# Active Faulting and Deformation of the Mongolian Altay Mountains

**Laura C. Gregory**

Thesis submitted to the University of Oxford

for the degree of Doctor of Philosophy

in

Earth Sciences




Department of Earth Sciences

and

University of Oxford

Trinity, 2012

Supervised by Dr. Richard T. Walker and Dr. Conall MacNiocaill

# Declaration

The contents of this thesis are all my own work, except where otherwise stated. The views and opinions expressed herein are mine and not necessarily those of any other person or body unless so attributed.

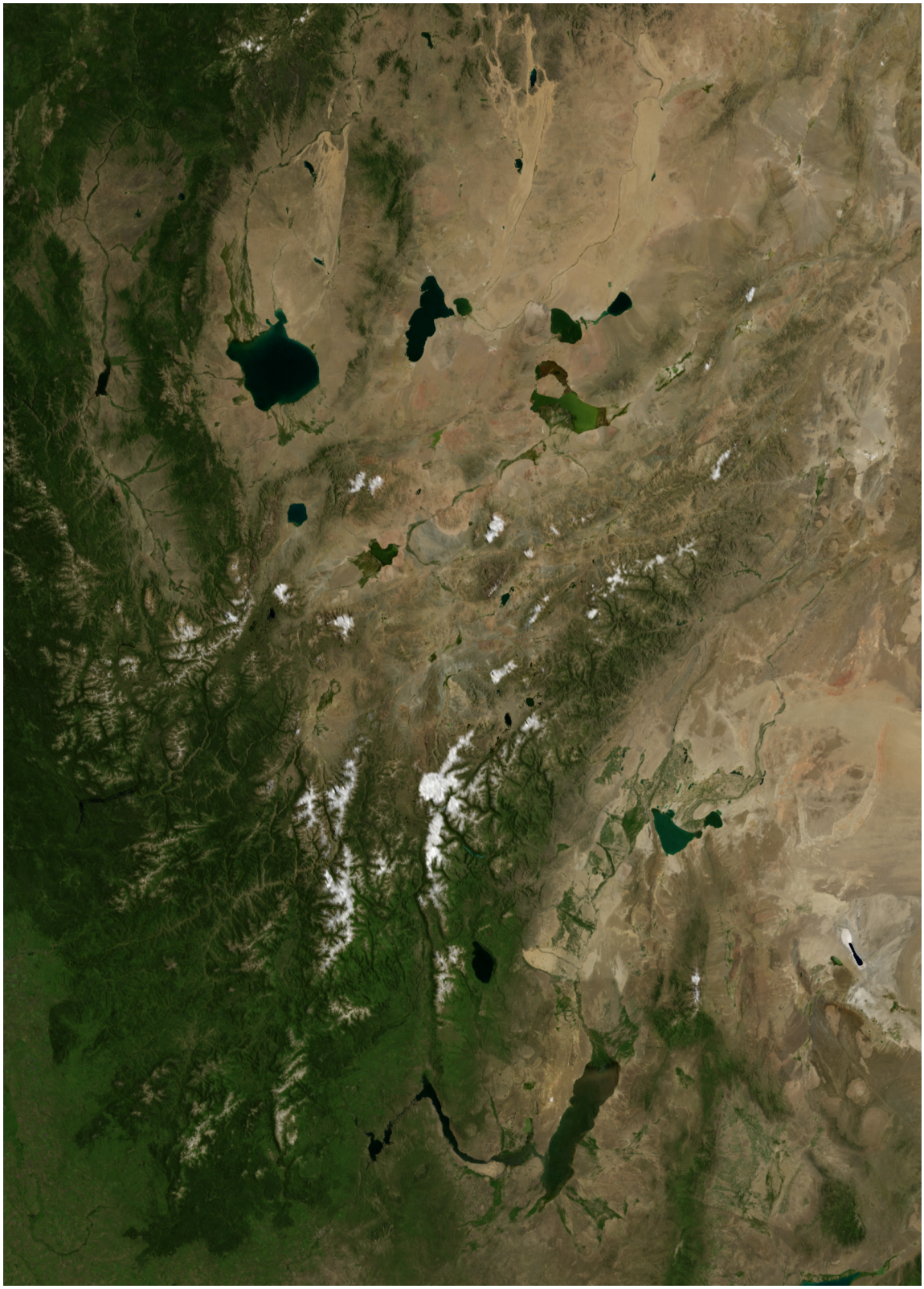

*...how many years can a mountain exist, before it's washed to the sea?*
-Bob Dylan

For my Dad

# Abstract

Active Faulting and Deformation of the Mongolian Altay Mountains

Laura C. Gregory
Exeter College, Oxford

*Trinity Term, 2012*

In this thesis, I use multiple techniques to investigate the active faulting and deformation of the Altay Mountains, Western Mongolia. The Altay are an intracontinental transpressional mountain range, which are deforming in the far-field of the India-Asia collision. An anastomosing network of dextral faults strikes NNW–SSE, and accommodates NE–SW oriented shortening by rotating anticlockwise about vertical axes. I begin by characterising the Altay faults, and add to what is already known about their surface expression with new observations of active faulting and three previously undescribed ancient earthquake ruptures. I use $^{10}$Be cosmogenic dating and uranium-series dating on pedogenic carbonate to estimate the average Quaternary rate of slip for two of the major fault zones in the Altay. The slip rate on the Ölgiy fault is constrained to 0.3–2.1 mm yr$^{-1}$. Results from the Hovd fault are ambiguous, demonstrating the complications encountered with application of Quaternary dating techniques. I measure palaeomagnetic directions from Cretaceous to Pliocene-aged sediments in the eastern Altay to constrain the degree of anticlockwise rotation. Results from thermal demagnetisation of specimens indicate that the eastern Altay has not undergone significant rotation, in contrast with previous studies from the Siberian Altay that reveal almost 40° of anticlockwise rotation. This suggests that the eastern-most Altay fault is too young to have experienced significant rotation, or is kinematically different from the Siberian Altay. I apply apatite fission track (AFT) dating and track length modeling to the central Altay. Results from AFT dating show rapid cooling in the late Cretaceous due to the distal assembly of Central Asia, suggesting that there was pre-existing topography at the start of the Late Cenozoic phase of deformation, the timing of which is constrained to have initiated at least 20 Myr ago. My work demonstrates that combining results from techniques that cover a variety of time scales quantifies the evolution of active faulting and deformation in the region.

# Extended Abstract

Active faulting and deformation in continental collision zones are typically distributed across a region that may be several thousands of kilometres in width as measured from the main collisional margin. This far-field deformation is poorly understood in terms of how strain is distributed on faults in the upper crust and how the regional patterns of deformation evolve over geological time scales. The kinematics of deformation can be determined by making measurements and observations of the rates and styles of faulting and mountain building, using different techniques applicable to different timescales of deformation. With quantification of the rates and styles of continental deformation, we can start to address questions on the dynamical forces driving the deformation.

In this thesis, I investigate the Altay Mountains in western Mongolia, which are actively deforming at the very northern edge of the India-Asia collision zone. The convergence between India and Asia has formed the largest example of active continental deformation on earth, with several zones of faulting and uplift extending across a region over 2500 km wide. Despite being located over 2000 km away from the India-Asia suture zone, the Altay accommodate approximately 7 mm $yr^{-1}$ of shortening, or 10–20% of the total convergence of India with Asia. Faults in the Altay are long (>500 km) sinuous dextral strike-slip faults that strike NNW–SSE, which is oblique to the NNE–SSW orientation of maximum shortening. The deformation in the Altay is transpressive, and the faults rotate anticlockwise about

vertical axes to accomodate shortening. Faults in the Altay are capable of having $M_w$ 8.0 earthquakes, as demonstrated both in the historical record of earthquakes as well as ancient surface ruptures that have occured within the last 2000 years. These surface ruptures are very well preserved due to the region's arid climate. Given the size, elevation (peaks >4000 m), and earthquake history of the region, it is relatively poorly studied in terms of quantifying the rates of faulting and uplift. In order to improve our understanding of the active deformation of the Altay, I present results from several techniques that quantify the rate and styles of active tectonics on a variety of time scales.

In Chapter 1, I provide a introduction to continental deformation as well as the active tectonics of the Altay and summarise what is known about the region. Each of the subsequent chapters focuses on a different method, with the timescale covered increasing from chapter to chapter: starting with observations of faulting in the geomorphology of the Altay, to Quaternary fault slip rates, to geological measurements of rotation and mountain building. I conclude by incorporating my results that span a range of timescales in order to discuss the rates and styles of deformation throughout the evolution of deformation in the region. The importance of assessing earthquake hazard in western Mongolia is also highlighted, as well as how this work may aid our understanding of the dynamics of continental deformation.

In Chapter 2, I describe the surface expression of active faults in the Mongolian Altay. There are 5 major fault zones, and I provide evidence for the Quaternary activity of each fault, some of which have been previously described, and some that were not known to have been active in the Late Quaternary until this work. The aim of the chapter is to add to the established observations of the region, many of which were made prior to the availability of high-resolution satellite imagery. This work helps to improve the understanding of the kinematics of faulting. For example, it was previously thought that many of the faults in the central Altay had shut

down, or were moving very slowly, probably because little field work had been conducted in the remote, high central Altay. Evidence of active faulting in the Central Altay is less clear because the region has experienced a greater degree of erosion due to glaciers and likely greater precipitation from being located near the drainage divide of the mountains, thus obscuring the surface trace of active faults. I also present descriptions of three previously unknown ancient earthquake ruptures, and estimate their moment magnitude based on the length of the rupture and classic earthquake scaling laws. These newly discovered ruptures are combined with previously described earthquake ruptures in terms of earthquake moment release, to estimate the slip rates of the Altay faults over the past ∼1000 years, which comes to ∼6.5 mm $yr^{-1}$. I also provide evidence that the amount of cumulative, horizontal displacement of the faults is at least 3–8 km, based on right-laterally offset rivers, in order to place constraint on the duration of strike-slip faulting in the Altay, based on the average estimated rates of faulting and ultimately comparable to rates and amounts of rotation and uplift derived from additional methods.

In Chapter 3, I use two independent Quaternary dating techniques to estimate the average slip rate across two of the major Altay faults, on the basis of fault-displaced alluvium. At one location, on the Ölgiy fault, the slip rate is well constrained by robust dating results. In contrast, results were difficult to interpret from a site on the Hovd fault, and this study highlights the need to apply multiple dating techniques. At the Ölgiy site, two debris flows (F1 and F2) are displaced by 26–61 m and 12–30 +8/-4 m respectively, and I use both $^{10}$Be cosmogenic boulder dating and U-series dating on pedogenic carbonate to constrain the timing of abandonment of the debris flows. Uranium series dating is used to estimate the minimum age of surface abandonment, and $^{10}$Be cosmogenic dating provides the maximum constraint. The ages for the F1 surface are between 47.7 ± 9.3 and 70 ± 8.7 kyr, and can be combined with the estimate of displacement to place bounds on the slip rate of 0.3–1.6 mm $yr^{-1}$.

The abandonment of F2 is between 18–25.9 ± 2.6 kyr, which resolves a slip rate of 0.3–2.1 mm $yr^{-1}$. Slip rates estimated for the two surfaces are in good agreement, and suggest that the slip rate of the Ölgiy fault is between 0.3–2.1 mm $yr^{-1}$. For the Ar Hötöl site on the Hovd fault, the geochronologic results are less straightforward. $^{10}$Be cosmogenic exposure ages are between 18 to >300 kyr for an alluvial fan displaced by 30–60 m. Boulders collected from an active river channel suggest that present-day inheritance in the boulders is on the order of 30 kyr, but the variance in surface boulder ages is likely not solely due to inheritance. A cosmogenic depth profile suggests that the surface was either abandoned at ∼170 kyr, or that the $^{10}$Be system is saturated, and the surface has been exposed for over 300 kyr. This suggests that either the Hovd fault has a very slow slip rate, or the displacements measured on the fan surface are not representative of the amount of Quaternary fault slip over the last 170–300 kyr, either because there are several active strands of the Hovd fault in the region or the streams that were used to estimate displacement are significantly younger than the abandonment of the alluvial fan.

In Chapter 4, I present palaeomagnetic results from samples collected in Cretaceous and younger sediments in the Dzereg Basin of the eastern Altay mountains. This work was done to place constraints on the vertical axis rotations of the Altay, as only one other palaeomagnetic study has been done in the Altay. Previous estimates from Oligocene and younger sediments from the Chuya Basin in the Siberian Altay suggested that the Altay have experienced up to 39±8° of anticlockwise rotation. Palaeomagnetic results from the Dzereg Basin provide reliable declinations, with palaeomagnetic directions from 10 sites that pass a fold test and include magnetic reversals. The declinations are not significantly rotated with respect to the expected directions, suggesting that faults in the eastern Altay have not experienced a large degree of vertical axis rotation. These results imply that either the eastern Altay are deforming in a different style than the Siberian Altay, or that the eastern-most

faults of the Altay are younger than those in the west, and have not rotated to a measurable degree.

In Chapter 5, I constrain the Late Mesozoic and Cenozoic cooling history of the central Altay based on results from apatite fission track (AFT) dating. This low-temperature technique resolves the cooling history of rock samples through the upper 2–3 kilometres of the crust. Fission track central ages are between 60–93 Ma, implying that the rocks cooled through the apatite partial annealing zone (60–110°C) in the Late Cretaceous, and have not exhumed more than ∼2 km since that time. Central fission-track ages are much younger in the central Altay than the eastern Altay, which yields ages that are generally Jurassic in age, suggesting that there may have been remnant topography in the central Altay at the initiation of Cenozoic deformation in the region. Track length data were modeled to place better constraint on the cooling history of the region, yielding evidence for Cenozoic cooling in the central Altay from at least ∼20 Ma, although the precise timing is poorly constrained. These low-temperature thermochronology results implies that the central Altay have been active since at least the early Miocene, but more low-temperature work is necessary to evaluate the evolution of Cenozoic deformation across the region.

I conclude the thesis by comparing the rates of faulting and rotation using a simplified kinematic model, and discuss the manner by which shortening strain is accommodated on dextral strike-slip faults. The measured cumulative displacement of 3–8 km on the dextral faults is significantly less than what would be expected from the high estimates of rotation in the Siberian Altay. I suggest two end-member models for the deformation of the Altay: one with high rotation implying that shortening is only taken up by rotation and significant right-lateral slip, and another model in which the shortening is taken up as a large amount of crustal thickening, with little rotation and small amounts of right-lateral slip. Some of the discordance between these two models may arise from the faults in the eastern Altay being younger than

the faults in the west. The kinematics of deformation is probably represented by a combination of the two end member models, and more work is necessary to quantify the more poorly defined constraints.

# Acknowledgements

I begin by thanking my supervisors Richard and Conall for guiding me through the past four years. Richard, thank you for having the scientific clarity to find sense in my ideas for the Altay and for consistently showing me and guiding me through the exciting big picture in our work. Conall, thank you for keeping me focused, and for constant encouragement and scientific insight into our work on the Altay. I must thank several colleagues for their contribution to the science of this thesis, mostly through enriching discussions on the work, as well as lab work. Ed, thank you for sharing my passion for the active tectonics of the Altay, for help in the field, and for being a mentor and a friend. Andy Carter, thanks for teaching me how to rigorously count fission tracks and for the fun discussions on the tectonics of the whole of Asia. Alex Thomas, thanks for all of the help with the lab work and interpretations of the geochemistry, and for your insight into my slip-rate studies. Josh West, thank you for enlightening discussions of Mongolian geology, and for lugging all of those rocks around Mongolia. Rachel, thank you for being a fantastic fourth year student, and producing some of the best analytical results in this thesis through careful lab work. I thank Cassie Fenton, Christoph Schnabel, and Shen Xu for good quality processing of my cosmogenic samples and data at SUERC. I thank Tony Watts and Alex Densmore for a thorough examination of this thesis, and for insightful and enjoyable discussion during my viva.

Mongolia is probably one of the most beautiful, adventurous, and geologically

interesting places to do field work, and I must thank several of my Mongolian colleagues for making the months spent in the field both successful and enjoyable. Tulga, Bayasgalan, and Tsolmon, thank you for your scientific input to the trips and incredible logistical support. Nara and Gana, thank you for being such talented drivers, and for taking care of us all in the field during our 'adventures'. Deegii, Deagi, Amgaa, Mo, and Muggi thank you for your friendship and help during field work.

I thank my friends and colleagues in S4, for their engaging scientific support and close friendship throughout the years. John, Marcus, Ivana, and Mike, thank you for not only being mentors through the DPhil years and the computer support, but for being close friends. I thank Susi, Rich, and Helen for being simply lovely and great friends, and I will miss you all so very much. Mark, thank you for all of the good times in the Pmag lab, and Gio and Sarah too. I also thank the Barry and the COMET+ research group for supporting me through the years, even though I am not technically a 'geophysicist'. I also thank the faculty of the Oxford Earth Science department, for providing a stimulating research environment.

I could not have made it through this DPhil without the amazing times had with friends inside and outside of the department. I thank my friends and housemates Katie, Chris, and Dan, especially for all of the laughs and for putting up with my American-ism. Katie, Al, Tristan, Emily, Susie, Rich W., Helen, Mark, Giovanni, Naomi, Owen, Rich P., and loads of others, thank you for all of the fun times (and there were a lot), and for the friendship. I thank the BGC for the good times and the w(h)ine. The girls (and Chris) of the Exeter College Boat Club are thanked for distracting me from my DPhil.

I thank Joe, Jim, Dave, Alexa, Emily, Laura and too many others to name from the University of Florida Geology department, for encouraging my passion for rocks and all things geology from the very beginning.

Ben, thank you for making me so incredibly happy, always.

And finally, I thank my parents, Chris and Bill, and my sister Amanda, for encouraging and inspiring me from the start, and especially my Dad for instilling my love of science.

# Contents


Declaration . . . . . iii

Abstract . . . . . vii

Extended Abstract . . . . . ix

Acknowledgements . . . . . xv

Contents . . . . . xxii

List of Figures . . . . . xxviii

List of Tables . . . . . xxx

**1 Introduction** **1**

1.1 Earthquakes and Continental Deformation . . . . . 1

1.2 Seismicity of the Altay . . . . . 5

1.3 The kinematics of faulting . . . . . 7

1.4 Geological history of the Altay . . . . . 9

1.5 Geomorphology of the Altay . . . . . 12

1.6 Climate of the Altay and surrounding region . . . . . 15

1.7 Motivation of Study . . . . . 17

1.7.1 A note on nomenclature . . . . . 19

**2 Active faults and ancient earthquake ruptures of the Altay** **21**

2.1 Introduction . . . . . 21

2.2 Methodology . . . . . 24

2.2.1 Remote sensing and field identification of active faults . . . . . 24
2.2.2 Empirically derived moment magnitudes . . . . . 28
2.2.3 Cumulative fault displacements . . . . . 30
2.3 Map of active faults . . . . . 34
2.3.1 The Har-Us-Nuur fault zone . . . . . 36
2.3.2 The Hovd fault zone . . . . . 44
2.3.3 The Ölgiy fault zone . . . . . 57
2.3.4 The Sagsay Fault Zone . . . . . 75
2.3.5 The Hoton Nuur/Fu Yun fault zone . . . . . 93
2.4 Newly discovered ancient earthquake ruptures . . . . . 110
2.4.1 The Sair Uul Rupture . . . . . 110
2.4.2 The Fiery Horse rupture . . . . . 125
2.4.3 The Tsengel Hyarhan rupture . . . . . 135
2.5 Discussion . . . . . 143
2.5.1 Cumulative displacement . . . . . 143
2.5.2 Reverse faulting . . . . . 147
2.5.3 Preservation of Quaternary faulting . . . . . 148
2.5.4 Earthquakes . . . . . 150
2.5.5 Evolution of faulting in the Altay . . . . . 153

**3 Average Quaternary rates of fault slip 157**

3.1 Introduction . . . . . 157
3.2 Quaternary dating techniques for measuring fault slip rates . . . . . 158
3.3 Slip rate of the Ölgiy fault . . . . . 160
3.3.1 Site description . . . . . 160
3.3.2 Measurement of lateral displacements . . . . . 164
3.3.3 U-series dating of pedogenic carbonate rinds: methods and results . . . . . 171

3.3.4 $^{10}$Be terrestrial cosmogenic nuclide dating: methods and results 184
3.3.5 Exposure age calculation . . . . . 188
3.3.6 Average Late Quaternary slip rate of the Ölgiy fault . . . . . 198
3.4 Slip rate of the Hovd fault . . . . . 201
3.4.1 Site description . . . . . 203
3.4.2 TCN results and depth profile modeling . . . . . 212
3.4.3 Exposure history of the Ar Hötöl site . . . . . 220
3.5 Discussion . . . . . 222
3.5.1 Reliability of slip rate estimates . . . . . 222
3.5.2 U-series dating . . . . . 223
3.5.3 Predicted slip rate of the Hoton Nuur fault . . . . . 224
3.5.4 Tectonic implications of the Altay fault slip rates . . . . . 226

**4 Vertical axis rotations of the eastern Altay 229**
4.1 Introduction . . . . . 229
4.2 Stratigraphy of the Dzereg Basin . . . . . 233
4.3 Palaeomagnetic methods . . . . . 239
4.3.1 Palaeomagnetic sampling and experiments . . . . . 242
4.3.2 Rock magnetic experiments . . . . . 243
4.4 Results . . . . . 243
4.4.1 Magnetic tests . . . . . 246
4.5 Discussion . . . . . 250
4.5.1 Reliability of the data . . . . . 250
4.5.2 Rotation of the Dzereg Basin . . . . . 251

**5 Low temperature thermochronology of the central Altay 255**
5.1 Introduction . . . . . 255
5.1.1 Geological history of the region . . . . . 258

5.2 AFT methods and sample collection . . . . . 261
5.2.1 Analytical Methods and Samples . . . . . 268
5.3 Results . . . . . 274
5.4 Thermal History Models and Discussion . . . . . 277

**6 Discussion and Conclusions** **289**
6.1 Summary of results and interpretations . . . . . 291
6.2 Hypotheses for the active deformation of the Altay . . . . . 294
6.3 Future Work . . . . . 299
6.4 Broader impacts and concluding remarks . . . . . 301

**Bibliography** **307**

**Appendices** **327**

**A Appendix 1** **327**

# List of Figures


1.1 SRTM DEM of central Asia . . . 3
1.2 Earthquakes, GPS velocities, and active faults . . . 6
1.3 Schematic diagram of faulting in western Mongolia . . . 8
1.4 Tectonic map of Central Asia, from (*Briggs et al.*, 2009) . . . 10
1.5 Drainage divide and topographic profiles across the Altay . . . 13
1.6 Landsat image of the Altay region . . . 16
1.7 Earthquake hazard map of Mongolia . . . 18

2.1 Active faults and ancient surface ruptures of the Altay Mountains . . . 23
2.2 Photos of the Chuya earthquake rupture . . . 27
2.3 Schematic diagram of the orientations of shear in the Altay . . . 29
2.4 Examples of confidence rating on river displacements . . . 33
2.5 DEM of the Har-Us-Nuur Fault . . . 35
2.6 ASTER image of lakes damed by fault-uplifted topography . . . 37
2.7 Field photos of the Jid palaeo-earthquake rupture . . . 40
2.8 Quickbird image of the Jigjig rupture and HUN stream terrace displacement . . . 42
2.9 ASTER image of the Ih HUN rupture fissures filled with snow . . . 43
2.10 SRTM DEM of the Hovd fault and its palaeo-earthquake ruptures . . . 45
2.11 ASTER imagery of the northern Hovd fault . . . 47
2.12 Landsat images of pull-apart basins on the southern Hovd fault . . . 50

2.13 Quickbird imagery of the Ar Hötöl surface rupture . . . . . 52
2.14 River offsets along the Hovd fault . . . . . 53
2.15 Aster GDEM restoration of Hovd fault river displacements . . . . . 55
2.16 Landsat imagery of several river displacements on the south Hovd fault 57
2.17 DEM of the Ölgiy Fault . . . . . 59
2.18 Landsat image of the region surrounding Tas Uul . . . . . 60
2.19 IKONOS imagery of the Ölgiy fault near Tas Uul . . . . . 62
2.20 Photos of the Ölgiy fault near Tas Uul . . . . . 63
2.21 ASTER imagery of dry valleys on the Ölgiy fault . . . . . 64
2.22 Diagram of a typical Altay flower structure . . . . . 66
2.23 Photos of reverse faulting on the Ölgiy fault . . . . . 67
2.24 Photos from the central Ölgiy fault . . . . . 69
2.25 SPOT imagery of the Höh Serkhiin Uul . . . . . 71
2.26 River displacements along the Ölgiy fault . . . . . 72
2.27 Reconstructed Landsat imagery of displaced rivers . . . . . 74
2.28 SRTM DEM of the Sagsay fault . . . . . 76
2.29 ASTER and Kompsat-2 imagery of landslides along the Sagsay fault . 77
2.30 Photo of landslides and fault scarps along Sogoog Uul . . . . . 78
2.31 Photo of a strike-slip scarp along the Sagsay fault . . . . . 79
2.32 Kompsat-2 imagery of the central Sagsay fault . . . . . 81
2.33 ASTER imagery of the Sagsay fault near Tal Nuur . . . . . 82
2.34 Photos of the Sagsay fault near Tal Nuur . . . . . 84
2.35 Landsat imagery of the southern Sagsay fault . . . . . 85
2.36 Kompsat-2 imagery of Monh Hyarhan Uul . . . . . 86
2.37 Kompsat-2 imagery of the Sagsay rupture . . . . . 89
2.38 Kompsat-2 imagery of the Sagsay rupture . . . . . 90
2.39 Photos of the Sagsay surface rupture . . . . . 91

2.40 Drainage displacements along the Sagsay fault . . . . . 92
2.41 DEM of the Hoton Nuur and Fu Yun fault zone . . . . . 94
2.42 Quickbird imagery of the Hoton Nuur fault . . . . . 95
2.43 ASTER and Quickbird imagery of the Dayan Nuur glacial deposits . 98
2.44 Photos of the Hoton Nuur fault through the Dayan Nuur moraines . . 99
2.45 Quickbird imagery and photo of displaced moraine edge along the Hoton Nuur fault . . . . . 100
2.46 Photos of a damaged tree along the Hoton Nuur fault zone . . . . . 101
2.47 Landsat image of the faults surrounding Tsengel Hyarhan Uul . . . . 104
2.48 ASTER imagery of faults surrounding Tsengel Hyarhan Uul . . . . . 105
2.49 Photos of faults surrounding Tsengel Hyarhan Uul . . . . . 106
2.50 Plot of river displacements along the Fu Yun fault . . . . . 108
2.51 ASTER imagery of drainage displacements along the Fu Yun fault . . 110
2.52 Map of the Sair Uul rupture . . . . . 111
2.53 Photos of a vertical scarp and sag pond along the Sair Uul rupture . 112
2.54 Photos of the Sair Uul rupture . . . . . 114
2.55 Kompsat-2 imagery of the Sair Uul rupture . . . . . 116
2.56 Photos of strike-slip features along the Sair Uul rupture . . . . . 117
2.57 Photos of displacements along the Sair Uul Rupture . . . . . 118
2.58 SPOT-5 imagery of the southern section of the Sair Uul rupture . . . 120
2.59 SPOT-5 imagery of the southern section of the Sair Uul rupture . . . 121
2.60 Photos of the southern portion of the Sair Uul rupture . . . . . 122
2.61 Photos of tension fissures on the southern Sair Uul rupture . . . . . 123
2.62 SRTM DEM overview of the Fiery Horse rupture . . . . . 126
2.63 ASTER and Kompsat-2 imagery of the northern section of the Fiery Horse rupture . . . . . 128
2.64 Displaced stream riser along the Fiery Horse rupture . . . . . 129

2.65 ASTER and Kompsat-2 imagery of the southern Fiery Horse Rupture 130
2.66 Photos of ground deformation along the Fiery Horse Rupture . . . . . 132
2.67 Photos along the Fiery Horse Rupture . . . . . 133
2.68 Photos of displacement along the Fiery Horse rupture . . . . . 134
2.69 Landsat image of the faults surrounding Tsengel Hyarhan Uul . . . . 136
2.70 Kompsat-2 imagery of the Tsengel Hyarhan rupture . . . . . 137
2.71 Kompsat-2 imagery of the Tsengel Hyarhan rupture . . . . . 138
2.72 Photo of Tsengel Hyarhan rupture . . . . . 139
2.73 Photo of Tsengel Hyarhan fissures . . . . . 140
2.74 Photos of Tsengel Hyarhan fissures . . . . . 141
2.75 Photos from the Tsengel Hyarhan rupture . . . . . 142
2.76 Various states of rupture preservation . . . . . 149
2.77 Drainage divide of the Altay mountains . . . . . 154

3.1 Location of the Ölgiy fault . . . . . 161
3.2 ASTER and Kompsat-2 imagery of the Ölgiy slip rate site . . . . . 164
3.3 Quickbird imagery of the Ölgiy slip rate site . . . . . 165
3.4 3D DEM of the Ölgiy slip rate site . . . . . 166
3.5 Field photos of stream displacements . . . . . 167
3.6 Diagram of vertical scarp at the Ölgiy site . . . . . 169
3.7 Photos of pedogenic carbonate on pebbles . . . . . 173
3.8 Correction for detrital Th in carbonate samples . . . . . 177
3.9 OxCal results of Bayesian analysis . . . . . 180
3.10 OxCal results from combining samples from F2 . . . . . 183
3.11 Field photos of boulder samples . . . . . 187
3.12 Plot of $^{10}$Be age results . . . . . 193
3.13 Diagram for the timing of the abandonment of surface F2 . . . . . 194
3.14 Diagram for the timing of the abandonment of surface F1 . . . . . 195

3.15 Diagram for the evolution of surface morphology . . . . . 197
3.16 Overview map of the Hovd fault . . . . . 201
3.17 ASTER and Quickbird overview of the Ar Hötöl site . . . . . 204
3.18 Quickbird image of the Ar Hötöl fan system . . . . . 205
3.19 Annotated Quickbird image of the Ar Hötöl sampling site . . . . . 206
3.20 DEM of the Ar Hötöl site . . . . . 207
3.21 Photos of the Ar Hötöl fault . . . . . 209
3.22 Photos of the Ar Hötöl site . . . . . 210
3.23 Diagram of slope displacement . . . . . 211
3.24 Photos of samples from Ar Hötöl . . . . . 213
3.25 Depth profile of $^{10}$Be concentrations for Ar Hötöl . . . . . 219
3.26 DEM and quickbird imagery of the Hoton Nuur slip rate site . . . . . 225
3.27 STRM DEM with slip rates of the Altay faults . . . . . 227

4.1 Map of the Altay with VAR study localities indicated . . . . . 232
4.2 Landsat overview map of the Dzereg Basin . . . . . 234
4.3 ASTER imagery and geological map of the northeast Dzereg Basin . 237
4.4 Photos of the Dzereg Basin strata . . . . . 238
4.5 Zijderveld plots from the northern group . . . . . 247
4.6 Zijderveld plots from the NE group . . . . . 248
4.7 Zijderveld plots from the southern group . . . . . 249
4.8 Curie temperature test results . . . . . 250
4.9 Stereoplots of site means and fold test . . . . . 252
4.10 Mean directions from age groups . . . . . 254

5.1 Photos of mountain morphology from the eastern and western Altay . 256
5.2 Overview of previous AFT studies in the Altay region . . . . . 259
5.3 Diagram for counting fission tracks . . . . . 264

5.4 Photos of etched tracks on apatite grain and mica print . . . . . 265
5.5 Photo of a poor quality apatite grain . . . . . 269
5.6 Map of AFT sample localities . . . . . 270
5.7 Vertical transects of AFT samples . . . . . 272
5.8 Plot of age versus elevation for AFT samples . . . . . 277
5.9 Cooling histories of Altay samples . . . . . 280
5.10 Time-temperature models of the oldest and youngest AFT samples . 283
5.11 Schematic diagram of sample cooling histories . . . . . 284
5.12 AFT ages plotted on DEM of the central Altay . . . . . 286
5.13 Overview of AFT results from the Altay . . . . . 288

6.1 Summary map of the Altay Mountains . . . . . 291
6.2 Simplified diagram for rotation calculation . . . . . 295
6.3 Earthquake hazard map of Mongolia . . . . . 305

A.1 Vertical profiles from the Ölgiy site . . . . . 330
A.2 Vertical profiles along debris flow F1 . . . . . 331
A.3 Vertical profiles along debris flow F2 . . . . . 332
A.4 Ar Hötöl depth profile model trade-offs . . . . . 333

# List of Tables


1.1 Glossary of Mongolian terms . . . . . 20

2.1 Summary of satellite data used in this thesis . . . . . 25
2.2 Hovd fault river displacements . . . . . 54
2.3 Ölgiy river displacements . . . . . 73
2.4 Sagsay river displacements . . . . . 93
2.5 Hoton Nuur-Fu Yun river displacements . . . . . 109
2.6 Average slip and length of Altay surface ruptures . . . . . 152

3.1 Surface displacement measurements . . . . . 168
3.2 U-series results . . . . . 176
3.3 OxCal modeling inputs and results . . . . . 179
3.4 OxCal modeling inputs and results, with the two samples from F2 combined, all shown with $1\sigma$ uncertainties . . . . . 182
3.5 $^{10}$Be data Table . . . . . 192
3.6 Estimates of the Ölgiy slip rate . . . . . 200
3.7 Ar Hötöl $^{10}$Be boulder exposure age calculations . . . . . 215
3.8 $^{10}$Be concentrations of depth profile samples from the Ar Hötöl fan (A1) 217

4.1 Palaeomagnetic sampling site localities and ages . . . . . 239
4.2 Palaeomagnetic data . . . . . 245

5.1 AFT samples . . . . . 273
5.2 AFT analytical data . . . . . 275

A.1 Profile height measurements . . . . . 328
A.2 $^{10}$Be blanks table . . . . . 329

# Chapter 1

# Introduction

## 1.1 Earthquakes and Continental Deformation

There is a fundamental difference between the plate tectonic deformation that occurs on oceanic plates and the distributed deformation that occurs on the continents (*McKenzie*, 1972; *Molnar and Tapponnier*, 1975). Earthquakes and tectonic deformation at oceanic plate boundaries are generally restricted to a narrow zone that is limited to a few 10's to 100's of kilometres surrounding the boundary. This is in contrast with continental plate boundaries, where earthquakes and distributed deformation can occur over several thousands of kilometres away from the convergent margin. This far field deformation of the continents is poorly understood in terms of the spatial and temporal distribution of strain onto upper crustal structures. Any one seismogenic fault on the continents may be moving more slowly than its oceanic plate-boundary counterpart because it is part of a distributed network of active faults, but continental faults play an important role in regional tectonics, and they are capable of producing earthquakes that can be large (greater than $M_w$ 8), destructive, and difficult to anticipate (e.g. *Jackson*, 2001). There is also much debate on how diffuse deformation of the continents is accomplished on a longer time scale (i.e. $>$ 1 m.y.) in terms of building and destroying mountain ranges and how

these processes relate to the rheology of the lithosphere and the underlying dynamics of the principle driving forces of deformation (e.g. *Jackson*, 2002; *Burov and Watts*, 2006; *Bürgmann and Dresen*, 2008).

Regions of active continental deformation provide the opportunity to observe the spatial and temporal distribution of strain on a variety of timescales. The collision between India and Asia forms the largest area of active tectonics on Earth, with several zones of faulting and uplift developed over a region that extends thousands of kilometres into the Eurasian continent (Figure 1.1). Earthquake hazard and the fundamentals of deformation are generally poorly quantified for the far-field active regions of Central Asia, which includes mountain ranges such as the Kunlun, Quilian Shan, Tien Shan, Göbi Altay, Altay, Hanguy, and Sayan. These regions of relatively slow strain accumulation can be difficult to investigate using purely geodetic methods because of poor data coverage and incomplete historical records, or simply because the region is deforming relatively slowly and has an infrequent earthquake record. Deformation on a geological time-scale is also relatively poorly known in the far-field of the India-Asia collision due to the remote locations of many of the Central Asian mountain ranges. A focus of this thesis is to gain a better understanding of the kinematics of deformation involved in the far-field of the India Asia collision, in order to address the dynamics of continental deformation.

This thesis presents research from the Altay Mountains of western Mongolia, which are located 2500 km from the India-Asia suture zone, and are one of the most distal results of the collision. The Altay region appears to be deforming relatively rapidly on decadal timescales, accommodating 10 to 20% of the total shortening from the motion of India (based on Global Positioning System (GPS) measurements, *Wang et al.*, 2001; *Calais et al.*, 2003; *Zhang et al.*, 2004; *Gan et al.*, 2007). In contrast to the Himalaya and Tien Shan ranges further south, where shortening is predominantly accomodated by thrust faults oriented perpindicular to the convergence

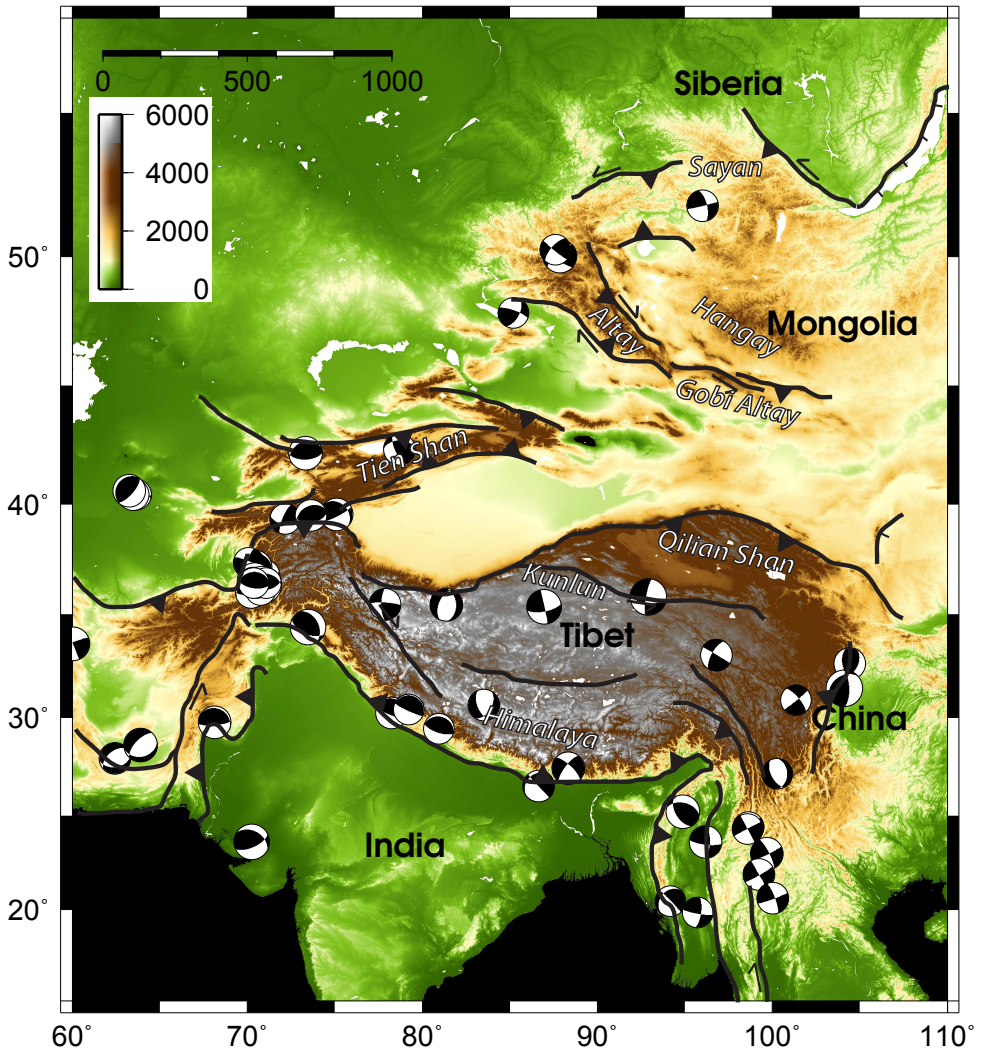


**Figure 1.1:** SRTM shaded relief image of central Asia. Major fault zones and the types of faulting are indicated by thick black lines. Double-couple solutions are all earthquakes greater than $M_s$ 6.5 available from the global CMT catalog, 1977–2011.

direction, much of the deformation in the Altay is accomodated in a transpressive regime. Large strike-slip faults striking NNW–SSE are the main features accommodating deformation in the Altay. These faults have accumulated several kilometres of right-lateral displacement and are capable of producing up to $M_w$ 8 earthquakes (*Baljinnyam et al.*, 1993). The region is suggested to rotate anticlockwise about vertical axes, in order to accommodate NE–SW oriented shortening on the NNW–SSE

striking dextral faults (*Bayasgalan et al.*, 2005).

The cold arid climate of Mongolia allows for good preservation of faulting and deformation features in the landscape, such as pre-historic earthquake ruptures and cumulative Quaternary fault displacements (e.g. *Baljinnyam et al.*, 1993; *Walker et al.*, 2006; *Nissen et al.*, 2009b). Also, the high topographic relief of the Altay potentially preserves the total vertical uplift due to Cenozoic deformation, based on the assumption that ancient planation surfaces have been uplifted and preserved on the tops of many mountains (e.g. *Jolivet et al.*, 2007). The highest mountain peaks in the Altay reach over 4000 m, and the region has a high average elevation ($\sim$ 2300 m *Baljinnyam et al.*, 1993). This is in part due to the elevation of the intervening basins, which are between 1500 and 2500 m in elevation, and thus the overall topographic relief in the range is generally of the order of 2000 m. Fault and deformation features are rapidly eroded in many regions of active deformation, but their preservation in the Altay allows for the determination of the rates and styles of deformation over a range of timescales, from a single earthquake event, to rates of faulting in the Quaternary, to the million year tectonic deformation. Despite the opportunity to apply a wide range of tools for the investigation of active tectonics and deformation, the Altay are relatively poorly studied when compared to other major active mountain ranges of the world, due to the region's remote setting and political situation until the early 1990's. As a result, the kinematics of deformation in the Altay, including both the rates and patterns of faulting and deformation, are in general poorly quantified, and therefore questions on the dynamics of the regional deformation, mainly how and why tectonic stress is transmitted through space and time over the whole of Central Asia, remain largely unanswered.

## 1.2 Seismicity of the Altay

Western Mongolia accommodates at least 10 mm $yr^{-1}$ of NNE–SSW oriented shortening, based on GPS estimates, with approximately 7 mm $yr^{-1}$ taken up by the Altay with respect to Siberia (stable Eurasia; *Calais et al.*, 2003). This shortening is reflected in the regional seismicity (Figure 1.2). Over the past century, four earthquakes of close to magnitude 8 or higher have occurred within or just west of western Mongolia. One of these occurred in the Altay, the 1931.08.10 M 7.9 Fu Yun earthquake in Xinjiang, China (*Richter*, 1958; *Baljinnyam et al.*, 1993; *Klinger et al.*, 2011). Two earthquakes occurred on the left-lateral Bulnay fault system to the northeast of the Altay: the 1905.07.09 $M_w$ 8.0 Tsetserleg event, shortly followed by the 1905.07.23 $M_w$ 8.3–8.5 Bulnay event (*Schlupp and Cisternas*, 2007). The left-lateral 1957.12.04 M 8.3 Göbi Altay earthquake is the fourth great Mongolian event in the past century, and it occurred on the sinistral faults to the southeast of the Altay (*Kurushin et al.*, 1997). Historical records of seismicity in Mongolia and the surrounding regions prior to the last century are nonexistent, but because of good preservation, there is abundant geomorphic evidence for large earthquakes that have occurred over the past few hundreds and even 1–2 thousands of years. The surface ruptures of ancient earthquakes that occurred hundreds of years ago in the Altay are fresh enough to determine key parameters about the causative earthquake event. It is sometimes even possible to determine a reliable sequence of events for a single fault strand (e.g. *Klinger et al.*, 2011). In chapter 2, I describe at least three ancient surface ruptures, which were previously unknown, and combine the scaling information of these events with the known earthquakes in the region to discuss the seismicity of the Altay over the past 1–2 thousand years.

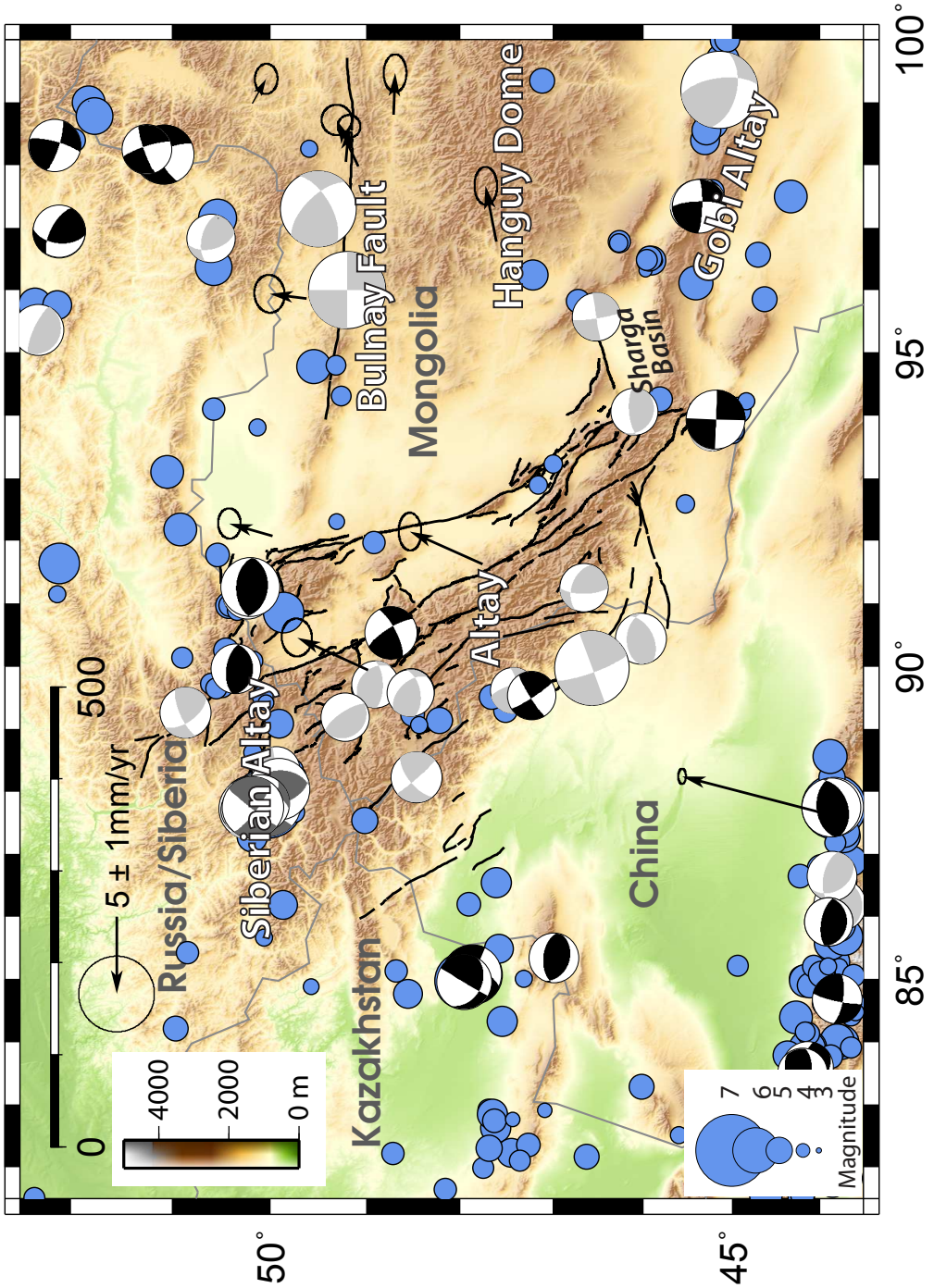


**Figure 1.2:** SRTM shaded relief image of the Altay. GPS velocities are relative to stable Eurasia (and are shown with station names, *Calais et al.*, 2003), blue circles are earthquakes plotted from the Engdahl catalog (*Engdahl et al.*, 1998), black double-couple solutions are from *Sloan et al.* (2011), dark grey double-couple solutions are from *Nissen et al.* (2007), and light grey double couples are solutions determined or cataloged by *Bayasgalan et al.* (2005, other references within). Active faults are plotted in black, political boundaries are plotted in grey.

## 1.3 The kinematics of faulting

Shortening in the Altay is accommodated on a series of parallel and anastomosing dextral strike-slip and reverse oblique-slip fault zones (Figure 1.2). The faults are up to 500 km long and strike NNW–SSE, which is oblique to the regional NNE–SSW maximum shortening direction derived from GPS measurements (*Calais et al.*, 2003). Based on the fault orientations and type of slip, the Altay are suggested to shorten in a transpressional manner, likely by rotating about a vertical axis or axes (Figure 1.3, *Baljinnyam et al.*, 1993; *Cunningham et al.*, 1996, 2003b). Anti-clockwise rotations are also suggested from the comparison of earthquake slip-vector azimuths with GPS vectors, which are not parallel (*Bayasgalan et al.*, 2005). This is in contrast to the faulting directly east of the Altay in the Göbi Altay and along the Bulnay fault zone, where GPS vectors are directed east-west and parallel to the large sinistral faults, requiring pure shear deformation (Figure 1.2). Whilst the modern day measurements of the pattern of strain accumulation are in agreement with large-scale vertical axes rotations, the longer-term transpressive deformation is poorly quantified and based on only one palaeomagnetic study in the Chuya Basin of the Siberian Altay (*Thomas et al.*, 2002). The distribution of the long term geological rotation patterns in the Altay has not been determined.

The style of slip that occurs on the Altay faults is often dependent on the fault orientation. Faults that strike between 340° –350° are typically pure strike-slip whereas faults with strikes between about 320° –340° are suggested to have a significant reverse component of motion based on the orientation of the faults relative to the maximum shortening direction determined from GPS, as well as the few reverse faulting earthquakes that have been recorded on more E–W striking faults (e.g. *Bayasgalan et al.*, 1999). Reverse or oblique reverse-dextral faulting due to NE–SW shortening on NW–SE striking faults is also observed in outcrops of active fault zones and bedrock geology (e.g. *Cunningham et al.*, 1996, 2003b; *Cunningham*, 2007; *Baljin-*

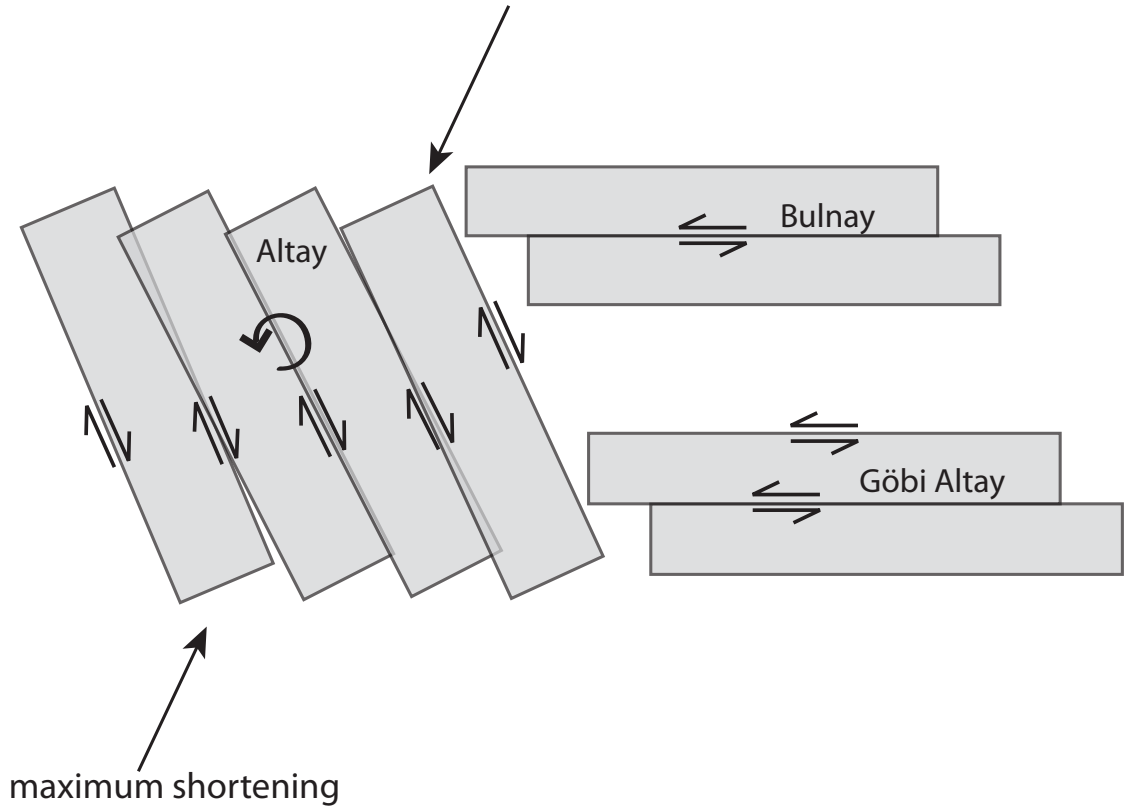


**Figure 1.3:** Schematic diagram of the kinematics of faulting and rotation in the Altay and surrounding region. The Altay region rotates to accommodate shortening along dextral faults at an oblique orientation to maximum shortening. The sinistral faults to the east of the Altay, in the Göbi Altay and Bulnay regions, are accommodating pure shear with no rotation.

*nyam et al.*, 1993, and references from the Russian literature within *Baljinnyam et al.* (1993)). In many cases, the trace of active reverse faults coincides with broad fault zones in outcrop where Paleozoic basement rock is thrust over Mesozoic sedimentary units, particularly along major restraining bend mountain ranges. Restraining bend mountain ranges are found throughout the Altay in westerly bends of the dextral NNW-striking faults (e.g. *Cunningham*, 2007). The NNW–SSE strike of the faults follows the inherited structural grain of the basement Palaeozoic arc complexes (*Cunningham*, 1998, Figure 1.4). Rock outcrops within the active Altay fault zones are frequently composed of marble and fault gouge, associated with the Palaeozoic-aged faulting in the region. Evidence for active, Quaternary faulting can be found as fault

scarps in alluvium along the base of high relief, but there are several examples of active strike-slip faults that are located well above the base of mountains, as well as faults that strike across flat basins with no associated relief. There are a few estimates of the average Quaternary slip rates for the Altay faults (*Baljinnyam et al.*, 1993; *Walker et al.*, 2006; *Nissen et al.*, 2009a,b; *Frankel et al.*, 2010), and existing studies suggest horizontal dextral slip is generally between 1–2 mm $yr^{-1}$.

## 1.4 Geological history of the Altay

The Altay region has a complex Phanerozoic history that starts with its nucleation as subduction-accretion complexes along the Siberian craton margin in the very latest Proterozoic (*Sengör et al.*, 1993). Various oceanic and continental fragments were amalgamated in a continuous process that lasted most of the Palaeozoic, forming the bulk of Mongolian basement rock in the process of assembling central Asia (Figure 1.4; *Traynor and Sladen*, 1995; *Sengör and Natal'In*, 1996; *Badarch et al.*, 2002; *Windley et al.*, 2007; *Briggs et al.*, 2007; *Levashova et al.*, 2010) and shaping a dominant structural grain that is aligned with the ancient arc and terrane boundaries (*Cunningham*, 1998). Thus active deformation is localised in the Altay (and the nearby Göbi Altay) because the region has a mechanically weak rheology due to the geological history, which has been reactivated. The trend of the structural grain is generally NNW–SSE in the Mongolian Altay and gradually bends to strike E–W in the Gobi-Altay. Throughout the Paleozoic, a long succession of suturing phases, synchronous with localised sinistral strike-slip shear, produced the high grade metamorphic rocks that are currently exposed as bedrock in the Altay Mountains (e.g. *Briggs et al.*, 2009). The bedrock of the Mongolian Altay comprises island arcs, ophiolites, accretionary complexes, and granitic plutons, representing the closure of the Palaeo-Asian Ocean in the Permian (at least 250 Ma, *Badarch et al.*, 2002; *Windley et al.*, 2007). The rocks involved were buried to depths up to 20 km, and

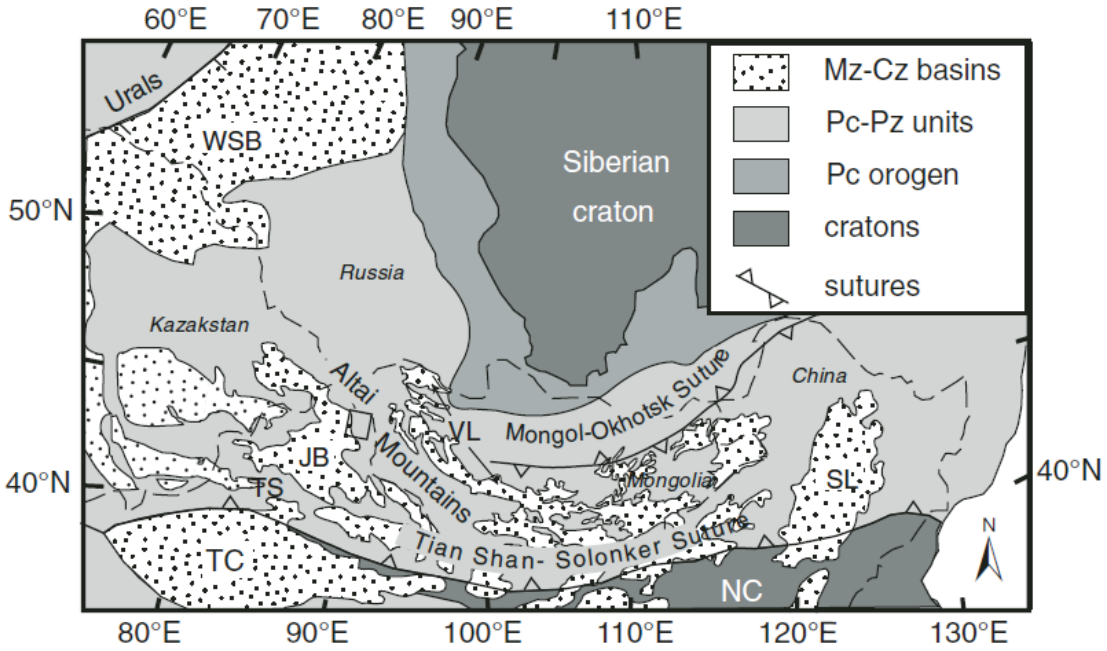


**Figure 1.4:** General tectonic map of central Asia, from *Briggs et al.* (2009), showing the ages and boundaries of the major cratons, terranes, and orogens that comprise the bed rock of the region. Abbreviations are: JB: Junggar basin, NC: North China craton, SL: Songliano basin, TC: Tarim craton, VL: Valley of the lakes, WSB: West Siberian basin.

subsequently exhumed during the Permian to Jurassic along major fault boundaries (*Briggs et al.*, 2009).

It is uncertain how tectonism throughout the Paleozoic was expressed at the surface, but it is likely that there was significant topographic relief at the start of the Mesozoic, and that the landscape was subjected to rapid erosion, based on thick clastic sediments deposited during the Mesozoic in the neighboring Junggar Basin in China and Dzereg and Dariv basins of Mongolia (*Allen and Vincent*, 1997; *Sjostrom et al.*, 2001; *Howard et al.*, 2003). The intensity of tectonism in the region generally decreased from the Permian onwards, but the region was probably subjected to deformation from distal events as the amalgamation of central Asia continued, until at least the Late Jurassic (*Yin and Nie*, 1996; *Dumitru and Hendrix*, 2001; *Badarch et al.*, 2002; *De Grave and Van den haute*, 2002; *De Grave et al.*, 2007). Late Juras-

sic to early Cretaceous cooling events have been suggested in low-temperature thermochronologic investigations from the Altay region (*De Grave and Van den haute*, 2002; *Vassallo*, 2006; *Yuan et al.*, 2006; *Jolivet et al.*, 2007; *Vassallo et al.*, 2007a; *De Grave et al.*, 2008; *Briggs et al.*, 2009; *Glorie et al.*, 2012a,b). This deformation is associated with either the closure of the Mongol-Okhotsk ocean to the southeast, or with the collision of the Lhasa terrane on what was the southern margin of Asia at the time (currently the central Tibetan Plateau).

Following the distal effects of collisions in the Mesozoic and associated cooling in the Altay, the region seems to have experienced relative tectonic quiescence for the Late Cretaceous and much of the Cenozoic. During what might have been ∼50 My of inactivity, it has been suggested that the pre-existing topographic relief was mostly leveled off to produce a low-relief erosional surface that possibly extended south from the Russian Sayan ranges to the Tien Shan and northern Tibet (*Cunningham*, 2011; *Bullen et al.*, 2001; *Jolivet et al.*, 2001, 2007). Deformation in the Altay region was reactivated at some time in the Cenozoic, due to the collision and continued indentation of India into Central Asia (e.g. *Tapponnier and Molnar*, 1979). It is somewhat unclear how the timings, styles, and rates of deformation have progressed across the Altay region through the Cenozoic. Conflicting low temperature thermochronology results suggest that the western Altay may have experienced tectonic activity from the early Miocene (*Yuan et al.*, 2006), whilst workers in the eastern Altay and the Siberian Altay suggest that the full onset of Cenozoic deformation that has produced the present-day relief in the Altay did not begin until more recently (initiating within the last 8 Myr, *De Grave and Van den haute*, 2002; *Vassallo*, 2006; *Jolivet et al.*, 2007; *Vassallo et al.*, 2007a; *De Grave et al.*, 2008; *Glorie et al.*, 2012a,b). Sedimentation records in the basins surrounding the Altay are consistent with regional uplift following the Oligocene. Sedimentary basins on the eastern margin of the Altay have an Oligocene unconformity, which is overlain by Miocene aged debris-rich fluvial sed-

imentary units (*Howard et al.*, 2003; *Cunningham*, 2011; *Cunningham et al.*, 2003b). An increase in conglomeritic deposits in the Plio-Pleistocene in the eastern Altay basins may imply an increase in tectonism in the last 5 Myr (*Howard et al.*, 2003).

## 1.5 Geomorphology of the Altay

Topography in the Altay generally follows the NNW–SSE trend of active faults (Figure 1.5). The mountain range is wide in the northwest (400–500 km) and narrows to the southeast where it meets the Göbi Altay mountains (100–200 km). Many basins with high elevations of at least 2000 m separate the NNW–SSE elongated mountain ranges in the eastern portion of the Altay. Basins on the outer flanks of the Altay are lower in elevation than those found within the range. The drainage divide of the east and west Altay mostly follows the Mongolian-Chinese border, which is significantly west of the centre of the mountain range (Figure 1.5). The region directly surrounding the drainage divide is characterised by steep-sided mountains with frequent U-shaped glacial valleys and little relationship between the known active faults and relief. Towards the west, the high relief topography gradually degrades to a sharp boundary with the Junggar Basin in China. The shape of topography west of the drainage divide is in contrast with the region to the east of the divide, where elongate anastomosing mountain ranges are bounded by major active faults, active alluvial fans, and intervening basins, as far east as the Depression of Great Lakes in Mongolia (Figure 1.5).

Some authors have addressed the asymmetric shape of the Altay and the difference in topographic morphology across the region. *Cunningham* (2005) suggested that crustal thickening in the Altay has led to inflation of the lower crust, and extrusion of less viscous lower crustal material towards the north led to regional uplift in the Siberian Altay, explaining the high relief in the region and lack of associated faulting. *Cunningham* (2005) and *Nissen et al.* (2009a) also suggest that the Altay

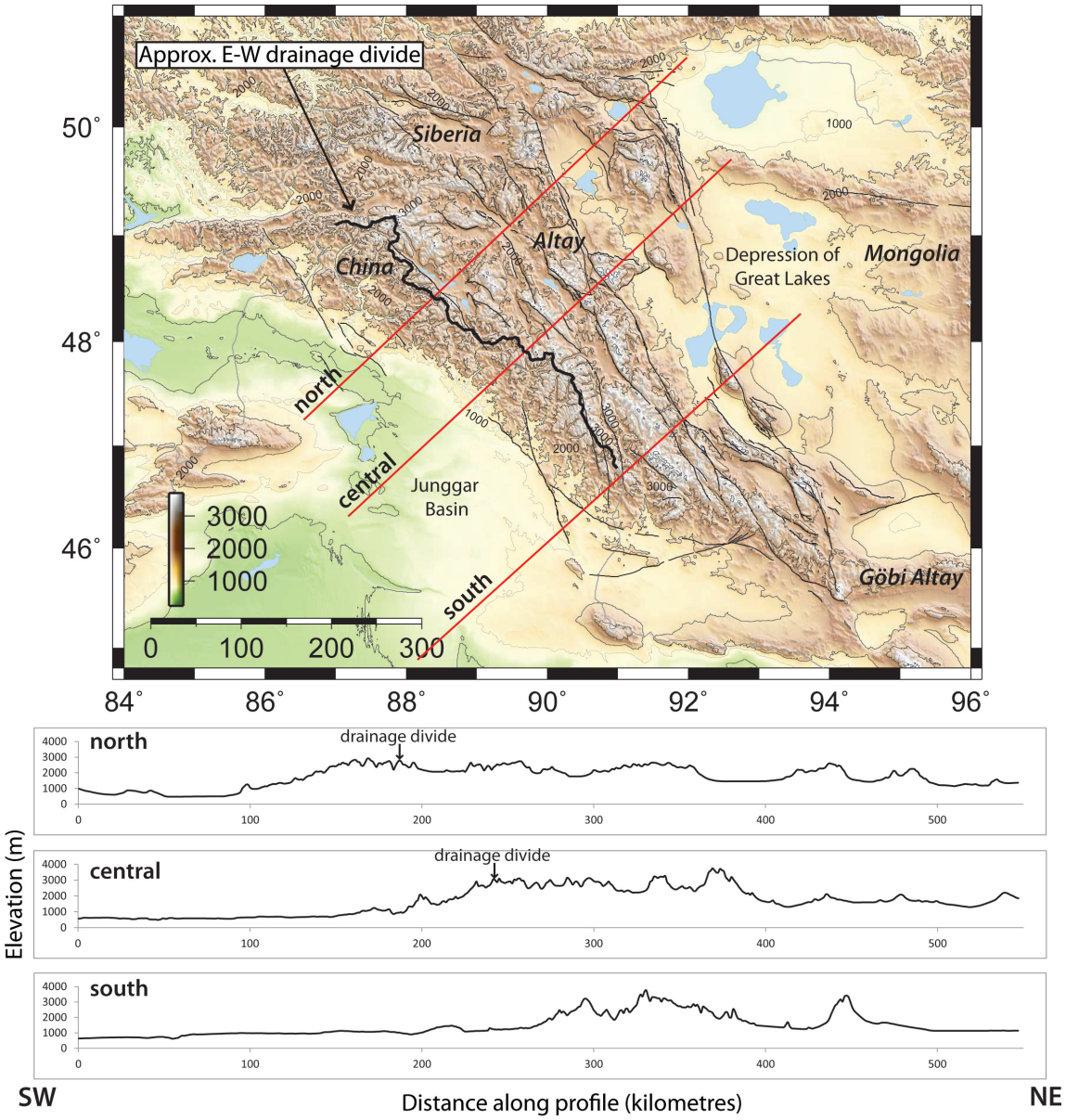


**Figure 1.5:** SRTM DEM of the Altay Mountains, with 500 m contour intervals (1000 m intervals are labeled), and three topographic profiles across the region, locations indicated by red lines. The heavy black line is the drainage divide between the northeast and southwest Altay, which follows the political border between Mongolian and China. The drainage divide is located close to the western side of the Altay, leading to an asymmetrical shape of topography from the southwest to the northeast. Political boundaries are mapped as grey lines.

are wider than would be expected for a transpressional mountain range because as deformation has evolved, faults in the center of the mountain range have rotated to an orientation that requires more work to be done against gravity, thus leading to the formation of new faults on the outer edge of the mountain range. They imply that the faults in the high Altay, along the drainage divide, have essentially shut down, which is why faulting on the edges of the range is more clearly expressed as fault controlled, anastomosing mountain ranges (visible in Figure 1.5).

A regionally preserved Late Cretaceous erosional surface is commonly suggested to cover much of the Altay and the Göbi Altay (*Cunningham*, 2011; *Cunningham et al.*, 2003a; *Ritz et al.*, 2003; *Jolivet et al.*, 2007; *Cunningham*, 2007). This planation surface is often preserved on mountain summits that are over 4000 m in elevation, and it is suggested that the surface is a peneplain, which by definition is a nearly featureless, gently undulating land surface of considerable area that has been produced by erosion almost to base level (e.g. *Hetzel et al.*, 2011; *Jackson*, 1997, cf.). A Mesozoic-aged period of stability in low temperature thermochronologic data is used to suggest that peneplain surfaces in the Altay and Göbi Altay formed during the Jurassic. The period of thermal stability is extrapolated as tectonic quiescence that lasted for about 150 Myr, during which the erosional peneplain surface was preserved and subsequently uplifted during the last 5 Myr due to Cenozoic deformation (*Jolivet et al.*, 2007). Where observed in the field, the peneplain is described as being cut through basement rock and not representing stratigraphic surfaces, with polygonal and striped ground morphology (*Jolivet et al.*, 2007). It is also concluded that the preservation of the Mesozoic surfaces indicates locally very low erosion rates since about ∼150 Ma in the Altay, and based on the presumed low erosion rates, that the current relief represents the total tectonic uplift since the formation of the peneplains, where they are observed (*Jolivet et al.*, 2007; *Cunningham*, 2007; *Nissen et al.*, 2009a). Peneplain surfaces are more commonly found in the eastern Altay,

and have not been clearly identified in the region surrounding the main drainage divide indicated in Figure 1.5.

## 1.6 Climate of the Altay and surrounding region

Mongolia is landlocked and thus the modern day climate of the region is continental, and the Altay region is generally arid and cold. The high mountains across central Asia add local complexities to climate, by deflecting storms as well as having orographic and rain-shadow effects on climate (*Gillespie et al.*, 2008). Precipitation in Central Asia is the result of advection by westerly winds from the Atlantic and Mediterranean, and much of the summer precipitation is evaporated and re-precipitated elsewhere (*Kurita et al.*, 2003). Precipitation in Mongolia is concentrated in the summer months, and less than 10% of the mean annual precipitation falls in the winter (*Morinaga et al.*, 2003). Most of the precipitation between November and March is solid due to average temperatures below 0°C. In the Altay, the lowest monthly mean temperatures are around -30°C and occur in January, which is also the month with the greatest recorded snow depth (recorded between 1940–1992 in the city of Hovd, *Morinaga et al.*, 2003). Currently, there is more vegitation and precipitation in the northwestern parts of the Altay: mainly in China, Russia, and the regions surrounding the Mongolian border with these countries (Figure 1.6). The region experiences a progressively drier climate towards the eastern parts of the mountain range that border the Depression of Great Lakes (Figure 1.5). Annual precipitation is around 250 mm $yr^{-1}$ at basin level and more than 300 mm $yr^{-1}$ at elevations above 3000 m in the northwest corner of the Mongolian Altay that borders Russia and China (*Tarasov et al.*, 2000). However, in the city of Hovd, Mongolia, on the eastern margin of the mountains, the average annual precipitation is much less, estimated as approximately 150 mm $yr^{-1}$ between 1940–1992 (*Morinaga et al.*, 2003). Most of the mountains that are greater than ∼3500 m elevation are capped by

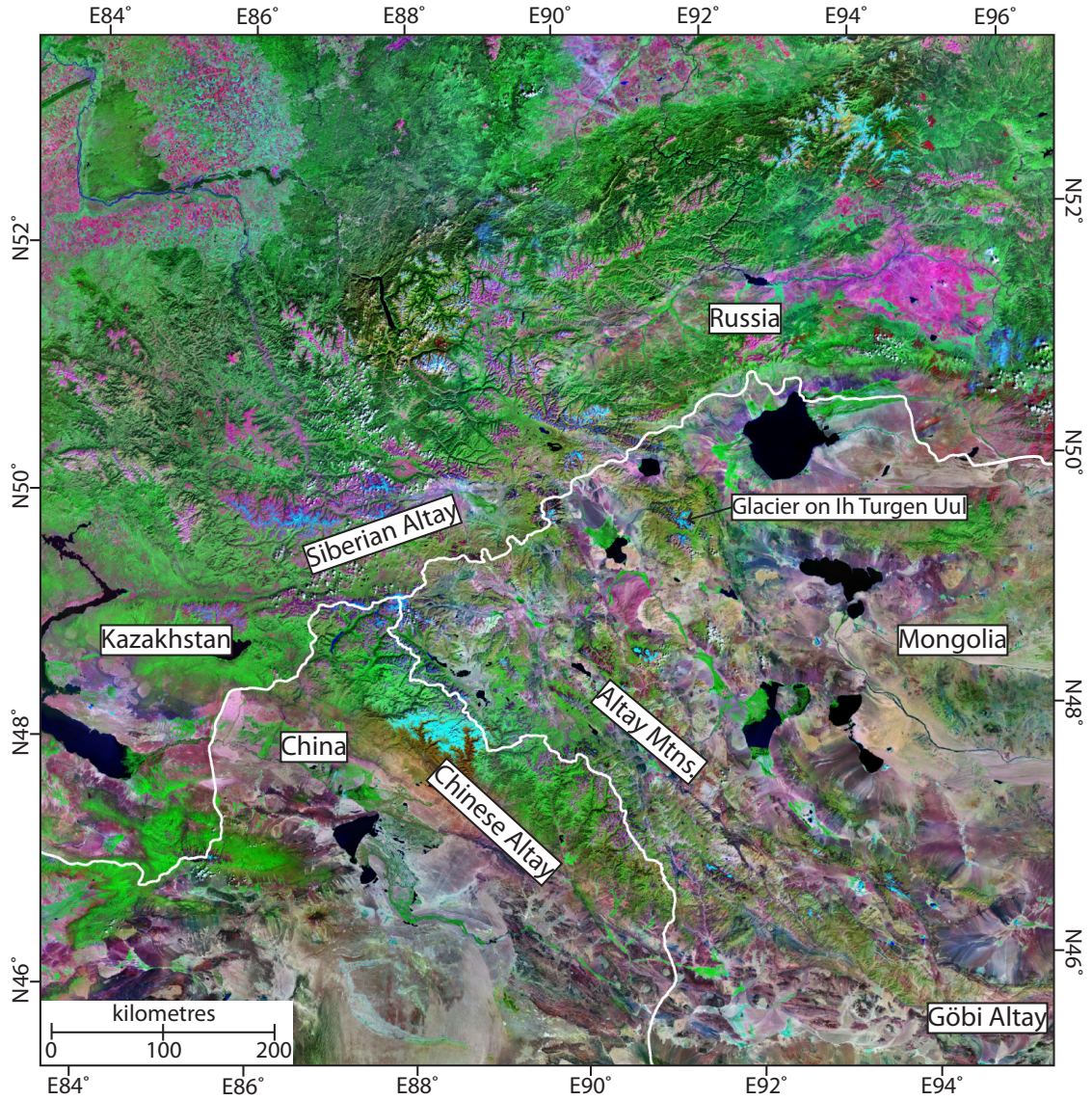


**Figure 1.6:** Landsat image of the Altay Mountains and surrounding region. The image is a MrSID panchromatic-sharpened composite, with bands 742 plotted as red, green, blue and a resolution of 14.25 m/pixel. Vegetation is strongly reflected in band 4, and thus vegetated regions generally appear green in this image, highlighting the difference in climate across the region. In general, the Siberian and Chinese Altay, and the northwestern parts of the Mongolian Altay, are wetter than the eastern Mongolian Altay. Snow and ice are reflected in band 2, and the bright blue regions across mountain peaks are mostly glaciers.

glaciers, though the glaciers are currently retreating and have been since the Little Ice Age (Figure 1.6, e.g. *Grunert et al.*, 2000; *Dundon and Ganbold*, 2009).

Palaeoclimate studies of Northern China indicate that central Asia has experi-

enced a dry, semiarid to arid climate since the Cretaceous, that was occasionally interrupted by warmer, wetter periods (*Hendrix et al.*, 1992). The region was affected by late Cenozoic glaciations, and likely experienced two to three glaciations in the Pleistocene (*Owen et al.*, 1997; *Tarasov et al.*, 1999; *Grunert et al.*, 2000; *Lehmkuhl and Haselein*, 2000; *Grunert and Lehmkuhl*, 2004; *Gillespie et al.*, 2008). The western Altay had a greater extent of Pleistocene glaciation, and in the eastern Altay, Pleistocene glaciers were restricted to isolated mountain ranges (*Lehmkuhl et al.*, 2004). The difference in glacial extent is suggested to be due to the decreasing gradient in precipitation from west to east across the Altay, suggesting that the precipitation gradient persisted from at least the Pleistocene until today. Major Pleistocene glacial advances took place during MIS (marine isotope stage) 2 and 4, which are associated with the LGM (last glacial maximum, approximately 15–25 kyr) and around approximately 70 kyr, respectively.

## 1.7 Motivation of Study

This thesis has several motivations, both in terms of better quantifying and documenting active tectonics in the Altay, and gaining insight into the spatial-temporal evolution of the India-Asia collision and the dynamics of continental deformation. A straightforward motivation of this thesis is to provide constraints on rates and styles of active deformation in the Mongolian Altay, because a limited amount of work has been done to characterise and quantify the active tectonics of the region. Whilst there are a few groups that have investigated the active tectonics of the region, much of the work has been focused on the very outer edges of the Altay. Very few researchers have ventured into the center of the mountain range (with the exception of *Baljinnyam et al.*, 1993; *Frankel et al.*, 2010), particularly the northwestern corner of the Mongolian Altay that borders Russia and China. Gaining a better regional understanding of active faulting is also important in terms of the earthquake hazard

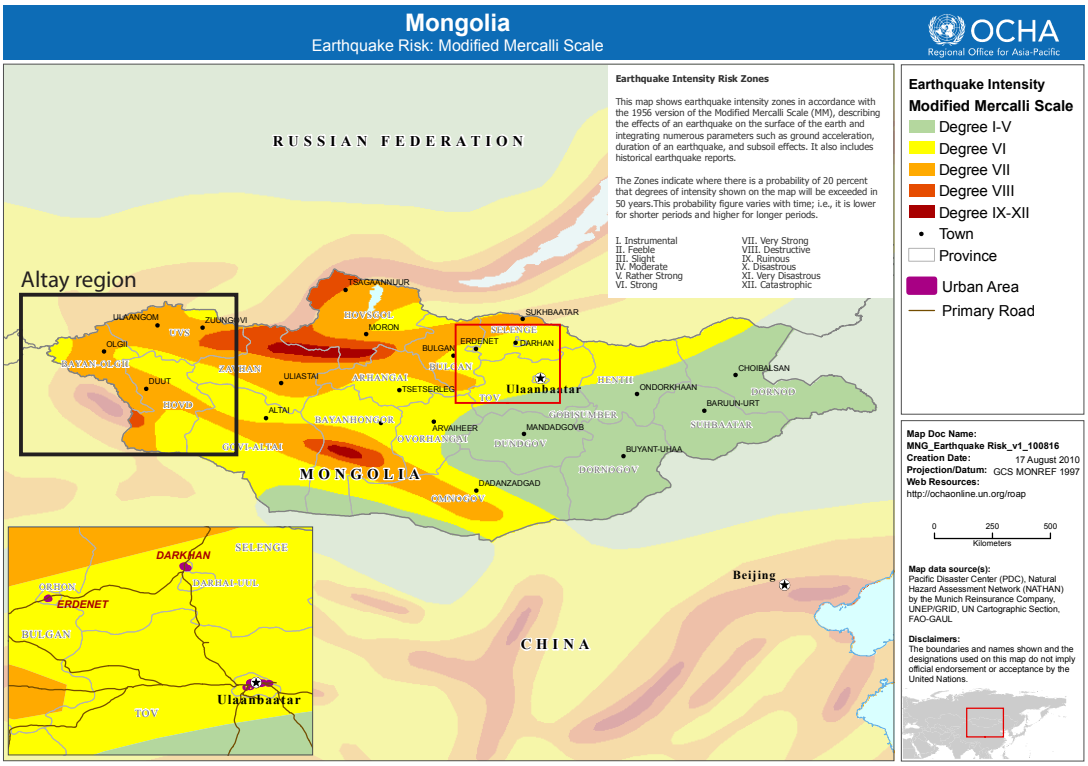


**Figure 1.7:** Earthquake hazard map of Mongolia, from the United Nations Office for the Coordination of Humanitarian Affairs Regional Office for Asia and the Pacific (OCHA-ROAP, http://preventionweb.net/go/15692). The modified Mercalli scale intensities indicate a 20% probability that the degree of of shaking intensity will be exceeded in the next 50 years. The map is largely based on the locations of earthquakes in the last century, but also takes into account factors such as subsoil effects on expected ground accelerations.

in Mongolia and the surrounding countries. The available earthquake hazard map is shown in Figure 1.7, which indicates regions where various levels of earthquake shaking are probable. One motivation of this thesis is to explore whether earthquake hazard maps that are based on earthquakes that occurred during the last century are appropriate for regions where the earthquake cycle for any one active intracontinental fault may have a repeat time significantly longer than historical earthquake records (e.g. *Stein et al.*, 2012). Faults with long repeat times that are still 'active' thus may not be indicated on probabilistic hazard maps.

Without a good understanding of the kinematics of deformation in the Altay, the region cannot be utilised to better understand the dynamics of deformation, both in

terms of the evolution of the India-Asia collision and the overall controls on continental deformation. One question that drives this work is 'How and why strain is transmitted over $>$ 2000 km of continental lithosphere due to the motion of India?'. Investigating the rates and evolution of faulting and mountain building in the distal, intracontinental Altay mountains may help to answer this question, and similar questions on the overall strength of the lithosphere. For example, better knowledge of the location and rates of active faulting may help to determine whether active mountain ranges, such as the Altay, have a relatively diminished strength. Longer term investigations in the timing of mountain building may determine if this is due to the longevity ($>$ 100 m.y.) of deformation of the region. Constraints on the timing of deformation in the far-field, relative to the timing of deformation over the whole India-Asia collision, may reveal aspects of the long-term strength of the continents and the spatial-temporal progression of large continent-continent collisions. Do the differences in modern day topography and active strain accumulation across this massive continental collision zone correspond to heterogeneities in lithospheric rheology? All of these questions cannot be addressed in this thesis, but they certainly provide motivation for the work that follows.

### 1.7.1 A note on nomenclature

Throughout this thesis, I generally use the Mongolian names for geographical and fault related terms, for example 'Sair Uul' (Dry Mountain) or 'Tsagaan Nuur' (White Lake). The same convention is used on figures and it is obvious when I refer to a feature such as a mountain on the figure. Because Mongolian is not a common language, I provide a glossary of Mongolian terms in Table 1.1, but the three most common terms I use are: uul for mountain, nuur for lake, and gol for river. The faults and palaeoearthquake ruptures that were not known before my work have been assigned appropriate names in Mongolian as well.

**Table 1.1:** Glossary of Mongolian terms

| | |
|---|---|
| alt | gold |
| ar | behind |
| bayan | rich |
| davaa | mountain pass |
| göbi | desert |
| gol | river |
| hötöl | a low pass |
| har | black |
| hungui | no humans |
| ih | big, great |
| jigjig | little |
| nuruu | mountain range |
| nuur | lake |
| sair | dry |
| tas | vulture |
| tsagaan | white |
| us | water |
| uul | mountain |

There are also a few things that the reader should keep in mind. North is to the top of all imagery, unless otherwise stated. Each chapter of this thesis is based in a different methodology, and thus each chapter has a separate methodology section in order to maintain the coherence of the chapters. The field work for this thesis was conducted in the summers of 2008, 2009, and 2010, by myself and my colleagues: mainly Richard Walker, Tsolmon Amgaa, A. Joshua West, Conall Mac Niocaill, Gantulga Bayasgalan, and Edwin Nissen. I also note throughout the thesis where other scientists have contributed to the research.

# Chapter 2

# Active faults and ancient earthquake ruptures of the Altay

## 2.1 Introduction

In this chapter, I describe the surface expression of the active faults in the Altay (Figure 2.1). The aim of the chapter is to expand on the established observations of active faults distributed across the region, and to improve our understanding of the kinematics of faulting in the Altay. I suggest some changes to the previously suggested deformation regimes by characterising several previously unknown or poorly known faults in the central and northern parts of the mountains. Earthquake ruptures that have occurred within the past few thousand years yield insight on the seismic behaviour of the faults on a time scale that is significantly longer than the modern day seismic record, which is admittedly limited. With an extended earthquake catalog, it may be possible to make connections between the observations of modern day strain across the mountains with estimates of Quaternary slip rates.

I present the observations from my analysis of high-resolution satellite imagery and from three field expeditions in the region. My work builds on the work of

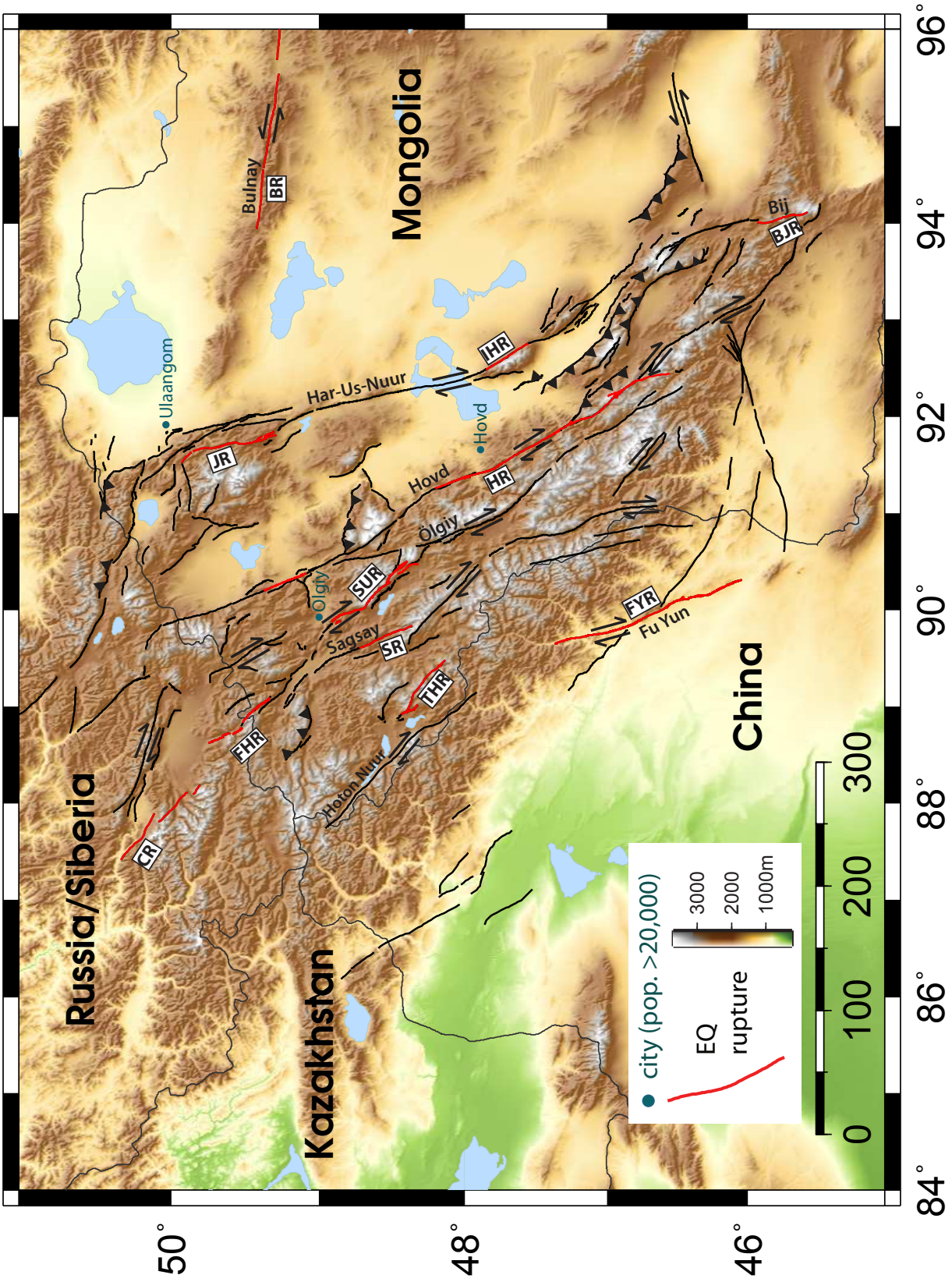
Mongolia
Russia/Siberia
Kazakhstan
China
Bulnay
BR
Ulaangom
Har-Us-Nuur
JR
JHR
Hovd
HR
Ölgiy
SUR
Sagsay
SR
THR
FHR
Hoton Nuur
CR
Bij
BJR
FYR
Fu Yun
city (pop. >20,000)
EQ rupture
3000
2000
1000m
0
100
200
300
84°
86°
88°
90°
92°
94°
96°
46°
48°
50°

*Baljinnyam et al.* (1993), and utilises recent advances in availability of high resolution satellite imagery, as well as field work in previously unexplored (geologically) regions. *Baljinnyam et al.* (1993) used Landsat data and aerial photos to make detailed observations and interpretations of the active faulting across Mongolia, as well as making use of observations in Russian language papers (e.g. *Khil'ko et al.*, 1985). Using high resolution imagery, I present detailed visual evidence for active faulting, combined with field based evidence. In this chapter, I also set up the background for the rest of this thesis, identifying and testing hypotheses for the deformation of the Altay throughout the chapter. I end with a discussion of the evolution of faulting across the Altay through time, from the million year time scale through to the present day.

**Figure 2.1** ***(preceding page)*:** ASTER GDEM (30 m/pixel) shaded topography with active Altay faults mapped in black, based on field work and remote sensing, and partially based on existing maps in *Baljinnyam et al.* (1993); *Cunningham et al.* (2003a); *Walker et al.* (2006); *Cunningham* (2007); *Nissen et al.* (2007); and *Klinger et al.* (2011). Faults zones are labeled in black text, and all known and ground-truthed surface ruptures are mapped in red (including ruptures that occurred within the past century). Rupture abbreviations are BJR: Bij Rupture, BR: Bulnay Rupture, CR: Chuya Rupture, FYR: Fu Yun Rupture, HR: Hovd Rupture, IHR: Ih Hun Rupture, JR: Jid Rupture, SR: Sagsay Rupture, SUR: Sair Uul Rupture, and THR: Tsengel Hyarhan Rupture.

## 2.2 Methodology

### 2.2.1 Remote sensing and field identification of active faults

Remote sensing of active faulting was conducted before and after field seasons using available digital elevation model (DEM) and high resolution raster datasets such as Kompsat-2, Quickbird, ASTER, and Landsat 7 (Table 2.1). Where possible, remote observations of surface ruptures were ground-truthed in the field; it is noted throughout the chapter where this was not possible, and sections of surface ruptures that were not visited in the field are generally mapped as dotted lines. Each of the Altay fault zones is described in detail, based on the expression of the fault features at the surface observed in the field and remotely, as well as summaries of prior work. Although many of the earthquake ruptures described in Section 2.3 are identified for the first time in this thesis, I also include descriptions of known ancient earthquake ruptures, which are analysed using recently available high-quality satellite imagery.

The fault map displayed in Figure 2.1 is an amalgamation of several datasets: (1) fault traces that were ground-truthed and documented in the field by myself and my colleagues, (2) fault traces that I identified remotely in available satellite imagery, (3) pre-existing digital traces mapped by R. Walker, and (4) fault traces that were well described in previous studies, mainly *Baljinnyam et al.* (1993); *Cunningham et al.* (2003a); *Walker et al.* (2006); *Cunningham* (2007); *Nissen et al.* (2007); and *Klinger et al.* (2011). Throughout this chapter, the evidence for the location of mapped faults is described, as well as whether the evidence was observed in the field, remotely, or by others. The majority of the traces in Figure 2.1 are mapped as I observed them, with previous work and available digital traces supplementing regions that I did not visit in the field or where available imagery is of a poor quality. Any traces that were ground-truthed in the field by other workers are mapped based on the published descriptions.

**Table 2.1:** Summary of satellite data used in this thesis

| Dataset | Resolution (m/pixel) | Bands | Availability |
|---|---|---|---|
| SRTM | 90 | N/A | complete coverage |
| ASTER GDEM | 30 | N/A | complete coverage |
| Landsat 7 | 30 | 1–8[a] | complete coverage |
| ASTER | 15 or greater | visible green, red, and near-IR[b] | partial |
| Kompsat-2 | 4 MS, 1 PAN[c] | visible, blue, green, red and near-IR, black and white[d] | partial |
| Quickbird | 2.4–2.8 MS, 0.6 PAN | visible blue, green, red, and near-IR[e] | partial |
| SPOT-5 | 2.5 PAN | black and white (PAN) | partial |

[a]wavelengths: 0.45–0.52, 0.52–0.60, 0.63–0.69,0 .77–0.90, 1.55–1.75, 10.40–12.50, 2.09–2.35, 0.52–0.90 $\mu$m respectively
[b]wavelengths: 0.52–0.60, 0.63–0.69, 0.76–0.86 $\mu$m respectively
[c]MS: multispectral, PAN: panchronomatic
[d]wavelengths: 0.45–0.52, 0.52–0.60, 0.63–0.69, 0.76–0.90, 0.50–0.90 $\mu$m respectively
[e]wavelengths: 0.45–0.52, 0.52–0.60, 0.63–0.69,0 .76–0.90 $\mu$m respectively

Evidence of Late Quaternary faulting was used to determine whether particular strands of the faults in the Altay can be considered as 'active'. In general, there is a very good level of preservation in the Altay of fault-related features such as scarps and cumulative strike-slip features such as sag ponds and mole tracks. The good preservation is in part due to the region's semi-arid climate, as well as particularly good preservation in regions of high elevation due to the effects of ground freezing. *Baljinnyam et al.* (1993) noted that surface ruptures that occur in regions of thick permafrost often result in very complicated deformation patterns as a result of the ground breaking into blocks, like shattering ice, and may involve significant rotation of blocks within the fault zone. The fault may also be expressed as a long single shear fracture in the surface soil or permafrost layer. The deformation patterns are well preserved in permafrost, because the breaks in the ground are well defined, and little erosion has occurred due to the generally cold climate and frozen ground. Similar features were also documented along the 2002 $M_w$ 7.9 Denali surface rupture, which occurred on permafrost ground (*Schwartz et al.*, 2012). The very cold climate and presence of permafrost may explain some of the very large deformation features described throughout this chapter. The effects of permafrost are particularly apparent along the 2003 Chuya earthquake event in the Russian Altay, which is discussed further in Section 2.3.4. I include a few photos of the rupture that were taken in the months following the event (courtesy of E. Nissen) to demonstrate the expression of a fresh earthquake rupture (Figure 2.2).

As introduced in Chapter 1, the strike-slip faults in the Altay are oriented at a highly oblique angle to the orientation of the axis of maximum compression in the region. The faults are aligned with the Paleozoic-aged structural grain, and therefore are not necessarily at the 'optimal' orientation for accommodating shortening, which would be as reverse faults oriented approximately perpendicular to maximum shortening (i.e. $\sigma_1$). Instead, shortening is mostly taken up along strike-slip faults,

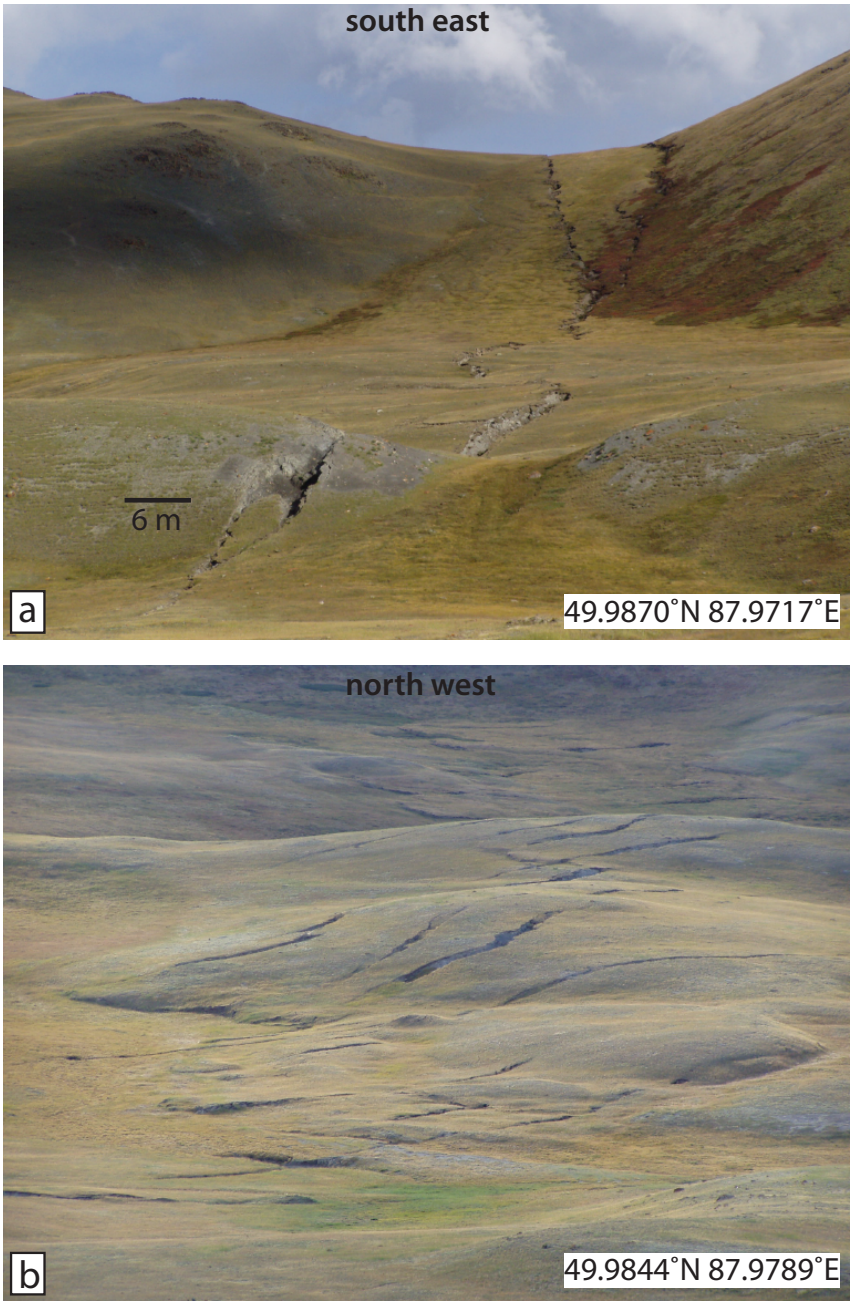


**Figure 2.2:** Photos of the 2003 $M_w$ 7.2 right-lateral Chuya surface ruptures, courtesy of Ed Nissen and taken in the months following the event. (a) shows a single fissure in the foreground, about 10 m wide and 5 m deep, as well as a split in the fissure along the base of the hillside. (b) shows an area of NNW–SSE oriented tension fissures and WNW–ESE oriented pressure ridges across a zone up to 100 m wide.

which are probably rotating (*Bayasgalan et al.*, 2005). However, the style of faulting varies with the fault strike. This is schematically depicted in Figure 2.3. For example, fault zones in the Altay that strike anti-clockwise from the general trend of faults (e.g. oriented towards the west) are observed to have a significant dip-slip component of motion, which is expected to be reverse based on the fault orientation relative to the stress field. The variation of faulting style based on fault orientation is observed in the field, where reverse fault exposures in outcrop occur on more east-west striking fault zones. Reverse faulting earthquakes are also observed on east-west striking faults, in central moment tensor (CMT) solutions (Figure 1.2, Chapter 1; *Bayasgalan et al.*, 2005; *Sloan et al.*, 2011). This relationship works at the scale of 1 to 100's of metres along fault-caused ground deformation features as well, though mostly for a different reason. Tensional ground deformation features, such as sag ponds, are expected and observed to have a ∼NE–SW oriented strike, and compressional ground deformation features, such as mole tracks, strike NW–SE. These smaller-scale structural relationships arise from interactions of the propagating earthquake rupture with the surface, which is a stress-free boundary and tends to cause the rupture to propagate as splay fault strands (*Scholz*, 2002). If sag ponds and pressure ridges with the correct orientation relative to the overall strike of the fault are observed along the fault zone, they confirm active dextral strike-slip faulting. The orientations of small extensional and compressional ground deformation features are an expression of small tensional and compressional bends of the fault at the very surface, and do not necessarily reflect the behaviour of the fault at depth.

### 2.2.2 Empirically derived moment magnitudes

Several earthquake scaling laws relate certain characteristics of earthquakes and faults, such as coseismic slip, rupture length, and fault length, with the magnitude of the earthquake event (or more accurately the dynamic stress drop in the event)

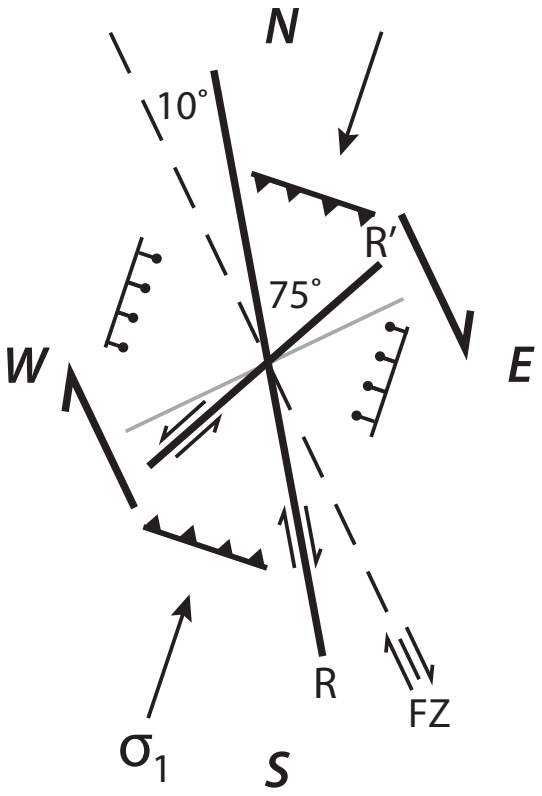


**Figure 2.3:** Schematic diagram of the orientations of shear in the Altay. $\sigma_1$ is oriented as the maximum shortening direction in the region, with the dashed line representing the general strike of the Altay fault zones (FZ). R and R' are the two sets of Riedel shears that may develop into surface features in strike-slip fault zones. The generally expected orientations of reverse and extensional faults are also indicated, with reverse faults striking more E–W than the Altay strike-slip faults, and with extensional faults striking more N–S, based on the orientation of maximum shortening.

and properties of the fault (e.g. total displacement; *Scholz*, 1982; *Cowie and Scholz*, 1992c; *Scholz*, 2002; *Wells and Coppersmith*, 1994). On geological time scales, the total accumulated fault displacement ($d_{max}$) is empirically related to fault length, as a function of the shear strength of the rock (*Cowie and Scholz*, 1992a,b). For single earthquakes, the earthquake magnitude $M_w$ approximately scales with the average surface displacement $\bar{u}$ and to the length $L$ and depth of the surface rupture, based on $M_w = \mu A \bar{u}$, where $A$ is the area of the rupture and $\mu$ is the modulus of rigidity of the crust (approximately $3 \times 10^{10}$ N m$^{-2}$; *Wells and Coppersmith*, 1994; *Scholz*,

2002). The equation $\overline{u} = \alpha L$ demonstrates that the average slip in an earthquake is related to the rupture length ($L$) by a constant $\alpha$, which is empirically determined to be approximately 5–10 $\times$ $10^{-5}$ for intraplate earthquakes (*Scholz*, 1982). The $\alpha$ ratio essentially represents the strain released during the earthquake, and can be related to the stress drop in the earthquake ($\Delta$) through the modulus of rigidity by $\Delta\sigma = \mu\alpha$. Therefore $\alpha$ should be constant for all earthquakes, if $\mu$ is uniform (e.g. *Jackson*, 2001). The range for $\alpha$ is generally found to be greater for intraplate than interplate earthquakes, suggesting that the average stress drop in intraplate events is slightly greater than for those at plate boundaries. This may be because faults at plate boundaries are typically very straight and long, with fewer geometric irregularities and higher long-term slip rates than faults within the continental interiors, which implies that interplate faults are weaker (*Scholz*, 1982; *Jackson*, 2001).

From source parameters of historical earthquakes, *Wells and Coppersmith* (1994) determined log-linear regressions between earthquake magnitude and surface rupture length. The correlation between magnitude and rupture length does vary as a function of the style of faulting, but for each type of faulting the empirically determined regression is statistically sound to the 95% confidence level. In order to estimate the moment magnitude for the ancient surface ruptures in the Altay, I use $M_w = a + b * log(SRL)$, where $SRL$ is the surface rupture length in kilometres and $a$ and $b$ are empirical coefficients determined for strike-slip faults, with values $a = 5.16$ and $b = 1.12$ (*Wells and Coppersmith*, 1994). I calculate the moment magnitude for all previously reported ruptures in the Altay and the ruptures that were discovered and documented during my own field work.

### 2.2.3 Cumulative fault displacements

Geomorphic features can be used to estimate the cumulative horizontal displacement across the major strike-slip faults of the Altay. The regional drainages generally cross

the faults at perpendicular or slightly oblique angles. The drainages only represent total fault displacement if the perpendicular drainages were in place during the initial stages of fault activity (*Lacassin et al.*, 1998; *Hubert-Ferrari et al.*, 2002). Large rivers that are perpendicular to the NNW–SSE trend of the faults record the clearest offsets. The most obvious river displacements are preserved where there is relief on both sides of the faults, such that the path of the river is confined to steep-sided valleys in the vicinity of the fault, and the fault-caused displacements of the river path are easily preserved. Major river offsets are listed in tables in each fault sub-section and discussed in the text for all faults possible.

Ratings on a scale of 1 to 5 are assigned for my level of confidence that any apparent river offset results from cumulative horizontal fault displacement, with examples of rivers with each rating level shown in Figure 2.4. A rating of 5 has the highest confidence, and implies that the displacement of the river is only due to strike-slip fault motion (Figure 2.4–5). Lower numbers are assigned for offsets that are successively less clear. A rating of 4 is assigned if the river was either at an oblique angle to the fault, or somewhat influenced by local topography or geologic contacts in a way that could impart some apparent offset (Figure 2.4–4). A rating of 3 is given to an offset that had the above issues to a more severe degree (or more than one issue). 3 is also assigned if there is a large uncertainty in the actual amount of fault-related offset, usually because the river meanders close to the fault, thus some displacement could be due to a pre-existing bend in the river (Figure 2.4–3), or because it was difficult to determine if rivers actually matched up in the past because of stream recapture or because the connecting stream is dry. A confidence rating of 3 is also assigned for rivers in a complicated region of faulting, such as a splay in the fault trace or where the river crosses several overlapping fault strands. A rating of 2 is assigned for offsets that had several of the issues already stated to a greater severity, especially for increasing difficulty in linking up the offset rivers on

either side of the fault, such as where the river follows a fault parallel valley (Figure 2.4–2). A confidence rating of 2 is also assigned to rivers that are displaced where a significant change in slope occurs where the river crosses the fault. A rating of 1 has the lowest confidence that the offset measured actually represents displacement caused by fault slip. This rating is assigned to the most severe cases of outside influence to the drainage pattern, specifically from a topographic obstruction that the river is forced to flow around such as a ridge of sediment built up where the river exits the range front (Figure 2.4–1) or a fold over a blind thrust fault. If a river offset has a rating of 1 or 2, I have very little confidence that the measured amount of horizontal displacement has been caused solely by strike-slip faulting.

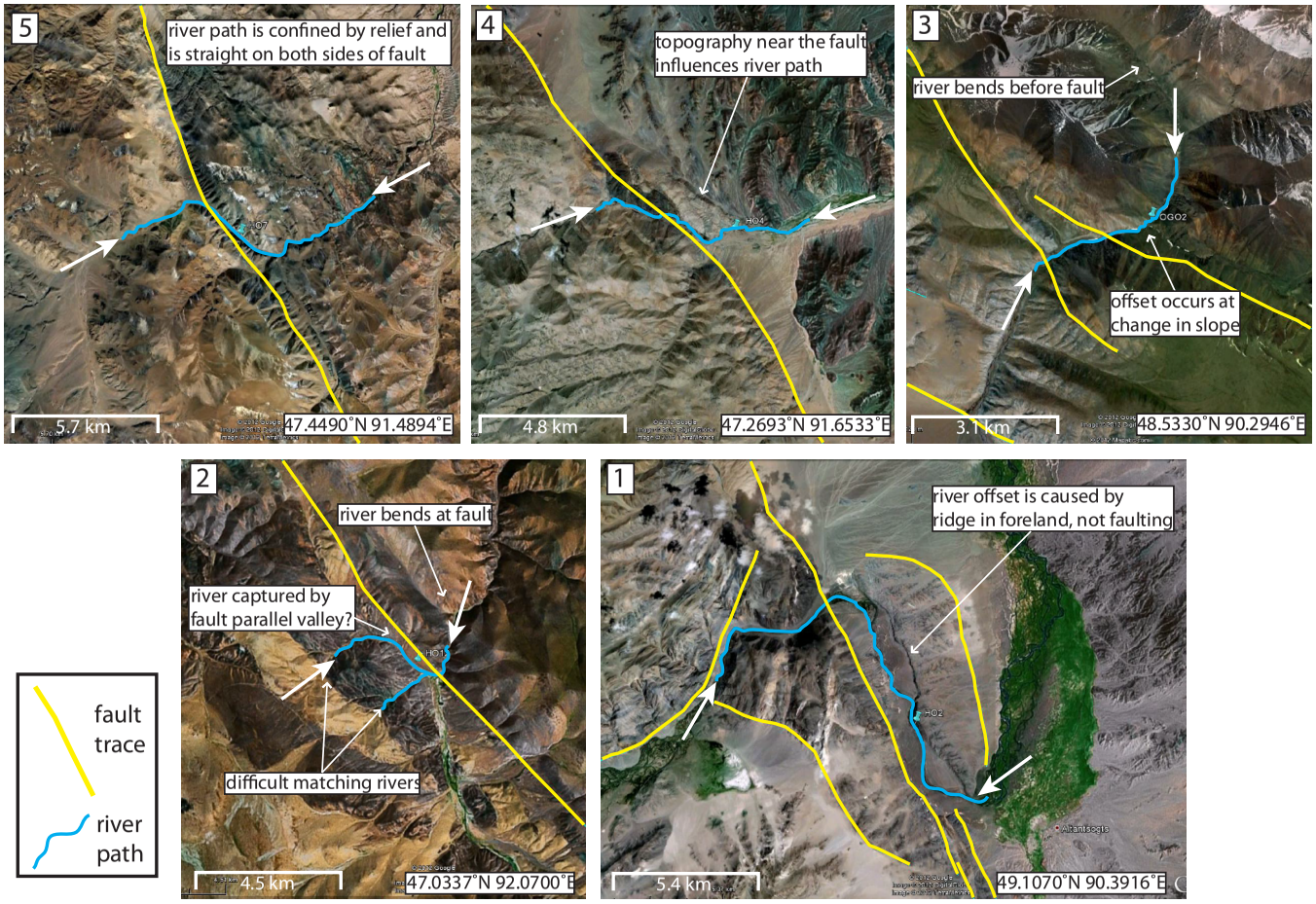


**Figure 2.4:** Google Earth screen shots showing examples of the different levels of confidence assigned to river displacements. The criteria for determining the level of confidence are described for each offset are outlined in this section.

## 2.3 Map of active faults

In this chapter, the Altay active faults are divided into five main zones, named from east to west: Har-Us-Nuur, Hovd, Ölgiy, Sagsay, and Hoton Nuur/Fu Yun (Figure 2.1). These fault zones include multiple fault strands, some of which are already named in the literature. I mostly keep the established fault strand nomenclature consistent with previous publications, but in some cases this is not possible because a fault may have multiple names or the same name was used for different faults. Fault strands that are along the same lines of NNW–SSE strike are grouped into zones, in attempt to clarify issues arising from nomenclature. Grouping of faults into fault zones at the northern and southern extremes of the Altay is less consistent because in these regions the faults are less continuous and have highly variable orientations. I describe the tectonic geomorphology from north to south along each fault, starting with the Har-Us-Nuur fault zone in the east. Part of the descriptions are a summary from the literature, with added information from my own field work and remote-sensing observations. The faults in the eastern Altay are typically well described in the literature, but less is known about the faults in the central and western Altay.

In general, I do not describe the details of several faults that lie outside of the Mongolian borders, because I did not visit these faults in the field and very little is known about them. This particularly includes the faults that bound the very north western Altay, and several strands of faults in the Siberian Altay that strike mostly east-west (Figure 2.1). The Siberian Altay faults are suggested to have a sinistral sense of slip (*Thomas et al.*, 2002), although the $M_w$ 7.2 2003 right-lateral Chuya earthquake (CR on Figure 2.1) suggests that the faults may be dextral and more related to the style of active faulting that dominates in the Mongolian Altay.

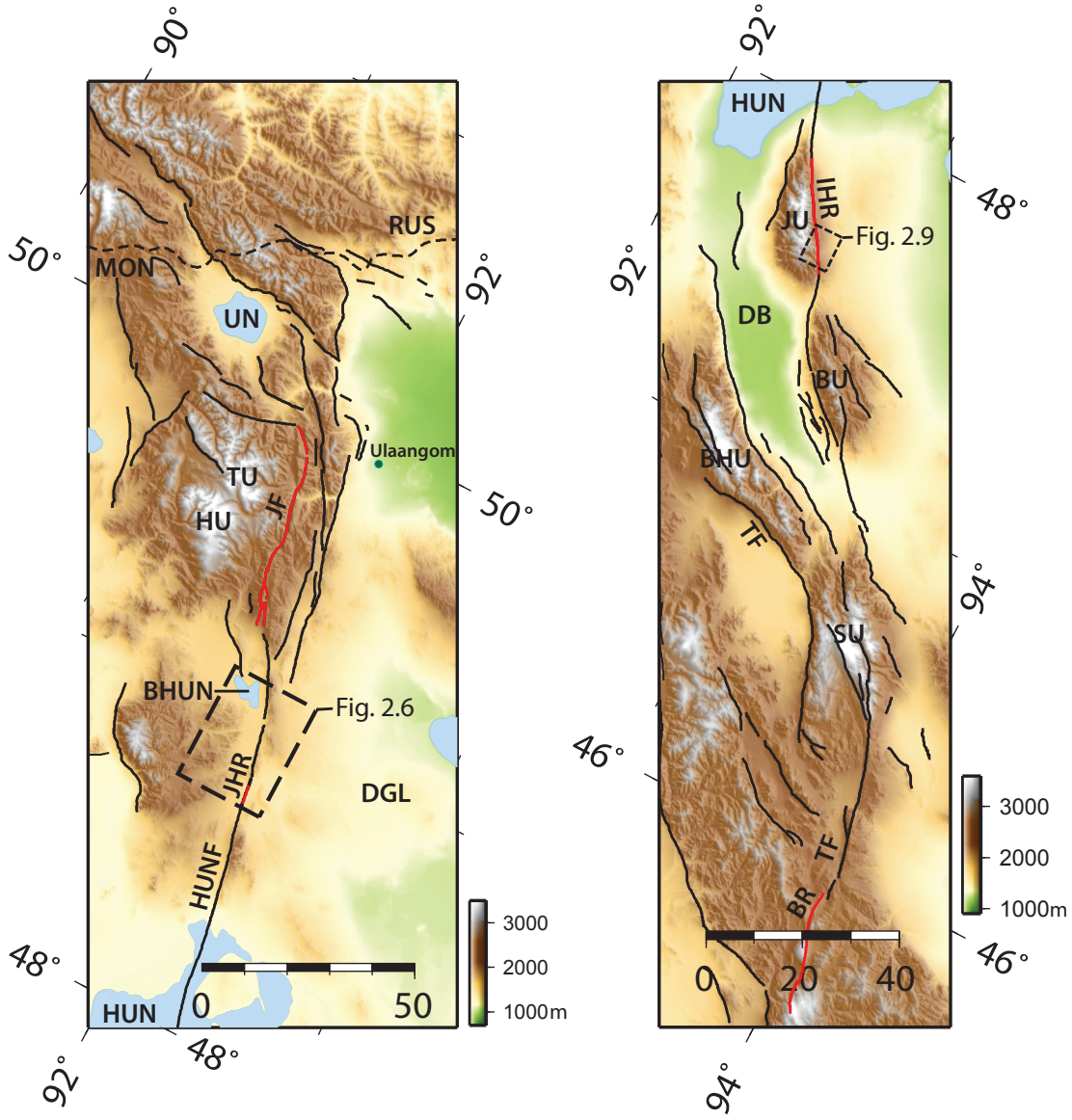


**Figure 2.5:** SRTM images of the northern (left) and southern (right) Har-Us-Nuur fault zone. Ruptures are mapped in red, active faults are mapped in black. Figures 2.6 and 2.9 are outlined by the black dashed rectangle. Political boundaries are mapped as dashed lines. Abbreviations are BHU: Bataar Hyaraan Uul, BHUN: Baga Har-Us-Nuur, BR: Bij Rupture, BU: Bumbat Uul, DGL: Depression of Great Lakes, HU: Harhirra Uul, HUN: Har-Us-Nuur, HUNF: Har-Us-Nuur Fault, IHR: Ih HUN (Har-Us-Nuur) Rupture, JF: Jid Fault, JHR: Jigjig HUN Rupture, JU: Jargalant Uul, MON: Mongolia, RUS: Russia/Siberia, SU: Sutai Uul, TF: Tonhil Fault, TU: Turgen Uul, UN: Üüreg Nuur, ZB: Dzereg Basin.

### 2.3.1 The Har-Us-Nuur fault zone

The Har-Us-Nuur (HUN) fault zone is at least 500 kilometres long and forms the far eastern boundary of the Altay range, bordered by the Depression of Great Lakes to the east (Figure 2.1). The northern end of the fault breaks up into several strands around Turgen Uul and Harhiraa Uul, with some potentially active faults continuing north past Uureg Nuur and into the Siberian Altay (Figure 2.5). The Jid fault is a strand of the HUN fault zone that cuts through Turgen and Harhiraa Uul, and was the focus of a study of an ancient earthquake rupture by *Walker et al.* (2006). *Walker et al.* (2006) also suggested that the Quaternary slip rate of the Jid fault is close to 1 mm $yr^{-1}$ based on displacements of alluvial fans of assumed post-glacial age (10–15 kyr). South of Harhiraa Uul the fault is relatively straight with a strike of 350° and there is very little topography associated with it. There are several small lakes on this section of the fault that are formed by water pooling where the fault has produced low relief topography, most notably the Baga Har-Us-Nuur (Figure 2.6). The low relief along the HUN fault is generally the final hindrance to eastward drainages of the Altay before reaching the internally drained Depression of Great Lakes (Figure 2.5).

The HUN fault passes through Har-Us-Nuur, and on the southern side of the lake forms two classic restraining bends that uplift Jargalant Uul to 3800 m and Bumbat Uul to about 3400 m (Figure 2.5). The Dzereg Basin lies on the southwest side of these mountains, and has been the site of several publications on the kinematics of faulting of the push up mountains (*Cunningham et al.*, 2003a), the Mesozoic and Cenozoic basin stratigraphy (*Howard et al.*, 2003), the Cenozoic uplift of the mountains (*Vassallo*, 2006), and the Quaternary slip rate of the Dzereg faults (*Nissen et al.*, 2009a,b). Baatar Hyarhan Uul and Sutai Uul bound the southwest side of Dzereg Basin, and are also formed by restraining bends along the Tonhil Fault, which is well described by *Munkhuu* (2006). Many of the thrust strands bounding the

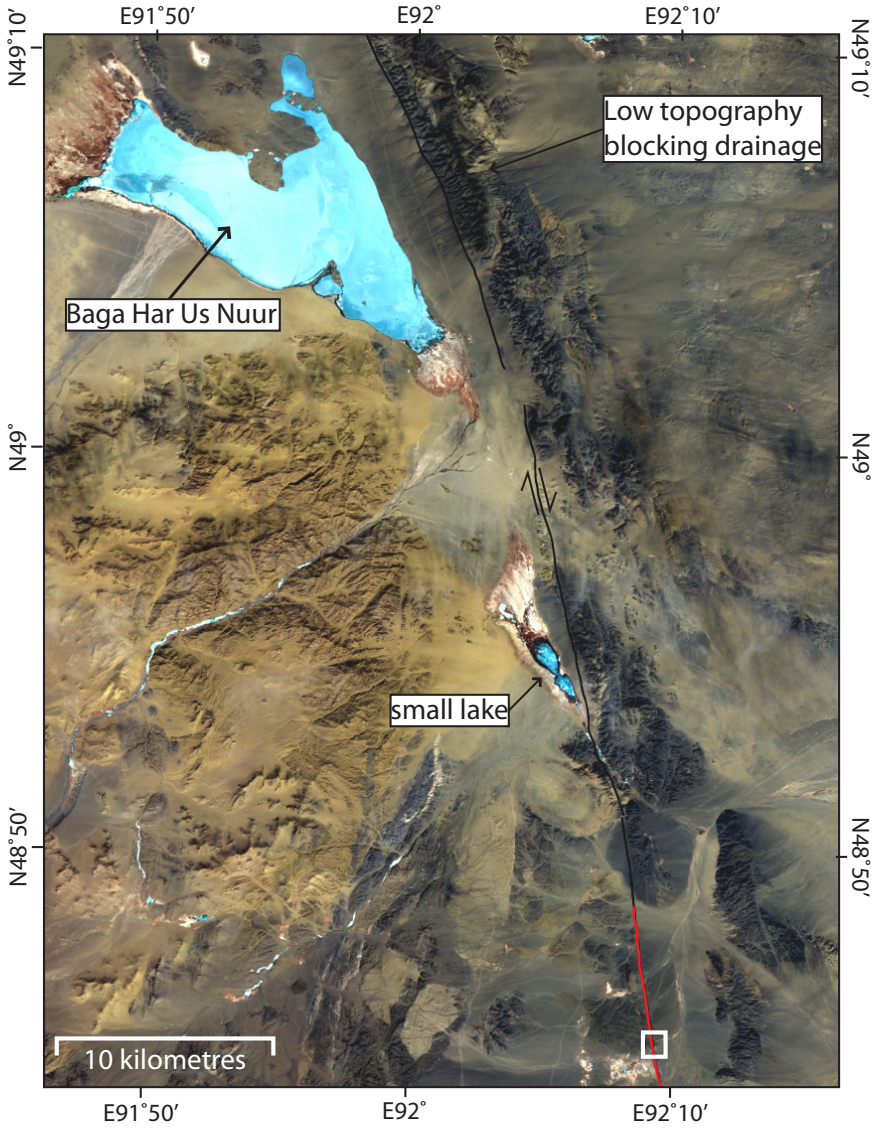


**Figure 2.6:** ASTER image (15 m/pixel) of the Har-Us-Nuur fault where the growth of low topography along the fault has formed a local closed basin, Baga Har-Us-Nuur. Figure 2.8 is marked as a white box in the bottom right corner, and the Jigjig scarp is traced in red.

restraining bend mountains produce clear scarps in Quaternary cover (*Nissen et al.*, 2009b). The Dzereg thrust faults also uplift the Mesozoic and Cenozoic sediments that I targeted for palaeomagnetic study in Chapter 4. The transpressional ranges surrounding Dzereg Basin form the approximate southern termination of the main strand of the Har-Us-Nuur fault, though several strands further south form the Tonhil

fault, which continues further south from Sutai Uul (Figure 2.5; *Munkhuu*, 2006).

In order to estimate Quaternary rates of vertical uplift and shortening, *Nissen et al.* (2009a) measured slip rates across several faults surrounding Baatar Hyarhan Uul- including a rate across several foreland ridges (locally called 'forebergs') and across two range bounding faults. From optically stimulated luminescence (OSL) dating, they determined ages of several alluvial deposits cut by the faults, and calculated offsets based on field GPS surveys of the surfaces. They found vertical displacement rates across the two faults to be between 0.1–0.6 mm $yr^{-1}$, and suggested a horizontal shortening rate of 0.7–2.4 mm $yr^{-1}$ from the vertical rate, using the dip of the thrust faults and total structural shortening across foreland ridges.

A dextral slip rate was also measured in the region, on the north eastern side of Jargalant Uul and along a portion of the Har-Us-Nuur fault that has displaced several abandoned alluvial fans. *Nissen et al.* (2009a) calculated a slip rate of 2.4±0.4 mm $yr^{-1}$ from a minimum cosmogenic nuclide age estimate of 74 kyr (modeled from a nuclide depth profile) on a fan displaced by 175±30 m. OSL dating performed on the same alluvial fans was inconsistent, and disregarded because aliquots may have been contaminated by feldspar grains, or the quartz grains may have been too immature to have developed strong OSL dosimetric qualities.

### Earthquakes

There are several ancient surface ruptures along the Har-Us-Nuur fault. The Jid palaeo-earthquake occurred on the northern part of the HUN fault (Figure 2.5a), and is described in detail by *Walker et al.* (2006). The rupture is characterised by a series of left-stepping tension fissures and right-stepping mole tracks, sometimes with linear fissures parallel to the strike of the fault that are continuous for several hundreds of metres. Deformation features are visible in the field or in satellite imagery nearly continuously for the length of the rupture, which is thought to be the full 90 km

length of the Jid fault. From the length of the rupture and the minimum right-lateral displacement that was measured (3.2 m), the earthquake was likely a $M_w$ 7.4–7.5 event. A paleoseismic trench was dug along the surface rupture by *Walker et al.* (2006), and using OSL dating, they constrained the occurrence of the most recent event to between 870–980 years ago. The Jid event is the only paleoearthquake that has been directly dated in the Altay, and I use the level of preservation (and degradation) along the Jid surface ruptures as comparison to other ruptures in the Altay, in order to provide some relative age constraint (Figure 2.7).

There are potentially two earthquake ruptures along the central portion of the HUN fault, one described by *Nissen et al.* (2009b) and one that I observed remotely (Figure 2.5). They are named the Ih HUN Rupture and Jigjig HUN scarp respectively. I describe the Jigjig 'rupture', or scarp, in this part of the chapter, instead of Section 2.4, because it has not been ground-truthed in the field. As such, it is not certain whether the features observed are the result of a single earthquake, or if they result from cumulative fault motion. A series of depressions and linear scarps is observable for at least 8 km on Google Earth imagery, from 48.8287°N, 92.1385°E to 48.7275°N, 92.1631°E, up to the point where no high resolution imagery is available. The scarp can be picked out as a series of fissures or low ponds that are 10 to 40 m long, some of which have white material that may be evaporite deposits formed due to past water ponding (Figure 2.8). There are localities where water has been ponded along the scarp, as well as an example of a river terrace riser that is right-laterally displaced by about 10 m (Figure 2.8b). Tension fissures, mole tracks, and displaced streams originating from one earthquake event are generally displaced by less than 10 m for all of the surface ruptures documented in the Altay, implying that the Jigjig displacements result from multiple earthquakes (Section 2.4). Features that are the result of a single earthquake (less than 10 m wide) are readily observed in Quickbird (0.6 m/pixel) and KOMPSAT-2 panchronomatic (1 m/pixel) imagery, but they

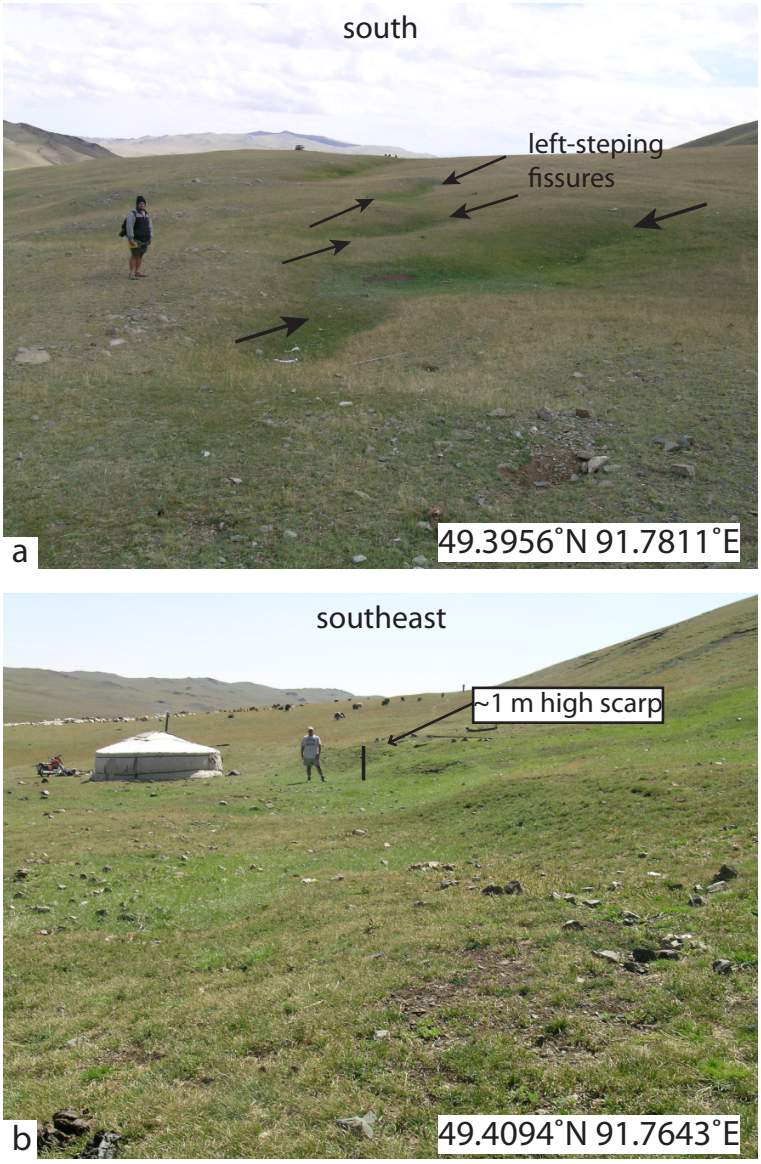


**Figure 2.7:** Photos of the Jid palaeo-earthquake, courtesy of Richard Walker and published in *Walker et al.* (2006). (a) shows a series of left-stepping tension fissures, with the long axes of the fissures rotated clockwise from the strike of the fault, which is approximately N–S in this photo. (b) shows a 1 m high vertical scarp along the rupture where the strike of the fault is about 310°, more to the west than the majority of the rupture.

are not possible to observe in lower resolution imagery (e.g. Landsat raster data, 30 m/pixel). The Jigjig scarp looks promising in the available Quickbird imagery on Google Earth, but the scarp should be documented in the field and followed to its ends to determine whether it is an ancient surface rupture. Field observations

are also necessary to estimate the magnitude and relative timing of the possible earthquake event.

Ground observations of the Ih HUN rupture were described in *Nissen et al.* (2009b). The palaeo-rupture is continuous for 30 km in the field, mainly expressed as left-stepping depressions in the ground that strike approximately N–S. The rupture is obvious even in ASTER imagery, as the fissures are filled with either snow or water (Figure 2.9). The fissures are typically 5–15 m long and 1–1.5 m wide on the minor axes of the fissure. From the size of the features and the rupture length, *Nissen et al.* (2009b) estimated that the causative event was likely a $M_w$ 7.0 earthquake. They estimated that the earthquake occurred within the last 900 years, by comparison with the level of preservation on the Jid palaeo-rupture to the north (*Walker et al.*, 2006).

*Khil'ko et al.* (1985) and *Munkhuu* (2006) described a surface rupture, the Bij rupture, along the southern portion of the HUN fault, also known as the Tonhil fault (Figure 2.5). It was described as having a 1 m high scarp along strike, and both left and right lateral offsets, with dextral offsets between 2 to 3 m. The length of the rupture is about 40 km, and it is suggested to have occurred between 500 to 1000 years ago. The surface rupture length of 25 km yields a moment magnitude of $M_w$ 7.0 for the Bij event, using the methods described in Section 2.2.2.

### Cumulative displacement

The best estimate of total offset on the HUN fault zone comes from the Jid strand, where *Walker et al.* (2006) described cumulative right lateral displacement of about 1 km of the region surrounding the Burgastay river, where the fault has a slight bend to the right. A pull-apart basin and several rivers, including the Burgastay, are restored with 1 km of displacement. Ideally, cumulative horizontal drainage displacements can be measured where a river system passes across the fault in a

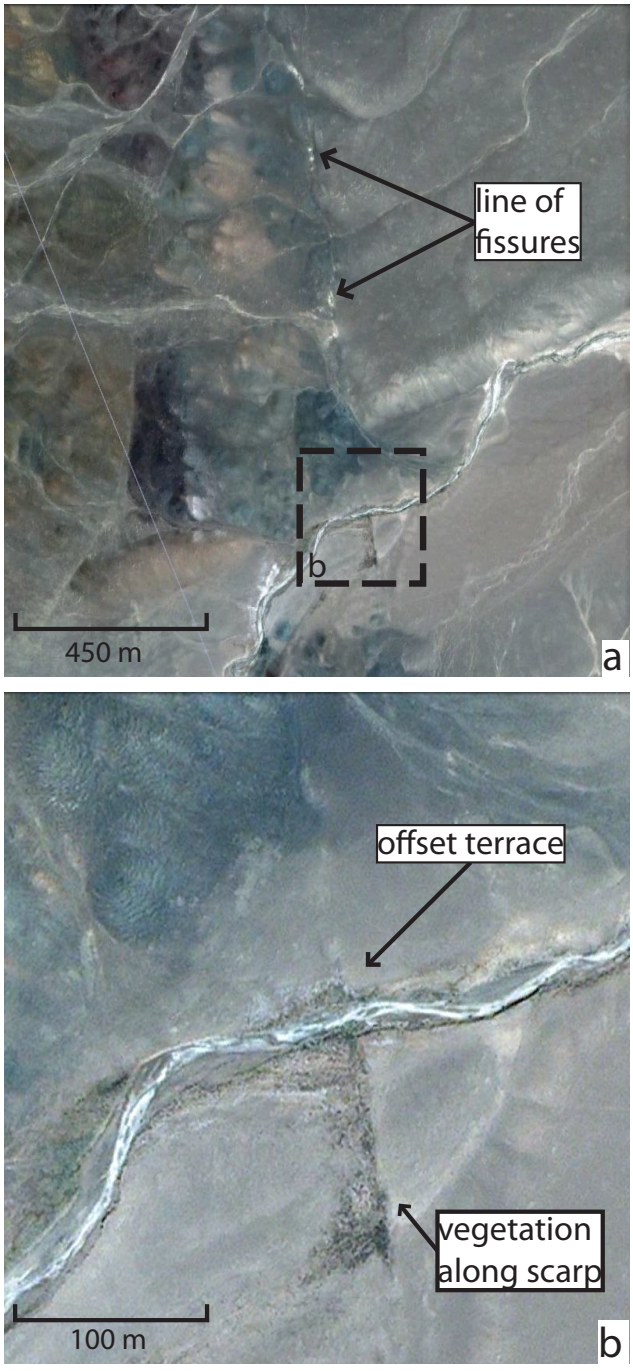


**Figure 2.8:** Quickbird imagery (from Google Earth) of the Jigjig 'rupture' along the HUN fault. (a) shows a line of possible fissures in the alluvium. (b) shows a stream terrace that is displaced by about 10 m. The centre of image (a) is at 48.757°N, 92.153°E.

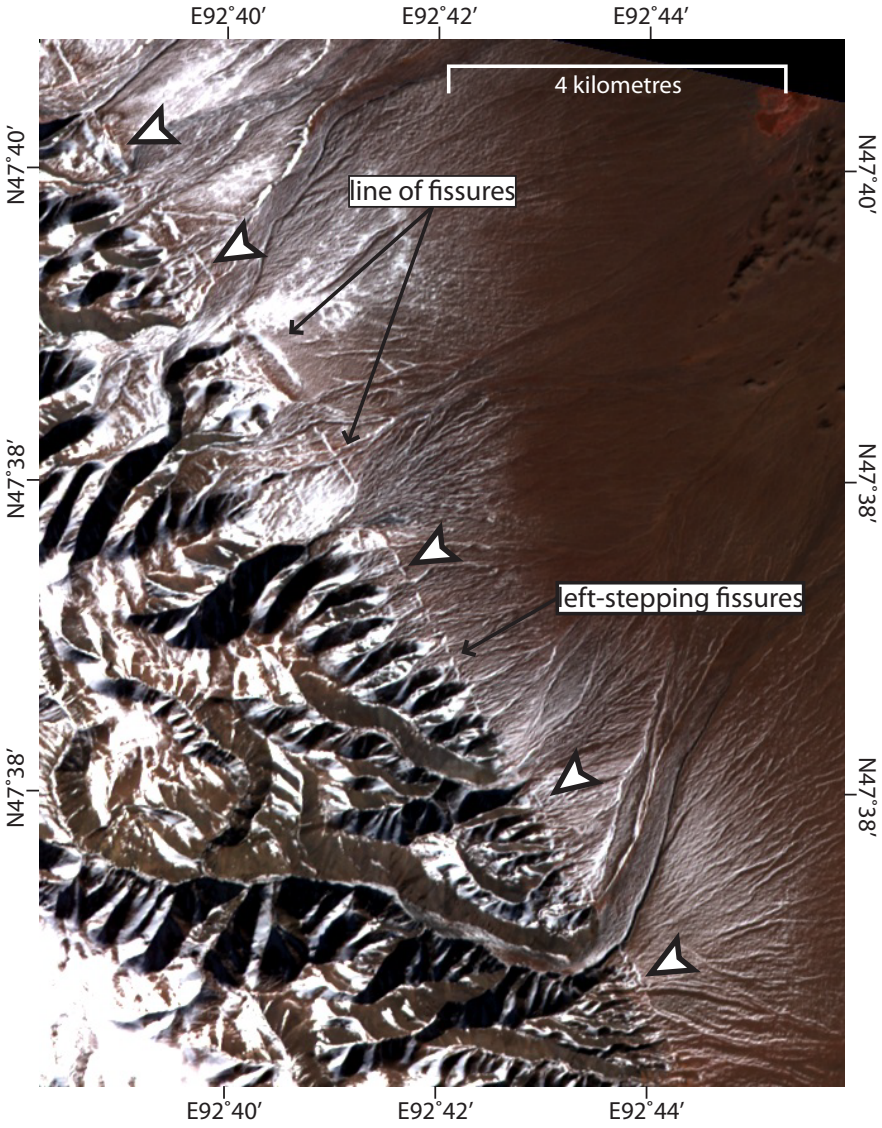


**Figure 2.9:** ASTER imagery of the Ih HUN rupture on the south eastern range front of Jargalant Uul. Lineations and fissures are clear because they were filled with snow when the image was captured. Lines of fissures and right-stepping tension fissures are indicated by arrows.

region where there is topographic relief on both sides of the fault, preserving the path of the river as it cuts through topography. Where drainages cross the fault as they exit the range front, the displaced path of the river is poorly preserved on geological time scales. Where it crosses major rivers, the HUN fault zone mostly follows the base of mountain ranges, rather than cutting through high relief, which

decreases the potential for preserving river displacements.

### 2.3.2 The Hovd fault zone

The Hovd fault (Figure 2.1) is the longest fault in the Altay, with strands that form a zone over 560 km in length. The strike of the fault varies between about 315° and 340°. The northern end of the Hovd fault zone extends north of the Mongolian-Russian border, where it breaks up into several shorter faults to the north of Ih Türgen Uul (Figure 2.10). The Hovd fault may be continuous into the Siberian Altay, where there is some evidence for active faulting as lineations in the surface morphology over a zone approximately 70 km long to the north of a 30 km stepover (Figure 2.10). However, clear evidence of Quaternary faulting in the suggested northern continuation of the Hovd fault is partially obscured in the available imagery (on Google Earth) by dense vegetation and erosion due to Quaternary glaciations.

Ih Türgen is a restraining bend mountain (i.e. *Cunningham*, 2007), formed either as a strike-slip termination at the end of the Hovd fault zone, or as a result of the 30 km stepover in the fault (Figure 2.10). Ih Türgen has classic characteristics of a restraining bend mountain, with peaks over 4000 m that stand out from the lower surrounding topography and bounding thrust faults on the eastern, south western, and possibly north western sides of the mountain. Where the main strand of the Hovd fault bounds the eastern range front, it likely has a significant reverse component of slip uplifting Ih Türgen. Topography is steepest along the eastern side of the mountain, associated with the Hovd fault, and drainages at the range front are steeply incised, indicating active reverse faulting (Figure 2.11a).

South of Ih Türgen, there are several ridges in the mountain foreland, about 1–2 km away from the range front, which block the Hovd river as it exits the range front. Just north of the town of Altantsots, the river is displaced by 10 km (Figure 2.11b,

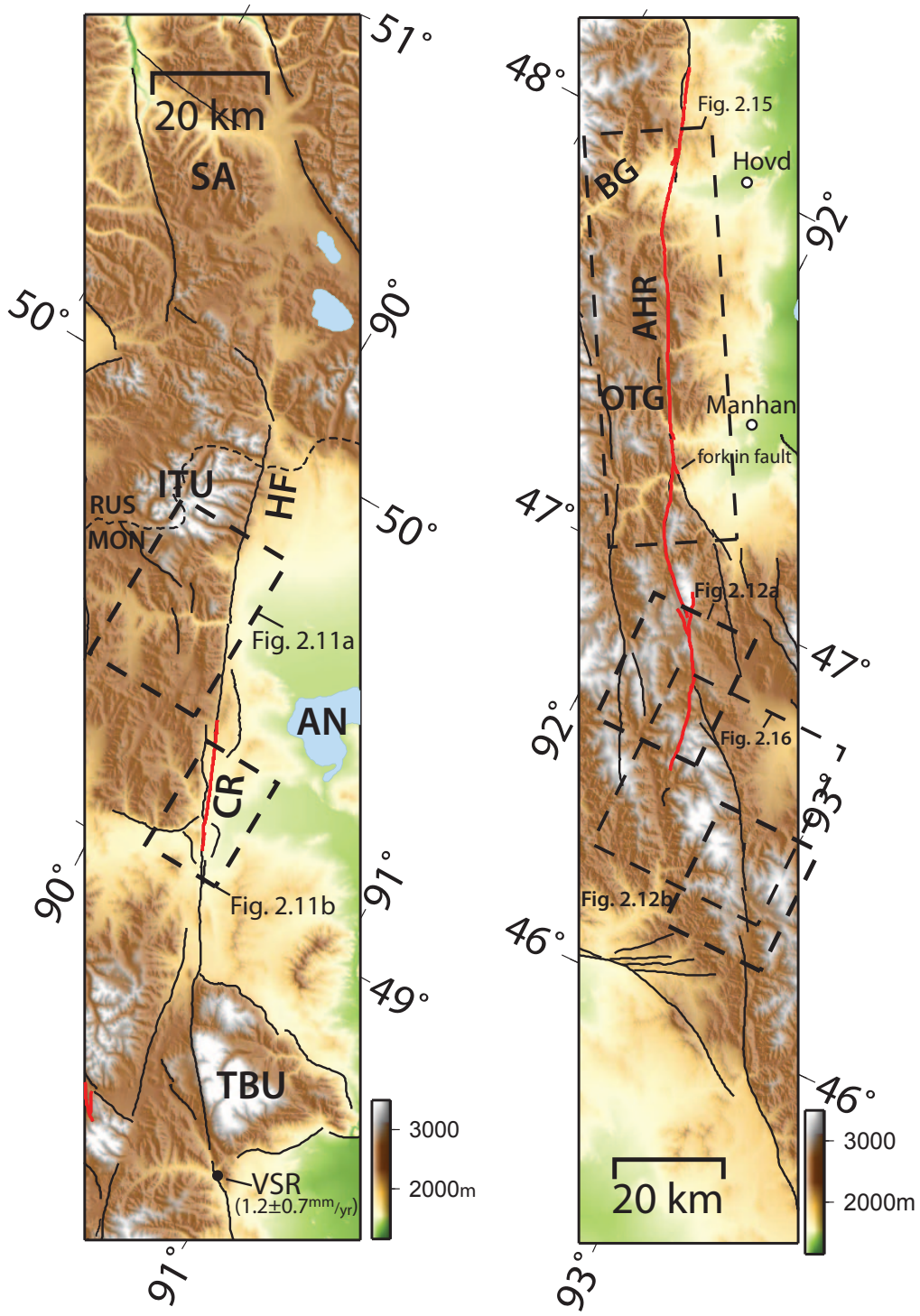


**Figure 2.10:** SRTM DEM (30 m/pixel) of the northern and southern trace of the Hovd fault. Active faults are mapped in black, palaeo-earthquake surface ruptures are mapped in red. Political boundaries are mapped as dashed lines. Abbreviations are AHR: Ar Hötöl rupture, AN: Atchit Nuur, BG: Buyant Gol, CR: Chihteyn Rupture, DTG: Dund Tsenkher Gol, HF: Hovd Fault, IT: Ih Turgen Uul, MON: Mongolia, RUS: Russia/Siberia, SA: Siberian Altay, TBU: Tsambagarav Uul, VSR: *Vassallo* (2006) slip rate.

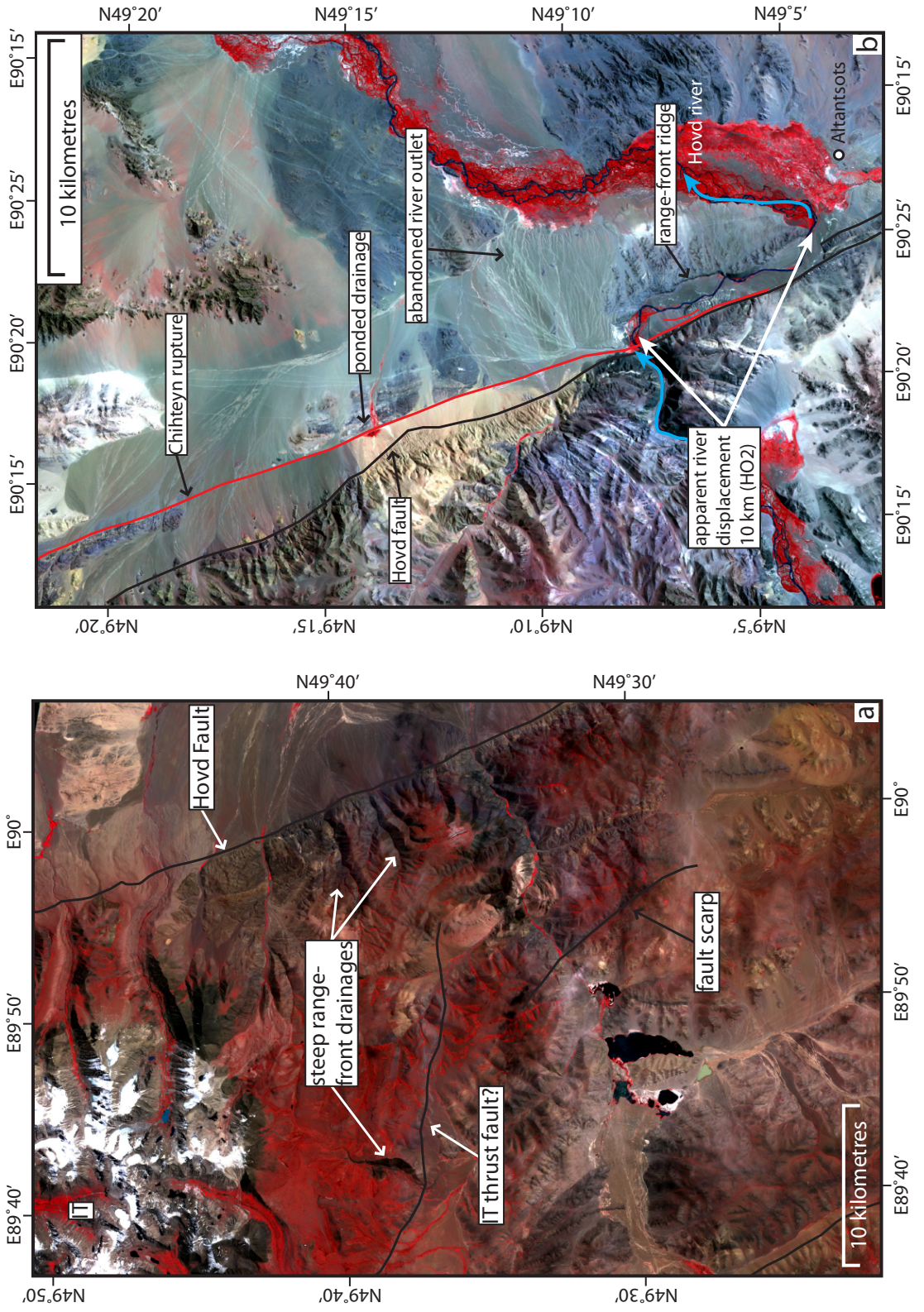
N49°20′
N49°15′
N49°10′
N49°5′
E90°15′
E90°25′
E90°20′
E90°15′
10 kilometres
Chihteyn rupture
ponded drainage
abandoned river outlet
range-front ridge
Hovd river
Altantsots
b
Hovd fault
apparent river displacement 10 km (HO2)
N49°20′
N49°15′
N49°10′
N49°5′
E90°15′
E90°25′
E90°20′
E90°15′
N49°40′
N49°30′
E90°
E89°50′
E89°40′
Hovd Fault
steep range-front drainages
fault scarp
IT thrust fault?
a
10 kilometres
N49°50′
N49°40′
N49°30′
E90°
E89°50′
E89°40′

offset HO2 in Section 2.3.2). Though this may be interpreted as a right-lateral strike-slip displacement, it is not possible to determine the influence of the foreland ridge on the path of the river. The river currently flows south around the ridge to exit into the Achit Nuur valley, potentially exaggerating any fault-caused right-lateral displacement. There is evidence for strike-slip motion on this portion of the Hovd fault, along the Chihteyn surface rupture. This rupture is described by *Khil'ko et al.* (1985) as having a dip-slip component along a segment in the centre of the rupture, which uplifts the eastern side of the fault, opposite to that of the nearby topography. They described a west facing scarp that is 0.5 to 2.0 m high. The northern segment of the rupture shows evidence of strike-slip motion, with *en-echelon* tension cracks that strike clockwise to the strike of the fault by approximately 30° to 50° (with an azimuth of 010° –030°). Drainages have ponded against the trace of the central part of the Chihteyn rupture, indicating a reverse scarp high enough to block the flow of small streams exiting the range (Figure 2.11b).

One of the most prominent features along the Hovd fault is Tsambagarav Uul, which is described by *Cunningham* (2007) as a triangular mountain in map view (Figure 2.10), bounded by thrusts on three sides, and situated at a restraining bend formed at a slight left step in the fault. *Vassallo* (2006) conducted a slip rate study on the south western flanks of Tsambagarav Uul (at 48.4348°N, 90.9790°E, Figure 2.10) using $^{10}$Be cosmogenic dating of boulders collected from a river terrace and a

**Figure 2.11** ***(preceding page)*:** ASTER imagery (15 m/pixel) of geomorphic evidence for Quaternary activity on the northern Hovd fault. (a) The restraining bend mountain, Ih Turgen (IT), in the top left of the image can be identified by white snow and glaciers on the peaks. The Hovd fault is clear at the range front, with steep drainages and high relief on the upthrown side of the fault indicative of dip-slip faulting. There are several other active faults on the southern side of Ih Turgen, probably part of the system of faults uplifting the push-up mountain. (b) Trace of the Chihteyn rupture and the 10 km displacement of the Hovd river. There are several ponded drainages on the western, upslope side of the rupture (indicated by vegetation, which appears red). The river displacement is not necessarily only caused by faulting, because a large ridge blocks the exit of the river from the range front (river displacement HO2 in Section 2.3.2).

displaced fan. He estimated an averaged age for the two surfaces of $20.1 + 18.5/ - 4.0$ kyr by integrating the youngest boulder ages from the two surfaces, with the assumption that these samples represent the actual age of the abandonment of the surfaces, with little influence of inheritance, and that the two surfaces are the same age because they have similar horizontal displacements. Any older boulders were assumed to have high levels of inheritance. Two depth profiles of cosmogenic nuclide concentrations were measured from the site, but both were inconclusive. Using horizontal displacements of $20 \pm 1$ and $25 \pm 5$ for the river terrace and the alluvial fan edge, respectively, *Vassallo* (2006) estimated a slip rate of $1.2 \pm 0.7$ mm yr$^{-1}$ for the Hovd fault.

South of Tsambagarov, the Hovd fault strikes along the base of low topography, where eastward-flowing rivers coming off the range are offset by approximately 2 km as a result of dextral slip of the fault (e.g. offsets HO3–HO5, Table 2.2). There is a major surface rupture, the Ar Hötöl rupture, along this section of the fault, first described by *Khil'ko et al.* (1985) and summarised below. The Hovd fault crosses Buyant river just west of the city of Hovd (pop. 29,000), and crosses high relief south of Hovd (Figure 2.15). There is no vertical displacement in topography across the fault through this region, and there are no large bends in the strike of the fault or corresponding restraining bend mountains. Also, the Ar Hötöl rupture through the high relief is dominantly strike-slip, with locally occurring vertical scarps documented by *Baljinnyam et al.* (1993). They attributed these scarps to local changes in strike of the fault, rather than an overall significant dip-slip component, because the dip directions of the vertical scarps were not consistently in one direction. The lack of vertical offsets and the horizontal displacement of several rivers along this section are indicative of nearly pure dextral strike-slip faulting. North of the Dund Tsenkher river (south of the city of Manhan), the fault forks into two strands (Figure 2.10).

South of the fork in the Hovd fault, there is a series of left-stepovers that have

produced elongate pull-apart basins (Figure 2.12). The basins are 3 to 8 km across on their diagonal, and indicate local extensional faulting due to the fault stepovers. South of 46°N, the fault exits the high mountainous terrain and runs along the western side of low topography. The strike of the Hovd fault at this southern-most part is between 290° and 310° and the main component of slip is dip-slip, up on the east side, indicated by the sharp change in slope at the fault and the steepness of gulleys on the upthrown side (Figure 2.10). At ∼45.5°N, the Hovd fault meets the Tonhil fault and coalesces into the complicated region of interaction between the dextral Altay faults and sinistral Göbi Altay faults (Figure 2.1).

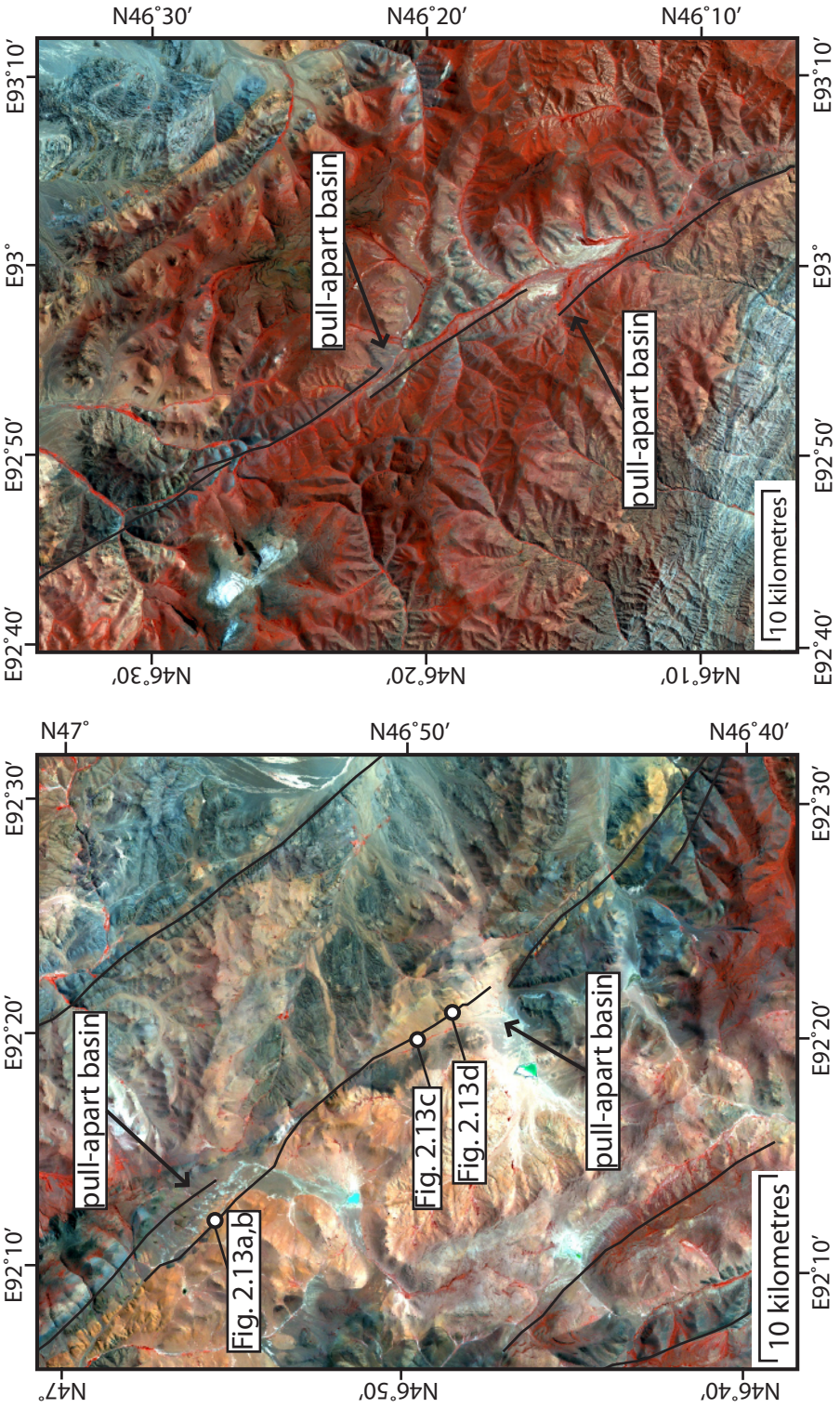


**Figure 2.12:** Landsat images (30 m/pixel, RGB=421) of pull-apart basins along left-steps or bends in the Hovd fault, which introduces a normal component of motion. The elongate basins can be picked out as flats, which are white in the band combination used, occupied by ephemeral lakes.

### Earthquakes

The Chiteyn rupture is described to be approximately 30 km in length (*Khil'ko et al.*, 1985). This length would result from an earthquake moment magnitude of approximately $M_w$ 6.8 (Section 2.2.2, *Wells and Coppersmith*, 1994). The rupture is reported to have a vertical scarp along the central section ranging from 0.5 to 2.0 m high, but no dimensions were reported for the fissures, sag ponds, or mole tracks that were found (*Khil'ko et al.*, 1985). These strike-slip features were described to dominate the rupture at its northern and southern ends. It is difficult to find the rupture in high resolution (0.6 m/pixel) Quickbird satellite imagery (from Google Earth), which suggests that it might be older than some of the other reported ruptures in the Altay, or has been eroded more heavily. *Khil'ko et al.* (1985) came to a similar conclusion on the age of the rupture based on observations of the rupture in the field and comparison with other ruptures in Mongolia. They assigned the rupture an age of 1000 to 1500 years, although it should be noted that they were working before any of the ruptures in Mongolia had been dated by Quaternary methods.

The most significant rupture on the Hovd fault, the Ar Hötöl rupture, runs along the central section of the fault adjacent to Hovd city (Figure 2.10). The rupture was described in detail by *Baljinnyam et al.* (1993); here I summarise their observations and have made slight adjustments to the map of the rupture using available Quickbird imagery (Google Earth) where they were unsure of the location. The rupture is very clear on Quickbird imagery, because the tension fissures and mole tracks that are typical of the Ar Hötöl rupture are at least several metres long, which is larger than the image resolution (0.6 m/pixel, Figure 2.13). The rupture is approximately 215 km long and extends from 48.5550°N 91.2550°E to 46.5550°N 92.4403°E. *Baljinnyam et al.* (1993) described sag ponds that are commonly 40 to 50 m long (8–10 m wide) with a trend of 350–010°, and mole tracks that are 15 to 20 m long (2–3 m high) with a trend of 280° –300°. The size and orientations of these features are indicative of

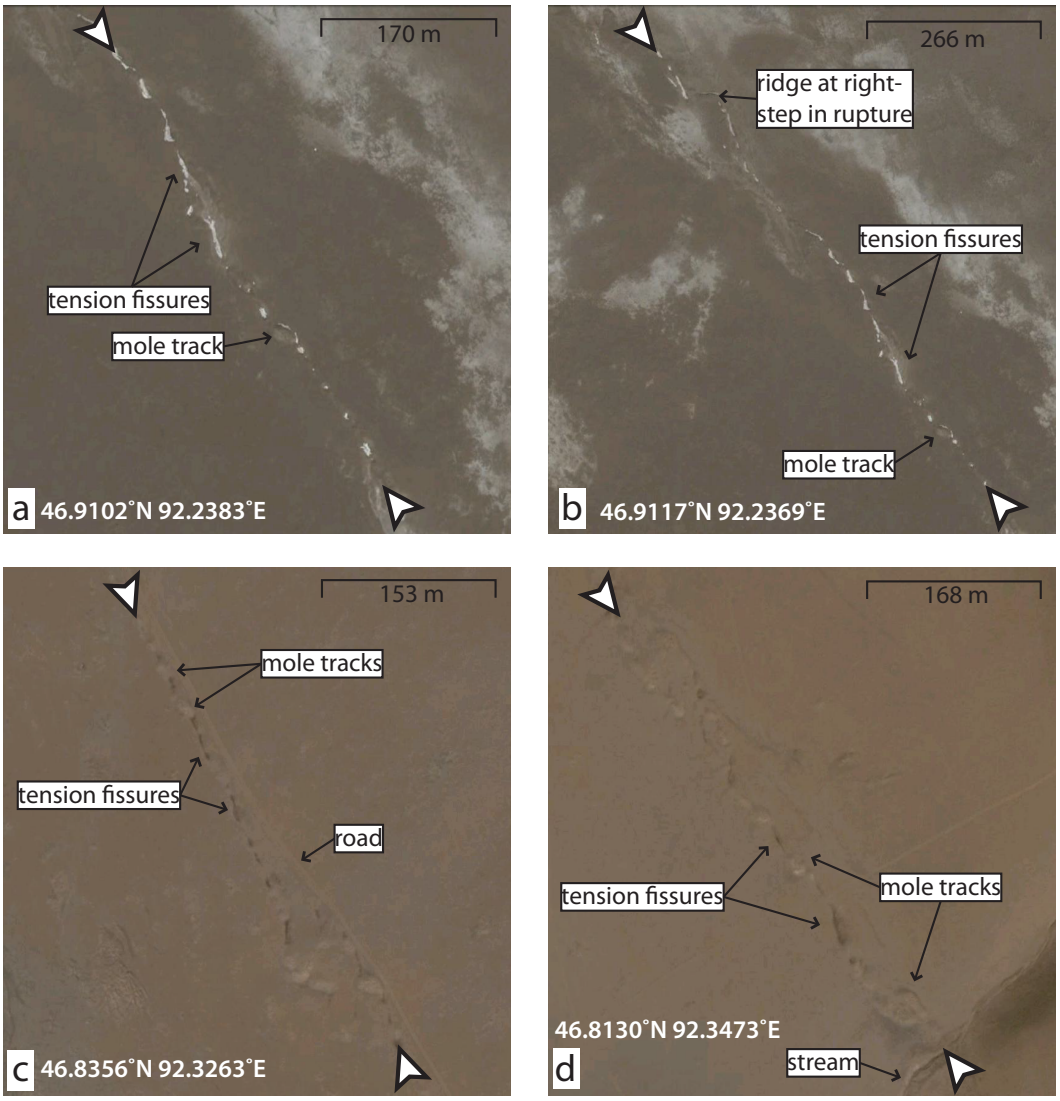


**Figure 2.13:** Quickbird imagery (0.6 m/pixel, from Google Earth) of the Ar Hötöl surface rupture. In each image, the trace of the rupture from north to south is indicated by white arrows. In (a) and (b), tension fissures are filled with snow, and appear white, and in all images the mole tracks are visible as circular features that are brighter on the southern side than the northern side, because of illumination and shadow from the sun. In (c) and (d), tension fissures are very dark, from shadow or possibly from having more vegetation because of the pooling of water. The tension fissures are left stepping, and where there are left (contractional) steps in the trace of the rupture, there are often large pressure ridges. Location of panels is indicated in Figure 2.12.

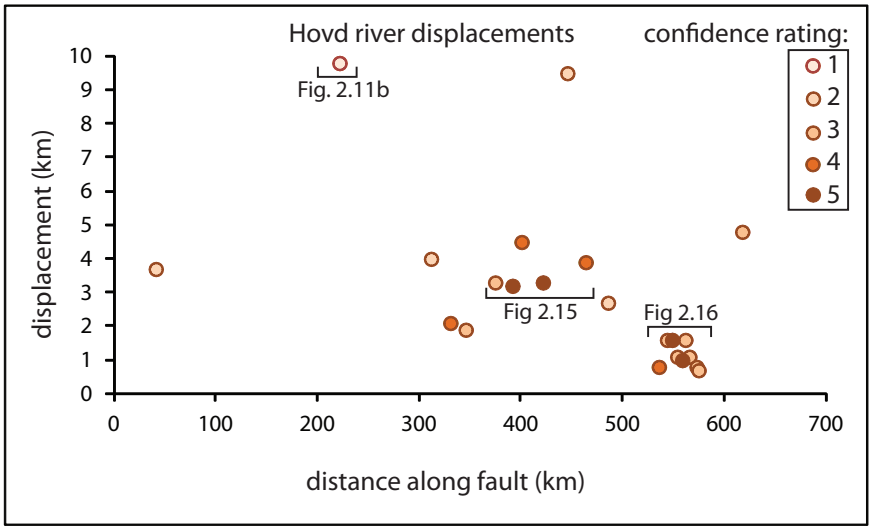


**Figure 2.14:** Plot of mapped river offsets from north to south along the Hovd fault zone. Different shades of orange represent the level of confidence in each measurement, with lighter colours being low confidence (rating of 1) and the darkest orange as high confidence (5). The criteria for assigning confidence levels is outlined in Section 2.2.3.

significant right-lateral slip in the earthquake. *Baljinnyam et al.* (1993) documented many displacements of streams and gullies, commonly offset by approximately 5 m, with a maximum offset of $7.5 \pm 3$ m in the central section of the fault. A limit on the maximum age of the earthquake is inferred from a $5.5 \pm 1$ m displacement of of a grave circle typical of the Uiger Turks, who ruled in Mongolia between approximately 745–840 AD. From the rupture length, the earthquake that made the Ar Hötöl surface ruptures was approximately a $M_w$ 7.8 event (Section 2.2.2, *Wells and Coppersmith*, 1994).

### Cumulative displacement

The Hovd fault has more mapped kilometre scale right-lateral river displacements than the other Altay faults. This is probably because large portions of the fault pass through high topography, leading to good preservation (Section 2.2.3). Offsets are listed in Table 2.2 and displayed in Figure 2.14, with the level of confidence assigned

**Table 2.2:** Hovd fault river displacements

| Offset name | Offset amount (km) | Confidence | Latitude (°N) | Longitude (°E) |
|---|---|---|---|---|
| HO1 | 3.7 | 2 | 50.3527 | 89.1091 |
| HO2 | 9.8 | 1 | 49.0962 | 90.3836 |
| HO3 | 4 | 2 | 48.4126 | 91.0015 |
| HO4 | 2.1 | 4 | 48.2942 | 91.1920 |
| HO5 | 1.9 | 3 | 48.1511 | 91.2572 |
| HO6 | 3.3 | 3 | 47.9168 | 91.4110 |
| HO7 | 3.2 | 5 | 47.7767 | 91.4782 |
| HO8 | 4.5 | 4 | 47.7070 | 91.5507 |
| HO9 | 3.3 | 5 | 47.5411 | 91.6806 |
| HO10 | 9.5 | 2 | 47.3506 | 91.8270 |
| HO11 | 3.9 | 4 | 47.2209 | 91.9500 |
| HO12 | 2.7 | 2 | 47.0378 | 92.0626 |
| HO13 | 0.8 | 4 | 46.6973 | 92.5110 |
| HO14 | 1.6 | 3 | 46.6631 | 92.5793 |
| HO15 | 1.6 | 5 | 46.6317 | 92.6405 |
| HO16 | 1.1 | 3 | 46.6064 | 92.6792 |
| HO17 | 1 | 5 | 46.5698 | 92.7269 |
| HO18 | 1.6 | 3 | 46.5441 | 92.7485 |
| HO19 | 1.1 | 3 | 46.5193 | 92.7729 |
| HO20 | 0.8 | 3 | 46.4520 | 92.8317 |
| HO21 | 0.7 | 3 | 46.4428 | 92.8375 |
| HO22 | 4.8 | 3 | 46.1044 | 93.0873 |

for each offset. Offsets range from about 700 m to 10 km, while the majority of rivers are displaced less than 5 km, and rivers displaced by less than 500 m were not mapped. There are two rivers that appear to be displaced by almost 10 km (offsets HO2 and HO10), but for both of these, it is difficult to determine how much offset, if any, is due to fault activity. HO2 is discussed in the beginning of this section (see Figure 2.11b), and offset HO10 places little to no constraint on total fault motion because the path of the river at this locality seems to be strongly influenced by the shape of a granitic contact. For offset HO10, far from the fault, the river is quite straight but the path of the river is complicated close to the fault (Figure 2.15).

All of the other offsets on the Hovd fault are less than 5 km, with varying levels of confidence based on the ratings described in Section 2.2. A portion of the fault just to the south of Bulgan Gol has five obvious offsets (HO7–HO11) that line up

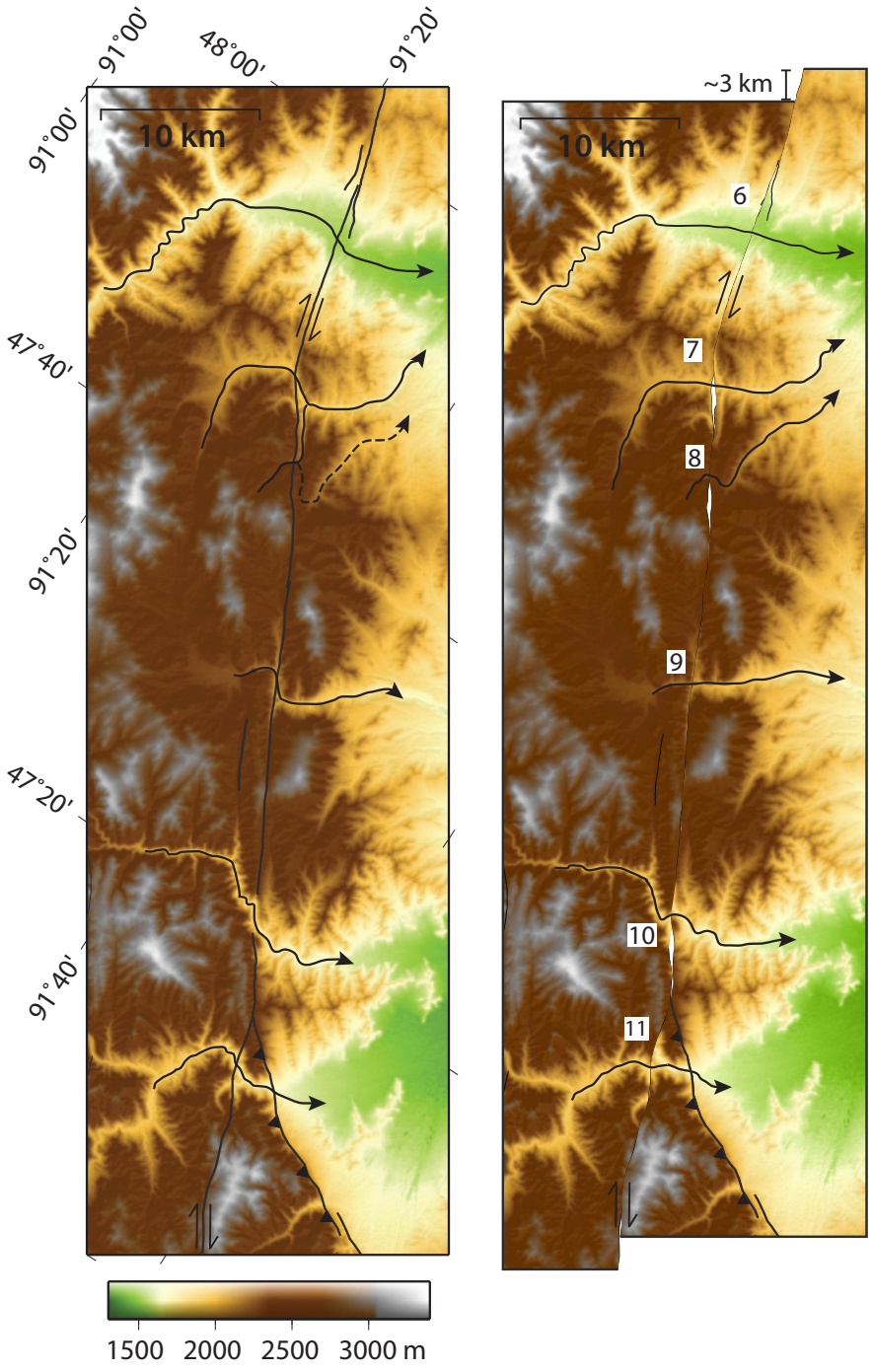


**Figure 2.15:** Aster GDEM shaded relief image of the central Hovd fault. The image on the right has been restored to represent approximately 3 km of horizontal motion along the fault. Each number represents the offset listed in Table 2.2, i.e. 6 is offset HO6. Figure location shown in Figure 2.10.

when reconstructed back about 3 km (Figure 2.15). Offsets HO7 and HO9 have a confidence rating of 5 because there is high relief on both sides of the fault and the offset river gorges are steep and perpendicular to the fault. Offset HO8 has a lower confidence rating of 4, because there is less certainty that the west and east river valleys met up in the past. The eastern, downstream river no longer connects up with the upstream, western river, as the upstream river has been re-directed to the north where offset HO7 occurs. Offset HO11 also has a rating of 4 because the river gorge is not perpendicular to the fault on the western side, and the bend in the river does not occur right at the fault (although the exact location of the fault is not very clear). The river crosses two strands of the Hovd fault, but the eastern strand seems to be accommodating mostly dip-slip motion and there is no lateral displacement of the river. Further south, there is another section of the Hovd fault that passes through high topography, crossing several rivers that also preserve high confidence displacements (Figure 2.16).

Because strike-slip faults may be active long before the formation of rivers that are large enough to accumulate kilometre-scale displacements, the river offsets that I measure in the Altay may underestimate the total cumulative fault displacement. It follows that the maximum displacement that I measure on each fault is closest to the total strike-slip displacement, with the exception of reasonably rejected offsets such as HO10. For the offsets with reasonable levels of confidence (greater than 3) there is a range in amount of displacement, up to almost 5 km but as low as 0.7 km (Table 2.2). There are many displacements less than 0.5 km along the fault, but documenting them here is beyond the scope of my thesis. For the Hovd offsets, there is little correlation between offset confidence level with either the amount of offset or the location of the offset along the fault (Figure 2.14), with the exception of the two displacements that are close to 10 km, which are unreliable.

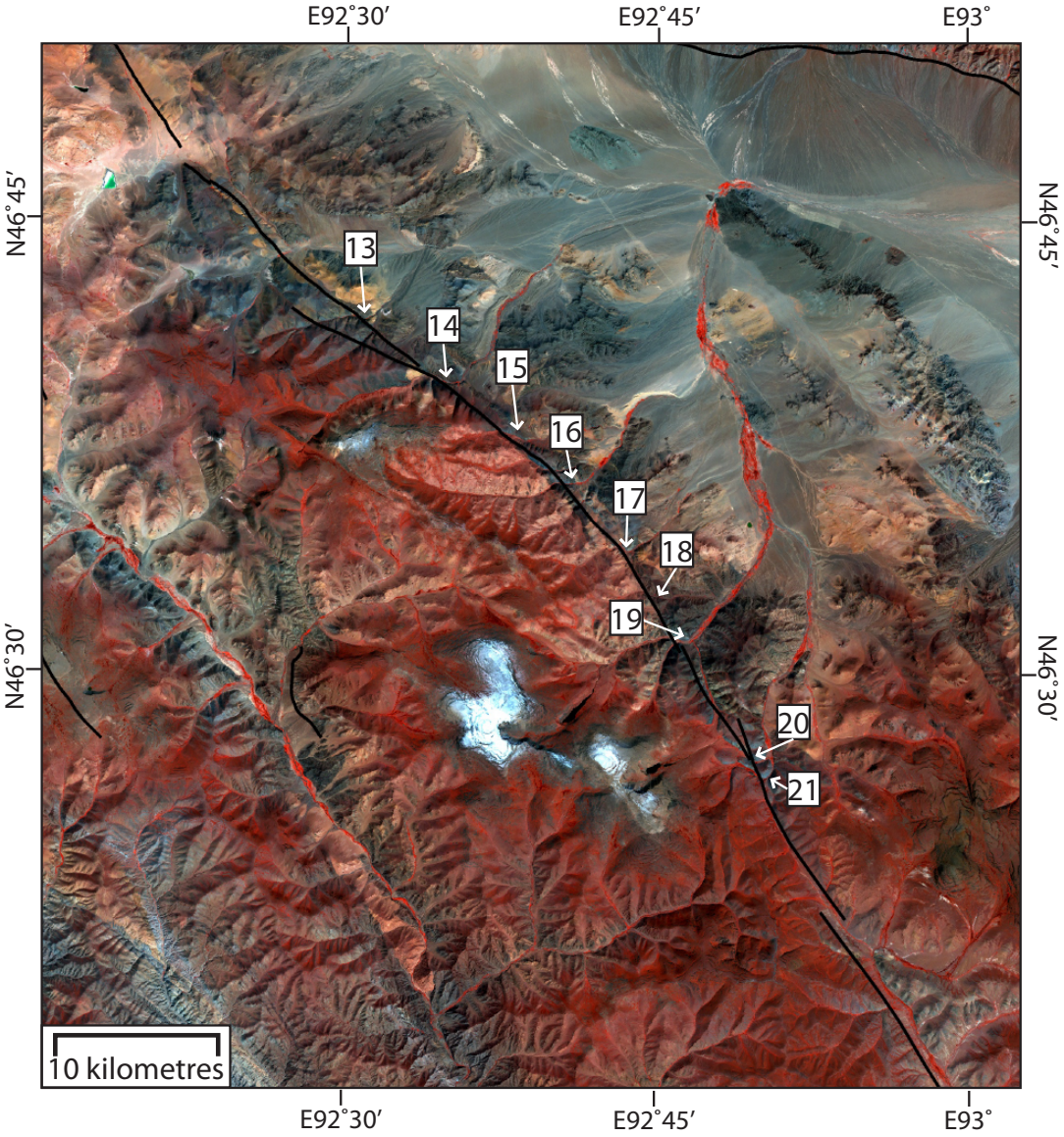


**Figure 2.16:** Landsat imagery (30 m/pixel, RGB = bands 421) of several rivers that are displaced by the Hovd fault by about 0.7 to 1.6 km. The rivers, which appear bright red in the image, can be easily observed. The numbers correspond to the offset number listed in Table 2.2, figure location shown in Figure 2.10.

### 2.3.3 The Ölgiy fault zone

The Ölgiy fault zone is a major strike-slip fault between the Hovd and Sagsay fault zones (Figure 2.17; e.g. *Baljinnyam et al.*, 1993). Several parts of the fault have not been investigated in detail. Various strands of the fault have different names,

including Tölbö Nuur (*Baljinnyam et al.*, 1993) and Höh Serh-Tsagaan Salaa (*Frankel et al.*, 2010), but I refer to it as the Ölgiy fault zone as it passes close to the city of this name, in order to be consistent with the names of the Sagsay and Hovd faults. I visited several sections of the Ölgiy fault in the summers of 2008–2010 and can contribute an updated description of the extent and continuity of the fault and the discovery of two previously-unknown earthquake ruptures (Section 2.4). There were no known palaeo-earthquake ruptures on the Ölgiy fault prior to this field work.

The northernmost strands of the Ölgiy fault occur along the margins of the Siberian Chuya and Kurai depressions (Figure 2.17). On the south western side of the depressions, there are dextral strike-slip faults that were unrecognised prior to the 2003 September 27 $M_w$ 7.2 Chuya earthquake in the Siberian Altay (*Nissen et al.*, 2007). While it is difficult to link the segmented faults of the Siberian earthquakes with a continuous fault zone in the Mongolian Altay, the style of right-lateral shear on the Siberian faults in surface ruptures, synthetic aperture radar interferometry (InSAR) data, and bodywave modeling from the Chuya earthquake indicates that the causative faults are dextral strike-slip faults, which are related to the Mongolian Altay faults (*Nissen et al.*, 2007). Faults in the Kurai Mountains (Figure 2.17) are thought to accommodate sinistral motion (*Delvaux et al.*, 1995), but the 2003 earthquake certainly indicates that the Chuya faults are dextral. There are also a number of kilometre-scale right lateral displacements along the Kurai fault.

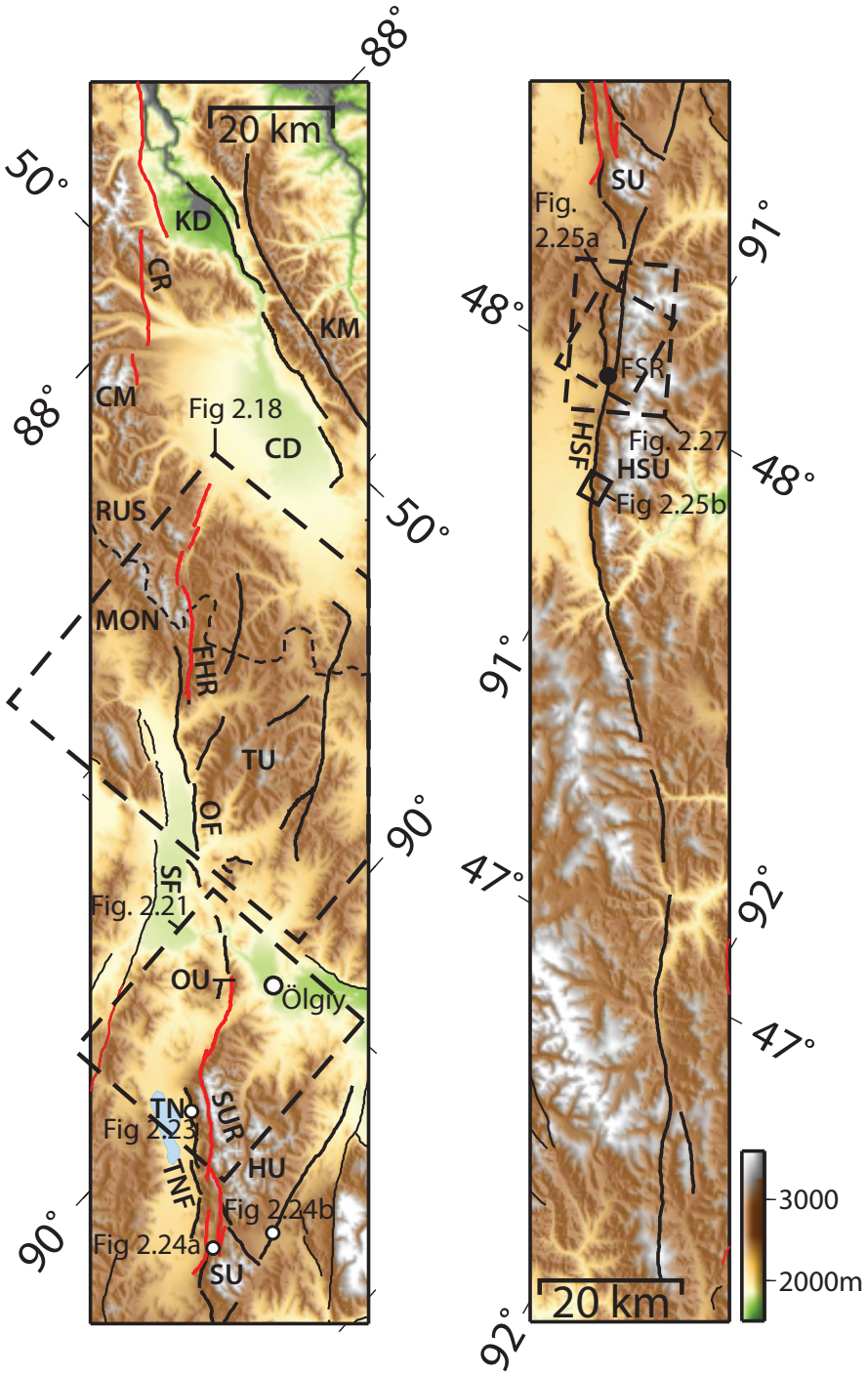


**Figure 2.17:** SRTM images of the northern, central, and southern Ölgiy fault. Ruptures are mapped in red, active faults are mapped in black. Political boundaries are mapped as dashed lines. Abbreviations are CD: Chuya Depression, CM: Chuya Mountains, CR: Chuya Rupture, FHR: Fiery Horse Rupture, FSR: *Frankel et al.* (2010) slip rate site, HSF: Höh Serh Fault, HSM: Höh Serkhiin Uul, HU: Hungui Uul, KD: Kurai Depression, KM: Kurai Mountains, OF: Ölgiy Fault, OU: Ölgiy Uul, MON: Mongolia, RUS: Russia/Siberia, SF: Sagsay Fault, SU: Sair Uul, SUR: Sair Uul Rupture, TN: Tolbo Nuur, TSF: Tsagaan Salaa Fault, TU: Tas Uul.

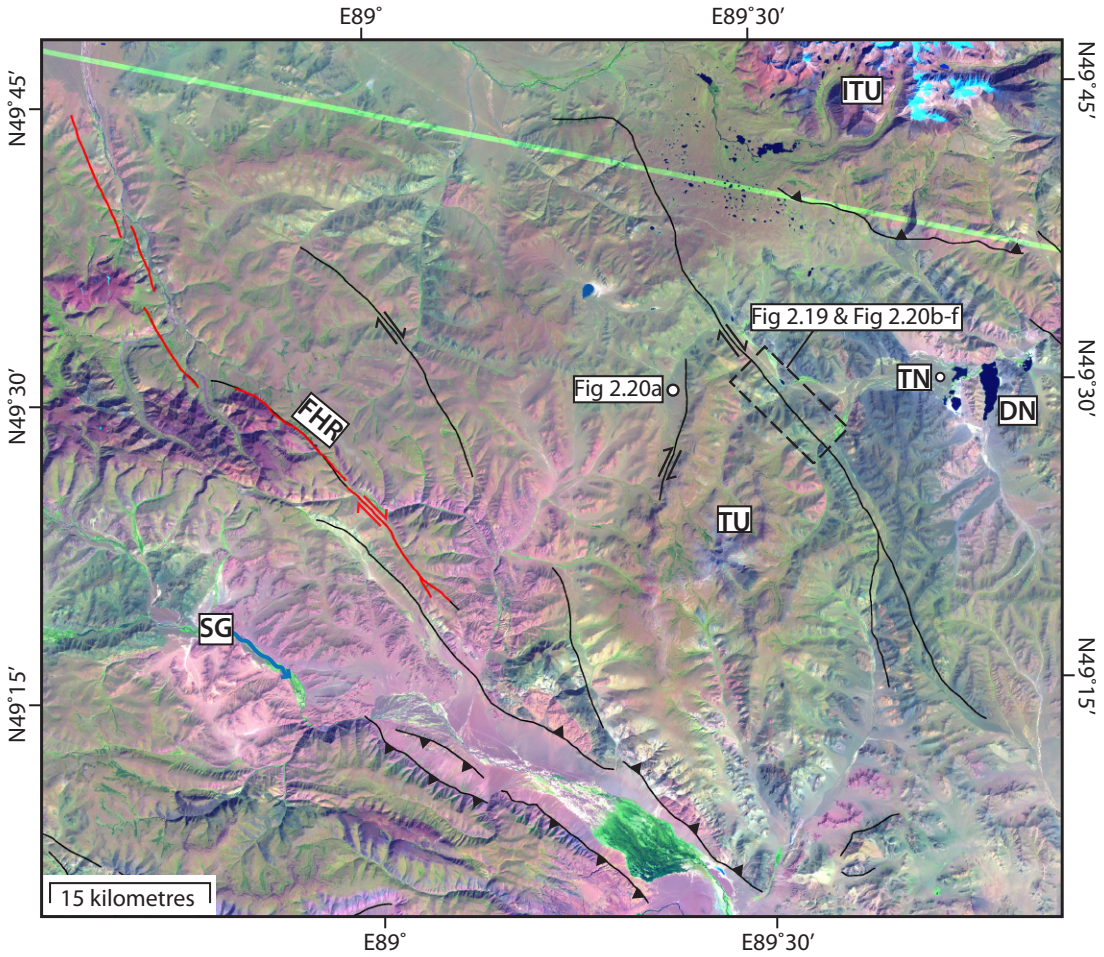


**Figure 2.18:** Landsat image of the active faults surrounding Tas Uul (RGB = 741). Active faults are mapped in black, ancient surface ruptures are in red. Figure 2.19a is indicated by a black dashed rectangle. Abbreviations are: DN = Dün Nuur, FHR = Fiery Horse Rupture, ITU = Ih Turgen Uul, SG = Sogoom Gol, TN = Tsagaannuur (town), TU = Tas Uul.

South of the Mongolian-Siberian border, there are active faults surrounding Tas ('vulture') Uul, and I group these strands with the Ölgiy fault zone, though they are not continuous with the main Ölgiy fault. There is evidence of Late Quaternary faulting along several ridges to the west of Tsagaanuur Town (Figure 2.18), as discontinuous linear scarps in alluvium (Figure 2.20a) and tension fissures and continuous linear scarps (Figures 2.19, 2.20b–f). In Figure 2.19, the fault can be traced continuously and probably has a dip-slip component, up on the southwest side, in

places where there is a sharp change in slope at the fault (Figure 2.20c), though elsewhere the fault strikes across Quaternary alluvium and does not seem to influence relief (Figure 2.19c,d). The strike of the fault is between 320° to 330°, and discrete sag ponds that are 2 to 5 m wide, up to 10 m long, and less than 1 m deep were documented in the field (Figure 2.20d). There is some evidence for displaced streams, however it is difficult to confirm that the right-lateral offsets in several streams are a result of faulting, because the change in slope at the fault may affect the course of the stream (Figure 2.19b and 2.20d). A well-defined series of left-stepping tension fissures and mole tracks are visible in Ikonos imagery through an alluvial fan (imagery from Google Earth, Figure 2.19c, d). It is possible that this section of faulting is a palaeo-surface rupture, but the full length of the 'rupture' was not found in the field, so I have included it in this section to confirm a previously-unknown active strand of the Ölgiy fault.

On the western side of Tas Uul, there is a previously unknown surface rupture, the Fiery Horse rupture, that is described in Section 2.4. There are probably several other active faults in the region, uplifting the southwest side of Tas Uul (Figure 2.17). There is little evidence for active faulting in the region to the south of Tas Uul and north of the city of Ölgiy, making it difficult to connect the faults surrounding Tas Uul with the main Ölgiy fault (Figure 2.17), although the faults south of Ölgiy are in line with, and have the same strike as, the Fiery Horse and Chuya earthquake ruptures (Figure 2.17).

There is evidence of Quaternary faulting on the western side of the low mountains that are directly west of Ölgiy city (pop. approx. 30,000), surrounding what I call 'Ölgiy Uul' (Figure 2.17). These mountains, along with Hungui Uul to the south, are an excellent example of the correlation between the direction of a fault's strike and its sense of slip; where the fault strikes ∼NW–SE, it has a dip-slip component uplifting Ölgiy Uul and Hungui Uul, confirmed to be reverse in places where the fault

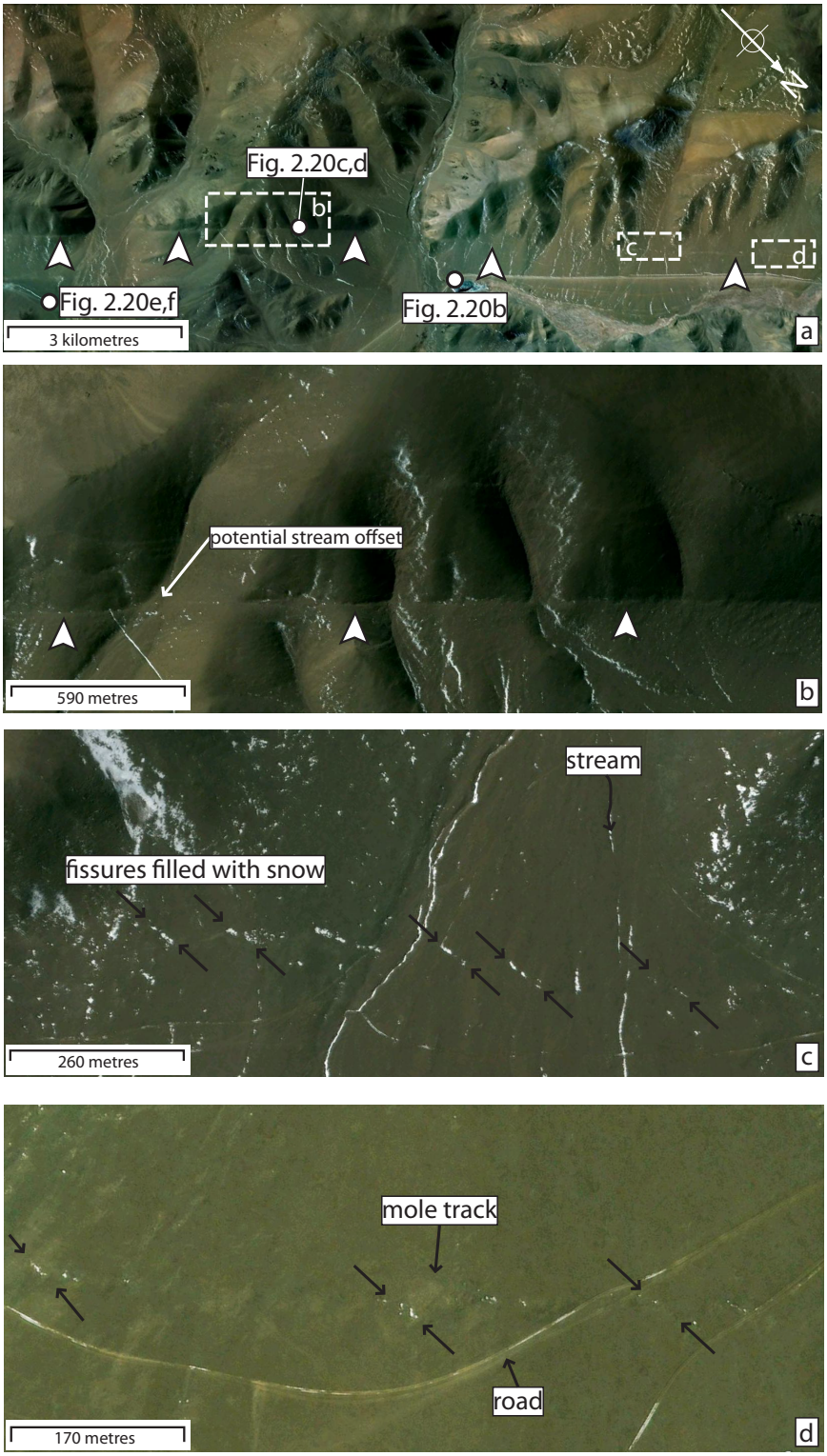


**Figure 2.19:** IKONOS imagery, from Google Earth, of the Ölgiy fault on the northern side of Tas Uul. (a) Evidence of Quaternary faulting is clear in across the centre of the image, located in some places at the base of local relief (left side) and elsewhere can be traced several 100 metres away from the range front (right side). In (b), the fault is observed to have a dip-slip component, and there is also stream that is potentially displaced right-laterally by faulting. (c) shows left-stepping tension fissures in Quaternary alluvium (indicated by arrow pairs), which are easy to see because they are filled with snow. In (d) there are more tension fissures with some snow, with mole tracks that show up as lighter bumps because they reflect illumination from the sun (from the top of the image, i.e. southwest). Photos in Figure 2.20 are indicated by white circles.

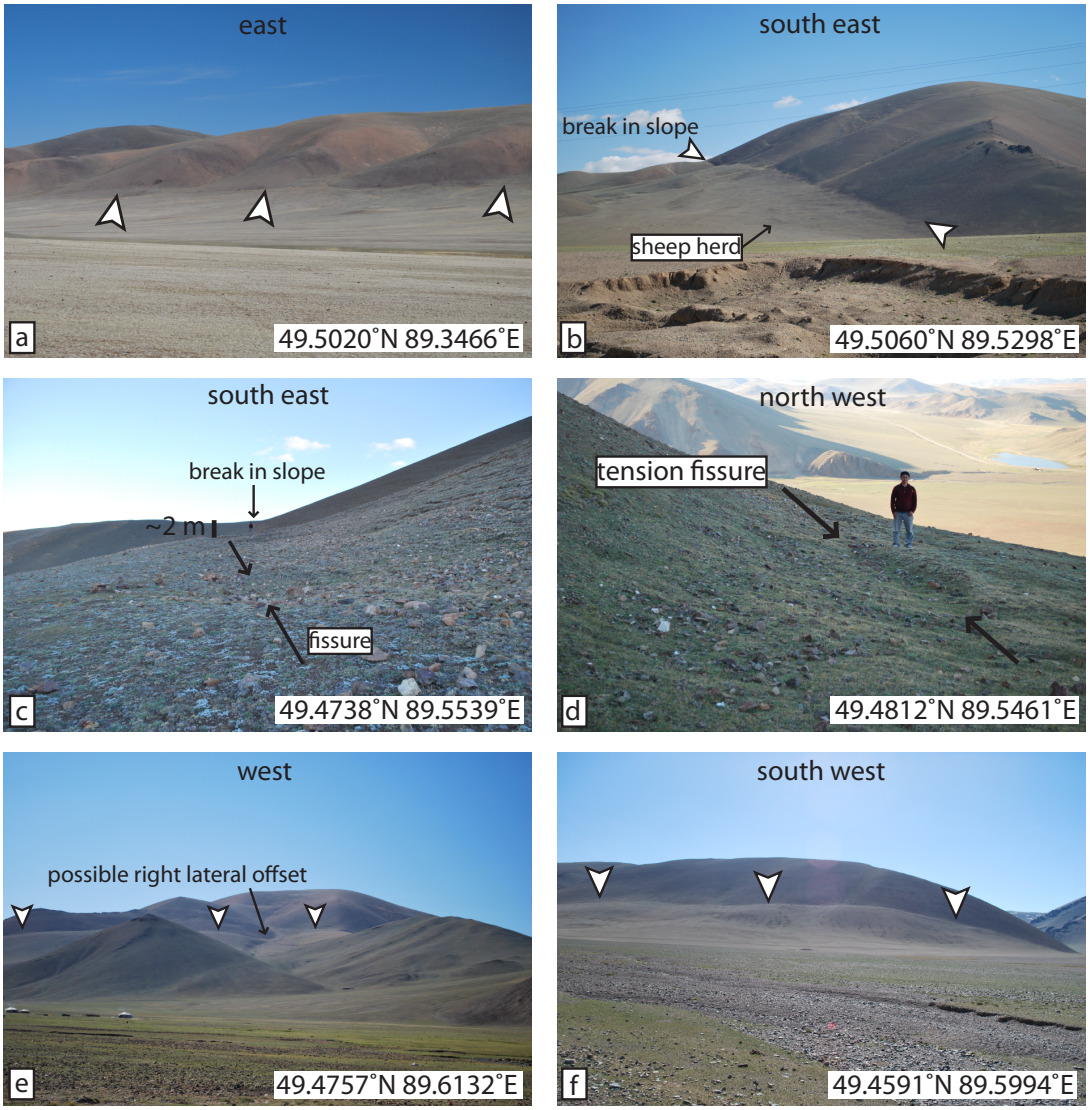


**Figure 2.20:** Photos of the Ölgiy fault on the northern side of Tas Uul. (a) A linear scarp cuts through Quaternary alluvium as well as the range front on the north western side of Tas Uul. (b) A clear scarp runs up the slope of a ridge near Tsagaannur town. Active faulting has produced a sharp break in slope on the horizon. (c) and (d) are from the scarp in (b). In (c) there is a break in slope along the fault at both the horizon and in the middle distance (where person stands), and a small fissure in the foreground. In (d) there are clear tension fissures that have long axes approximately parallel to the strike of the fault. (e) A right-lateral offset in a stream flowing off the ridge, possibly offset by faulting. (f) The continuation of the scarp further to the south of (b).

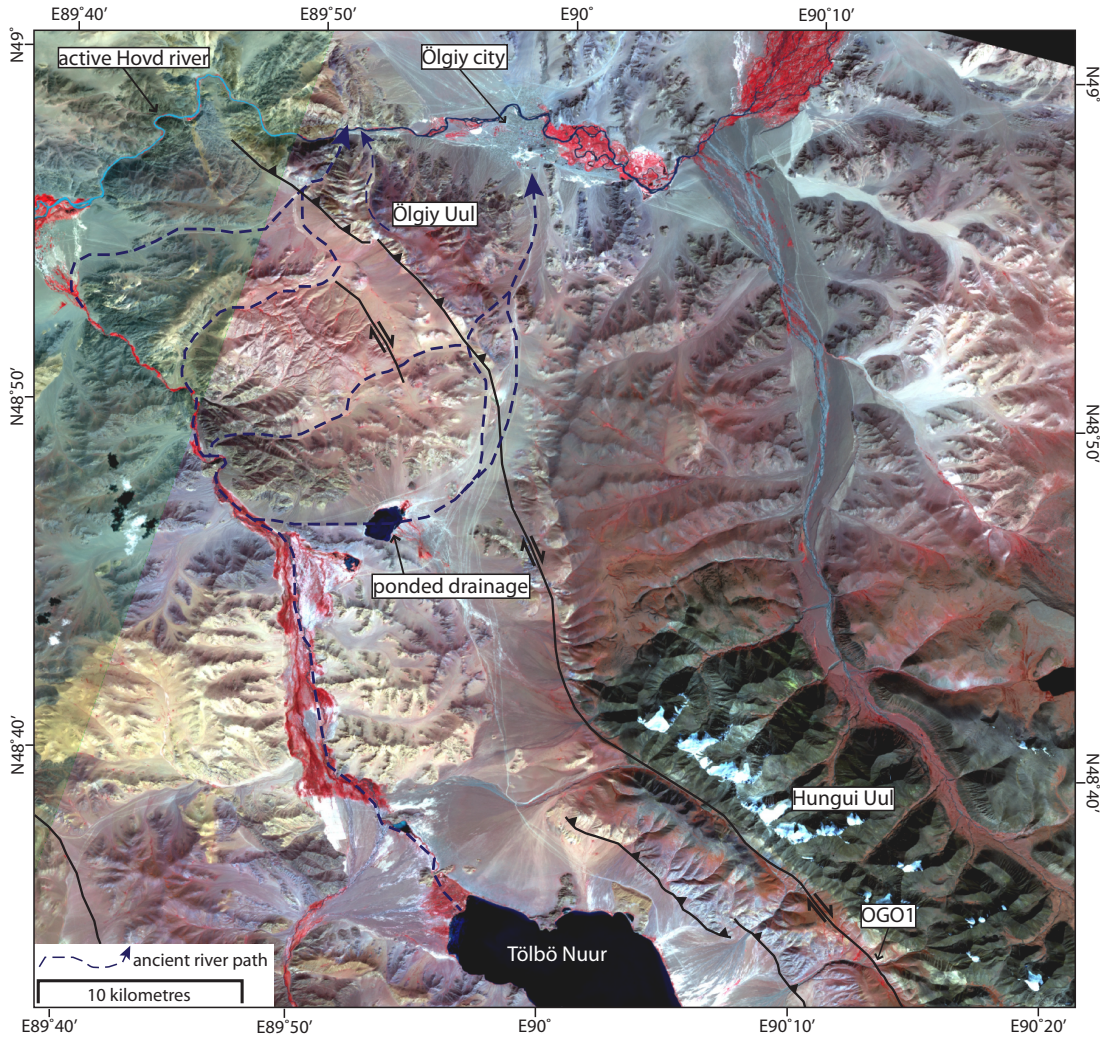


**Figure 2.21:** ASTER imagery of dry valleys along the Ölgiy fault near Ölgiy city. The dashed lines indicate potential paths where the Hovd river, as well as drainages from Tölbö Nuur, may have flowed in the past. Several of the ancient river courses carved steep gorges in the mountains. Where the fault strikes more to the west, there is a significant dip-slip component uplifting Ölgiy and Hungui Uul. Black lines indicate active faults. The through going strike-slip fault in Hungui Uul preserves dextral stream displacements, one of which is indicated by OGO1 (as listed in Table 2.3).

outcrops at the base of Hungui Uul. The two mountain ranges are separated by a flat valley, which the Ölgiy fault crosses with a more northerly strike of 340°–350°and accommodates pure strike-slip motion, based on the presence of a recent strike-slip surface rupture (the Sair Uul rupture, Section 2.4) across the valley and the lack of a vertical scarp. The newly discovered Sair Uul surface rupture terminates at the base

of Ölgiy Uul (Figure 2.17), where the rupture features suggest a significant reverse component, whereas the remainder of the rupture to the south is nearly pure strike-slip. The region surrounding Ölgiy Uul and Hungui Uul also has clear evidence of the effect of active dip-slip faulting on drainage patterns. The Hovd river currently flows to the east through a steep gorge in Ölgiy Uul, but there are several steep dry valleys carved into the mountains where the river may have incised as the growth of topography progressed (Figure 2.21). The valley between Ölgiy Uul and Hungui Uul is also a dry valley, as it is possible that drainages from Tölbö Nuur flowed north to join the Hovd river, but the valley was abandoned due to faulting in the region. There are several shallow ponds in the region, which appear to have formed as the through-going drainage networks were abandoned (Figure 2.21).

Along Hungui Uul (Mongolian for 'no humans mountain') on the eastern side of Tölbö Nuur, the Ölgiy fault breaks into parallel reverse and strike-slip strands where there is a left-stepping bend in the main Ölgiy fault zone (Figure 2.21). The fault has a half-flower structure in cross-section, with the frontal dip-slip fault branching off from the main through-going strike-slip fault, based on the morphology of the faults at the surface and the style of dip-slip faulting observed at the range front in the field in outcrop (shown schematically in Figure 2.22). The strike-slip strand cuts through high topography, where drainages are located parallel to the fault in a steep gorge behind the range front (Figure 2.22). There are right-lateral offsets of 1–2 km in some of the major drainages along this portion of the fault, confirming dextral slip on the main through going portion of the fault. There is a step in elevation across the strike-slip fault through Hungui Uul, and presumably the fault was initially an oblique-slip fault, but the shortening component of slip has since migrated to the south as a separate structure. Faulting expressed as a flower structure in cross-section is characteristic of a left-step in the strike of Altay fault zones (e.g. *Cunningham*, 2007).

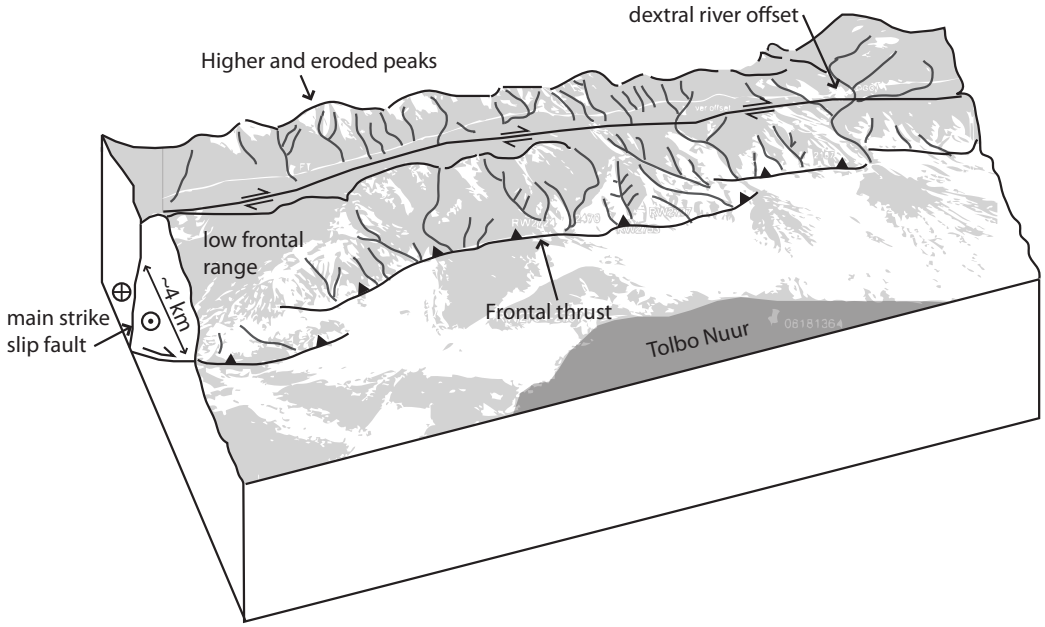


**Figure 2.22:** Diagram of the Ölgiy fault at a typical left-stepping compressional bend, overlain on a Google Earth image of the bend in the fault near Tölbö Nuur, forming Hungui Uul (shown in map view in Figure 2.21). The fault has produced a flower structure in cross-section, with reverse slip partitioned onto faults at the front of the range, and a through-going main strike-slip fault that has created a valley behind the range front. Several rivers are displaced along the strike-slip linear valley. Total relief (from high peaks to the range-front reverse fault) is ∼1.5 km, and the strike-slip strand is ∼4 km from the range-front thrust (which dips ∼40–55° from field measurements in outcrop).

The frontal thrust has uplifted several abandoned alluvial fans by 6 to 12 m (Figure 2.23a, b). Along the base of these fans, recent uplift has exposed outcrops of fault gouge, with scarps in the alluvium above the gouge outcrops (Figure 2.23). One gouge zone approximately 50 m wide is exposed in a river gulley. The faulted rocks are topped by a shallow eastward-dipping (less than 10°–20°) alluvial layer approximately 1 m thick. In outcrop, the fault gouge dip shallows towards the surface, from 40°–55° at the base of the outcrop to ∼20° at the surface (Figure 2.23c). The gouge is composed of green to blue-grey schist with quartz veins and a moderate foliation that follows the dip of the fault zone. The schist rocks grade into quartzite schist away from the range front, with the active fault scarp in the alluvial

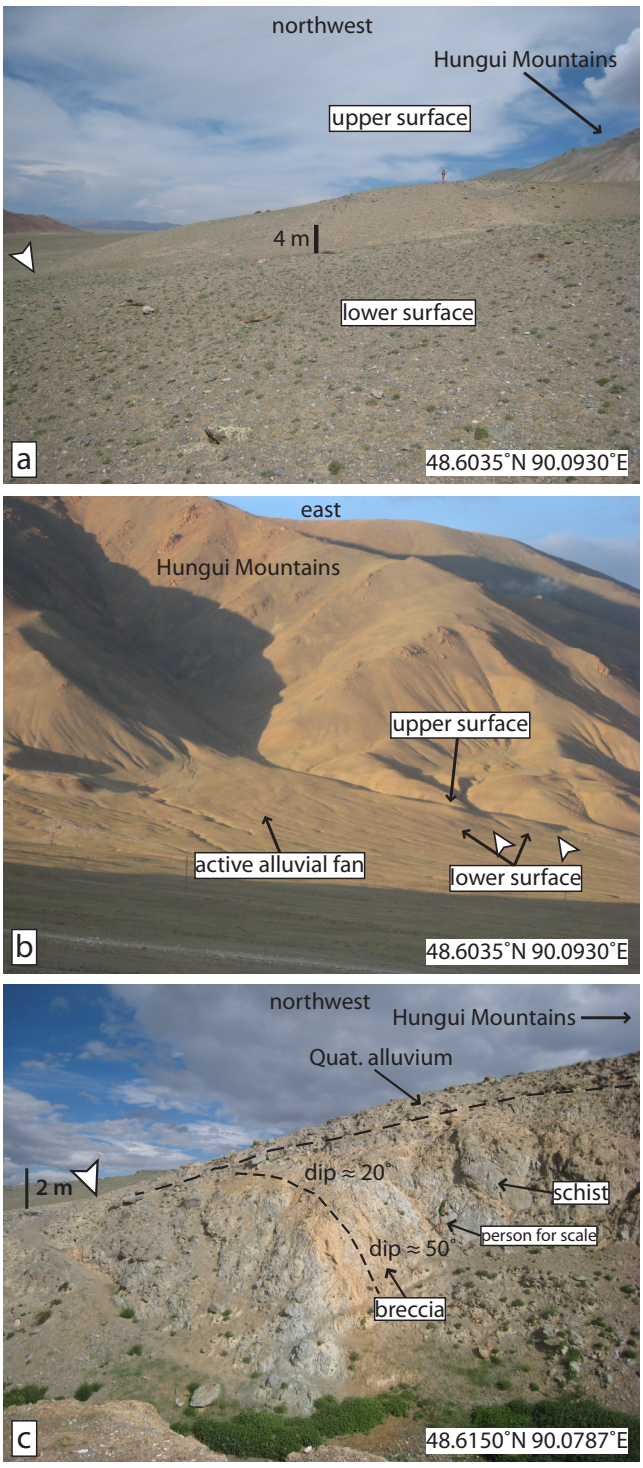


**Figure 2.23:** (a) and (b) are field photos of remnant alluvial fan surfaces uplifted by cumulative motion on the Hungui Uul thrust fault. There are two abandoned surfaces uplifted above the active fan level visible in (b). The upper surface is probably an older remnant, and has accommodated more dip-slip motion than the lower surface. (c) shows a brecciated fault zone in outcrop, exposed by a stream cutting through recently uplifted material. The fault rocks dip shallowly near the surface, but are more steeply dipping with depth (orientations traced by dashed lines). White arrows indicate the location of an active fault trace. Location of photos is indicated in Figure 2.17.

cover located above the fault gouge outcrop (Figure 2.23c). The entire fault zone that is exposed is highly altered with orange and red mineralised rocks throughout. Other fault exposures were found in river gulleys along the section of the fault north of Tölbö Nuur, on the western side of Hungui Uul where the fault strikes more to the north (330°–350°, at 48.7083°N, 90.0072°E). At this locality, the fault accommodates mostly strike-slip motion and the dip of the fault in the exposures is nearly vertical, between 80°–90° and shallowing close to the surface. Dextral-slip tension fissures from the Sair Uul rupture were observed in the overlying alluvium directly above the vertical fault exposure.

South of Hungui Uul and Tölbö Nuur, there is a triangular restraining-bend mountain called Sair Uul (Mongolian for 'dry mountain'). Sair Uul is bound on three sides by oblique dextral-reverse faults (Figure 2.17). The southern termination of the Sair Uul surface rupture occurs on the western side of Sair Uul (Section 2.4). There is evidence for multiple fault strands surrounding the mountain, with several scarps observable in satellite imagery and the field, as well as steepened gulleys on the upthrown side of reverse faults (Figure 2.24 and Section 2.4). The shape in map view of Sair Uul is very similar to the much larger Tsambagarav Uul directly northeast (see Figure 2.10 compared with Figure 2.17). The peaks of Sair Uul host valley glaciers and reach just over 3900 m.

*Frankel et al.* (2010) measured slip rates on the Höh Serh-Tsagaan Salaa strand in the central portion of the Ölgiy fault zone, south of Sair Uul. They determined rates for two strands of the fault: the eastern Höh Serh fault that accommodates dextral motion and the western Tsagaan Salaa fault that accommodates reverse motion (Figure 2.25). With dextral and reverse slip partitioned onto the two faults, they found separate right-lateral and shortening slip rates of $0.9 + 0.2/-0.1$ mm yr$^{-1}$ and $0.3 \pm 0.1$ mm yr$^{-1}$, respectively. Offsets were measured using SPOT satellite imagery and DEMs produced by differential GPS in the field, and the displaced surfaces were

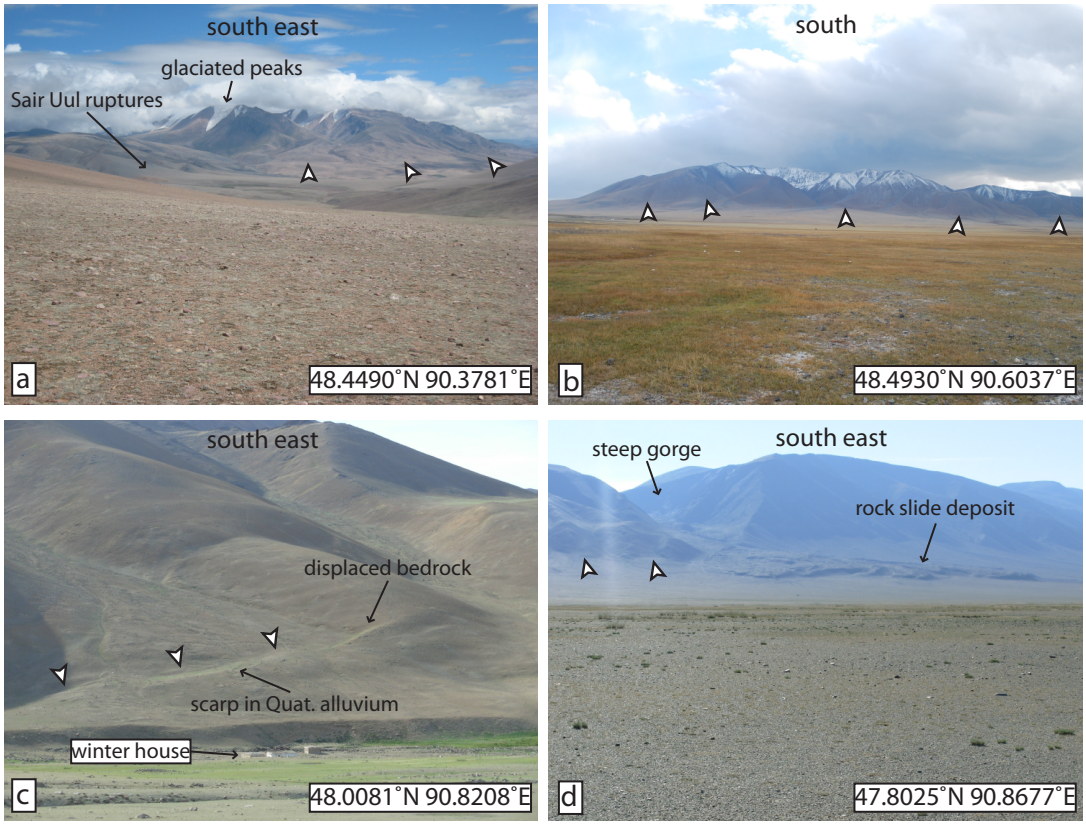


**Figure 2.24:** Photos from the central Ölgiy fault. (a) shows the glaciated peaks of Sair Uul from the western side of the mountain, with the locality of the Sair Uul ruptures and range bounding thrusts indicated. (b) is a photo of the north eastern side of Sair Uul, with reverse faulting lineations in Quaternary cover indicated. The locality of the slip rate study in *Frankel et al.* (2010) is indicated in (c). A clear right-lateral displacement of the bedrock-alluvium contact is indicated, as well as fault scarps. (d) is a photo of the large debris flow along the Höh Serkhiin section of the Ölgiy fault. Photo localities are indicated on Figure 2.17 (a,b) and Figure 2.25 (c, d).

dated with $^{10}$Be cosmogenic nuclides on individual large cobbles and boulders. The strike-slip rate is derived from dextral offsets of $17.5 \pm 4.5$ m and $15.7 \pm 6.5$ m of channels in an alluvial fan and the offset of the contact between a bedrock ridge and alluvium of $19.3 \pm 2$ m (Figure 2.24c). The average offset of $17.5 \pm 1.8$ m, is divided by the weighted mean age of $18.8 \pm 2.6$ kyr (from 5 samples) to calculate the dextral slip rate of $0.9 + 0.2/-0.1$ mm yr$^{-1}$. The shortening slip rate comes from a fault scarp in late Pleistocene alluvium. The scarp height ranges between $4.2 \pm 0.5$ m and $6.4 \pm 0.5$ m with a mean of 5.5 m and standard deviation of 1.2 m.

Ages for the alluvium at this site are between $38.6 \pm 3.5$ and $58.5 \pm 5.3$ kyr with a mean of 44.8 kyr and standard deviation of 6.8 kyr. Age results are tightly clustered and consistent with a single population, in terms of their probability distribution function (pdf). The slip rate at this site was calculated by converting a vertical uplift rate of 0.1 mm $yr^{-1}$ to a horizontal shortening rate of $0.3 \pm 0.1$ mm $yr^{-1}$ with an observed fault dip of 25°.

To the east and continuing south of the slip rate sites lie Höh Serkhiin Nuruu (Mongolian for 'Blue Wild Goat Mountains'), which are formed along nearly 100 km of the Ölgiy fault zone as part of a transpressional bend (Figure 2.17). The fault has a reverse component along the base of the mountains, evidenced by reverse scarps in the foreland alluvium and steep drainages in the hanging wall of the fault. The Höh Serkhiin range is asymmetric in cross-section, with a much steeper western range front, bounded by the Höh Serh fault. Along a section of the fault where strike-slip and reverse components are partitioned onto separate strands, cumulative river displacements of 0.5 to 4.0 km are preserved due to the fault cutting through topography (Figure 2.25a). Mole tracks and tension fissures were also observed in the field along this strand (*Frankel et al.*, 2010). Further south along the Höh Serkhiin range, there is a large rock slide at the exit of a steep gorge (Figure 2.25b, 2.24d). South of the Höh Serkhiin Uul, the location and existence of active faulting is difficult to determine, and little is known about the active faulting in this part of the Altay. It was not possible to follow clear fault features in the field, as the southern continuation of the Ölgiy fault, if it does continue, is through high topography with difficult access. At this southern extent of the Ölgiy fault, an approximate fault trace is mapped based on available Landsat imagery, but this trace has not been ground-truthed.

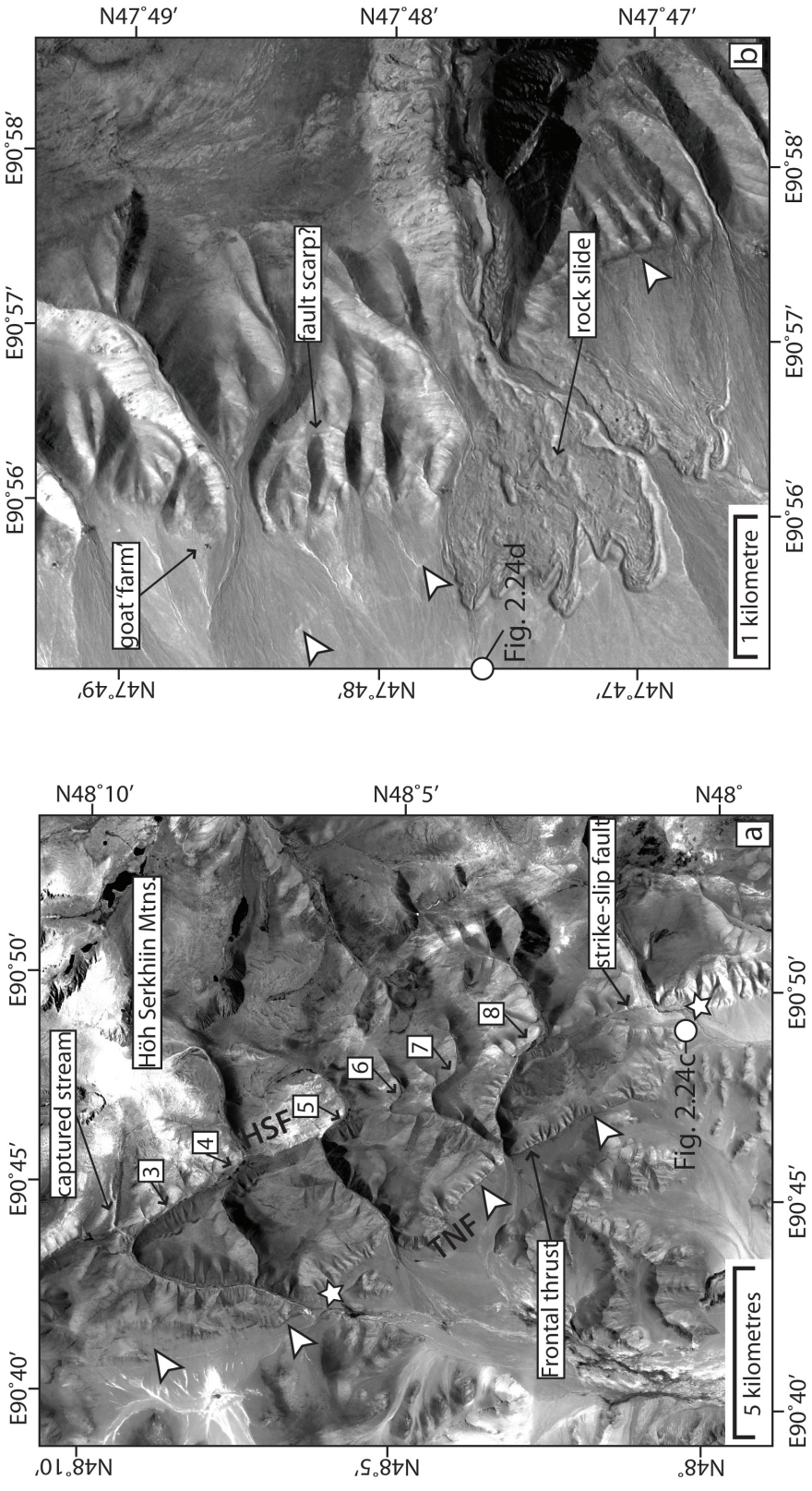


**Figure 2.25:** SPOT imagery of the Höh Serkhiin Uul. (a) Several drainage displacements occur where the faulting is partitioned into dextral strike-slip and reverse faulting, each number corresponds to an offset listed in Table 2.3, i.e OGO3 is the most northerly drainage offset in the figure. The stars indicate the localities of slip rate studies in *Frankel et al.* (2010). (b) A large rock slide along the main range-bounding fault. The exact surface trace of the fault is ambiguous, and may be close to the mountain range, where a dark lineation is visible, or located a few hundred metres away from the range front, where vertical scarps were observed in the field (and indicated by arrows in the figure).

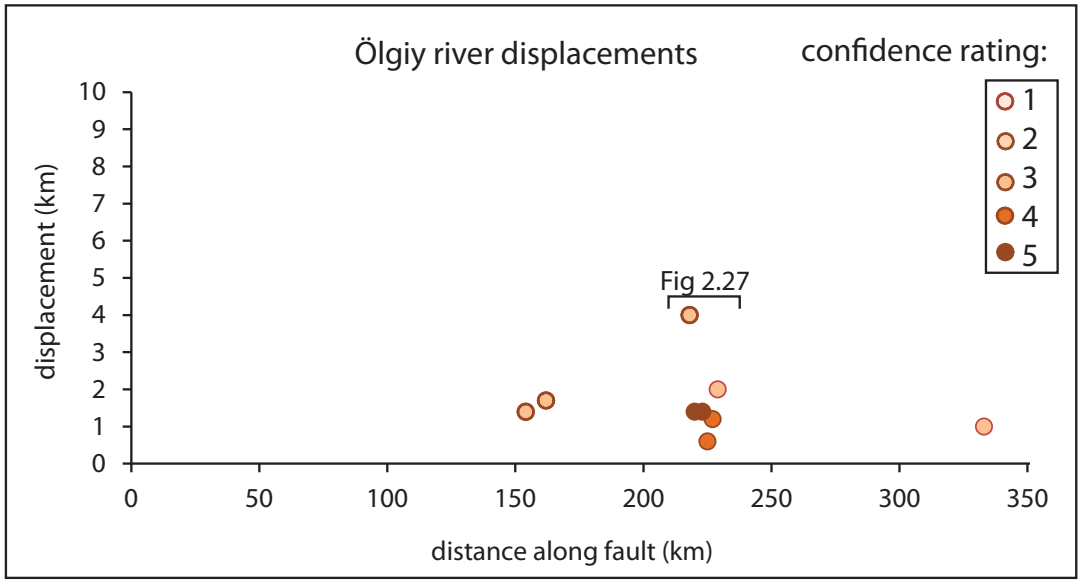


**Figure 2.26:** Plot of river displacements from north to south along the Ölgiy fault zone. Different shades of orange represent the level of confidence in each measurement, with lighter colours representing lower confidence and darker colours representing higher confidence. The criteria for assigning confidence levels are outlined in Section 2.2.3.

### Cumulative displacement

River displacements on the Ölgiy fault are preserved along sections where the fault strikes through topography, and as on the Hovd fault, there are no large river or stream displacements in places where the fault is located at the base of a range front (Section 2.3.2). Offsets are displayed in Figure 2.26 and listed in Table 2.3. Large-scale offsets on the Ölgiy fault have a more restricted range than offsets on the Hovd fault, with measurements between 500 m and 4.0 km. Stream displacements OGO1 and OGO2 occur within the Hungui Uul where the Ölgiy fault is partitioned into strike-slip and reverse faulting, and cumulative strike-slip offsets are likely to be less than on portions of the fault that are mostly strike-slip (Figures 2.21 and 2.22). These offsets are minimum estimates of cumulative fault slip, because the streams did not exist prior to the uplift of the Hungui Uul, and any right-lateral motion on the fault prior to mountain building (if there was any) would not be represented

**Table 2.3:** Ölgiy river displacements

| Offset name | Offset amount (km) | Confidence | Latitude (°N) | Longitude (°E) |
|---|---|---|---|---|
| OGO1 | 1.4 | 3 | 48.5789 | 90.2191 |
| OGO2 | 1.7 | 3 | 48.5345 | 90.3030 |
| OGO3 | 4.0 | 3 | 48.1403 | 90.7449 |
| OGO4 | 1.4 | 5 | 48.1254 | 90.7563 |
| OGO5 | 1.4 | 5 | 48.0993 | 90.7777 |
| OGO6 | 0.6 | 4 | 48.0830 | 90.7884 |
| OGO7 | 1.2 | 4 | 48.0697 | 90.7985 |
| OGO8 | 2.0 | 3 | 48.0525 | 90.8027 |
| OGO9 | 1.0 | 3 | 47.3153 | 91.5936 |

in the stream displacements. Offsets OG01 and OG02 also have a relatively low confidence rating, because the bending of the stream at the fault could be a result of the change in topographic gradient as the streams cross the fault, rather than cumulative right-lateral motion.

Figures 2.25b and 2.27 show at least six drainage displacements (OGO4–OGO8 in Table 2.3) along another section of the Ölgiy fault where active faulting is partitioned into strike-slip and reverse components, onto the Höh Serh and Tsagaan Salaa segments respectively. The displacements are only preserved where there is topography on both sides of the strike-slip fault, and like the displacements along Hungui Uul discussed above, the stream displacements are probably not representative of the absolute total cumulative horizontal motion on the Ölgiy fault because the streams were probably initiated after the growth of topography. Figure 2.27b–d show different increments of displacement. For displacements of 0.9, 1.4, and 4.2 km, different drainages are progressively restored across the fault. The restoration of streams at different cumulative displacements may imply that the maximum amount of 4.2 km represents the cumulative offset along this portion of the fault, which approximately reconstructs offset OGO4 listed in Table 2.3, and smaller displacements may represent successive stream capture and the progression of displacement through time. However, the maximum displacement may be an overestimate, because if the

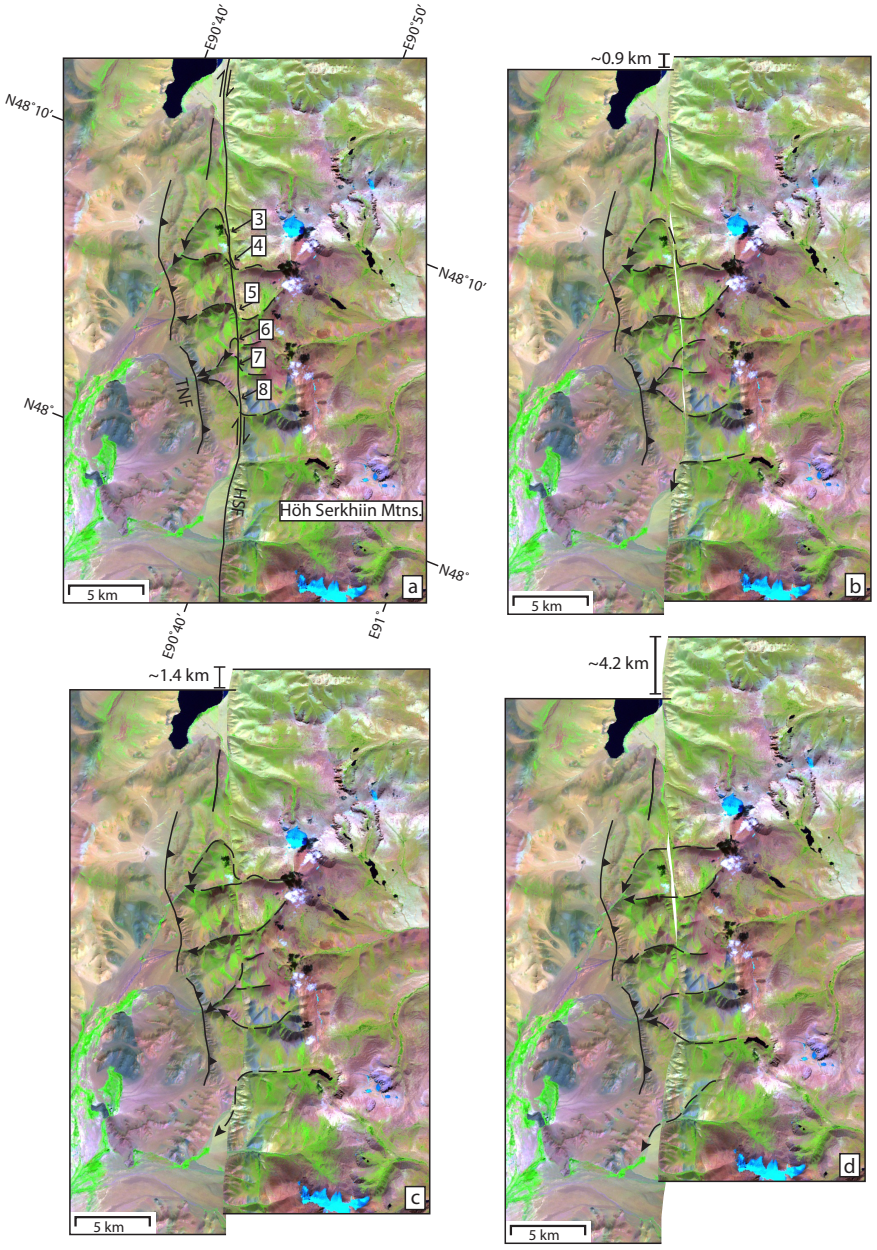


**Figure 2.27:** Landsat imagery of at least 6 stream displacements along the Ölgiy fault. (a) Numbers 3–8 correspond to offsets listed in Table 2.3. (b) to (d) represent increasing amounts of reconstruction of right-lateral displacement along the Höh Serh strike-slip fault.

drainages are coincidentally equally spaced, restoring by greater amounts than the actual fault-displacement could realign drainages that were not actually connected in the past.

### 2.3.4 The Sagsay Fault Zone

The Sagsay fault zone consists of several strands that together are at least 400 km long and strike roughly NNW–SSE (Figure 2.28). The fault has a significant reverse component in places, where several linear mountain ranges are uplifted along westerly transpressional bends in strike (e.g. Buyant Uul). Where the fault strikes NNW–SSE, the sense of slip appears to be predominantly strike-slip, and cumulative river displacements are preserved. The Sagsay fault zone is best known for the Sagsay surface rupture, which was first reported by *Khil'ko et al.* (1985) and later described by *Baljinnyam et al.* (1993). *Khil'ko et al.* (1985) suggested that long-term deformation along the Sagsay fault is not significant, but in this section I show evidence of clear active faulting and large cumulative displacements along the entire Sagsay fault zone, suggesting that it is an important component of active deformation in the Altay.

At the northern end of the Sagsay fault and near the village of Sogoog, Sogoog Uul seems to be uplifted along dip-slip faults, which strike about 300° on both the north eastern and south western sides of the mountains (Figure 2.28). In satellite imagery and in the field, dip-slip Quaternary fault scarps and landslide scarps share similar characteristics and they must be carefully distinguished, because both features are a vertical scarp that is several metres high. Stream incision of the upthrown side of the faults and within the landslide material both have more steeply incised channels than the surrounding alluvium, also causing the features to appear similar. However, landslides can be identified in satellite imagery based on their surface morphology (Figure 2.29) and in the field because a landslide scarp is curvilinear, whereas fault scarps are generally straight. There are some places along the Sogoog range front where it is difficult to distinguish between landsliding and faulting, because the main scarp at the crown of a landslide is similar to a discontinuous reverse scarp (e.g. Figure 2.29c), and in order to attribute a scarp to faulting, one must be sure there

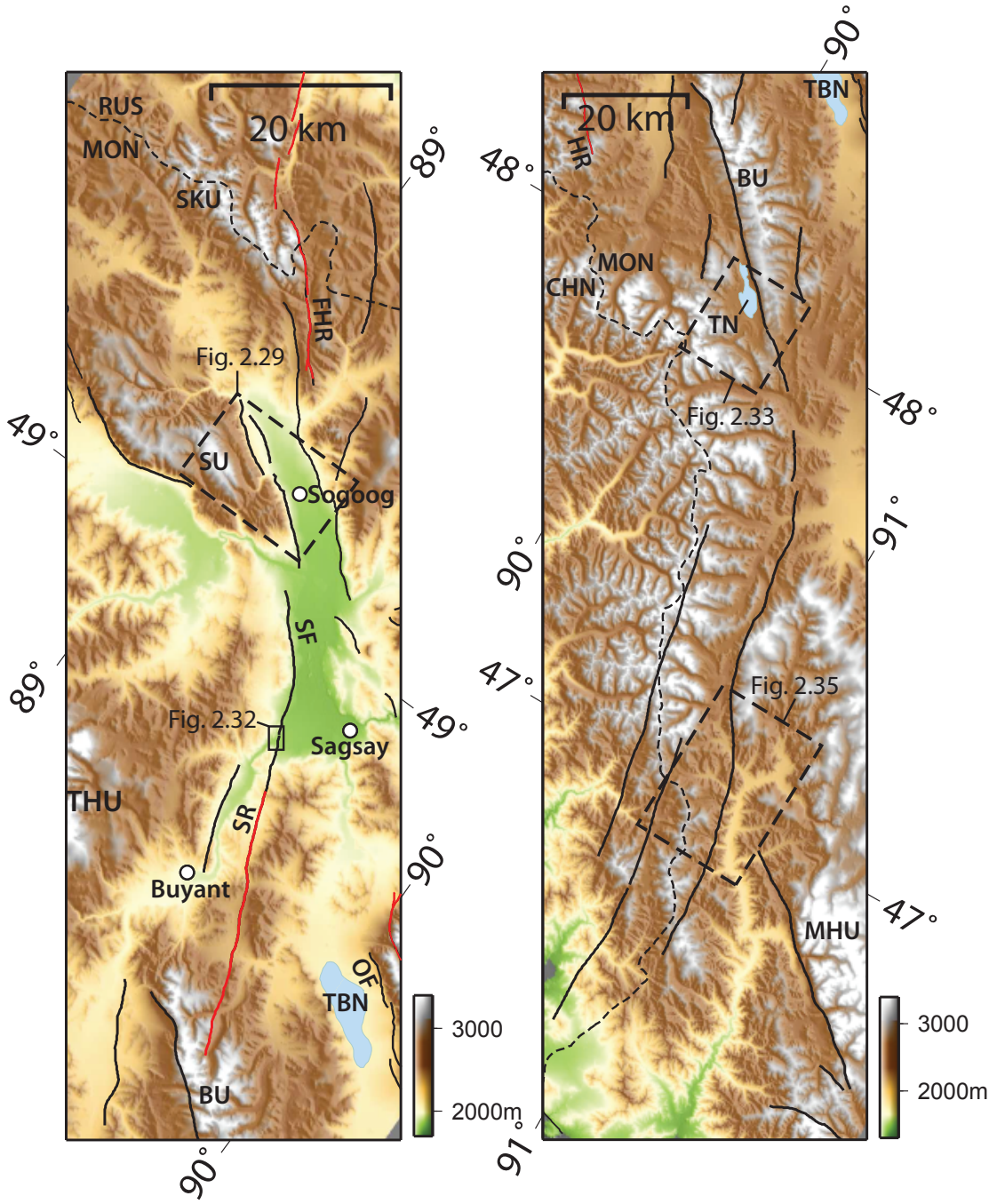


**Figure 2.28:** SRTM DEM of the northern and southern Sagsay fault zone. Active faults are mapped in black and ancient earthquake ruptures are mapped in red. Political boundaries are mapped as dashed lines. Abbreviations are: BU: Buyant Uul, CHN: China, FHR: Fiery Horse Rupture, HR: Hoton Rupture, MHU: Monh Hyarhan Uul, MON: Mongolia, OF: Ölgiy Fault, RUS: Russia/Siberia, SF: Sagsay Fault, SKU: Siilkhem Uul, SR: Sagsay Rupture, SU: Sogoog Uul, TBN: Tölbö Nuur, THU: Tsengel Hyarhan Uul, TN: Tal Nuur.

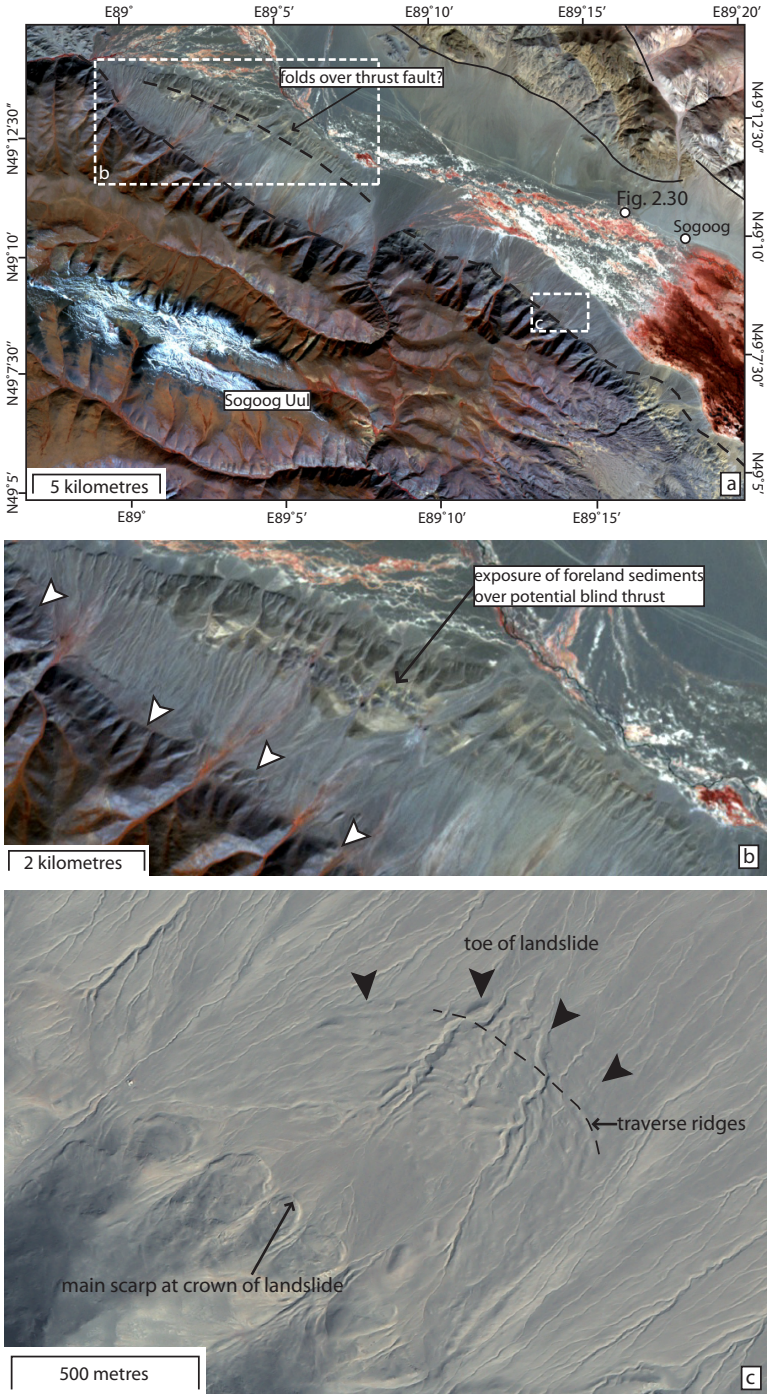


**Figure 2.29:** ASTER (a and b) and Kompsat-2 panchronomatic (1 m/pixel) (c) imagery of landslides and and presumed faults in Quaternary alluvium along the Sagsay fault near the city of Sogoog. (a) Dashed black lines are presumed traces of faults at the base of Sogoog Uul and in the foreland of the mountain range. Locations of (b) and (c) are indicated. In (b), buff coloured units outcrop in the foreland of Soogog Uul over what is possibly a blind thrust fault (similar to the exposure in the Dzereg Basin, in Chapter 4). Vertical scarps at the range front are indicated by white arrows, but it is unclear whether these are due to active faulting or are scarps of fossil landslides. (c) The vertical scarp at the toe of the landslide indicated by black arrows, which can be distinguished from a fault scarp based on the presence of traverse ridges and a main scarp at the crown of the landslide. The toe scarp is also irregular, which would not be expected from a linear fault.

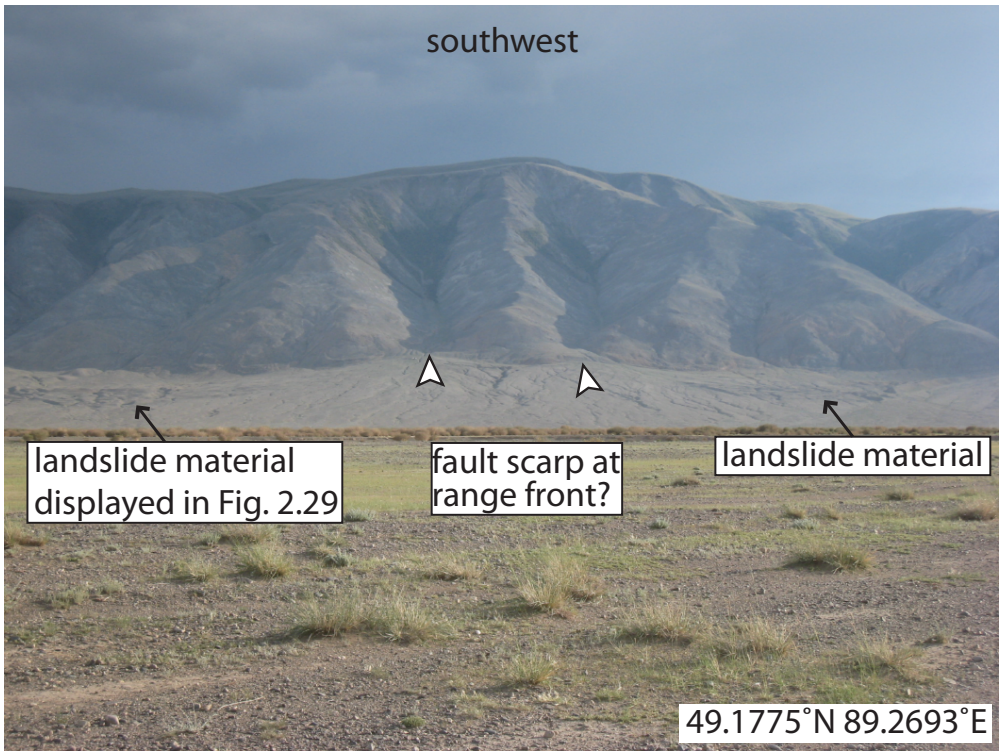


**Figure 2.30:** Photo of landslides and fault scarps along the northern margin of the Sogoog Uul. Both the landslide material and fault scarps have led to stream incision that is visible in the photo, but the scarp at the toe of the landslide material has a more rounded and irregular shape. Potential fault scarps are also much closer to the range front in this photo. Photo locality is shown in Figure 2.29a.

is no fossil landslide material downslope from the scarp. 'Blind' thrusts can also be difficult to identify. In the foreland of the northern strand of the fault that bounds Sogoog Uul, there is a broad zone of uplifted material located several kilometres in the foreland of the range (Figure 2.29a,b). The ridge of buff and grey-coloured material in Figure 2.29b is possibly basin sediments uplifted over a blind thrust fault.

South of Sogoog, near the town of Sagsay, the fault strikes about 320° and has a strike-slip component that is expressed by stream displacements where the fault cuts across a series of Quaternary alluvial fans, similar to the fault trace visible in Figure 2.32 further to the south. Samples for optically stimulated luminescence (OSL) dating were collected in 2009 from a pit in the fan surface, and are currently

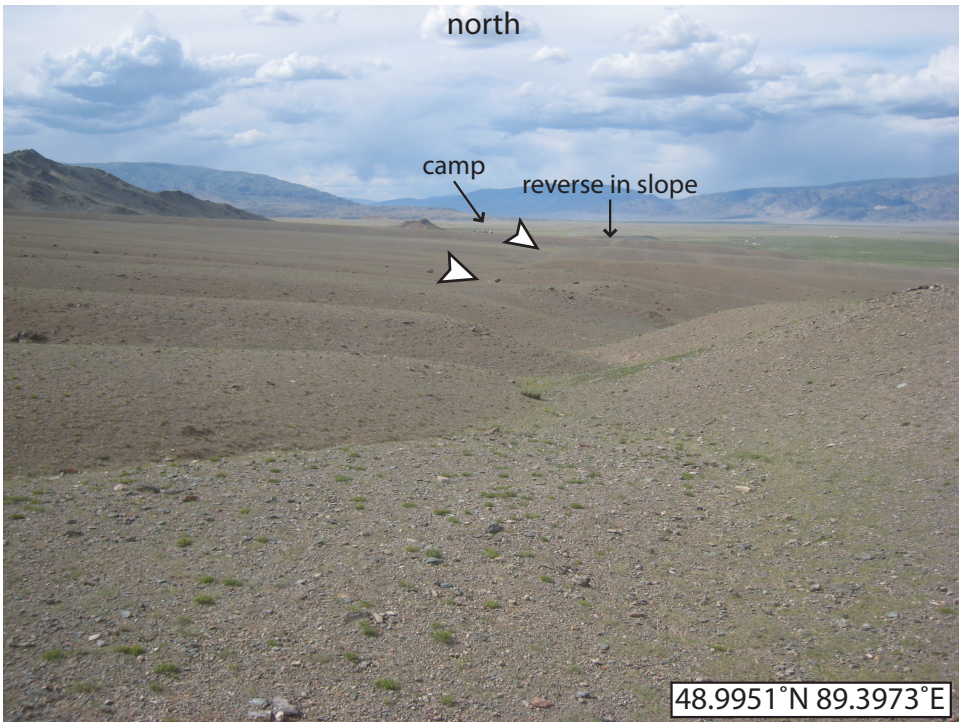


**Figure 2.31:** Photo of fault scarp in Quaternary alluvium. The scarp has a slight reverse component, uplifted on the east side (right of image), causing a reverse in slope along strike. White arrows point to the scarp (Photo R. Walker).

being processed (Figure 2.31).

The Sagsay fault is clear in Kompsat-2 imagery near where it crosses the Sagsay tributary of the Hovd Gol (Figure 2.32). On this section of the fault, the Quaternary expression suggests mostly strike-slip motion, with a series of sag ponds and mole tracks that are around 50 m long and 1–2 m deep (Figure 2.32b). Where the fault crosses a large alluvial fan, the trace appears to have a vertical component that uplifts material on the east side of the fault, opposite to the gradient of the fan surface and what would be expected from local topography (Figure 2.32c). The discontinuous reverse scarps occur along a portion of the Sagsay fault that is mostly strike-slip, and are probably a local feature, akin to the cumulative growth of mole tracks due to irregularities in the fault strike near the surface. On the south side of the Sagsay River, the fault seems to break into several strands parallel to and south

a
2 kilometres
Sagsay river
Man-made
drainage channel
b
c
N48°52′
N48°50′
E89°30′
E89°30′
b
sag ponds
bridge built on fault scarp
pressure ridge
400 metres
c
road
winter house
restraining bend
scarps in alluvium
down slope
500 metres

of the Sagsay river. On the south side of the low mountains south of Sagsay town, the Sagsay surface rupture is exceptionally preserved along a 30 km strand of the fault (described below).

South of the Sagsay rupture lies Buyant Uul, also called Mengildyk Uul by *Cunningham* (2007), with glaciated peaks that are over 3600 m high (Figure 2.28). Buyant is a linear mountain range that is formed along a section of the Sagsay fault that strikes 310°. There are several other active strands of the fault in the western foreland of the mountain range (as mapped in Figure 2.28). Fault-related features are particularly clear along the southern end of the mountains, near Tal Nuur (Figure 2.33), whereas recent glaciation and erosion along the higher peaks of Buyant Uul have obscured clear evidence of ground deformation. Northeast of Tal Nuur, there are lineations visible in ASTER imagery at the base of the range, as well as several shutter ridges that have diverted drainages flowing off the mountains (Figures 2.34a and 2.33b). Shutter ridges attest to a right lateral sense of motion, but it is likely that the fault also accommodates reverse slip. Just south of Tal Nuur (where the Sagsay fault dips eastward), the dip-direction of the fault is reversed, uplifting material on the western side of the fault (Figures 2.34b and 2.33c). *Cunningham* (2007) classified the mountain range as the termination of the strike-slip fault southeast of the mountain, but it seems likely that the Sagsay fault on the north side of the mountain range is related to the strike-slip faults to the south.

**Figure 2.32** ***(preceding page)*:** (a) Kompsat-2 imagery of the Sagsay fault expressed in Quaternary alluvium. White arrows indicate the surface trace of the fault. (b) shows a series of sag ponds and pressure ridges, as well as a bridge built on the vertical fault scarp where it crosses the Sagsay river. (c) displays scarps in an alluvial fan, which are expressed as a reverse in the slope that may be due to a reverse component to faulting on this strand (although opposite what may be expected from topography), or are likely a series of cumulative mole tracks.

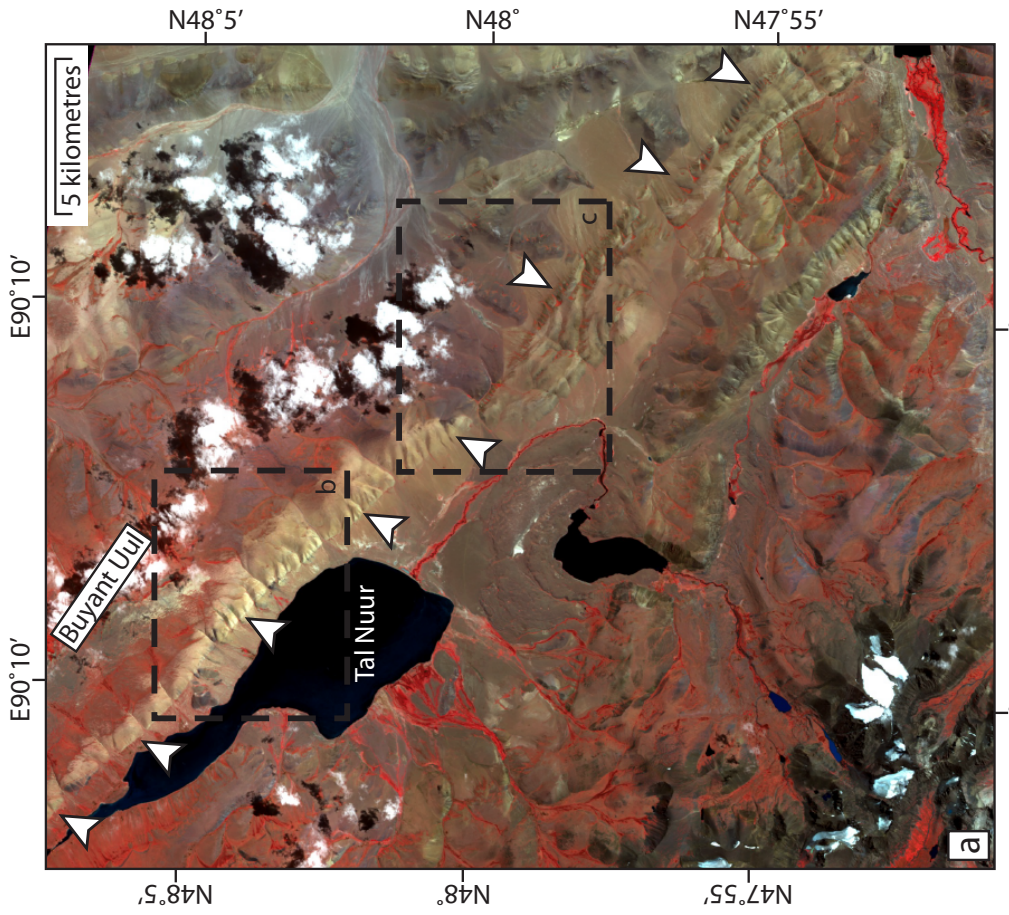


**Figure 2.33:** (a) ASTER imagery of the Sagsay fault along Tal Nuur; white arrows point to the trace of the fault. In (b) there are several shutter ridges along the range front, as well as a linear scarp. (c) shows the reverse of slip south of Buyant Uul and Tal Nuur, with uplifted topography on the western side of the fault.

South of ∼47.7°N, there are several possible fault strands that strike roughly 350° and seem to accommodate mostly strike-slip motion (Figure 2.28). These faults have not been fully investigated in the field, and several cross the Mongolian-Chinese border, making them difficult to visit. There are right-lateral drainage displacements along the faults, attesting to dextral strike-slip, and lineations that could be fault-related are frequently observed in satellite imagery, but more work is needed to fully characterise these strands of the Sagsay fault (Figure 2.35).

Monh Hyarhan Uul, with peaks over 4200 m and relief of 2000 km, is uplifted along a fault with a WNW strike of about 310°(Figure 2.28). Monh Hyarhan can be considered as part of the Sagsay faulting system because it is essentially along strike from Buyant Uul and the Sagsay earthquake ruptures, and branches off from the southern terminations of the Sagsay strike-slip strands described above (Figure 2.28). The faulting along the base of Monh Hyarhan is likely to be predominantly reverse. However, indications of Late Quaternary activity are scarce, probably because fast erosion acting in the foreland surrounding the high and glaciated peaks destroys Quaternary fault scarps before they can be preserved. There are a few localities on the south western side of the mountain where there are potential reverse scarps in alluvial fans at the base of the range (Figure 2.36).

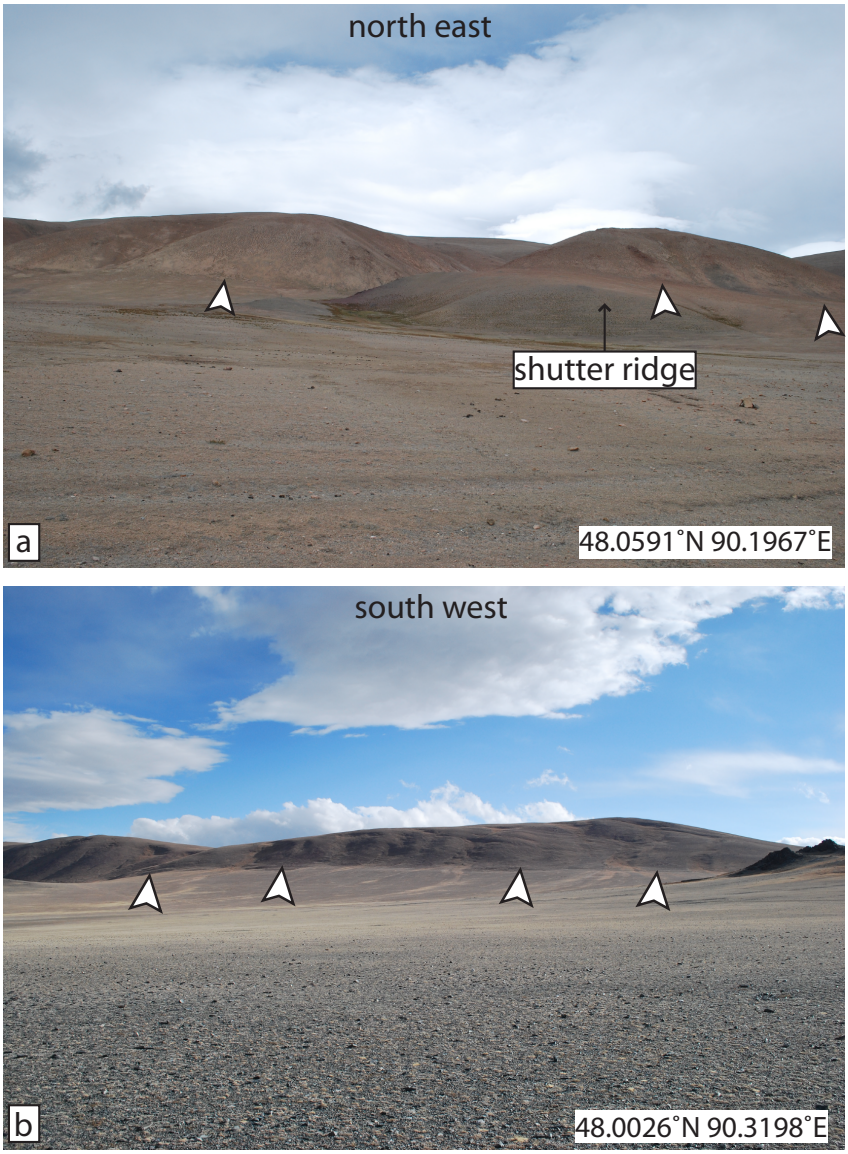


**Figure 2.34:** Photos of the Sagsay fault near Tal Nuur. (a) shows the fault along the ridge just to the east of Tal Nuur, where dextral strike-slip motion has created a shutter ridge by displacing topography in the mid-ground relative to topography in the background. The trace of the active fault can be seen as a dark lineation at the change in slope in the background, indicated by white arrows and visible in Figure 2.33. (b) shows fault scarps at the base of a ridge, but facing the opposite direction to (a). Photo locations are shown in Figure 2.33.

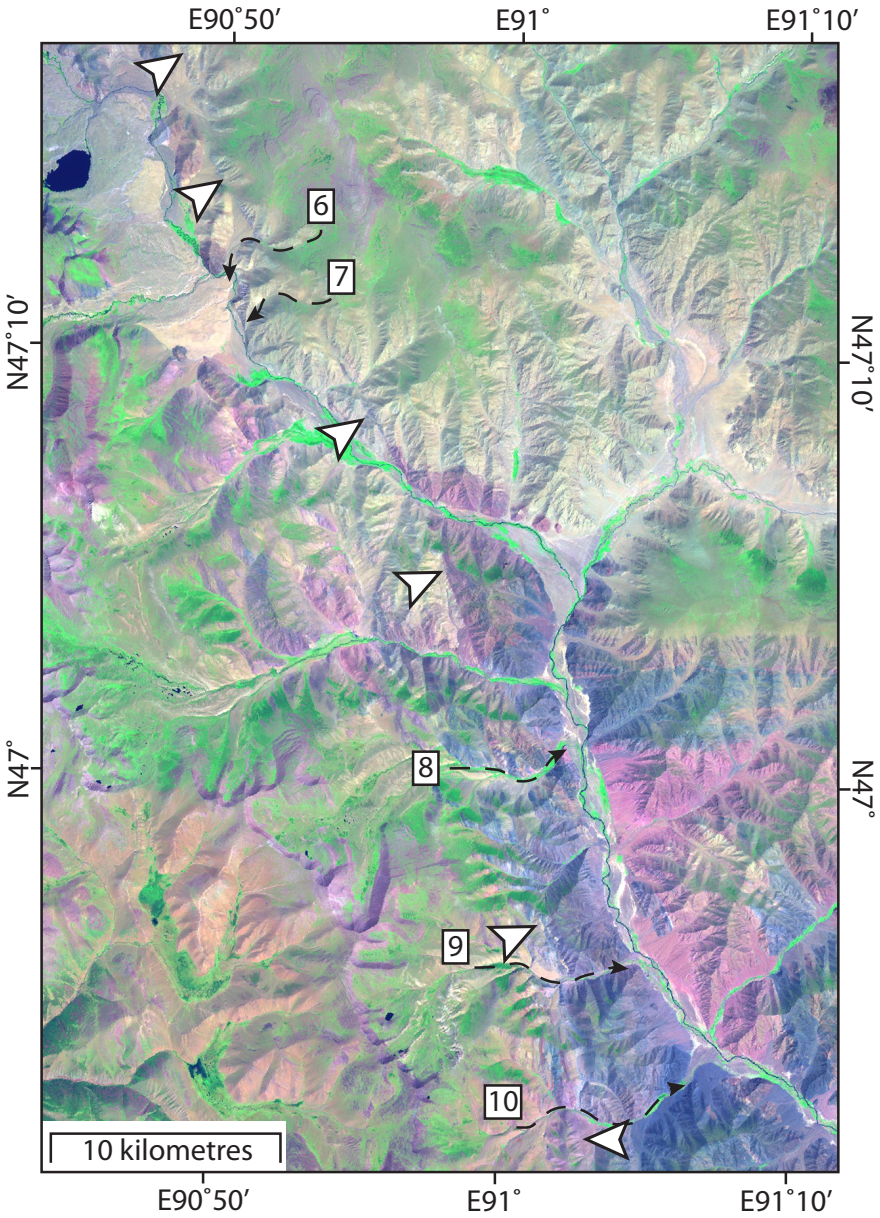


**Figure 2.35:** Landsat imagery of the southern strands of the Sagsay fault (RGB = 741). The fault is visible as a lineation at the base of several low ridges, and in many places seems to follow a bedrock contact between the more mafic rock (deep pink to purple in the plotted bands) and more granitic buff coloured rock. There are several drainage displacements along this section of the fault, attesting to dextral strike-slip motion. Numbered displacements are listed in Table 2.4.

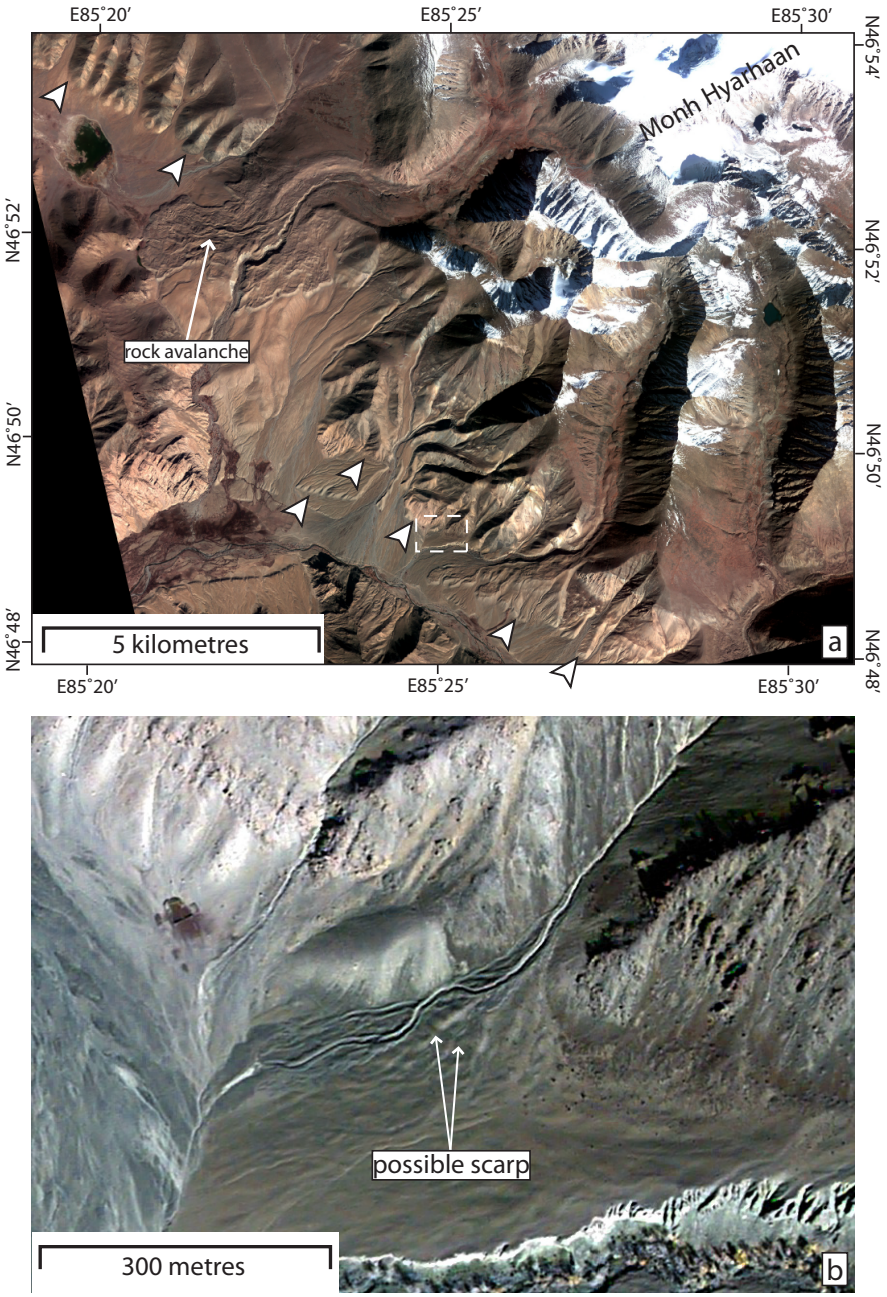


**Figure 2.36:** Kompsat-2 imagery of Monh Hyarhan Uul. RGB is plotted as red, green, and blue spectral bands (4 m/pixel), with the 1 m resolution panchromatic band also plotted in (b). (a) Several possible scarps are visible surrounding the Monh Hyarhan massif, but these scarps are generally discontinuous and it may be difficult to distinguish between fault scarps and landslide scarps. (b) The white box in (a) outlines the locality of (b), which shows a steep scarp in the alluvium.

### Earthquakes

The Sagsay surface rupture is located on the central part of the Sagsay fault zone (Figure 2.28). The rupture is well preserved, with similarities to the level of preservation observed along the Ar Hötöl and even Bulnay surface ruptures (*Khil'ko et al.*, 1985; *Baljinnyam et al.*, 1993). I contribute an updated documentation of the rupture, utilising Kompsat-2 high-resolution imagery (Figures 2.37 and 2.38). The rupture is approximately 40 km long and has a strike between about 315° and 340°. Tension fissures and mole tracks were observed by *Khil'ko et al.* (1985) and *Baljinnyam et al.* (1993) to be up to 40 to 50 m long, 2 m deep, or in the case of mole tracks, 2 to 3.5 m high (Figure 2.39b, c). From a rupture length of 40 km, the Sagsay earthquake was probably close to a $M_w$ 7.0 (Section 2.2.2; *Wells and Coppersmith*, 1994).

Horizontal displacements of streams crossing the rupture were estimated to be on average 2.5 m and at least 3 m by *Khil'ko et al.* (1985) and *Baljinnyam et al.* (1993), along with maximum and average vertical displacements of 2 m and 0.5 m, respectively. Much of the rupture cuts through alluvial fans, with streams that are perpendicular to the strike of the fault. Some stream displacements of 7–8 m are visible in Kompsat-2 imagery (Figure 2.38b). These displacements are likely to be the result of more than one event, because this is much greater than the measurements made by *Khil'ko et al.* (1985) in the field. Also displacements on the order of 7–8 m are more than what would be expected from a 40 km rupture length, which should only be approximately 1.5 m, based on Table 2C in *Wells and Coppersmith* (1994), where $log(MD) = a + b * log(SRL)$ (MD is maximum displacement, SRL = 40 km, and a and b are empirically determined). There is a vertical component along sections of the rupture, but the uplifted side is not consistent: in some places the fault uplifts material on the western side of the fault, and sometimes on the eastern side of the fault, evidenced by vertical scarps observed in the field (Figure

2.39) and incised streams on the uplifted side of the fault in imagery (Figures 2.37 and 2.38). The accommodation of reverse motion is generally correlated with the strike of the fault, where the rupture has a more westerly strike it is more likely to have a reverse component than pure strike-slip. The size of earthquake features, the amount of slip in the event, and the potential for multiple earthquakes in the Late Quaternary/Holocene along the Sagsay rupture portion of the fault all attest to the significance of the Sagsay fault.

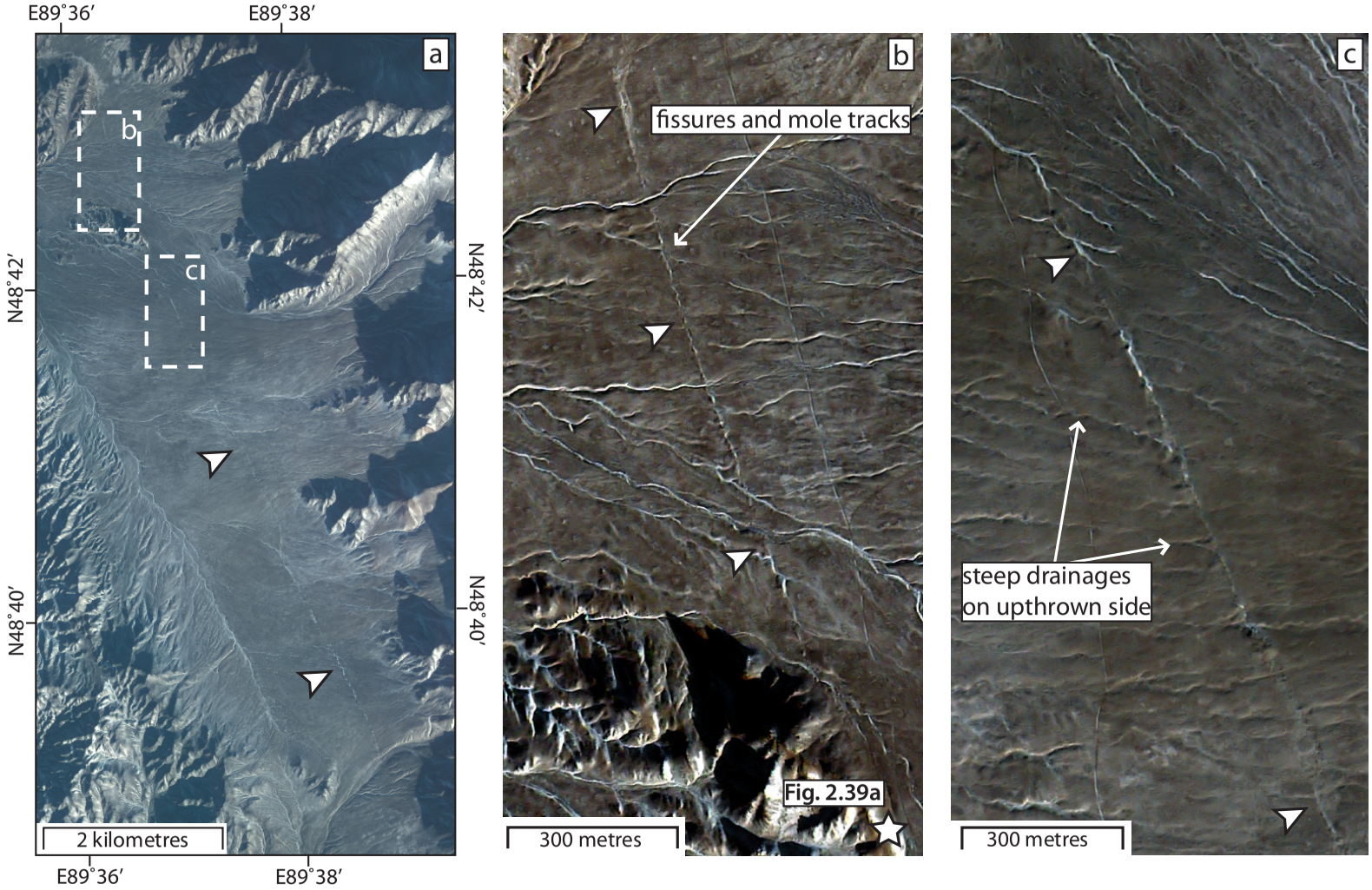


**Figure 2.37:** Kompsat-2 imagery of the Sagsay rupture. (a), (b) The rupture is visible as a series of white lineations, which are probably filled with some snow, striking NW across a relatively flat alluvial plain. (c) Drainages are more incised on the west side of the fault, indicating that the section of the rupture shown has a vertical component, uplifting the west side of the fault. The uplift is opposite to the direction of uplift further south on the rupture (Figure 2.38).

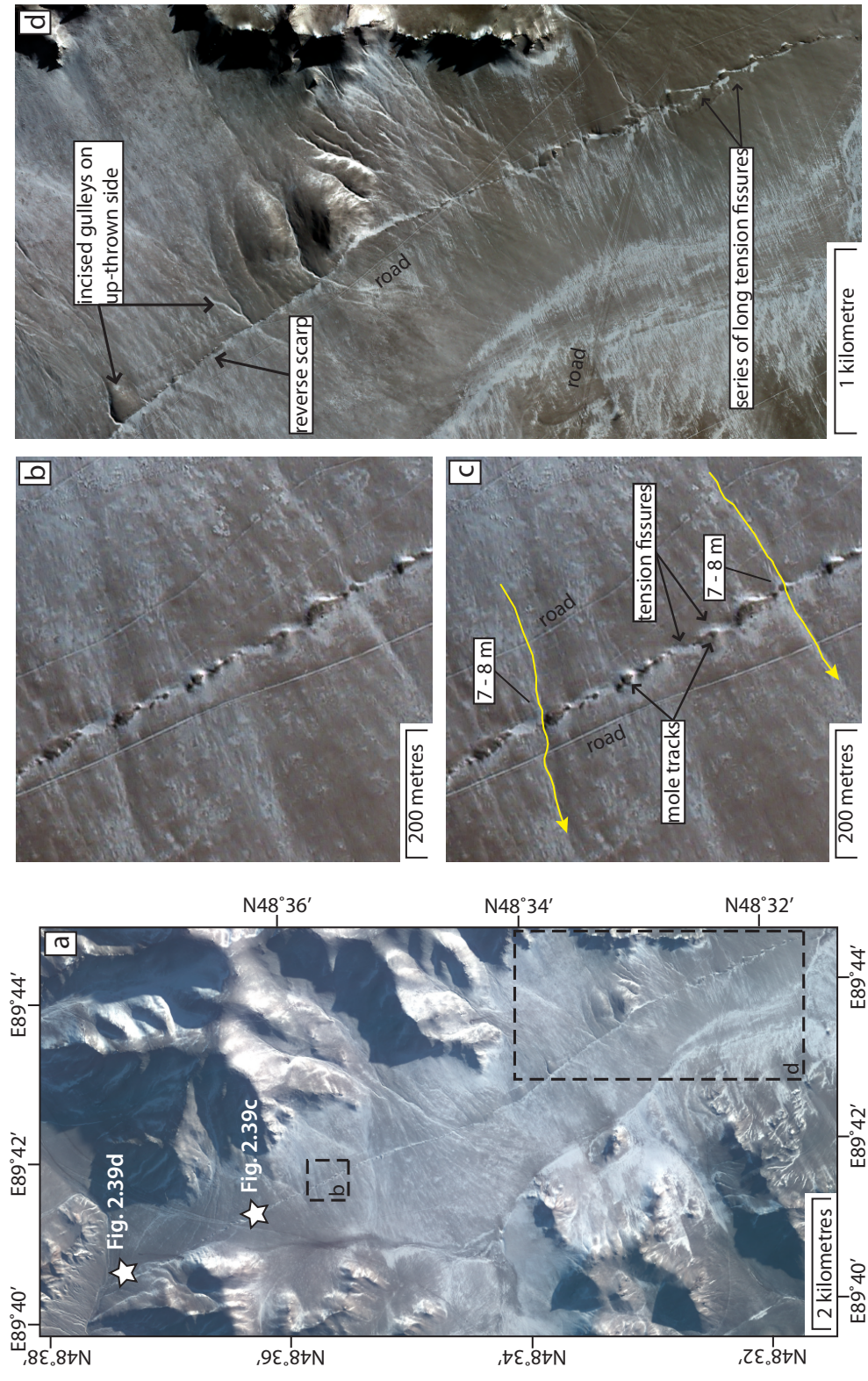


**Figure 2.38:** Kompsat-2 imagery of the southern portion of the Sagsay surface rupture. (b) and (c) show original and annotated examples of displaced streams, mole tracks, and right-stepping tension fissures along a part of the rupture that is pure strike-slip. (d) The upthrown side of the rupture is on the eastern side along this section, evidenced by steep drainages on the upthrown side. A series of *en-echelon* tension cracks is visible in the lower corner.

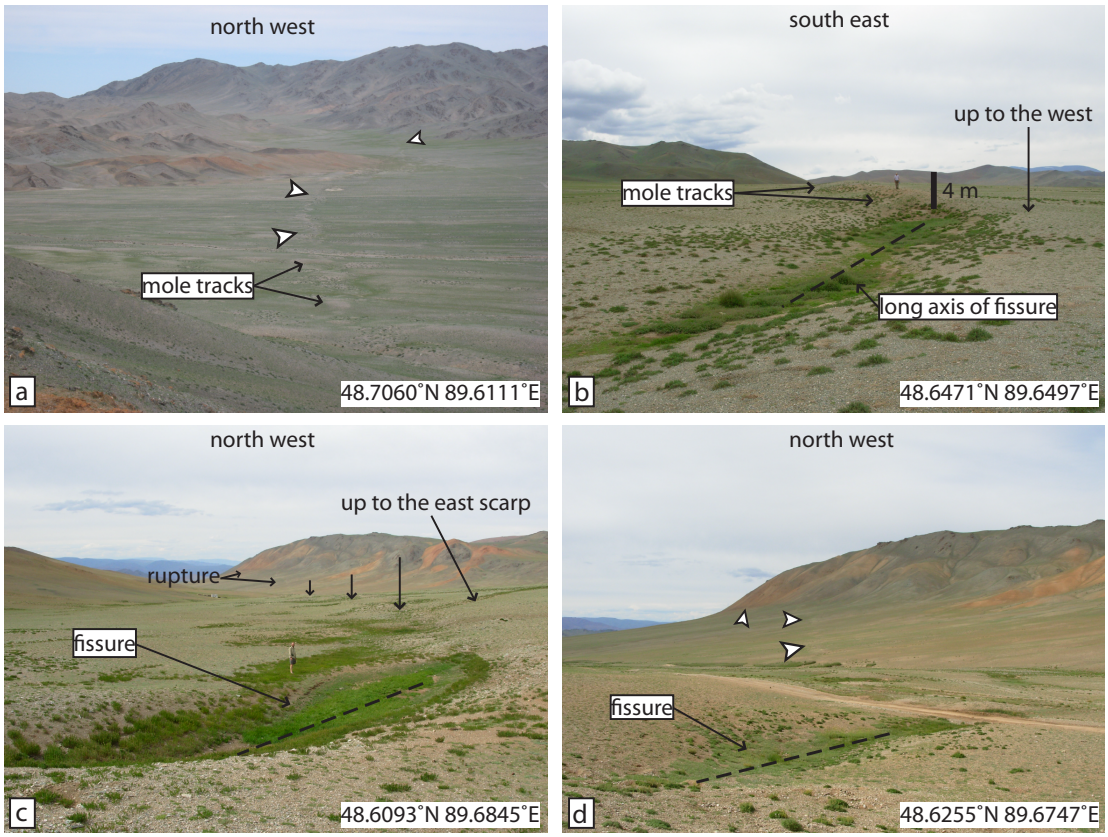


**Figure 2.39:** Photos of the Sagsay surface rupture. (a) shows the northern-most part of the rupture, which is visible as a continuous series of buff-coloured mole tracks and green fissures through the center of the image, indicated by white arrows. Water pools in the fissures, causing them to be more vegetated than the surroundings. (b) shows a series of fissures and hummocky mole tracks, with a local reverse scarp on the western side of the fault. (c) is from the southern end of the Sagsay rupture, where there are a series of large steep-sided fissures, up to 40 m long and possibly the result of several earthquakes, as well as uplifted ground on the eastern side of the fault. (d) is taken from close to the same vantage point as Figure 11 in *Baljinnyam et al.* (1993). There is a sag pond in the foreground, with the rupture trace across the hillside in the background. Photo locations are indicated on Figures 2.37 and 2.38.

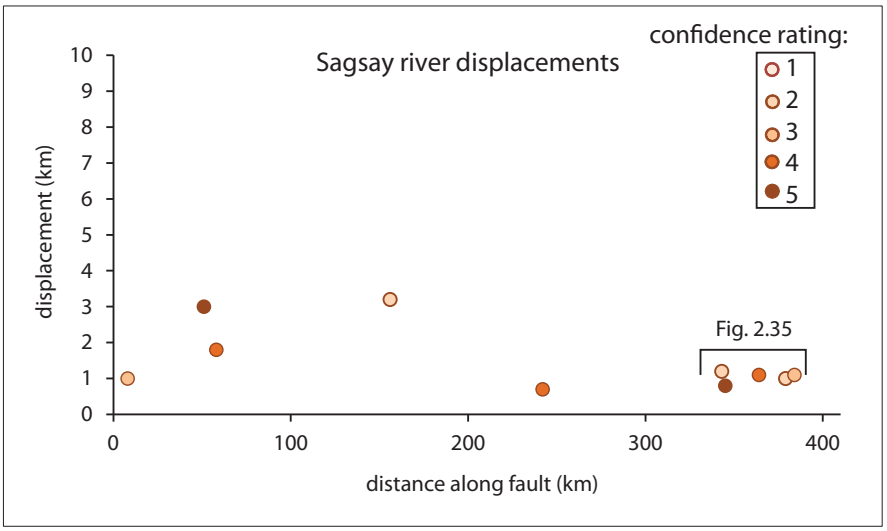


**Figure 2.40:** Plots of river displacements mapped from north to south along the Sagsay fault zone. Different shades of orange represent the level of confidence in each measurement, with lighter orange being low confidence and darker orange being high confidence. The criteria for assigning confidence levels are outlined in Section 2.2.3.

### Cumulative displacement

Right-lateral drainage displacements are found along nearly all of the major strands of the Sagsay fault. Displacements are plotted in Figure 2.40 and listed in Table 2.4. The cumulative right-lateral displacement along the Sagsay fault seems to be between 1 and 3 km, although most of the displacements are closer to 1 km. As on the other Altay faults, many of the drainage displacements are observed where the fault is located within high relief, where the displacement of drainages probably underestimates total fault displacement, because the drainages have only existed since the uplift of topography, which maybe have occurred after the initiation of strike-slip faulting. Despite this, the river displacements confirm active strike-slip faulting of the southern portion of the Sagsay fault (Figure 2.35), where there is a lack of imagery and the fault has not been investigated in the field.

**Table 2.4:** Sagsay river displacements

| Offset name | Offset amount (km) | Confidence | Latitude (°N) | Longitude (°E) |
|---|---|---|---|---|
| SGO1 | 1 | 3 | 49.7008 | 88.6490 |
| SGO2 | 3 | 5 | 49.4188 | 89.0013 |
| SGO3 | 1.8 | 4 | 49.1391 | 88.5694 |
| SGO4 | 3.2 | 2 | 48.6274 | 89.6708 |
| SGO5 | 0.7 | 4 | 48.0002 | 90.2938 |
| SGO6 | 1.2 | 2 | 47.2072 | 90.8547 |
| SGO7 | 0.8 | 5 | 47.1882 | 90.8709 |
| SGO8 | 1.1 | 4 | 47.0442 | 90.9852 |
| SGO9 | 1 | 2 | 46.9221 | 91.0347 |
| SGO10 | 1.1 | 3 | 46.8711 | 91.0475 |

### 2.3.5 The Hoton Nuur/Fu Yun fault zone

The Hoton Nuur and Fu Yun fault zone forms the most westerly of the clearly defined fault zones in the Altay. The two faults are difficult to connect in the high peaks of the central Chinese Altay (Figure 2.1), but I group them together in this section because they are along strike of one another and it is possible that they may form one through-going fault. There is good evidence that both strands are active strike-slip faults, with localised reverse motion. The Fu Yun fault had a $M_s$ 7.9 earthquake in 1931, with tension fissures and horizontal offsets that attest to right-lateral slip (*Richter*, 1958; *Baljinnyam et al.*, 1993; *Klinger et al.*, 2011). The Hoton Nuur fault was not specifically recognised by previous workers in the Altay, although a vague trace is mapped as a dashed line on some maps (see Figure 3 in *Baljinnyam et al.*, 1993). There is clear evidence for active faulting along the Hoton Nuur strand in the field, as well as surrounding the neighboring Tsengel Hyarhan Uul and on the flanks of Tavan Bogd massif (Figure 2.41). The Hoton Nuur fault strand mostly runs along the eastern base of the high peaks that form the drainage divide of the whole of the Altay, which is also the Mongolian-Chinese political border (Figure 2.41).

As mapped in Figure 2.41, the northern portion of the Hoton Nuur fault runs along the western side of a large glacial valley, with Hoton Nuur in the center of

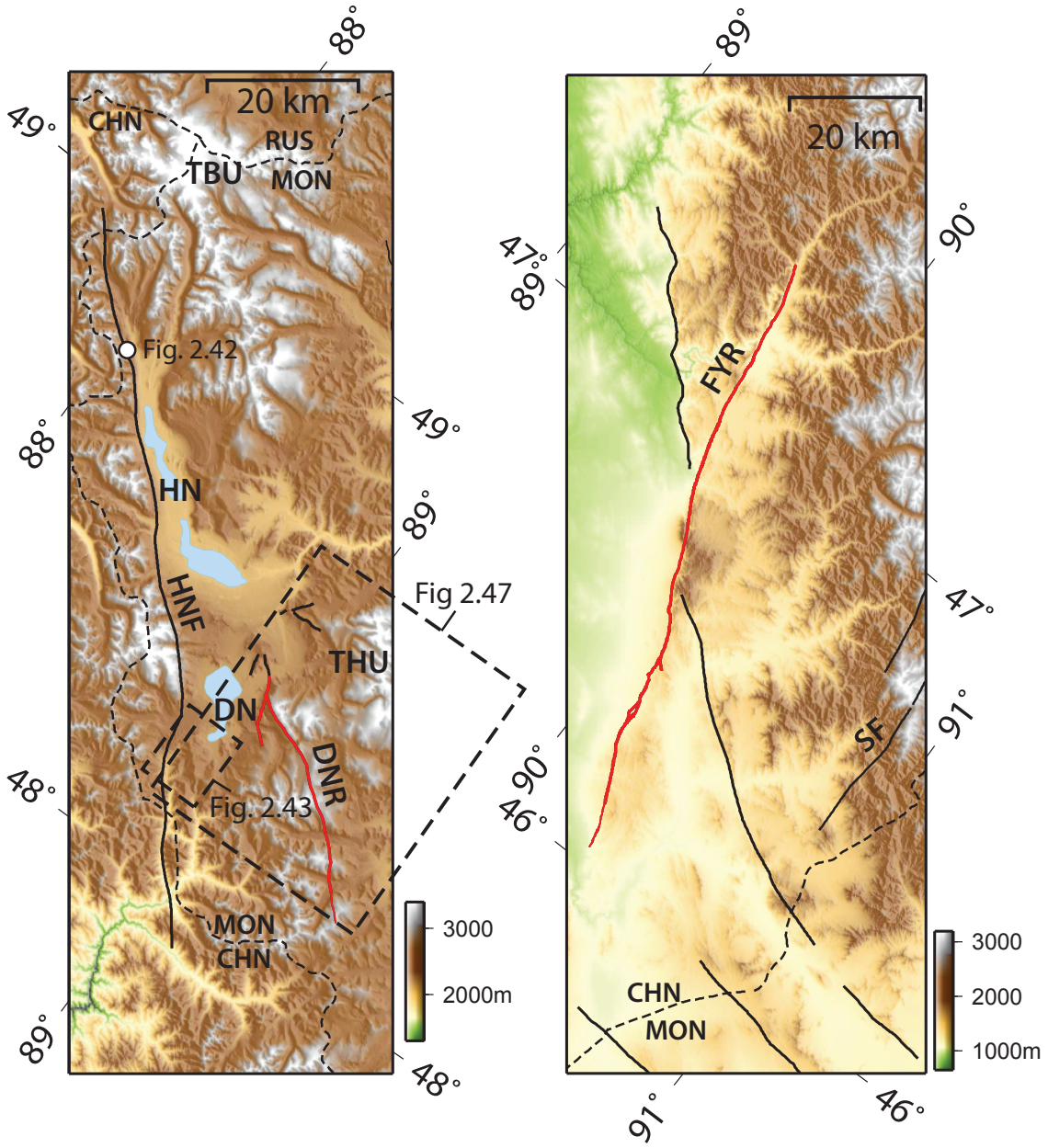


**Figure 2.41:** SRTM DEM of the Hoton Nuur and Fu Yun fault zone. Active faults are mapped in black and ancient earthquake ruptures are mapped in red. Political boundaries are mapped as dashed lines. Abbreviations are CHN: China, DN: Dayan Nuur, DNR: Dayan Nuur Rupture, FYR: Fu Yun Rupture (and fault), HN: Hoton Nuur, HNF: Hoton Nuur Fault, MCB: Mongolian-Chinese border, MON: Mongolia, RUS: Russia/Siberia, SF: Sagsay Fault, TBU: Tavan Bogd Uul, THU: Tsengel Hyarhan Uul.

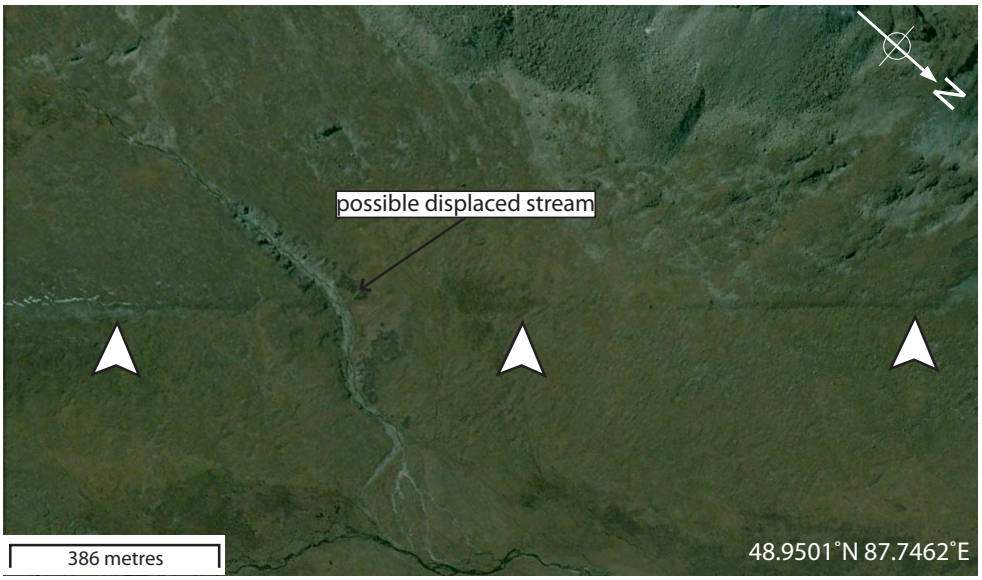


**Figure 2.42:** Quickbird imagery (Google Earth) of the Hoton Nuur fault. The fault runs along the base of the Hoton Nuur valley, south of the Tavan Bogd massif. A NE-facing scarp is visible in the image, indicated by white arrows, which are on the downthrown side.

the valley. Along the lake, there is not much evidence for Late Quaternary faulting, because the undulations and complicated drainage patterns in glacial deposits and outwashes along the lake make it difficult to distinguish stream displacements, sag ponds, and mole tracks due to faulting from hummocks and pools in the glacial deposits surrounding the fault. There are a few localities in the northern part of the valley where a sharp scarp in Quaternary alluvium seems likely to be related to active faulting (Figure 2.42). The scarp is probably a reverse scarp, with the west side uplifted, in agreement with the surrounding topography, and the scarp is continuous for at least 11 km in Google Earth imagery. It has not been investigated in the field, as it is difficult to reach, but is clearly related to faulting in the available imagery.

South of Dayan Nuur, a series of left-stepping sag ponds crosses a dissected alluvial fan, which is overlain by several glacial deposits (Figure 2.43). The sag ponds range in length from 10 m to 300 m, suggesting that they are the result of

cumulative right-lateral motion of the Hoton Nuur fault (Figures 2.43b and 2.44). The long axes of the fissures strike between about 330° to 005°, which is either parallel to, or clockwise to, the strike of the fault (330°, Figure 2.43b). Some fissures have been altered, by either water pooling in the depressions or small streams crossing the fault zone. The longest fissures are potentially multiple features that were connected by small streams running between the individual ponds.

The surface expression of faulting is discontinuous to the north and south of the series of fissures displayed in Figure 2.43b. Several deposits of glacial moraines and outwash cross the projected path of the Hoton Nuur fault, and similar to the region surrounding the scarp recognised in Figure 2.42, definitive features that are result of faulting cannot be distinguished from the hummocks and small kettle pools that occur on the surface of the glacial deposits indicated on Figure 2.43a. These moraine and probably outwash deposits are elevated approximately 30 m above the surrounding alluvium, and they are visible as a distinct deposit in satellite imagery (Figure 2.43) and in the field (Figure 2.44).

Figure 2.45a shows evidence of faulting as a series of sag ponds and lineations in gently undulating alluvium. Also shown is altered orange coloured fault rock that outcrops along strike, which is typically found along Altay faults (see Chapter 1). The fault intersects a glacial deposit, possibly a moraine, exiting the high peaks along the Altay drainage divide (also indicated on Figure 2.43a), and there is a series of fissures observed within the uneven surface of the deposit that are potentially due to active faulting (Figure 2.45b). Both the base of the moraine and the crest of a ridge on the edge of the moraine are displaced right-laterally by approximately 30 m. The displaced moraine is the basis of a slip rate study, described further in chapter 3, where I sampled boulder tops from the crest of ridge in Figure 2.45c for $^{10}$Be cosmogenic dating, but for which I do not yet have results.

While investigating the Hoton Nuur fault in 2010 in the field, I found possible

indications of past earthquake events in the form of damaged trees, which are included in this thesis out of interest. There is a body of work on the study of the effect of earthquake rupture on trees along the zone of surface rupture (*Meisling and Sieh*, 1980; *Lin and Lin*, 1998; *Carver et al.*, 2004). Directly along the trace of the fault, trees are often found with cracked trunks and temporary asymmetric growth and branching due to the shaking and rupturing of the ground during an earthquake. Tree rings from damaged trees often show a reduction in width around the time of the earthquake, and radiocarbon data from damaged tree rings can even be used to place age constraints on ancient earthquakes (e.g. *Jacoby et al.*, 1997; *Wells et al.*, 1999). Along the southern section of the Hoton Nuur fault, several trees show signs of damage (Figure 2.46). These include changes in growth direction, which can occur if a tree is knocked over during an event such as an earthquake, storm, or landslide, but then survives the event and continues growing. Several trees showed distinct changes in morphology as well as some cracking. Because they were found along the zone of faulting, they may be related to ancient earthquake events. However it is possible that the trees were damaged during large storms or landsliding.

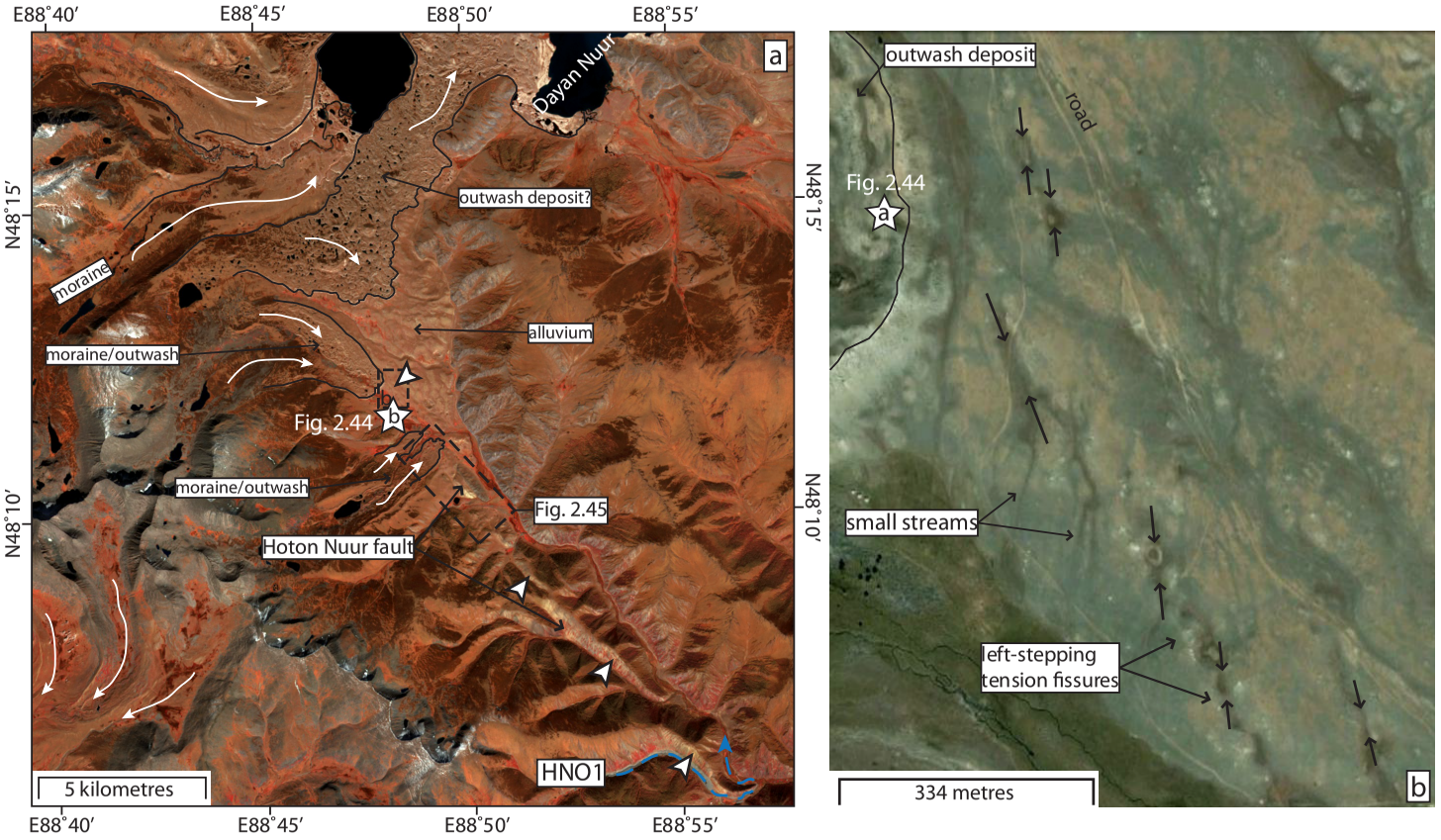


**Figure 2.43:** ASTER (a) and Quickbird Google Earth (b) imagery of the Hoton Nuur fault where it crosses several glacial deposits southwest of Dayan Nuur. In (a) the flow directions of ice and glacial outwash is indicated by white lines along the main moraines and outwash deposits. The Hoton Nuur fault follows orange-coloured altered outcrops, and the trace of the fault in Quaternary deposits is indicated by black and white arrows. HNO1 and blue dashed line indicate the river displacement in Table 2.5. (b) shows a set of clear left stepping fissures that attest to right-lateral strike-slip faulting along the Hoton Nuur fault, which have probably been widened and connected in some places by water ponding. The fissures cross hummocky alluvium, and the toe of a glacial outwash deposit, elevated ∼30 m above the alluvium, is indicated in the top left corner.

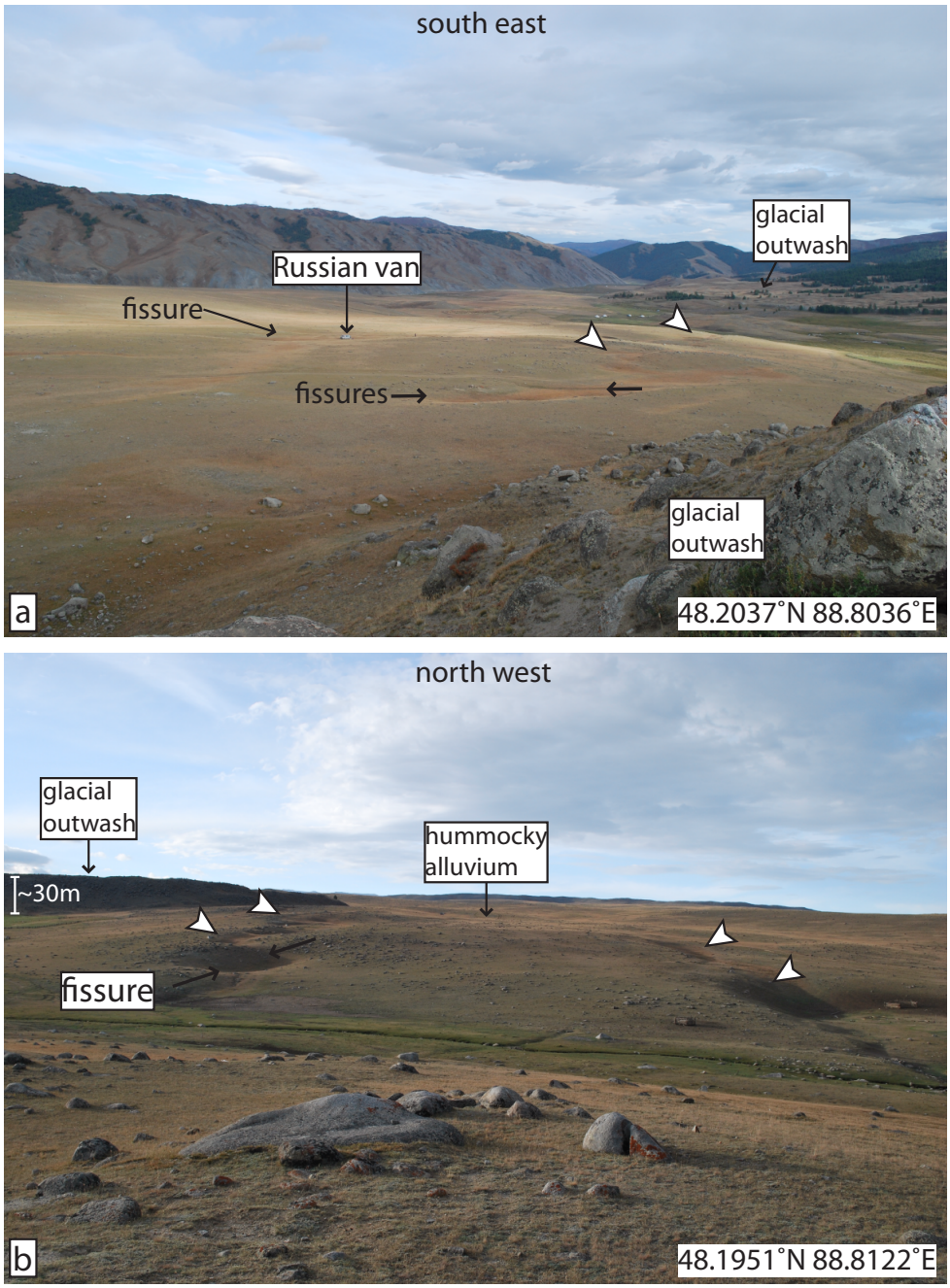


**Figure 2.44:** Field photos of the Hoton Nuur fault through the Dayan Nuur moraines. Photos are taken from the two stars in Figure 2.43. Two lines of left-stepping fissures that are several tens of metres long are visible in the undulating alluvium in the mid ground of the photos. In (a), the glacial outwash deposit that was sampled for a slip rate study is indicated in the distance, and in (b) the moraine/outwash deposit outlined in Figure 2.43 is also indicated, which is at least 30 m above the underlying alluvium.

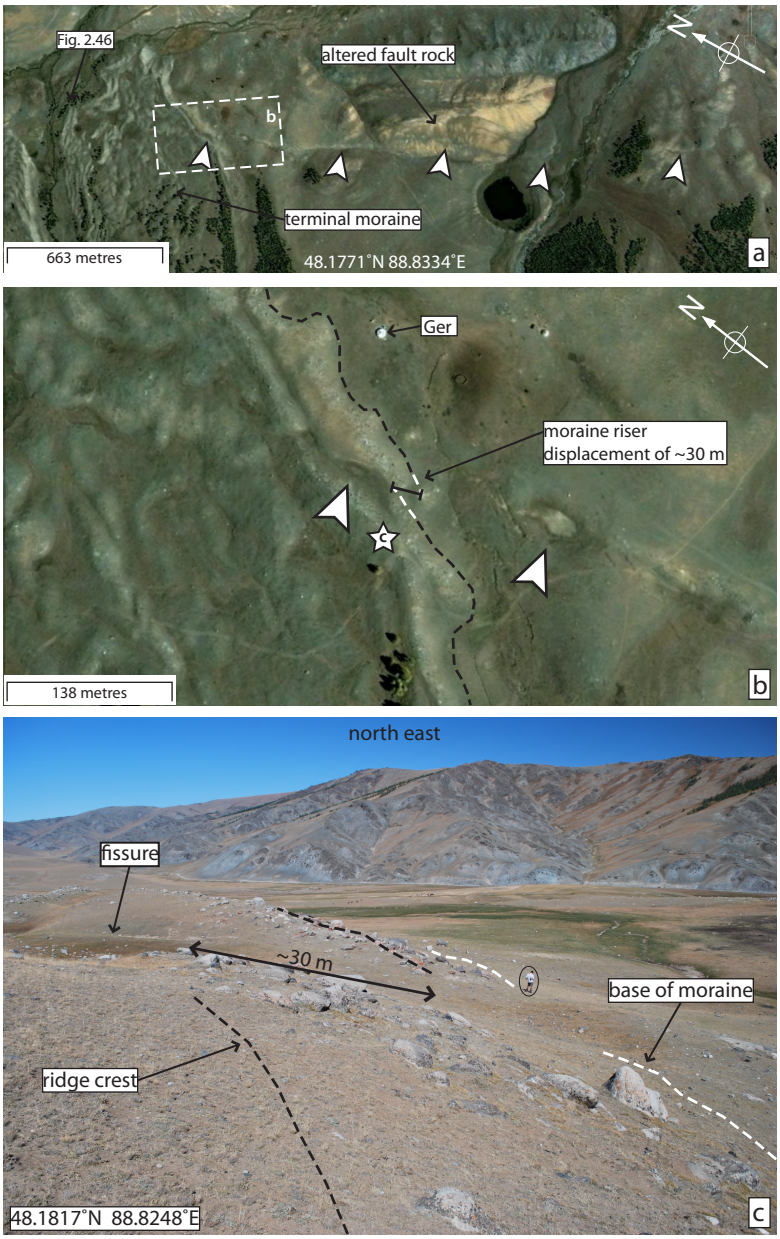


**Figure 2.45:** Quickbird imagery (Google Earth) and photo of the Hoton Nuur fault through a terminal moraine. The fault cuts across a bedrock ridge that has the orange mineralised rock typically observed along Altay faults (a). In (b), cumulative fissures are visible within the older moraine surface on the right of the image. Where the fissures intercept the younger terminal moraine, the edge of the moraine is right-laterally displaced. White dashed lines indicate projection of the riser to the fault. Several ponds along strike of the fault could be fault-related fissures. (c) shows a photo of the displaced moraine and moraine fissures, taken from the star in (b). Both the base of the moraine and the crest of a ridge on the edge of the moraine are displaced. The locality of (a) is indicated in Figure 2.43.

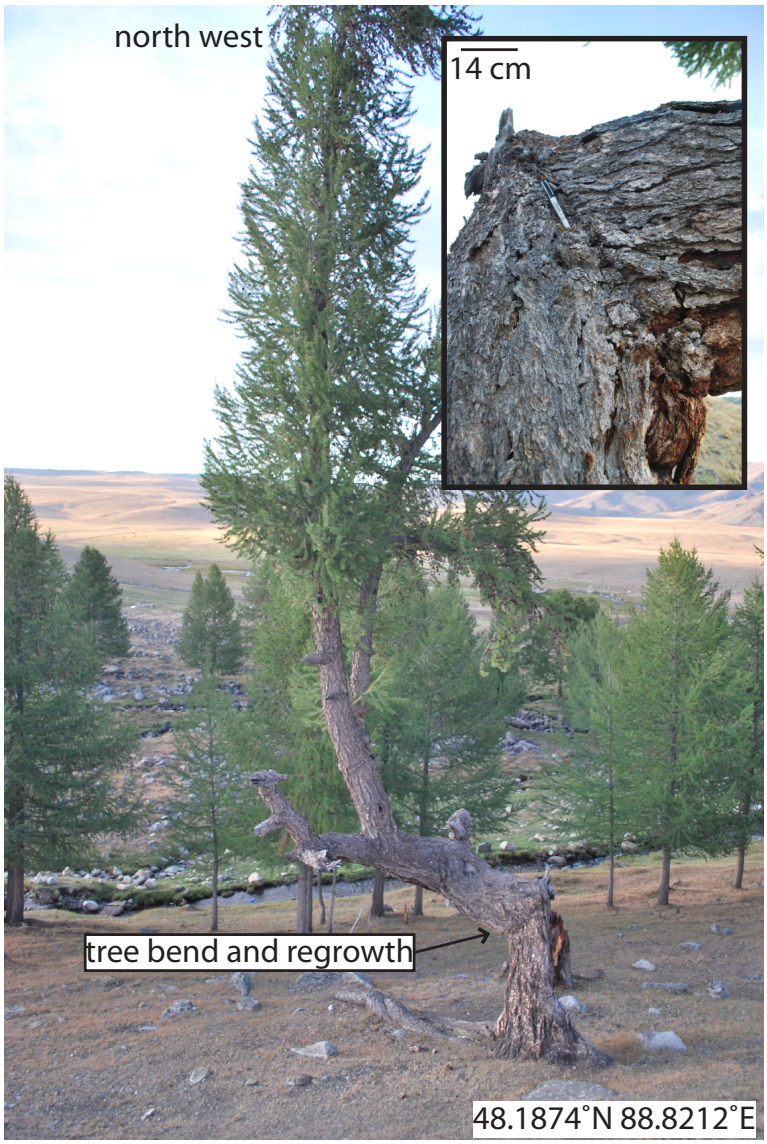


**Figure 2.46:** Photos of a damaged tree along the Hoton Nuur fault. There is a large bend in the trunk and evidence of a change in growth direction at the bend. Locality is indicated on Figure 2.45.

To the east of the main Hoton Nuur fault, there are several faults surrounding Tsengel Hyarhan Uul, including what is likely an ancient earthquake rupture (Figure 2.47). Tsengel Hyarhan Uul is twice as long as it is wide, with peaks above 3900 m. Based on the elongate shape of topography and the identification of several active faults surrounding Tsengel Hyarhan Uul, the range is probably being uplifted along a bend in a strike-slip fault, very similar to Buyant Uul and Monh Hyarhan Uul along the Sagsay fault. However it is difficult to relate Tsengel Hyarhan to a particular Altay fault zone, and the discontinuous faults surrounding the range may be related to the Hoton Nuur faulting, or even branches of the Sagsay fault zone (Figure 2.1). In this north western part of the Altay, it is generally difficult to find clear evidence for active faulting that is continuous for much more than 100 km, probably due to either the effect of recent glaciation and erosion causing deterioration of fault scarps or possibly because faults in the central Altay simply move more slowly, or are shorter and more discontinuous, than faults on the margins of the Altay (e.g. *Cunningham*, 2005; *Nissen et al.*, 2009b). The contrast between the expression of faulting along the margins of the Altay with faulting in the central Altay is expanded further in Section 2.5.

Figures 2.48 and 2.49 show ASTER imagery and field photos of the faults that can be identified surrounding Tsengel Hyarhan Uul. Details of an ancient earthquake rupture, mapped in red in Figure 2.47, are given in Section 2.4. One fault, indicated in Figures 2.48a and 2.49a, has a NE–SW strike, which is uncommon in the Altay and may be accommodating localised left-lateral slip. This is further suggested by fissures that are right-stepping and oriented anticlockwise from the strike of the fault (Figure 2.49b), although in some places it is difficult to distinguish between hummocks in the landscape and fissures due to faulting. Other faults surrounding the range are visible as lineations in Quaternary alluvium in satellite imagery, but had somewhat degraded scarps in the field (Figure 2.48a). A branching fault on the

south side of Tsengel Hyarhan Uul was clear in the field, including several localities where a series of grassy depressions were observed, likely due to dextral strike-slip faulting (Figure 2.49b, c, and d; and Figure 2.48b). I tentatively connect the field and remote sensing observations on the southern flanks of Tsengel Hyarhan with similar observations near Chickertee Nuur as part of one earthquake rupture, the Tsengel Hyarhan rupture, which is described in more detail in Section 2.4.

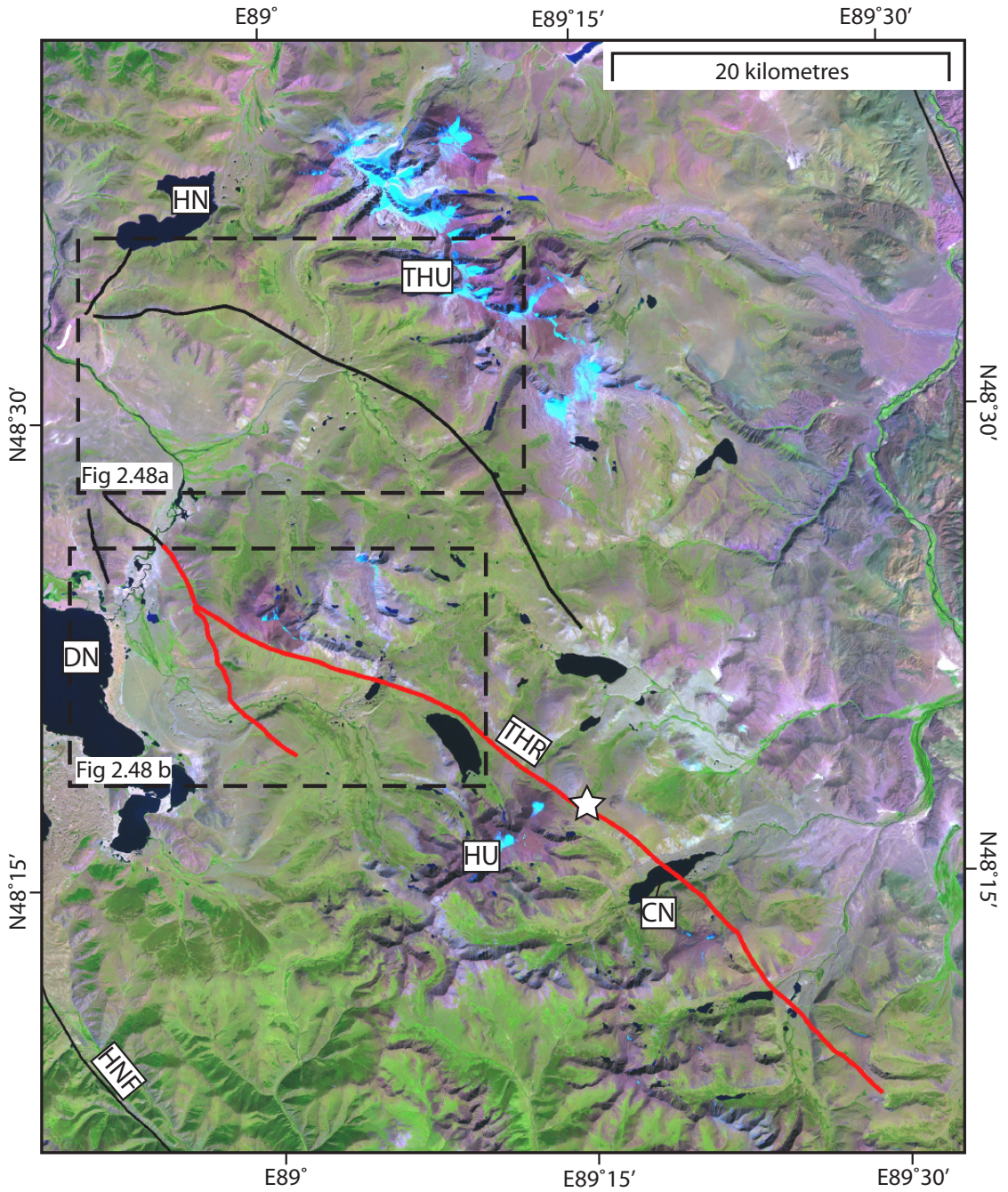


**Figure 2.47:** Landsat image of the faults surrounding Tsengel Hyarhan Uul (RGB = 741). Abbreviations are CN: Chickertee Nuur, DN: Dayan Nuur, HN: Har Nuur, HNF: Hoton Nuur Fault, HU: Halagash Uul, THR: Tsengel Hyarhan Rupture, THU: Tsengel Hyarhan Uul. ASTER images in Figure 2.48 are indicated by dashed rectangles. White star indicates the locality of ruptures described in Section 2.4, and Figure 2.75.

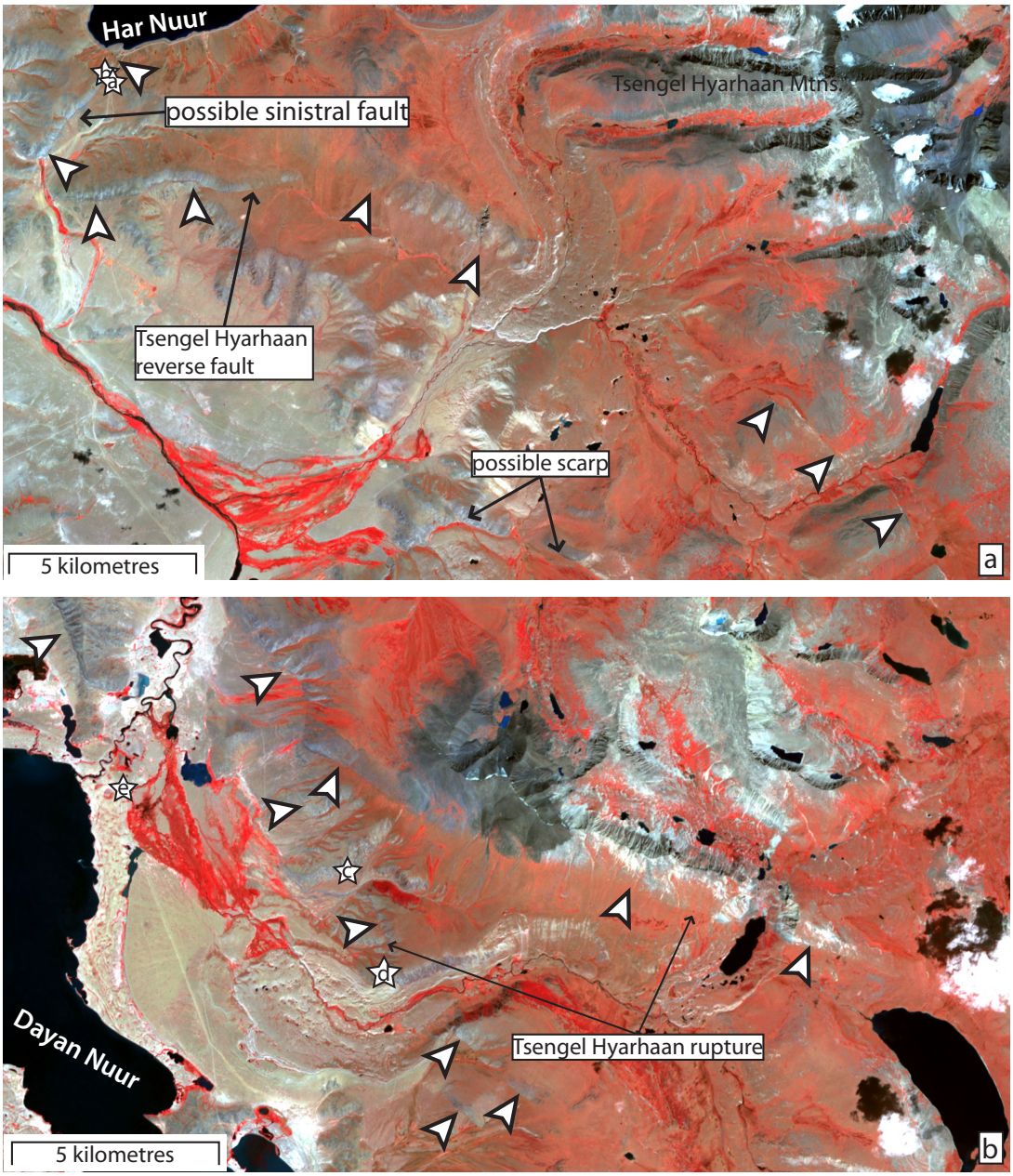


**Figure 2.48:** ASTER imagery of faults surrounding Tsengel Hyarhan Uul. Stars indicate the localities of photos in Figure 2.49. White arrows indicate potential fault strands. In (a) there is a small NE–SW striking fault that may be a sinistral strike-slip fault, based on its orientation and right-stepping fissures. In (b), the northern end of the Tsengel Hyarhan rupture cuts across the base of a low range, and is split into two strands surrounding the topography.

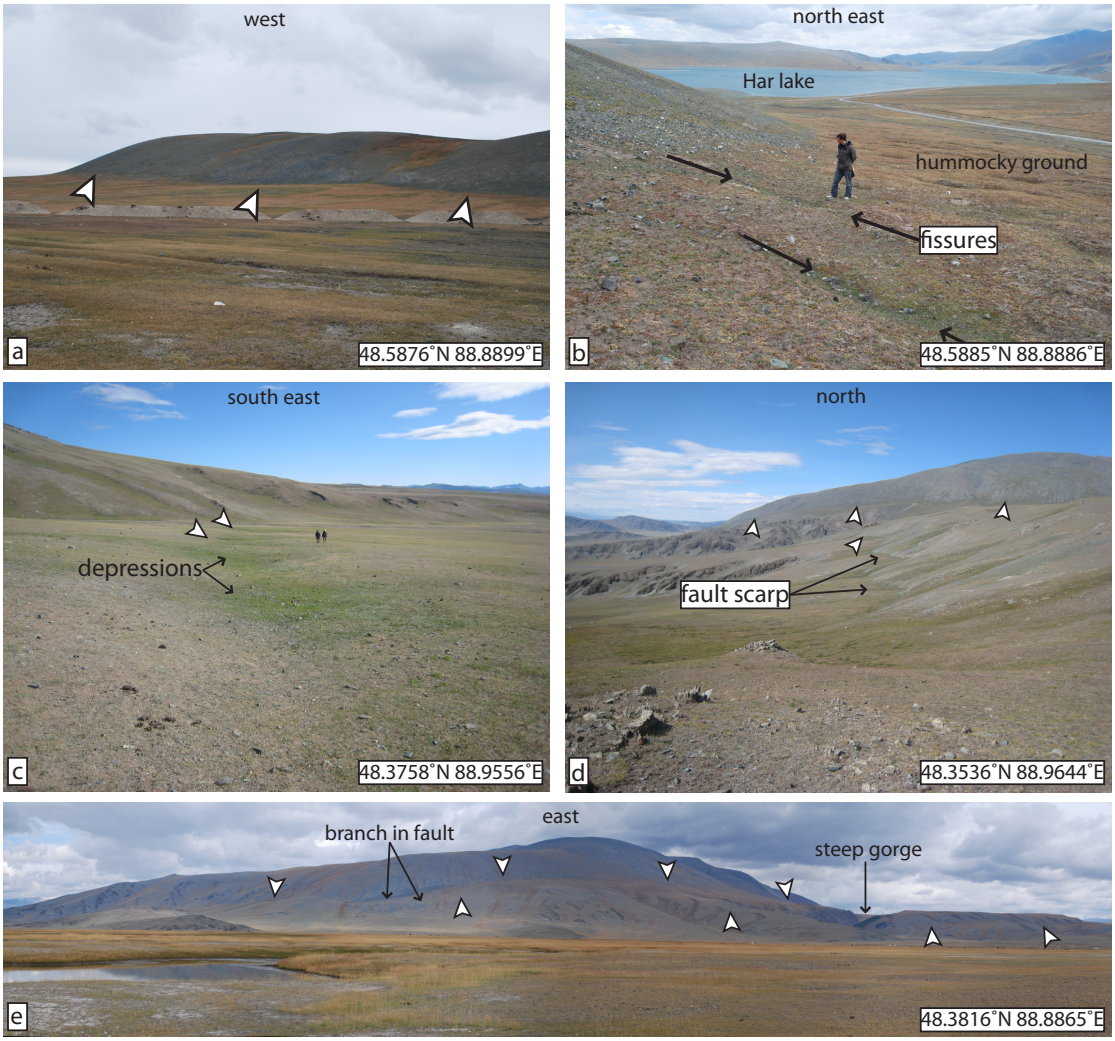


**Figure 2.49:** Field photos of faulting surrounding Tsengel Hyarhan Uul. (a) and (b) are taken from the possibly left-lateral fault extending south of Har Nuur. (b) shows possible right-stepping grassy fissures at the base of the scarp in (a). (c) and (d) Grassy depressions and linear scarps found in the field that are potentially features of the northern end of the Tsengel Hyarhan rupture. (e) Panorama of the branching faults surrounding Tsengel Hyarhan Uul.

The strike of the Fu Yun fault (340°–350°) is oblique to the general NW–SE trend of the structural grain and bedding planes of the Palaeozoic rocks that it cross-cuts (Figures 2.41 and 2.51a). This is not unusual for the Altay faults, but it does imply that the Fu Yun fault accommodates nearly pure strike-slip motion, and this is confirmed by the lack of continuous vertical scarps and the lack of any change

in relief across the fault. There are also a number of west flowing streams exiting the Altay that are right-laterally displaced as they cross the fault, offset by amounts ranging from a few hundred metres up to 3 km.

### Earthquakes

The only events previously known to have occurred on the Hoton Nuur-Fu Yun fault zone are the earthquakes on the Fu Yun fault. The $11^{th}$ August 1931 $M_s$ 7.9 Fu Yun earthquake is well described in the literature (*Richter*, 1958; *Chen and Molnar*, 1977; *Molnar and Deng*, 1984; *Shi et al.*, 1984; *Baljinnyam et al.*, 1993; *Klinger et al.*, 2011) and I review it briefly here. I provide a description of the likely palaeoearthquake on the Hoton Nuur fault zone, along Tsengel Hyarhan Uul, in Section 2.4.

The surface rupture of the 1931 Fu Yun event is mapped to be between 160 and 180 km long (*Shi et al.*, 1984; *Klinger et al.*, 2011). It is interesting to note that the length of the Fu Yun rupture is significantly less than what would be expected for a M 7.9 event. If the *Wells and Coppersmith* (1994) relation for strike-slip faults is used, the rupture length would be expected to be around 280 km (Section 2.2.2). The average coseismic slip in the event (from 290 offset measurements) is $6.3 \pm 1.2$ m (*Klinger et al.*, 2011), and a maximum slip of 9 to 14.6 m was suggested by *Shi et al.* (1984). There are discontinuous vertical scarps along the Fu Yun rupture, attesting to local components of normal and reverse faulting in places. Vertical displacements between 1 and 3.6 m were measured, some of which are suggested to have resulted from subsequent aftershocks (*Shi et al.*, 1984; *Baljinnyam et al.*, 1993). Successively larger horizontal offsets, up to 64.5 m but generally less than 37 m, were observed by *Klinger et al.* (2011). They suggest that these offsets are the cumulative result of at least four older earthquakes, with an average slip of 6.3 m, and based on the slip distributions along the fault, they suggest that the Fu Yun fault obeys a characteristic slip model.

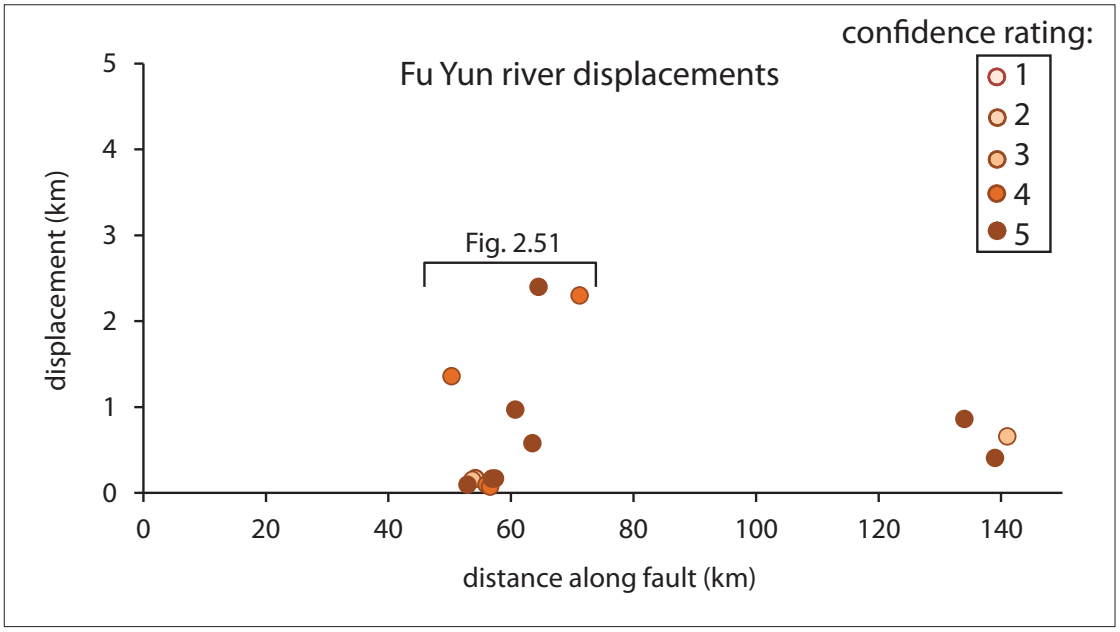


**Figure 2.50:** Plot of river displacements along the Fu Yun fault strand, part of the Hoton Nuur/Fu Yun fault zone. The Hoton Nuur offset is not displayed, because the two faults can not be joined as one fault zone. Different shades of orange represent the level of confidence in each measurement, with light orange being lower confidence and dark orange being higher confidence. The criteria for assigning confidence level is outlined in Section 2.2.3.

### Cumulative Displacement

Drainage displacements along the Fu Yun fault are plotted in Figure 2.50 and listed in Table 2.5. Preservation of long term displacements along the Hoton Nuur section of the fault is quite poor. There is only one locality on the Hoton Nuur section that has a displacement with even a medium level of confidence (HN01). At HNO1, a major east-flowing river seems to be displaced across the fault, but there is a topographic ridge impeding the course of the river (Figure 2.43). Along the Fu Yun section of the fault, there are several drainage displacements where west-flowing drainages exiting the Altay cross the fault (Figure 2.51). A large portion of the Fu Yun fault is along a major NNW–SSE valley, and the surrounding rivers drain into the valley, rather than crossing the fault. Maximum displacements are up to 2.4 km where large gorges

**Table 2.5:** Hoton Nuur-Fu Yun river displacements

| Offset | Offset amount (km) | Confidence level | Latitude (°N) | Longitude (°E) |
|---|---|---|---|---|
| HNO1 | 2.25 | 3 | 48.0990 | 88.9306 |
| FYO2 | 1.36 | 4 | 46.9307 | 89.7931 |
| FYO3 | 0.10 | 5 | 46.9092 | 89.8017 |
| FYO4 | 0.15 | 3 | 46.9013 | 89.8059 |
| FYO5 | 0.17 | 2 | 46.8969 | 89.8080 |
| FYO6 | 0.10 | 4 | 46.8814 | 89.8160 |
| FYO7 | 0.07 | 4 | 46.8760 | 89.8190 |
| FYO8 | 0.17 | 5 | 46.8738 | 89.8198 |
| FYO9 | 0.17 | 5 | 46.8701 | 89.8212 |
| FYO10 | 0.97 | 5 | 46.8418 | 89.8369 |
| FYO11 | 0.58 | 5 | 46.8185 | 89.8487 |
| FYO12 | 2.40 | 5 | 46.8103 | 89.8552 |
| FYO13 | 2.30 | 4 | 46.7589 | 89.8982 |
| FYO14 | 0.86 | 5 | 46.2350 | 90.1859 |
| FYO15 | 0.41 | 5 | 46.2012 | 90.2117 |
| FYO16 | 0.66 | 3 | 46.1852 | 90.2235 |

cross the fault. Much smaller displacements are measured in streams with restricted catchment areas (Figure 2.51b).

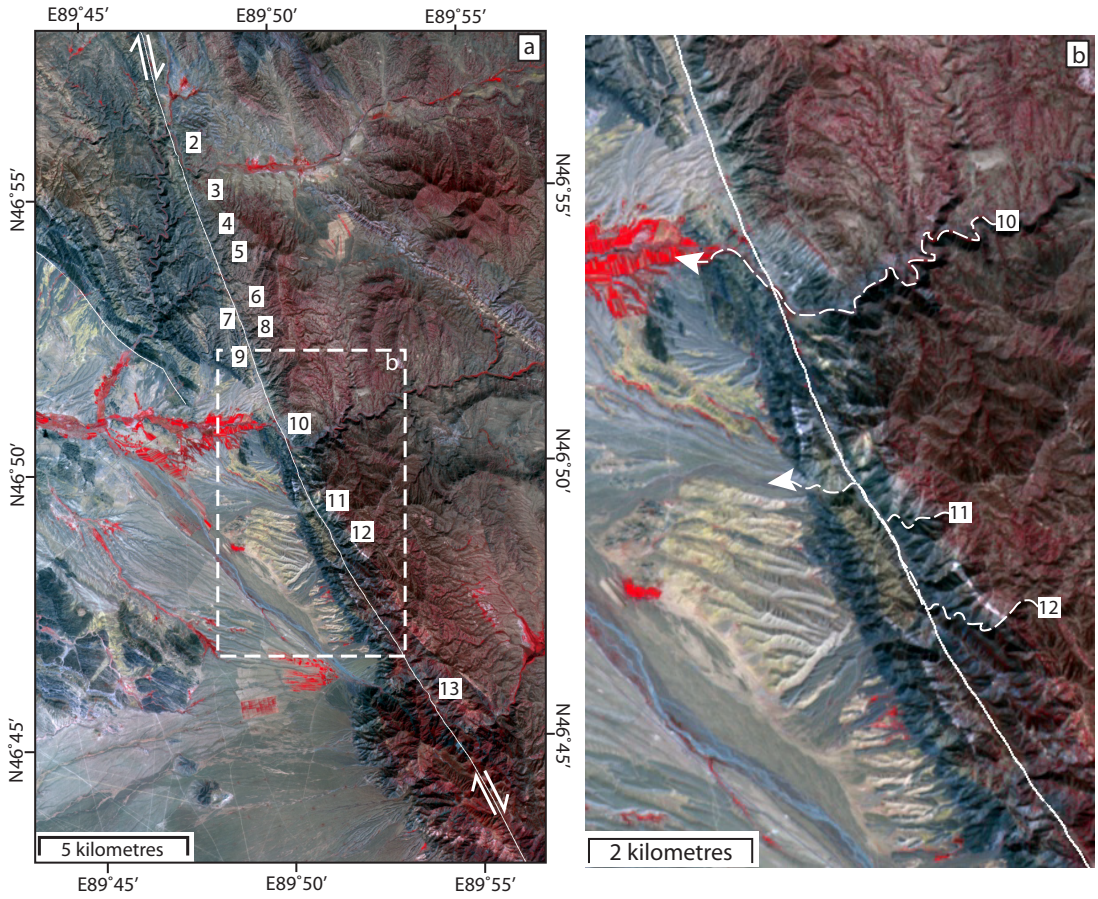


**Figure 2.51:** ASTER imagery of displacements along the Fu Yun fault where the fault crosses several west flowing drainages. (a) shows an overview of the region, where the regional bedding trend strikes oblique to the Fu Yun fault. Numbers correspond to offsets listed in Table 2.5. In (b), offset FYO11, which has a relatively small catchment area, joins the larger FYO12.

## 2.4 Newly discovered ancient earthquake ruptures

### 2.4.1 The Sair Uul Rupture

A previously unknown surface rupture along the central part of the Ölgiy fault zone was discovered in the field in 2008, named the 'Sair Uul' rupture after the mountain that is at its southern termination (Figure 2.52). The rupture zone is approximately 80 km long. The northern termination of the rupture is 9 km west of Ölgiy city, and the central strand extends along the NW flanks of and through Hungui Uul. The

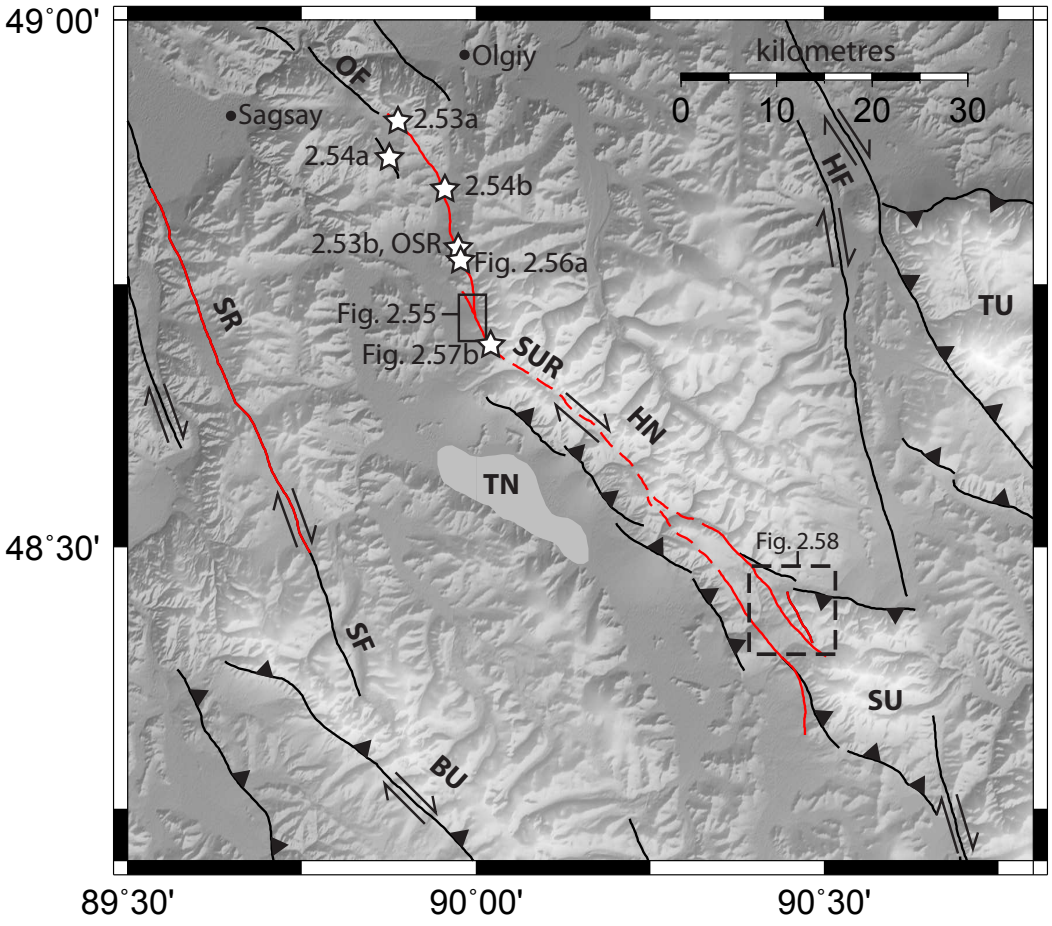


**Figure 2.52:** SRTM 90 m DEM with the Sair Uul (SUR) and Sagsay (SR) ruptures mapped in red. Towns are indicated with closed circles. The dashed line indicates a section of the Sair Uul rupture that was not ground-truthed in the field. Stars indicate photo locations from the labeled figure numbers. Abbreviations are BU: Buyant Uul, HF: Hovd Fault, HN: Hungui Nuruu, OF: Olgiy Fault, OSR: Ölgiy slip rate site, SF: Sagsay Fault, SU: Sair Uul, TN: Tolbo Nuur, TU: Tsambagaraav Uul.

sense of slip of the rupture is dominated by dextral slip, with a dip-slip component on the northern 8.5 km (Figure 2.53).

The strike of the northern termination of the rupture is 315° and it has a continuous 1.5 m high vertical scarp, uplifted on the northeast side of the fault (Figure 2.53). There is a 5 km long strike-slip strand parallel to and directly southwest of the dip-slip scarp, with lineations that are clear in satellite images as a series of

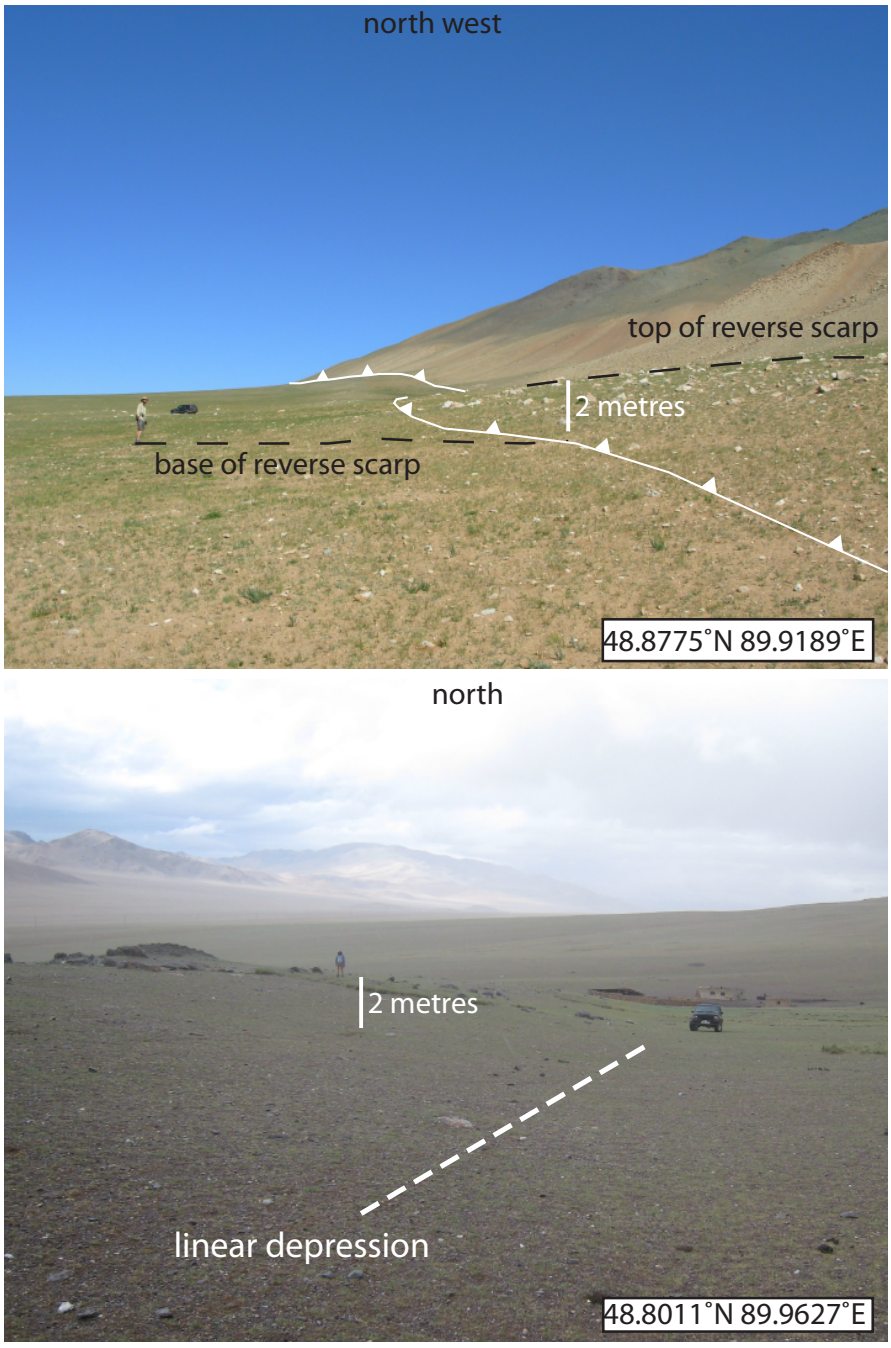


**Figure 2.53:** (a) Field photo of a 1.5 m high scarp on the northern termination of the Sair Uul rupture. (b) Photo of a linear depression along the Sair Uul rupture with a dip-slip component uplifting the western side of the fault. Photo localities are indicated on Figure 2.52.

*en-echelon* fissures. However, in the field, these fissures were linked and covered in vegetation, possibly related to springs and ponding of water along the fault (Figure 2.54a). It cannot be confirmed that the line of depressions is directly related to the Sair Uul paleoearthquake, and it is not included in the formal map of the rupture but is noted as a possible splay fault. The strike of the main rupture is nearly north-south (340°–350°) where it crosses a flat valley and the main road from the south into Ölgiy. On this more northerly-striking portion there is no vertical scarp and the rupture is dominantly strike-slip. There are several tension fissures and mole tracks that are clear in satellite imagery and obvious in the field, including a nearly continuous 2 km long depression that is about 2 m deep and 5 m wide (Figure 2.54b). Long linear features several hundreds of metres long are observed elsewhere on Altay ruptures (*Walker et al.*, 2006), and the long depression observed on the Sair Uul rupture is probably related to faulting, but may have been exploited by a stream.

Roughly 18 km south of Ölgiy city, the rupture strikes 340° to 350° and there is a linear depression that is approximately 500 m long with one side uplifted by about 4 m to the west, opposite what may be expected from the surrounding topography (Figure 2.53). South of this depression, the rupture passes east and upslope of a mineralised ridge and the site of an old copper mine, where there are several ephemeral streams incised into steep alluvial fans that are offset by 15–20 m, forming the focus of the Ölgiy slip rate study in Chapter 3 (labeled OSR in Figure 2.52). The mineralised ridge exposes faulted rocks with slickensides that have a plunge/trend of 64°/008° and a rake of 300°, indicating a nearly N–S slip vector when projected onto a horizontal plane, as well as a dip-slip component of motion. This fault surface is probably an exposure of a Paleozoic basement fault that has been exploited by Cenozoic faulting (e.g. *Cunningham*, 1998).

South of the copper mine, rupture features were observed in the field and in satellite imagery almost continuously for approximately the next 14 km south along

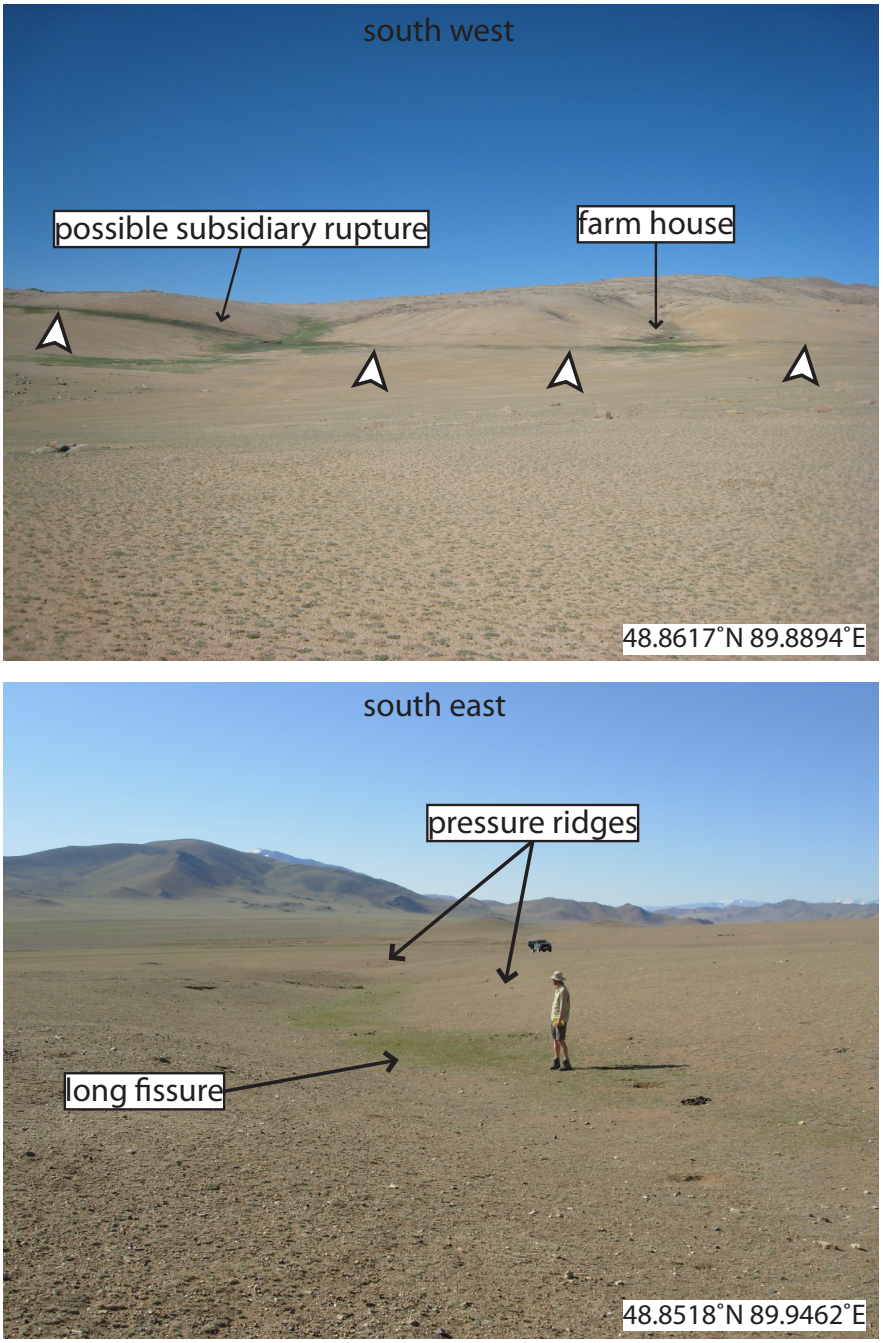


**Figure 2.54:** Field photos from the Sair Uul rupture. (a) shows the subsidiary rupture to the west of the main Sair Uul rupture, which was difficult to identify as a rupture in the field as vegetation covers much of the feature. (b) shows part of a long depression observed along the main rupture. There are pressure ridges along the depression, but the depression is continuous around the ridges, possibly due to stream capture of individual depressions.

strike. The rupture continues through a saddle at the base of the main range front, where several pressure ridges (or mole tracks) and tension fissures (or sag ponds) were observed that are 5–10 m wide, 5–50 m long, and about 2 m deep or high (Figure 2.56a, labeled on Figure 2.52). Some of these features are probably too large to be the result of a single earthquake, and may be the result of surface deformation from several earthquakes. The long axes of tensional features strike 360°, which is about 15–20° clockwise from the strike of the fault (340°) and typical of dextral strike-slip faulting.

South of the saddle in topography pictured in Figure 2.54, the rupture is visible in the Hungui Uul foreland as a series of left-stepping fissures through active alluvial fans (Figure 2.55a). The fissures are up to 50 m long, 5 m wide, and 2 m deep, with a strike that is 15–20° clockwise from the main rupture trend (Figure 2.57a). The rupture features are clear in alluvial fans and the younger river terraces cut into the fans, and the only surface on which they are not found is the active river channel. There are very well-preserved fault-related features observed in high resolution Kompsat-2 imagery (1 m/pixel), including two parallel series of fissures (Figure 2.55c). Each of the fissures is 20–50 m long and rotated clockwise to the strike of the fault, indicating dextral slip. These fissure series cut through an alluvial fan, displace the riser between the fan and the southern side of the river in Figure 2.55c, and cut through two generations of river terraces (T1 and T2). The riser from T2 to the fan is displaced by approximately 2 and 10 m by the east and west fissures series respectively. The terrace riser from T2 to T1, on the northern side of T1, is displaced by 3.7 m (Figures 2.57a, 2.55c). There is at least one small rupture that branches out to the northwest from this section, approximately 3 km long and striking 335°, with a slight dip-slip component indicated by a scarp about 1 m high, up on the west side of the fault and opposite to the regional topography (Figure 2.55a).

Along the same range front as Figure 2.55, but further south (at 48.71°N, 90.01°E),

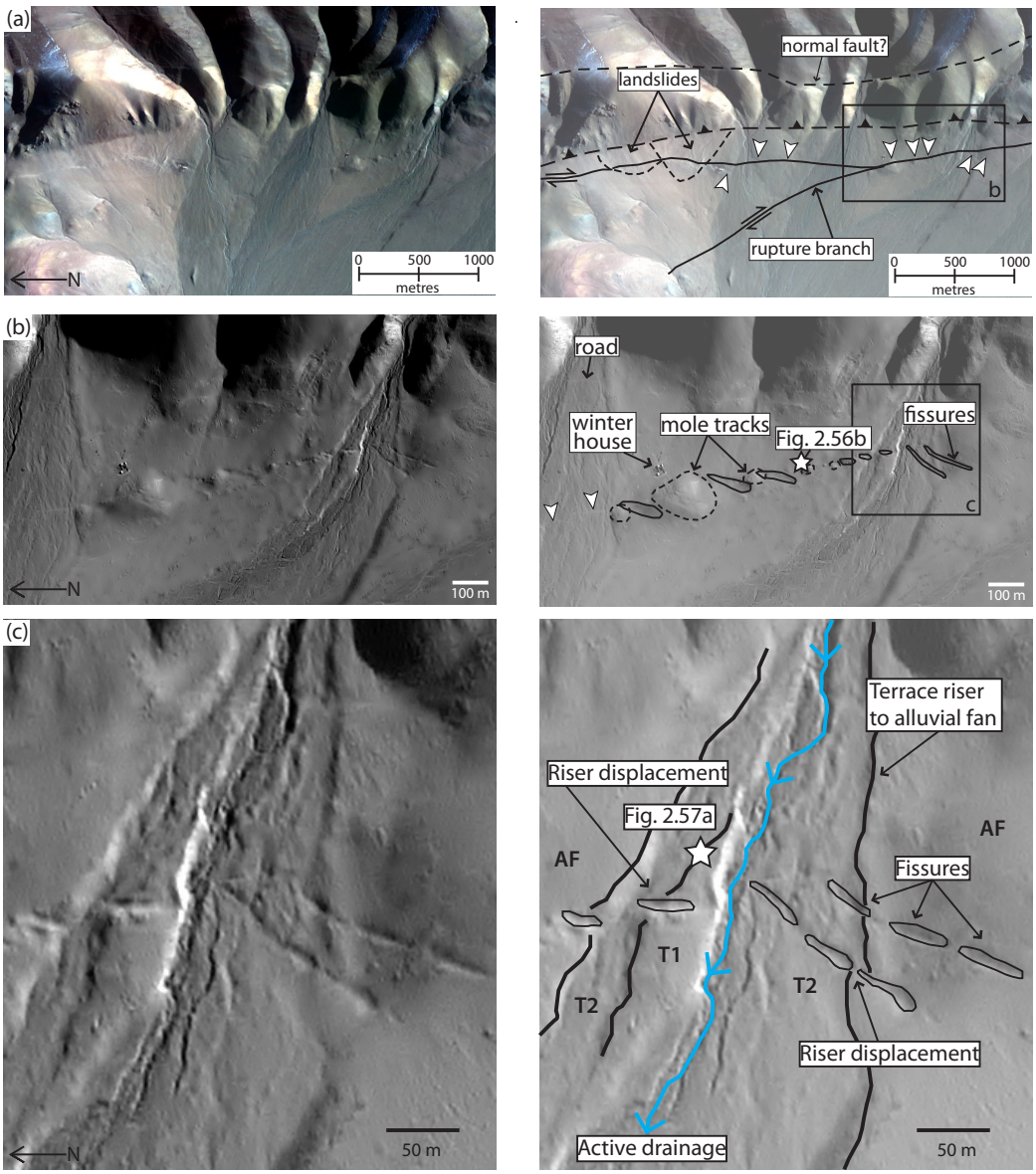


**Figure 2.55:** Original and annotated Kompsat-2 images from the central section of the Sair Uul rupture. Images have been rotated such that north is to the left of the images. (a) Views of the Hungai range front where the rupture cuts through alluvial fans. A potential normal fault behind the range is indicated, as well as areas of landslid material. White arrows indicate sag ponds and mole tracks along the trace of the fault. (b) Clear fissures and mole tracks through an active alluvial drainage system. Illumination is from the right side of the figure in this orientation, and it picks out the highs and lows of fissures and pressure ridges. (c) Detailed view of long fissures, where displaced terrace risers are indicated by black lines and arrows where offset. There are at least two generations of river terraces, where T1 is a remnant terrace above T2, which is incised by the active stream (indicated by blue line). AF is the surrounding alluvial fan.

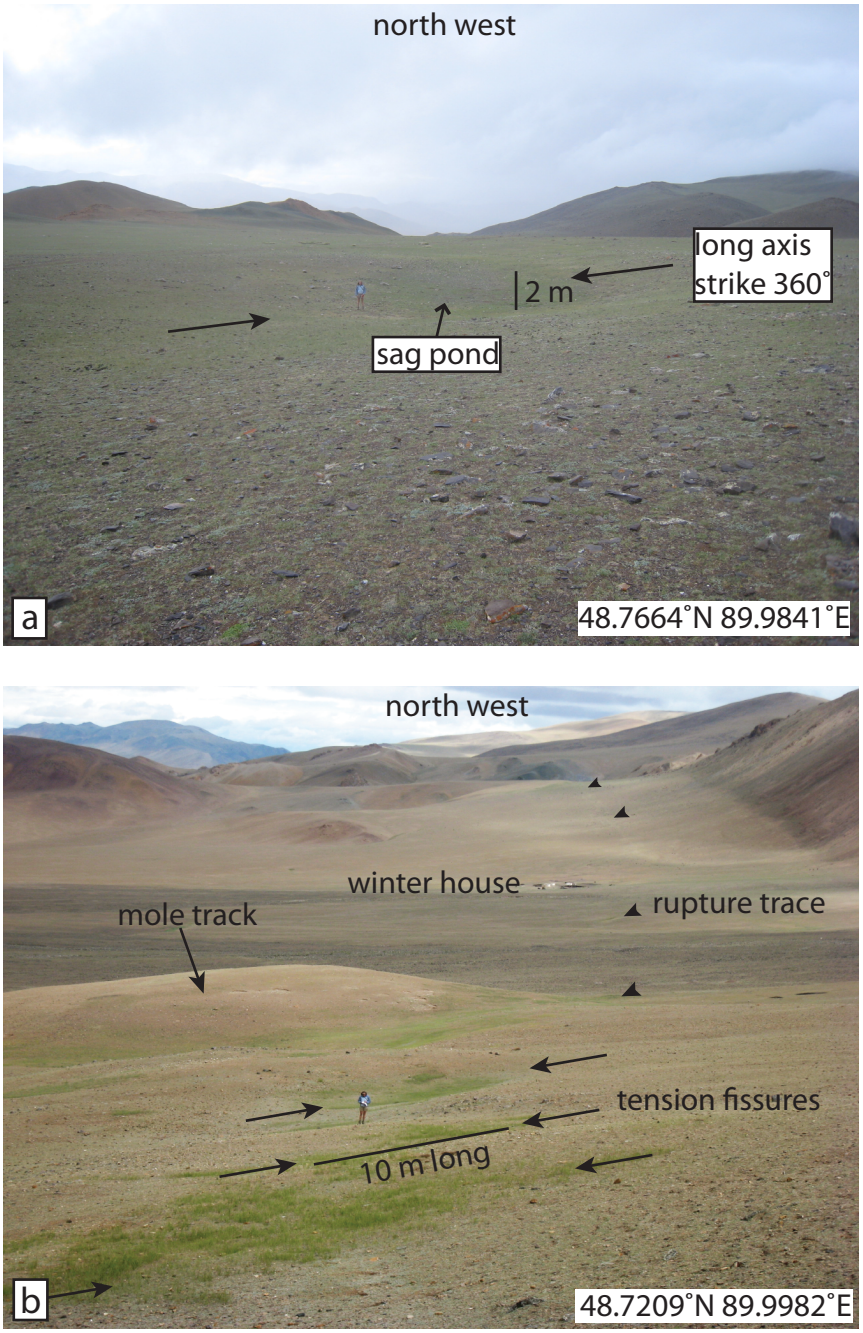


**Figure 2.56:** Photos of strike-slip features along the Sair Uul rupture (a) Large sag pond along the rupture. The sag pond is about 5 m wide, 15 m long and 2 m deep, and has a strike of about 360°, which is rotated clockwise from the strike of the rupture. Locality labeled on Figure 2.52. (b) Series of left-stepping tension fissures and a large mole track (200 m across) in the foreground, visible in satellite imagery in Figure 2.55b. The rupture continues in the mid-ground through the active river channel and terraces, and in the background through the foreland of Hungui Uul. Locality labeled on Figure 2.55.

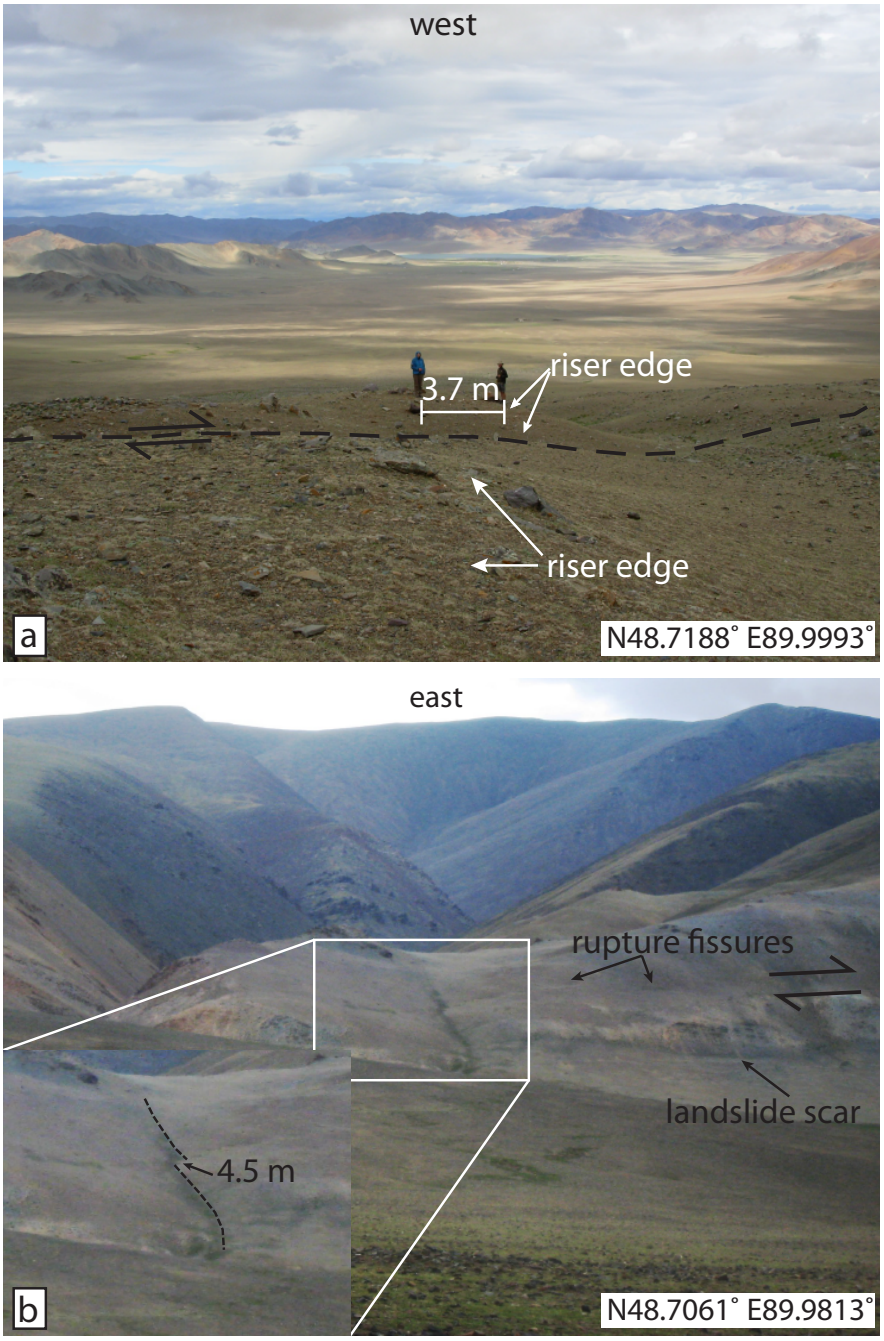


**Figure 2.57:** Photos of displacements along the Sair Uul rupture. (a) Stream terrace riser displaced by about 3.7 m, locality indicated in Figure 2.55c. The edge of the riser on both sides of the fault is indicated by arrows. (b) Stream displaced by about 4.5 m along a line of fissures. A landslide scar is indicated, and landslide deposits were found below the scar in the field. Locality indicated in Figure 2.52.

the rupture crosses a river gorge and is located high on the flank of the mountains, striking 335°. Metamorphosed fault rock outcrops in the side of the gorge directly below a saddle in the range front where there is a series of 5–10 m long tension fissures. In outcrop, the fault dip is nearly vertical and the edge of the river gorge in which the fault outcrops is displaced by about 20 m. Where the rupture zone crosses a small stream, the southern stream bank is displaced by 4.5 m (Figure 2.57b). Along this part of the rupture, there are several landslides located directly below the trace of the fault.

The rupture strike changes to between 300°–310° as it intersects the rocky interior of Hungui Uul, where it was difficult to investigate in the field and very steep topography makes the rupture unclear in satellite imagery (along the dashed portion in Figure 2.52). There is a large landslide several hundred metres long on the likely rupture zone, which is 3–5 km behind the main range front and frontal thrust (e.g. Figure 2.22). It is possible that this landslide was caused by shaking in the earthquake, a typical phenomenon observed along large magnitude earthquakes in steep and glaciated mountains (e.g. the 2002 $M_w$ 7.5 Denali earthquake, Alaska, *Jibson et al.*, 2006).

South of Hungui Uul, the rupture crosses high (2700 m) but relatively flat topography and is visible as grassy depressions (Figure 2.60a). The southern termination of the surface rupture is complex, with several strands observed in the field and in satellite imagery over a zone of 5 km (Figure 2.58). There is a clear 2 m high, 700 m long vertical scarp through an alluvial fan where the rupture crosses a dry valley with ponded streams (Figures 2.60b, 2.59b). The scarp is quite steep, and therefore relatively fresh, and there are left-stepping depressions along the base of the scarp, suggesting a strike-slip component of motion. On the flanks of Sair Uul there are several strands of fissures, and one segment of the rupture is located along a series of gulleys that are displaced by 100–300 m (Figures 2.59a and 2.61c,d). The rupture

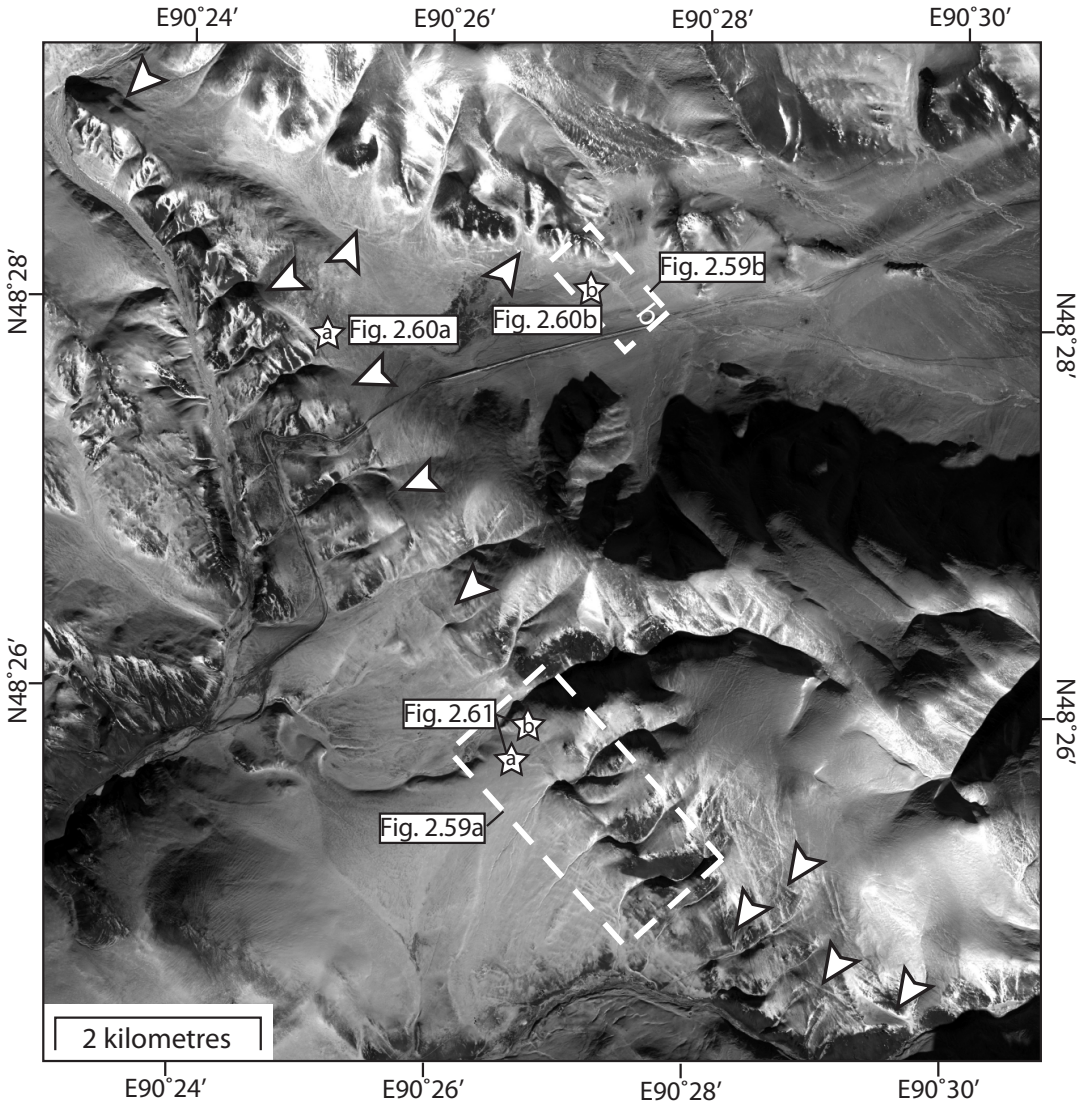


**Figure 2.58:** SPOT-5 imagery (2.5 m/pixel) of the southern section of the Sair Uul rupture, showing an overview of the termination of the rupture, where several rupture traces were observed. White dotted rectangles outline images in Figure 2.59, and the location of this figure is indicated in Figure 2.52.

was not found further south than the northwest side of Sair Uul.

The majority of the features along the Sair Uul rupture are indicative of right-lateral strike-slip. The main exception to this is the northernmost 8.5 km termination, where there is a continuous 2 m high reverse scarp uplifted on its northeast side. The scarp occurs where the strike of the rupture veers more to the west, and it is in-

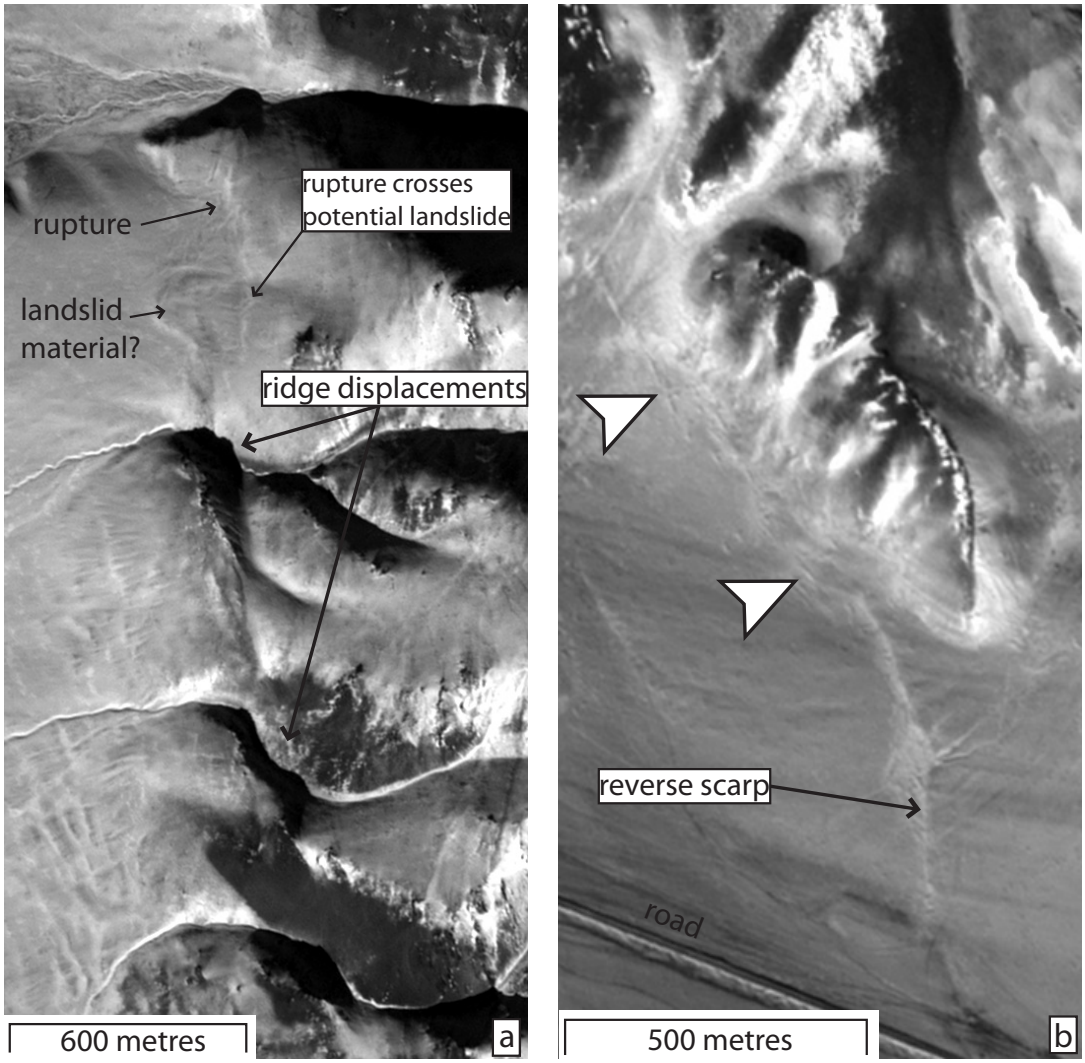


**Figure 2.59:** SPOT-5 imagery (2.5 m/pixel) of the southern section of the Sair Uul rupture, showing the areas outlined in rectangles in Figure 2.58. (a) Several ridges are displaced on the western flanks of Sair Uul. The rupture is visible as light coloured depressions along strike of the displaced ridges. (b) Fresh reverse scarp, up on the right side of the image.

teresting to note that this follows the general regional trend in the Altay of reverse or oblique slip found where faults strike to the WNW. There are several discontinuous vertical scarps at other localities, mentioned above, but these are not consistently up to either the northeast or southwest, and often face against what would be expected from the regional topography; these dip-slip faulting features are likely due to local

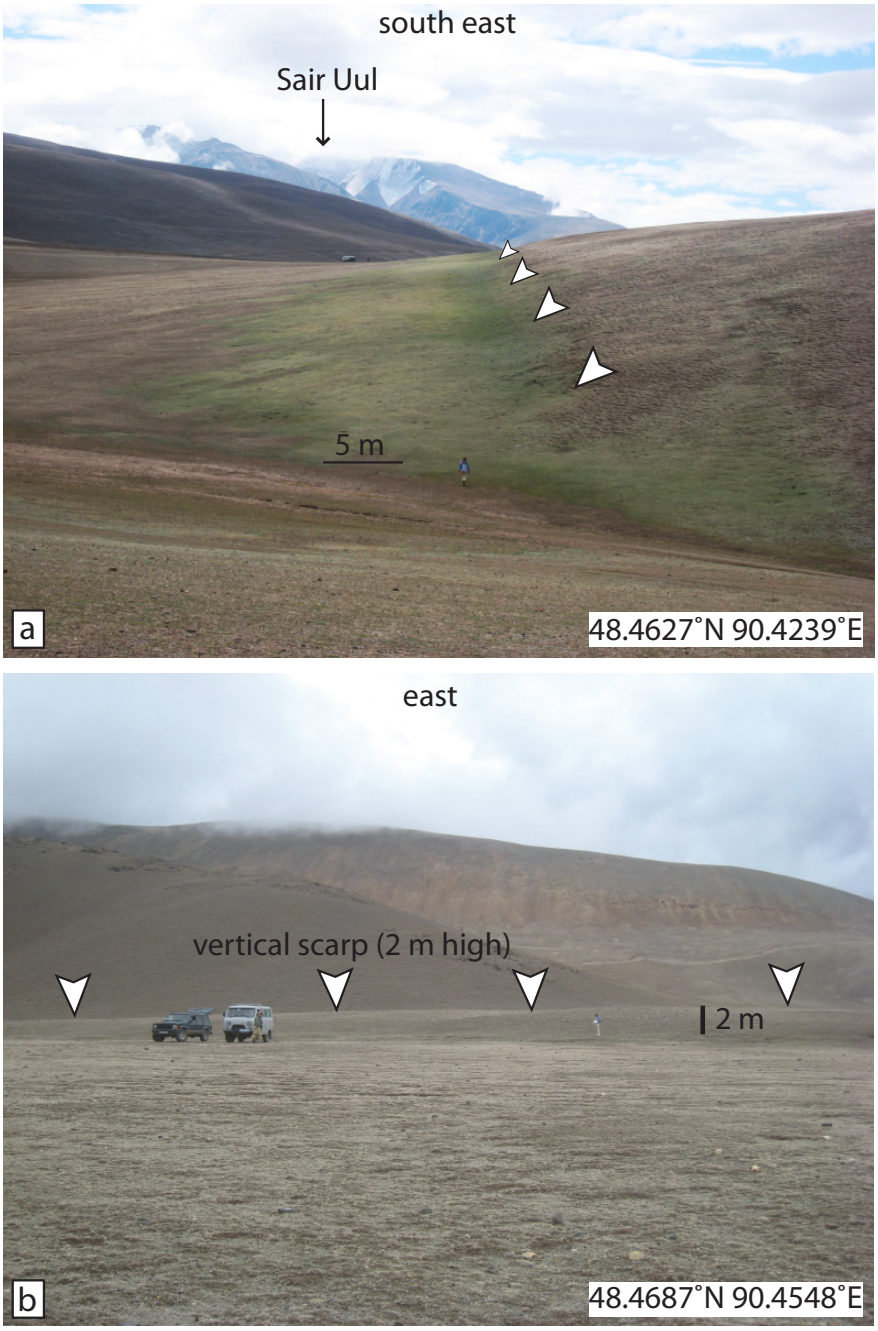


**Figure 2.60:** Photos from southern section of the Sair Uul rupture. (a) Grassy depressions along the base of the ridge, possibly with a slight dip-slip component uplifting the west side of the fault. (b) View of approximately 2 m high scarp along one strand of the rupture. There are some depressions at the base of the scarp, indicating a strike-slip component. Photo localities are indicated in Figure 2.58.

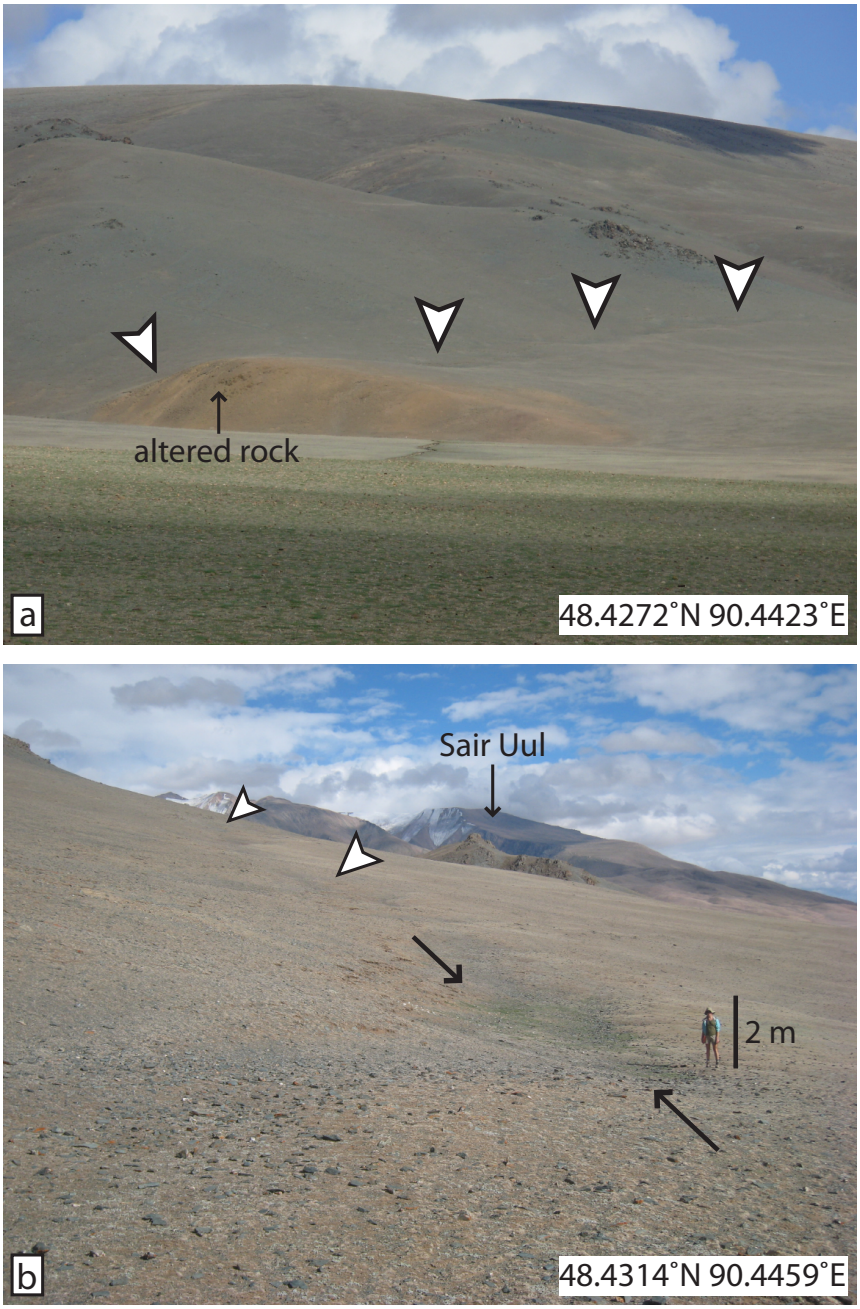


**Figure 2.61:** Photos from the southern portion of the Sair Uul rupture (a) Arrows indicate grassy depressions that are 5–10 m long on the hillside. Altered rock that is formed along Paleozoic faults and commonly found along the active Altay faults, is indicated. (b) Photo of the fissures in (a). Photo localities are indicated in Figure 2.58.

irregularities in the propagation of the rupture at the surface and are not due to a significant overall oblique component of the rupture. The vertical scarp that is 700 m long and 2 m high near the southern end of the rupture is another more continuous reverse faulting feature (Figure 2.60b and Figure 2.59b), but it was found where the surface expression of the fault comprises several complex strands near the end of the rupture (Figure 2.58). The southern termination of the rupture occurs at Sair Uul, a push-up mountain formed at a transpressional bend in the Ölgiy fault and also a possible impediment to the propagation of the earthquake.

Most of the tension fissures and pressure ridges that I observed have widths of 2–5 m, but some features are up to tens of metres wide. Fissures and mole tracks range in length from 10 to 50 m, with some continuous linear depressions up to 2 km long. In comparison to other known surface ruptures in western Mongolia such as the Ar Hötöl or the Bulnay, on average these features are smaller, but of the size that is to be expected from the length of the rupture, based on fault scaling laws (e.g. *Wells and Coppersmith*, 1994), because the Sair Uul rupture is only about a fifth of the length of the largest palaeoearthquakes in Mongolia. However some features of Sair Uul are much larger in size than expected given the length of the rupture (Figure 2.56a, Figure 2.55b), and may be the result of cumulative paleoearthquakes.

For the measured surface rupture length of 83 km, the magnitude of the earthquake is estimated to be $M_w$ 7.3 from empirically determined parameters of continental strike-slip faults (*Wells and Coppersmith* (1994), see Section 2.2.2). The characteristic size of features, surface rupture length, and estimated magnitude of Sair Uul rupture are similar to the the same features of the 1990.06.20 $M_w$ 7.3 Rudbar-Tarom earthquake in NW Iran, which had a surface rupture that was also 80 km long (*Berberian et al.*, 1992). For Sair Uul, the average of all field measurements of strike-slip displacement is approximately 4 m. If this average displacement is used to empirically calculate the source magnitude, the resulting magnitude of

$M_w$ 7.7 is significantly larger. The size of the features relative to the length of the rupture is verification that I can confidently join the northern and southern sections of the rupture, which I was able to trace in the field, through the middle of Hungui Uul, where I have no field confirmation of the rupture. If the northern and southern surface ruptures were caused by different events, I would expect smaller average offsets and significantly smaller surface features. If the two strands of the rupture represented two separate events, they would be less likely to reach the surface in such an consistent manner. However, it is also possible that the average offset is overestimated, because smaller offsets of 1–2 m or less are not as likely to be preserved. Despite this, I am still confident that the Sair Uul rupture represents one event based on the size of rupture features and the similarity of the surface expression of the northern and southern portion of the rupture. A very rough estimate of the repeat time of the earthquake can be made with the assumption that the slip rate of the Ölgiy fault is between about 1 and 2 mm yr$^{-1}$ (Chapter 3 *Frankel et al.*, 2010). The average coseismic displacement of 4 m divided by the approximate slip rate suggests a repeat time of 2000–4000 years for similar magnitude earthquakes on this section of the fault.

### 2.4.2 The Fiery Horse rupture

Another previously unknown palaeoearthquake was discovered in satellite imagery and mapped in the field north of the village of Sogoog (Figure 2.62). The local people attributed the surface features to the ancient tracks of a fiery horse, inspiring the name for the Fiery Horse Rupture. The rupture runs NW–SE from 47.72°N, 88.63°E to 49.34°N, 89.07°E. The northern part of the rupture, which extends into Russia and was not visited in the field, is very obvious as several strands in satellite imagery (Figure 2.63). Along the northern-most strands, there are characteristic left-stepping tension fissures filled with snow or vegetation that have the same mor-

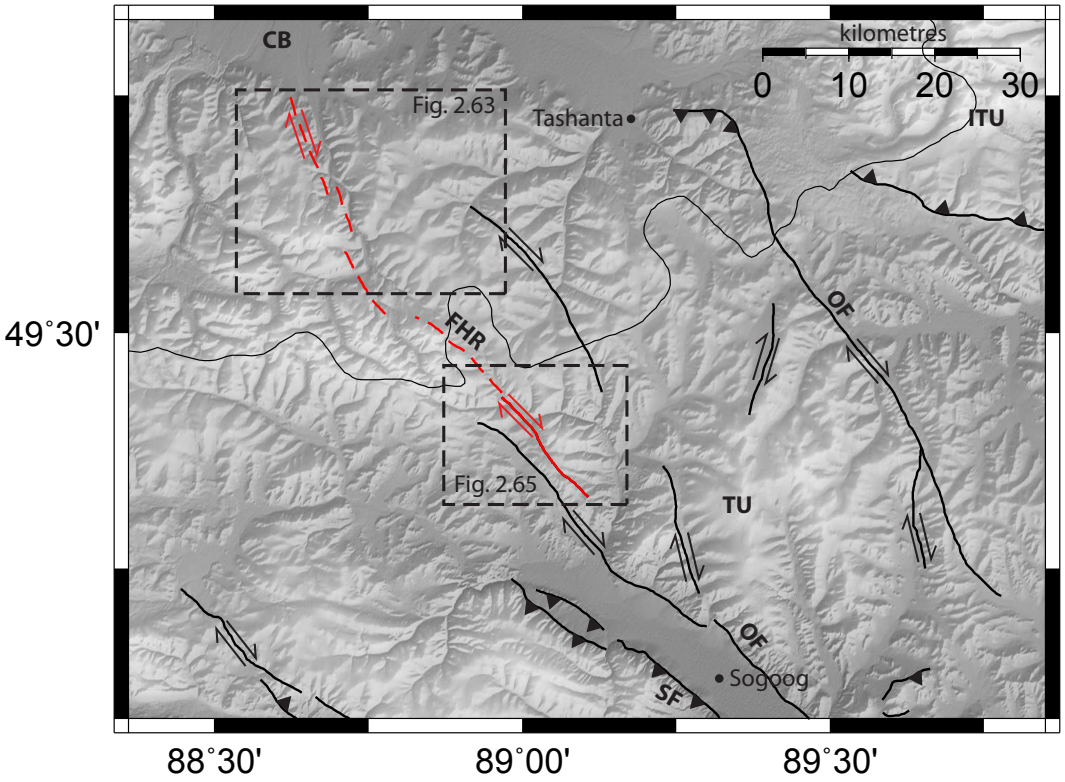


**Figure 2.62:** SRTM 90 m DEM overview of the Fiery Horse rupture. Ruptures are mapped in red and towns are indicated with closed circles. The dotted line indicates a section of the rupture that was not ground-truthed in the field. Abbreviations are CB: Chuya Basin, FHR: Fiery Horse Rupture, ITU: Ih Turgen Uul, SF: Sagsay Fault, OF: Olgiy Fault.

phology in imagery as the southern section of the rupture that was ground-truthed in the field. The long axes of fissures are generally oriented about 020° clockwise from the strike of the fault, although some fissures are parallel to the rupture strike. There are several displaced stream risers along the northern section that are offset by 15–20 m, possibly recording cumulative displacement (Figure 2.64). Some sections of this northern part of the fault are not as clear in satellite imagery, but based on the similarities of features visible in satellite imagery with those observed in the field, and on the general size of features, I am confident that the rupture is continuous from north to south. Parts of the rupture that are not clear in satellite imagery are

along steep slopes and are mostly covered by landslides or snow.

Ground deformation features along the southern section of the Fiery Horse rupture are excellently preserved as a series of *en-echelon* tension fissures and vertical scarps in some places (Figures 2.65 and 2.66). A continuous strand of the rupture is shown in Figures 2.65b and 2.66a, b. Tension fissures are observed to have a large range in size: some fissures are approximately 1 m across and up to 3.5 m long, whilst many features are significantly larger, up to 10 m across and 50 m long (Figures 2.67 and 2.66c, d). The strike of the long axes of the tension fissures varies along the rupture with the strike of the fault. Where the fault strikes more to the west (310° –320°), the fissures are nearly aligned with the trace of the rupture or even rotated anticlockwise (less than 310°, Figure 2.66c), and where the strike is more northerly (330°), fissures are generally rotated clockwise to the strike of the rupture (greater than 330°).

There are few localities where horizontal displacement could be measured, but the width of fissures and pressure ridges can be used to approximate the horizontal displacement that occurred during the earthquake. The width of a fissure in the direction that is parallel to the local trace of the fault is ideally a measure of the extension of the fissure, correlating to strike-slip displacement parallel to the fault (e.g. *Walker et al.*, 2006). Most of the features that can be attributed to one earthquake were between 1.0–3.5 m across in the direction parallel to fault strike, and these displacements are used to approximate the average displacement of the earthquake (Figure 2.66). This method is not ideal, because the fissures may be modified by subsequent ponding of water or collapse of the side of the fissure. Very large horizontal displacements were measured along an ephemeral stream perpendicular to the strike of the fault (at 49.4072°N, 89.0031°E, and shown in Figure 2.68b, c). Both the active stream and the stream bank are displaced by 10–15 m, and this must represent cumulative slip in several earthquakes.

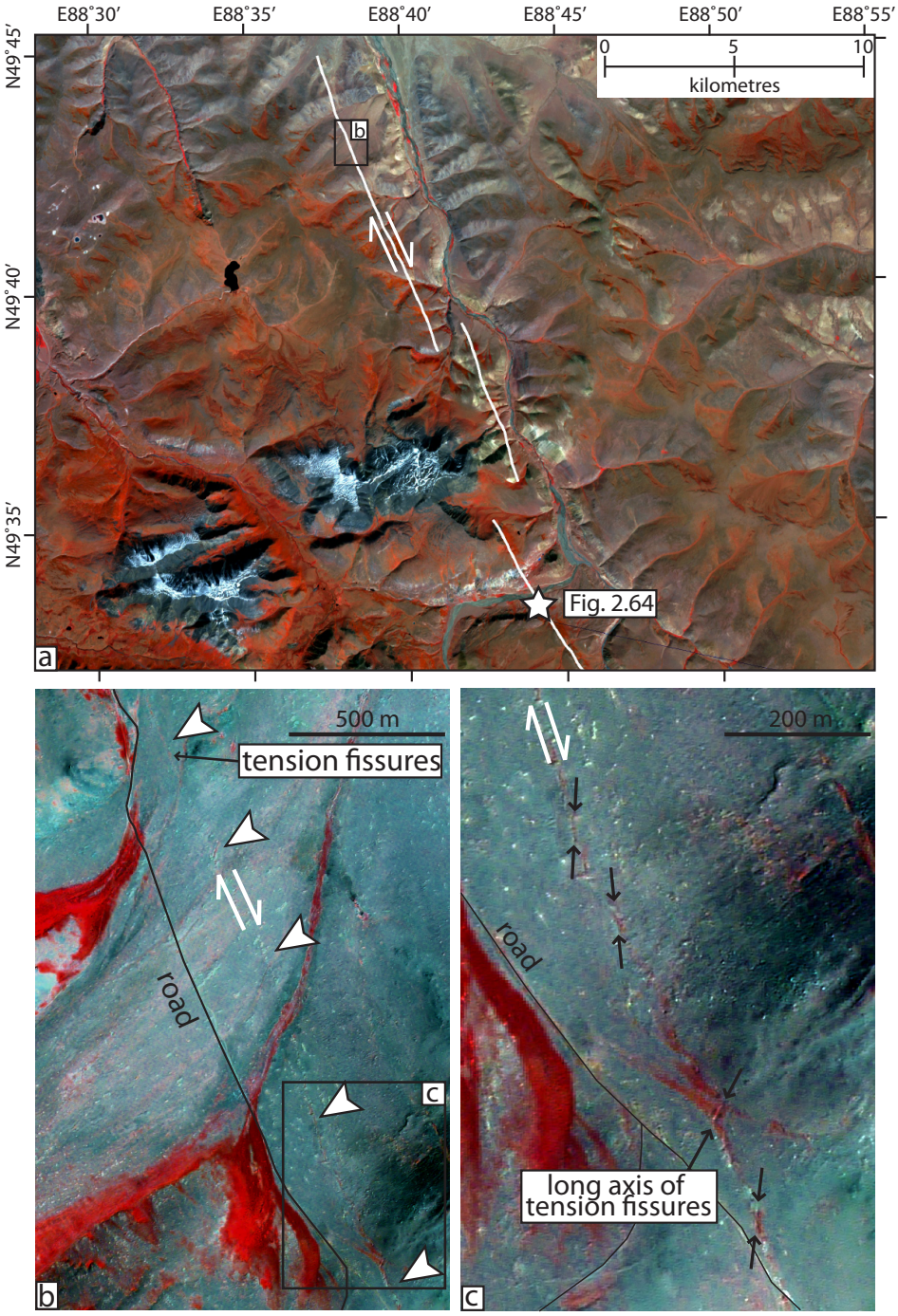


**Figure 2.63:** (a) ASTER image of northern strands of the Fiery Horse rupture. (b) and (c) are panchromatic-sharpened (1 m resolution) multi-spectral (4 m) Kompsat-2 images (with RGB plotted as near-infrared, blue, and green bands). (b) shows a section of surface ruptures that is continuous for over 2 km. (c) Fissures are obvious as red depressions that are filled with more vegetation, which is strongly reflected in the near-infrared band, than the surrounding alluvium. The long axes of the *en-echelon* fissures are rotated clockwise with respect to the strike of the fault.

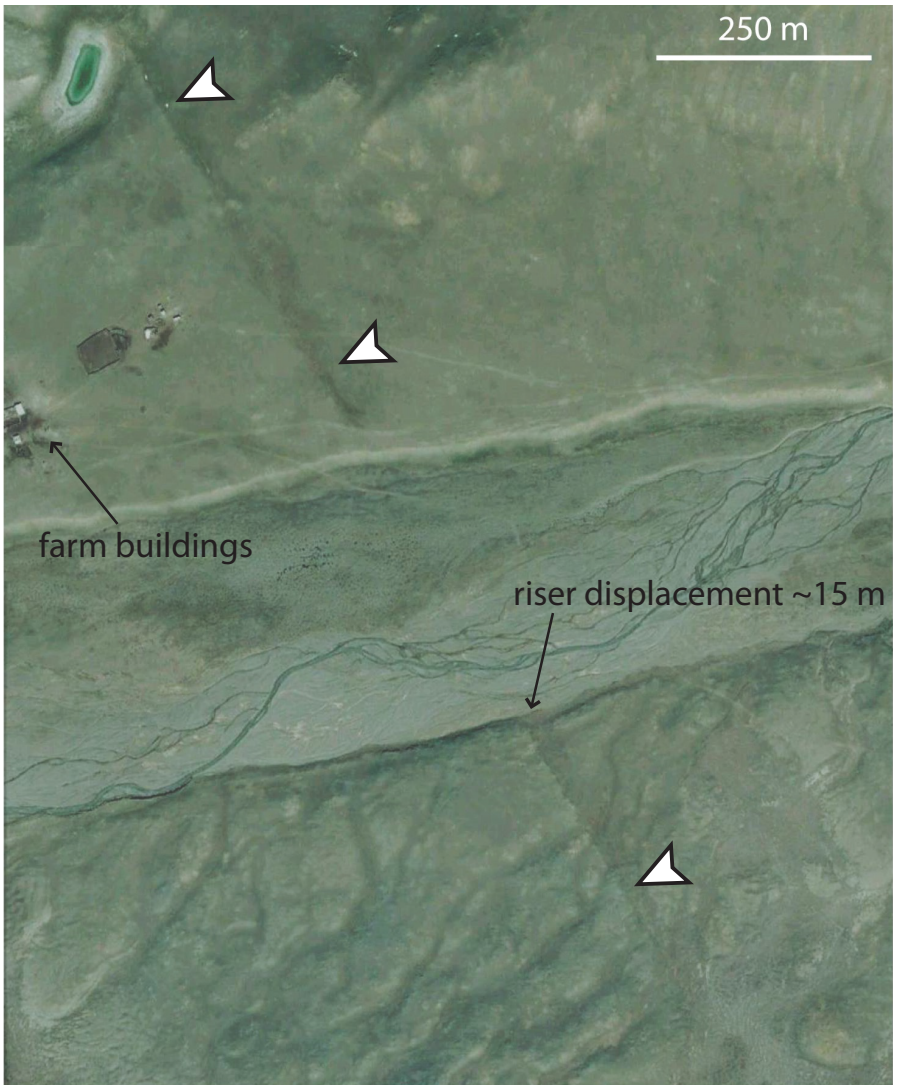


**Figure 2.64:** Quickbird imagery (from Google Earth) of the Fiery Horse rupture and a displaced stream riser. The riser is displaced by approximately 15 m. The center of the image is 49.5617°N, 88.7314°E. Location is shown in Figure 2.63.

Along a right stepping bend in the rupture (at 49.39°N, 89.02°E; Figure 2.65), there are several large sag ponds and a 2 m high vertical scarp that is continuous for several hundred metres, with fissures observed at the base of the scarp (Figure 2.66d, e). The fault likely has a significant normal component along this section of the rupture, based on the orientation of the fault (more to the north) and presence of large tensional features. The rupture was followed further south, where deformation

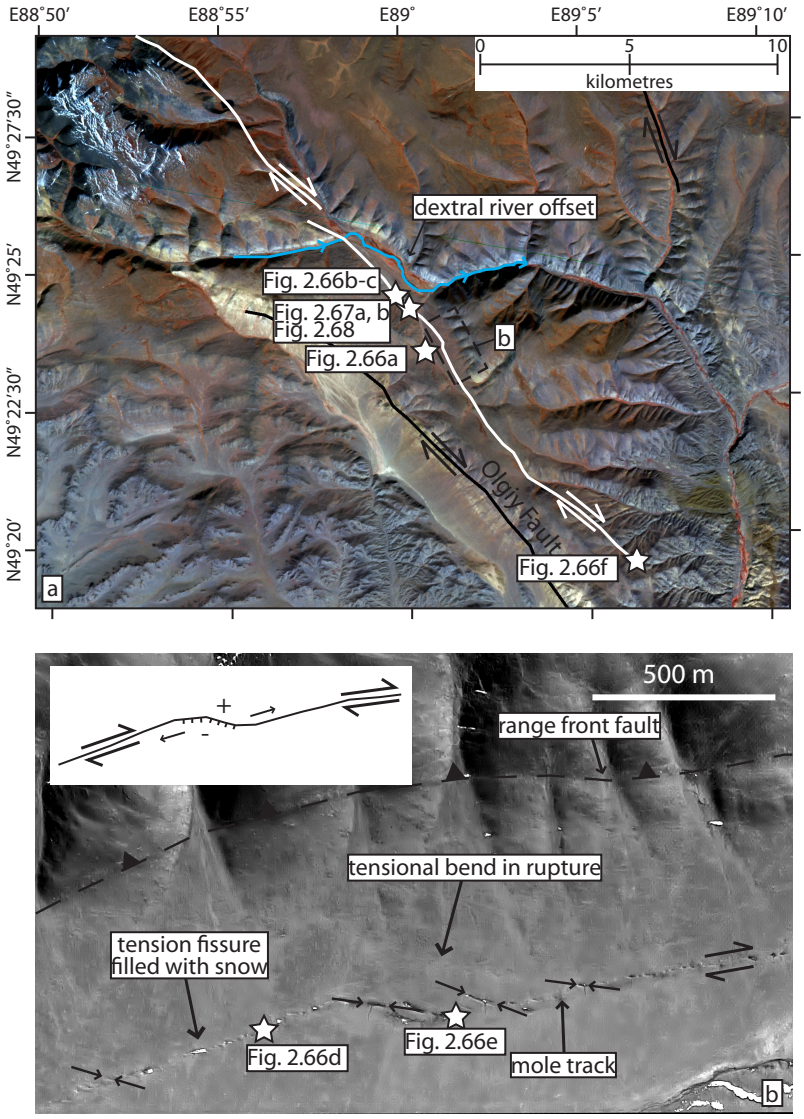


**Figure 2.65:** ASTER (a) and Kompsat-2 (b) panchromatic (1 m/pixel) imagery of the southern Fiery Horse rupture. (a) A drainage crossing the fault is displaced by 3.0 km. In (b) arrow pairs point to the long-axes of tension fissures, which are also obvious as white depressions (filled with snow). Discontinuous scarps are formed along a transtentional bend in the rupture, which appear darker in the image due to shadowing. The inset in (b) shows the geometry of faulting in the right-stepping tensional bend in the portion of the rupture shown.

features are less identifiable. There is also a small vertical scarp near the southern end of the rupture, probably with a normal component based on the strike of the fault (Figure 2.66e).

Like the Sair Uul rupture, features along the Fiery Horse rupture are generally indicative of dextral strike-slip faulting. Left-stepping *en-echelon* fissures, right-stepping mole tracks, and right-lateral horizontal offsets of stream banks consistently attest to dextral slip. However, a normal component of slip is inferred along a section of the rupture where the geometry of faulting implies a transtentional bend, shown in Figure 2.65. The inset in Figure 2.65 outlines the extensional sense of slip on the right-stepping bend, suggesting that vertical scarps found in the vicinity of the bend are the result of localised normal faulting (e.g. Figure 2.66e). This transtentional bend is unusual, as a normal component of slip is mostly absent from the dominantly transpressional Altay mountains. Notable exceptions where transtensional faulting is present are the pull-apart basins along the Hovd fault, described early in this chapter, and in localised sections of the Jid fault (*Walker et al.*, 2006). Tensional fissures were also found at the base of the vertical scarps on the Fiery Horse rupture, and these tensional features as well as some very large fissures (greater than 10 m) attest to extensional faulting at the surface in the rupture bend (Figure 2.66d).

The Fiery Horse rupture is approximately 60 km long, which correlates with an approximate magnitude ($M_w$) 7.1 earthquake (*Wells and Coppersmith*, 1994). Features along the rupture are fresh, which suggests that the earthquake is amongst the youngest of the palaeoearthquakes in the Altay, and it is likely a few hundred years old. The size of features and horizontal displacement varies along the rupture. Features that are probably the result of the most recent earthquake suggest average displacements between 1 and 3.5 m, and whilst these are not ideal estimates of average strike-slip displacement, the along-strike widths of tension fissures are in agreement with a magnitude between $M_w$ 7.0 and 7.5 (based on empirical relations

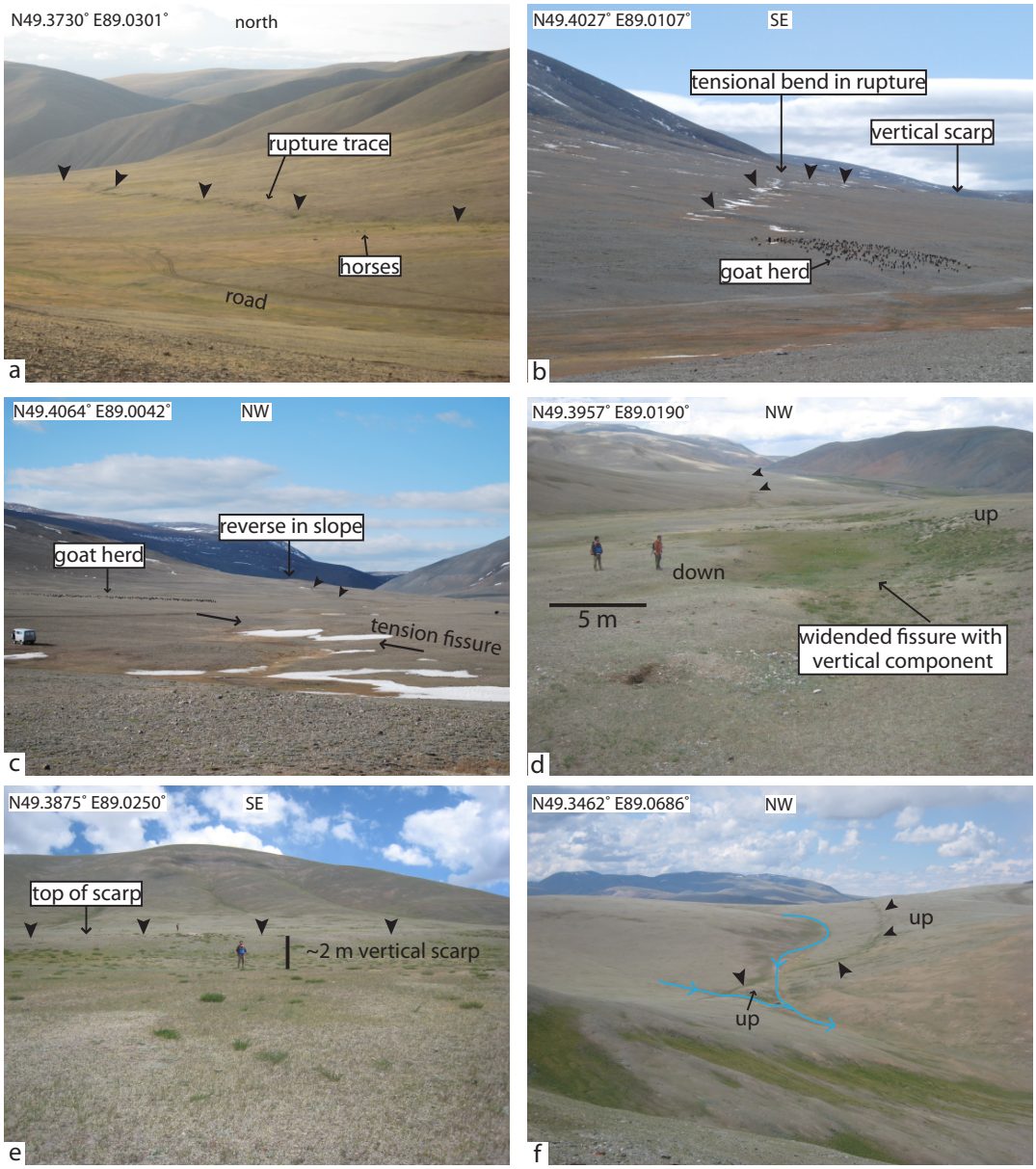


**Figure 2.66:** Photos of ground deformation along the Fiery Horse rupture. (a) and (b) show a series of tension fissures, also shown in Figure 2.65. There is a right-step in the rupture indicated, with large tensional fissures in the bend. (c) Sag ponds that are up to 50 m long (see Russian van at left for scale), and rotated anti-clockwise from strike along a part of the rupture with a more westerly strike. A reverse in slope is visible on the horizon along strike of the rupture. (d) A large fissure, possibly widened by water ponding, with a vertical scarp along the tensional bend in the rupture indicated in (b). (e) 2 m high vertical scarp along the tensional bend in the rupture in (b). (f) Fissures near the end of the rupture, with a vertical component uplifting the east side of the fault. Photo localities are indicated in Figure 2.65.

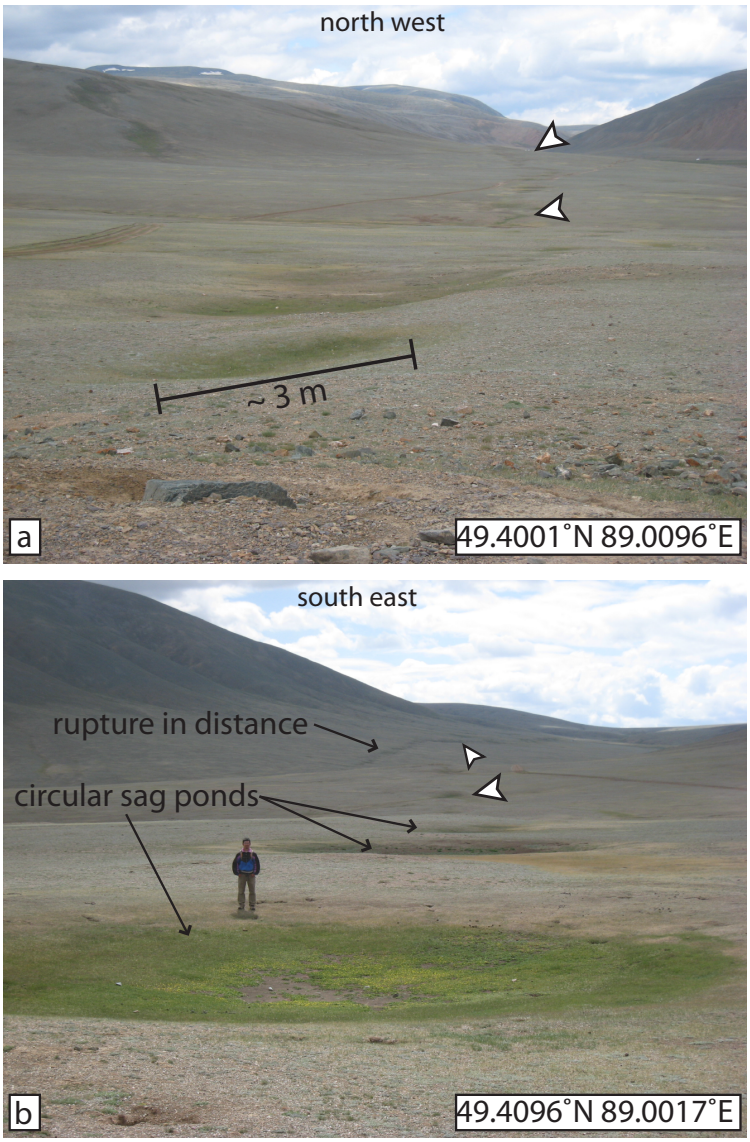


**Figure 2.67:** Photos highlighting the range in size of tensional features along the Fiery Horse rupture. (a) *En-echelon* fissures are rotated clockwise from the strike of the rupture, and are between 2.5 and 3.5 m long and approximately 1 m wide. (b) A series of rounded sag ponds 10–15 m wide, possibly altered by pooling of water over time, with the effect of ponding heightened due to the presence of permafrost.

in *Wells and Coppersmith*, 1994). Many of the ground deformation features observed are much larger than would be expected for a magnitude 7.1 earthquake, particularly the along-strike widths of sag ponds and stream displacements that are on the order of 10 metres or more. These features likely are the result of cumulative slip on the

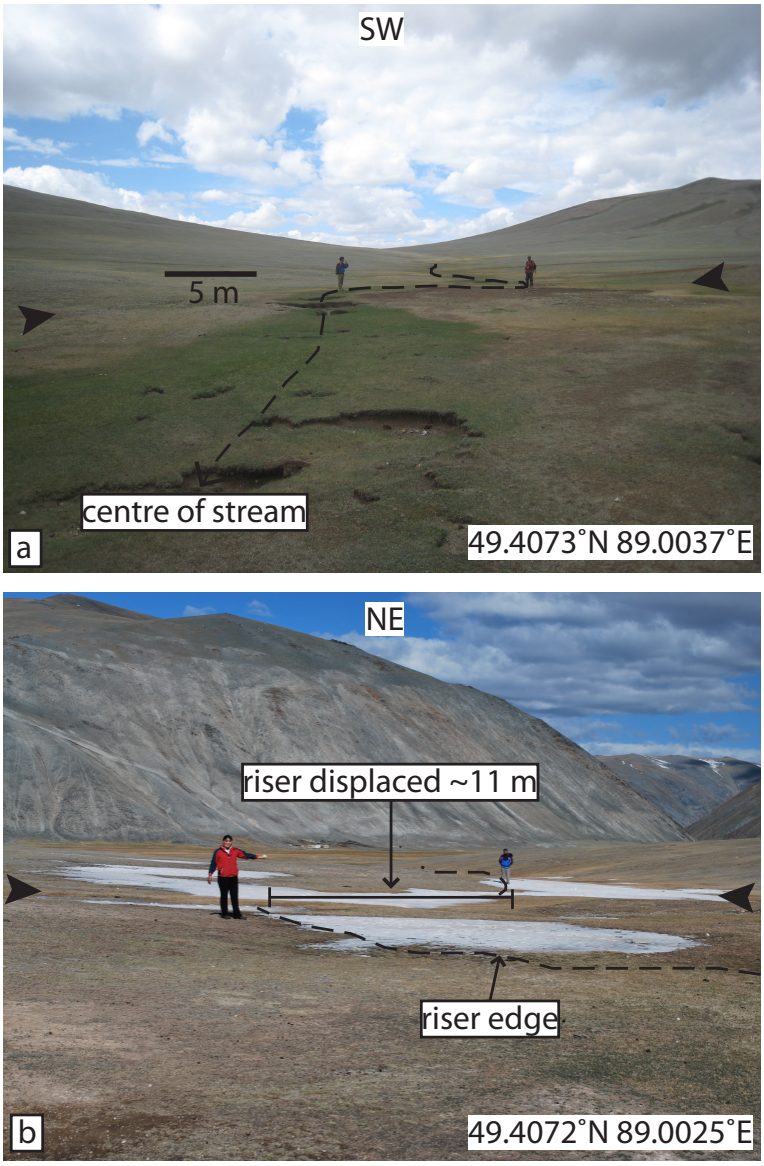


**Figure 2.68:** Photos of dextral displacements along the Fiery Horse rupture. (a) Displacement of the center of an ephemeral stream by about 11 m. (b) Displacement of the stream bank by approximately the same amount. Large tension fissures were observed to be in line with the bank displacements (Pictured in Figure 2.66c). These larger displacements are the result of cumulative offset of the fault.

fault during the Holocene, demonstrating that the Fiery Horse section of the faults surrounding Tas Uul (at the northern end of the Ölgiy/Sagsay faults) is capable of repeated earthquakes. These faults were not clearly recognised before the discovery of the Fiery Horse rupture, but are important for accommodating deformation in the

Altay, and should be included in future maps of the Altay faults.

### 2.4.3 The Tsengel Hyarhan rupture

Evidence of a surface rupture is visible in satellite imagery and was documented in the field along a previously unknown strand of the Hoton Nuur fault south of Tsengel Hyarhan Uul (Figures 2.69 and 2.70). The features described in this section are also along strike from the faults surrounding Tsengel Hyarhan Uul, and may connect with the Tsengel Hyarhan faults to form a single continuous surface rupture (Figure 2.49c, d, and e). Features along the northern part of the rupture are described in Section 2.3.5, as they confirm the activity of faults surrounding Tsengel Hyarhan Uul (which I have grouped with the Hoton Nuur fault zone). Features of the southern section of the rupture are described here from south to north. The region crossed by the fault was heavily glaciated in the Late Quaternary, and much of the region crossed by the rupture comprises hummocky, proglacial or glacial deposits where it is difficult to distinguish features of the rupture from hummocks in the surface of deposits. The southern portion of the rupture is visible in satellite imagery, although discontinuously, and was documented in the field. Another section of the rupture was observed on a plateau in the topography along strike from, and 20 km to the northwest of, the southern end of the rupture (starred locality in Figure 2.69).

The rupture is visible as a wide red scar cutting across a ridge in Kompsat-2 multispectral imagery (Figure 2.71a). This linear depression is oblique to the slope of the hill, and does not appear to be related to any drainages exiting the flat topography above (Figure 2.70 and 2.72a). There are distinct depressions within the scar itself, which are about 1–2 m wide. A series of fissures continues for approximately 1 km to the southeast along a high plateau in topography (Figure 2.72b). These fissures strike between 320°–330°, and are oriented parallel to the strike of the rupture. The depressions are quite degraded, and are between 1–2 m wide. The west side of the

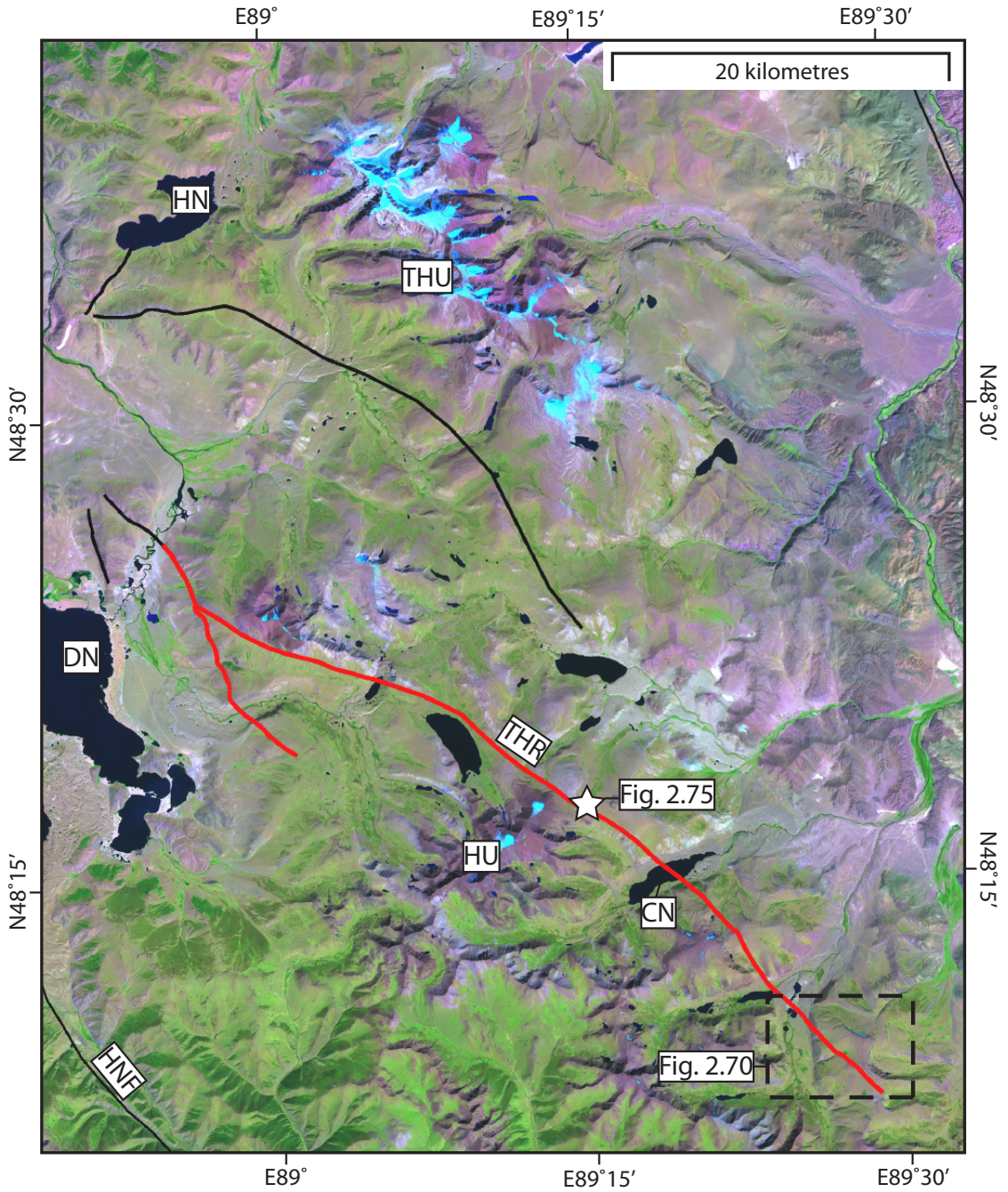


**Figure 2.69:** Repeat of Landsat image in Figure 2.69 of the faults surrounding Tsengel Hyarhan Uul (RGB = 741). Abbreviations are CN: Chickertee Nuur, DN: Dayan Nuur, HN: Har Nuur, HNF: Hoton Nuur Fault, HU: Halagash Uul, THR: Tsengel Hyarhan Rupture, THU: Tsengel Hyarhan Uul. White star shows the locality of ruptures pictured in Figure 2.75.

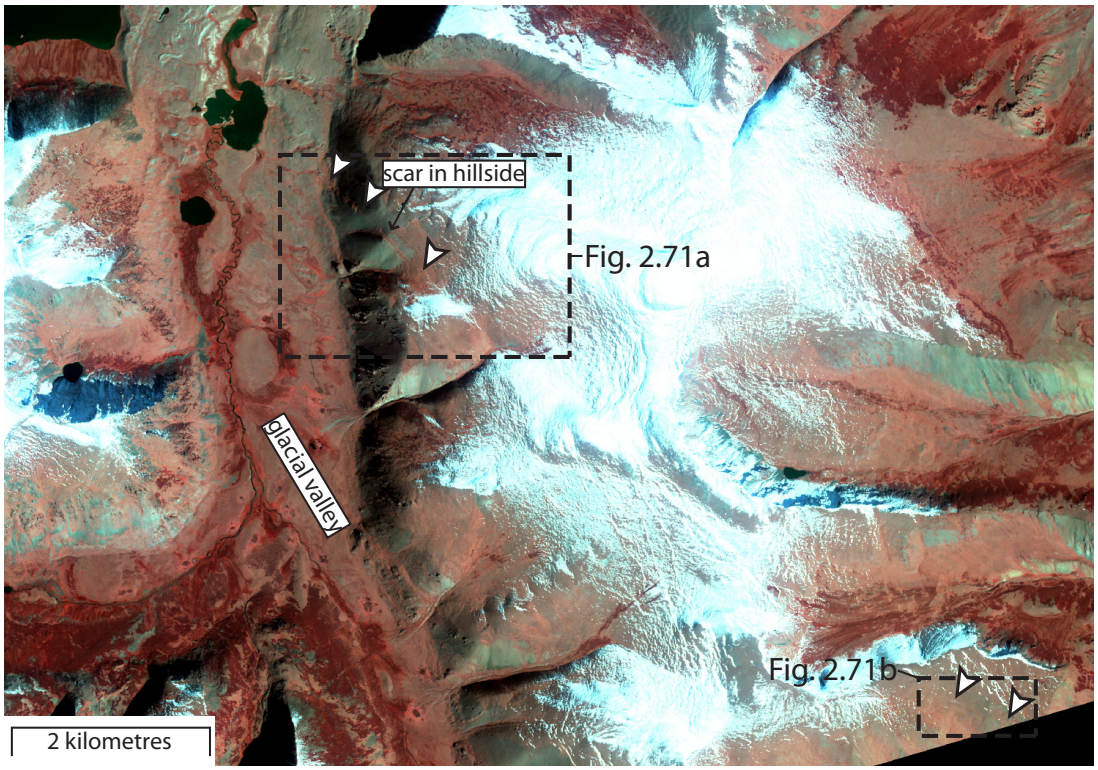


**Figure 2.70:** Kompsat-2 imagery of the Tsengel Hyarhan rupture, with RGB plotted as 4 m/pixel near-infrared, green, and blue spectral bands. The rupture scar is visible as a NW–SE striking red lineation in the hillside, but unfortunately the rest of the rupture is covered in snow. A U-shaped glacial valley is oriented approximately N–S through the image, with hummocky glacial deposits at the base of the valley. Location is shown in Figure 2.69

scarp is uplifted about 1 m relative to the east, and this change in height is most likely related to faulting because the plateau is flat.

A line of exceptionally fresh, *en-echelon* fissures cut across the valley floor a few hundred metres northwest of and parallel to the fault scarp in the hill side (Figure 2.73). These linear depressions are located on the hummocky surface of a moraine, and it is possible that they are not related to faulting, and instead are an inherent morphological feature of the moraine, particularly as they are not located directly along strike from the main rupture. However the fissures are distinct from any other features in the moraine, and they have a left-stepping, *en-echelon* pattern character-

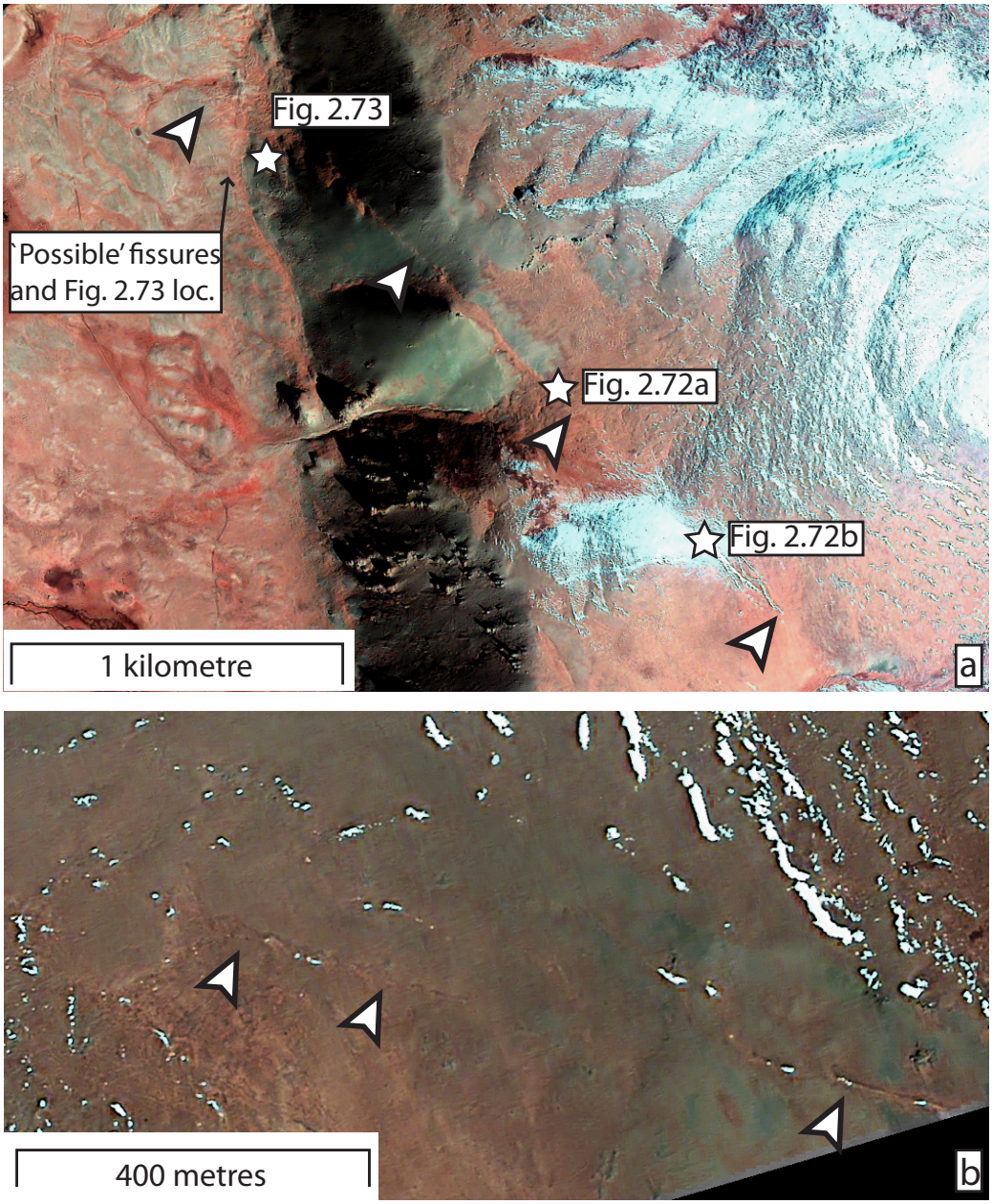


**Figure 2.71:** Kompsat-2 imagery of the Tsengel Hyarhan rupture, plotted the same as Figure 2.70, but pan-sharpened with the 1 m panchromatic band. (a) The rupture scar cuts across the hill side, and is somewhat visible as a lineation along the plateau of the high topography in the lower right of the image. The rupture appears red as a result of vegetation growing in depressions, reflected in the near-infrared band. (b) Faint lineations are visible that line up with the main rupture, which may be the continuation of the rupture. Snow has ponded in some features. Outline of (a) and (b) are shown in Figure 2.70.

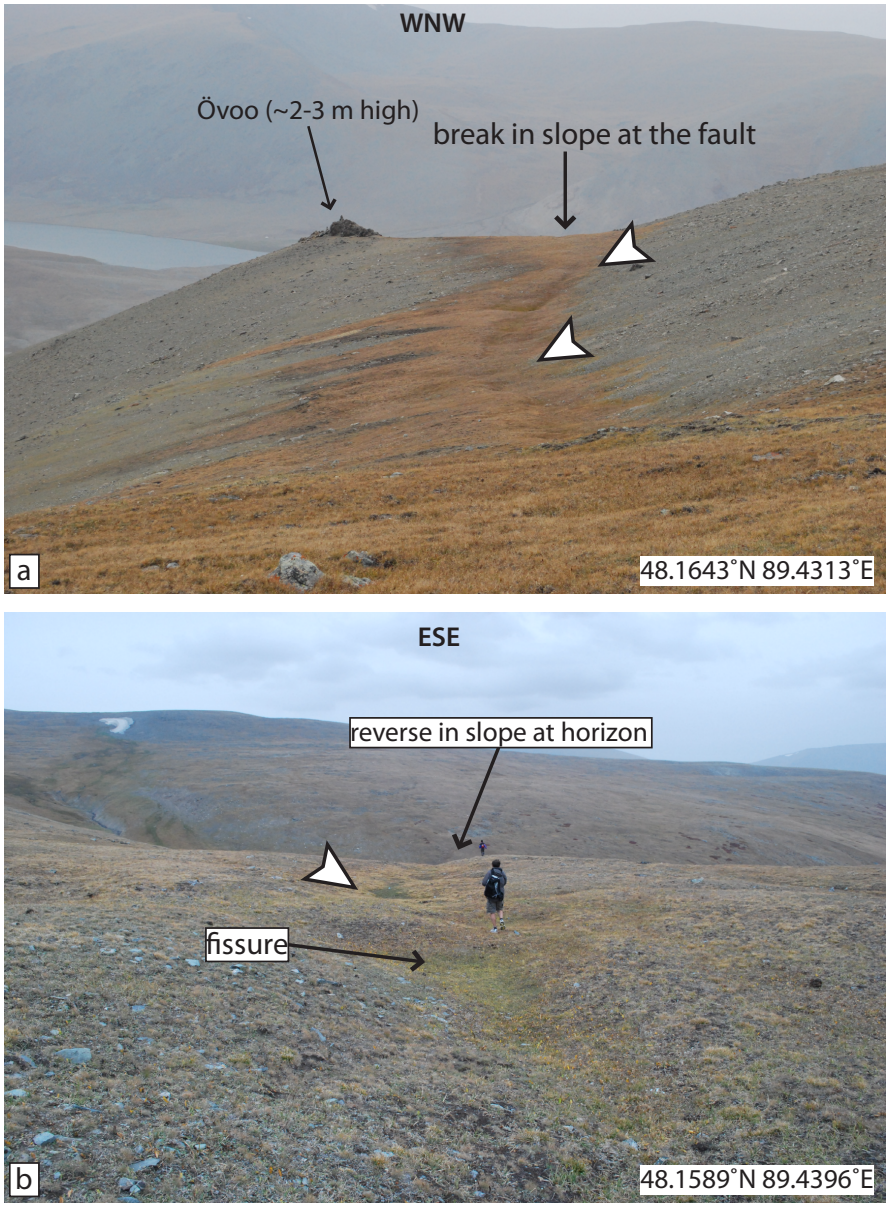


**Figure 2.72:** Photos of the Tsengel Hyarhan rupture where it is located on the top of a high plateau (over 2900 m). Photo locations are indicated by stars in Figure 2.71. (a) Linear depression just above the scar on the hill slope in 2.71a. The övoo is approximately 2–3 m high. Separate depressions are visible within the scar. (b) Line of depressions in the ground on the exposed plateau. The features are degraded, but are located along strike of the other rupture features described. A reversal in slope is visible on the horizon of the mid-ground, and the rupture possibly continues on the hillside in the background.

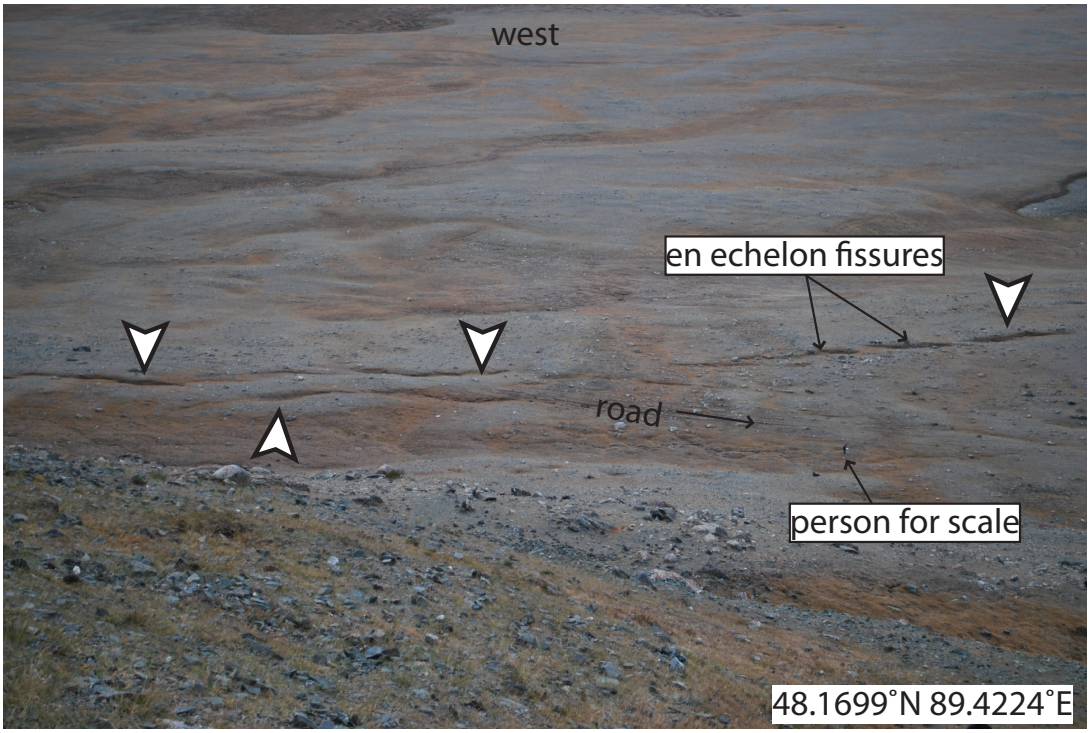


**Figure 2.73:** Photo of possible fissures in the moraine below the linear scar in Figure 2.71a. The fissures are left stepping, *en-echelon*, and fresher than other features of the moraine. Location of fissures is indicated by arrows and 'potential' fissures label in Figure 2.71.

istic of earthquake surface ruptures (Figure 2.74a). The fissures are continuous for approximately 200 m, and are up to 10 m long, 1–2 m wide, and 1 m deep. A slight reverse in slope, up on the southwest side, was observed (Figure 2.74b). The sides of the depressions are sharp, suggesting that they are relatively young features. They are likely more protected from the elements than ruptures in the high plateau in topography (nearly 3000 m), which if they are part of the same rupture, may explain why they appear to be more fresh. The preservation of active faulting features in Quaternary deposits is further expanded in the discussion of this chapter.

Tension fissures and linear vertical scarps were also found on a high plateau 20 km northwest of the sites described above, to the north of Chickertee Nuur (starred in Figure 2.47). These features are also exposed to strong winds, as well as snow. The

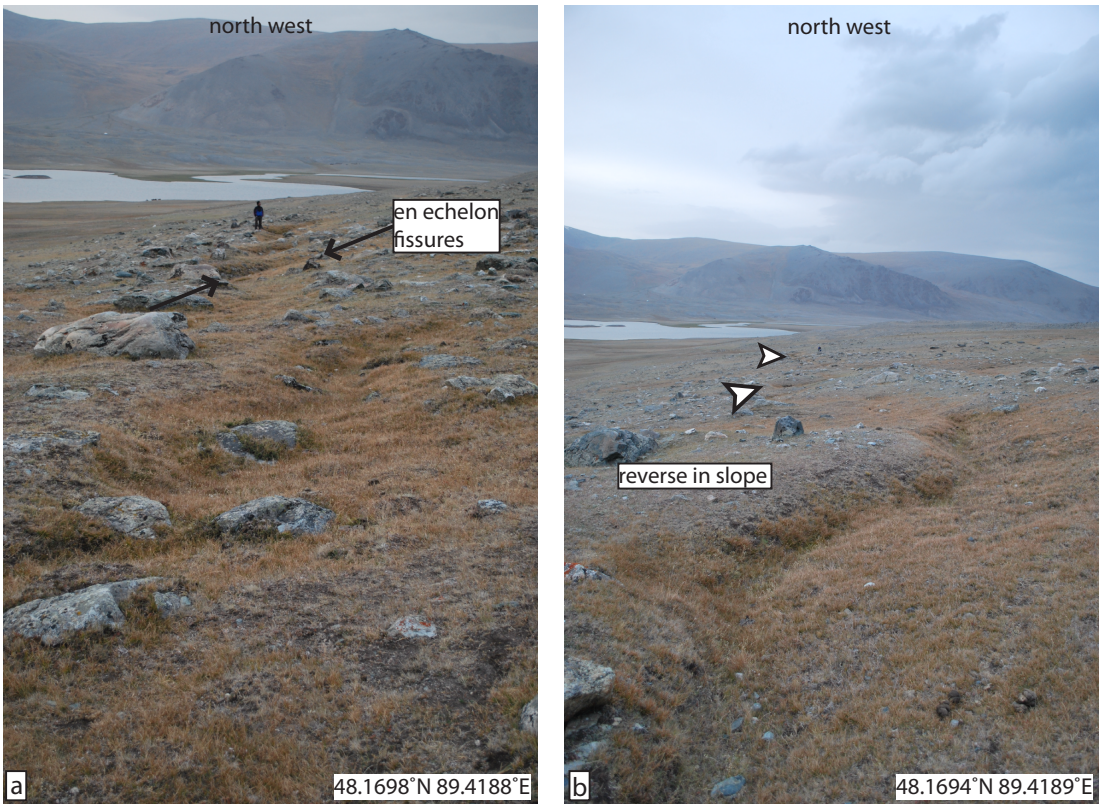


**Figure 2.74:** Photos of the potential fissures, photo locations indicated by stars in Figure 2.71. (a) A series of left-stepping linear features, 5–10 m long and 1–2 m wide, up to 1 m deep. (b) A reverse in the slope of the moraine surface.

features were filled with snow when I observed them in the field, but this helps in identifying the depressions in photos (Figure 2.75). The strike of the rupture is 300°, and it is preserved at elevations above 3100 m. The depressions are between 2–5 m wide, and approximately 5–10 m long, with more continuous vertical scarps that are 1 m high. If all of the features described above are the result of one earthquake rupture, and are continuous with the features observed along the base of Tsengel Hyarhan Uul, then the rupture is about 60 km long and would result from an earthquake of magnitude $M_w$ 7.1.

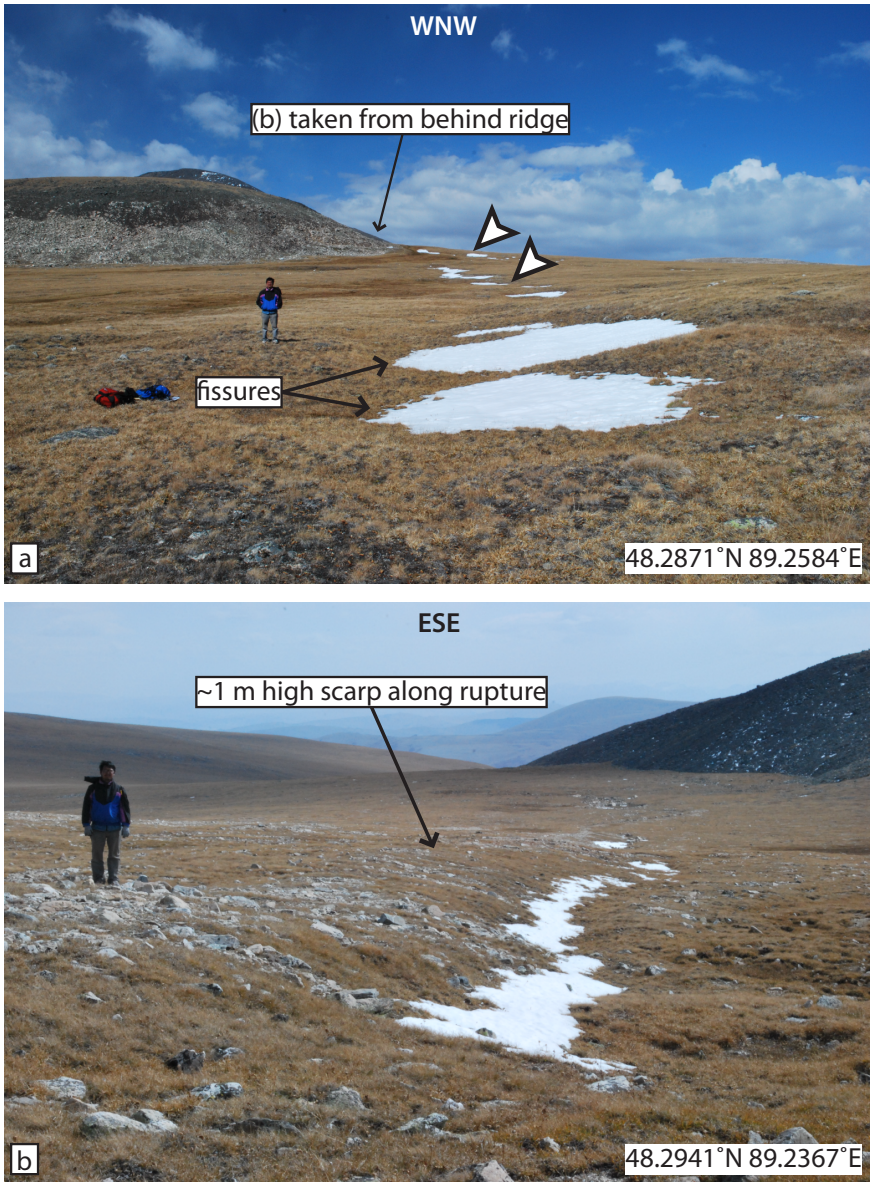


**Figure 2.75:** Photos of the possible continuation of the Tsengel Hyarhan rupture where it crosses a plateau in topography; the locality is shown in Figure 2.69. The rupture has a strike of 300°. (a) A line of fissures, which are about 5 m wide and filled with snow. There is a slight vertical component uplifting the east side of the fault. (b) 1 m high scarp, uplifting the east side of the fault, found in a saddle in the topography. The scarp is continuous for a few hundred metres, and the uplifted side is against the slight gradient in topography.

## 2.5 Discussion

From detailed investigation of the tectonic geomorphology of faults in the Altay, I discuss several hypotheses regarding the overall deformation of the region, on a variety of timescales. The dominant type of active faulting in the Altay mountains is dextral strike-slip. There is good evidence for dextral slip along all of the major fault zones in both the observed ground deformation features as well as the long term kilometre-scale drainage displacements. Historically recorded seismicity and surface ruptures preserved from the last (at least) 1000 years also consistently indicate dextral strike-slip faulting. I use these observations to discuss several aspects of active faulting in the Altay, including the long term displacement, the presence of reverse faulting, the preservation of Quaternary surface deformation in the Altay, and the evolution of deformation across the range, particularly based on observations from the north western Altay.

### 2.5.1 Cumulative displacement

Reliable horizontal drainage displacements are no greater than 5 km along all of the fault zones in the Altay. If I use a very rough estimate of an average Quaternary slip rate of 1 mm $yr^{-1}$ along each fault, and extrapolate over the duration of deformation in the Altay, horizontal displacements of around 5 km represent approximately 5 million years of cumulative fault displacement. The slip rate of 1 mm $yr^{-1}$ is a conservative estimate on the rate of slip, as many of the measured or estimated Quaternary slip rates (especially from the eastern Altay) are closer to at least 2 mm $yr^{-1}$ or more (*Nissen et al.*, 2009a,b; *Vassallo et al.*, 2005; *Vassallo*, 2006), though many quantitative estimates are within uncertainty of 1 mm $yr^{-1}$ (Chapter 3, *Vassallo*, 2006; *Nissen et al.*, 2009b; *Frankel et al.*, 2010). Thus horizontal offsets suggest that the Altay faults have been active (as strike-slip faults) for at least 3–5 Myr, assuming that the slip rates have remained constant over the entire life-span of the faults, and

that the few existing slip rate studies can be extrapolated over the length of the strike-slip faults. However, I must stress that the drainage displacements represent a minimum estimate of cumulative displacement. Obtaining maximum estimates of displacement requires E–W drainages in place when faulting is initiated, and more importantly, the potential to preserve river displacements must also exist when strike-slip faulting approximately begins. Because the best preserved river displacements occur along sections of the fault with high topography on both sides of the fault, in order to 'lock in' the course of the river and consistently record displacement, some topography must be present at the initiation of faulting. Widespread peneplain surfaces, existing thermochronology data, and sedimentation records all suggest that the Altay region had relatively low relief prior to late Cenozoic deformation, which suggests that the topography needed to preserve cumulative drainage offset was not likely present from the initiation of strike-slip faulting, and therefore my measurements of river displacements may underestimate the total strike-slip displacement of the Altay faults. The pull-apart basins along the Hovd fault are between 3 to 8 km wide along their long axes (Figure 2.12), and these may be better recorders of total displacement than drainages because the basin formation was more likely initiated near the time of strike-slip fault initiation. The maximum long-axis width of 8 km can be used as the approximate maximum strike-slip displacement, but this depends on the kinematics of individual basins and whether much of the basin development is accomplished by normal faulting. More information is on the faults surround the basins is necessary to quantitatively estimate the amount of strike-slip displacement, including the fault dips and the thickness of sedimentary deposits.

Just as horizontal displacement may be combined with fault slip rates to estimate the duration of strike-slip faulting in the Altay, the total vertical uplift, with estimates of vertical slip rate, can place constraints on the duration of reverse faulting in the Altay (e.g. *Nissen et al.*, 2009b). While the peaks of the highest mountains in the

Altay are around 4000 m in elevation, the relief across the range is generally no more than about 2000 m because the lowest elevations are mostly above 1700 m. Many of the mountains in the Altay are suggested to have peneplain surfaces preserved on their summits, which are the remnants of a Mesozoic low-relief surface (*Cunningham*, 2005; *Jolivet et al.*, 2007, described in Chapter 1). This implies that the relief observed today is the total relief that has resulted from faulting over the duration of Cenozoic deformation, assuming that the overlying Cretaceous and Tertiary sediments were not very thick, which is reasonable given that low-temperature minerals such as apatite that are currently at elevations between 1500–2500 m have not been buried to a depth greater than 2–3 km since the Mesozoic (Chapter 5). Quaternary vertical uplift rates are between 0.1 to 0.6 mm $yr^{-1}$, from slip rate studies on reverse faults formed at the base of the Baatar Hyarhan, Bumbat, and Hoh Serkhiin Mountains, which are formed in restraining bends in the faults (*Nissen et al.*, 2009a; *Frankel et al.*, 2010). Therefore a rough estimate of 2 km of vertical uplift, divided by the range in slip rate estimates, suggests that vertical faulting has been active for at least 3.3 million years, but possibly up to 20 million years. The duration of fault-related uplift is therefore highly dependent on vertical slip rates, but it is difficult to estimate a vertical slip rate that is representative of the whole of the region, because the reverse faulting is discontinuous and widely distributed across the range. Rates of uplift determined from low-temperature thermochronology may provide better insight into the initiation of deformation in the Altay, and this is discussed in Chapter 5.

From the Quaternary slip rate estimates, and the expression of faulting, the style of deformation in the Altay is dominated by strike-slip faulting, with a small amount of shortening (from uplift on reverse faults). If Cenozoic deformation in the Altay has always involved slip along strike-slip and reverse faults at similar rates, then I can use the rough estimates of cumulative displacement to place constraints on the

initiation of deformation. For example, if the uplift rates are at the faster range of known estimates, and the topography has been formed in a relatively short amount of time (3.3 Myr), it implies that the horizontal river displacements are a reliable estimate of cumulative strike-slip faulting, because, if faults slip at 1–2 mm $yr^{-1}$, 3–6 km of horizontal displacement can be accommodated in 3.3 Myr. However if the uplift rates are much slower, and closer to 0.1 mm $yr^{-1}$, then I would expect to find much larger drainage displacements of at least 20 km (if the strike-slip faults are moving at a rate of 1 mm $yr^{-1}$). A slow vertical uplift rate would suggest that much of the strike-slip offset has not been recorded by the geomorphology. More information from thermochronology, as well as a detailed GIS study of the drainage patterns in the Altay, is necessary to place better constraint on the initiation, and evolving kinematics, of deformation in the region.

The pull-apart basin displacements of a maximum of 8 km in turn suggest that faulting in the Altay may be relatively young, because these displacements would be accommodated in broadly 3–16 Myr, assuming a range of fault slip rates between 0.5 to 2.8 mm $yr^{-1}$, based on the existing quantitative estimates of Quaternary slip rates on all of the Altay faults (*Vassallo*, 2006; *Nissen et al.*, 2009b; *Frankel et al.*, 2010, Chapter 3). However this constraint depends on whether slip rates are consistent along a single fault, how constant the fault slip rates are through time, and also whether the basin opening begins at the same time as strike-slip faulting was initiated. Given that the pull apart basins that I measured come from a restricted part of only one fault zone, a better analysis of the topography across the Altay is necessary to find a more robust distribution of cumulative slip indicators. Absolute bedrock displacements do not provide much insight into cumulative slip, because Mesozoic and younger rocks are scarce, making it difficult to distinguish between bedrock displacement due to Palaeozoic faulting and Cenozoic tectonics.

### 2.5.2 Reverse faulting

Transpressive push-up mountains and termination reverse faults are probably accommodating significant amounts of shortening across the Altay, in addition to the shortening that is accommodated by rotation of the region (e.g. bookshelf faulting; *Bayasgalan et al.*, 1999, 2005). The importance of reverse faulting in the Altay was also stressed by *Baljinnyam et al.* (1993) based on their field observations, and is further confirmed by my work in the central and north western Altay. *Baljinnyam et al.* (1993) noted that evidence for reverse faulting is much more difficult to confirm than evidence for strike-slip faulting, because scarps in Quaternary alluvium are often eroded or not preserved at all due to the location of faults at the base of large mountain ranges, where significantly more material is shed from the higher topography, and faults may even be blind thrusts. Like *Baljinnyam et al.* (1993), I find that my observations of Quaternary reverse faulting are less easy to interpret than those of strike-slip faulting (Figure 2.36), but I agree that reverse faults along these mountain ranges must play an important role in the deformation of the Altay due to their association with high topography.

It is interesting to note that reverse faulting scarps 1 to 2 m high are commonly found along surface ruptures, and even cumulative fault scarps, on sections of the faults that are mostly accommodating strike-slip. These local reverse scarps are generally discontinuous (a few tens of metres long at the most) and they often are uplifted opposite to what would be expected from the surrounding topography. I suggest that these scarps are probably just the result of the variation in strike of the fault at the surface only, and they do not represent the true behaviour of the fault at depth, with the exception of the continuous reverse scarp documented at the northern termination of the Sair Uul rupture (Figures 2.52 and 2.53).

### 2.5.3 Preservation of Quaternary faulting

Low erosion rates lead to good preservation of fault scarps, such that even faults that move at less than 1 mm $yr^{-1}$ have a strong expression in the landscape. In much wetter climates, identification of Quaternary evidence for slow moving faults is generally not possible. In general, the Altay region experiences very low annual precipitation, and therefore is expected to have very low erosion rates (only 100 to 300 mm $yr^{-1}$, as discussed in Chapter 1; *Tarasov et al.*, 2000; *Morinaga et al.*, 2003). From low-temperature thermochronology, I show in Chapter 5 that long-term erosion rates, approximately since the Mesozoic, have also been very slow. The Altay did experience periods of Late Quaternary glaciation and paleoenvironmental change (see Chapter 1; *Lehmkuhl and Haselein*, 2000; *Lehmkuhl and Owen*, 2005), but evidence of Quaternary faulting was still preserved through these changes. It follows that whilst the region may have experienced more intense erosion through these changes, particularly during de-glaciation, the average erosion rates were probably still quite low through the Quaternary.

As discussed in Section 2.2 and Chapter 1, and noted in *Baljinnyam et al.* (1993), the very cold climate in the high elevations of the Altay may also help to preserve faulting features for a very long period of time. This is partially due to the presence of permafrost, which produces steep cracks in the landscape during earthquake rupture, similar to features described along the $M_w$ 7.9 2002 Denali surface rupture (*Schwartz et al.*, 2012). Even where there is not extensive permafrost, the combination of cold climate and lack of erosion lends the area unique preservation potential, particularly for pre-historic earthquake ruptures. Surface ruptures are probably preserved well over 1000 years, based on the observation of surface ruptures that are even more degraded than the Jid rupture, which occurred between 870 and 980 years ago (*Walker et al.*, 2006, Figure 2.76).

The previously unknown surface ruptures described in Section 2.4 can be com-

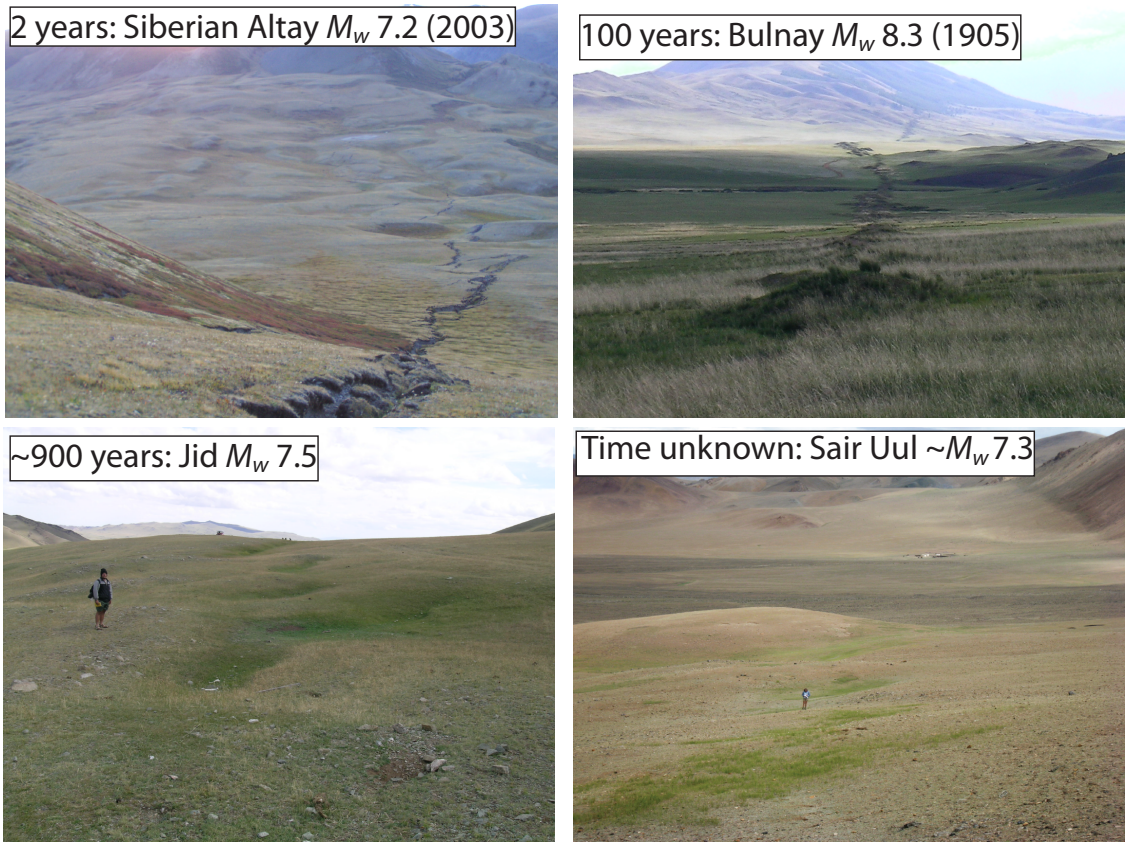


**Figure 2.76:** Photos from earthquake surface ruptures in the Altay and surrounding regions, at various states of preservation. Over time, the steep-sided ground ruptures of recent earthquakes degrade into the sloping fissures shown in the lower two images, taken along pre-historic ruptures.

pared with the Jid event to broadly estimate the timing of the events, though more precise methods such as seismic trenching are necessary to assign precise age estimates. Figure 2.76 shows earthquake ruptures in various stages of preservation, from 2 years to 100 years to approximately 900 years after the causative events. The Sair Uul rupture is also shown for comparison with the Jid earthquake. Many of the features along the Sair Uul rupture are similar in preservation to the Jid rupture, suggesting relatively similar timing of the two events to within a few hundred years. The sides of fissures are gently sloping and the fissures are shallow, implying that they have had time to be filled with material collapsing into the depression (see also Figures 2.56b and 2.61). The Fiery Horse rupture appears more fresh in satellite

imagery when compared with the Jid and Sair Uul ruptures, and therefore may have occurred more recently.

It is difficult to establish the relative timing of the Tsengel Hyarhan rupture. If the fissures observed in the glacial moraine are due to the most recent earthquake (and not some slumping process of the moraine), they suggest a relatively recent event, because the sides of the fissures are steeper than features observed along the other Altay prehistoric ruptures (Figure 2.74). The depressions and scarps of the Tsengel Hyarhan rupture that occur on high plateaus are not as well preserved, but the level of preservation may be the result of their location in the wetter parts of the mountain range and at high elevations where they are exposed to strong winds (Figure 2.72). As such, I would not expect the features to survive for as long on the high topography, and therefore the Tsengel Hyarhan rupture may be relatively youthful. In order to place more accurate constraints on the timing of all of the surface ruptures in the Altay, more quantitative work is necessary. Seismic trenching along several of the large ruptures, such as the Ar Hötöl and Sair Uul, would provide greater insight into the earthquake history of the region.

### 2.5.4 Earthquakes

The average displacements and lengths of the surface ruptures can be used to calculate a rough estimate of the combined slip rate of the Altay faults for the last 1000 years. I use a simple calculation outlined by *Brune* (1968) and applied by *Baljinnyam et al.* (1993). The sum of seismic moments of earthquakes along a fault is divided by the shear modulus, the area of the fault, and the time spanned by the history of earthquakes to calculate the rate of slip of the fault. To simplify the calculation, I multiply the average slip by the length of the rupture instead of calculating the seismic moment, and thus do not need to incorporate the shear modulus and the width of the faults (*Baljinnyam et al.*, 1993). To calculate the slip rate ($S$) of the

Altay as a whole, I assume that the faults are parallel and can simply add all of the earthquakes together, from the equation:

$$S = \frac{1}{Lt} \sum_{i=1}^{n} \overline{u}_i l_i \tag{2.1}$$

where $n$ is the number of earthquake events, listed in Table 2.6, along with the average displacement ($\overline{u}$) and length of each surface rupture ($l$). I add together the product of the average displacement and length of each event, and divide this sum by the average length of faults in the Altay ($L$ = 500 km) and the duration of time covered by the ancient ruptures ($t$ =∼1000 years). I also include the events that have occurred in the past century, which were recorded seismically but also have associated average displacements and rupture lengths measured in satellite imagery and in the field (*Nissen et al.*, 2007; *Klinger et al.*, 2011).

The sum of the average slip times length of all of the ruptures is 3292 km m, which results in an average strike-slip rate for the past 1000 years of 6–7 mm yr$^{-1}$. The rate is a rough estimate, because there are uncertainties in the timing of the earthquakes and in particular their average slip, as this was difficult to measure for many of the ruptures (discussed throughout the chapter). When *Baljinnyam et al.* (1993) made the same calculation based on their investigation of surface ruptures of the Altay, they assumed that all of the ruptures they observed occurred within the past 500 years, and they calculated a slip rate of about 10 mm yr$^{-1}$ from the three largest known events at the time (Fu Yun, Sagsay, and Ar Hötöl). It is now known that the ruptures of the Altay are preserved for longer than 500 years, and the slip rate is very dependent on the duration of time represented in the earthquake record. There is also the possibility that there are some events missing from the earthquake catalog in Table 2.6, because there are large regions of the Altay that have not been investigated in detail, particularly along the southern sections of the major fault zones. The central and southern parts of the mountains in particular

**Table 2.6:** Average slip and length of Altay surface ruptures

| Rupture | Slip (m) | Rupture length (km) | Reference |
|---|---|---|---|
| Jid | 3.2 | 90 | *Walker et al.* (2006) |
| Ih Hun | 2.5 | 30 | *Nissen et al.* (2009b) |
| Bij | 2.5 | 40 | *Munkhuu* (2006) |
| Chiteyn | ∼2 | 30 | *Khil'ko et al.* (1985) |
| Ar Hötöl | 4.5 | 215 | *Baljinnyam et al.* (1993) |
| Chuya | 1.2 | 60 | *Nissen et al.* (2007) |
| Sagsay | 2.5 | 36 | *Baljinnyam et al.* (1993) |
| Fu Yun | 6.3 | 160 | *Klinger et al.* (2011) |
| Sair Uul | 4 | 83 | This chapter |
| Fiery Horse | 3 | 60 | This chapter |
| Tsengel Hyarhan | 2 | 60 | This chapter |

may have surface ruptures from earthquakes of the past 1000 (or even up to 2000) years. Thus it is likely that my estimate of 6–7 mm $yr^{-1}$ underestimates the 1000 year fault slip rate.

The exceptional preservation of earthquake ruptures provides a unique setting for comparing the rates of slip on the faults and earthquake moment release over a range of timescales. From GPS, the Altay appear to be accommodating NNE–SSW shortening at a rate of about 7 mm $yr^{-1}$ (*Calais et al.*, 2003). This shortening is accommodated by vertical axis rotation of the right-laterally slipping faults. The kinematics of this style of deformation require that the total horizontal strike-slip rate on the NNW–SSE striking faults is greater than the over all shortening rate. Based on the shortening rate of 7 mm $yr^{-1}$ estimated by GPS measurements, the estimate of 6–7 mm $yr^{-1}$ for strike-slip faulting is less than what would be expected, but probably not by an order of magnitude. The strike-slip faulting rate is dependent on the rotation rate, and I provide an estimate of the strike-slip rate and total strike-slip displacement in the discussion of this thesis, following results from a palaeomagnetic study presented in Chapter 4. The 1000 year slip rate can also be compared with Quaternary rates of slip on all of the faults, and that comparison will be discussed later in the thesis.

### 2.5.5 Evolution of faulting in the Altay

In the Altay, there is a decrease from the northwest to the south and southeast in the amount of annual precipitation and evidence of glacial deposition and erosion (Chapter 1; *Morinaga et al.*, 2003). This change in climate conditions across the Altay may have an impact on fault preservation. The dry, almost desert-like climate of the easternmost fault zones has led to the exceptional preservation of fault features, which can be traced continuously for hundreds of kilometres. The eastern Altay faults were clearly recognised on Landsat 1 imagery by *Molnar and Tapponnier* (1975) prior to detailed field investigations of the region, along with the Fu Yun fault, which is also partially located in the dry desert climate of the southwest Altay, and a large earthquake was known to have occurred in the area (the 1931 Fu Yun event). Prior to my work, very little evidence for active faulting had been identified in the north western Altay, near the Mongolian borders with China and Russia (Figure 2.77). Based on the lack of published evidence for faulting in the north western Altay and the high Quaternary rates of slip on eastern Altay faults combined with the total topographic displacement, it has been suggested that faults in the central Altay are mostly inactive, and that the majority of slip has been accommodated on structures in the eastern, or possibly on both the eastern and western margins, of the mountain range in the Late Quaternary (e.g. *Cunningham*, 2007; *Nissen et al.*, 2009b).

Based on the hypothesis that deformation has migrated to the eastern margins of the Altay, *Nissen et al.* (2009b) suggested that faults in the central Altay may have shut down over time, or at least slowed. Because the Altay rotate about a vertical axis to accommodate shortening (*Bayasgalan et al.*, 2005), the strike-slip faults themselves may rotate into less optimal orientations relative to the regional principle stresses, and this rotation combined with the increase in gravitational forces due to the buildup of topography could have a 'slowing' effect on fault slip. This is a reasonable suggestion: rotation of strike-slip faults to non-optimal orientations

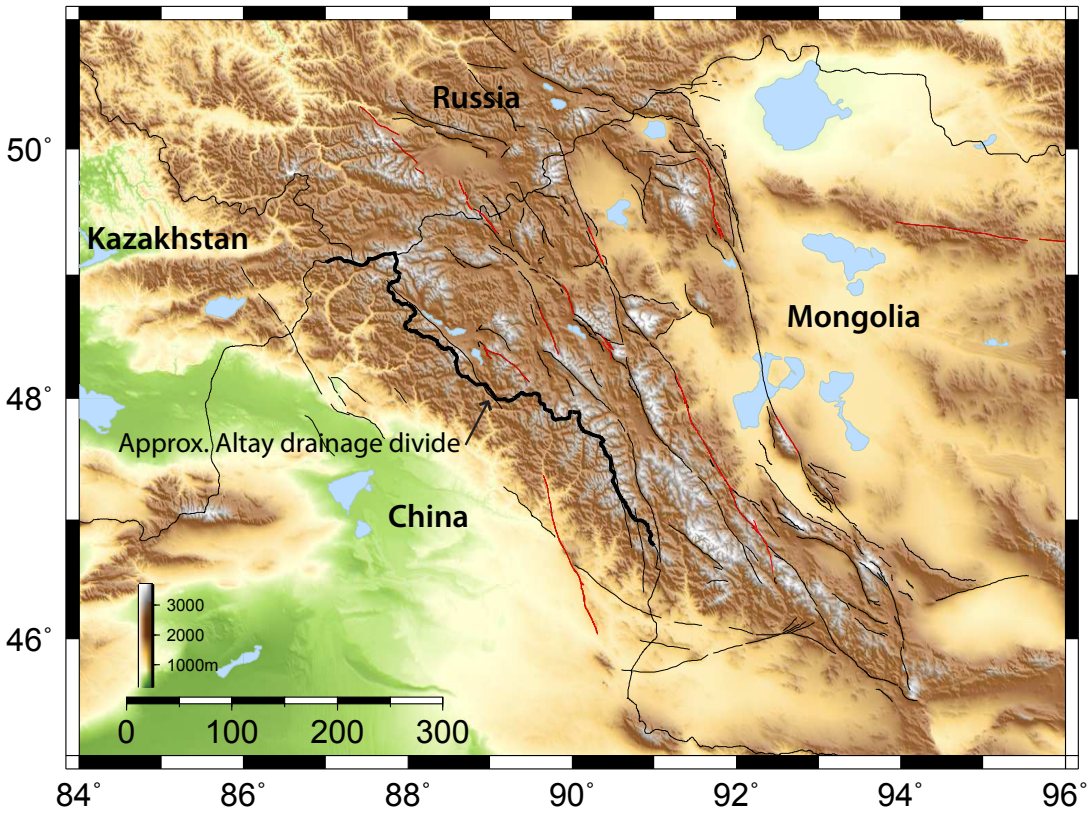


**Figure 2.77:** SRTM DEM of the Altay, with the approximate drainage divide of the range in bold black. The divide is asymmetrical and close to the western side of the mountains. It follows the political border between Mongolia and China.

relative to the stress field is known to lead to the progressive demise of faults as they rotate away from optimal orientations, and the initiation of splay faults and even new fault zones that continue accommodating the regional strain field (*Scholz et al.*, 2010). The Altay have an asymmetric topographic shape, with the drainage divide of the entire range located on the far western side of the mountains, along the political border between Mongolia and China (Figure 2.77). The region surrounding the drainage divide is characterised by steep mountains, that are not clearly related to traces of active faults. The relief surrounding the drainage divide of the Altay is in contrast with the shape of topography in the eastern parts of the range associated with the Sagsay, Ölgiy, Hovd, and Har-Us-Nuur faults, which has a basin-and-range

style of linear mountain ranges formed along the anastomosing strike-slip faults, separated by basins. Despite the rugged topography, my work has confirmed that while it may be difficult to identify, evidence of active faulting in the north western Altay can be recognised. Prior to my remote sensing and field investigations, the Hoton Nuur fault was not known to have been active in the Late Quaternary, and the faults surrounding Tsengel Hyarhan Uul and Tas Uul were not identified. The evidence for earthquake ruptures described along these faults is important in confirming that faults in the north western Altay have accommodated strike-slip deformation within the past 1000 years, and is in contrast with the previously suggested hypotheses that the faults in the central and north western parts of the Altay have effectively 'shut down'. Whether the faults in this region have average Quaternary slip rates similar to faults in the eastern Altay has yet to be tested.

# Chapter 3

# Average Quaternary rates of fault slip

## 3.1 Introduction

In this chapter, I present the results of slip rate studies conducted on two of the main Altay fault zones. The aim of the chapter is to provide a detailed discussion of Quaternary dating techniques when they are applied in semi-arid mountainous regions, and to outline the limitations inherent to the techniques. I apply $^{10}$Be boulder and depth profile dating, and uranium-series dating on pedogenic carbonate, to establish the timing of abandonment of landforms displaced by Quaternary faulting and show that the use of multiple and complimentary techniques is important for obtaining reliable results.

I first provide an overview of the application of Quaternary dating techniques, and the limitations encountered in each. I then present slip rate studies from the Ölgiy and Hovd faults. I treat each fault separately, presenting a well-constrained slip rate on the Ölgiy fault, which is in contrast with more ambiguous geochronologic results from the Hovd fault. This emphasizes the problems that can arise from uncertainties

and assumptions inherent in individual Quaternary dating techniques. In the Ölgiy slip rate study, I describe a detailed methodology for both $^{10}$Be cosmogenic nuclide dating and U-series dating, including a description of the calculation of ages from analytical results. The terrestrial cosmogenic nuclide (TCN) analytical methods described in Section 3.3.4 also apply for the Hovd slip rate study. For each of the faults, I describe the geomorphology of the site and the measurements of fault displacement, followed by the details of sample collection and analytical results. I discuss the slip rate calculation and geochronological assumptions for each site, and end with a discussion of the tectonic implications of the slip rates of the Altay faults, including the slip rate site on the Hoton Nuur fault presented in Chapter 2, for which I have yet to obtain geochronological results.

## 3.2 Quaternary dating techniques for measuring fault slip rates

Establishing the age of abandonment for Quaternary landforms provides quantitative constraints in studies of neotectonics, geomorphology, and paleoclimate, yet these studies are often hindered by the limitations of Quaternary dating techniques that arise from both analytical and geological uncertainties. These limitations can sometimes be overcome by combining complementary dating methods (e.g. *DeLong and Arnold*, 2007; *Kock et al.*, 2009; *Nissen et al.*, 2009b). Quaternary slip rate studies are important for assessing earthquake hazard along active faults and understanding the kinematics of active continental deformation in a variety of tectonic settings (e.g. *Brown et al.*, 2002; *Densmore et al.*, 2007a; *Frankel et al.*, 2007). Detailed Quaternary dating may also be used for investigations of landscape stability, which is of importance to communities living in regions with landslide hazards.

Late Quaternary dating techniques can be particularly difficult to apply in arid

to semi-arid mountainous environments. Suitable organic material for radiocarbon ($^{14}$C) dating is not often present in arid environments and the fine-grained sediments necessary for optically stimulated luminescence (OSL) dating may not be available in high energy alluvial systems (*Faure*, 1986; *Wintle and Huntley*, 1982; *Richards*, 2000). Terrestrial cosmogenic nuclide (TCN) dating is often used to constrain the abandonment of landforms in mountainous settings, and the method has been successfully applied in several studies in western Mongolia (e.g. *Ritz et al.*, 1995; *Nissen et al.*, 2009a; *Frankel et al.*, 2010). TCN age calculations rely on a knowledge of the production rate of cosmogenic isotopes *in situ* at a study locality (*Lal*, 1991), but there are systematic uncertainties in quantifying time-integrated production rates, particularly when the calibrated production rates are scaled to different latitudes, longitudes, and elevations. Uncertainties in $^{10}$Be production rates are reasonably quantified by empirical studies (*Lal*, 1991; *Stone*, 2000), whereas the uncertainties arising from pre- and post- depositional processes are often inconsistent and stochastic, leading to significant over or under estimates (respectively) of exposure ages, especially from $^{10}$Be boulder dating alone (*Gosse and Phillips*, 2001; *Putnam et al.*, 2010).

$^{238}$U-$^{234}$U-$^{230}$Th (U-series) dating of pedogenic carbonate that has accumulated *in situ* on pebbles in alluvium has been applied in regions where other Quaternary techniques may not be possible (*Ku et al.*, 1979; *Blisniuk and Sharp*, 2003; *Sharp et al.*, 2003; *Fletcher et al.*, 2011). The U-series method utilises short-lived intermediate isotopes from the uranium decay chain to constrain the age of carbonate growth, and in turn the stabilisation of the landform. The method has high analytical precision (requiring only small sample sizes), is based on well-defined decay constants, and can be used on samples aged up to 500 kyr (> 1 Myr for model $^{234}$U/$^{238}$U ages). U-series dating is possible because uranium is incorporated into carbonate during growth, whereas thorium is initially excluded, such that (ideally) all $^{230}$Th measured

in the sample is the daughter product of the initial uranium. However the potential for incorporation of initial $^{230}$Th may lead to problems in calculating U-series age. I have made efforts to correct for this 'detrital' thorium in the Ölgiy study.

The U-series technique has several advantages over other Quaternary dating techniques: the analytical uncertainties are relatively small, and because the surface must be stabilised before carbonate development is preserved, U-series results constrain the minimum age of surface abandonment. By combining U-series dating with $^{10}$Be TCN dating, it is possible to gain insight into the spread of TCN ages that occur due to pre- and post- depositional processes, placing a more accurate constraint on the geochronology of a displaced landform. This in turn provides a more reliable estimate of average rates of Quaternary fault slip.

## 3.3 Slip rate of the Ölgiy fault

The Ölgiy slip rate study presented in this chapter is the first to apply both U-series and cosmogenic nuclide dating techniques in the Altay, and amongst the first such studies in the world. The tectonic geomorphology of the Ölgiy fault is described in Chapter 2, along with a description of the published constraint of 0.9 +0.2/-0.1 mm yr$^{-1}$ on the slip rate of the Ölgiy fault (*Frankel et al.*, 2010, Figure 3.1).

### 3.3.1 Site description

The study site is located on the central part of the Ölgiy fault where the strike of the fault is ∼340°–350° and motion is nearly pure strike-slip (Figure 3.2a). The site is 20 km south of Ölgiy city, one of the major towns in the Altay mountains (Figure 3.1b). At the locality, the trace of the fault runs along the eastern side of a north-south bedrock ridge that is composed of large quartz bodies and copper ore. Several east-west oriented alluvial deposits are emplaced at gaps in the ridge (Figure 3.2b).

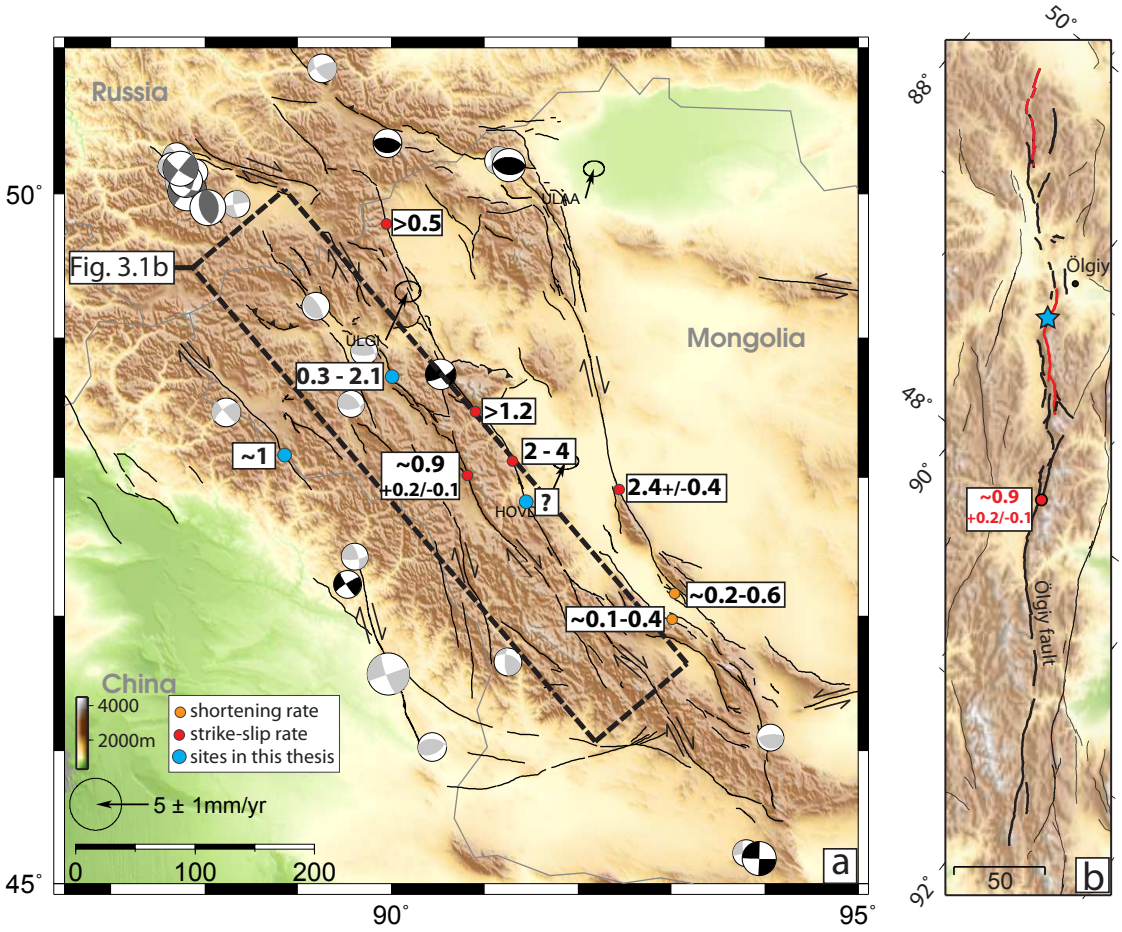


**Figure 3.1:** SRTM shaded relief images of the Altay (30 arc seconds/pixel). (a) GPS velocities are relative to stable Eurasia and show ∼ 7 mm/yr of northeast directed shortening across the Altay (*Calais et al.*, 2003). Earthquake focal mechanisms in black are from body-wave modeling in *Sloan et al.* (2011), those in dark grey are from *Nissen et al.* (2007), and light grey mechanisms are solutions modeled or catalogued by *Bayasgalan et al.* (2005, other references within). Active faults are plotted in black and political boundaries are grey. Published slip rate values from the Altay are indicated, including the sites discussed in this chapter. Red dots indicate strike-slip rates, orange dots indicate shortening rates, and blue dots indicate sites in this chapter. (b) The Ölgiy fault is plotted in bold black lines and known prehistoric earthquake ruptures are plotted in red. The Ölgiy slip rate site is indicated (blue star), as well as the site of *Frankel et al.* (2010) (red dot).

These abandoned landforms are incised by streams, and where they cross the dextral fault, the streams preserve right-lateral displacements (Figure 3.3). Near the site, there is an exposed fault plane in bedrock with slickensides oriented north-south and nearly horizontal (location shown on Figure 3.3). Any topography along the fault at

the site is probably due to right-lateral displacement that has made a reverse scarp by displacing the slope of the alluvial surface (described further in Section 3.3.2). The fault is located at the base of a topographic ridge that forms the north-western flank of the Hungui Mountains (Figure 3.2a). The Ölgiy site was selected because the alluvium is relatively protected from erosion by the surrounding ridges, and it preserves the best displacements in the area. Also the site is located on along a section of the fault that is likely to accumulate pure strike-slip motion, based on the strike of the fault, which is confirmed approximately 2–5 km to the north of the site where the fault strikes across a flat valley without any associated vertical displacements.

The study locality includes two alluvial deposits that were emplaced nearly perpendicular to the strike of the Ölgiy fault. The surfaces of the deposits, now abandoned, are incised by several streams (Figure 3.3). The two main streams at the site are more steeply incised on the west side of the fault (down slope, Figure 3.4). Although the two surfaces are similar in appearance, the dating results confirm that there are two distinct deposits, an older deposit 'F1' and a younger deposit 'F2' (Sections 3.3.3 and 3.3.4). There is also a potentially different generation of alluvium on the northern boundary of the site, although it was not sampled (labeled 'F1/F2?' on Figure 3.3). Based on the complicated nature of deposition at the site, I refrain from associating the northern surface with either of the deposits that were dated. Both of the deposits have abundant clasts on their surfaces that are angular and range in size from small pebbles to 2 m boulders. The composition of the clasts is metasedimentary with prominent quartz veins, and some are composed of pure vein quartz. The surfaces have slopes that dip between 10° and 20° . The stratigraphy of the deposit is poorly sorted with no visible structure, at both the surface and up to 2 m depth as visible in the stream channels. However, it was not possible to dig into the surface due to the remote locality and presence of large boulders throughout, so a

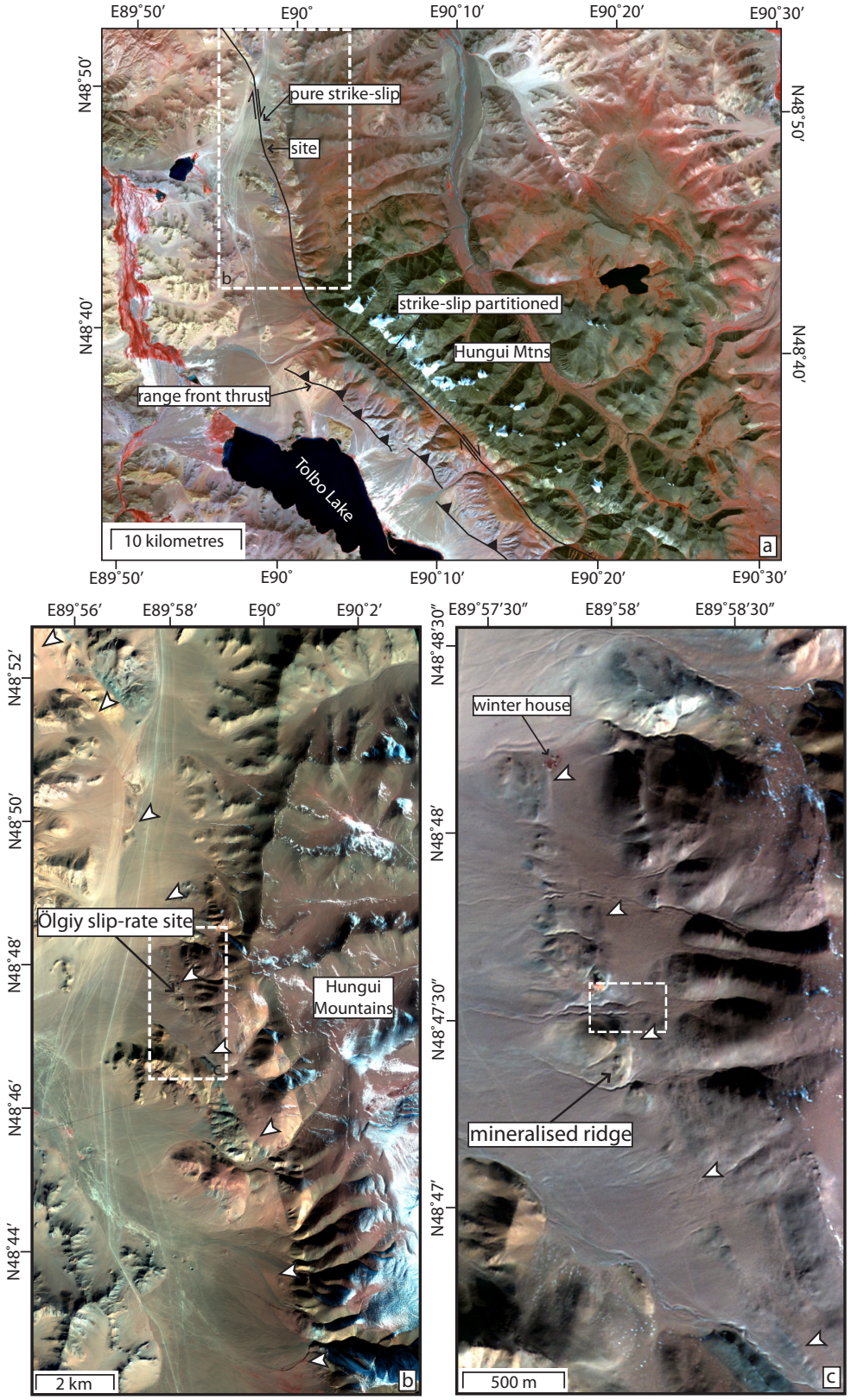
E89°50′
E90°
E90°10′
E90°20′
E90°30′
N48°50′
N48°40′
pure strike-slip
site
b
strike-slip partitioned
Hungui Mtns
range front thrust
Tolbo Lake
10 kilometres
a
E89°56′
E89°58′
E90°
E90°2′
N48°52′
N48°50′
N48°48′
N48°46′
N48°44′
Ölgiy slip-rate site
Hungui Mountains
2 km
b
E89°57′30″
E89°58′
E89°58′30″
N48°48′30″
N48°48′
N48°47′30″
N48°47′
winter house
mineralised ridge
500 m
c

detailed stratigraphy of the deposits could not be determined. Due to this ambiguity, I refrain from defining a specific transport mechanism for the two deposits, though based on the course nature of the sediments, clasts, and boulders, the deposits were likely emplaced relatively close (within a few kilometres) to their source.

### 3.3.2 Measurement of lateral displacements

To estimate the displacements of F1 and F2, I use field observations, high-resolution Kompsat-2 and Quickbird satellite imagery, and a digital elevation model (DEM) calculated from a field-based kinematic GPS survey. There are two streams incised into the abandoned surface that have dextral offsets where they intersect the fault (Figures 3.3 and 3.5). The active stream channels are 3–4 m wide, and on the western side of the fault they are more than 2 m deep (Figure 3.4). I use topographic profiles from the DEM to measure the displacement of the base of each stream on either side of the fault at a distance of 12–13 m from the fault (Figure 3.4). The width of the streams (measured from the DEM) is used to assign an uncertainty to the displacement measurement (e.g. *Frankel et al.*, 2010). Where the profiles are drawn on the DEM, the southern stream is displaced by 19±4 m and the northern stream is displaced by 12±4 m (inset on Figure 3.4). The two streams represent the displacement of surface F2, as the streams form the boundary between F1 and F2 and the deposition of the younger F2 deposit likely overprinted any preexisting

**Figure 3.2** ***(preceding page)*:** ASTER (15 m/pixel, a) and Kompsat-2 (4 m/pixel, b and c) imagery of the slip rate study site. White arrows point to the surface trace of the fault. (a) The Hungui Mountain range is shown, with the frontal thrusts that uplift the mountain. The main strike-slip fault is located behind the range front. (b) shows the western ridge of the Hungui mountains to the east of the fault, with the active trace of the fault indicated by white arrows. Where the fault veers away from the range front, it crosses a valley and produces no vertical features, implying pure strike-slip motion on this strand of the fault. (c) The fault runs behind a series of mineralised ridges, with alluvial deposits spaced between the ridges, fed from the main range front. There is a winter house situated in a sag pond formed along the fault. Outline in (c) is area covered by Figure 3.3.

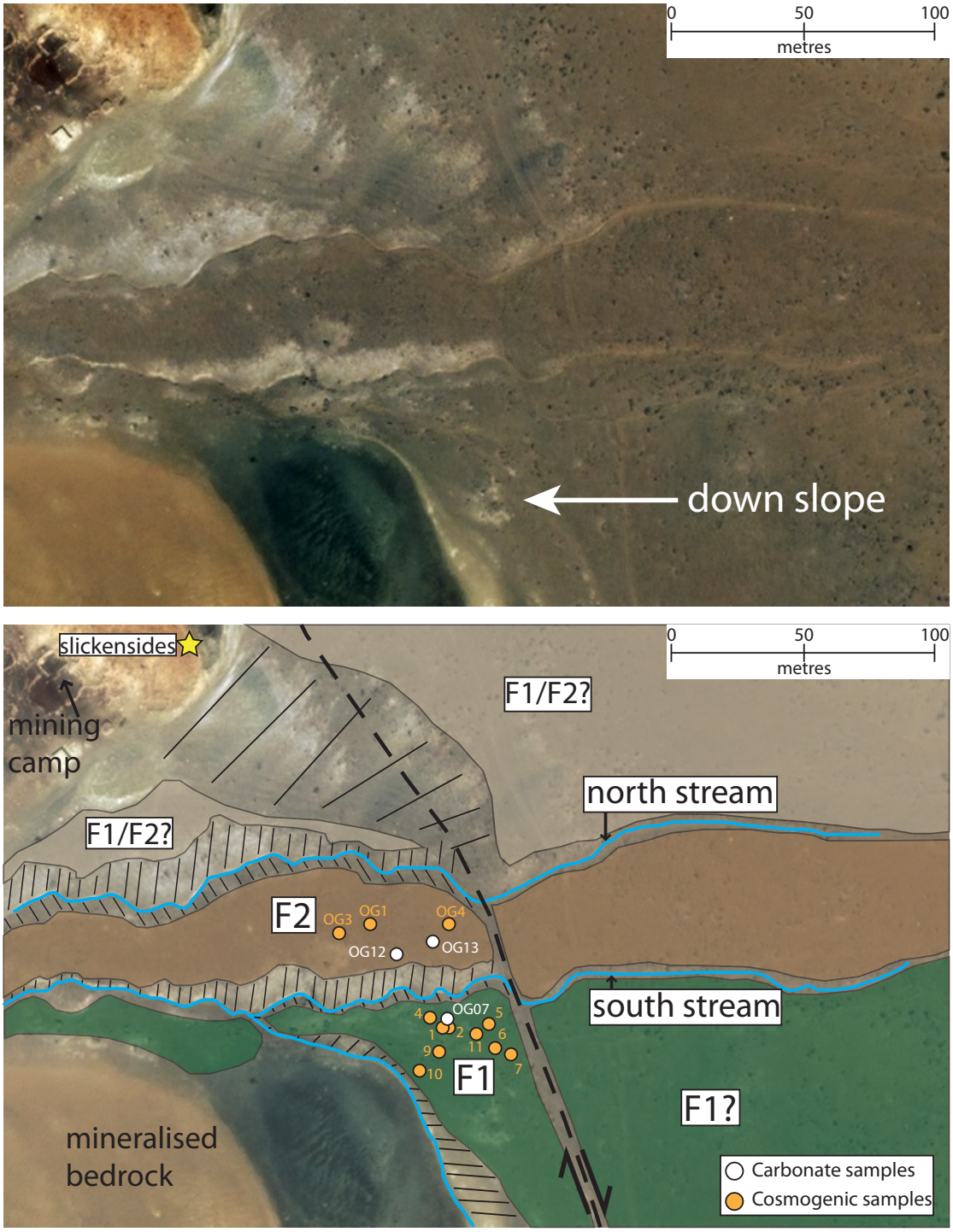


**Figure 3.3:** Quickbird imagery (0.6 m resolution) of the Ölgiy site. The lower panel is an annotated version of the upper image. Streams are traced in blue, surfaces outlined and coloured in green (F1) and brown (F2), with the fault mapped as a bold dashed line. Buff coloured surfaces (in the interpretation) were not sampled and may be F1, F2, or an older deposit (indicated by 'F1/F2?' box). Black hashing indicates steep stream risers. The site slopes down to the west (left of images). Sample localities are indicated by white (U-series) and orange (TCN) circles with respective sample numbers, and slickensides were measured at the yellow star.

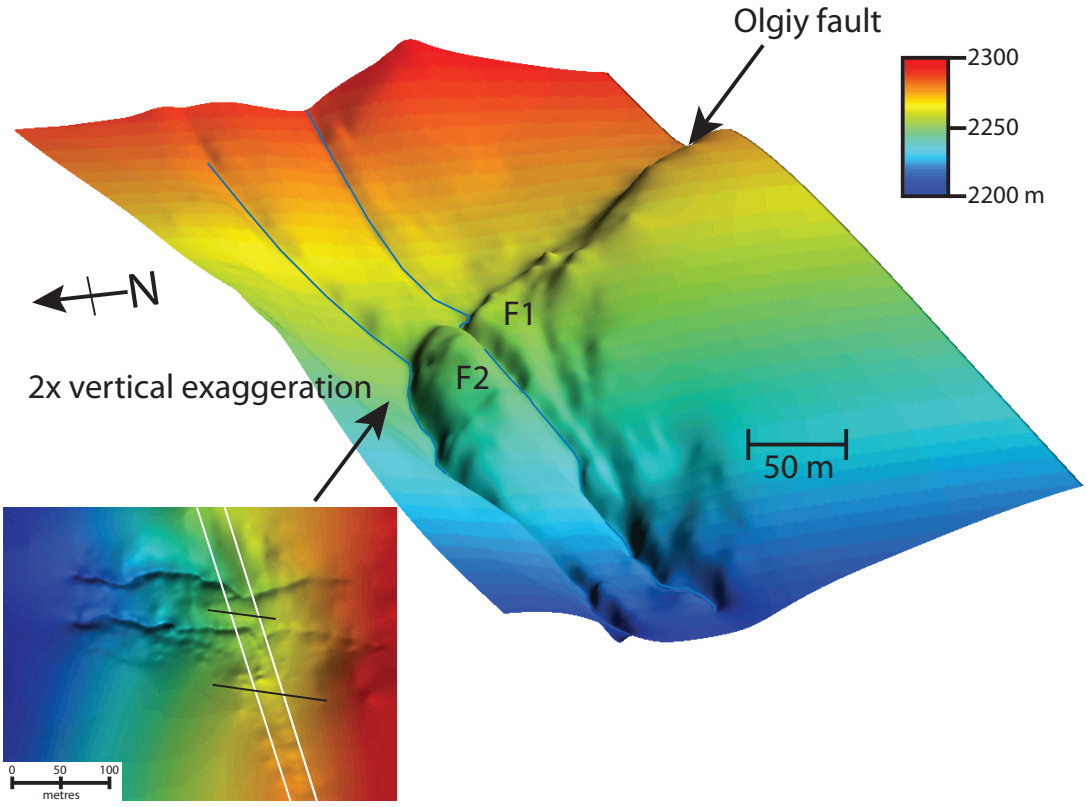


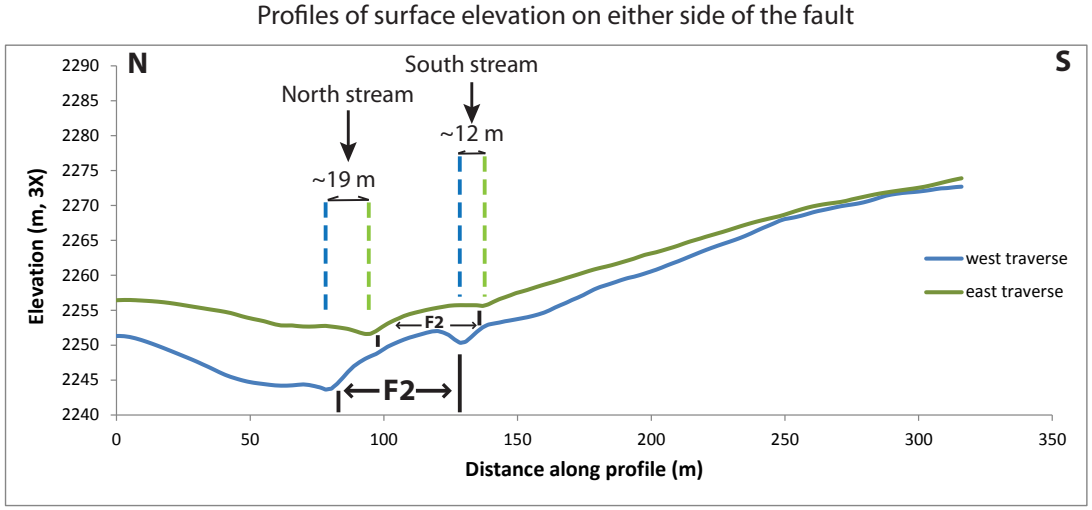


**Figure 3.4:** DEM made from a kinematic GPS survey. The 3D view highlights the apparent vertical scarp along the fault caused by dextral displacement of the landscape. White lines on inset (2D) show profile lines from the lower half of the figure, black lines on inset show scarp profile lines from Figure 3.6. On elevation profiles from the east and west sides of the fault, both streams can be picked out, with measurements of their displacements. F2 is visible as a distinct landform, particularly on the west side (downslope of the fault).

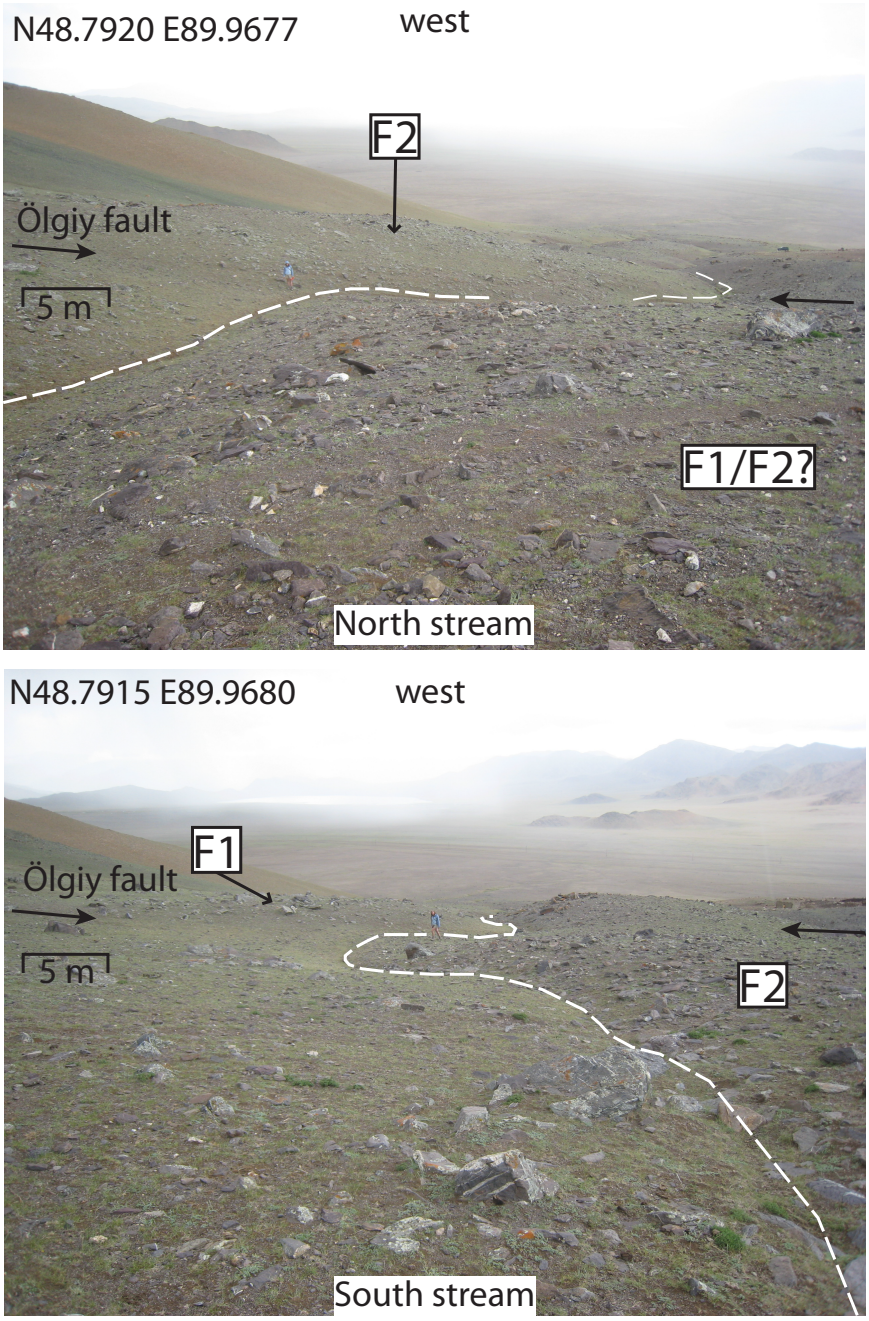


**Figure 3.5:** Photos of the northern and southern stream displacements. Streams are traced in white dotted lines, both are displaced right-laterally at the fault.

stream offsets.

Topography on the west side of the fault appears to be uplifted relative to the east side, producing a scarp along the fault (Figure 3.4). The strike of the Ölgiy fault

**Table 3.1:** Surface displacement measurements

| Feature | Strike | Dip | Fault strike | Plunge ($p$) | Scarp height (h) | Displacement (x) |
|---|---|---|---|---|---|---|
| F1 scarp | 195° | 13.8° | 343° | 08° | 5.7 ±2.1/2.8 m | 41 ± 15/20 m |
| F2 scarp | 183° | 13.4° | 343° | 05° | 2.6 ±0.7/0.4 m | 30 ± 8/4 m |
| S1 | | | | | | 12 ± 4 |
| S2 | | | | | | 19 ± 4 |

is oblique to the strike of the deposit surface, and therefore the right-lateral motion of the fault places the originally lower elevation material that is on the eastern, up-slope, side of the fault against higher elevation material that is on the western, down-slope side of the fault, creating an east-facing vertical scarp (Figure 3.6). With the assumption that the fault motion at the site is pure strike-slip, I use the height of the vertical scarp to estimate the maximum horizontal displacement required for creating the scarp, for both F1 and F2 (Figure 3.6). I find the plunge of the intersection line between the deposit surface and the fault plane ($p$), assuming a vertical fault. The orientation of the steepest direction of slope (essentially the 'dip') is measured from the field-based DEM (Figure 3.4), and I measured the height of the reverse scarp in several profiles across the fault (on each deposit); the average scarp heights are listed in Table 3.1. The average of orientation measurements and the plunges of the intersection between the fault and the surface are also listed in Table 3.1. Detailed measurements and topographic profiles are listed in Table A.1 and shown in Figures A.1, A.2, and A.3 in Appendix A. The slope of F1 has a slightly different dip direction compared to F2, so the plunges of the fault intersection lines are different. The horizontal displacement ($x$) required to create a vertical displacement of height $h$ is calculated from $tan(90 - p) = x/h$ (Table 3.1, Figure 3.6).

Based on the horizontal displacement calculated from the vertical scarp, I use a maximum estimate of 41 +15/-20 m for the offset of F1 and 30 +8/-4 m for the offset of F2. The uncertainties on the maximum displacement are based on differences in scarp height on 5 different profiles on each deposit (Appendix A). I take the mean displacement from each surface, and the uncertainties are the difference between the

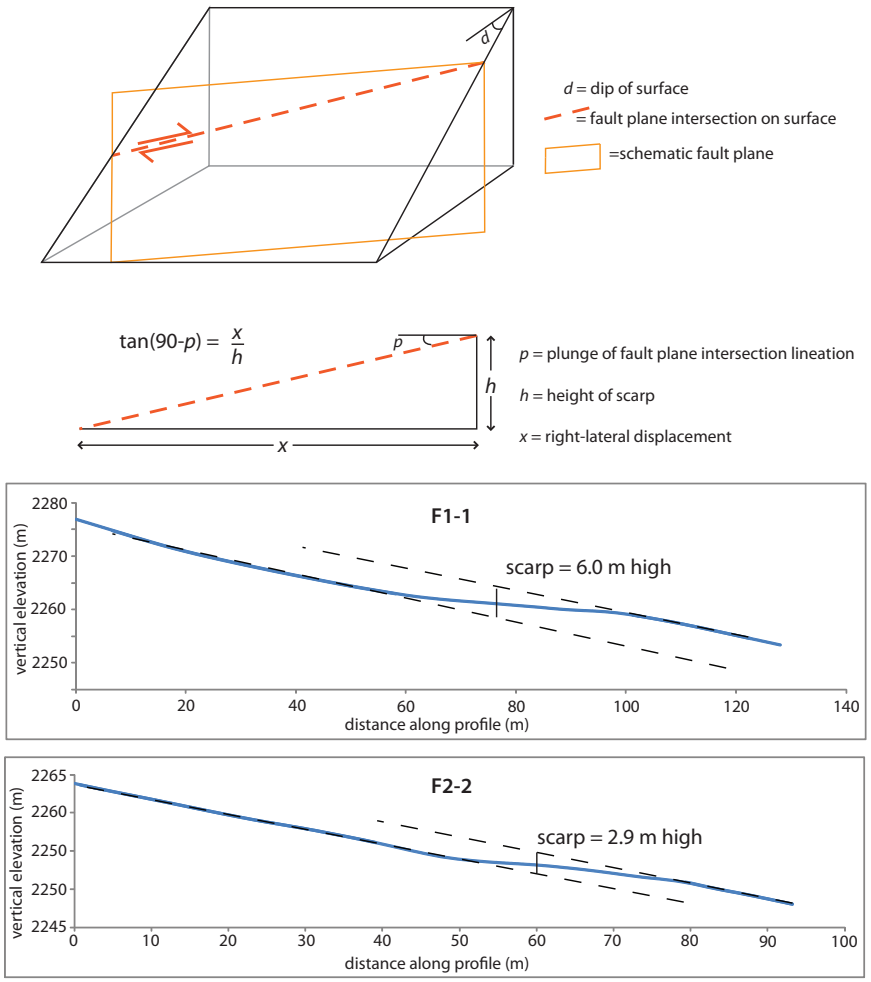


**Figure 3.6:** Diagram for calculating the displacement ($d$) necessary for creating an apparent reverse scarp of a measured height ($h$). The plunge of the fault plane intersection line is calculated with a stereonet from strike and dip measurements of the alluvial surface and the fault plane. The lower half of the figure shows profiles made down the slopes of F1 and F2 show the apparent vertical offset due to dextral motion along the Ölgiy fault. The profiles F1-1 and F2-2 are two examples from surfaces F1 and F2, respectively, of several profiles that were averaged to calculate the offsets of the deposits, listed in Table 3.1. All profiles are shown in Appendix A.

maximum and minimum measurements from the mean.

The offset of the streams is used to estimate the minimum displacement of F2, specifically that of the northern stream (Figure 3.3). The displacement of the stream may be an overestimate if there was a significant bend in the course of the stream at the fault right from the start of stream incision, perhaps caused by an obstruc-

tion that is not related to faulting. This is unlikely at the Ölgiy site because the catchment is small and the bends in the stream that exist today are mostly much smaller than the displacement of the stream currently observed at the fault. Also the displacement of S2 is 7 m greater than S1, thus the use of S1 to estimate minimum displacement is a conservative estimate. However there is the potential for either stream to underestimate the displacement of the deposit surface. There may have been some 'lag time' between the abandonment of the alluvium and the initiation of incision of the streams. Once stream incision began, displacement of the streams by faulting likely initiated in a relatively short amount of time because after several earthquakes over a few thousand years, there would be a large enough reverse scarp to dam the streams, in the way that they are currently inhibited to flow directly downslope.

The Quaternary dating techniques used in this study constrain the abandonment of the surface, and not necessarily the incision of the streams, and therefore the scarp measurement of the surface displacement is more directly correlated to the age constraints than the displacement of the streams. As such, the stream displacements place a minimum constraint on the offset of the alluvium, and the vertical scarp method provides a maximum constraint on fault offset. The scarp method may overestimate strike-slip offset if there is a reverse component of fault motion at the site, but any reverse slip component should be relatively small at the Ölgiy site, based on the pure strike-slip field expression of the most recent activity of the fault across the region. Also, the reverse scarp is of the opposite sense to the surrounding topography (Figure 3.2), and any reverse motion at the site would likely be a localised effect (as observed elsewhere in the Altay, e.g. *Baljinnyam et al.*, 1993). The deposits are uplifted on the western side of the fault, but the most obvious topography is on the eastern side of the fault (Figure 3.2). I would also expect steeply incised streams consistently located in the hanging wall of what would be an eastward dipping reverse

fault. By considering the slope displacements as maximum offsets, the possibility of localised reverse motion is incorporated into the slip-rate estimates, as well as the potential for the streams to underestimate fault displacement.

### 3.3.3 U-series dating of pedogenic carbonate rinds: methods and results

$^{238}$U-$^{234}$U-$^{230}$Th dating takes advantage of the intermediate nuclides produced in the $^{238}$U decay chain. Pedogenic carbonate accumulates on pebbles embedded in stable alluvium, within the top ~200 cm of the surface (*Birkland*, 1984). Uranium is relatively soluble in ground water and is incorporated into the carbonate in similar concentrations as in the water (relative to $Ca^{-2}$), whereas $^{230}$Th is insoluble in water, allowing for the fractionation of uranium from thorium at the time of carbonate formation (see *van Calsteren and Thomas*, 2006, for an overview). The radiogenic decay of U to $^{230}$Th allows for the timing of carbonate accumulation to be dated. The carbonate coatings on clasts generally show a progressively outward growth, with the oldest layers directly adjacent to the pebble, younging outwards in stratigraphic succession. When the technique was first applied, large sample sizes were necessary to obtain large enough ion concentrations (*Ku et al.*, 1979). However with modern MC-ICP-MS (multi-collector inductively coupled plasma mass spectrometry) techniques, it is possible to measure small samples of carbonate (<6 x $10^{-4}$ g), and the method is becoming more widely applied in Quaternary science and active tectonics (e.g. *Blisniuk and Sharp*, 2003; *Sharp et al.*, 2003; *Kock et al.*, 2009; *Fletcher et al.*; *Behr et al.*, 2010).

#### Sample preparation and analytical methods

Cobbles greater than 0.5 m wide were collected from F1 and F2 in the summer of 2009. Only pebbles that had carbonate crust growing on the underside were collected,

in order to insure that the carbonate grew *in situ*. Several samples were collected from the two surfaces, but based on the thickness and quality of the pedogenic carbonate rinds, carbonate from two separate samples were measured from F2 (MN09-OG12 and MN09-OG13), and one sample from F1 (MN09-OG7). The cobbles were collected from the top 10 cm of the surface (including exposed cobbles), where it appeared stable and undisturbed, and far from the margins of the alluvial surfaces or stream channels. Samples were processed by Rachel Garland, a fourth year student whom I worked with closely, under the supervision of Dr. Alex Thomas in the Oxford Earth Science geochemistry laboratories.

Pedogenic carbonate crusts were cross-sectioned with a diamond rock saw, rinsed with 18ΩM cm (Milli-Q) water and dried, before sub-samples were taken with a New Wave Research Micro Mill (Figure 3.7). Where possible, sub-samples were taken from trenches cut parallel to visible stratigraphic layering within the crust. Trenches were milled with a tungsten carbide drill bit, and were typically 200 $\mu$m wide. For each sub sample approximately 0.6–3 mg of powder was collected with a scalpel, and weighed in a micro centrifuge tube on a $\pm$ 0.00001 g balance.

Sub-sample powders were transferred to Teflon vials with 1 ml 18ΩM cm water, and were spiked with a mixed $^{229}$Th:$^{236}$U tracer solution. Total digestion of samples was undertaken with $HNO_3$ and HF. Equilibration of sample and spike isotopes was ensured by twice drying and redissolving the sample in concentrated $HNO_3$. Uranium and thorium were separated from each other and the sample matrix by anion exchange chromatography, using BioRad AG1 X8 resin (100–200 mesh). Briefly, the sample was loaded onto a 2 ml resin bed in 4 ml of 7.5N $HNO_3$ and the major ions were washed through the column with a further 4 ml of 7.5N $HNO_3$. The column

Pedogenic carbonate samples were processed and measured by Rachel Garland, with the help of Dr. Alex Thomas, as part of a fourth year project (*Garland*, 2010). Rachel measured sample MN09-OG12, and Alex measured samples MN09-OG13 and MN09-OG13. Rachel and Alex also performed data reduction and OxCal modeling, and Rachel wrote up the results as part of her project. Further data analysis and modeling was preformed by Alex Thomas and myself.

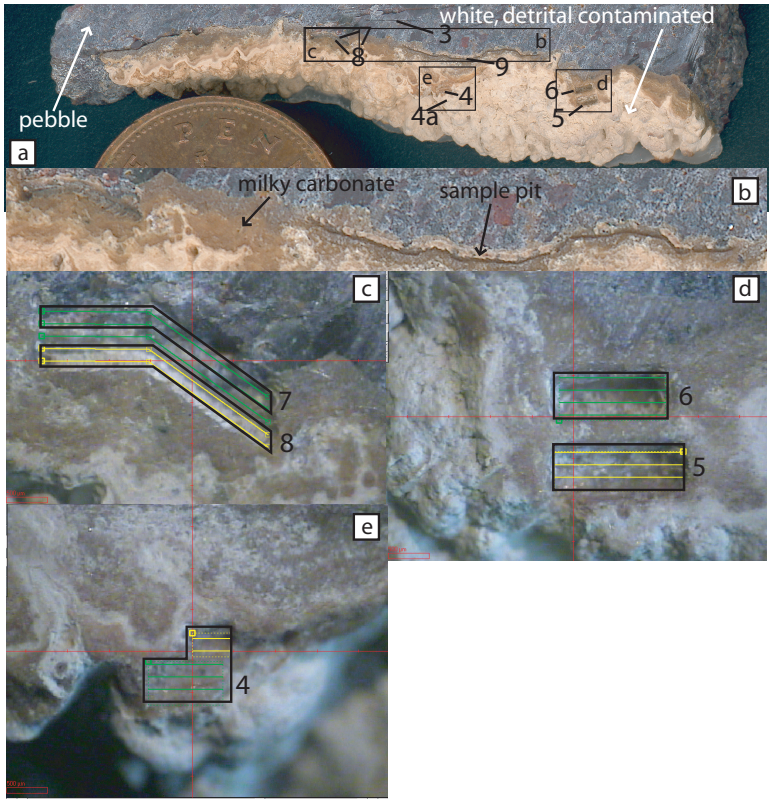


**Figure 3.7:** Photos of the carbonate crust from sample MN09-OG12. Insets show milling of subsamples. The milky buff coloured carbonate is ideal for dating, as the opaque white carbonate will have detrital contamination. Carbonate sampled closest to the pebble is more likely to date the initiation of carbonate growth.

was then converted to chloride form with 1.5 ml of 6N HCl, before Th was eluted in 6 ml of 6N HCl, and finally U was eluted in 6 ml water. Prior to measurement the Th and U fractions were dried down and converted to nitrate form before being dissolved in 2% $HNO_3$.

Measurement of Th and U isotope ratios was performed on a Nu Instruments MC-ICP-MS with a DSN-100 desolvating nebuliser sample introduction system. Minor isotopes, $^{234}U$, $^{230}Th$, and $^{229}Th$, were measured in an ETP ion counter detector while the larger ion beams were detected in Faraday collectors. Due to the small sample sizes, measurement protocols were optimized to characterize the uncertainties on such small beams. Uranium was measured statically with all isotopes measured

simultaneously. Each sample measurement was bracketed with two measurements of CRM-145 uranium standards: one at a similar $^{234}$U intensity to the samples, to assess the reproducibility of $^{234}$U/$^{238}$U and $^{238}$U/$^{236}$U ratios (using $^{238}$U/$^{235}$U as a proxy for the reproducibility of $^{238}$U/$^{236}$U); and one more concentrated so that higher precision corrections for mass bias and ion counter efficiency could be made. Th isotopes were measured dynamically, with both $^{230}$Th and $^{229}$Th measured in the same ion counter in two steps and $^{232}$Th in a Faraday collector. Each sample's Th fraction was doped with CRM-145 uranium standard so that signal instability between measurement steps could be made using the $^{235}$U beam (the $^{232}$Th is too small for these samples, and the $^{238}$U falls in a gap in the collector array). A separate measurement of a CRM-145 standard was made between sample analyses to characterize the mass bias and ion counter detector efficiency. A uranium standard is chosen here rather than a thorium standard, which may produce more accurate corrections, because of the need to limit the amount of thorium entering the sample introduction system and hence keep background contamination low. Prior to all measurements, assessments of the memory of the detector and the detector noise were made on a 2% $HNO_3$ solution by blocking the ion beam entirely. The contribution from tailing of the $^{238}$U and/or $^{232}$Th beam, to all other isotopes, was made by measuring at half masses on standard and sample solutions.

Isotope abundances are calculated accounting for the minor natural components of the $^{229}$Th:$^{236}$U tracer solution, and the procedural blanks. The total procedural blanks and their uncertainties are 65 $\pm$ 117 pg $^{238}$U, 9 $\pm$ 17 pg $^{232}$Th, and 0.7 $\pm$ 1.1 fg $^{230}$Th ($2\sigma$ errors based on 14 measurements of the total procedural blank processed alongside samples similar to those measured here). The final uncertainties in isotope abundances, which are dominated by the uncertainty in the blank correction, are up to 70%, but for the majority of samples (where the blank is a more minor component) total uncertainties are less than 10%.

### $^{238}$U-$^{234}$U-$^{230}$Th results

Uranium concentrations, U-series isotope ratios, and calculated ages are listed in Table 3.2. Ages are calculated from the measured ($^{230}$Th/$^{238}$U) and ($^{234}$U/$^{238}$U), using the age equation of *Broecker* (1963) in the isoplot software (*Ludwig*, 2003). Calculated ages show some agreement within each crust, but in some cases the order of the ages violates the stratigraphic order of outward growth from the pebble. This stratigraphic discrepancy can be accounted for by considering the initial isotopic composition of the sub-samples. Detrital contamination of silicic particulates within the authigenic carbonate will have incorporated $^{230}$Th and uranium with a potentially different ($^{234}$U/$^{238}$U), which will typically bias the ages to older values (*van Calsteren and Thomas*, 2006). To correct for this contamination, the measured ($^{232}$Th/$^{238}$U) is used as a proxy for the amount of contamination and the isotopic composition of the contaminant phase is assumed to be of approximately crustal composition. The crustal composition and associated uncertainties are estimated from the means and $2\sigma$ uncertainty of the U-series data archived in the EarthChem database (http://www.earthchem.org). While this is largely a dataset consisting of measurements of volcanic rocks, which are typically selected to avoid weathering products, it does provide the best available estimate of the isotopic composition of the likely contaminant.

Ages calculated from corrected ($^{230}$Th/$^{238}$U) and ($^{234}$U/$^{238}$U) are within error of stratigraphic order in all cases, and ages are not corrected to be less than zero (within error), giving some confidence to the initial $^{230}$Th and $^{234}$U correction used (Table 3.2, Figure 3.8). The detrital corrected ages for individual subsamples of the crust from F1 are between 42 ± 6 kyr to 19.6 ± 1.7 kyr. Ages from the two samples of the F2 surface are between 21 ± 4 kyr to 9 ± 5 kyr ($2\sigma$ uncertainties, neglecting outermost stratigraphic samples, which have large detrital contributions resulting in detrital corrected ages that range beyond the date they were sampled, Table 3.2).

**Table 3.2:** U-series results

| subsample ID | $^{238}$U conc. (ppm) | ($^{232}$Th/$^{238}$U) | ($^{230}$Th/$^{238}$U) | ($^{234}$U/$^{238}$U) | Age (kyr) | Detrital corr. age (kyr) | ($^{234}$U/$^{238}$U)initial |
|---|---|---|---|---|---|---|---|
| *Sample MN09_OG12* | | | | | | | |
| MN09_OG12_9 | 7.4 ± 1.4 | 0.080 ± 0.005 | 0.22 ± 0.04 | 1.188 ± 0.007 | 22 ± 4 | 15 ± 5 | 1.209 ± 0.016 |
| MN09_OG12_7 | 11.0 ± 0.8 | 0.0915 ± 0.0017 | 0.253 ± 0.011 | 1.182 ± 0.004 | 26.0 ± 1.2 | 17 ± 4 | 1.207 ± 0.016 |
| MN09_OG12_8 | 27.2 ± 2.1 | 0.0622 ± 0.0007 | 0.215 ± 0.007 | 1.184 ± 0.004 | 21.7 ± 0.7 | 16 ± 3 | 1.202 ± 0.011 |
| MN09_OG12_6 | 1.1 ± 0.2 | 0.127 ± 0.021 | 0.17 ± 0.10 | 1.338 ± 0.025 | 14 ± 10 | 4 ± 11 | 1.38 ± 0.04 |
| MN09_OG12_5 | 2.6 ± 0.3 | 0.043 ± 0.005 | 0.14 ± 0.05 | 1.303 ± 0.014 | 12 ± 5 | 9 ± 5 | 1.322 ± 0.017 |
| MN09_OG12_4 | 0.4 ± 0.2 | 0.54 ± 0.21 | 0.6 ± 0.4 | 1.56 ± 0.06 | 47 ± 43 | 3 ± 47 | 2.1 ± 0.5 |
| MN09_OG12_4a | 3.0 ± 0.3 | 0.72 ± 0.05 | 0.63 ± 0.06 | 1.297 ± 0.013 | 71 ± 10 | -12 ± 63 | |
| MN09_OG12_2 | 0.2 ± 0.2 | 1.1 ± 1.1 | 2.0 ± 2.2 | 1.57 ± 0.09 | | | |
| *Sample MN09_OG13* | | | | | | | |
| MN09_13-2-5 | 9.6 ± 2.6 | 0.0906 ± 0.0019 | 0.283 ± 0.007 | 1.186 ± 0.003 | 29.5 ± 0.8 | 21 ± 4 | 1.213 ± 0.016 |
| MN09_13-1-3 | 10 ± 4 | 0.0695 ± 0.0016 | 0.217 ± 0.007 | 1.178 ± 0.003 | 22.0 ± 0.8 | 16 ± 3 | 1.197 ± 0.012 |
| MN09_13-1-2 | 9 ± 5 | 0.0251 ± 0.0008 | 0.174 ± 0.008 | 1.192 ± 0.003 | 17.1 ± 0.9 | 14.9 ± 1.3 | 1.204 ± 0.005 |
| MN09_13-1-1 | 1.3 ± 0.8 | 0.064 ± 0.008 | 0.17 ± 0.06 | 1.239 ± 0.004 | 15.8 ± 7 | 10 ± 7 | 1.260 ± 0.013 |
| MN09_13-3-6 | 0.9 ± 0.7 | 0.022 ± 0.010 | 0.16 ± 0.12 | 1.231 ± 0.006 | 15 ± 13 | 13 ± 13 | 1.245 ± 0.012 |
| MN09_13-3-8 | 0.3 ± 0.1 | 0.35 ± 0.05 | 0.52 ± 0.12 | 1.219 ± 0.005 | 59 ± 19 | 24 ± 26 | 1.33 ± 0.09 |
| *Sample MN09_OG07* | | | | | | | |
| MN09_07-1-3 | 7.9 ± 1.2 | 0.121 ± 0.003 | 0.487 ± 0.010 | 1.257 ± 0.003 | 52.4 ± 1.3 | 42 ± 6 | 1.321 ± 0.025 |
| MN09_07-1-2 | 4.9 ± 0.8 | 0.131 ± 0.003 | 0.327 ± 0.009 | 1.194 ± 0.003 | 34.6 ± 1.1 | 22 ± 6 | 1.231 ± 0.025 |
| MN09_07-1-1 | 8.8 ± 7.5 | 0.0139 ± 0.0011 | 0.213 ± 0.015 | 1.215 ± 0.003 | 20.9 ± 1.6 | 19.6 ± 1.7 | 1.230 ± 0.004 |
| Detrital Composition (means and 2$\sigma$ of U-series data of rocks from the EarthChem database) | | 1.13 ± 0.37 | 1.10 ± 0.29 | 1.02 ± 0.16 | | | |

Uranium concentrations and measured U-series isotope activity ratios for sub samples of pedogenic carbonate crusts. Ages are calculated from the measured isotope ratios using the equation of *Broecker* (1963). The detrital corrected ages are calculated from isotope activity ratios corrected for detrital contamination, i.e. projected to a hypothetical $^{232}$Th free authigenic end-member, using an assumed detrital composition representative of crustal material. The ($^{234}$U/$^{238}$U) initial is the isotopic composition of the uranium at the time it was incorporated into the crust calculated with the detrital corrected age. All uncertainties are 2$\sigma$.

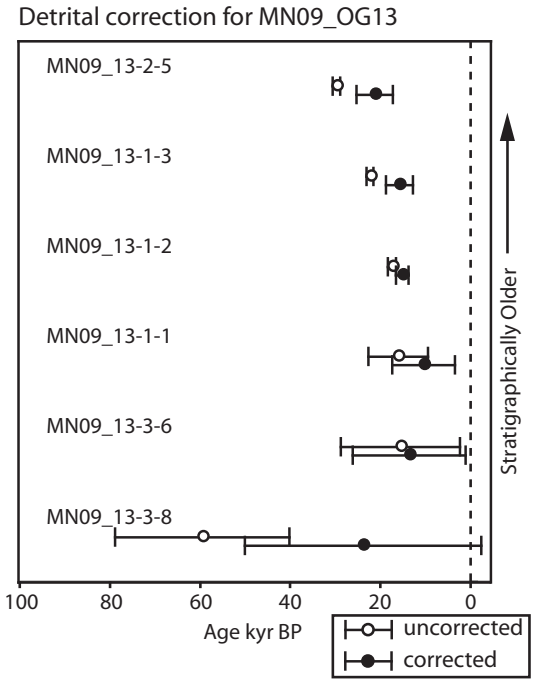


**Figure 3.8:** U-Th ages of sub-samples from pedogenic carbonate crust MN09-OG13. White dots are uncorrected ages of sub-samples of the crust, black dots are corrected for detrital contamination. Sub-samples are ordered stratigraphically with the oldest, nearest to the pebble, uppermost. Correction for detrital contamination is shown to result in younger ages and an increase in the uncertainty (shown at $2\sigma$).

### Bayesian statistical analysis of U-series results

Considered separately, the stratigraphic ages from each carbonate rind do not necessarily place constraint on the timing of stabilisation of the alluvial surface, which is the point in time that is relevant for using fault offsets of the alluvial deposits to estimate an average slip rate. Instead, the sequence of U-series results represents the growth of the crust through time. Because each individual age may have some contamination from the carbonate formed above and below the specific layer that was sampled, it is necessary to incorporate the full suite of results in calculating the time of initiation of crust formation. This is accomplished by undertaking a Bayesian statistical analysis procedure, utilizing the OxCal program (*Bronk Ramsey*, 2009). The basic premise of the analysis is that for each carbonate sample an age model

is constructed that places each sub sample in stratigraphic order within a sequence that is bounded by the initiation and end date of crust growth, with the assumption that the ages represent a random sampling of a uniform distribution between the boundaries of the model. Even the sub sample that was collected closest to the pebble surface may have some contamination from younger carbonate, thus the statistical treatment of the suite of results better predicts the probability of initiation of carbonate formation, because it is based on the full set of results instead of a single stratigraphic measurement.

Additional information based on what is known about the samples and the U-series system can be added to the Bayesian analysis in OxCal, which was originally constructed for radiocarbon dating. In the cases where the ages, when corrected for initial $^{230}$Th and $^{234}$U, have uncertainties that overlap with the date the samples were collected from the field (AD 2009), the additional constraint that the samples existed at the time of sampling is applied. This constraint is applied by adding an event to the young end of the age model with an age of -0.059 kyr (which is the year the samples were collected relative to time 0 in OxCal, *Bronk Ramsey*, 2009). Carbonate growth may continue up until the time of sampling. The OxCal statistical analysis takes into account the stipulation that even the oldest samples may have contamination from a younger layer of carbonate, and produces a carbonate growth sequence that is bounded by a statistically probable start and end date.

The results of the statistical analyses are given as mean, median, and start and end values, and these are detailed in Table 3.3. The model also produces probability distribution functions (PDF) for the age of each stratigraphic layer in the crust, shown in Figure 3.9. The effects of this approach are to reduce the uncertainties on the ages of the individual sub-samples while forcing the ages to be in stratigraphic order, as would be expected if the carbonate grows outward through time.

Because there are two samples from the F2 alluvial surface (MN09-OG12 and

**Table 3.3:** OxCal modeling inputs and results

| | Input (kyr BP) | | Modeled (kyr BP) 95% conf | | | | | | |
|---|---|---|---|---|---|---|---|---|---|
| Event | mean | $2\sigma$ | from | to | median | mean | $2\sigma$ | A(%) | C(%) |
| *Sample MN09_OG12* | | | Indices: Amodel = 92.6 Aoverall = 96.1 | | | | | | |
| Boundary Initiate | | | 27.948 | 14.972 | 19.6 | 20.5 | ±8.4 | 87.8 | |
| MN09_OG12_9 | 15.042 | ±5.462 | 20.792 | 14.591 | 17.5 | 17.6 | ±3.1 | 89.8 | 99.6 |
| MN09_OG12_7 | 17.403 | ±4.116 | 19.042 | 13.888 | 16.4 | 16.4 | ±2.6 | 109.8 | 99.8 |
| MN09_OG12_8 | 15.879 | ±2.694 | 17.264 | 12.768 | 15.0 | 15.0 | ±2.3 | 96.5 | 99.6 |
| MN09_OG12_6 | 3.804 | ±10.904 | 15.030 | 5.713 | 10.5 | 10.4 | ±4.9 | 69.9 | 99.6 |
| MN09_OG12_5 | 8.810 | ±5.180 | 12.019 | 3.563 | 7.8 | 7.8 | ±4.3 | 103.9 | 99.6 |
| MN09_OG12_4 | 3.082 | ±47.390 | 8.649 | -0.061 | 3.6 | 3.9 | ±5.2 | 140.5 | 99.8 |
| Sampling | -0.059 | ±0.002 | -0.057 | -0.061 | -0.059 | -0.059 | ±0.002 | 92.6 | 100 |
| Boundary End | | | -0.056 | -9.499 | -1.8 | -3.0 | ±7.5 | 92.8 | |
| *Sample MN09_OG13* | | | Indices: Amodel = 83 Aoverall = 83 | | | | | | |
| Boundary Initiate | | | 31.064 | 16.421 | 22.0 | 23.0 | ±9.6 | 89.6 | |
| MN09_OG13_2_5 | 20.955 | ±4.004 | 23.482 | 16.116 | 19.6 | 19.7 | ±3.8 | 90.8 | 99.4 |
| MN09_OG13_1_3 | 15.472 | ±3.020 | 18.303 | 14.252 | 16.1 | 16.2 | ±2.1 | 110.3 | 99.7 |
| MN09_OG13_1_2 | 14.816 | ±1.346 | 15.964 | 13.461 | 14.7 | 14.7 | ±1.3 | 102.7 | 99.8 |
| MN09_OG13_1_1 | 10.083 | ±6.928 | 15.186 | 7.407 | 11.9 | 11.7 | ±4.2 | 110.4 | 99.7 |
| MN09_OG13_3_6 | 13.309 | ±12.550 | 13.948 | 3.632 | 9.2 | 9.0 | ±5.4 | 106.9 | 99.5 |
| MN09_OG13_3_8 | 23.543 | ±26.192 | 10.692 | -0.059 | 5.0 | 5.2 | ±6.2 | 54.4 | 99.5 |
| Sampling | -0.059 | ±0.002 | -0.057 | -0.061 | -0.059 | -0.059 | ±0.002 | 92.6 | 100 |
| Boundary End | | | -0.053 | -10.175 | -2.0 | -3.3 | ±8.1 | 96.6 | |
| *Sample MN09_OG07* | | | Indices: Amodel = 99.5 Aoverall = 99.3 | | | | | | |
| Boundary Initiate | | | 81.732 | 36.151 | 49.2 | 55.0 | ±33.3 | 86 | |
| MN09_07-1-3 | 41.554 | ±5.574 | 46.294 | 35.147 | 40.8 | 40.8 | ±5.7 | 97 | 96.6 |
| MN09_07-1-2 | 22.176 | ±5.940 | 27.848 | 19.119 | 22.9 | 23.2 | ±4.7 | 109.2 | 98 |
| MN09_07-1-1 | 19.583 | ±1.698 | 21.175 | 17.844 | 19.5 | 19.5 | ±1.7 | 100.6 | 99 |
| Sampling | -0.059 | ±0.002 | -0.057 | -0.061 | -0.059 | -0.059 | ±0.002 | 92.5 | 100 |
| Boundary End | | | -0.056 | -37.963 | -8.0 | -12.9 | ±26.8 | 92.1 | |

Inputs to, and results from, Bayesian analysis of age data. A separate age model is constructed for each crust, consisting of: boundaries at the beginning and end of each sequence that define the start and end of crust growth; the sequence of events (i.e. the stratigraphically ordered sub-samples), and final event that constrains the minimum possible age of the crust (and individual sub-samples) to the date it was sampled from the field. The agreement indices, A, for each age model and for individual events are >60% (except for MN09_OG13_3_8). Convergence tests, C, are >95%, indicating that the modeled results are a realistic representation of the input data and model (*Bronk Ramsey*, 1995).

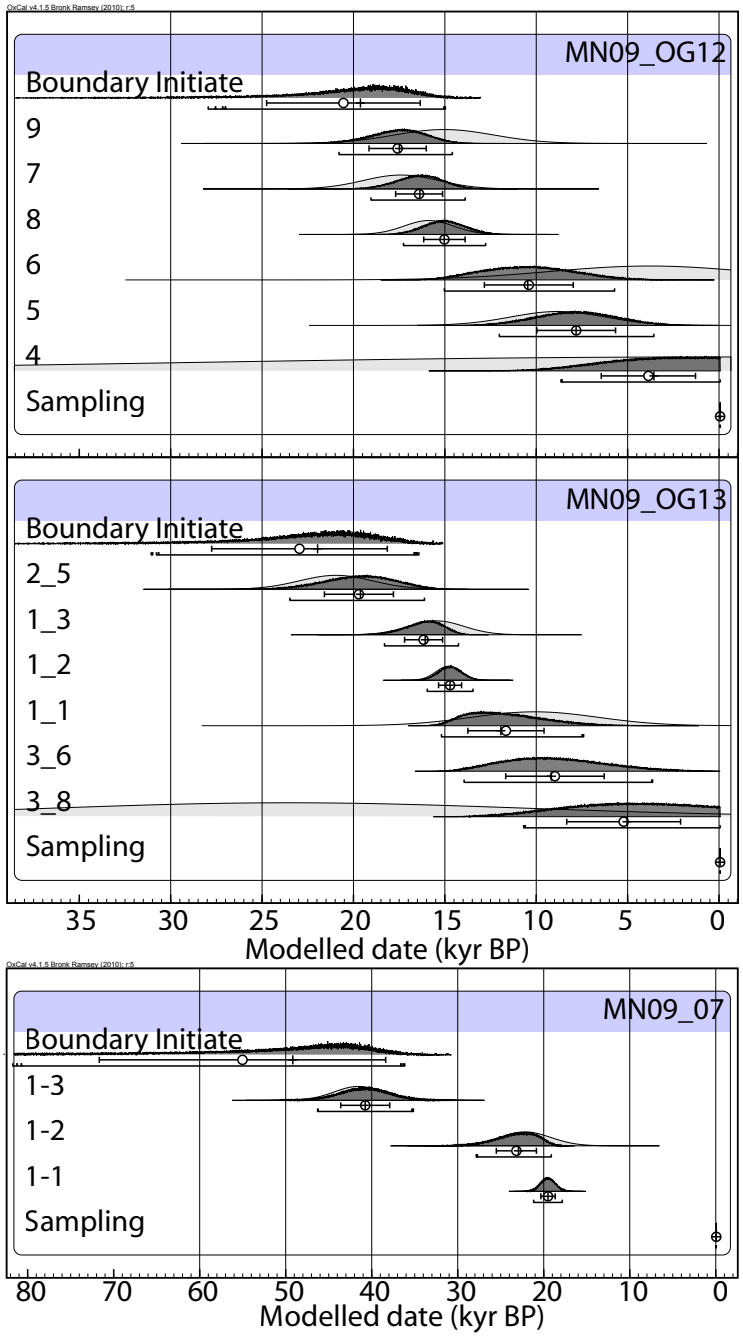


**Figure 3.9:** Results of the Bayesian analysis of the ages within each crust. For each crust sub-samples are ordered stratigraphically, with the oldest uppermost. The distributions of the input ages (corrected for detrital contamination) are shown in light grey, while those resulting from the additional constraints of the age models are in dark grey. Summary statistics of the modeled distributions that are shown below each distribution include: mean (open circle) and $1\sigma$, median (cross), and 95% interval of the age distribution (horizontal bar).

MN09-OG13), an additional model was run with the constraint that both carbonate rinds initiated growth at the same time, based on the assumption that carbonate growth on F2 started simultaneously for both samples. This is a reasonable assumption because, considered separately, the two samples have similar initiation ages. The result of modeling the two samples together provides an estimate of when carbonate began to accumulate on the two samples from the F2 surface, which is based on a larger dataset as it takes into account the results from each sub-sample of crust from both rinds. The results of modeling the samples together are presented in Figure 3.10 and Table 3.4, with $1\sigma$ uncertainties (instead of $2\sigma$) for comparison with the $^{10}$Be cosmogenic nuclide dating results. Sample MN09-OG07 is also presented in Table 3.4, with $1\sigma$ uncertainties listed.

The output PDFs do not have a normal distribution, because there tends to be a long 'tail' of old ages possible for the given inputs, but the older ages have a much lower probability (Figure 3.10). Because of this, the distribution tends to overestimate the age in terms of the mean and median values of the PDF. There is a greater probability that the ages are younger than the calculated median and mean values, particularly in the case of the mean value of the boundary initiate (open circles in Figures 3.9 and 3.10). However for the median ages, the distribution of results is taken into account and as a result it is less problematic in terms of overestimating the age. In terms of calculating fault slip rates, the age of initiation of carbonate growth is an approximation for the timing of stabilisation of a landscape, because carbonate pedogenesis does not occur in a high energy environment. Therefore the most useful aspect of the U-series results is the minimum age for growth initiation. In order to calculate the slip rate of the Ölgiy fault, I constrain the minimum ages of stabilisation/abandonment of the two surfaces by simply using the minimum constraint from the range of boundary initiate results from the OxCal model (in columns 'from' and 'to' in Table 3.4). For F1, the lower boundary initiate is 38.4 kyr from the one sample

**Table 3.4:** OxCal modeling inputs and results, with the two samples from F2 combined, all shown with $1\sigma$ uncertainties

| | Input (kyr BP) | | Modeled (kyr BP) 68.2% conf | | | | | | |
|---|---|---|---|---|---|---|---|---|---|
| Event | mean | $1\sigma$ | **from** | **to** | median | mean | $1\sigma$ | A(%) | C(%) |
| *Sample MN09_OG12* | | | | | | | | | |
| Boundary Initiate | | | 22.297 | 18.053 | 20.367 | 20.680 | ±2.302 | | 80 |
| MN09_OG12_9 | 15.042 | ±2.731 | 19.245 | 16.401 | 17.893 | 17.959 | ±1.419 | 80.8 | 98.7 |
| MN09_OG12_7 | 17.403 | ±2.058 | 17.810 | 15.374 | 16.629 | 16.663 | ±1.224 | 115.6 | 99.2 |
| MN09_OG12_8 | 15.879 | ±1.347 | 16.323 | 14.059 | 15.179 | 15.164 | ±1.120 | 100.5 | 98.4 |
| MN09_OG12_6 | 3.804 | ±5.452 | 13.180 | 7.955 | 10.501 | 10.450 | ±2.456 | 69.4 | 98 |
| MN09_OG12_5 | 8.810 | ±2.590 | 10.032 | 5.626 | 7.838 | 7.829 | ±2.160 | 103.9 | 98.1 |
| MN09_OG12_4 | 3.082 | ±23.695 | 5.0670 | -0.056 | 3.571 | 3.873 | ±2.585 | 140.5 | 98.9 |
| Sampling | -0.059 | ±0.001 | -0.058 | -0.060 | -0.059 | -0.059 | ±0.001 | 92.6 | 100 |
| Boundary End | | | -1.450 | 1.563 | | | | 90.9 | |
| *Sample MN09_OG13* | | | | | | | | | |
| Boundary Initiate | | | 22.297 | 18.053 | 20.367 | 20.680 | ±2.302 | | 80 |
| MN09_OG13_2_5 | 20.955 | ±2.002 | 20.489 | 17.150 | 18.936 | 19.046 | ±1.628 | 81 | 98.4 |
| MN09_OG13_1_3 | 15.472 | ±1.510 | 16.998 | 14.955 | 16.042 | 16.123 | ±1.010 | 111.8 | 99.1 |
| MN09_OG13_1_2 | 14.816 | ±0.673 | 15.347 | 14.080 | 14.712 | 14.710 | ±0.629 | 102.7 | 99 |
| MN09_OG13_1_1 | 10.083 | ±3.464 | 14.324 | 10.178 | 11.934 | 11.654 | ±2.083 | 110.4 | 98.9 |
| MN09_OG13_3_6 | 13.309 | ±6.275 | 12.256 | 6.616 | 9.175 | 8.979 | ±2.694 | 106.9 | 98.4 |
| MN09_OG13_3_8 | 23.543 | ±13.096 | 7.852 | 0.634 | 5.037 | 5.223 | ±3.117 | 54.5 | 98.1 |
| Sampling | -0.059 | ±0.001 | -0.058 | -0.060 | -0.059 | -0.059 | ±0.001 | 92.8 | 100 |
| Boundary End | | | -1.45 | 1.563 | | | | 90.9 | |
| *Sample MN09_OG07* | | | | | | | | | |
| Boundary Initiate | | | 57.023 | 38.435 | 49.175 | 55.025 | ±16.648 | | 86 |
| MN09_07-1-3 | 41.554 | ±2.787 | 43.737 | 37.775 | 40.757 | 40.751 | ±2.849 | 97 | 96.6 |
| MN09_07-1-2 | 22.176 | ±2.970 | 25.159 | 20.215 | 22.936 | 23.181 | ±2.330 | 109.2 | 98 |
| MN09_07-1-1 | 19.583 | ±0.849 | 20.347 | 18.644 | 19.503 | 19.501 | ±0.835 | 100.6 | 99 |
| Sampling | -0.059 | ±0.001 | -0.058 | -0.06 | -0.059 | -0.059 | ±0.001 | 192.5 | 100 |
| Boundary End | | | -0.057 | -14.428 | | | | 92.1 | |

Age models are constructed with the same parameters in Table 3.3, but samples MN09_OG12 and _OG13 were modeled with the assumption that carbonate growth was initiated at the same time. Here, all uncertainties are listed as $1\sigma$ errors for comparison with $^{10}$Be data.

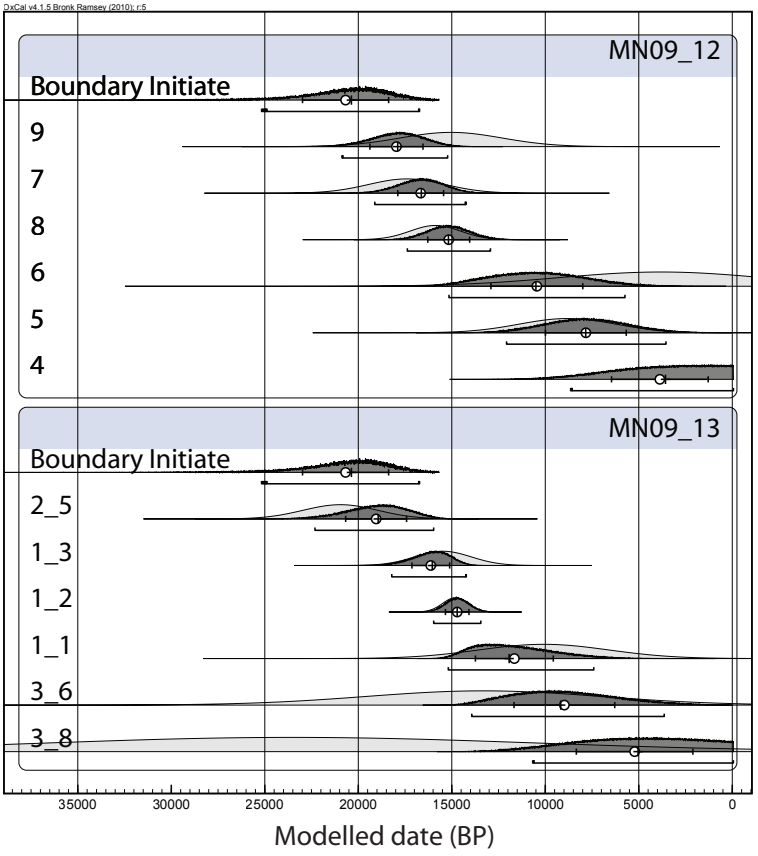


**Figure 3.10:** Results of the Bayesian analysis of the ages within each crust for modeling of the two samples from F2. The start and end date of both samples were stipulated to occur at the same time. The distributions of the inputted ages (corrected for detrital contamination) are shown in light grey, while those resulting from the additional constraints of the age models are in dark grey. Summary statistics that are shown below each model distribution include: mean (open circle) and $1\sigma$; median (cross) and 95% interval of the age distribution (horizontal bar).

measured (MN09-OG7, based on a range of 57.0 kyr to 38.4 kyr kyr). The results from the two separate pebbles measured from F2 are combined in a single OxCal model (samples MN09-OG12 and MN09-OG13, Figure 3.10), with the assumption that the initiation of carbonate growth on both pebbles occurred at the same time on the deposit (with the stabilisation of the deposit). The results of the combined OxCal model place the estimate of stabilisation of F2 before 18.0 kyr (from a range of 22.3 kyr to 18.0 kyr). Stabilisation is approximately equivalent to abandonment of the surface, because presumably the surface is no longer aggraded or degraded once

the system is stable enough for carbonate pedogenesis to begin and be preserved. Therefore the carbonate results are complimentary to $^{10}$Be results presented below, in that the U-series statistically probable growth initiation ages provide a cutoff date for the existence of the surface, a constraint that is important for interpreting the cosmogenic dates.

### 3.3.4 $^{10}$Be terrestrial cosmogenic nuclide dating: methods and results

$^{10}$Be is a long-lived isotope that is produced *in-situ* in quartz, mainly as a result of high-energy spallation reactions (with O and Si) due to cosmic rays (*Nishiizumi et al.*, 1989). The $^{10}$Be concentration in a sample is used to estimate the duration of exposure to cosmic rays, based mainly on empirically determined production rates (see *Gosse and Phillips*, 2001, for a thorough review). The concentration of cosmogenic nuclides in a sample reflects the duration of time the sample has been exposed. The concentration of a cosmogenic nuclide ($N$, atom g$^{-1}$) at depth $x'$ (in terms of mass per unit area, g cm$^{-2}$) from the surface can be generally represented as a function of time ($t$) by:

$$N(t) = \frac{Pe^{-x'L^{-1}}}{(\epsilon L^{-1} + \lambda)}\left[1 - e^{(\epsilon L^{-1}+\lambda)}\right] + N(0)e^{-\lambda t} \tag{3.1}$$

where $\epsilon$ is the mass erosion rate (g cm$^{-2}$ yr$^{-1}$), $P$ is the production rate (atom g$^{-1}$ yr$^{-1}$, dependent on several factors discussed further below), $L$ is the effective attenuation length of cosmic rays (~150 g cm$^{-2}$ for $^{10}$Be production in sediments, or effectively 200 cm *Lal*, 1991; *Brown et al.*, 1992), $\lambda$ is the radioactive decay constant (per year), and *N(0)* is the cosmogenic nuclide concentration already present at the initiation of surface exposure. Constant production and erosion rates are assumed in Equation 3.1, and there are three unknowns: $\epsilon$, $t$, and *N(0)*. Thus the erosion rate

($\epsilon$) and nuclide concentrations inherited from prior exposure *N(0)* must be assessed in order to determine accurate exposure ages.

The *in-situ* production rate of $^{10}$Be decreases exponentially with depth below the surface, due to the attenuation of cosmic ray flux through a material (e.g. *Lal*, 1991). The *in-situ* production rate at any time $P$ (atoms g$^{-1}$ s$^{-1}$) of a radionuclide at depth, $x$ (cm), is simplified as:

$$P(x) = P(0)e^{-\mu x} \tag{3.2}$$

where *P(0)* is the production rate at the surface, and $\mu$ is the absorption coefficient (cm$^{-1}$), where $\mu = \rho/\Lambda$ and $\rho$ is the density of the overlying rock (g cm$^{-3}$) and $\Lambda$ is the absorption mean free path for nuclear interacting particles in the rock column (g cm$^{-2}$). $1/\mu$ is equivalent to $\sim$50 cm for most crustal rock densities. If continuously exposed, the $^{10}$Be concentrations at the surface will reach a steady state where cosmogenic production and radioactive decay are in equilibrium, and the system is essentially saturated with $^{10}$Be. Erosion also plays a role in the equilibrium of the system, because in an eroding system, the top of the surface is constantly being replaced by the layer below, and thus removing $^{10}$Be from the system. Therefore prior to reaching secular equilibrium, the shape of a profile of nuclide concentrations at depth will be affected by the erosion rate of the surface, and it is possible to calculate both the age of exposure of the surface and the surface erosion rate based on the measured depth profile of $^{10}$Be concentrations. *Siame et al.* (2004) developed a chi-squared inversion method to model measurements of $^{10}$Be concentrations with depth. The inversion minimises the difference between the measured and expected nuclide concentrations based on the attenuation of production with depth. From the $\chi^2$ inversion, best fit constraints are placed on the erosion rate and exposure duration that have led to the concentrations in the measured $^{10}$Be profile. The inversion is

based on:

$$\chi^2 \equiv \sum_{i=1}^{N} \left( \frac{C_i - C(x_i, \epsilon, t)}{\sigma_i} \right)^2 \tag{3.3}$$

where $C_i$ is the measured $^{10}$Be concentration at depth $x_i$, $C(x_i, \epsilon, t)$ is the computed concentration with a given solution for $\epsilon$ (erosion rate) and $t$ (exposure time), and $\sigma_i$ is the analytical uncertainty at depth $x_i$. Minimising the $\chi^2$ quantity (3.3) gives the maximum likelihood for values of the modeled parameters ($\epsilon$, $t$). Because the deepest samples should have negligible $^{10}$Be concentrations if there are very low levels of geological inheritance in the alluvium, the inherited $^{10}$Be concentration can essentially be found by the offset of concentrations in the lower samples from the expected concentration with no inheritance (expected to be close to zero at depths > 200 cm), though this approach does not take into account any variance in inheritance levels through time.

In this section, I calculate the exposure ages of boulders collected from the surface of the deposits at the Ölgiy site, using the online CRONUS exposure age calculator (*Balco et al.*, 2008). With the calculation of exposure ages below, I describe the details for my choice of production rate, as well as my choice for the various parameters that are used to scale the empirically determined production rates to a local production rate at my slip rate site. In Section 3.4, I describe the results from a depth profile of $^{10}$Be concentrations in an alluvial fan on the Hovd fault, and use the chi-squared inversion from *Siame et al.* (2004) to place constraints on the erosion rate, inherited nuclide concentrations, and exposure age of the fan surface.

### Sample preparation and measurement

Samples from schistose metasediment (mostly conglomeritic) and vein quartz boulders were collected from the F1 and F2 deposits in the summers of 2008 and 2009. Eleven samples were collected from surface F1 (nine were measured) and six samples from surface F2 (three were measured). Most of the boulders that were sampled

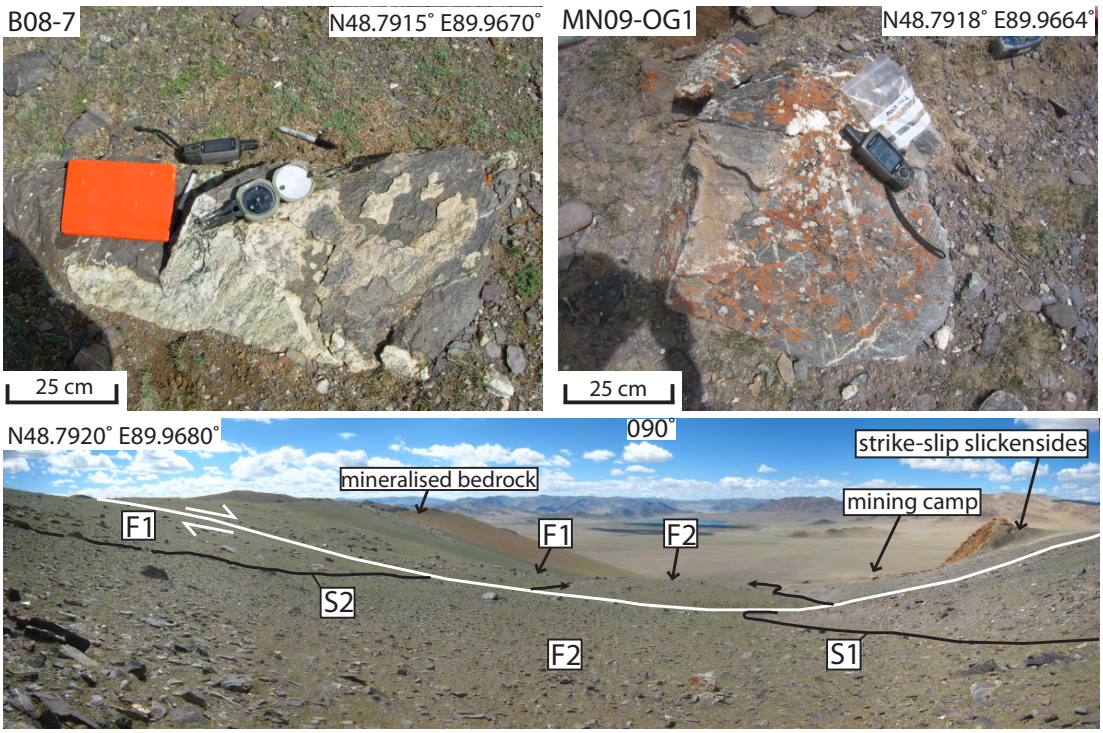


**Figure 3.11:** Examples of boulders sampled from F1 (left) and F2 (right) fan surfaces. Lower— Panoramic photo of the site, with labels for both alluvial surfaces (F1 and F2) and the two main streams (S1 and S2). The Ölgiy fault is traced in white where it crosses the site.

were 50 to 100 cm across, and all samples stood over 30 cm high above the surface (Figure 3.11). I was careful to sample boulders that had lichen or desert varnish and no evidence of recent disturbance (such as fresh rock exposed), in order to minimise the potential for complications in exposure history, and boulders from the edges of the surfaces or near stream channels were avoided. In order to have sufficient quartz for $^{10}$Be analyses, thick quartz veins present in the metasediment boulders were collected. Unfortunately, it was not possible to dig a depth profile pit for sampling because the deposits are composed of course sediment with abundant large boulders throughout.

At least 2 kg of material was collected for each sample. The top 2–6 cm of boulders were crushed using a jaw crusher and disc mill, and sieved to a fraction

of 250–700 $\mu$m. The approximate maximum thicknesses of samples were estimated during processing and the correction for sample thickness is included in exposure age calculations. Further sample preparation was carried out at the Scottish Universities Environmental Research Centre (SUERC) Cosmogenic Isotope Analysis Facility (CIAF) in East Kilbride, Scotland. Magnetic grains were separated using a Frantz separator. The resulting fraction was purified by several stages of etching in HF and heavy liquid separation, and checked for purity under optical microscope. Detailed processing is the same as that described in *Wilson et al.* (2008).

Once Be was isolated in samples through cation-exchange column chemistry, $^{10}$Be/$^{9}$Be ratios were measured on the accelerator mass spectrometer (AMS) at SUERC (*Freeman et al.*, 2004). Total procedural blanks were prepared alongside samples using approximately the same $^{9}$Be tracer mass as the samples. SUERC AMS measurements of $^{10}$Be/$^{9}$Be ratios are normalised to the reference standard NIST SRM4325 (which has a $^{10}$Be/$^{9}$Be ratio of 3.060 x $10^{-11}$, and is normalised to the 2002 Nishiizumi Be standard in the CRONUS age calculations, *Nishiizumi*, 2002). The measured blank $^{10}$Be/$^{9}$Be ratios are on the order of $10^{-15}$ (Table A.2 in Appendix A), and these values were subtracted from the sample $^{10}$Be/$^{9}$Be ratios, with the uncertainty of this correction included in the 1$\sigma$ concentration uncertainties. The total reported 1$\sigma$ uncertainties for $^{10}$Be concentrations include a standard conservative 2.5% preparation uncertainty (mainly from the uncertainty in the Be carrier solution, *Wilson et al.*, 2008), along with AMS measurement uncertainties for sample measurement, for measurement of the primary standard and for blank corrections.

### 3.3.5 Exposure age calculation

I used the online calculator CRONUS-Earth, Version 2.2, to calculate exposure ages (*Balco et al.*, 2008, at url: http://hess.ess.washington.edu). $^{10}$Be data are reported

in Table 3.5, with all data necessary for recalculating exposure ages (e.g. *Balco et al.*, 2008; *Dunai and Stuart*, 2009). Sample elevations were measured in the field with a hand-held GPS and converted into atmospheric depth in the CRONUS calculator (*Balco et al.*, 2008). The Be decay constant is not precisely determined but is 4.62 x $10^{-7}$ $yr^{-1}$ for the 2002 Nishiizumi standard, to which the CRONUS calculator normalises based on the standard used in the CIAF measurements. Decay constant uncertainty has very little effect on age calculations for samples that are relatively young ($10^4$ yrs), and because I have used a standard calculator, the ages are easily recalculated using adjusted constants.

The calibrated production rates for $^{10}$Be nuclides in samples due to muon flux and high-energy spallation must be scaled to the elevation and latitude of the site (e.g. *Stone*, 2000; *Dunai*, 2000; *Staiger et al.*, 2007). Muon flux in the CRONUS calculator is only varied by elevation, not by latitude or time (i.e. ignoring magnetic field effects), however muon production is only a few percent of the total surface $^{10}$Be production. High-energy spallation is the most significant component of production, and there are five different schemes generally used for scaling production rates. The simplest scaling scheme is from *Lal* (1991), improved by *Stone* (2000), which works on the variation of production rate by latitude and elevation (or atmospheric pressure). I use this time-varying production rate scaling scheme, with the modification of *Nishiizumi et al.* (1989) for correcting for the changing magnetic field over time from palaeomagnetic data (the 'Lm' scheme in CRONUS *Balco et al.*, 2008). This scheme does not take into account higher spherical harmonic fields, thus the scaling is based on a geocentric axial dipole (i.e. there is only magnetic variation according to latitude).

Azimuthal elevations of the horizon were measured at the sample locality, and I used these to calculate the shielding of cosmogenic rays by topography with the program described in *Balco et al.* (2008). The effect of topographic shielding is generally

quite small because the majority of incoming cosmogenic radiation is focused about the vertical (*Gosse and Phillips*, 2001). Shielding is negligible at the site (0.972), but is included in the age calculations. I also include estimates of sample thicknesses and densities to correct for the attenuation of flux through rock (listed in Table 3.5). The uncertainty typically associated with the thickness correction is small (1–2%; *Gosse and Phillips*, 2001).

Corrections for erosion of the boulder surface have not been applied for exposure age calculations in this study. Whilst there was no field evidence for *in-situ* spallation on the boulders that were sampled, this cannot be ruled out as much of the boulder surfaces were covered in lichen and could not be directly observed. Surface lowering may lead to anomalously low $^{10}$Be concentrations from late exposure, but I do not have an independent method for calculating the denudation of the surface surrounding the boulders. The only surface erosion rate that has been measured in the Altay comes from an alluvial fan near Har Us Lake, on the eastern side of the Altay (*Nissen et al.*, 2009b). From a $^{10}Be$ depth profile, *Nissen et al.* (2009b) calculated a very low surface erosion rate of 2.5 m Myr$^{-1}$. A denudation rate of this order of magnitude would not have a significant effect on samples of Late Quaternary age (*Gosse and Phillips*, 2001), and care was taken to sample boulders at a height of at least 30 cm to minimise the effects of surface erosion on exposure ages. The effect of either surface lowering or boulder surface erosion can in some ways be dealt with by integrating the oldest exposure age for calculating fault slip rates, but in some cases even boulders with the greatest cosmogenic nuclide concentrations may have experienced some post-depositional effects (*Hallet and Putkonen*, 1994). Surface coverage (from snow) is also an important consideration. If significant snow cover has occurred, for example about 1 m of cover for four months of the year, this could lead to up to a 5% difference in calculated ages from the actual exposure age (*Gosse and Phillips*, 2001). However, I also do not have a measure of snow cover in

the region of the site, and I have not included any cover corections.

### $^{10}$Be TCN results

The age calculation results incorporate corrections for shielding, elevation, sample thickness, and density (Table 3.5). From the $^{10}$Be exposure ages, there are two groups of exposure ages representing two distinct events— all samples from F1 are older than samples from F2 (Table 3.12). There is a large spread in the data from F1, with the calculated boulder exposure ages ranging from 40.8 ± 4.4 to 102.9 ± 13.3 kyr. With the exception of the oldest and youngest boulders, all are within one standard deviation (17.2 kyr) of the mean (65.3 kyr) of all samples (Figure 3.12). Ages from F2 are more tightly grouped than F1, with a moderate spread of data. Ages for the three samples measured range between 10.6 ± 1.2 to 25.9 ± 2.6 kyr, and two of three boulder ages are within 1$\sigma$ error (25.9 ± 2.6 and 21.3 ± 2.2).

### Age constraints on the timing of surface abandonment from $^{10}$Be cosmogenic dating

Because the U-series dating provides a minimum constraint on fan abandonment, I mainly focus on discerning the best maximum constraint on surface exposure from the cosmogenic nuclide results. If the boulders have had a complicated exposure history, several factors may influence the $^{10}$Be concentrations in my samples, leading to both over- or under- estimating the age of abandonment of the alluvial surface (e.g. *Brown et al.*, 1998; *Zreda and Phillips*, 2000; *Vassallo et al.*, 2011). Post-depositional processes may lead to underestimating the abandonment of a surface, because erosion of either the boulder surfaces themselves or denudation of the surface causes samples to be exposed to cosmogenic radiation at some time after the surface has been abandoned. Conversely, ages from boulder samples may overestimate the abandonment of a surface if they have been subjected to pre-depositional accumulation

**Table 3.5:** $^{10}$Be data Table

| Sample | Latitude (° N) | Longitude (° E) | Elevation[a] (m) | Thickness[b] (cm) | Density[b] (g cm$^3$) | Production rate[c] (at g$^{-1}$ y$^{-1}$) | | $^{10}$Be conc.[d] ($10^5$ a g$^{-1}$ $SiO_2$) | Exposure age[e,f,g,h] (ky) |
|---|---|---|---|---|---|---|---|---|---|
| | | | | | | spallation | muons | | |
| *Bayan Ölgiy F1* | | | | | | | | | |
| B08-1 | 48.7915 | 89.9667 | 2235 | 3 | 2.5 | 26.28 | 0.372 | 13.980 ± 0.489 | 48.2 ± 6.2 |
| B08-02 | 48.7915 | 89.9667 | 2236 | 3 | 2.5 | 26.3 | 0.372 | 17.310 ± 0.543 | 60.0 ± 7.4 |
| B08-04 | 48.7916 | 89.9666 | 2236 | 4 | 2.6 | 26.06 | 0.37 | 29.210 ± 1.015 | 102.9 ± 13.3 |
| B08-05 | 48.7916 | 89.9669 | 2243 | 3 | 2.6 | 26.4 | 0.372 | 20.240 ± 0.655 | 70.0 ± 8.7 |
| B08-06 | 48.7915 | 89.967 | 2245 | 3 | 2.6 | 26.44 | 0.373 | 11.910 ± 0.415 | 40.8 ± 5.2 |
| B08-07 | 48.7915 | 89.967 | 2246 | 4 | 2.6 | 26.25 | 0.372 | 18.290 ± 0.635 | 63.5 ± 8.1 |
| B08-09 | 48.7914 | 89.9667 | 2242 | 4 | 2.6 | 26.17 | 0.371 | 19.410 ± 0.677 | 67.7 ± 8.7 |
| B08-10 | 48.7914 | 89.9666 | 2241 | 5 | 2.6 | 25.95 | 0.37 | 19.540 ± 0.683 | 68.7 ± 8.8 |
| B08-11 | 48.7915 | 89.9669 | 2239 | 5 | 2.6 | 25.91 | 0.37 | 18.710 ± 0.695 | 65.9 ± 8.7 |
| *Bayan Ölgiy F2* | | | | | | | | | |
| MN09-OG01 | 48.7918 | 89.9664 | 2230 | 2 | 2.4 | 26.4 | 0.373 | 7.492 ± 0.115 | 25.9 ± 2.6 |
| MN09-OG03 | 48.7919 | 89.9662 | 2227 | 2 | 2.4 | 26.35 | 0.372 | 6.148 ± 0.109 | 21.3 ± 2.2 |
| MN09-OG04 | 48.7919 | 89.9668 | 2236 | 2 | 2.4 | 26.52 | 0.373 | 3.064 ± 0.077 | 10.6 ± 1.2 |

[a] Typical hand held GPS vertical uncertainties are 10–15 m.
[b] Used to correct for attenuation of flux through rock, with an attenuation length of 160 g cm$^{-2}$ (*Balco et al.*, 2008).
[c] Time-variant local production rate based on *Lal* (1991) and *Stone* (2000).
[d] All uncertainties are reported to 1$\sigma$ level.
[e] A shielding factor of 0.972 was applied to all samples, to correct for local topography.
[f] No erosion rate correction was used in age calculations, see Section 3.3.5.
[g] Ages were calculated using the CRONUS-Earth online calculator, v 2.2 (*Balco et al.*, 2008).
[h] Age uncertainties include internal and external errors.

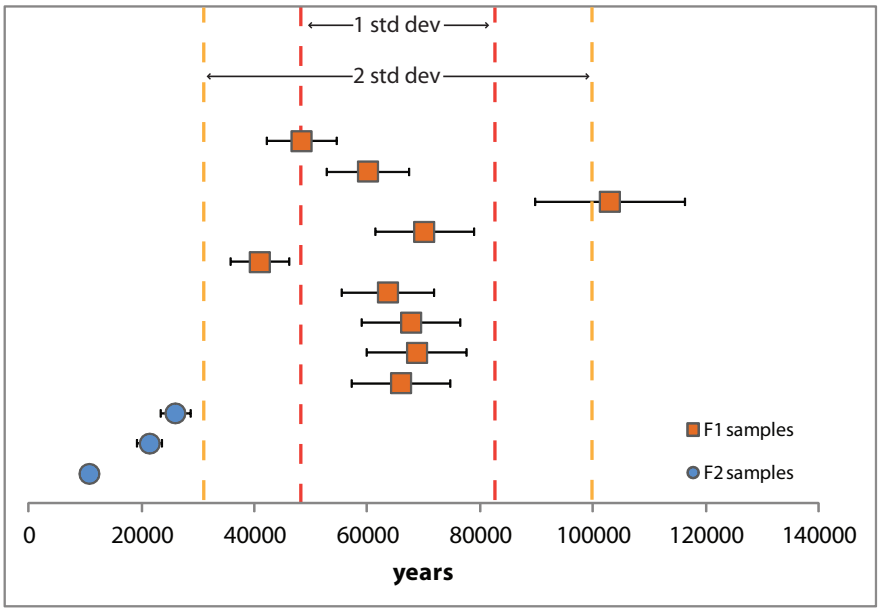


**Figure 3.12:** $^{10}$Be age results from the CRONUS calculator for F1 (orange) and F2 (blue). All uncertainties are displayed at the $1\sigma$ level. Samples from the two fans do not overlap in age, and the 1 and 2 standard deviation envelopes are indicated for the population of results from F1.

of cosmogenic nuclides during transport or from exposure as bedrock upstream, producing an 'inherited' signal in the $^{10}$Be concentrations. At the Ölgiy site, the range in boulder ages suggest a potentially complicated exposure history, and therefore I discuss the TCN concentrations in detail, alongside the U-series results, in order to provide a reliable maximum estimate of abandonment for each surface. Schematic diagrams of the age constraints from both $^{10}$Be and U-series dating, for each surface, are shown in Figures 3.13 and 3.14.

Typically, when interpreting nuclide concentrations measured in surface boulders, especially from glacial moraines, the calculated ages are assumed to underestimate surface exposure due to post-depositional surface lowering (*Hallet and Putkonen*, 1994; *Pallàs et al.*, 2010). In this case, the oldest TCN ages are used to establish the timing of exposure, with the stipulation that the estimated exposure age is a minimum. Erosion of the boulder surfaces themselves can also be problematic (*Hallet*

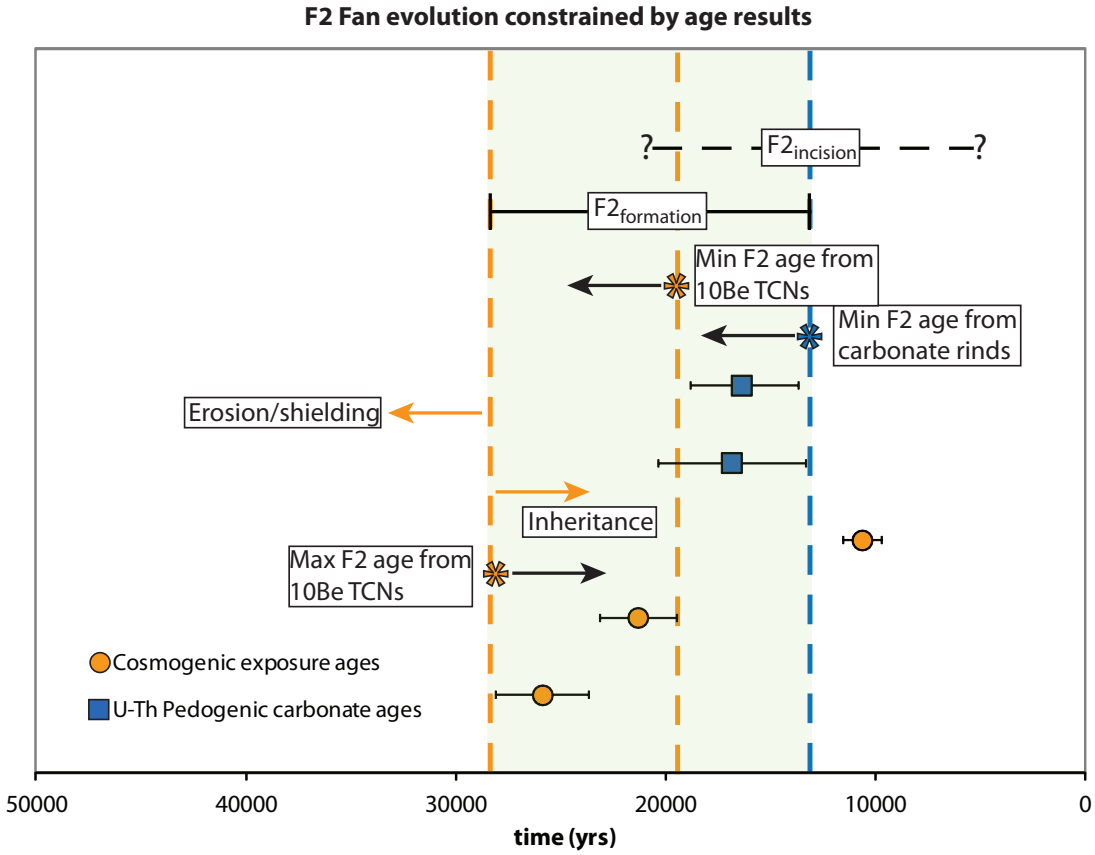


**Figure 3.13:** Time line of landscape abandonment and incision of alluvial surface F2. The orange bar indicates the oldest exposure age from cosmogenic dating, but if samples are affected by erosion, the actual age of abandonment is older than I have suggested. If the samples have an inherited signal, then the actual time of abandonment is younger than the boulder ages. The blue line indicates the minimum age of F2 abandonment from U-series dating. The dashed error bars for the incision the streams of F2 indicate the potential for lag time between the abandonment of the alluvial surface and the incision, and subsequent displacement, of the streams.

*and Putkonen*, 1994; *Matmon et al.*, 2005). Whilst the lack of correlation between the measured $^{10}$Be concentrations with boulder composition (Table A.2) implies that boulder surface erosion may be minimal, it is possible that some spallation or boulder surface erosion has occurred based on the large spread in data from the older surface.

Comparison of the cosmogenic and U-series dates for F2 shows that some post-depositional processes may have affected the boulder ages (Figure 3.13). Boulder sample MN09-OG4 (10.6 ± 1.2 kyr) is significantly younger than the age of stabil-

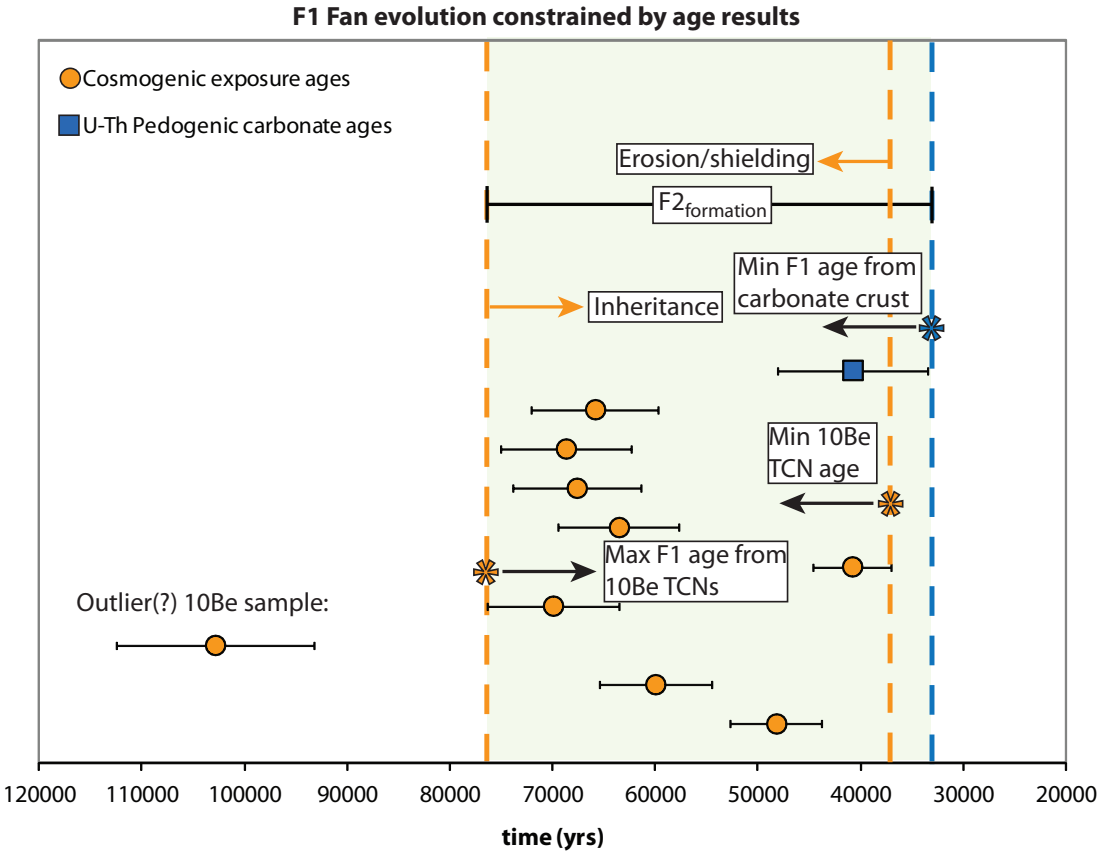


**Figure 3.14:** Time line of landscape abandonment of alluvial surface F1. The orange bar indicates the oldest exposure age from cosmogenic dating, but if samples are affected by erosion, the actual age is older than we have suggested. If the samples have an inherited signal, then the actual abandonment is younger than the minimum boulder ages. The blue line indicates the minimum age of F1 abandonment from U-series dating, which is close to the minimum age from TCN dating. The outlier boulder (sample B08-04) is beyond the 1 standard deviation of the mean of the boulder ages, but there is still the possibility that all of the other samples have had significant erosion, and B08-04 actually most closely represents the abandonment of the surface.

isation of the surface from the U-series dating (20.4 ± 2.3 kyr), implying that the exposure of boulder MN09-OG4 post-dates abandonment of the surface, presumably due to surface lowering. It follows that surface lowering may have affected other samples, both on F2 and F1. The range in $^{10}$Be concentrations from F1 also implies that the F1 surface has been subjected to some post-depositional processes, because in general, the effect of erosion becomes more pronounced on older surfaces (*Brown et al.*, 1998). Estimates for surface erosion rates from western Mongolia vary

from 1 m/100 kyr to as low as 2.5 m $Ma^{-1}$ (*Vassallo et al.*, 2007b; *Nissen et al.*, 2009b, respectively). *Vassallo et al.* (2011) suggests that even at these low erosion rates, boulders that are initially at different depths in the deposit can be exhumed at different rates based on the size of the boulders and the localised bar-and-swale morphology of the surface of the alluvium. Over time, the bar-and-swale topography of the fan surface is reduced, exposing boulders that were buried at the time of deposition, as well as causing smaller boulders to migrate from their original position as the surrounding surface is eroded away (Figure 3.15, reproduced from *Vassallo et al.*, 2011). This process is also observed on alluvial fans in southern California, in similar arid conditions, though on a very different lithology (granitic; *Matmon et al.*, 2006; *Behr et al.*, 2010).

Therefore the simplest interpretation of the data would be to use the oldest boulder dated from each of the deposits as an approximation for the maximum age of the deposits (102.9 ± 13.3 kyr and 25.9 ± 2.6 kyr for F1 and F2, respectively), with the stipulation that these ages may underestimate surface abandonment if all of the boulders have experienced some form of post-depositional erosion. This interpretation is particularly reasonable for F2, because the one sample that has anomalously low nuclide concentrations (MN09-OG4) is located on the crest of F2, close to the trace of the fault, where the alluvium may have been subjected to strong motion during a previous earthquake, leading to catastrophic erosion of the ridge (Figure 3.3). The two older boulders were collected further downslope, in the centre of the deposit and away from the two streams. Thus the maximum age of F2 seems well constrained as 25.9 ± 2.6 kyr.

However, the possibility of inherited $^{10}$Be nuclides accumulated prior to the deposition of the boulders must be considered as well. The effect of samples with inherited nuclides is likely to be stochastic (unless there is a particular store of similar clasts up stream), and may result in a small number of outliers in a TCN dataset that

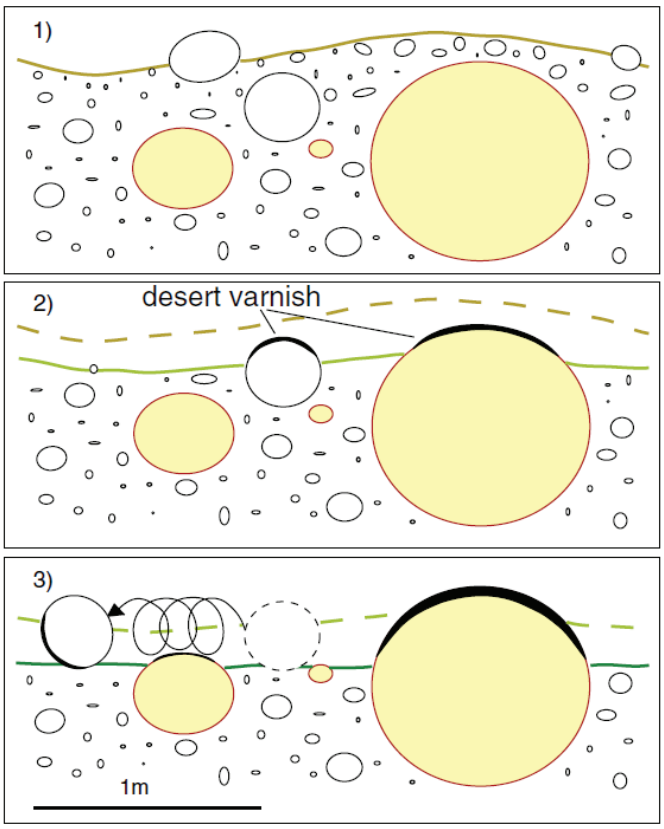


**Figure 3.15:** Diagram from *Vassallo et al.* (2011) that illustrates the evolution of surface morphology from an original bar-and-swale tread. The surface flattens over time and clasts of different sizes are progressively exhumed. The presence and patterns of desert varnish may help to determine what process has been active on any particular clast. The original depth and size of the clast relative to the surface morphology determines the preservation of the original position of the clast.

appear much older than the actual abandonment of the surface. In the Gobi-Altay of western Mongolia, *Vassallo et al.* (2011) found that whilst many boulder sample sites were affected by surface lowering, there were a small fraction of boulders with 100% greater levels of TCN concentrations than other samples from the same deposit. These outliers might be a result of the episodic nature of mass-wasting deposits in the arid Mongolian climate, which mix boulders with long prior residence time on hillslopes and high prior $^{10}$Be concentrations with boulders that have little pre-depositional exposure, resulting in a few randomly distributed samples with high levels of inheritance at the surface. The amount of inherited nuclides in a boulder

sample is not possible to quantify, as it is dependent on the length of time the sample was previously exposed in the catchment (*Vassallo et al.*, 2011).

At the Ölgiy site, sample B08-4 is suspect for having an inherited cosmogenic nuclide component for several reasons. The sample age lies well outside of one standard deviation of the mean of all boulder ages (Figure 3.12), and if B08-4 is excluded from the mean of all boulders, it is also outside of two standard deviations of the mean. If inheritance was not the cause of the anomalous $^{10}$Be concentrations in sample B08-4, then I would have to assume that surface lowering had a significant effect on all of the other boulders sampled (Figure 3.14). However it does not seem likely that all of the other samples have experienced late exposure, because I would expect the effect of surface lowering to be similar in small regions of the fan, and to have similar effects on boulders with the same composition and similar heights above the surface. Boulders in close proximity to B08-4 have significantly younger exposure ages, of 48.2 ±6.2 kyr and 60.0 ± 7.4 kyr, and is unlikely that post-depositional effects would affect a small area of the deposit in such a stochastic manner (see sample localities labeled on Figure 3.3). I therefore disregard sample B08-4 in my estimate of the abandonment of F1, and suggest that this sample might have been entrapped during the deposition of the alluvium after significant exposure within the catchment of F1. A similar approach to the variability in TCN concentrations within a catchment was taken by *van der Woerd et al.* (1998) and *Brown et al.* (2003). For the maximum abandonment of F1, I use the oldest boulder age within the remaining population of results (70.0 ± 8.7 kyr), with the assumption that there has been some surface lowering that has led to the spread in ages in the samples (Table 3.5).

### 3.3.6 Average Late Quaternary slip rate of the Ölgiy fault

I present a range of slip rates for the Ölgiy fault, calculated by dividing estimates of displacement by the geochronological results from both F1 and F2. My choices for

the boundaries of the slip rate estimates are summarised in Table 3.6, as described in each of the previous sections. All age constraints in this section are quoted at the $1\sigma$ level for comparison between U-series and cosmogenic results (see Tables 3.4 and 3.5).

### Slip rate from surface F1

The horizontal displacement of F1 is 41 +15/-20 m, calculated based on the vertical scarp across the fault (Section 3.3.2). The minimum age of F1 is taken from the lower bound of the initiation of crust formation in the OxCal model of sample MN09_OG07 (minimum used = 38.4 kyr, from the model output for boundary initiation of 38.4 kyr to 57.0 kyr, Table 3.4). For the maximum age of F1, I use the upper bound of 70 ± 8.7 kyr from the oldest of the $^{10}$Be cosmogenic boulder ages that lie within one standard deviation of the mean of all F1 boulder ages (Figure 3.12, Section 3.3.5). I divide the maximum age by the minimum displacement and the minimum age by the maximum displacement to reach a range of average slip rates over the past 38–70 kyr of 0.3 to 1.6 mm yr$^{-1}$.

### Slip rate from surface F2

F2 has a minimum displacement value of 12 ± 4 m, from the southern stream offset, and a maximum displacement value of 30 +8/-4 m from the horizontal displacement calculated based on the vertical scarp across the fault (Section 3.3.2). The timing of abandonment of F2 is established by the minimum constraint of the U-series dates and the maximum constraint from $^{10}$Be TCN boulder ages. The U-series age is 18.0 kyr (the minimum estimate from a range of 22.3–18.0 kyr) and the TCN age is 25.9 ± 2.6 kyr. Dividing the maximum and minimum age constraints by the minimum and maximum estimates of displacement, respectively, results in a slip rate range over the last 18–26 kyr of 0.3 to 2.1 mm/yr.

**Table 3.6:** Estimates of the Ölgiy slip rate

| Constraint | Minimum | based on | Maximum | based on |
|---|---|---|---|---|
| Age of F1 | 38.4 kyr | range of U-series boundary initiate (57.0–38.4 kyr) | 70.0 ± 8.7 kyr | oldest boulder age w/in 1 std. dev. of mean |
| Age of F2 | 18.0 kyr | range of U-series boundary initiate (22.3–18.0 kyr) | 25.9 ± 2.6 kyr | oldest boulder from F2 |
| Offset of F1 | 26 m | min. of scarp displacement (41 ± 15/20 m) | 61 m | maximum of scarp displacement |
| Offset of F2 | 12 ± 4 m | lesser stream displacement | 30 +8/-4 m | scarp method |
| slip rate of F1 | 0.3 mm $yr^{-1}$ | min offset/max boundary of max age | 1.6 mm $yr^{-1}$ | max offset/min age |
| slip rate of F2 | 0.3 mm $yr^{-1}$ | min bound of min offset/max bound of max age | 2.1 mm $yr^{-1}$ | max bound of displacement/min age |

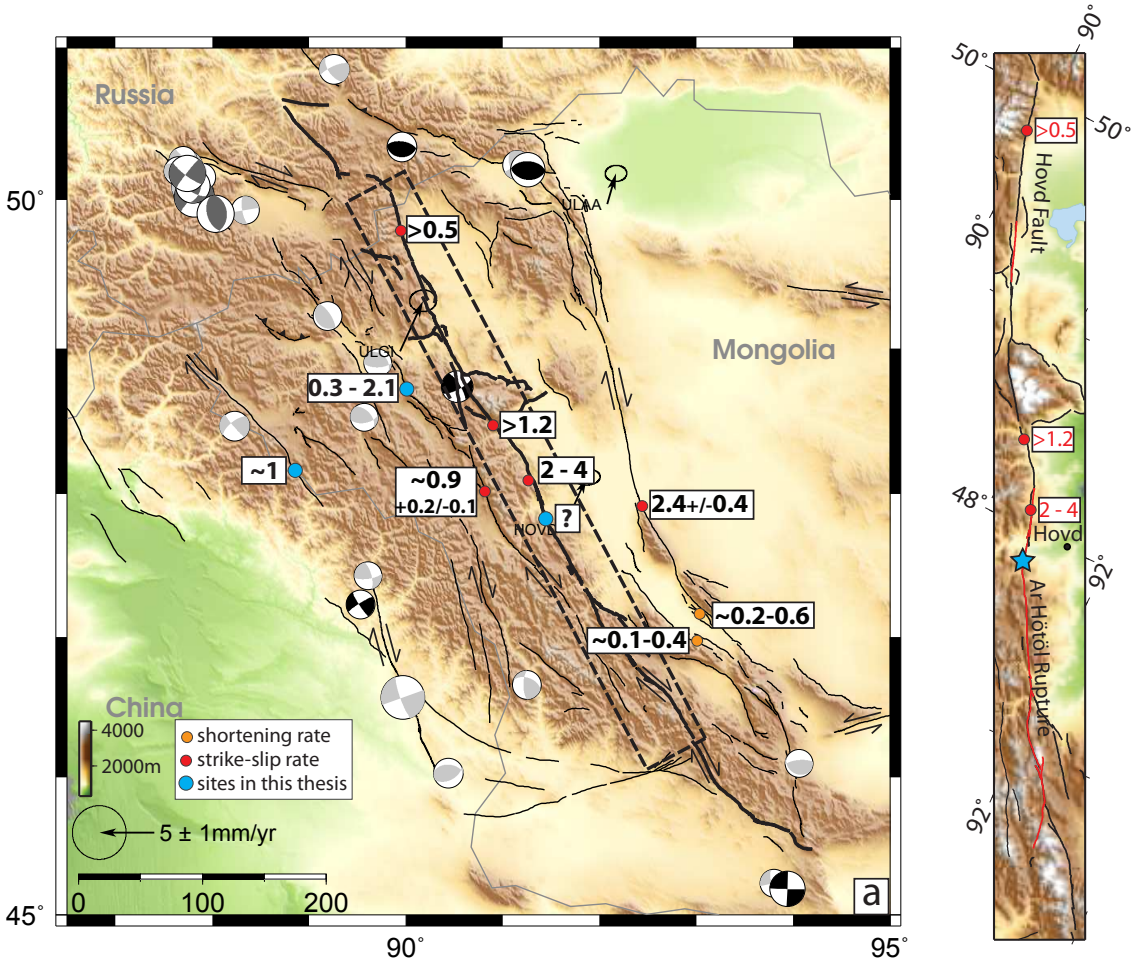


**Figure 3.16:** SRTM DEM (30 arc seconds/pixel) shaded relief imagery of the Altay and the Hovd fault. (a) GPS velocities are relative to stable Eurasia and show ∼ 7 mm/yr of northeast directed shortening across the Altay (*Calais et al.*, 2003), earthquake focal mechanisms in black are from models in *Sloan et al.* (2011), in dark grey are from *Nissen et al.* (2007), and light grey mechanisms are solutions modeled or catalogued by *Bayasgalan et al.* (2005) (other references within). Active faults are plotted in black, and strands of the Hovd fault zone are plotted as bold lines. Slip rate studies from the Altay are indicated, including the sites discussed in this chapter. Red dots indicate strike-slip rates, orange dots indicate shortening rates, blue dots indicate sites in this chapter. (b) The Hovd fault is plotted in bold black lines and known prehistoric earthquake ruptures are plotted in red. The Ar Hötöl slip rate site is indicated (blue star), as well as studies from *Vassallo* (2006) ($> 0.5$ and $> 1.2$ mm yr$^{-1}$) and *Baljinnyam et al.* (1993) (2–4 mm yr$^{-1}$).

## 3.4 Slip rate of the Hovd fault

The Hovd fault is one of the eastern-most faults of the Altay (Figure 3.16), and I describe the tectonic geomorphology of the fault zone in Chapter 2, and give a brief

overview of other slip rate studies conducted along the Hovd fault here. *Baljinnyam et al.* (1993) estimated a slip rate for the Hovd fault of 2 to 4 mm $yr^{-1}$, from the displacement of steep sides of a dry valley along the fault by about 75 m (with an uncertainty of 10 m). *Baljinnyam et al.* (1993) suggested that the valley was formed in the last glacial period, corresponding to the LGM (between 35–14 kyr in the Altay). However because of the lack of certainty in the origin of the valley, they suggest that the slip rate cannot be constrained by as well as 2–4 mm $yr^{-1}$. Instead, they suggested the broader constraint that slip is certainly more than 1 mm $yr^{-1}$ and less than 10 mm $yr^{-1}$, though even this estimate is not necessarily true without confirmation from quantitative dating techniques. Other estimates of the slip rate of the Hovd fault come from two separate localities where the fault has an oblique slip component (*Vassallo*, 2006). The northernmost estimate comes from the base of Ih Turgen Uul, where a right-laterally displaced river bank and vertical scarp in a river terrace were used to estimate horizontal and vertical slip rates, respectively. The alluvium is estimated to have been abandoned at 65 +35/-24 kyr from $^{10}$Be cosmogenic boulder dating. *Vassallo* (2006) suggest a maximum vertical slip rate of $\sim$0.2 mm $yr^{-1}$ and a minimum horizontal slip rate of $\sim$0.5 mm $yr^{-1}$. The second slip rate study in *Vassallo* (2006) is located on the southern corner of Tsambagaraav mountain, described in Section 2.3.2 of Chapter 2. A slip rate of $1.2 \pm 0.7$ mm $yr^{-1}$ was estimated on the basis of the youngest ages from $^{10}$Be cosmogenic dating of boulders. The results from two depth profiles were inconclusive.

In order to place a more robust estimate on the slip rate of the Hovd fault, an alluvial fan on the central Hovd fault was targeted for study. Samples were collected for $^{10}$Be boulder and depth profile dating, in order to use depth profile results to constrain the potential inheritance in surface boulders, as well as the erosion rate (e.g. *Nissen et al.*, 2009b). The fan was suspected to be of late Pleistocene age, possibly deposited during climatic pulses associated with MIS (Marine Isotope Stage) 2 or

4, consistent with the commonly observed association in western Mongolia between alluvial fan aggradation with the transitions from cold, dry glacial periods to warm, humid interglacials at the ends of the last two glacial stages (MIS 2 and 4, *Nissen et al.*, 2009b; *Frankel et al.*, 2010; *Vassallo et al.*, 2011). Unfortunately, the $^{10}$Be dating work is ambiguous, when results are considered from both boulders embedded in the alluvium and from a depth profile of nuclide concentrations. There are a variety of possible interpretations of the dating results of my study, but there is no unique scenario supported by the results. This study is included in this thesis to emphasize the problems that can arise in cosmogenic nuclide exposure dating and the necessity for using multiple Quaternary geochronometers to estimate fault slip rates, particularly in arid and mountainous environments.

### 3.4.1 Site description

A site was targeted for a slip rate investigation along a portion of the Hovd fault that was thought to accommodate pure strike-slip. The study is located on a portion of the fault that crosses a system of alluvial fans and river systems about 20 km southwest of Hovd city (Figure 3.17). The fault runs along a 1 km wide valley, through a fan system that slopes downwards along the valley to the Buyant River. The fault scarp is clear in the Quaternary alluvium of the fan and strike-slip motion at the site is supported by the lack of association of the scarp with any topography or restraining bend mountains. Also, the strike of the fault is consistent with pure strike-slip motion (340°–350°), and the scarp occurs along the dextral Ar Hötöl surface rupture (*Baljinnyam et al.*, 1993, described in Chapter 2). I refer to the site as the Ar Hötöl locality, after the surface rupture crossing the fan system.

The main alluvial fan at the site is labeled A1 on Figure 3.18. The fan has a gently undulating surface incised by several ephemeral streams, and the entire system is incised by a river channel and terrace system exiting from what appears

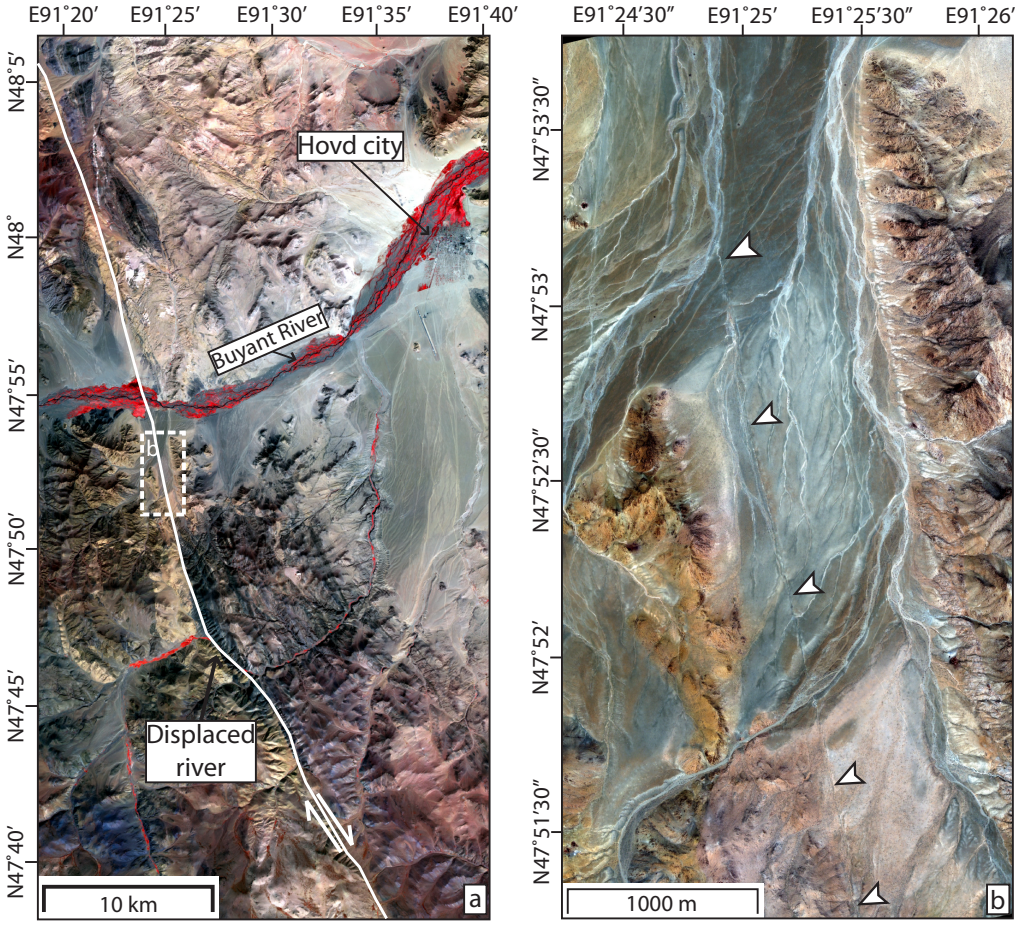


**Figure 3.17:** ASTER and Quickbird (0.6 m/pixel) imagery of the Ar Hötöl site. (a) The site is within 20 km of Hovd city, and is just south of the Buyant river. The Hovd fault is likely pure strike-slip though the area, and south of the site, there are prominent river displacements of more than 4 km. (b) Quickbird image of the system and rivers and alluvial fans crossed by the fault.

to be the main catchment that fed the fan (Figures 3.19 and 3.20). There are NE–SW oriented ridges in the surface of the fan, which have a relief of 2–5 m, which are possibly interfluves formed between the streams incised parallel to the ridge crests (indicated in Figures 3.19 and 3.20). Alternatively, the ridges may be original features of the fan, and the streams subsequently incised in the natural lows between ridges. Where the Hovd fault crosses the alluvial fan, two prominent streams are displaced by between 30–60 m (Figure 3.22, also indicated in Figures 3.19 and 3.20).

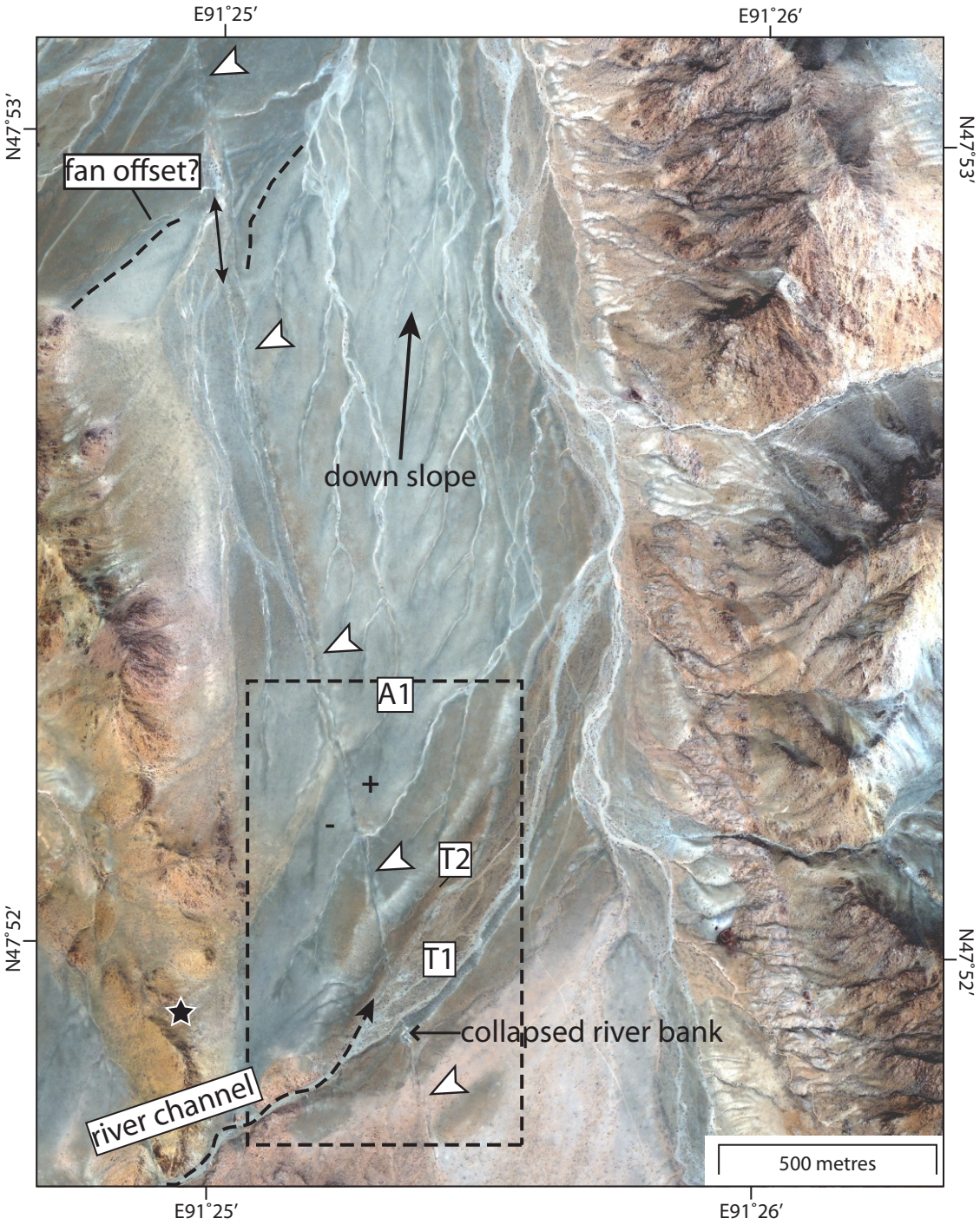


**Figure 3.18:** Quickbird image of the Ar Hötöl fan system, with the nomenclature for the main alluvial fan (A1) and river terraces (T1 and T2) indicated. The location of Figure 3.19 is outlined by dashed rectangle. The ephemeral main river that feeds the fan system is indicated by dashed curve. The fault scarp is indicated by white arrows. At the top of the image, the northern part of the fan seems to be displaced right-laterally by about 120 m. At the dating site, the east side of the fault is uplifted relative to the west. Black star in lower left shows location of photo in Figure 3.22a.

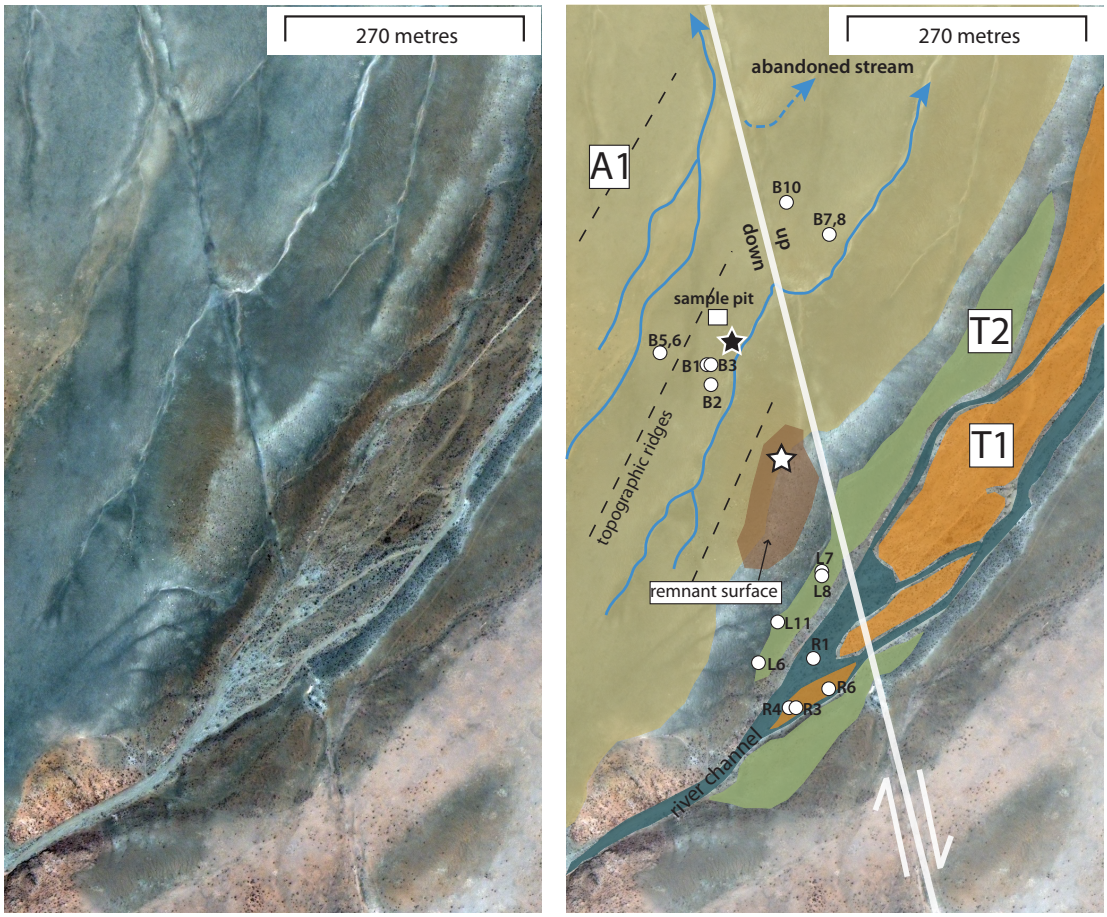


**Figure 3.19:** Quickbird image of the Ar Hötöl sampling site, right panel is the annotated version of the left. The extent of the main alluvial fan (A1) is coloured, as well as the river terrace T2, and terrace T1 which is slightly raised above the channels of the ephemeral river, but will not necessarily be preserved during high river activity. Channels cut into T1 are coloured in blue. A remnant of an older fan surface that was elevated relative to A1 is coloured in brown. Cosmogenic sample localities are indicated by white dots, and the sampling pit is indicated by the white box. White star shows the location of photos in Figure 3.21, black star shows the locality of the photo in Figure 3.22b. The material on the southwest side of the stream is a different colour from A1 in satellite imagery (see image covering a larger area in Figure 3.17), and is not assigned to any particular fan or terrace.

The northern most of the two streams has been beheaded and currently flows north along the fault scarp. The abandoned part of the north stream on the east side of the fault preserves an offset of at least 40–60 m, estimated from the extents of the stream banks on the DEM. The topography of the fan is displaced as well, and there

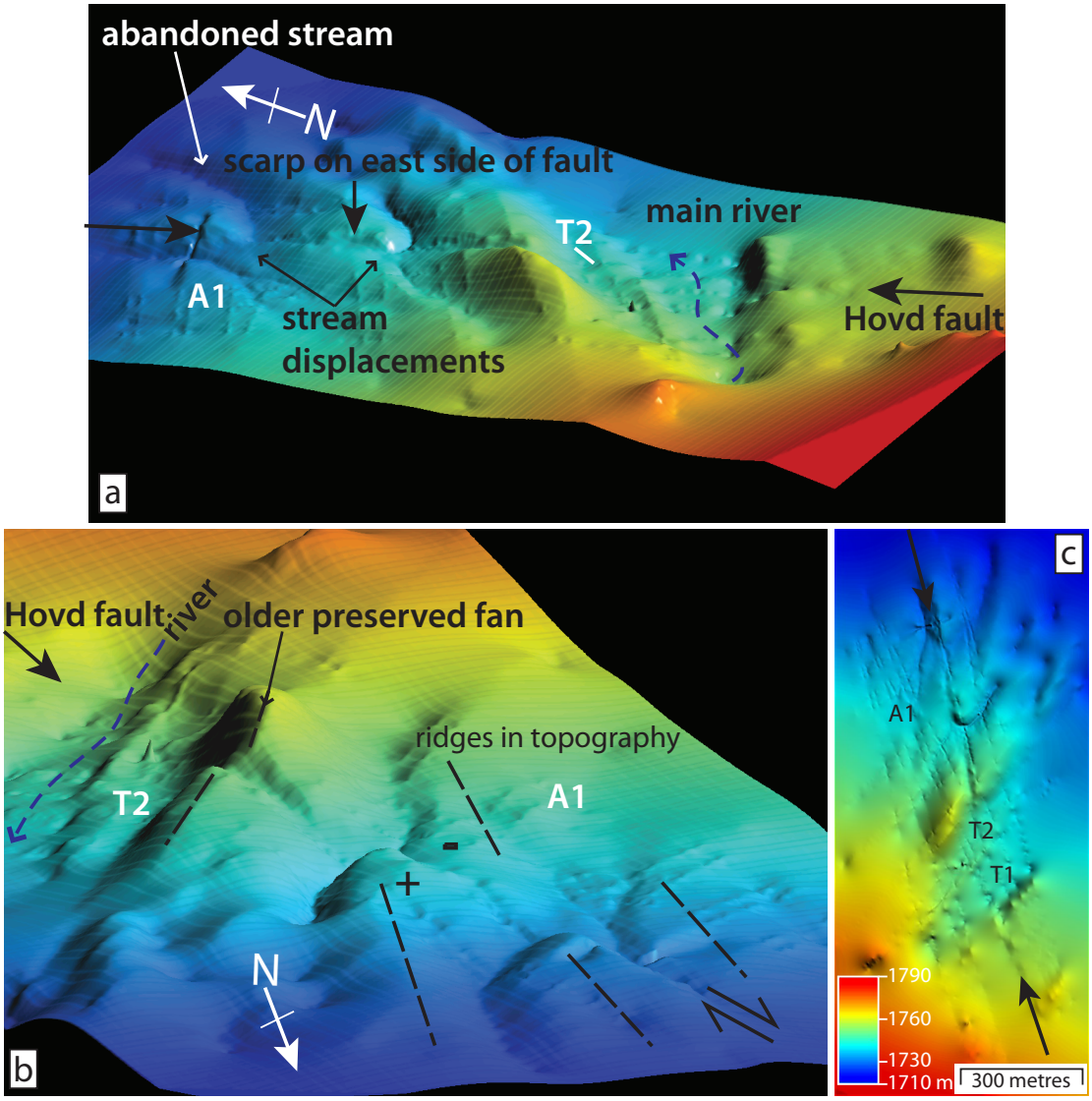


**Figure 3.20:** Views of the DEM made from a kinematic GPS survey of the Ar Hötöl site, with 1.5 times vertical exaggeration and illuminated from the southeast in (a) and (c), and from the northwest in (b). The main river is indicated as the low valley cut into the fan system, along with the abandoned T2 terrace on the side of the river. Where the fault crosses the surface of A1, the east side of the fault is uplifted relative to the west, producing a steep scarp in the alluvium, which is in shadow in (a). The two streams are displaced right-laterally along the fault. The northernmost stream has taken a new course along the fault, and left an abandoned gulley on the east side of the fault. The high in topography on A1 may be an abandoned alluvial fan, it also has a different colour in Quickbird imagery (Figure 3.19). Panel (c) shows a 2D view of the DEM, with scale.

is a vertical scarp in some places, particularly on the ridges of the fan, with uplifted material on the east side of the fault (Figure 3.20).

The uplift on the eastern side of the fault is unexpected, because based on the orientation of the fault relative to the slope of the surface, material on the western side of the fault should be uplifted relative to the east. Right-lateral slip through the site should displace material that was previously down-slope of the fan on the east side of the fault against material that is upslope, and at a higher elevation. Pure right-lateral slip should form a vertical scarp that is down on the northeast side, if the fan surface was originally flat and slip is purely dextral. In this sense, slip on the Hovd fault at this site should have the opposite effect on topography as slip on the Ölgiy fault as described in Section 3.3.2. The Ölgiy fault is oriented clockwise to the downslope direction of the alluvial surfaces, and dextral faulting creates a reverse in the slope, up on the downslope side of the fault (see diagram in Figure 3.23). At the Ar Hötöl site the fault is oriented anticlockwise to the down-slope direction of the fan surface, and right-lateral motion should create a scarp that appears to be downthrown on the down-slope side of the fault. However, the scarp formed along the fault at the Ar Hötöl site generally appears to uplift the east side of the fault. Thus the vertical scarp must be formed by some other process, possibly by a reverse component of slip on the Hovd fault through the site, uplifting the east side of the fault, though this may be a localised effect as the fault is generally pure strike-slip through the region.

Along the river valley indicated in Figure 3.19, a terrace T2 is preserved ∼2–3 m above the channels of the ephemeral river on both sides of the channel. Within the broad river channel, there is another surface, T1, that is not so much a terrace but a surface that stands approximately 50 cm above the active drainage. This surface is probably transient, and may be heavily eroded or even destroyed when the river is particularly active. The surface is covered in boulders and cobbles ($<$ 1 m across), some of which are loose on the top of the surface. On the north side of the channel, the riser between the river and T2 is displaced by ∼7–8 m, possibly as a result of

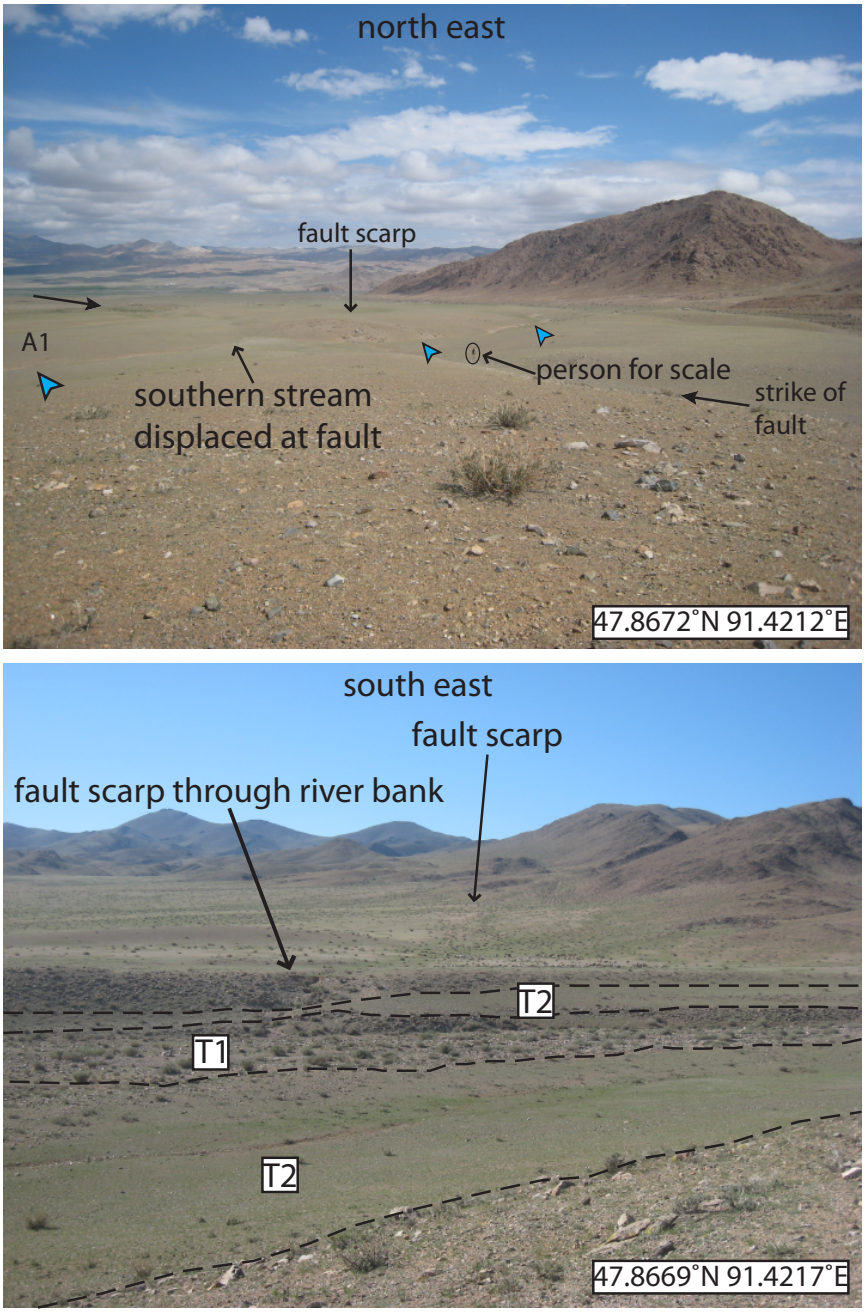


**Figure 3.21:** Photos of the Hovd fault through the Ar Hötöl site. Upper panel shows the south stream displacement on the main alluvial fan (A1). The fault is visible as a series of vertical scarps, uplifted on the eastern side of the fault. The southern stream is indicated by blue arrows. View is down the valley towards the Buyant River. The lower panel shows the main river and upper and lower terraces (T2 and T1) at the site, which are outlined by dashed lines. Damage to the river bank is visible along the fault, and the fault scarp continues in the distance.

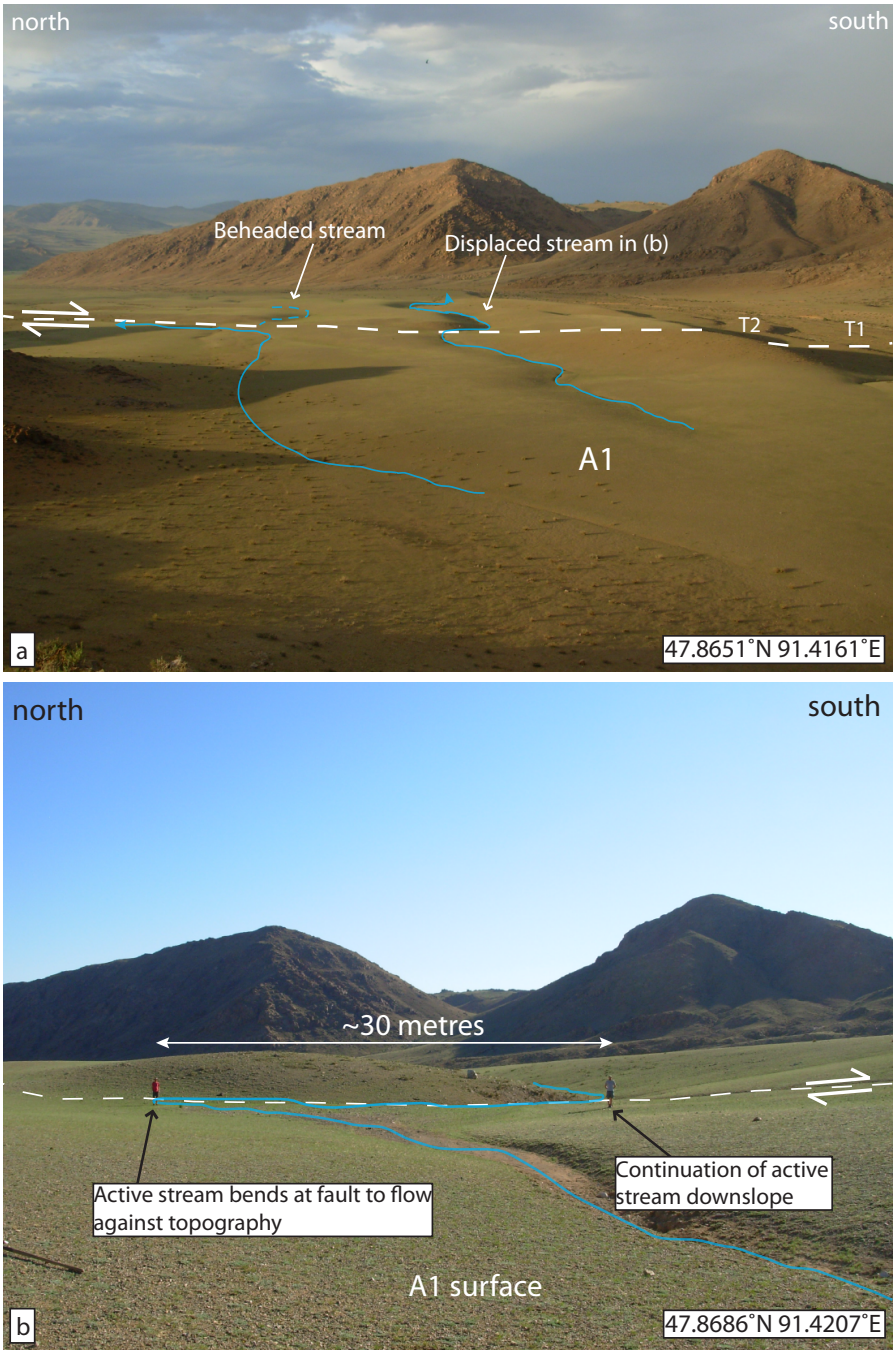


**Figure 3.22:** Photos of the displaced streams that flow across A1 at the Ar Hötöl site.

the Ar Hötöl earthquake. The same riser on the south side of the channel is poorly preserved and collapsed along the fault, and does not record fault displacement (Figure 3.18). The alluvium on the south side of the channel, above the riser from

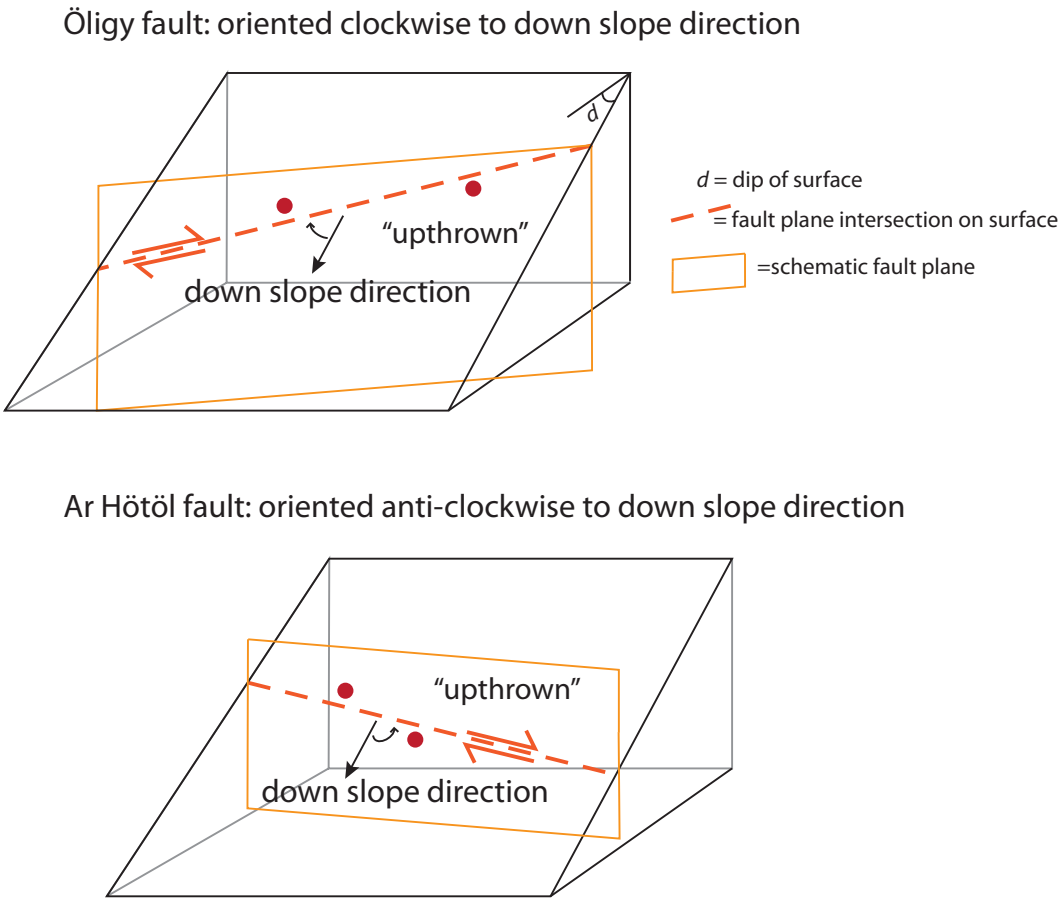


**Figure 3.23:** Diagram of slope displacement on the Ölgiy and Ar Hötöl faults. In the case of a clockwise rotated fault (relative to the down-slope direction of the surface), a vertical scarp uplifted on the lower part of the surface is formed. In the case of an anticlockwise rotated fault, a vertical scarp uplifted on the upper part of the surface is formed. The red dots move closer to one another as fault slip progresses, but stay at the same elevation.

T2, seems to be of a different fan generation from A1, because it has a much lighter colour in satellite imagery and is sourced from the granitic rock directly southwest of the surface (Figure 3.19). This surface was not dated. The riser from T2 to the unknown fan surface is disrupted along the fault, but it is difficult to estimate the riser displacement. On the north side of the channel, the riser between T2 and the A1 fan surface is displaced right-laterally but it is also not possible to place a precise estimate on the fault displacement because the riser is indistinct (Figure 3.19).

### 3.4.2 TCN results and depth profile modeling

#### $^{10}$Be concentration in surface boulders

Eight samples were measured (from six boulders) from the A1 surface, four samples were measured from T2, and four samples were measured from T1. I was careful to sample quartz rich granitic and meta-granitic boulders that were located away from any of the active channels on the surface, and only collected samples that had evidence for stabilisation such as desert varnish or that were 'cemented' into the surface. Most samples stood at least 30 cm above the surface, though a few from A1 were lower than is normally sampled due to the lack of suitable boulders available for sampling. The exception to these sampling criteria are samples from T1, because the surface is essentially the active river channel and loose boulders were collected in order to place constraints on the inherited nuclide component in the results from A1 and T2. Boulder samples were processed as outlined in Section 3.3.4, and the analytical results are shown in Table 3.7. Cosmogenic exposure ages were calculated in the CRONUS online calculator (*Balco et al.*, 2008), with the time-variant production rate of *Lal* (1991) and *Stone* (2000) scaled to the latitude and elevation of the Ar Hötöl site. Because the samples were collected from a wide valley with relatively low surrounding topography, I do not apply a topographic shielding correction. I assume minimal erosion of the surface, but this assumption cannot be confirmed by the $^{10}$Be depth profile results outlined below.

Boulders collected from the active river system of a sample site can reveal the inherited nuclide concentration that may be present in the surface boulders deposited within the system due to pre-depositional exposure, if transport mechanisms remain constant through time (e.g. *Brown et al.*, 1998; *Vassallo et al.*, 2011). If a consistent level of inheritance is found, then the average concentrations can be subtracted from the sample concentrations to deal with inheritance. The $^{10}$Be concentrations in samples from T1 are consistent, ranging between 4.8–6.8 x $10^5$ at $g^{-1}$, equivalent to




**Figure 3.24:** Upper panels show photos of the pit sampled for the depth profile of $^{10}$Be concentrations. Pebbles were taken at 25 cm intervals. The sample number is indicated in the photos just above the layer that was sampled. Numbers at the end of each sample indicate the depth in centimeters from the surface, e.g. AH08-DP30 was taken at 30 cm depth. Lower panel shows sample AH B5/6, which had saturated $^{10}$Be concentrations. Arrow on boulder points to north. Pit and sample locations are shown on Figure 3.19.

~23–33 kyr of exposure. This suggests that there may be a reasonably high level of inherited nuclides in samples collected from the stable portions of the Ar Hötöl site, but only if similar transport processes brought the samples to the system.

$^{10}$Be concentrations from T2 have a wider range, from 12–18 x $10^5$ at $g^{-1}$, corresponding to exposure ages of 60–90 kyr. Even with a presumed inherited $^{10}$Be component subtracted from the samples, precise timing for exposure of the terrace is difficult to constrain from the results. The number of samples measured was limited by funding, and there are too few samples to determine if any are obvious outliers. The scattered $^{10}$Be concentrations suggest that the terrace boulders have experienced a rather complicated exposure history, perhaps involving both inherited nuclide concentrations and episodes of exposure and reburial, prior to being exposed in the terrace surface observed at present.

The $^{10}$Be concentrations measured in samples from the alluvial fan are also suggestive of a complicated exposure history, even more so than the river terrace samples. $^{10}$Be concentrations from A1 range from 3.7 to 62 x $10^5$ at $g^{-1}$, corresponding to an order of magnitude difference in exposure duration between the individual samples, of 17 kyr to much greater than 300 kyr. The boulder with the highest $^{10}$Be concentration is in steady state equilibrium between production and radioactive decay, and it is not possible to calculate an exposure age for the sample (although one is listed in Table 3.7 to demonstrate the range in exposure histories between the samples). I discuss the possible scenarios that could lead to such a large spread in ages in conjunction with the results from the depth profile described below.

### $^{10}$Be depth profile results

Samples for measuring a depth profile of $^{10}$Be concentrations were collected from the A1 fan surface, at the locality shown on Figure 3.19. An approximately 2 m pit was dug into the surface at a site that was far from any channel margins or irregularities

**Table 3.7:** Ar Hötöl $^{10}$Be boulder exposure age calculations

| Sample | Latitude (° N) | Longitude (° E) | Elevation[a] (m) | Thickness[b] (cm) | Density[b] (g cm$^3$) | Production rate[c] (at g$^{-1}$ y$^{-1}$) | | $^{10}$Be conc.[d] ($10^5$ a g$^{-1}$ $SiO_2$) | Exposure age[e,f,g,h] (ky) |
|---|---|---|---|---|---|---|---|---|---|
| | | | | | | spallation | muons | | |
| *Ar Hötöl alluvial fan 1 (A1)* | | | | | | | | | |
| AH B1 | 47.8680 | 91.4201 | 1731 | 6 | 2.4 | 18.00 | 0.315 | 10.140 ± 0.358 | 50.6 ± 6.5 |
| AH B2 | 47.8679 | 91.4201 | 1734 | 6 | 2.4 | 18.04 | 0.315 | 12.960 ± 0.455 | 64.9 ± 8.4 |
| AH B3 | 47.8680 | 91.4201 | 1731 | 6 | 2.4 | 18.00 | 0.315 | 25.120 ± 0.812 | 127.2 ± 16.2 |
| AH B5 | 47.8684 | 91.4195 | 1729 | 4 | 2.5 | 18.22 | 0.316 | 61.170 ± 2.079 | 320.8 ± 43.7 |
| AH B6 | 47.8684 | 91.4915 | 1729 | 4 | 2.5 | 18.22 | 0.316 | 61.840 ± 2.104 | 324.5 ± 44.2 |
| AH B7 | 47.8696 | 91.4216 | 1721 | 4 | 2.5 | 18.11 | 0.315 | 3.648 ± 0.131 | 18.3 ± 2.3 |
| AH B8 | 47.8696 | 91.4216 | 1721 | 4 | 2.4 | 18.13 | 0.315 | 3.868 ± 0.130 | 19.4 ± 2.4 |
| AH B10 | 47.8697 | 91.4212 | 1721 | 5 | 2.3 | 18.03 | 0.315 | 3.786 ± 0.132 | 19.1 ± 2.4 |
| *River terrace 2 (T2)* | | | | | | | | | |
| AH L6 | 47.8651 | 91.4210 | 1742 | 5 | 2.6 | 18.23 | 0.316 | 18.180 ± 0.644 | 90.5 ± 11.8 |
| AH L7 | 47.8660 | 91.4219 | 1736 | 5 | 72.6 | 18.15 | 0.316 | 16.760 ± 0.585 | 83.7 ± 10.8 |
| AH L8 | 47.8660 | 91.4219 | 1738 | 5 | 2.6 | 18.18 | 0.316 | 15.460 ± 0.536 | 77.0 ± 9.9 |
| AH L11 | 47.8656 | 91.4213 | 1740 | 5 | 2.6 | 18.20 | 0.316 | 12.090 ± 0.423 | 60.0 ± 7.7 |
| *River terrace 1 (T1)* | | | | | | | | | |
| AH R1 | 47.8651 | 91.4216 | 1740 | 5 | 2.4 | 18.26 | 0.316 | 4.798 ± 0.152 | 23.8 ± 2.9 |
| AH R3 | 47.8646 | 91.4214 | 1742 | 5 | 2.5 | 18.26 | 0.316 | 5.705 ± 0.200 | 28.2 ± 3.6 |
| AH R4 | 47.8646 | 91.4213 | 1742 | 5 | 2.4 | 18.29 | 0.317 | 5.426 ± 0.178 | 26.8 ± 3.3 |
| AH R6 | 47.8648 | 91.4218 | 1740 | 5 | 2.6 | 18.20 | 0.316 | 6.848 ± 0.215 | 33.9 ± 4.1 |

[a] Typical hand held GPS vertical uncertainties are 10–15 m.
[b] Used to correct for attenuation of flux through rock, with an attenuation length of 160 g cm$^{-2}$ (*Balco et al.*, 2008).
[c] Time-variant local production rate based on *Lal* (1991) and *Stone* (2000).
[d] All uncertainties are reported to 1$\sigma$ level.
[e] No shielding factor was applied.
[f] No erosion rate correction was used, see Section 3.3.5.
[g] Ages were calculated using the CRONUS-Earth online calculator, v 2.2 (*Balco et al.*, 2008).
[h] Age uncertainties include internal and external errors.

in the fan surface, on a flat portion of the fan with no surficial evidence for animal burrows (local relief is <0.5 m). Pebbles were collected from ~25 cm intervals, with approximately 1 kg of material sampled from each layer (Figure 3.24). The pebbles sampled were at least ~2 cm or or greater in diameter, and the material was generally quartz-rich granite with some metasedimentary clasts, which were residing in a sandy matrix. The top 10–20 cm of the pit is a soil layer, with brown vegetation and root systems mixed with poorly stratified sediments that had lower clast concentrations than the rest of the pit. Below the soil layer the material is sandy with abundant clasts, concentrated in horizontal layers. At about 30–35 cm depth, there is a carbonate rich layer with several clasts coated in white friable carbonate. Most of the carbonate clasts are coated on the underside of the pebble while *in-situ*, indicative of stability, but a few pebbles were found with coatings on the tops of the pebbles as well. The stratigraphy below 40 cm is generally faint, but there are horizons approximately 5–20 cm thick with similar clast sizes, and a roughly undisturbed stratigraphy can be identified down the majority of the pit wall (Figure 3.24).

Pebbles from each sample interval were processed as outlined in Section 3.3.4, with chemical processing and analytical measurements performed at the NERC CIAF facility. Pebbles from each layer were crushed together, and included approximately 1 kg of material per sample. $^{10}$Be concentrations and 1$\sigma$ analytical uncertainties are listed in Table 3.8 for each sample interval, and the concentrations are plotted against depth in Figure 3.25a. The very top sample was taken from pebbles on the surface of the alluvial fan, and this sample has an anomalously lower $^{10}$Be concentration than the sample below it at 30 cm. The remaining $^{10}$Be concentrations show a clear exponential decrease with depth, suggesting that the stratigraphy of the fan has not been disturbed and the profile of concentrations is robust. The very high levels of $^{10}$Be concentration in the top portion of the profile suggest a long duration

**Table 3.8:** $^{10}$Be concentrations of depth profile samples from the Ar Hötöl fan (A1)

| Sample | Depth (cm)[a] | $^{10}$Be concentration ($10^5$ at $g^{-1}$) |
|---|---|---|
| AH08-DP00 | 0 | 30.63 ± 0.82 |
| AH08-DP30 | 30 | 33.36 ± 0.88 |
| AH08-DP50 | 50 | 29.19 ± 0.79 |
| AH08-DP75 | 75 | 23.21 ± 0.61 |
| AH08-DP100 | 100 | 19.69 ± 0.53 |
| AH08-DP125 | 125 | 17.45 ± 0.47 |
| AH08-DP150 | 150 | 14.34 ± 0.39 |
| AH08-DP175 | 175 | 14.18 ± 0.37 |

[a]Sample depths correspond to the top of the layer sampled, as measured down from the top of the pit. Each layer was between 2–5 cm thick.

of exposure, possibly even long enough to have reached steady-state equilibrium between production and radioactive decay. The surface sample (AH08-DP00) may have an anomalous concentration because of some disturbance at the surface, or mixing of more recently deposited clasts with those that have been exposed for the full duration of fan abandonment, and therefore the top sample is not included in the depth profile modeling below. Concentrations in the deepest samples from the Ar Hötöl depth profiles are suggestive of a significant contribution from geologically inherited nuclides, with concentrations on the order of 14 x $10^5$ at $g^{-1}$, equivalent to ∼70 kyr of exposure time. Sediments at 170 cm and greater depth should be mostly shielded from cosmogenic radiation and have low concentrations, particularly if the surface has experienced some lowering due to erosion.

To determine the exposure age of A1 and to try and place some constraint on the erosion rate, the chi-squared inversion described in Section 3.3.4 is used to minimise the difference between the expected exponential decay profile of $^{10}$Be concentration at depth and the measured concentrations of my samples (*Siame et al.*, 2004). The high $^{10}$Be concentrations of the depth profile suggest that the surface has been exposed for much longer than originally expected, based on comparison with other

Chi-squared inversion modeling was performed by Dr. A. Joshua West, using a home-built matlab script.

constraints on the timing of alluvial fan deposition in the Altay (Table 3.7, e.g. *Nissen et al.*, 2009b; *Frankel et al.*, 2010). The simplest best-fit solution to the $\chi^2$ inversion (discounting the top sample AH08-DP00) is a profile that is in steady state equilibrium, and has been exposed for a minimum of 300 kyr (green line in Figure 3.25b). This is a reasonable solution, as at least one of the boulder samples (AH B5/6) also reflects a saturated $^{10}$Be concentration. The best fit modeled profile has an inherited $^{10}$Be concentration of 8.0 x $10^5$ at $g^{-1}$ (or approximately 70 kyr), which is significantly more than the $^{10}$Be concentrations measured in boulders from the active river channel (T1, ages of ∼30 kyr). The T1 boulder samples likely experienced a somewhat different pre-depositional history from the pebbles collected at depth in the fan surface, and may have experienced a shorter duration of residence time (exposed) in the catchment. Because the profile is in equilibrium between $^{10}$Be production and radioactive decay, it is difficult to place constraints on the erosion rate of the surface. The best fit value for erosion of the profile is approximately 3.7 m $Ma^{-1}$, but this rate is very poorly constrained by the model— see Appendix A, Figure A.4 for a visualisation of the trade-offs between erosion rate, exposure duration, and inheritance. The effect of surface erosion is to increase the total shielding experienced by the samples, reducing the amount of $^{10}$Be in the samples from what would be expected if there were zero erosion. The loss of material in the time between surface abandonment and sampling causes the exponential shape of the $^{10}$Be concentration profile to become less pronounced, but it is difficult to establish the rate of erosion based on the shape of a profile in equilibrium. The lowest two samples are relatively poorly fit to the modeled profile, suggesting some disturbance at depths greater than 1.5 m, though there was no evidence for a different layer in the stratigraphy of the pit.

A more complicated scenario may explain the existence of the younger boulders on the fan surface, as well as the younger material collected from the surface for

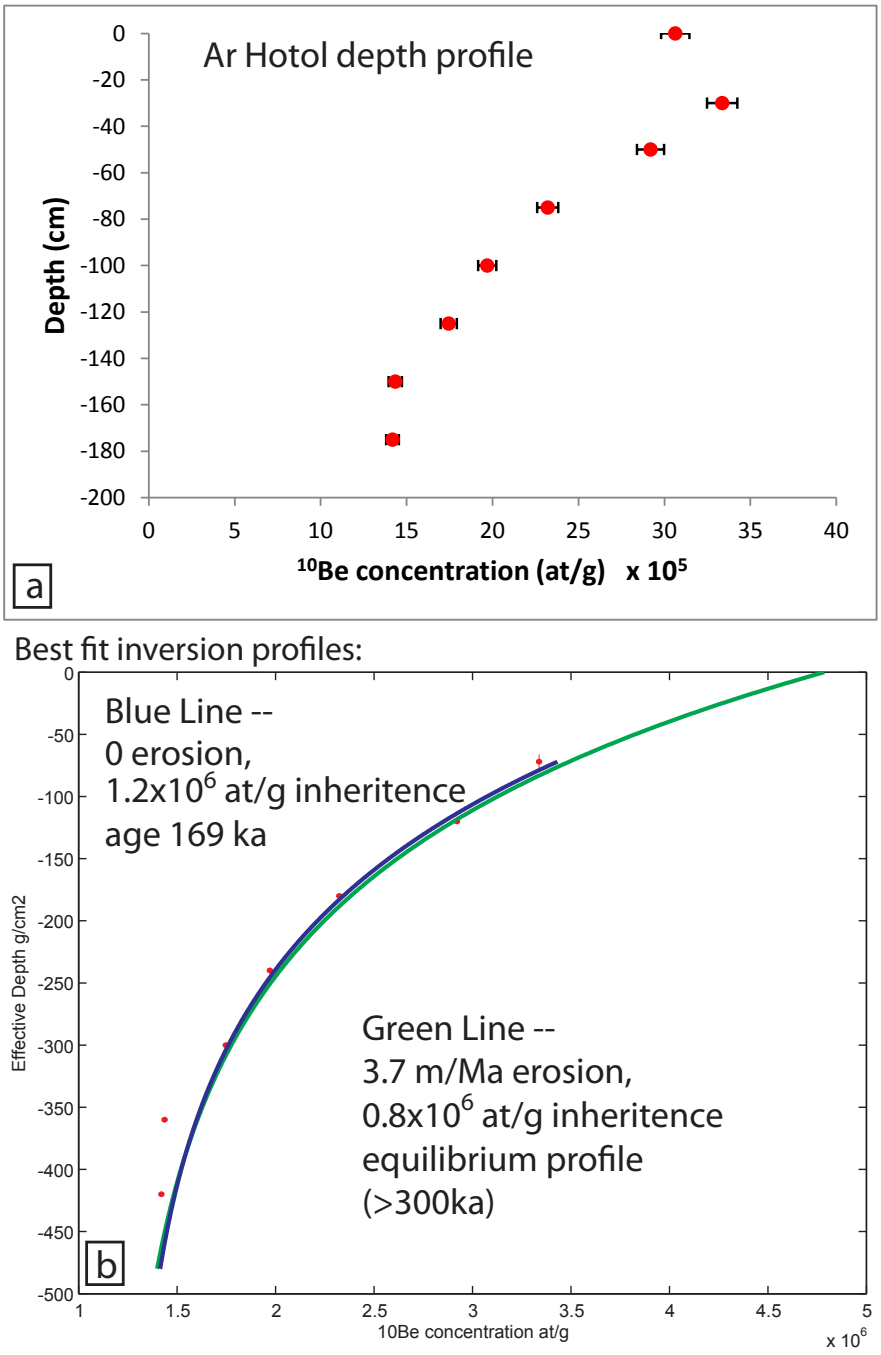


**Figure 3.25:** The upper panel shows a vertical profile of $^{10}$Be concentrations measured from many clasts at each depth, indicated by the red dots and shown with $1\sigma$ error bars. The lower panel shows the best fit models for $^{10}$Be concentrations, with profiles for no erosion (blue line) and with erosion (green line). In both profiles, the upper most sample (AH08-DP00) is not included, due to the anomalously low $^{10}$Be concentration. Incorporating erosion results in an equilibrium profile, with no constraint on surface abandonment.

the depth profile. The fan surface may have been abandoned some time ago, but subsequently experienced some resurfacing and deposition of fresh material on the surface, possibly related to the last one or two deglaciations in the region (at MIS 2 and 4). The more recent events would have been at a much smaller scale than the initial deposition of the fan, as there are high $^{10}$Be concentrations at depths of 30 cm (sample AH08-DP30). These events may have deposited effectively 'young' boulders and sediments to the top of the surface, whilst leaving large 'old' boulders exposed. The scenario can be modeled by keeping the surface height constant through time (i.e. a constant sample locality depth), with effectively no erosion. If the sample that was collected at 30 cm depth is assumed to be near the surface after abandonment of the fan (but before 'resurfacing'), the model results in a best-fit exposure age of approximately 170 kyr, with inherited nuclide concentrations of 12 x $10^5$ at $g^{-1}$ (blue line, Figure 3.25b). This scenario involves a rather complicated exposure history, and while it is a bit more reasonable given the slip-rate that was expected on this fault, based on the rates between 1.2–4 mm $yr^{-1}$ determined by *Vassallo* (2006) and *Baljinnyam et al.* (1993) and stream displacements of less than 60 m, it is not possible to discern between the complicated scenario described here and the potential for a much longer exposure duration, with an equilibrium profile of $^{10}$Be concentrations.

### 3.4.3 Exposure history of the Ar Hötöl site

My initial interpretation of the $^{10}$Be concentrations in the boulder samples was that the boulders with anomalously high concentrations had high levels of inheritance, and the abandonment of the alluvial fan was closer to the exposure ages from the boulders with lower concentrations, equivalent to exposure durations of between 20 to 65 kyr, made even younger if an inherited nuclide component (equivalent to 23–33 kyr) was subtracted from the age estimates. This assumption was made because the best prior constraint on the slip rate of the Hovd fault is $\sim 1.2 \pm 0.7$ mm $yr^{-1}$

(*Vassallo*, 2006), and thus the younger boulders would constrain a similar rate of slip given the stream displacements of 30–60 m. However, the depth profile of nuclide concentrations confirms that the fan has had a much longer duration of exposure than suggested from the majority of the boulder samples. If the age of the site could be well constrained by the depth profile modeling, to either $>$ 300 kyr or approximately 170 kyr (which is poorly constrained), the 30–60 m displacement of the streams is suggestive of a very low slip rate of at most 0.4 mm yr$^{-1}$ by taking the maximum displacement and minimum age, or significantly lower if the depth profile is in equilibrium. Given the cumulative displacement, other Quaternary slip rate estimates, and the recent earthquake history, it seems highly unlikely that the Hovd fault has a slip rate much less than 0.5–1 mm yr$^{-1}$.

There are a few scenarios that could explain the low, and poorly constrained, Quaternary slip rate estimate from the Ar Hötöl site. Both the depth profile and the boulder ages place constraints on the exposure of the alluvial fan surface, but this age constraint is incorporated into the slip rate calculation based on the displacement of shallow streams incised into the surface of the fan. If the incision of the streams significantly post-dates abandonment of the fan, the averaged fault slip rate may be under-estimated considerably. Since incision, the streams should be reliable recorders of displacement, because the vertical scarp along the fault preserves the displaced path. If the slip rate averaged since fan abandonment at the Ar Hötöl site is indeed slower than expected, perhaps the faulting at the surface is not representative of the main fault zone. At the site, the fault scarp cuts through the fan surface and the river terraces and terrace risers, but it is possible that deformation was taken up along other surface faults in the region for some portion of the 170 to >300 kyr existence of the fan surface. There is little evidence for older, surrounding faults along strike of the main Hovd fault zone, but if the scarps have not been active within the late Pleistocene, it is possible that they have been substantially degraded. In any case,

the results and geomorphic interpretations from the Ar Hötöl site are not likely to be representative of the true Quaternary slip rate of the Hovd fault.

## 3.5 Discussion

### 3.5.1 Reliability of slip rate estimates

Both the Ölgiy and Ar Hötöl slip rate studies reveal that the application of multiple Quaternary dating techniques can place a more reliable constraint on the timing of abandonment of fault displaced landforms. At the Ölgiy site, complementary $^{10}$Be and U-series techniques place independent maximum and minimum estimates on surface abandonment, which adds a high degree of confidence to the slip rate estimate of 0.3–2.1 mm yr$^{-1}$ for the fault. The slip rates estimated from the two different surfaces, F1 and F2, are in agreement, also suggesting that the slip rate is reliable. The horizontal slip rate of 0.9 +0.2/-0.1 mm yr$^{-1}$ from *Frankel et al.* (2010) falls within my range of slip rates from the Ölgiy site, and while it is possible that I have been too conservative in providing such a large range in rates, I have taken all possible interpretations of the geomorphology and geochronology into account.

The Ar Hötöl study demonstrates the problems that can occur when using Quaternary dating techniques. The boulder and depth profile $^{10}$Be results revealed a more complicated exposure history than was originally expected. The depth profile results confirm that $^{10}$Be boulder dating alone may be unreliable if pre- and post-depositional processes have affected the samples, which is the case elsewhere in the Altay (*Nissen*, 2008; *Nissen et al.*, 2009b; *Vassallo et al.*, 2011). $^{10}$Be measurements are expensive, and therefore the number of samples that can be collected is often limited, but careful site and sample selection can sometimes alleviate problems associated with complex depositional histories. In some cases, however, it may be impossible to predict what combination of sample and site geomorphology will pro-

vide reliable results. Unfortunately, I do not have much confidence in the rough estimate of slip from the Ar Hötöl fan surface, in part because it is substantially slower than the rate estimated by *Vassallo* (2006), and more work is necessary to reliably determine the slip rate of the Hovd fault at this and other sites. An averaged Quaternary slip rate significantly lower than 1 mm $yr^{-1}$ on one of the eastern-most faults in the Altay would have important tectonic implications, suggesting that the faulting pattern across the Altay has migrated in a previously unanticipated manner.

### 3.5.2 U-series dating

Complimentary results from U-series and $^{10}$Be exposure dating demonstrate the potential for U-series dating to be used more frequently, particularly when working in regions where other techniques are problematic. In the Ölgiy study, the timing of stabilisation of the fan from the U-series dates was able to confirm that at least some surface lowering had affected the $^{10}$Be concentrations in boulder samples, making interpretation of the spread of boulder ages possible. More work can be done to improve the U-series method, especially towards dealing with detrital contamination of the carbonate and comparing U-series ages for stabilisation with other chronological methods for establishing the abandonment of alluvium. Because the method provides a minimum constraint on surface abandonment, U-series alone can only provide maximum slip rates. While the upper bounds on fault slip are important to constrain, particularly when estimating earthquake hazard, the method must be applied with an independent technique in order to constrain minimum rates of fault slip. Another useful result of U-series dating is an insight into the climatic history of a region. For example, results from all of the Ölgiy samples suggest progressive carbonate growth until the present day, implying that climate conditions have been favorable for carbonate pedogenesis since at least ∼40 kyr.

### 3.5.3 Predicted slip rate of the Hoton Nuur fault

I do not describe the details of the Dayan Nuur slip rate site mentioned in Chapter 2, because samples for TCN dating were collected in the final field season of my DPhil (2010), and have not yet been measured at the CIAF. However, I can provide a very rough estimate of the slip rate of the Dayan Nuur fault, based on the presumed age of a terminal moraine suspected to have formed during the Last Glacial Maximum (LGM) in Mongolia. The LGM is suggested to have reached peak glaciation between 30–35 kyr, with terminal moraines reaching about 2000 m at the Turgen-Harhirra massif on the Har-Us-Nuur fault (*Lehmkuhl*, 1998). At the Dayan Nuur site a terminal moraine surface is displaced along the fault, and the edge of the moraine can be reconstructed by ∼30 m of slip using a kinematic DEM (Figure 3.26). The displacement combined with the presumed age of approximately 30 kyr is suggestive of a slip rate on the order of 1 mm $yr^{-1}$ for the Dayan Nuur fault. It is possible that the displaced terminal moraine is from an older glacial advance, but the $^{10}$Be boulder exposure ages will place a better constraint on the abandonment of the moraine.

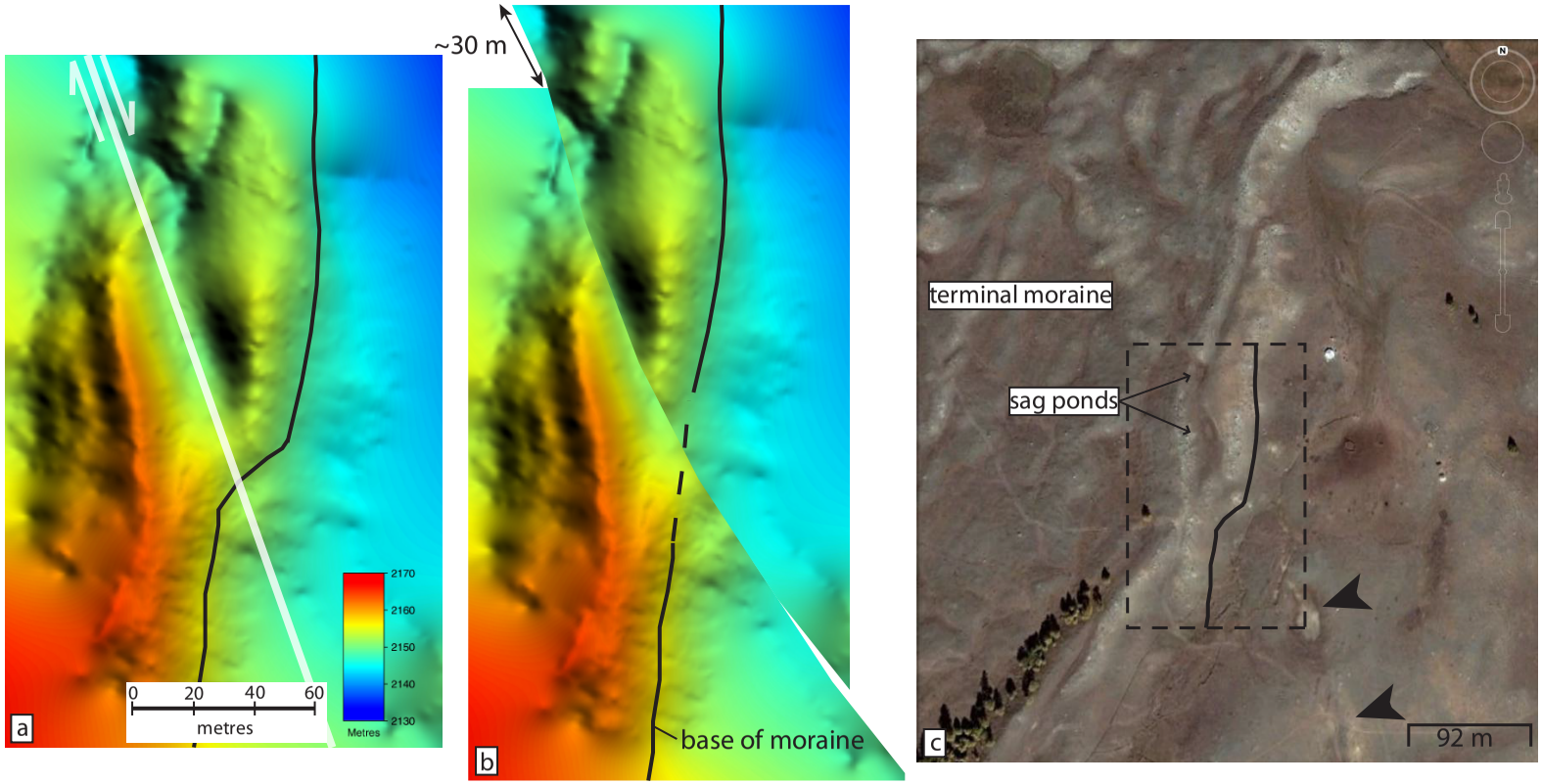


**Figure 3.26:** Overview figure of the Hoton Nuur slip rate site. (a) and (b) display a DEM produced from a kinematic GPS survey. (a) shows the right-lateral Hoton Nuur fault (white line) where it intersects the riser of a moraine edge (black line). This same DEM is reconstructed in (b) to account for right lateral motion of the fault and some closure of what might be a sag pond formed as a result of strike-slip faulting. The edge of the moraine reconstructed with 30 m of fault slip. (c) is a Quickbird image, from Google Earth, of a larger portion of the moraine edge, with the region of the DEM indicated as well as the riser edge. A series of sag ponds and ground disruptions caused by the fault are indicated with arrows, and sag ponds are visible even in the complicated surface of the terminal moraine.

### 3.5.4 Tectonic implications of the Altay fault slip rates

In order to understand the tectonics of faulting across a region, Quaternary fault slip rates must be robust and based on reliable Quaternary dating work. More work is necessary to fully understand the deformation along the Altay faults, but I can begin to make some modifications to what was previously suggested for the kinematics of the Altay strike-slip faults. Slip rates determined from the Ölgiy fault, which is essentially in the center of the mountain range, are indistinguishable from rates estimated for the easternmost faults of the Altay (Figure 3.27). Therefore even if topography and active faulting has expanded outwards through time, strain accumulation has not migrated away from the centre of the range. On the Hoton Nuur fault, one of the western-most faults of the Altay, the displacement of a moraine that is likely of at least mid to late Pleistocene age confirms that the fault has been active at least in the last few 10 to 100 thousand years. Whether the Hoton Nuur fault is moving more slowly than faults on the eastern and western edges (and now centre) of the Altay has yet to be determined, and the implications of the Hoton Nuur site will be dependent on the geochronological results.

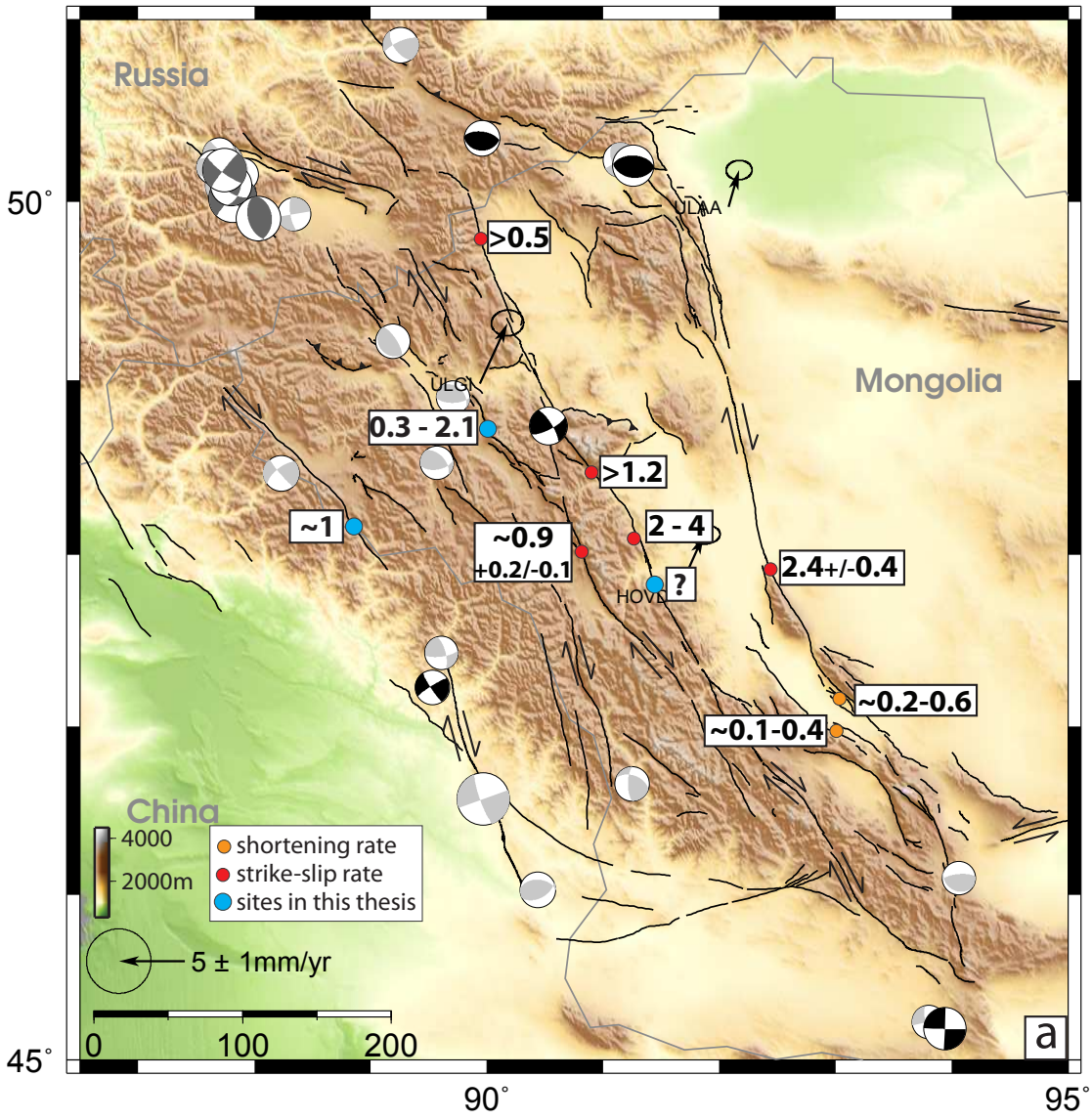


**Figure 3.27:** SRTM shaded relief image of the Altay (30 arc seconds/pixel). GPS velocities are relative to stable Eurasia and show $\sim 7$ mm yr$^{-1}$ of northeast directed shortening across the Altay (*Calais et al.*, 2003), earthquake focal mechanisms in black are from *Sloan et al.* (2011), in dark grey are from *Nissen et al.* (2007), and light grey mechanisms are solutions modeled or catalogued by *Bayasgalan et al.* (2005, other references within). Active faults are plotted in black. Slip rate studies from the Altay are indicated, including the sites discussed in this chapter. Quaternary slip rates are relatively consistent across the known Altay fault zones. Red dots indicate strike-slip rates, orange dots indicate shortening rates, blue dots indicate sites in this chapter (which are strike-slip).

# Chapter 4

# Vertical axis rotations of the eastern Altay

## 4.1 Introduction

A tenet of the style of deformation of the Altay is that the region rotates about a vertical axis (or axes) in order to accommodate NNE–SSW directed shortening along right-lateral strike-slip faults that strike NNW–SSE (*Baljinnyam et al.*, 1993; *Bayasgalan et al.*, 2005). Regional anticlockwise rotation is evident with the comparison between well-defined earthquake slip vectors and the direction of GPS velocities across the mountains: slip vector azimuths are oblique to the GPS directions and parallel to the NNW-striking active faults (*Bayasgalan et al.*, 2005, GPS velocities are plotted in Figure 4.1). While vertical axis rotation of the region is clearly required from the geodetic and seismic data, very little observation has been made on the longer term geological record of rotation in the region. Evidence of tectonic rotation on a geological time scale, including the amount and time-averaged rates of rotation, can be found by comparing measured palaeomagnetic declinations to the expected direction of the palaeomagnetic field. Yet there is only one existing study of Ceno-

zoic palaeomagnetic directions in the Altay, conducted by *Thomas et al.* (2002) on samples collected from the Siberian Altay. In the Chuya depression, they estimated palaeomagnetic anticlockwise rotations of 39 ± 8° relative to stable Eurasia. They sampled Oligocene to Pleistocene clays and sandstones, and found dual-polarity and stable chemical remanent magnetisations, carried by magnetite, which are deviated with respect to the reference pole. They suggested that the rotation arises from left-lateral shear along the faults surrounding the Chuya Basin, but these faults are in fact probably dextral strike-slip faults, as evidenced by the right-lateral 2003 $M_w$ 7.2 Chuya earthquake.

In order to better quantify rotation in the Altay and investigate the continuity of rotation across the region, Cretaceous to Pliocene sediments were sampled from the Dzereg Basin for palaeomagnetic investigation. The Dzereg Basin is formed in an overall transtensional bend in the Har-Us-Nuur fault, and is surrounded by several restraining bend mountain ranges formed along smaller steps in the same fault system (Figure 4.1). The topography surrounding the Dzereg Basin is suggested to be relatively young, formed only within the last 3–8 Ma on the basis of low-temperature thermochronology studies (*Jolivet et al.*, 2007). There are several motivations for selecting the Dzereg Basin as a palaeomagnetic study locality. Appropriate material for palaeomagnetic study is limited in the Altay, and the Dzereg Basin is the only known locality to preserve uplifted Miocene and younger-aged sediments in the Mongolian part of the Altay. Volcanic rocks are also an appropriate target for palaeomagnetic study, but there are no known Cenozoic volcanics in the Altay. Good age constraints are also required to interpret palaeomagnetic directions, and in the Dzereg Basin stratigraphic ages were previously determined by several authors (*Shuvalov*, 1968, 1969; *Khosbayar*, 1973; *Devyatkin et al.*, 1975; *Sjostrom et al.*, 2001; *Howard et al.*, 2003). Whilst local basin-scale rotations can often overprint the regional rotations that are the focus of this study, the structural evolution of Dzereg is well known based

on the excellent exposure of active faults, folds, and uplifted stratigraphic units, and can therefore be corrected for in palaeomagnetic data by restoring sample directions to their tilt-corrected orientations. The degree of Cenozoic rotation along the Hovd fault in the Dzereg Basin can also be used to test the age of initiation of faulting and mountain building, given assumptions about how these rates relate to rotation. For example, if the mountains are very young as suggested by low-temperature thermochronology, relatively small amounts of rotation may be expected for the Dzereg Basin in only 3–8 Ma of faulting. In this chapter, I present the palaeomagnetic results and discuss the resulting rotations, or lack thereof, from the stable Eurasia reference pole. The negligible rotations found in Dzereg are then discussed further in relation to the evolution of deformation and total rotation in the Altay in Chapter 6.

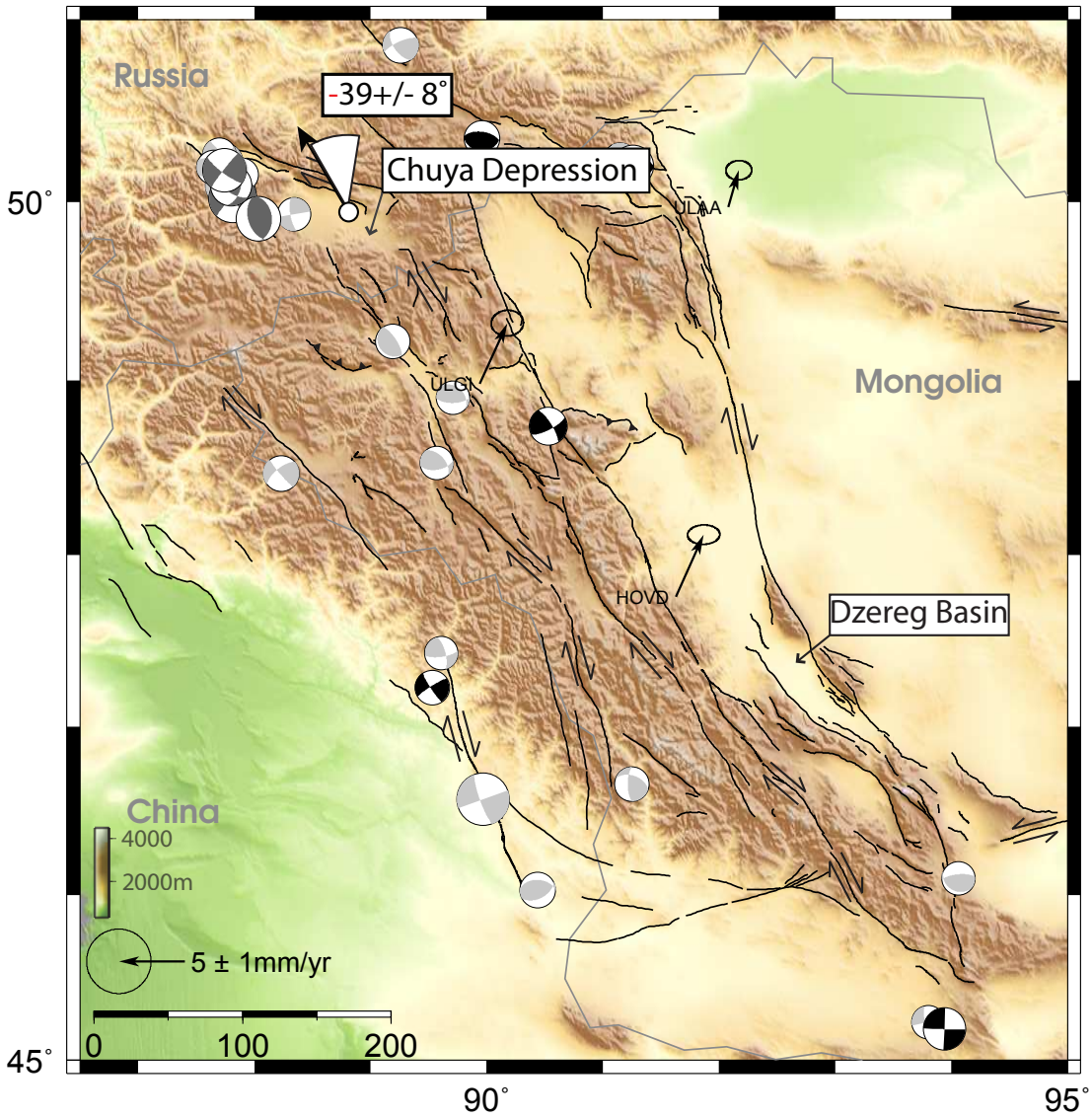


**Figure 4.1:** SRTM shaded relief image of the Altay (30 arc seconds/pixel). Vertical axis rotation estimate in the Chuya Basin is from *Thomas et al.* (2002). This chapter focuses on results from the Dzereg Basin on the eastern margin of the Altay. Displayed GPS velocities are relative to stable Eurasia and show $\sim 7$ mm yr$^{-1}$ of northeast-directed shortening across the Altay (*Calais et al.*, 2003). Earthquake focal mechanisms in black are from *Sloan et al.* (2011), in dark grey are from *Nissen et al.* (2007), and light grey mechanisms are solutions modeled or catalogued by *Bayasgalan et al.* (2005, other references within). Active faults are plotted in black (from Chapter 2). Slip vectors from *Bayasgalan et al.* (2005) are not plotted but are generally parallel to the Altay faults.

## 4.2 Stratigraphy of the Dzereg Basin

The Dzereg Basin lies between several transpressional massifs along the Har-Us-Nuur fault (Figure 4.2). The basin and surrounding mountains are the site of several key studies in the Altay, including slip rate studies summarised in Chapter 2 (*Nissen et al.*, 2009a,b); and investigations of the Mesozoic and Cenozoic stratigraphy and structure of the basin and active faults (*Cunningham et al.*, 1996; *Sjostrom et al.*, 2001; *Howard et al.*, 2003; *Cunningham*, 2007). Continuous outcrops of Mesozoic and Cenozoic strata are exposed in the range fronts of the Jargalant, Bumbat, and Baatar Hyarhan mountains, uplifted by active thrust faults that have propagated into the foreland. Oriented palaeomagnetic cores were collected from 16 sites in 2009, in three different regions of the basin (Figure 4.2). The three stratigraphic sections sampled are uplifted along kinematically different strands of the faults surrounding Dzereg Basin, and as a result, have distinguishable tectonic orientations. Sampling from the same units over a variety of structural orientations adds confidence to the palaeomagnetic results, not only by producing duplicate samples of the same unit in different areas, but also because the sampling strategy helps to determine whether local, fault-caused rotations have affected the samples. If local rotations have occurred, corrected sample directions will not necessarily agree across the different sampling localities. The three sampling localities cover the length and width of the basin, and were specifically chosen because each locality has a well-constrained Oligocene and younger stratigraphy. I briefly summarise the stratigraphy of the sampled sections here.

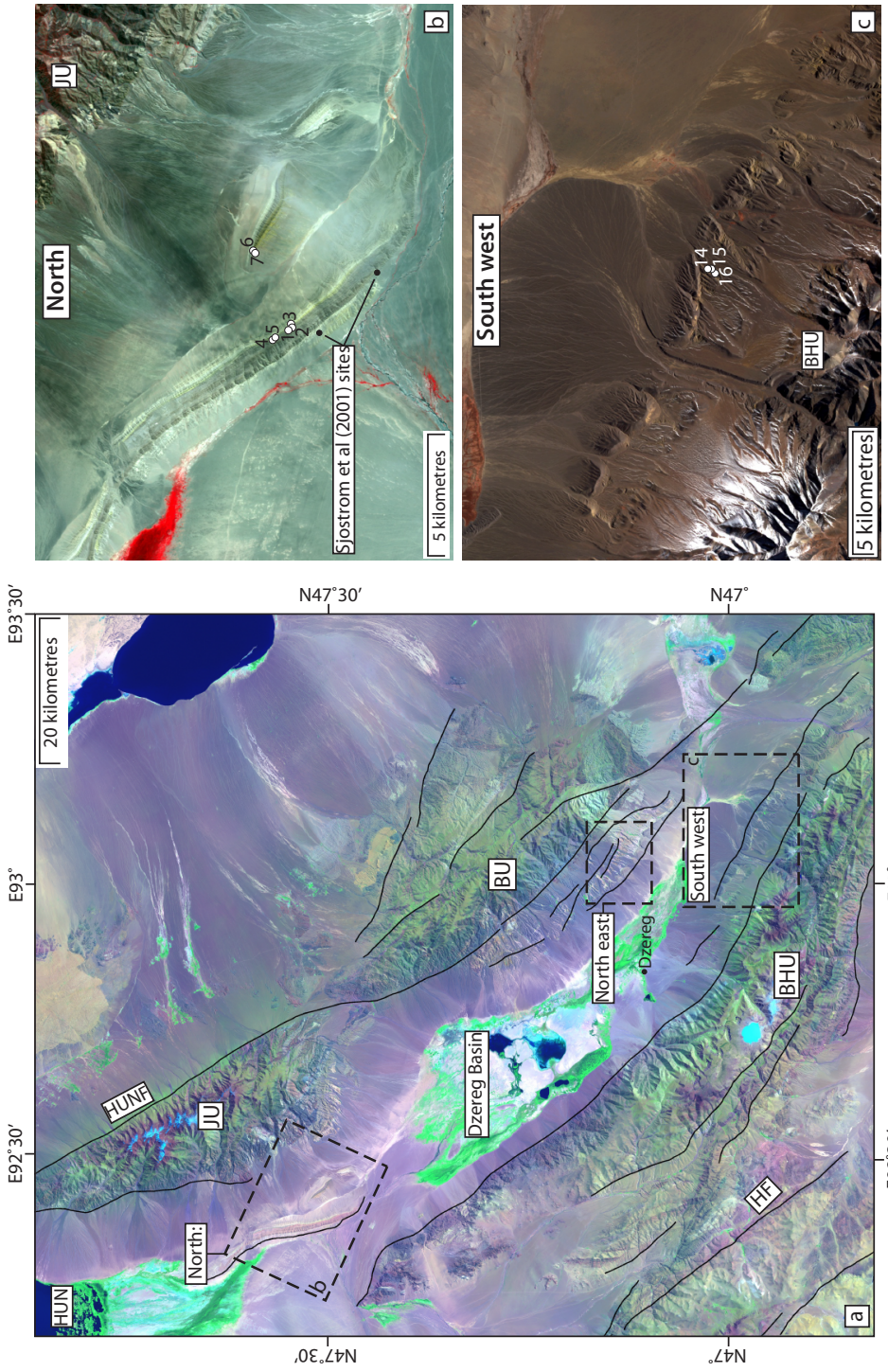


**Figure 4.2:** (a) Landsat image (RGB = 741) of the Dzereg Basin, with the three different sampling localities indicated (North, North east, and South west). Figure 4.3 is indicated by dashed rectangle labeled North east. Abbreviations are BHU: Baatar Hyarhan Uul, BU: Bumbat Uul, HF: Hovd Fault, HUN: Har-Us-Nuur, HUNF: Har-Us-Nuur Fault, and JU: Jargalant Uul. The town of Dzereg is indicated. (b) and (c) are ASTER images of the northern and southwestern sampling localities, with sample sites labeled.

*Sjostrom et al.* (2001) investigated the Mesozoic strata in the Dzereg Basin and surrounding regions, and used extensive paleontologic work for the relative dating of the sedimentary units (*Shuvalov*, 1968, 1969; *Khosbayar*, 1973; *Devyatkin et al.*, 1975). They described the Oshin Nuruu site on the southwest flanks of Jargalant Mountain, which was targeted for the northern-most palaeomagnetic sampling site in this chapter (sites 1–7 in Table 4.1, Figure 4.2). *Sjostrom et al.* (2001) described the Lower to Middle Jurassic sections as comprising sandstone with some pebbly conglomerate and siltstone layers within (Figure 4.4c). There are two separate exposures uplifted on what were suggested by *Cunningham et al.* (1996) to be two splay thrust faults from the main Jargalant faults. The palaeomagnetic sites for analysis in this chapter were collected from stratigraphically above the Jurassic sections described by *Sjostrom et al.* (2001), in what were likely to be Jurassic to Cretaceous aged red conglomeratic sandstone units and grey to yellow coarse-grained sandstone units. Sites 1–5 were collected from the sediments uplifted by the western-most thrust fault, and sites 6 and 7 from the units uplifted by the eastern thrust (Figure 4.2b). Samples were collected from finer grained mudstone and siltstone units interbedded with the conglomerates. Sediments on the eastern ridge were more coarse grained, including 1–2 mm sized pebbles within much of the sandstone and mudstone units, and were less consolidated than those from the western ridge.

Sites 8 through 13 were collected from Cenozoic strata uplifted in the range front of Bumbat Mountain (Figure 4.3), from sedimentary sequences described by *Howard et al.* (2003). They provided details of the biostratigraphy that was first outlined by *Devyatkin et al.* (1975) on the basis of paleontology. The sites are part of a syncline-anticline pair that has folded Upper Jurassic to Plio-Pleistocene sediments, which are unconformably overlain by Quaternary alluvial fans. A similar sedimentary sequence is also uplifted on the opposite side of the basin, where sites 14–16 were collected (Figure 4.2). No major folds were identifiable in the field on the southwest side of

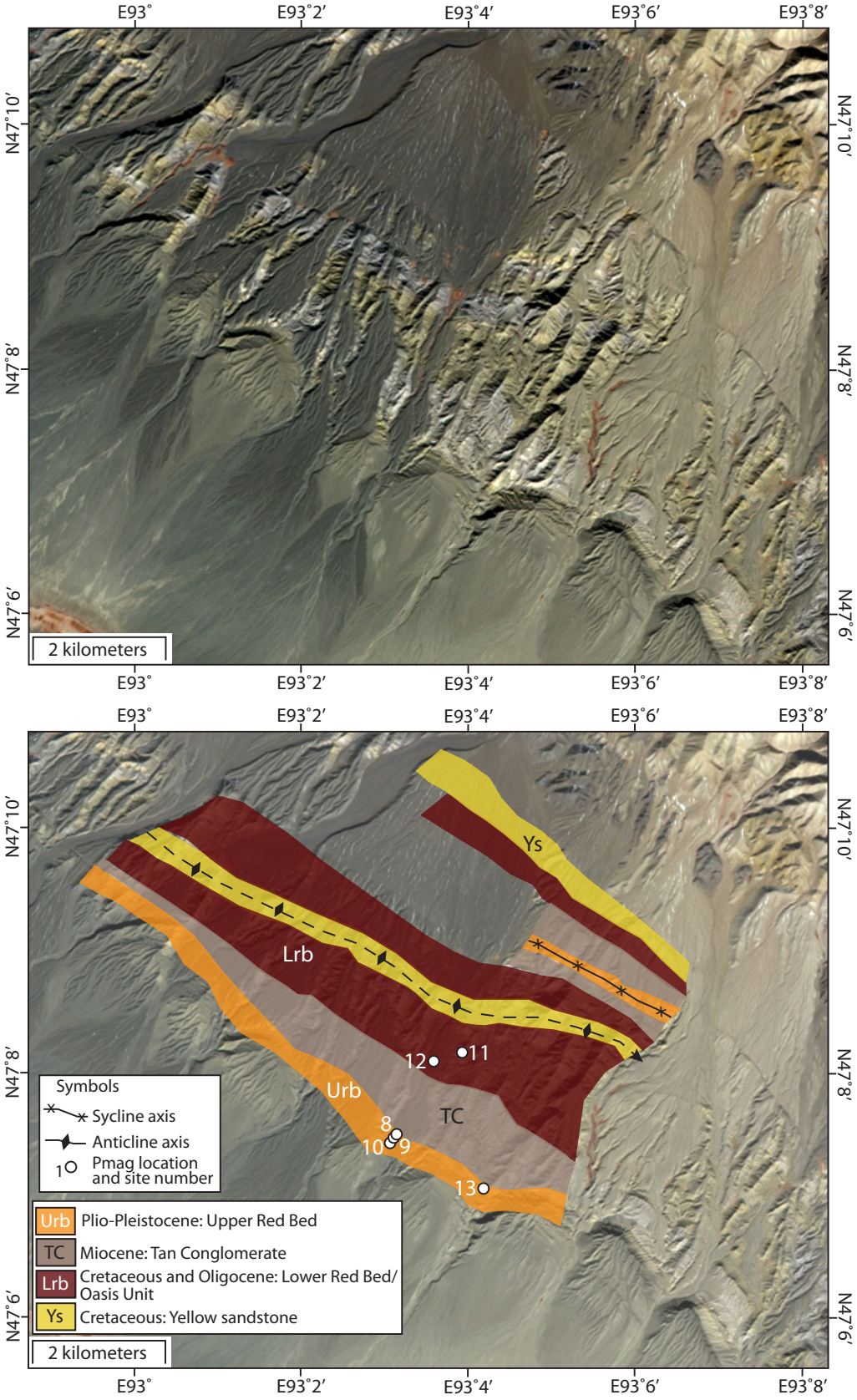
E93°
E93°2′
E93°4′
E93°6′
E93°8′
N47°10′
N47°8′
N47°6′
2 kilometers
Ys
Lrb
Urb
TC
11
12
8
9
10
13
Symbols
Sycline axis
Anticline axis
Pmag location and site number
Urb Plio-Pleistocene: Upper Red Bed
TC Miocene: Tan Conglomerate
Lrb Cretaceous and Oligocene: Lower Red Bed/ Oasis Unit
Ys Cretaceous: Yellow sandstone

the Dzereg Basin, and the succession consistently dips southwest towards Baatar Hyarhan Mountain.

The Cretaceous and younger stratigraphy is divided into four groups: the Cretaceous Lower Red Beds, the Oligocene Oasis Unit, the Miocene Tan Conglomerates, and the Pliocene Upper Red Bed/Pleistocene Conglomerates (*Howard et al.*, 2003). Two sites were collected from the Oasis Unit, stratigraphically above the unconformable boundary with the Cretaceous Lower Red Beds. The Oasis Unit consists of medium-grained buff-coloured sandstone, with interbedded siltstone, and is approximately 140 m thick (Figure 4.4d). The unit is suggested to represent renewed Oligocene tectonism in the Altay. The overlying Miocene strata comprise coarse grained conglomerates, and were not suitable for palaeomagnetic investigation. The Pliocene Upper Red Beds are conformable with the Miocene sequence, and are mostly composed of interbedded, fining upwards and red-stained conglomerates and siltstones. Several sites were sampled from this unit on both the north-eastern and south-western side of the basin. Sediments on the south-eastern side of Dzereg were similar in colour, sorting, grain size and stratigraphic relationships between interbedded layers to those sampled on the north-eastern side in the Upper Red Bed Unit.

**Figure 4.3** ***(preceding page)*:** ASTER imagery (15 m/pixel) of the sampling sites from the northeast side of the Dzereg Basin. The lower panel shows a geologic map of the area modified from *Howard et al.* (2003), with the ages of the units mapped labeled and sampling localities indicated. The region includes a syncline-anticline pair.

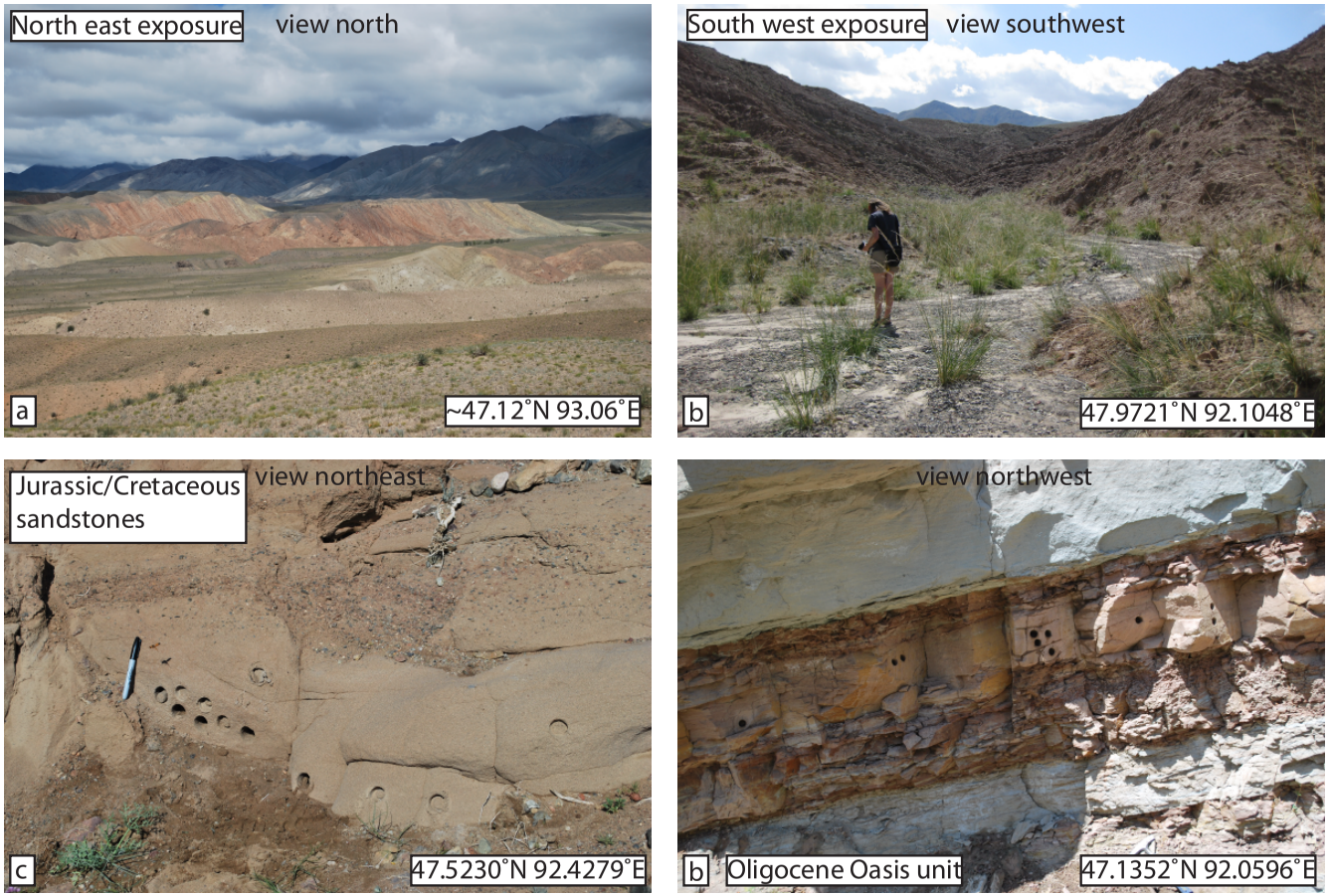


**Figure 4.4:** Photos of the exposures of Cenozoic and Mesozoic sediments in the northeast and southeast Dzereg Basin. (a) shows strata uplifted by northeast-dipping thrust faults, which have tilted the landscape towards Bumbat Mountain in the background of the photo. (b) shows the Upper Red Bed Plio-Pleistocene sediments uplifted on the flanks of Baatar Hyarhan Mountain, dipping towards the peaks of Baatar Hyarhan in the background. (c) Cretaceous sandstones with palaeomagnetic drill holes at site 6. (d) Oligocene Oasis Unit, with interbeded red sandstones (sampled, site 12) and yellow sandstones with some cross bedding.

**Table 4.1:** Palaeomagnetic sampling site localities and ages

| Site | Latitude (N°) | Longitude (E°) | Strat grp. | Age | Bedding S/D[1] |
|---|---|---|---|---|---|
| *North Dzereg* | | | | | |
| Site 1 | 47.5221 | 92.3811 | ON[2] | Jurassic-Cretaceous | 336/40 |
| Site 2 | 47.5219 | 92.3814 | ON | Jurassic-Cretaceous | 336/40 |
| Site 3 | 47.5219 | 92.3817 | ON | Jurassic-Cretaceous | 343/45 |
| Site 4 | 47.5294 | 92.3791 | ON | Jurassic-Cretaceous | 342/42 |
| Site 5 | 47.5292 | 92.3796 | ON | Jurassic-Cretaceous | 340/48 |
| Site 6 | 47.5230 | 92.4279 | ON | Jurassic-Cretaceous | 322.5/23 |
| Site 7 | 47.5227 | 92.4274 | ON | Jurassic-Cretaceous | 320/24 |
| *North east Dzereg* | | | | | |
| Site 8 | 47.1250 | 93.0524 | Urb | Plio-Pleistocene | 130/24 |
| Site 9 | 47.1250 | 93.0522 | Urb | Plio-Pleistocene | 132/26 |
| Site 10 | 47.1247 | 93.0520 | Urb | Plio-Pleistocene | 130/33 |
| Site 11 | 47.1364 | 93.0663 | Oasis | Oligocene | 125/23 |
| Site 12 | 47.1352 | 93.0596 | Oasis | Oligocene | 128/20 |
| Site 13 | 47.1171 | 93.0701 | Urb | Plio-Pleistocene | 090/28 |
| *South west Dzereg* | | | | | |
| Site 14 | 46.9732 | 93.1048 | Urb | Plio-Pleistocene | 113/52 |
| Site 15 | 46.9722 | 93.1051 | Urb | Plio-Pleistocene | 107/50 |
| Site 16 | 46.9711 | 93.1038 | Urb | Plio-Pleistocene | 101/65 |

[1]Bedding strike and dip are listed as an average of measurements collected in the region surrounding the site; dip is measured in the direction 90° clockwise from strike.
[2]ON: Oshin Nuruu section (from *Sjostrom et al.*, 2001)

## 4.3 Palaeomagnetic methods

A natural remanence magnetisation (NRM) is acquired by suitable minerals in the presence of the Earth's magnetic field, forming the base of the study of palaeomagnetism. The primary magnetisation of a rock occurs when the rock forms, and is parallel to the geomagnetic field at the time (e.g. *Butler*, 1992; *Merrill et al.*, 1998). In sedimentary rocks, the magnetic direction of the rock is set during and following deposition. Detrital magnetic minerals, such as hematite, are subjected to the torque of the Earth's magnetic field, and are physically aligned with the field during deposition (see *Tauxe*, 2010, for a detailed review of the process). The magnetisation of sediments is known as a detrital remanent magnetisation (DRM) and can be related to the applied external field $\mathbf{B}$. A magnetic moment $\mathbf{m}$ placed in a field $\mathbf{B}$ will have a torque $\Gamma$ acting on the magnetic particle, of $\Gamma = \mathbf{m} \times \mathbf{B} = mB\sin\theta$, where $\theta$ is the angle between the moment of the particle and the external field.

The detrital remanence of a sample is fixed when the magnetic particles in the sediment can no longer move in response to the geomagnetic field. Thus the orientation of the field is recorded in sedimentary rocks during deposition, and can be used to determine the subsequent rotation undergone by a region due to tectonic vertical axis rotations. Post-depositional processes may have an affect on the magnetisation, with changes mostly arising from chemical alteration and the acquisition of a chemical remanent magnetisation (CRM) or due to compaction of the sediments, which results in a shallowing of the magnetic inclination. These effects can sometimes be determined by step-wise demagnetisation of palaeomagnetic samples, in order to isolate magnetisations with different coercivities, which is the resistance to demagnetisation. The primary component of magnetisation will generally have a higher coercivity and be more resistant to demagnetisation. Post-depositional growth of altered minerals such as goethite may carry a relatively strong magnetisation, but the CRM carried by alterations can generally be thermally demagnetised when heated. In order to deal with low-temperature CRM, and various other potential post-depositional magnetisations, samples are heated in a field free oven, such that the overprinting magnetisations are randomised at increasing temperatures, which allows for the remaining primary magnetisation to be measured. Magnetic tests for the initial susceptibility of each sample and the behaviour of susceptibility over a range of temperatures in select samples are also performed, in order to characterise the minerals holding the different magnetisations in the samples. These tests are particularly aimed to determine the temperature at which the magnetic remanence is unblocked, the Curie temperature, which enables the identification of the main magnetic carriers.

The palaeomagnetic results must pass reliability tests to confirm that the magnetisation in the samples is in fact primary, and can be related to the age of the sediments (*Van der Voo*, 1990). There are generally seven tests (Quality, or Q-factors)

that may be applied to samples, but the samples need not pass each test to prove that the magnetisation is primary. Q-factors are outlined by *Van der Voo* (1990) as applied to Virtual Geomagnetic Poles (VGP), which are essentially the ancient orientation of the magnetic field relative to the sampling locality, but Q-factors can also be applied to studies where obtaining a VGP is not the primary goal, in the case of investigating vertical axis rotations. The Q-factors outlined by *Van der Voo* (1990) are briefly described here to facilitate discussion on the reliability of palaeomagnetic results from the Dzereg Basin. (1) The age of the rock must be well determined (within a half-period), and (2) a sufficient quantity of samples must be measured with adequate statistical precision. (3) Samples must be demagnetised in order to isolate potential overprinting components of magnetisation, and the primary component is generally the highest coercivity direction. (4) Field tests are an important Q-factor for interpreting palaeomagnetic results, and in sedimentary rocks, the fold test is the most widely used test. A positive fold test will result in an increase in the precision of sample grouping as the strata are unfolded to their flat lying position, but in order to be statistically significant, the test requires enough samples with stable directions collected from sufficiently varying bedding orientations. (5) Structural coherence is necessary to relate the palaeomagnetic core samples to deformation in the upper crust. This factor (5) is important in the case of vertical axis rotation studies, because the potential for local, basin-scale rotations must be considered when extrapolating results to regional rotations. (6) The presence of reversals is an important test of primary magnetisation, because if regional magnetic resetting has occurred, reversed directions will not be preserved, though it is not a guarantee that the rocks have not been remagnetised. The final test of reliability (7) is that the directions obtained are not similar to any younger palaeopoles, which would suggest that the sample was remagnetised at the time that the measured directions match a younger palaeomagneitc pole. I discuss my results in the context of these tests in

section 4.5.1, but start by confirming that the age of the samples well determined, based on the stratigraphy outlined in section 4.2.

### 4.3.1 Palaeomagnetic sampling and experiments

Samples were collected in the field using a gasoline powered hand drill, and were oriented with a magnetic compass. Due to the low magnetic intensity of the sediments, no correction for magnetic interference from the outcrop was necessary. Just over 160 core samples were collected from 16 sites in three different regions of the Dzereg Basin (Figure 4.2, Table 4.1). Samples aged from Late Cretaceous to Plio-Pleistocene were collected, based on the stratigraphy of the region outlined by *Sjostrom et al.* (2001) and *Howard et al.* (2003), briefly described in section 4.2.

Samples were carefully wrapped in the field and further processing was done at the University of Oxford palaeomagnetic laboratory. Core samples were cut into 1–2 standard sized specimens using a custom saw, and a few of the more delicate samples were cut by hand with a utility knife and sanded to remove metal from the knife. Samples were stored and measured in a magnetically shielded room, with an internal field <200 nT. A pilot batch of 1–2 specimens from each site was thermally step-wise demagnetised at relatively narrow temperature intervals of 50°C steps up to 500°C, followed by narrowing to 20°C steps to 620°C, and to 10°C steps until demagnetised (up to about 700°C). After analysing the preliminary samples, a series of thermal steps up to 700°C were chosen for demagnetisation of the remaining samples (generally at 60°C steps to 540°C, followed by 20°C steps to 700°C). Magnetic measurements were made on samples in between each heating step, on the Oxford 2-G 3-axis cryogenic magnetometer. Best fit magnetic components found during demagnetisation were determined for linear segments on orthogonal plots, using the least-square regression analysis implemented in the Super IAPD program (`http://www.geodynamics.no/software.htm`). The orthogonal plot is a display of

the horizontal and vertical (declination and inclination) projection of the magnetisation at each temperature step (e.g. Figure 4.5; *Zijderveld*, 1967).

### 4.3.2 Rock magnetic experiments

In order to better characterise the carriers of magnetisation in samples, magnetic tests were performed on samples. Initial susceptibility was measured for all samples, and Curie temperature measurements were carried out on a select group of powdered samples (representing the variety in age and composition in the sampling sites) using a KLY-2 susceptibility bridge with a CS2 heating unit. In these experiments, the susceptibility of a finely crushed sample is incrementally measured during heating and cooling. The magnetic carrier can be determined from the change in magnetic susceptibility with temperature, in particular the value for the Curie temperature of the sample, which occurs when the magnetic ordering is destroyed with an accompanying loss of susceptibility (e.g. *Merrill et al.*, 1998).

## 4.4 Results

Palaeomagnetic data from sites that have consistent and stable remanent magnetisations are listed in Table 4.2. Representative Zijderveld diagrams and thermal demagnetisation paths are displayed in Figures 4.5, 4.6, and 4.7 from the three different regions of the Dzereg Basin shown in Figure 4.2. The intensities of natural remanent magnetisations (NRM) range from around 1 to 44 mA/m, with generally lower intensities in samples that had less stable directions. The highest intensities were found from a site that yielded inconsistent directions (site 9). A low coercivity component was frequently removed from samples at lower temperatures (up to ~250°C), which can generally be attributed to the present day field (north and steep, e.g. Figure 4.6). Many samples lost a significant percentage of intensity at temperatures up to ap-

proximately 120°C, which may be indicative of the presence of goethite imparting a CRM. However, once this low coercivity component was removed, a stable magnetic direction could generally be found from the higher temperature measurements (e.g. sample M916-3, Figure 4.7). Samples were fully demagnetised at much higher temperatures, between 560–700°C, indicating that both magnetite and hematite may be contributing to the primary magnetisation, as the Curie temperatures are 580°C for magnetite and between 675° to 725°C for hematite (*Merrill et al.*, 1998).

Both *in-situ* and tilt-corrected directions for the stable high coercivity components are listed in Table 4.2. The tilt correction was made for each site based on the strike and dip of the strata that were sampled (Table 4.1). In order to test for tectonic rotation of the samples as well as inclination flattening during compaction, the tilt-corrected directions can be compared to the expected VGP (virtual geomagnetic pole) for the time of deposition. VGPs were calculated from the apparent polar wander path (APWP) for Eurasia catalogued by *Torsvik et al.* (2012) for the Dzereg Basin using the GMAP2003 program (available at `http://www.geodynamics.no/software.htm`). The degree of rotation for each site is the difference between the measured tectonic corrected declination ($D_{tc}$) and the expected declination for a given stratigraphic age based on the VGP. The flattening of a site is the difference between the expected inclination and tilt-corrected, measured inclination ($I_{tc}$).

Uncertainties at the 95% confidence level for the rotation and flattening were determined following methods in *Demarest* (1983). Uncertainties are based in part on the classic *Fisher* (1953) statistics for the probability distribution of two dimensional cone of 95% confidence ($\alpha_{95}$). A small correction factor is added to the uncertainty, in line with *Demarest* (1983), which takes into account the precision of the results as well as the inclination of samples. The uncertainties for rotation of declinations increase as inclinations steepen, and as inclination approaches 90°, a range of 0–360°

**Table 4.2:** Palaeomagnetic data

| Site | n/N[a] | $D_{is}$[b] | $I_{is}$[b] | $D_{tc}$[c] | $I_{tc}$[c] | $\alpha_{95}$[d] | $\kappa$[d] | Exp D[e] | Exp I[e] | Rotation[j] | Error | Flattening | Error |
|---|---|---|---|---|---|---|---|---|---|---|---|---|---|
| *North Dzereg* | | | | | | | | | | | | | |
| Site 1 | 5/9 | 000.0 | 53.1 | 029.0 | 27.9 | 9.1 | 71.7 | 030.4 | 68.6 | -1.4 | 10.6 | 40.7 | 7.7 |
| Site 3 | 4/4 | 310.4 | 70.7 | 048.0 | 53.1 | 17.6 | 28.1 | 030.4 | 68.6 | 17.6 | 25.1 | 15.5 | 14.3 |
| Site 6 | 9/10 | 051.2 | 70.2 | 052.9 | 47.2 | 17.8 | 9.3 | 030.4 | 68.6 | 22.5 | 22.4 | 21.4 | 14.4 |
| Site 7 | 5/5 | 025.8 | 64.5 | 037.2 | 41.9 | 14.9 | 27.3 | 030.4 | 68.6 | 6.8 | 17.5 | 26.7 | 12.2 |
| *NE Dzereg* | | | | | | | | | | | | | |
| Site 8 | 8/15 | 198.8 | -25.6 | 190.6 | -47.0 | 14.0 | 16.7 | 183.5 | -67.9 | 7.1 | 17.8 | 20.9 | 11.5 |
| Site 11 | 9/14 | 209.9 | -10.1 | 208.7 | -32.9 | 14.3 | 14.0 | 188.6 | -67.9 | 20.1 | 15.2 | 35.9 | 11.7 |
| Site 12 | 10/10 | 209.4 | -0.8 | 208.5 | -19.3 | 7.6 | 41.8 | 188.6 | -67.9 | 20.1 | 9.3 | 48.3 | 6.5 |
| *SW Dzereg* | | | | | | | | | | | | | |
| Site 14 | 2/13 | 012.8 | -0.9 | 006.0 | 49.5 | - | - | 003.5 | 67.9 | 2.5 | 32.0 | 18.4 | 19.5 |
| Site 15 | 14/14 | 008.1 | 9.8 | 357.9 | 58.1 | 6.8 | 35.6 | 003.5 | 67.9 | -5.6 | 12.2 | 9.8 | 5.9 |
| Site 16 | 8/13 | 183.1 | 13.1 | 177.7 | -50.7 | 4.8 | 132.6 | 183.5 | -67.9 | -5.8 | 8.8 | 17.2 | 4.5 |

[a] n/N is number of specimens used in site means (n) over the number of samples measured (N)
[b] $D/I_{is}$ are the declination and inclination of the primary magnetic vector of the site, in geographic coordinates (*in-situ*)
[c] $D/I_{tc}$ are the declination and inclination of the primary magnetic vector with the tectonic correction at the site
[d] $\alpha_{95}$ is the semi-axis of the cone of 95% confidence, and $\kappa$ is a precision parameter
[e] Expected declination and inclination are from VGPs recalculated for the Dzereg Basin from *Torsvik et al.* (2012), depending on the age of the site[g,h,i]
[f] Positive polarity VGPs are used when the polarity of the site is positive, and corresponds to the Dec listed in parentheses in *g, h, and i.* [g] Jurassic/Cretaceous reference VGP (150 Ma): Dec = 210.4° (30.4°), Inc = -68.6° , $\alpha_{95}$ = 3.0
[h] Oligocene reference VGP (20 Ma): Dec = 188.6° (008.6°), Inc = -67.9°, $\alpha_{95}$ = 3.0
[i] Pliocene reference VGP (10 Ma): Dec = 183.5° (003.5°), Inc = -67.9°, $\alpha_{95}$ = 3.0
[j] Rotation and flattening parameters, and associated errors at the 95% confidence level, are calculated from methods outlined by *Demarest* (1983)

for declination is possible.

Rotations of individual sites from the expected declination are between 22° clockwise to 6° anticlockwise. The site rotations are combined into groups based on their stratigraphic age and discussed further in Section 4.5. The majority of samples yield inclinations that are shallower than those predicted from the reference poles by >10°, and have likely experienced inclination flattening. This shallowing phenomenon is common amongst sedimentary rocks due to compaction, particularly in central Asia, where sedimentary samples commonly have measured inclinations that are 20° shallower than expected (*Tauxe and Kent*, 2004). The majority of sites have experienced inclination shallowing of approximately equal to or less than 20°, though a few have significantly more flattening (sites 1, 11, and 12). However, the shallowing of inclinations does not affect the sample declination, and this shallowing is useful because it suggests a primary magnetisation acquired before lithification.

### 4.4.1 Magnetic tests

The results of susceptibility tests are shown in Figure 4.8, for select sites that have stable demagnetisation vectors as well as one site with inconsistent directions (site 9). Samples from sites 3, 9, and 11 display a characteristic *Hopkinson* effect, which is an increase in susceptibility just before the Curie temperature drop in susceptibility, and is often associated with the unblocking temperature of the magnetisation (*Tauxe*, 2010). The loss of susceptibility around 560°C is characteristic of magnetite being the primary carrier of magnetisation, and most samples display a drop in susceptibility in this range. Some samples also lose the remaining susceptibility around 680–700°C, suggesting that hematite is also present in those samples.

In some cases, the statistics of the mean directions from a site are quite poor, with high $\alpha_{95}$ values and low $\kappa$ values. Whilst there is no specific acceptable standard for $\alpha_{95}$ and $\kappa$, values of $\alpha_{95} < 15$ and $\kappa > 30$ are considered to be typical for good quality

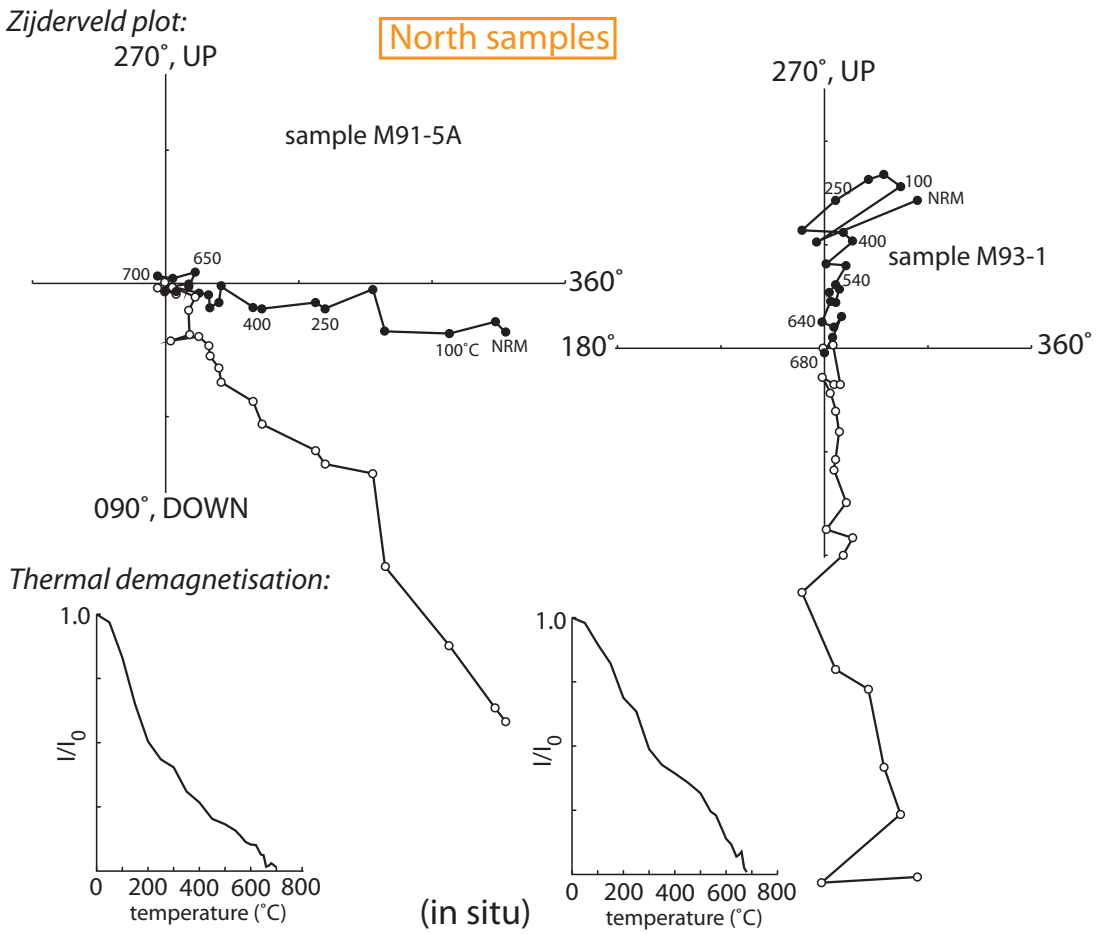


**Figure 4.5:** Examples of thermal demagnetisation Zijderveld diagrams from the northern group of sites. Plots are shown *in-situ* with no tectonic correction. Open points indicate the inclination, and closed points are the sample declination. North is to the right of the plot, and magnetic directions are fit as vectors through the measurements that are directed from high to low temperature. $I/I_0$ on the thermal demagnetisation plot is the magnetic intensity of the sample divided by the NRM (initial) intensity.

studies. The poor statistical values arise from sites that have a low number of stable specimens, and that generally have primary components of magnetisation that are relatively weak (e.g. sites 11 and 14). Many specimens have a large component of noise in final demagnetisation steps at high temperatures, and this is probably due to alteration and growth of secondary minerals during heating, which are formed as clays break down at high temperatures. In susceptibility tests of samples with secondary mineral growth, the cooling curve shows a large increase in susceptibility

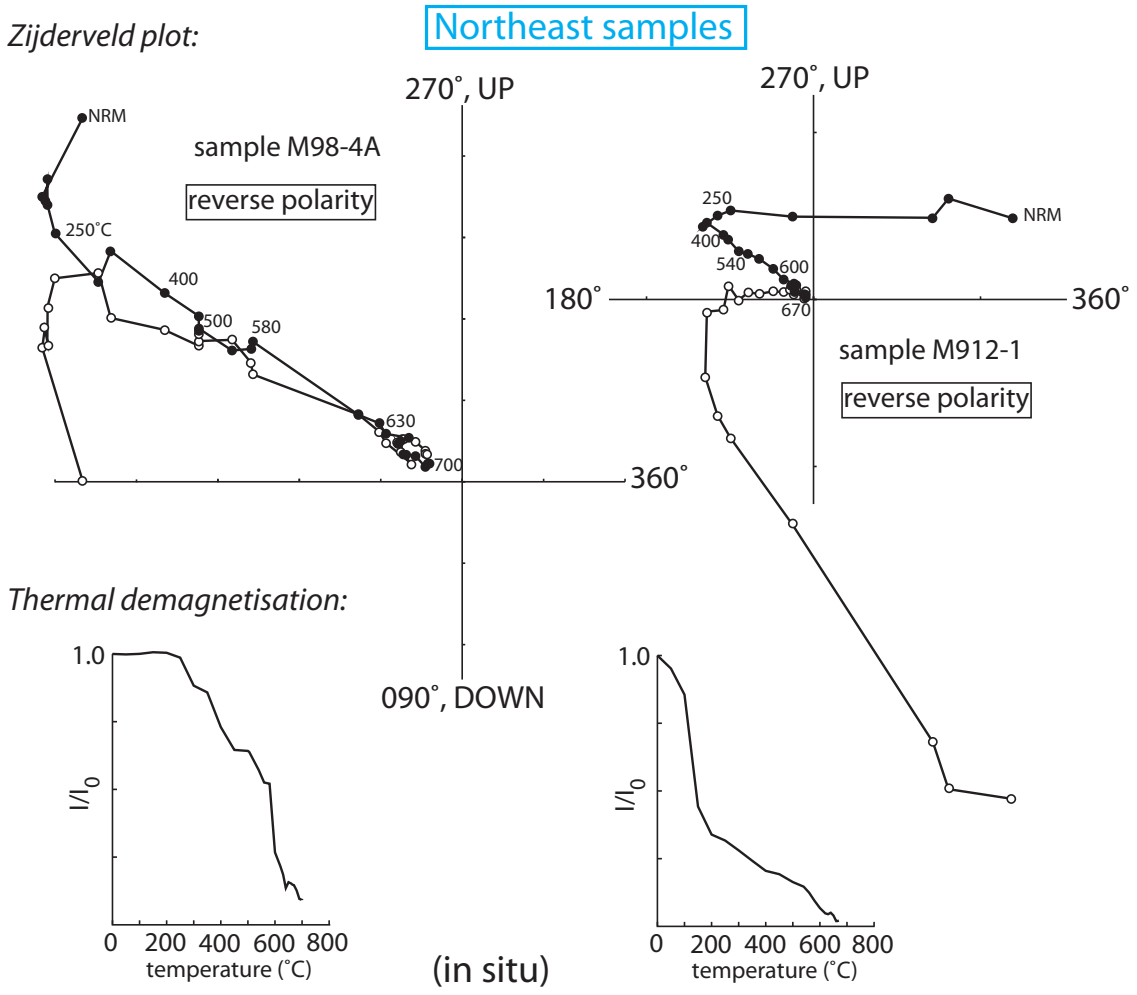


**Figure 4.6:** Examples of thermal demagnetisation Zijderveld diagrams from the northern eastern group of sites. Samples have a low temperature component with normal polarity that is probably a modern day field overprint, with a higher temperature component that is reversed, with a declination to the SW as shown. Plots are shown *in-situ* with no tectonic correction. Open points indicate the inclination, and closed points are the sample declination. North is to the right of the plot, and magnetic directions are fit as vectors through the measurements that are directed from high to low temperature. $I/I_0$ on the thermal demagnetisation plot is the magnetic intensity of the sample divided by the NRM (initial) intensity.

during cooling, with sharp increases at the magnetite Curie temperature, implying the growth of magnetite. During demagnetisation, the secondary growth of altered minerals that are magnetic does not affect the sample declination, because the directions in the mineral growth are randomised in the shielded oven, but the mineral

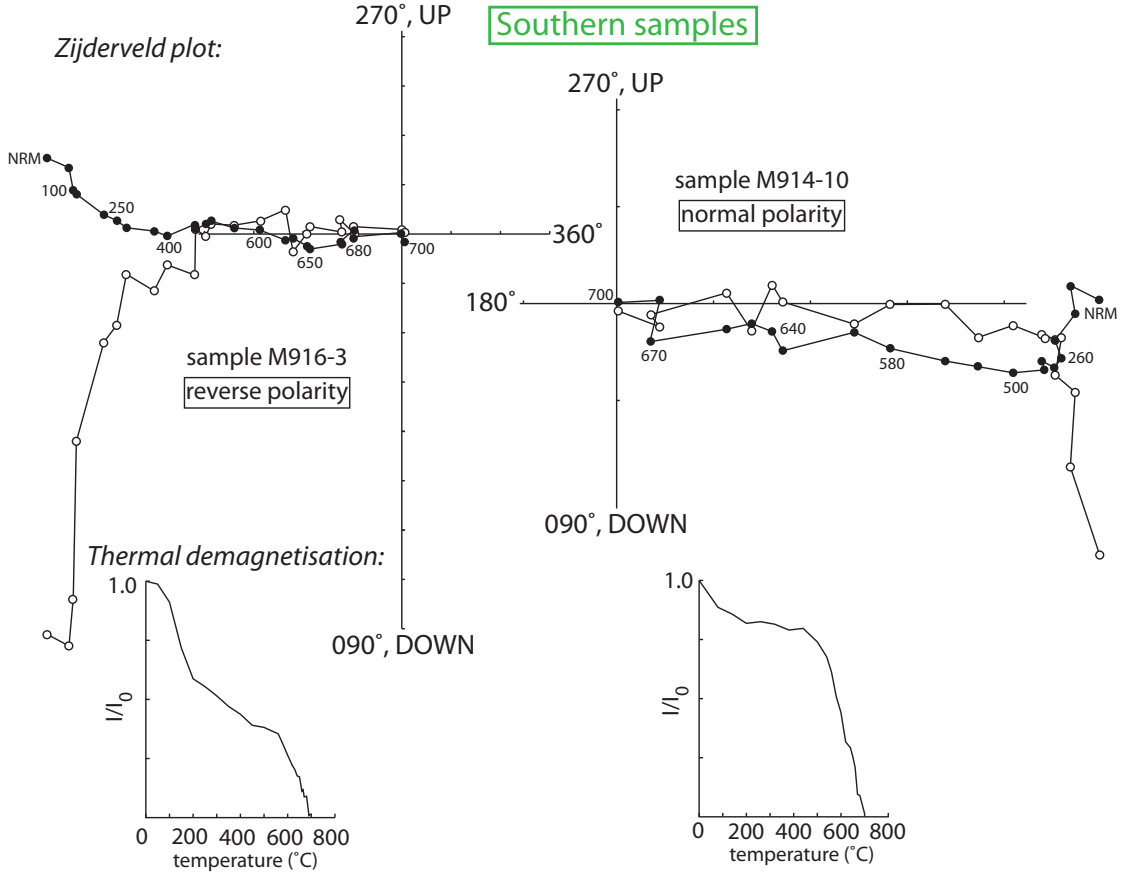


**Figure 4.7:** Examples of thermal demagnetisation Zijderveld diagrams from the southern group of sites, with normal and reverse polarities. Plots are shown *in-situ* with no tectonic correction. Open points indicate the inclination, and closed points are the sample declination. North is to the right of the plot, and magnetic directions are fit as vectors through the measurements that are directed from high to low temperature. $I/I_0$ on the thermal demagnetisation plot is the magnetic intensity of the sample divided by the NRM (initial) intensity.

alteration does produce noise in the data.

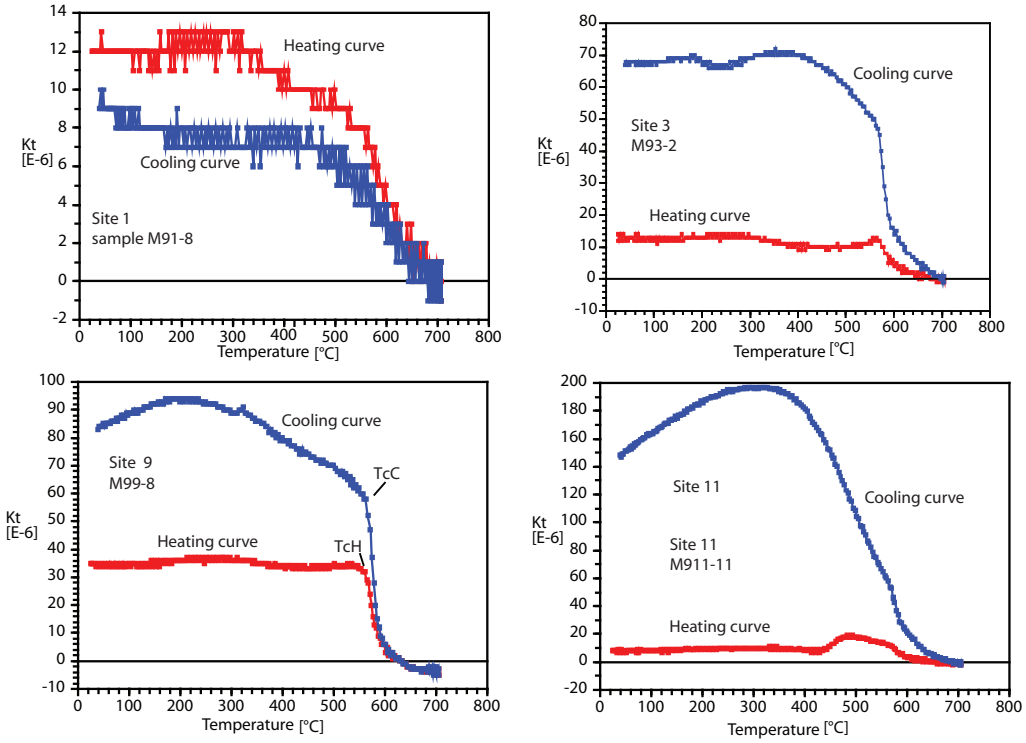


**Figure 4.8:** Results from Curie temperature tests on four example samples. TcH indicates the Curie temperature when heating, which is indicated by a sharp drop in susceptibility. TcC is the Curie temperature during cooling, and is the end of the steep increase in susceptibility during cooling. Most samples show some alteration during heating, evidenced by the higher susceptibility during cooling than heating, although this is not observed in site 1. Samples have Curie temperatures around 560–580°C, indicating that magnetite is the primary magnetic carrier. Site 3 shows a steepening in slope at around 650°C, which may indicate the presence of hematite.

## 4.5 Discussion

### 4.5.1 Reliability of the data

Tilt correction of the sites results in better grouping of the mean directions, and directions from all of the sites can be combined into a statistically significant fold test, positive at the 95% confidence level, using the classic *McElhinny* (1964) approach (Figure 4.9). For the fold test, the site directions are incrementally restored back to horizontal from the stratigraphic orientations. The $\alpha_{95}$ and $\kappa$ values are calculated for each 10% increment. If magnetic directions in the samples have been

reset since deposition, the precision of the results ($\alpha_{95}$) is predicted to worsen and the grouping (essentially $\kappa$) will decrease, because the samples are essentially 'blind' to the structure of the fold. If the directions are primary, the measures of precision and grouping will improve, because the samples migrate to the 'true', tilt-corrected site mean.

Unfolding of the Dzereg Basin sites by up to 90% results in a higher $\kappa$ value for the mean of all sites, which would not be the case if samples were remagnetised during or after tectonic tilting occurred. This passing of the fold test confirms that the isolated magnetic components are primary. Fold tests were also performed on groupings of the sites by age, but none of the groups produced a statistically significant fold test. This is likely because there is little variability in bedding orientations within each age group, and the fold tests would be improved by sampling from units of the same age, but from strata with variable orientations.

Also attesting to primary magnetisation, there are several sites that have reversed polarity, exhibited in the Cretaceous and Cenozoic sequences (Figure 4.9). While this is not necessarily confirmation of primary magnetisation, it does add confidence to the reliability of the directions. Tilt-corrected directions are distinct from the present day field in the region, which has a north declination and a steep inclination of approximately 65°, suggesting that the measured directions are not the result of a present-day overprint. A steeply dipping, northerly overprint was found at low temperatures in several sites, but this component was removed by stepwise heading (e.g. sample M912-1, Figure 4.6).

### 4.5.2 Rotation of the Dzereg Basin

The mean palaeomagnetic directions measured from each of the Jurassic-Cretaceous, Oligocene, and Plio-Pleistocene sediments are displayed in Figure 4.10. The predicted declination and inclination for the samples, based on VGPs calculated from

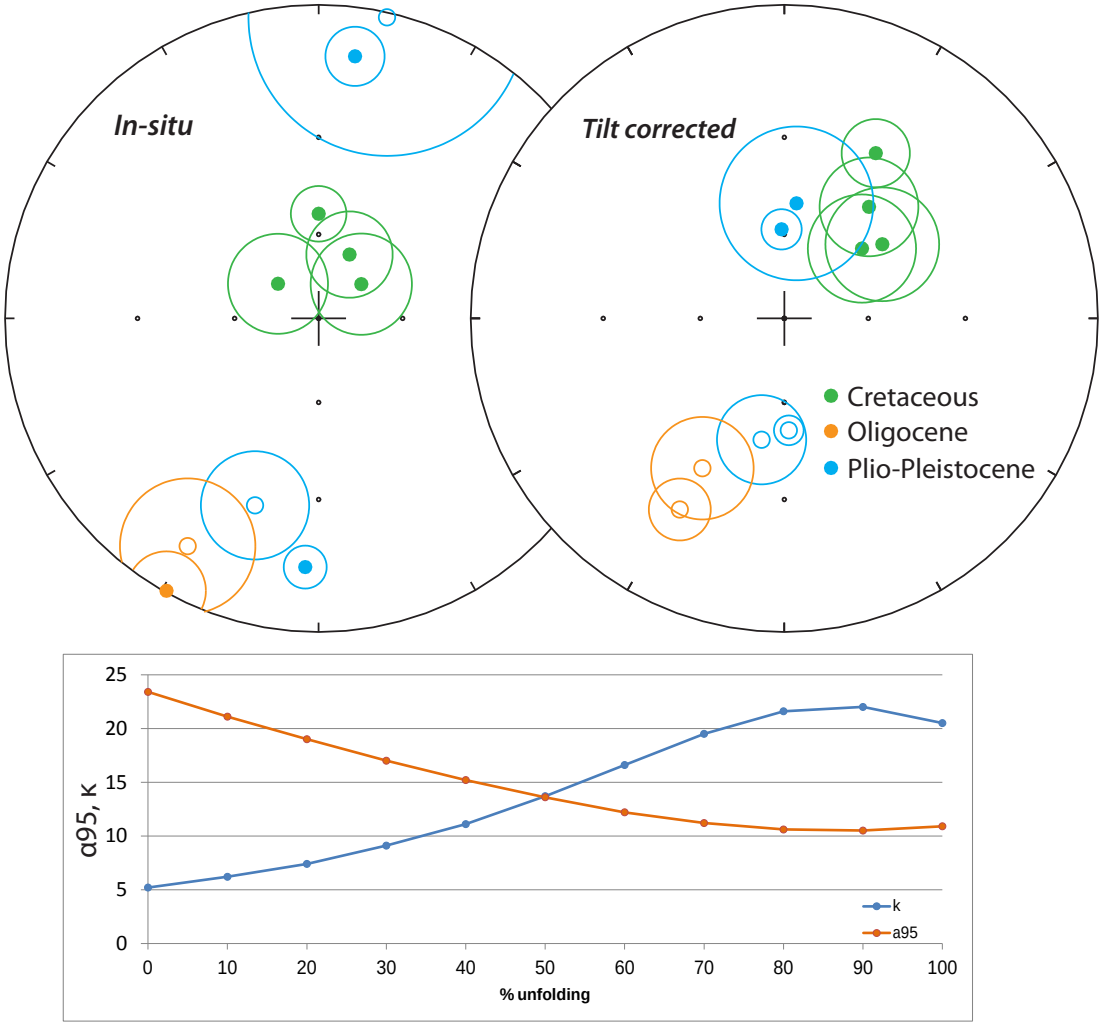


**Figure 4.9:** *In-situ* and tilt corrected site means and $\alpha_{95}$ cones of uncertainty are shown on the stereoplots (lower hemisphere projection) for all stable and consistent sites. Closed circles indicate positive directions and open circles indicate negative directions, and all sites are plotted as a single (normal) polarity. The lower panel shows the results of the fold test that includes all sites, with a higher $\kappa$ value, indicating greater precision, with 90–100% unfolding.

*Torsvik et al.* (2012) are also shown as squares on the same figure, with dashed lines indicating the expected declination. The mean inclinations are more shallow than what is expected from the VGPs, confirming that some degree of flattening has occurred, probably as a result of compaction. The mean declinations are not dissimilar from those predicted by the VGPs, and even the oldest group is well within the 95% cone of uncertainty of the expected declination (Jurassic/Cretaceous

D=40.6° ± 15.4°, compared to the VGP D=30.4° ± 3.0°). The Plio-Pleistocene grouping has the lowest uncertainty, and the mean declination is not rotated with respect to the expected declination (Pliocene D=003.4° ± 7.1°, compared to a VGP D=003.5° ± 3°).

The results from the Dzereg Basin suggest that the region has not undergone a measurable amount of palaeomagnetic rotation. The results are of high quality, and pass several field tests that attest to primary magnetisation, including reversal and fold tests. The ages of the strata are generally well defined, based on paleontological work, geologic mapping, and stratigraphy (*Devyatkin et al.*, 1975; *Sjostrom et al.*, 2001; *Howard et al.*, 2003). The lack of rotation in the Dzereg Basin is in strong contrast with both the existing palaeomagnetic results from the Chuya Basin in the Siberian Altay (*Thomas et al.*, 2002), and with the anticlockwise rotations predicted by geodetic data and the pattern of faulting (*Bayasgalan et al.*, 2005; *Cunningham*, 2005). In the Chuya Basin, anticlockwise rotations of 39 ± 8° have been suggested on the basis of palaeomagnetic data from Oligocene and younger aged sediments, with reasonable tests of reliability. Whether the rotation is the result of heterogeneous and local basin-scale rotation due to faulting, or represents large scale vertical axis rotation of the mountain belt, is difficult to determine without additional information on the duration of active faulting, as well as the kinematics of strike-slip faulting and total fault offsets (e.g. *Walker and Jackson*, 2004). Based on the topographic expression of active faulting and mountain building, it seems possible that the faults surrounding the Dzereg Basin are younger than those acting on the Chuya Basin, and have not yet accumulated significant slip to cause rotation. Constraints on the initiation of deformation, along with long-term fault displacement, may provide insight into the lack of rotation measured in eastern Altay. In Chapter 6, I discuss the discrepancy between results from the Chuya and Dzereg Basins in the context of the kinematics and rates of faulting presented in the previous chapters, as well

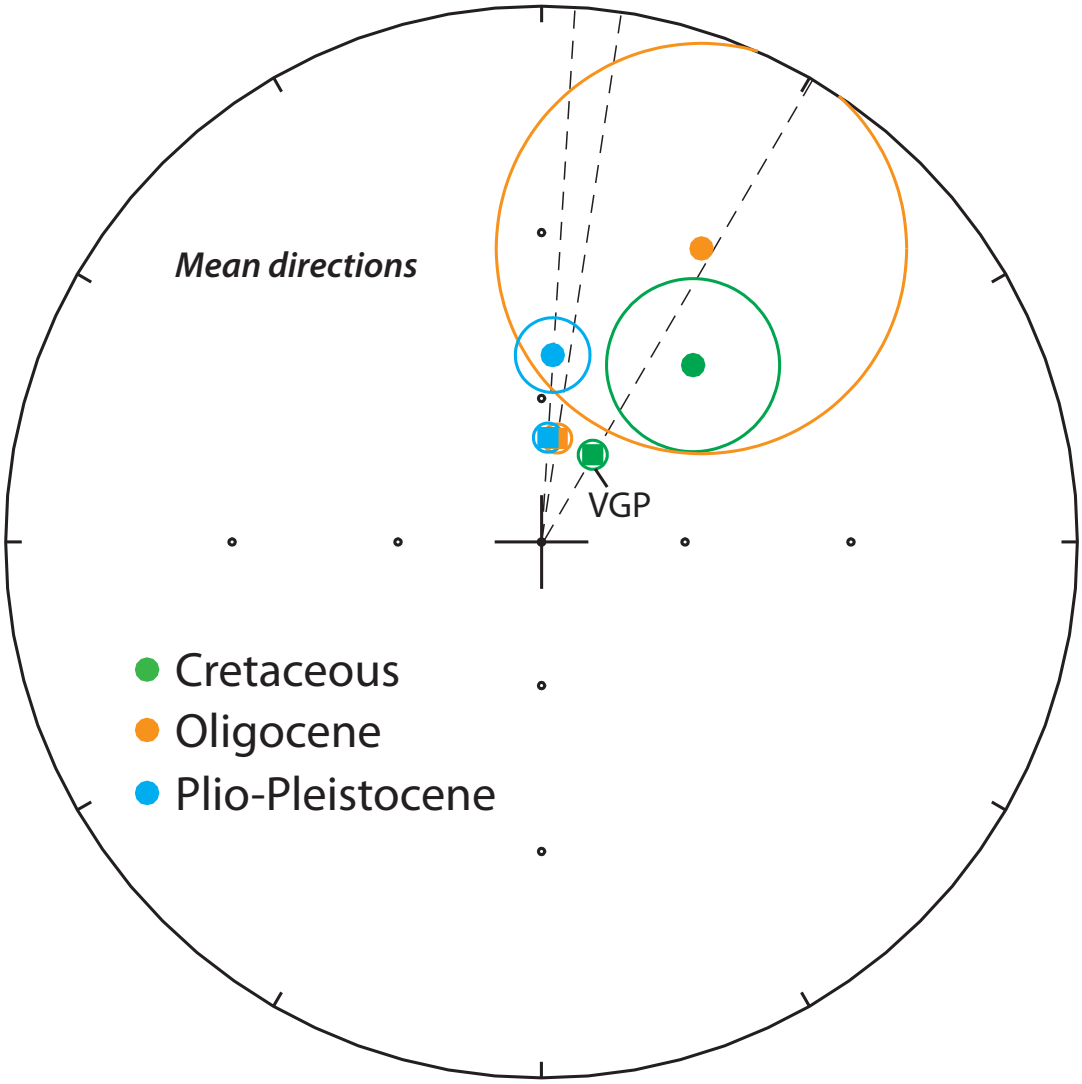


**Figure 4.10:** The mean directions for sites from each age group are plotted as coloured circles, with the VGPs plotted as squares in the same colours. Dashed lines show the expected declination based on each VGP for the Jurassic/Cretaceous (150 Ma), Oligocene (20 Ma), and Plio-Pleistocene (10 Ma). The stratigraphic groups are not rotated with respect to the expected poles, within uncertainties, but do demonstrate significant inclination shallowing.

as results from low temperature thermochronology, which adds constraint to the geological evolution of the Altay, as presented in the next chapter.

# Chapter 5

# Low temperature thermochronology of the central Altay

## 5.1 Introduction

Low-temperature thermochronology has the potential to link observations of long-term, geological continental deformation with short-term (Quaternary to the modern day) measurements of the rates and styles of strain accumulation on active faults. Apatite fission track (AFT) techniques provide constraints on the timing and rates of cooling of rock on geological time scales, but in the upper few kilometres of the crust, thus possibly illuminating the most recent deformation. The Altay mountains provide a unique setting for understanding far-field and large scale deformation of the crust, as the region is actively deforming due to the convergence between India and Asia that occurs over 2500 km to the southwest (e.g. *Tapponnier and Molnar*, 1979). As outlined in Chapter 1, the timing and the style of the progression of deformation in central Asia throughout the Phanerozoic is not fully understood.

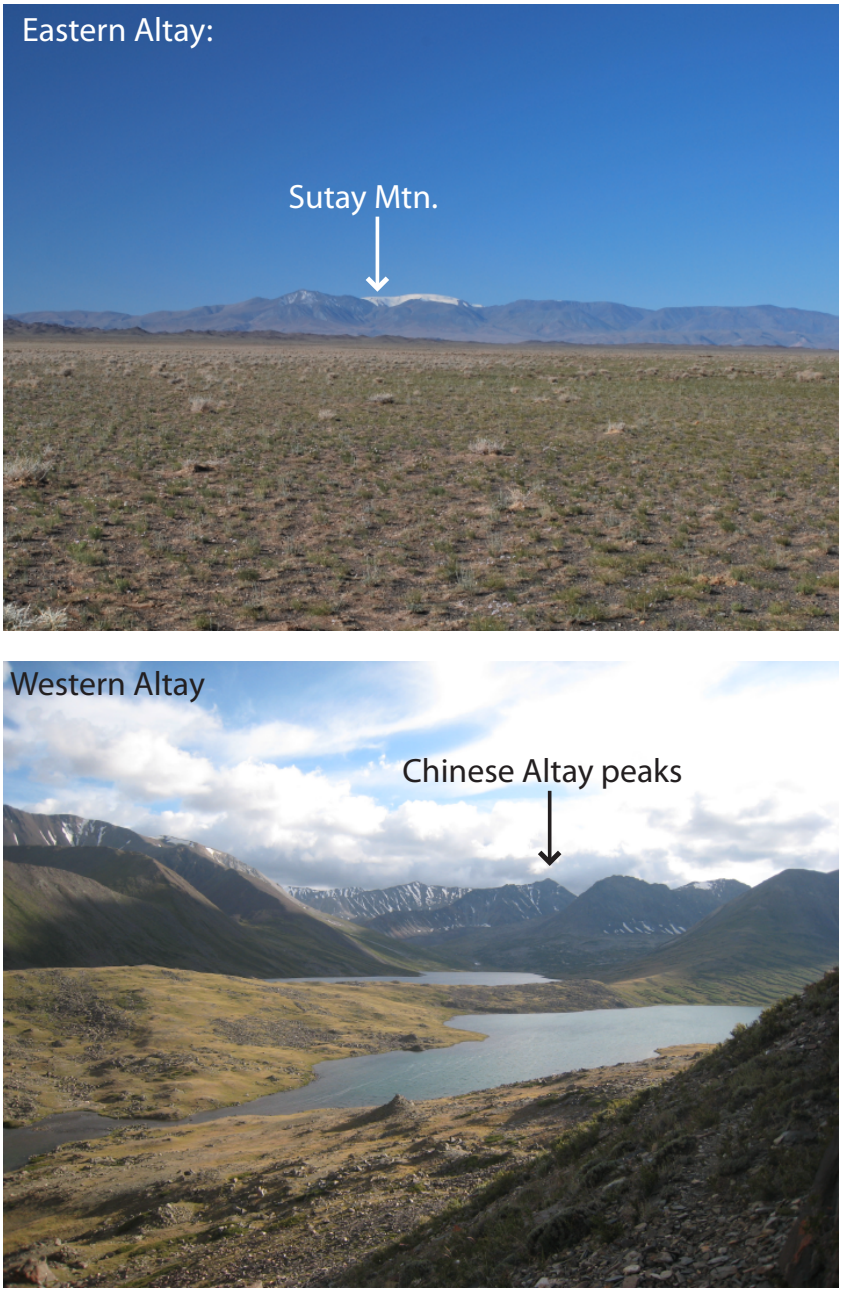


**Figure 5.1:** Photos that demonstrate the difference in morphology between the eastern and western mountains of the Altay. The upper panel shows Sutay mountain, one of the push-up mountains along the Har-Us-Nuur fault in the southeast Altay. Sutay is thought to be topped by a peneplain surface (though currently glaciated), and is relatively flat. The lower panel shows steep sided peaks of the Chinese Altay near the drainage divide, taken from the near the sampling locality of AFT sample ALT-25. The region is characterised by steep, U-shaped valleys and glacial moraines with abundant glacial lakes.

Cooling histories modeled from AFT results indicate rapid cooling in the late Miocene to early Pliocene from the Gobi-Altay and Siberian Altay (*De Grave and Van den haute*, 2002; *De Grave et al.*, 2007; *Jolivet et al.*, 2007; *Vassallo et al.*, 2007a; *De Grave et al.*, 2009), but these studies are limited to the very northern or south-eastern Altay. There are no results from the central Mongolian Altay, and older (Oligocene to early Miocene) cooling ages are reported for the western Altay (*Yuan et al.*, 2006). There is also a difference in the geomorphology of the mountains between the eastern and western Altay. The eastern Altay is characterised by dry climate, low erosion rates (e.g. *Nissen et al.*, 2009b), and individual mountain ranges or massifs. The western Altay experiences a wetter climate and has high, almost continuously mountainous topography with steeper sides and peaks, and few isolated massifs (Figure 5.1). These inconsistencies from west to east in cooling histories and geomorphology may arise from a few factors. Problems in modeling recent uplift with low temperature thermochronology and the simple lack of data in the Altay might result in an apparent discrepancy in the timing and patterns of late Cenozoic deformation across the region. A longstanding difference in climate across the E–W drainage divide may affect the uplift history of the range if erosion, and thus denudation, is significantly stronger in magnitude on the western side. It is also possible that the present topographic patterns could result from pre-existing topography in the western Altay or the migration of deformation from west to east (discussed in Chapter 2, *Nissen et al.*, 2009b). In this chapter, I test these hypotheses with AFT results from samples collected in the central Altay. Cooling histories from the central Altay, close to the drainage divide, allow for the comparison of the timing of deformation across the range, in order to infer whether the differences in results from west to east are due to tectonics, geomorphology, methodological problems, or any combination of these factors.

### 5.1.1 Geological history of the region

A detailed description of the geological history of the Altay is provided in Chapter 1, Section 1.4, but I briefly summarise the Phanerozoic geology of the region here. The Altay bedrock is a series of arc, ophiolite, and accretionary complex fragments amalgamated during the Palaeozoic, as part of the closure of the Palaeo-Asian Ocean and the long-standing assembly of central Asia against the Siberian craton (*Sengör et al.*, 1993). Several microcontinents and continental fragments of presumably late Precambrian age are suggested to make up portions of the Mongolian basement, particularly in central Mongolia, and these cratons are surrounded by fold and thrust complexes of late Precambrian to Paleozoic age (e.g. *Traynor and Sladen*, 1995; *Sengör and Natal'In*, 1996; *Badarch et al.*, 2002; *Windley et al.*, 2007; *Briggs et al.*, 2007; *Levashova et al.*, 2010). The Proterozoic and early Phanerozoic tectonics of central Asia formed a dominant structural grain that follows the various ancient arc and terrane boundaries (*Cunningham*, 1998). In Mongolia, this structural grain is oriented mostly NNW–SSE in the Altay, and it gradually bends to strike more E–W in the Göbi Altay.

During the Permian and throughout the Mesozoic, the region was also subjected to deformation from the increasingly distal amalgamation of central Asia, probably including the collision of the Lhasa block and the closure of the Mongol-Okhotsk Ocean in the Jurassic (e.g. *Yin and Nie*, 1996; *Dumitru and Hendrix*, 2001; *Badarch et al.*, 2002; *Briggs et al.*, 2009). The most recent tectonism in the area is attributed to the convergence between India and Asia, which is suggested to have initiated as long ago as approximately 30 Ma or as recently as 5 Ma.

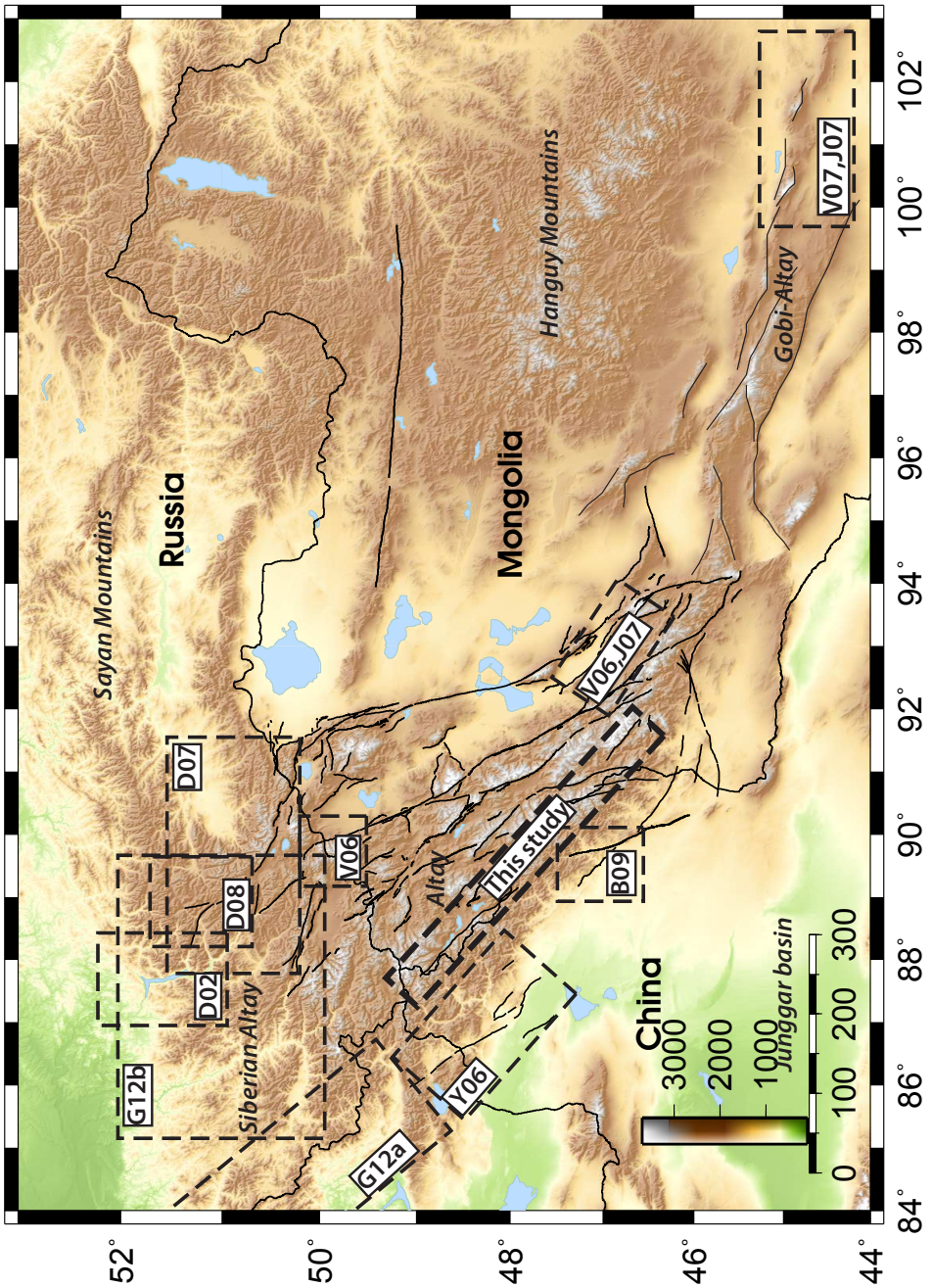


**Figure 5.2:** SRTM DEM shaded relief image of the Altay region (30 arc seconds/pixel), including the Gobi and Siberian Altay. Outlined rectangles indicate the general areas of prior thermochronologic work. Abbreviations are B09: *Briggs et al.* (2009), D02: *De Grave and Van den haute* (2002), D07: *De Grave et al.* (2007), D08: *De Grave et al.* (2008), G12a: *Glorie et al.* (2012a), G12b: *Glorie et al.* (2012b), J07: *Jolivet et al.* (2007), V06: *Vassallo* (2006), V07: *Vassallo et al.* (2007a), Y06: *Yuan et al.* (2006)

Cenozoic deformation due to the convergence between India and Asia has occurred in central Asia from the region north of the Tarim Basin to the Tien Shan and the Altay (e.g. *Tapponnier and Molnar*, 1979; *Sobel and Dumitru*, 1997; *Yin et al.*, 1998; *Jolivet et al.*, 2001; *Cunningham*, 2005). The exact timing of Cenozoic deformation in the Altay and Göbi Altay is unclear, and may have begun from as long ago as the Oligocene (*Howard et al.*, 2003, 2006; *Yuan et al.*, 2006; *Glorie et al.*, 2012b) to as recently as 5–10 Ma (*De Grave and Van den haute*, 2002; *Vassallo*, 2006; *Jolivet et al.*, 2007; *Vassallo et al.*, 2007a; *Buslov et al.*, 2008), or beginning in the Oligocene but intensifying in the Pliocene (*De Grave et al.*, 2007; *Glorie et al.*, 2012a). The sedimentary record begins to coarsen during the Oligocene in the neighboring Junggar, Dzereg, and Dariv basins on the western and eastern sides of the Altay, with sandstones and conglomeratic material potentially indicating the growth of nearby topography (*Yin et al.*, 1998; *Howard et al.*, 2003, 2006; *Chen et al.*, 2011). From low-temperature thermochronology, the discrepancy of at least 20 million years between different studies may be suggestive of west to east spatial growth of topography, with older cooling histories in the western Altay (*Yuan et al.*, 2006), and younger, more rapid cooling of the restricted push-up mountains in the eastern and Göbi Altay (e.g. *Jolivet et al.*, 2007; *Vassallo et al.*, 2007a, see Figure 5.2), though rapid uplift in the last 5 My has also been suggested in parts of the Siberian Altay to the north (*Buslov et al.*, 2008).

Many of the regions sampled are thought to preserve peneplain surfaces leveled during the Late Mesozoic to early Cenozoic, which have now been uplifted and preserved even in regions of high relief (∼1.5–2 km) as a result of low erosion and recent uplift (*Jolivet et al.*, 2007, described further in Chapter 1). The term peneplain is used to denote a a nearly featureless, gently undulating land surface of considerable area that has been produced by erosion almost to base level (e.g. *Hetzel et al.*, 2011; *Jackson*, 1997, cf.). Whilst the flat surfaces that top many of the high mountains in

the Altay generally fit the description of a peneplain, more information is necessary to determine the precise Cenozoic formation and history of the surfaces, particularly by quantifying erosion rates over geological time scales (e.g. *Strobl et al.*, 2012). Topography topped by peneplain surfaces suggests that the current relief represents the total (Cenozoic) uplift, because the highest elevations have not been significantly denuded, which is true only if the surfaces are validated as peneplains. Confirming the preservation of peneplains is important because topographic relief, where peneplains are preserved, may be essentially equal to total rock uplift (*England and Molnar*, 1990). If the high elevations have been significantly eroded, then it is not possible to unravel the impact of erosion on estimates of total rock uplift from low temperature thermochronology data. In the Altay, if the planation surfaces have been preserved, the low-temperature thermochronology systems used to suggest recent uplift have not been fully reset, because (with a typical geothermal gradient of 30°C/km) even rocks from the lowest elevations (1–2 km below the peneplain surface) were not at sufficiently high temperatures to completely record Cenozoic uplift.

## 5.2 AFT methods and sample collection

Apatite fission track techniques allow for the measurement of the thermal history of rocks on geologic timescales, based on the formation of damage zones ('fission tracks') in the crystal lattice of apatite grains due to the spontaneous nuclear fission decay of $^{238}$U (*Price and Walker*, 1963, see *Tagami and O'Sullivan* (2005) and references within for an updated review, as well as other articles within the same special issue). The duration of time that a rock has spent above a certain temperature is reflected in the density of fission tracks in apatite grains, relative to the uranium content of the grains. Fission tracks are not permanent features, and exposure to elevated temperatures causes a self-repair process known as annealing. Fission tracks in the crystal lattice are fully repaired in apatite at temperatures $>\sim$110–120°C if heating is

maintained for geological timescales, at which point the AFT system is reset (*Laslett et al.*, 1987; *Ketcham et al.*, 1999). Fission tracks are only partially annealed over a range of lower temperatures, which is termed the partial annealing zone (PAZ). Within the PAZ for apatite of between 110° ± 10° to 60°C, annealing takes place at a rate that is dependent on the temperature and the duration of time that the rock remains in the PAZ. The density of tracks, and thus the estimated age, is a function of the mean track length in the sample, since track length controls the probability of a track intersecting the plane of observation. For reasonably long mean track lengths ($> 13\mu$m) an age can be viewed as a crude measure of when the sample cooled through the PAZ, but shorter mean track lengths have experienced a more complex cooling history. For this reason modeling AFT age and length data are needed to understand the true nature of the sample cooling history.

More than one method has been developed for making fission track measurements, and I describe the external detector method (EDM), which I used to analyse bedrock samples from the Altay. The specific analytical procedure that was applied to the Altay samples is described below, but first I provide a general summary of EDM counting and AFT age calculations. The aim of the EDM for counting is to directly measure the density of spontaneous, fossil tracks in multiple grains in a sample, and to determine the concentration of uranium in the same grains that are counted, so that the density of fossil tracks can be directly related to the uranium content, and the distribution of uranium, in each grain that is counted. In order to measure the spontaneous tracks, apatite mineral separates are mounted in epoxy and polished to expose the internal mineral surfaces. This avoids contamination by implantation of tracks from uranium that is external to the apatite grain. Since fission tracks are very small, they must be enlargened by chemical etching in order to observe tracks by conventional optical microscopy (Figure 5.3, *Price and Walker*, 1962). Once etched, the apatite grain mount represents a record of spontaneous fission decay, i.e.

the daughter product of uranium in the sample. Therefore age determination also requires measurement of the parent isotope. This is achieved by using an external detector to record fission tracks produced by activation of the uranium atoms in the sample apatite grains. The detector is a thin sheet of mica attached to the surface of each grain mount, and grain mount-detector pairs are packaged together with glass standard 'dosimeters' to be irradiated at a well-thermalised reactor. The samples are bombarded by thermal neutrons, causing fission tracks to be induced in the mica detector from contact with the apatite grain surfaces, and the density of induced tracks on the mica is therefore the result of the uranium content at the surface of the apatite grains. The density of tracks on the detector for the glass dosimeter packaged with the samples, which contains a known concentration of uranium, provides a measure of the neutron flux that the samples experience.

The mica detectors are etched after cooling, and mounted next to the apatite grain mount. The induced tracks on the mica detectors reflect the amount and distribution of uranium in the apatite grains. The outlines of grains are a mirror image of the grain mount, and an automated stage attached to a good quality optical microscope allows for the precise location of grains relative to their track print on the mica (Figure 5.4). The density of spontaneous tracks $\rho_s$ and induced tracks $\rho_i$ can then be determined for the same area on each grain counted, in order to solve the age equation below (Equation 5.1). The analyst must be careful to avoid non-track features on the grain surface, and to count portions of the grains that have a homogeneous uranium distribution, which can be determined from the pattern of tracks on the mica detector for any grain. The dosimeter track density $\rho_d$ must also be determined.

The age equation for the EDM counting is:

$$t_i = \frac{1}{\lambda_d} ln \left( 1 + \lambda_d \zeta g \rho_d \frac{\rho_{s,i}}{\rho i, i} \right) \tag{5.1}$$

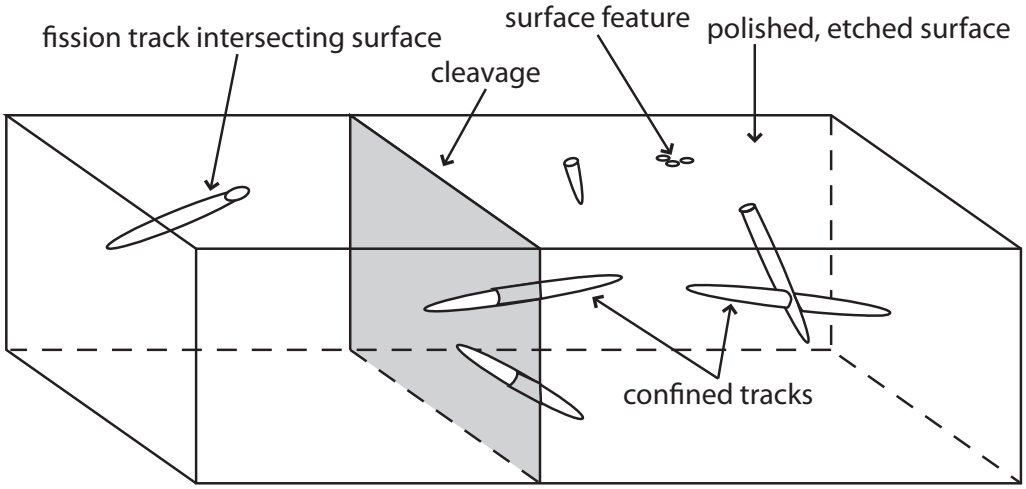


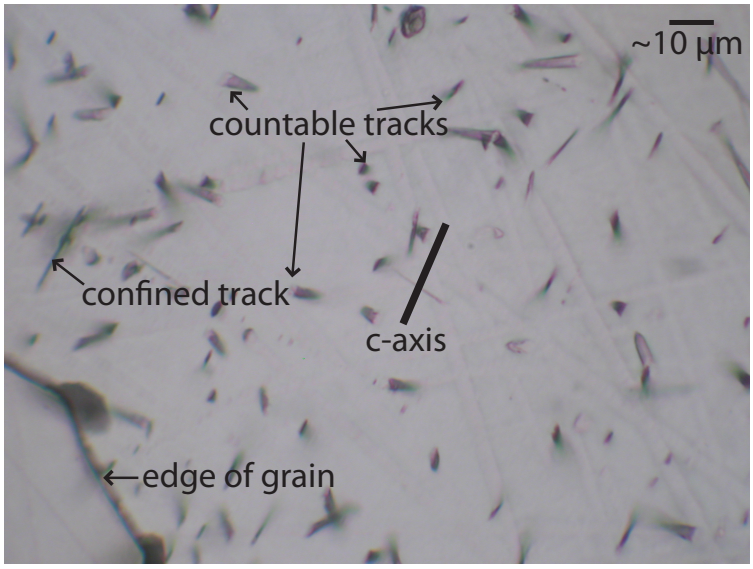


**Figure 5.3:** Schematic diagram for the different tracks revealed by etching a polished apatite grain, based on Figure 10 in *Tagami and O'Sullivan* (2005). Tracks intersecting the surface are counted, while surface features that are not tracks must be avoided. Confined tracks that intersect other tracks should be measured for track length determinations. Tracks intersecting cleavage may have been artificially expanded by the opening of cleavage and should be avoided if possible. Lower panel shows a grain from sample ALT-39, with confined tracks and countable tracks intersecting the grain surface indicated.

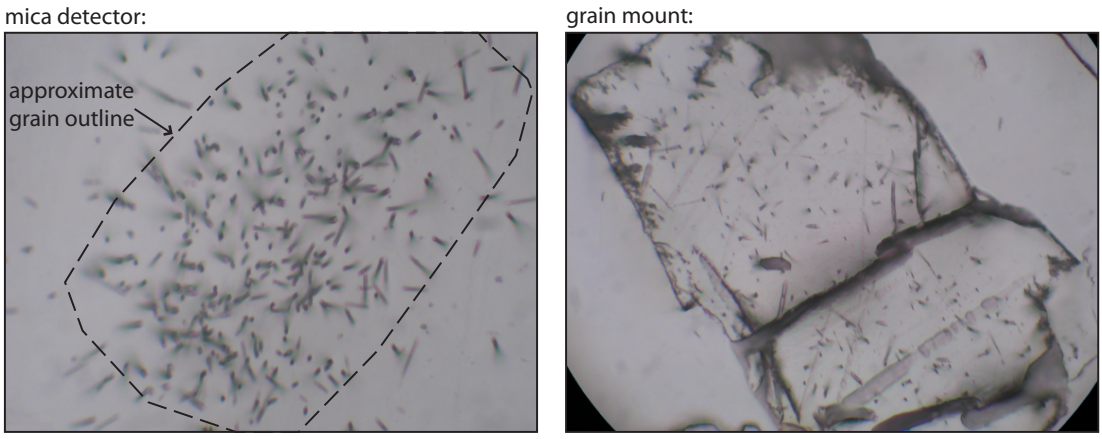


**Figure 5.4:** Photos of etched tracks on mica print (left), which mirrors the apatite grain on the right. Based on the shape of the grain, tracks from the same area on the grain can be counted on the mica. It is noted that the mica image is an example of poor contact between the detector and the grain, and should not be counted.

where $i$ is a single measured apatite grain, $t_i$ is the fission track age of grain $i$ in years, $\lambda_d$ is the decay constant of $^{238}$U (1.55125 x $10^{-10}$ $a^{-1}$, *Jaffey et al.*, 1971), $\zeta$ is a unique user-specific calibration factor determined based on EDM counting of fission track age standards ($zeta = 325 \pm 11.6$ or $338 \pm 5$ for analyses presented in this chapter, determined based on methods outlined in *Hurford*, 1990), and $g$ is a geometry factor, equal to 0.5 based on the $4\pi/2\pi$ geometry of tracks measured on a polished apatite surface, which contains tracks from above the surface (from material that is removed during polishing) and below the surface (from the lower part of the apatite grain that remains on the mount after polishing, e.g. *Laslett et al.*, 1984; *Donelick et al.*, 2005). $\rho_{s,i}$ is the spontaneous fission track density measured in the grain, equal to $(N_{s,i}/\Omega_i)$ where $N_{s,i}$ is the number of tracks counted over area $\Omega_i$ (tracks $cm^{-2}$), and $\rho_{i,i}$ is the induced fission track density, equal to $(N_{i,i}/\Omega_i)$ where $N_{i,i}$ is the number of tracks counted over area $\Omega_i$ on the mica detector (tracks $cm^{-2}$). The symmetric error for a single grain AFT age is:

$$\sigma_i = \left[\frac{1}{N_{s,i}} + \frac{1}{N_{i,i}} + \frac{1}{N_d} + \left(\frac{\sigma_\zeta}{\zeta}\right)^2\right]^{1/2} \tag{5.2}$$

where $N_i$ is the number of tracks counted from the uranium standard for calculating $\rho_d$, and $\sigma_\zeta$ is the error of $\zeta$. The pooled AFT age ($t_{pooled}$) for a population of grains in a sample is:

$$t_{pooled} = \frac{1}{\lambda_d} ln \left( 1 + \lambda_d \zeta g \rho_d \frac{\sum N_{s,i}}{\sum N_{i,i}} \right) \tag{5.3}$$

and the uncertainty of the pooled age is:

$$\sigma_{pooled} = \left[ \frac{1}{\sum N_{s,i}} + \frac{1}{\sum N_{i,i}} + \frac{1}{N_d} + \left( \frac{\sigma_\zeta}{\zeta} \right)^2 \right]^{1/2} \tag{5.4}$$

Further discussion of the derivation of the equations is provided by *Hurford* (1990), *Tagami and O'Sullivan* (2005), and *Donelick et al.* (2005).

The data from a population of grains in a sample are reported as the central age, which is equivalent to the pooled age when the distribution of single grain ages has a Poisson distribution. However, over dispersion of the single grain ages can occur due to bad counting, bad contact between the grain and the mica detector, or to differences in grain annealing rates due to variable compositions of apatites from a single sample. The central age provides a percentage measure of the dispersion amongst the single grain ages, and when there is over dispersion in the data, assuming a good experiment, the results must be interpreted by taking into account differences in apatite compositions.

Confined track lengths are measured in the same grains that are counted for age determination, in order to model the distribution of track lengths with sample age (although if there is good confidence that the sample has a single age population, lengths can be measured in other grains). There are two types of confined tracks that are revealed during etching, based on the feature that they intersect: tracks in tracks (TINTs) and tracks in cleavage (TINCLEs, Figure 5.3). All track length measurements are made on horizontal tracks (*Laslett et al.*, 1982), mainly from TINTs, because TINCLEs may be artificially lengthened by the opening of cleavage; also

because cleavage and fractures tend to have a preferred grain orientation, TINCLE data can introduce a length-angle bias. An etched un-annealed track in apatite has a mean length of 16 $\mu$m, and any features significantly longer than this are not fission tracks. The orientation of the track relative to the crystallographic axis must be measured as well, in order to minimise the effects of etching efficiency relative to track orientation and anisotropic track annealing. A minimum of 50–100 tracks must be measured in a sample for thermal history modeling. A full description of the biases, both user- and naturally-introduced, in track length measurements and AFT counting is provided by *Donelick et al.* (2005).

Bias in thermal history models may arise from apatite compositional effects on annealing rates, which affect the distribution of measured track lengths (e.g. *Barbarand et al.*, 2003; *Donelick et al.*, 2005). Apatite is a phosphorus-bearing mineral and has the following general chemical formula: $Ca_5(PO_4)_3$[F,Cl,OH]. End member compositions arise from exchange between the three anions (F, Cl, and OH), to form fluorapatite, chlorapatite, and hydroxyapatite. The most common apatite found in nature is fluorapatite, but chlorapatites and other compositions are also frequently found. The kinetics of annealing, as well as etching characteristics, are dependent on the composition of the apatite, and must be considered when measuring and modeling confined track lengths. Cl content in particular is correlated with annealing kinetics, with the general association of a higher closure temperature with greater Cl content. Several measurable kinetic parameters can be used to evaluate the potential effect of Cl content (as well as other kinetic effects), although they are not to be used as a direct proxy. The length of etch pits on the grain surface, called $D_{par}$, is one common kinetic parameter, and is known to be positively correlated with Cl weight percent (*Donelick*, 1993). However the association of $D_{par}$ with kinetic properties is not fully understood and may be affected by other element substitutions leading to a variety of apatite compositions and changes in annealing parameters (*Barbarand*

*et al.*, 2003). $D_{par}$ should be used as a guideline and a warning of compositional controls on annealing if $D_{par}$ is particularly large. Typical $D_{par}$ values of 1.5 $\mu$m–3.0 $\mu$m are generally indicative of apatites with low Cl weight percent, but again this is not always the case (*Carlson et al.*, 1999; *Ketcham et al.*, 1999).

Problems with counting AFT samples may also occur due to the quality of the apatite grains. The area chosen for counting must be relatively free of surface defects and cannot include large cracks due to cleavage. Low or zoned uranium content is also problematic; with low U content, there will not be sufficient tracks induced on the mica detector for determining $\rho_i$, and if the U content is zoned, a large enough area with consistent track densities will not be found. The quality of apatites in samples from the Altay is often very poor (e.g. *Nissen*, 2008), with significant cracks and inclusions, as well as low and zoned U content (Figure 5.5). As a result, despite obtaining sufficient apatite in mineral separates for nearly 80% of the Altay samples collected in 2009, less than 50% of the samples with apatite separates could be counted.

### 5.2.1 Analytical Methods and Samples

Forty-two samples were collected for fission-track analysis from a NW–SE directed transect along the eastern side of the Altay drainage divide and the Mongolian-Chinese border (Figure 5.6, Table 5.1). Vertical transects were collected where possible, and the general aim was to collect as many samples as possible from the lower parts of the mountain valleys or the hanging walls of major thrust faults in order to capture the deepest rocks, which are most likely to have the fission-track system partially 'reset' by heating in the PAZ since the Cretaceous (see Section 5.1.1). Vertical transects that yielded results were taken from Tavanbogd and Monh Hyarhan Mountains (Figure 5.7). A vertical transect up a large massif can often reveal the cooling rate due to uplift on the bounding fault system. Ideally a difference of least 2000 m

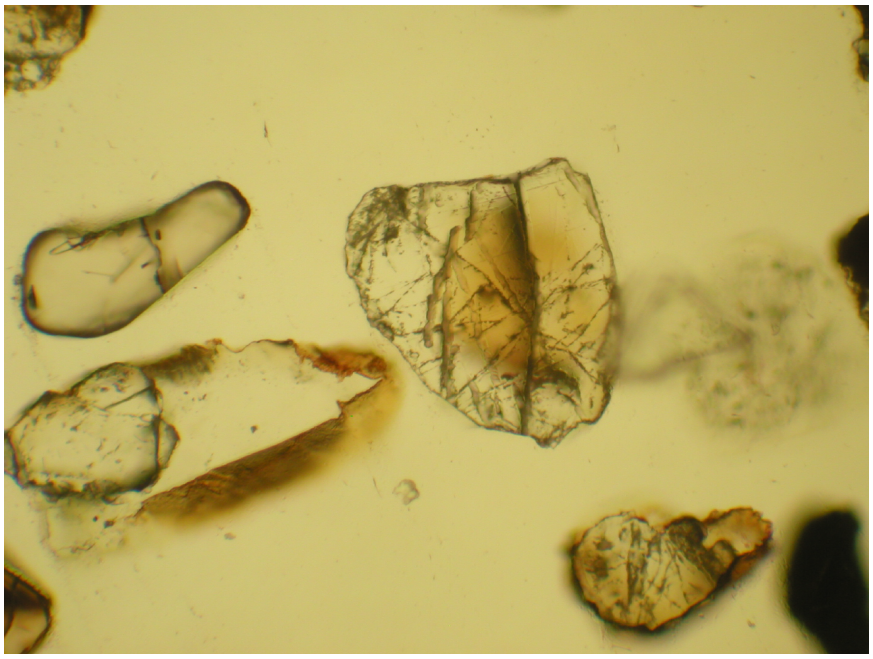

**Figure 5.5:** Photo of a poor quality apatite grain from sample ALT-8. The numerous cracks and defects in the surface makes it difficult to find a clear part of the grain large enough for reliable counting, and there are almost no fission tracks observed because of low U content (confirmed by the mica prints for this sample, which have very low track density). This sample could not be measured.

between the upper- and lower-most samples is required, though this was difficult to obtain in the Altay due to sparse outcrop at the base of major mountains.

Samples were crushed, milled, rinsed, sieved, and put through standard liquid and magnetic separation techniques in order to obtain concentrated apatite separates. Thirty-one samples had sufficient apatite to continue with processing and irradiation, following standard procedures for the London Fission Track Research Group (e.g. *Hurford and Carter*, 1991). Apatites were mounted in epoxy on glass, and etched in 5 N $HNO_3$ at 20°C for 20 s followed by vigorous rinsing in water. Grain mounts were polished to reveal apatite grains, then mounts were packed with mica external detectors and Corning glass (CN5) dosimeters and irradiated at the FRM 11 thermal neutron facility at the University of Munich, Garching, Germany. Fission-track densities from thirteen samples were measured on grain mounts, mica detectors,

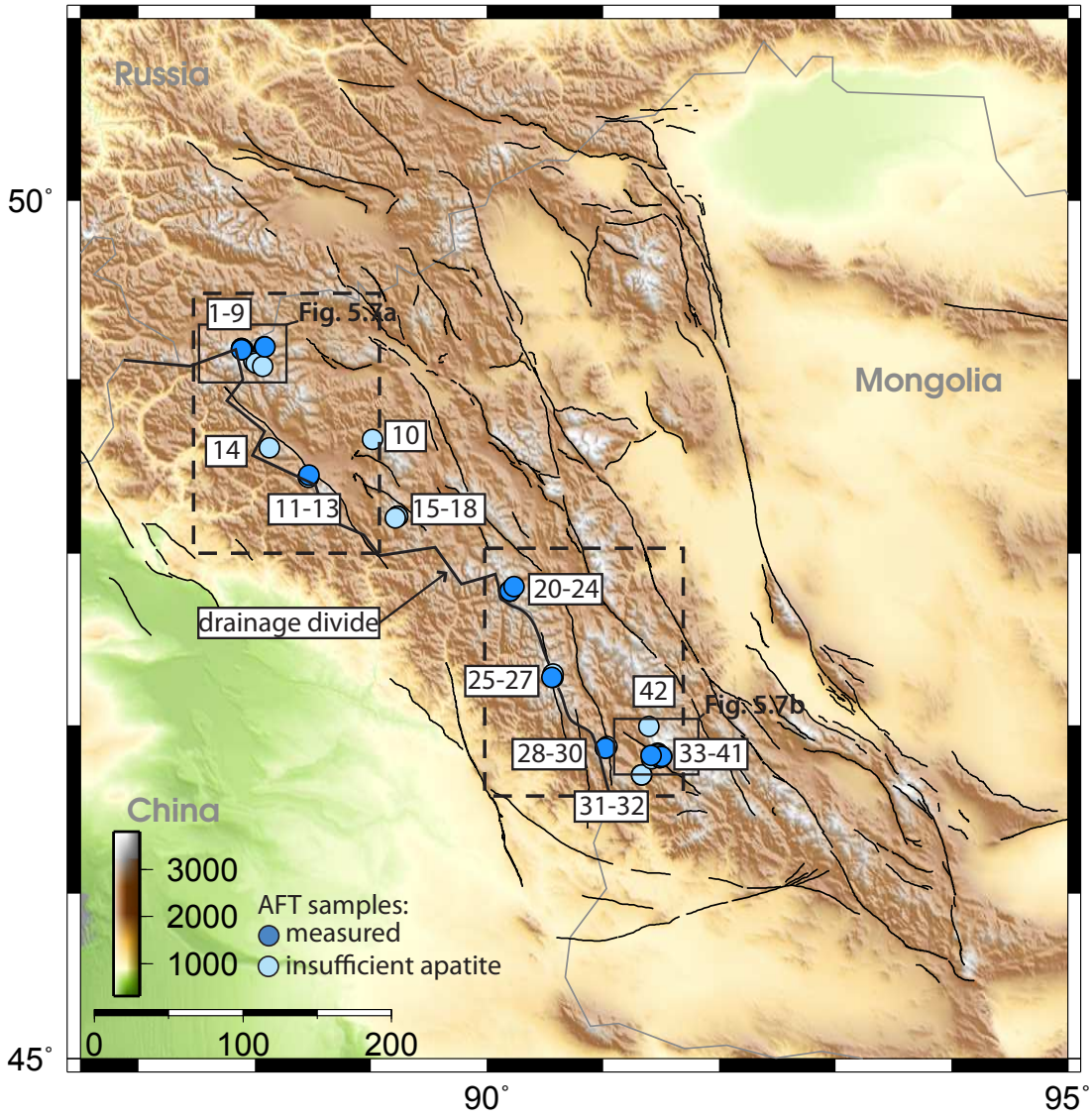


**Figure 5.6:** SRTM DEM of the Altay with sample numbers labeled and indicated by blue circles. Samples were collected in a transect along the drainage divide of the Central Altay. Light blue circles indicated samples that were collected, but either did not contain sufficient apatite or good enough quality apatite to be measured, or were sampled in proximity to another sample. Darker blue samples indicate measured samples discussed in this chapter. Dashed rectangles indicate the localities of the northern and southern panels in Figure 5.12, solid rectangles indicate locations of Figure 5.7.

and dosimeters using an optical microscope at 1250x magnification. Central ages are reported, but will be the same as ages calculated using Equation 5.3, with $1\sigma$ uncertainties from Equation 5.4, if there is no significant dispersion in the grain ages. Track lengths were measured when the density of tracks in apatite grains was sufficient to have revealed TINTs, and only samples with at least 60 track length measurements have been used in the thermal history measurements. I counted the majority of the measurable samples (based on a zeta factor of 325 $\pm$ 11.6), aside from three more difficult samples (ALT-2, 4, and 24), which were counted by A. Carter (using a zeta factor of 338 $\pm$ 5). My zeta calibration was determined based on the analysis of 13 standard samples (including Durango, Mt. Dromedary, and Fish Canyon apatite standards, see *Hurford*, 1990, for zeta calibration techniques).

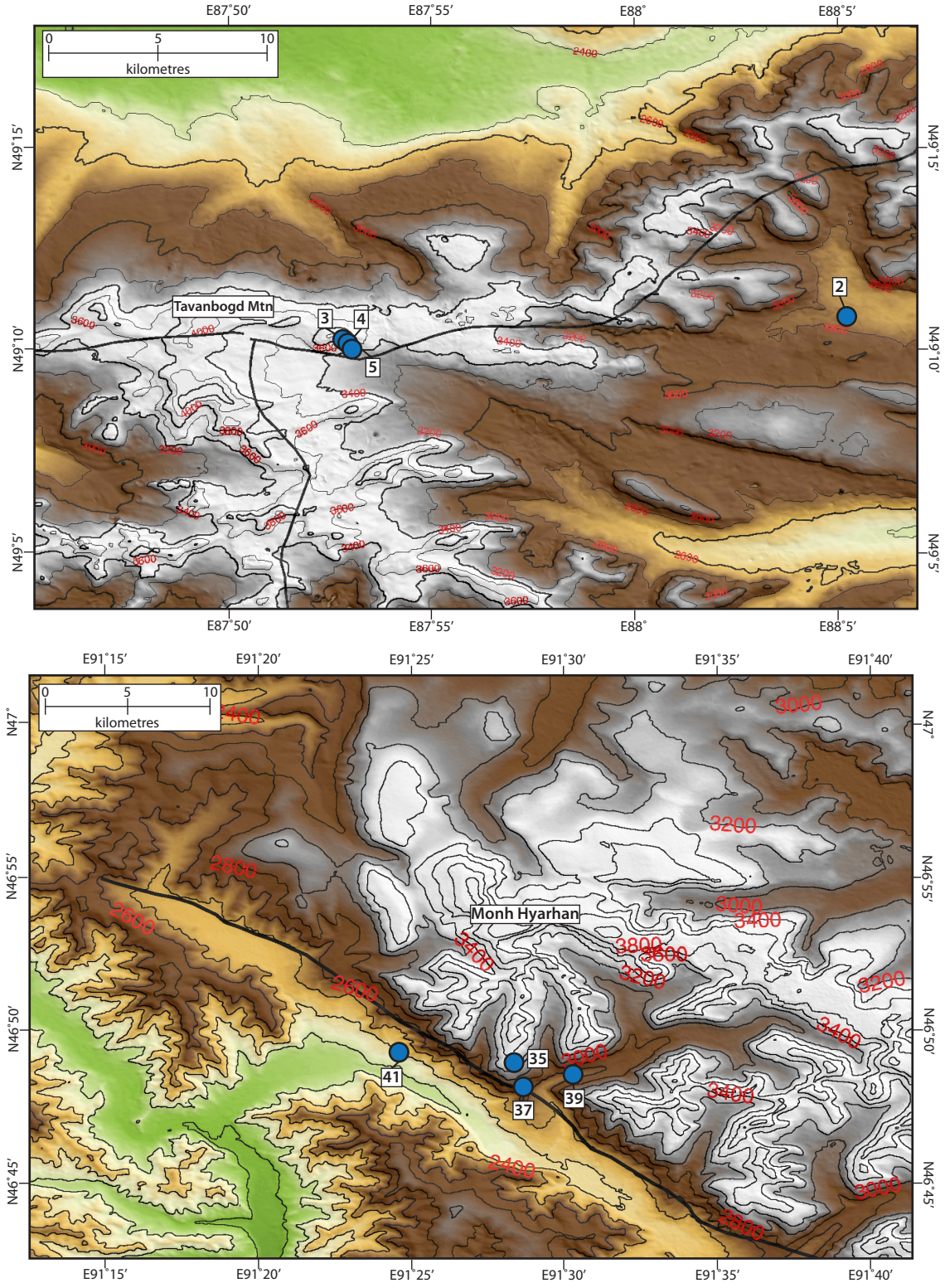


**Figure 5.7:** ASTER GDEM image (30m/pixel) of the two vertical transects of AFT samples that yielded results. Samples numbers are labeled and indicated by blue circles. Transects were made on Tavanbogd Mountain (a) and Monh Hyarhan Mountain (b).

**Table 5.1:** AFT samples

| Sample | Latitude (°N) | Longitude (°E) | Elevation (m)[a] | Lithology | Region | Analysed |
|---|---|---|---|---|---|---|
| ALT-01 | 49.1812 | 88.0829 | 2752 | Meta-sandstone | Tavanbogd Mtn | |
| ALT-02 | 49.1826 | 88.0891 | 2732 | Meta-sandstone | Tavanbogd Mtn | x |
| ALT-03 | 49.1713 | 87.8846 | 3852 | Granodiorite | Malachin peak | x |
| ALT-04 | 49.1712 | 87.8850 | 3845 | Granite | Tavanbogd Mtn | x |
| ALT-05 | 49.1660 | 87.8876 | 3417 | Granite | Tavanbogd Mtn | x |
| ALT-06 | 49.1656 | 87.9019 | 3281 | Sandstone | Tavanbogd Mtn | |
| ALT-07 | 49.1003 | 87.9899 | 2733 | Siltstone | Tavanbogd Mtn | |
| ALT-08 | 49.0908 | 88.0095 | 2619 | Sandstone | Tavanbogd Mtn | |
| ALT-09 | 49.0710 | 88.0671 | 2675 | Meta-sediment | Tavanbogd Mtn | |
| ALT-10 | 48.6560 | 89.0129 | 2440 | Schist | Tsenger Hyarhan | |
| ALT-11 | 48.4419 | 88.4603 | 2365 | Schist | Hoton Nuur | |
| ALT-12 | 48.4409 | 88.4639 | 2362 | Schist | Hoton Nuur | |
| ALT-13 | 48.4522 | 88.4672 | 2295 | Schist | Hoton Nuur | x |
| ALT-14 | 48.6102 | 88.1257 | 2368 | Granite | Zagast Gol | |
| ALT-15 | 48.2159 | 89.2304 | 2467 | Quartzite | Chigerty Nuur | |
| ALT-16 | 48.2156 | 89.2311 | 2500 | Felsic dyke | Chigerty Nuur | |
| ALT-17 | 48.2167 | 89.2295 | 2442 | Granodiorite | Chigerty Nuur | |
| ALT-18 | 48.2055 | 89.2084 | 2572 | Granodiorite | Chigerty Nuur | |
| ALT-19 | 47.7837 | 90.1994 | 2525 | Granite | Chigerty Nuur | |
| ALT-20 | 47.7844 | 90.2007 | 2547 | Schist | Chigerty Nuur | |
| ALT-21 | 47.7843 | 90.2008 | 2553 | Granite | Chigerty Nuur | |
| ALT-22 | 47.7843 | 90.2010 | 2553 | Granite | Chigerty Nuur | x |
| ALT-23 | 47.7843 | 90.2010 | 2557 | Granite | Chigerty Nuur | |
| ALT-24 | 47.8103 | 90.2344 | 2526 | Diorite | Chigerty Nuur | x |
| ALT-25 | 47.2799 | 90.5581 | 2777 | Granite | Bulgan Gol | x |
| ALT-26 | 47.2795 | 90.5684 | 2738 | Schist | Bulgan Gol | |
| ALT-27 | 47.2987 | 90.5684 | 2775 | Meta-sediment | Bulgan Gol | |
| ALT-28 | 46.8648 | 91.0187 | 2320 | Gneiss | Monh Hyarhan | |
| ALT-29 | 46.8646 | 91.0185 | 2325 | Gneiss | Monh Hyarhan | x |
| ALT-30 | 46.8736 | 91.0352 | 2220 | Schist | Monh Hyarhan | |
| ALT-31 | 46.7068 | 91.3320 | 1741 | Pegmatite | Bulgan Gol | |
| ALT-32 | 46.7070 | 91.3327 | 1729 | Schist | Bulgan Gol | |
| ALT-33 | 46.8344 | 91.4728 | 3766 | Schist | Monh Hyarhan | |
| ALT-34 | 46.8287 | 91.4715 | 3626 | Quartzite | Monh Hyarhan | |
| ALT-35 | 46.8164 | 91.4707 | 3331 | Meta-sediment | Monh Hyarhan | x |
| ALT-36 | 46.8096 | 91.4866 | 2802 | Gneiss | Monh Hyarhan | |
| ALT-37 | 46.8073 | 91.4886 | 2566 | Gneiss | Monh Hyarhan | x |
| ALT-38 | 46.8152 | 91.5063 | 2670 | Gneiss | Monh Hyarhan | |
| ALT-39 | 46.8150 | 91.5061 | 2652 | Gneiss | Monh Hyarhan | x |
| ALT-40 | 46.8029 | 91.4192 | 1992 | Granite | Monh Hyarhan | |
| ALT-41 | 46.8204 | 91.4148 | 2065 | Granite | Monh Hyarhan | x |
| ALT-42 | 46.9921 | 91.3933 | 3206 | Granite | Monh Hyarhan | |

[a]Typical hand held GPS vertical uncertainties are 10–15 m

## 5.3 Results

The track densities, central ages and counting statistics for all 13 samples analysed are listed in Table 5.2, and the central ages are plotted against elevation in Figure 5.8. The central ages are (mostly) late Cretaceous, with one sample of Paleocene age, ranging from 93.1 ± 4.2 to 60.2 ± 2.4 Ma. Two samples have abnormally high age dispersion and low percent $\chi^2$ values that fail the $\chi^2$ test, which is essentially a test of the variation of the age distribution and indicates over dispersion if $\chi^2$ is $< 5\%$ (samples ALT-22 and ALT-35, Table 5.2). These samples are not significant outliers, as the central age and mean track length data are not inconsistent with results from other samples. Failure to pass the $\chi^2$ test generally comes from extra Poissonian variation amongst the measured grains in a sample, which may arise from grains sourced from different populations (e.g. in sedimentary or metamorphic rocks), compositional variations, or poor counting technique. The samples do not have any indication of compositional control on grain ages (from $D_{par}$ measurements, Table 5.2), and apatites in the samples are unlikely to have a variable source, although ALT-35 is a meta-sedimentary rock (ALT-22 is granitic). Relatively fewer grains were counted for these two samples— generally the analyst aims to count at least 20 grains, but fewer grains are counted if the samples lack suitable grains for counting (e.g. Section 5.2). Because there is no indication that the samples are outliers of the dataset, I include them in discussion of the results below.

A simple cooling history often results in a strong correlation between elevation and age, because rocks at higher elevations will have an older apparent AFT age as a result of passing through the PAZ earlier than rocks at the base of the same tectonic package (e.g. *Brown et al.*, 1994). However, in general samples from the Altay do not show a simple correlation (Figure 5.8). Samples collected from the highest elevations have old AFT ages, but there is no distinct trend for all of the samples in the plot of age versus elevation, even within vertical profiles sampled on

**Table 5.2:** AFT analytical data

| Sample[a] | No. Grains | $\rho_d^b$ | $N_d$ | $\rho_s^c$ | $N_s$ | $\rho_i^d$ | $N_i$ | $P(\chi^2)^e$ | % AD[f] | Central age (Ma ± 1$\sigma$) | $D_{par}$ $\mu$m | MTL[g] ($\mu$m ± 1$\sigma$) | Std. dev. of MTL | No. tracks for MTL |
|---|---|---|---|---|---|---|---|---|---|---|---|---|---|---|
| ALT-02 | 20 | 1.398 | 7750 | 0.994 | 515 | 3.057 | 1601 | 4.58 | 15.2 | 75.4 ± 4.8 | 2.07 | 13.2 ± 0.16 | 1.39 | 80 |
| ALT-03 | 23 | 1.445 | 8012 | 3.260 | 2299 | 8.342 | 5804 | 77.30 | 0.4 | 92.3 ± 2.5 | 2.29 | 13.4 ± 0.10 | 1.13 | 130 |
| ALT-04 | 20 | 1.398 | 7750 | 2.125 | 1125 | 5.819 | 3225 | 11.26 | 9.3 | 82.6 ± 3.5 | 1.98 | 14.3 ± 0.15 | 1.30 | 80 |
| ALT-05 | 12 | 1.445 | 8012 | 0.650 | 186 | 1.601 | 504 | 42.58 | 0.5 | 86.1 ± 7.4 | 2.05 | 12.3 ± 1.19 | 3.36 | 8 |
| ALT-13 | 17 | 1.398 | 7750 | 1.101 | 399 | 3.522 | 1337 | 85.39 | 0 | 67.4 ± 3.9 | 1.55 | 11.8 ± 0.33 | 1.66 | 25 |
| ALT-22 | 12 | 1.445 | 8012 | 1.243 | 191 | 3.803 | 642 | 0.19 | 33.8 | 70.8 ± 9.3 | 1.88 | 13.5 ± 0.38 | 1.24 | 11 |
| ALT-24 | 20 | 1.398 | 7750 | 0.387 | 292 | 1.223 | 940 | 7.27 | 20.3 | 75.1 ± 6.3 | 1.98 | 14.4 ± 0.91 | 1.29 | 2 |
| ALT-25 | 21 | 1.445 | 8012 | 2.420 | 880 | 9.149 | 3425 | 15.95 | 3.5 | 60.2 ± 2.4 | 1.83 | 11.9 ± 0.19 | 1.88 | 101 |
| ALT-29 | 11 | 1.406 | 7796 | 1.277 | 281 | 3.265 | 704 | 88.86 | 0 | 90.6 ± 6.5 | 1.80 | 12.6 ± 0.49 | 2.23 | 21 |
| ALT-35 | 14 | 1.398 | 7750 | 3.008 | 2327 | 7.305 | 5627 | 0.02 | 12.8 | 93.1 ± 4.2 | 2.03 | 13.6 ± 0.13 | 1.40 | 112 |
| ALT-37 | 15 | 1.406 | 7796 | 2.042 | 1197 | 5.204 | 3103 | 14.07 | 7.4 | 87.3 ± 3.6 | 2.29 | 12.9 ± 0.15 | 1.64 | 113 |
| ALT-39 | 23 | 1.445 | 8012 | 1.395 | 1374 | 3.931 | 4034 | 77.36 | 0 | 79.5 ± 2.6 | 2.20 | 12.9 ± 0.24 | 1.85 | 61 |
| ALT-41 | 16 | 1.398 | 7750 | 0.796 | 334 | 72.041 | 861 | 51.92 | 0.7 | 87.5 ± 5.7 | 2.00 | 14.0 ± 0.36 | 1.79 | 25 |

[a]Latitude, longitude, and elevation are listed in Table 5.1.
[b]$\rho_d$ and $N_d$ denote the average density and total number of tracks induced on the mica detector of the dosimeter.
[c]$\rho_s$ and $N_s$ denote the average density and total number of spontaneous tracks on apatite grains in a sample.
[d]$\rho_i$ and $N_i$ denote the average density and total number of induced tracks on the mica detector for a sample.
[e]$P(\chi^2)$ is a measure of the Poissonian variation in a sample, $< 5\%$ indicates overdispersion, which may be due to counting errors or multiple age populations in a sample (*Galbraith*, 1981).
[f] % AD is the percentage of age dispersion in a sample.
[g]MTL is the mean track length.

Tavan Bogd and Monh Hyarhan massifs (Figure 5.7). Old AFT ages are measured in samples collected at low elevations, and young AFT ages are measured in samples collected from elevations over 2500 m. Because the entire region has a relatively high elevation (>1500 m), there is scant bedrock at elevations less than 2000 m, which limits the relief that is possible to sample to ∼1500 m. There is also a lack of correlation between mean track length (MTL) and age, other than the shortest MTLs are measured in the youngest samples (Figure 5.8).

The lack of correlation between elevation and central age suggests that the elevation of topography at the present day is not closely related to the Mesozoic exhumation history of the region. In other words, samples that reached the most shallow levels in the crust in the past are not necessarily at the present highest elevations, and some relative change in position in the rock column between samples may have occurred, but the resolution of the dataset does not permit any detailed interpretations. A lack of correlation between age and elevation may also arise if the palaeo-geothermal gradient was low, in which case the amount of exhumation that has occurred is not sufficient to show age offsets. In order to place better constraints on the regional cooling in the Altay, I apply a numerical inverse model of the thermal history of samples with sufficient track length data in the next section.

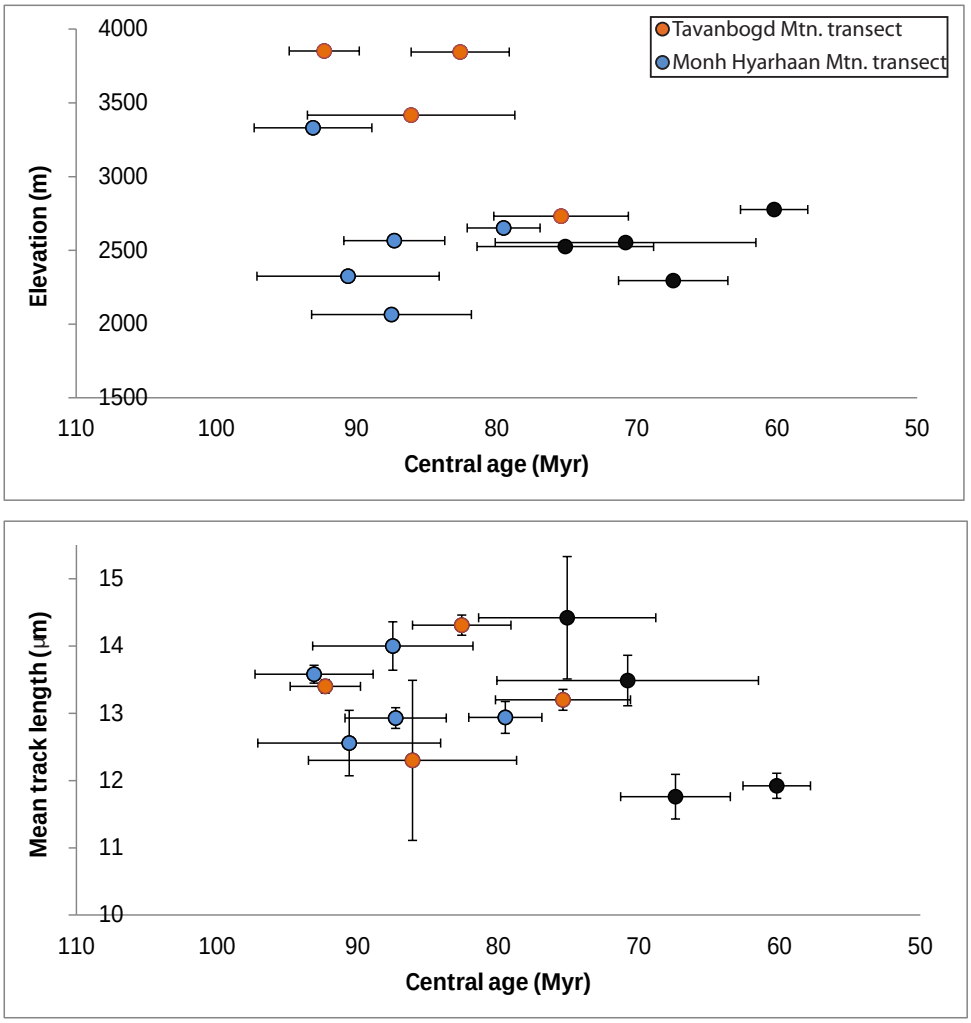


**Figure 5.8:** Plot of age versus elevation (upper panel) and mean track length (lower panel) for AFT samples analysed. There is not a consistent relationship between age and elevation, other than the highest elevated samples are amongst the oldest. The same is true for MTL and age— there is no correlation, other than that the youngest samples have the shortest MTL. The two transects that were measured are indicated by coloured symbols and maps of the sample transects are shown in Figure 5.7.

## 5.4 Thermal History Models and Discussion

The thermal histories of samples were modeled using the HeFTy program based on fission track length and age data for samples that have sufficient track length measurements (*Ketcham*, 2005). The HeFTy inverse model provides a set of statistical best-fit cooling histories for the input track length and age measurements, based on

Monte Carlo simulations. The annealing model of *Ketcham et al.* (2007) was used, which takes into account compositional variation amongst samples and the angle of confined tracks relative to the crystallographic axis of a mineral grain. Because the composition of the grain and the orientation of tracks relative to the c-axis have a significant effect on annealing, the *Ketcham et al.* (2007) model improves agreement between empirical annealing models and measurements, as well as removing the anomalous late cooling events that often resulted from the first AFT annealing models (e.g. *Laslett et al.*, 1987).

In HeFTy, 'good' fit thermal history paths are determined when the predicted model path length distribution fits the measured distribution, to a degree predicted by the Kolmogorov-Smirnov (K-S) probability test (see *Ketcham et al.* (2000) for a full description of the K-S test utilised in HeFTy). The K-S test compares the cumulative distribution functions (cdf) of both the modeled and measured track distributions, and also takes into account the number of measured tracks. The result of the K-S test is essentially the 'probability of a worse fit' of a random sampling of the modeled track length distribution from that which was measured. 'Acceptable' fit paths are those that cannot be ruled out as being sufficiently close to the data distribution. 'Good' fit paths are those that fit what would be predicted by a random sampling of the measured data.

In HeFTy models, the initial track length was set based on the average $D_{par}$ measured in each sample (between 1.55–2.29, Table 5.2), and was close to 15.95 $\mu$m for all samples. Each model is then set up following recommendations in *Ketcham et al.* (2000) and *Ketcham* (2005). The model constraints are chosen to be as simple as the data that are being modeled, such that added complexity is not invoked when interpreting the models. Initial conditions are set by picking points and drawing boxes surrounding the points in the time-temperature ($t$-$T$) space. Only a few simple constraints were placed on all of the models of the Altay samples. The highest

temperature $t$-$T$ constraint was assigned to be greater than the measured central age by at least 40 million years, which stipulates that the central age represents cooling from depths greater than the PAZ. The lowest temperature $t$-$T$ constraint is set to the temperature at which the sample was collected, 20°C at 0 Ma. In between these standard HeFTy constraints, additional constraints were set such that the sample approximately reached the PAZ around the time of the central age that was measured (±50 Ma), and then an additional path was typically allowed between the central age constraint and the present day. Large boxes were drawn surrounding these constraints, such that no tight constraints were added to the model. A two-stage, episodic cooling was allowed within each parameter space box ('2E'), to allow for variability or 'noise' in the model because the complexity of the $t$-$T$ path is not well known. Each sample has a slightly different set of constraints, but these are based on the measured data and were chosen as not to strictly confine the model to an expected cooling history. When run, HeFTy searches the model space, and finds good and acceptable fit paths to the data. The models were run until 100 good fit paths were found.

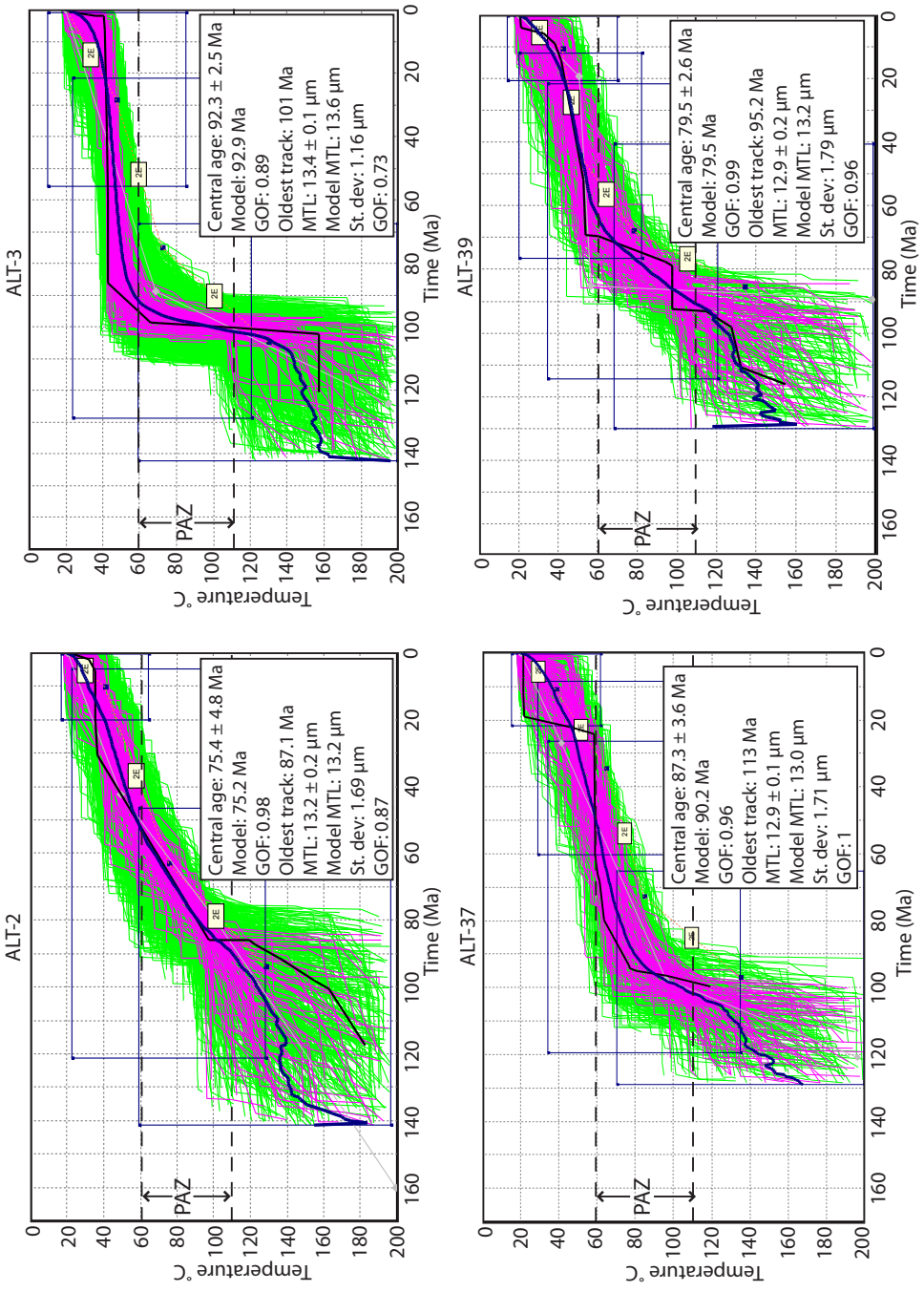


**Figure 5.9:** HeFTy time-temperature models of several samples that had sufficient confined track length measurements, based on the annealing model of *Ketcham et al.* (2007). Results of each model are also listed, including the goodness of fit (GOF) for age and mean track length (MTL). The region below the closure temperature for apatite is not constrained by the model, because fission tracks are fully annealed at higher temperatures. Thin blue boxes indicate the parameter space that was set for the model run shown, thick blue line indicates the average model cooling path, and the black line is the 'best fit' path. Pink lines indicate good fit paths, green lines have an acceptable fit. '2E' boxes indicate a 2 stage, episodic cooling within each parameter space box. The partial annealing zone (PAZ) is indicated for the approximate temperatures that tracks experience partial annealing, with the closure temperature for Altay set at 110° ± 10°.

Figures 5.9 and 5.10 show the statistical good and acceptable fit paths predicted by HeFTy for several Altay samples. The resulting $t$-$T$ paths are dominated by a Cretaceous cooling event, which is ubiquitous in low-temperature thermochronologic data from the Altay region (e.g. *De Grave and Van den haute*, 2002; *Yuan et al.*, 2006; *Vassallo et al.*, 2007a). The cooling histories are only reliable up to temperatures in the deeper part of the PAZ, and the 'oldest track' parameter listed in figures 5.9 and 5.10 is a guideline for the age up to which the model is valid. Sections of the cooling paths older than the oldest tracks are not constrained by the data. Similarly, sections of the cooling paths below the low temperature part of the PAZ, at ∼60°C, will not be directly constrained by the AFT data. The AFT models do not constrain the onset of cooling, and therefore not the intensity of the event, as the rocks may have been cooled from very high temperatures over a long or short period of time before reaching the PAZ in the Late Cretaceous (Figure 5.11). However it is clear that the samples resided within the upper 2–3 km of the crust by the Paleocene, with the assumption of a normal geothermal gradient of ∼30°C/km, or temperatures of 60°–80°C at 2–3 km depth. Since the oldest samples reached the top of the PAZ by the end of the Cretaceous, any later Cenozoic denudation could not have been significant. However it is possible that several hundred metres of overlying rock have been removed since the Late Cretaceous, because shallow fluctuations of the sample at temperatures lower than the PAZ (or approximately the top ∼1–1.5 km of crust) are not reflected in fission track data. Because the majority of samples reached low temperatures in the Early Cenozoic and were not subsequently buried to a significant depth, they do not record evidence of the recent uplift of the Altay recognised along the Har-Us-Nuur fault and in the Siberian Altay (*De Grave and Van den haute*, 2002; *De Grave et al.*, 2007; *Jolivet et al.*, 2007; *Vassallo et al.*, 2007a; *De Grave et al.*, 2009).

However there is one sample that remained at temperatures greater than ∼60°C fol-

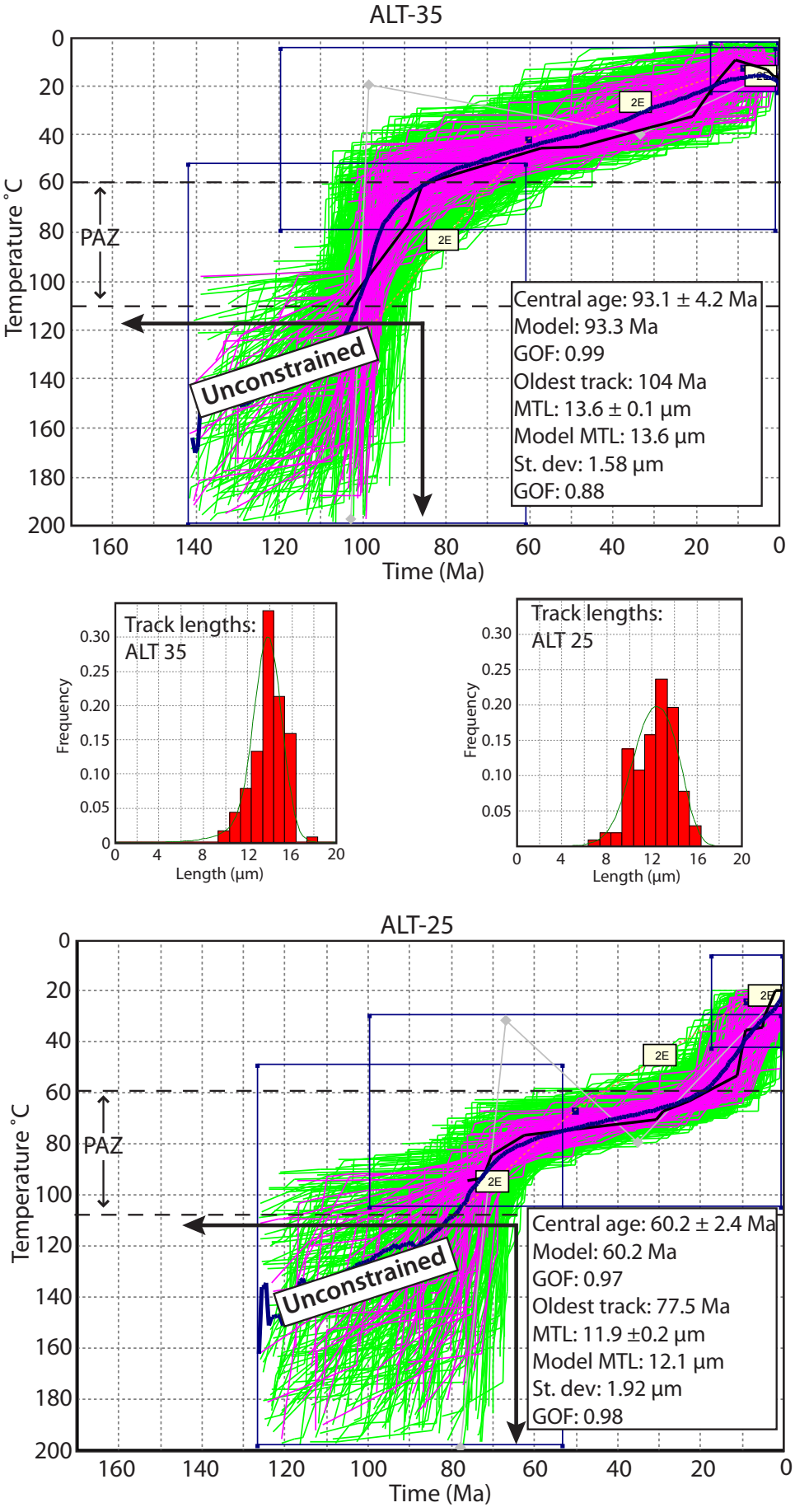
ALT-35
Temperature °C
Time (Ma)
PAZ
Unconstrained
2E
Central age: 93.1 ± 4.2 Ma
Model: 93.3 Ma
GOF: 0.99
Oldest track: 104 Ma
MTL: 13.6 ± 0.1 µm
Model MTL: 13.6 µm
St. dev: 1.58 µm
GOF: 0.88
Track lengths:
ALT 35
Frequency
Length (µm)
Track lengths:
ALT 25
ALT-25
Central age: 60.2 ± 2.4 Ma
Model: 60.2 Ma
GOF: 0.97
Oldest track: 77.5 Ma
MTL: 11.9 ±0.2 µm
Model MTL: 12.1 µm
St. dev: 1.92 µm
GOF: 0.98

lowing the Late Cretaceous event (ALT-25, Figure 5.10). The shorter track lengths and young central age suggest that the sample spent some time in the PAZ with relatively little exhumation, prior to accelerated cooling beginning approximately 10–30 Ma, as reflected in the thermal history model. The Late Cenozoic cooling event can be attributed to deformation from the ongoing collision between India and Asia, which is certainly reflected in the active deformation of the Altay (Chapters 2 and 3). Recent cooling is only clearly defined in one sample, and even this sample was residing quite shallow in the PAZ, therefore there is only a broad constraint on the precise timing of the event. However, it is clear that there is no evidence of a very significant degree of Cenozoic cooling initiated or accelerated within only the last 3–8 Ma, as suggested by *Jolivet et al.* (2007) and *Vassallo et al.* (2007a) from samples in the push up mountains of the Eastern and Göbi Altay, and from some workers in the Siberian Altay (*De Grave and Van den haute*, 2002; *Buslov et al.*, 2008). In general, the precise age of Cenozoic cooling is poorly constrained by the apatites throughout the region, because they have not been at high enough temperatures since the Late Cretaceous (and even older). Many of the previous studies based the prediction of young cooling ages on outdated models that are known to produce artifact late-stage cooling (e.g. *Laslett et al.*, 1987). Artifact cooling has been dealt with in more recent models (*Ketcham et al.*, 2007), but much of the work on fission track modeling in the Altay was done before the updated models were established, or the adjusted models were not used. A rough model was run with the central ages and lengths reported from the eastern Altay with the *Ketcham et al.* (2007) annealing model, and young cooling was very poorly constrained.

**Figure 5.10** ***(preceding page)*:** HeFTy time-temperature inverse models of the youngest and oldest AFT samples. Models were run as described in Figure 5.9. The oldest samples (e.g. ALT-35) record late Cretaceous cooling, and the youngest sample capture the recent, late Cenozoic cooling history. Together they suggest three stage cooling for the central Altay.

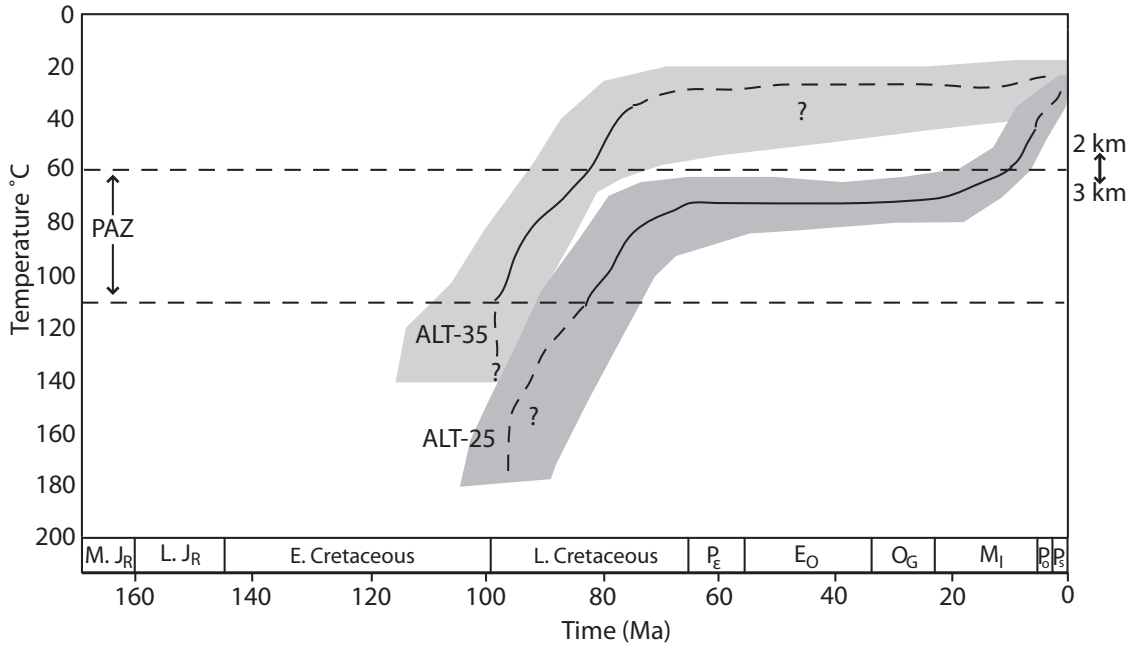


**Figure 5.11:** Schematic diagram of the cooling histories of oldest and youngest samples. The oldest sample is at a higher elevation today, and probably was at a shallower part of the crust than the youngest sample. The youngest sample remained deep, or hot, enough to record residence time in the PAZ until recent Cenozoic tectonism brought the sample to the surface today. The youngest samples reflect uplift initiation approximately 20 Ma.

The modeling results from the central Altay suggest that, while not very well constrained, far-field deformation from the convergence of India and Asia was potentially active in at least the Early Miocene in the Altay region, and probably during the Oligocene (*Yuan et al.*, 2006). These results agree with estimates of cooling from the western Altay (*Yuan et al.*, 2006), as well as with estimates based on sedimentation rates in the Dzereg and Dariv basins on the eastern side of the range (*Howard et al.*, 2003, 2006), and in the Junggar Basin to the west (*Yin et al.*, 1998; *Chen et al.*, 2011). Clastic sedimentation in these basins suggests the existence of nearby topography in the Mesozoic, with a period of relative quiescence indicated by more fine grained material in the Paleocene, followed by coarse grained sandstones and conglomerates from the Oligocene. *Howard et al.* (2006) suggested that mountains along the Hovd fault had formed by the Oligocene, and that a more recent increase

in coarser material in the Dzereg Basin in the Plio-Pleistocene may be indicative of topography generated on the boundaries of the Dzereg Basin. This is in line with more recent accelerated uplift found by *Jolivet et al.* (2007) on the push-up mountains along the Har-Us-Nuur fault, surrounding Dzereg Basin.

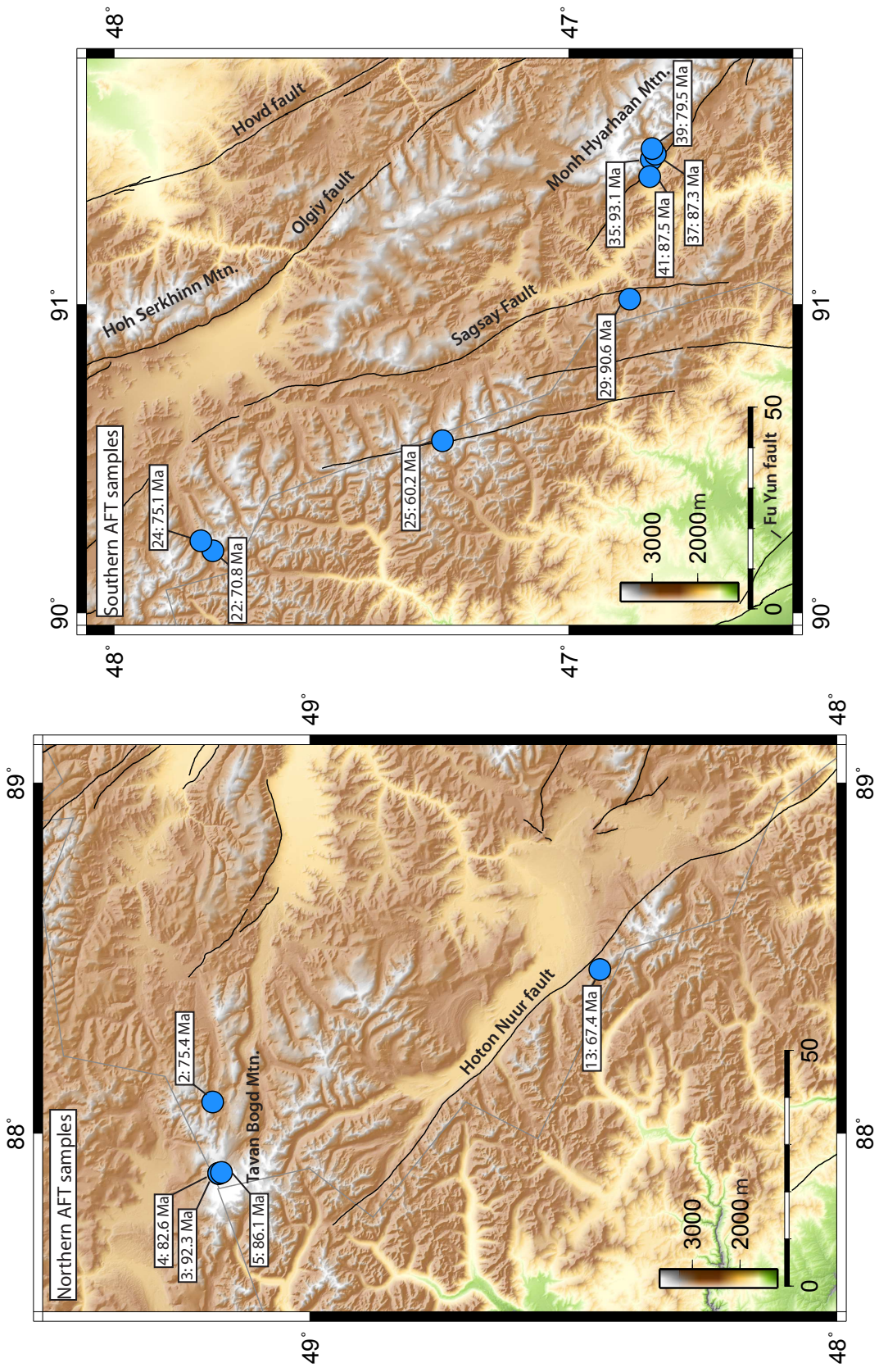


**Figure 5.12:** ASTER GDEM (30 m/pixel) of the region sampled for AFT analysis, with sample locations and central ages indicated. Only samples measured are plotted, and the first number in the boxes indicate the sample number, followed by the age. See Table 5.2 for additional age data. Fault zones that are labeled are fully described in Chapter 2. Locations are indicated on Figure 5.6.

The Paleocene and Upper Cretaceous AFT central ages derived in this chapter and from other studies along the Altay drainage divide and Siberian Altay are significantly younger than those from the eastern Altay, which are generally restricted to the Jurassic (Figures 5.12 and 5.13). These results suggest that the Mesozoic period of deformation ended more recently in the western Altay, whether it was related to either the closure of the Mongol-Okhotsk or collision of the Lhasa block. It was previously suggested that the late Jurassic and early Cretaceous was a period of tectonic quiescence in the Altay (*Jolivet et al.*, 2007), but AFT results suggest that the region was still undergoing extensive exhumation until at least the late Cretaceous. It seems unlikely that a widespread peneplain surface was established to the extent that is suggested for the eastern Altay prior to Cenozoic reactivation of mountain building (*Jolivet et al.*, 2007). There are no confirmed peneplains in the central Altay, and whilst some mountains in the central Altay are topped by relatively flat topography, the youngest samples measured come from the base of topography that has been heavily denuded by Quaternary glaciations, along the drainage divide (Figure 5.1). It is also possible that some topographic relief, remnant from fast cooling during the late Cretaceous and early Paleocene, persisted through reactivation in the Cenozoic. It follows that, in regions with young AFT central ages, the topography observed today is not necessarily only derived from late Cenozoic deformation. The region is tectonically active (Chapters 2, 3), but the potential for inherited topography must be considered when estimating the total Cenozoic deformation in the Altay. The implications of these results for the evolution of topographic relief across the region will be combined with observations of the active faulting in the Altay, and discussed further in Chapter 6.

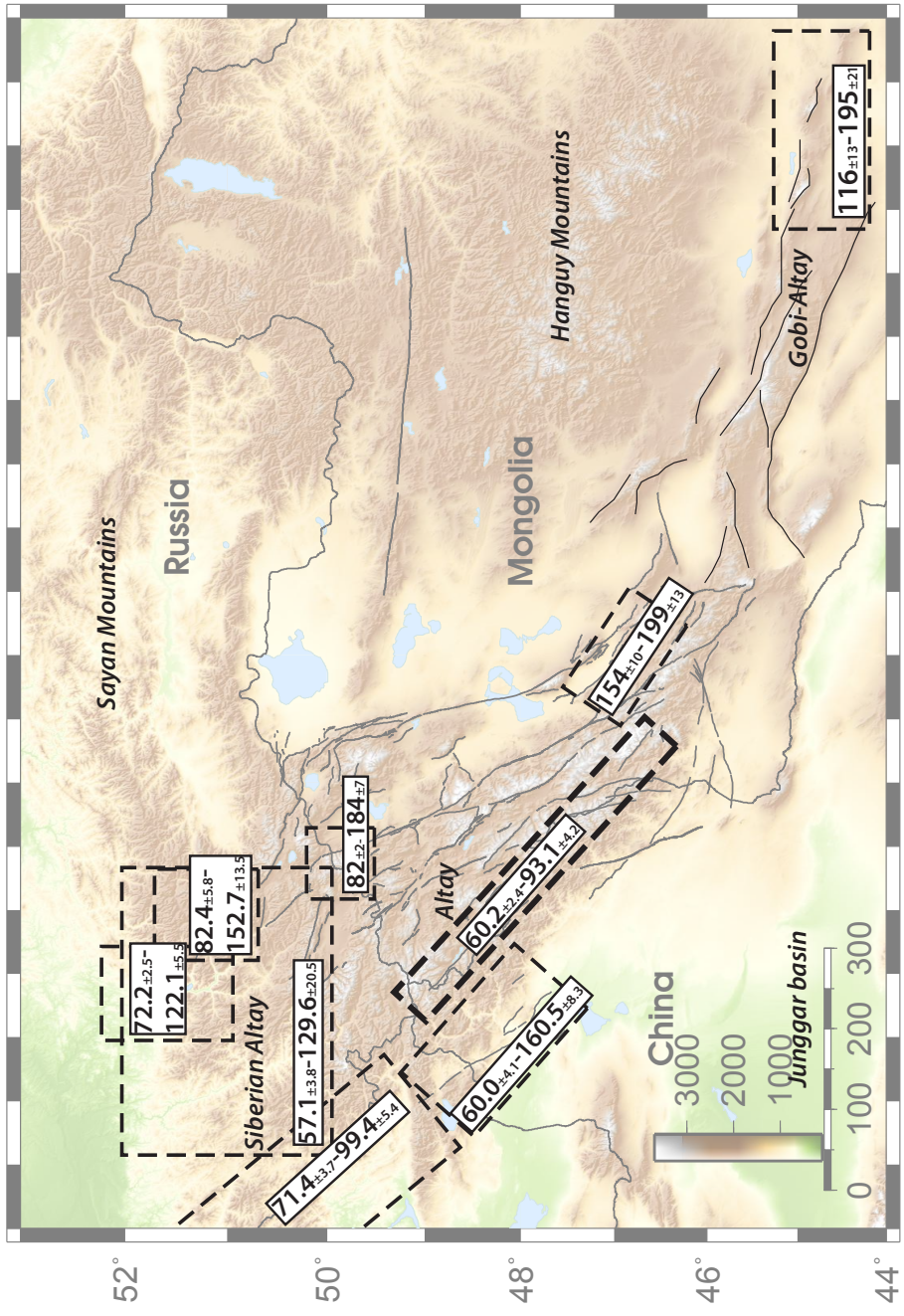


**Figure 5.13:** SRTM DEM shaded relief image of the Altay region (30 arc seconds/pixel), including the Gobi and Siberian Altay. Outlined rectangles indicate the general areas of prior thermochronologic work, with insets indicating the range of central ages resulting from AFT studies (this Chapter; *De Grave and Van den haute*, 2002; *De Grave et al.*, 2008; *Glorie et al.*, 2012a,b; *Jolivet et al.*, 2007; *Vassallo*, 2006; *Vassallo et al.*, 2007a; *Yuan et al.*, 2006). The lower bound on central ages young towards the west, suggesting Mesozoic deformation was active more recently in the western and Siberian Altay.

# Chapter 6

# Discussion and Conclusions

Throughout this thesis, I presented evidence for the rates, styles, and timing of active deformation in the Altay mountains on a variety of time scales. The results and observations of this work enable a comparison of deformation in the Altay over different time scales and, along with previously established constraints, elucidate the evolution of active faulting and mountain building over time. In this discussion, I will first summarise each chapter and highlight the key results, as well as questions that have yet to be answered. I then compare the rates and styles of deformation found from the different techniques, from time scales that range from the modern day GPS velocities and ancient earthquake patterns, to the Quaternary rates of slip, to the geological evidence of deformation. Comparison between these results allows me to re-evaluate the accuracy of the less reliable constraints, and to address hypotheses for the deformation of the Altay. I conclude with an outline of future aims for this work, and I highlight the potential impact of this thesis, in both the understanding of continental deformation and the need to realise the earthquake hazard in Western Mongolia.

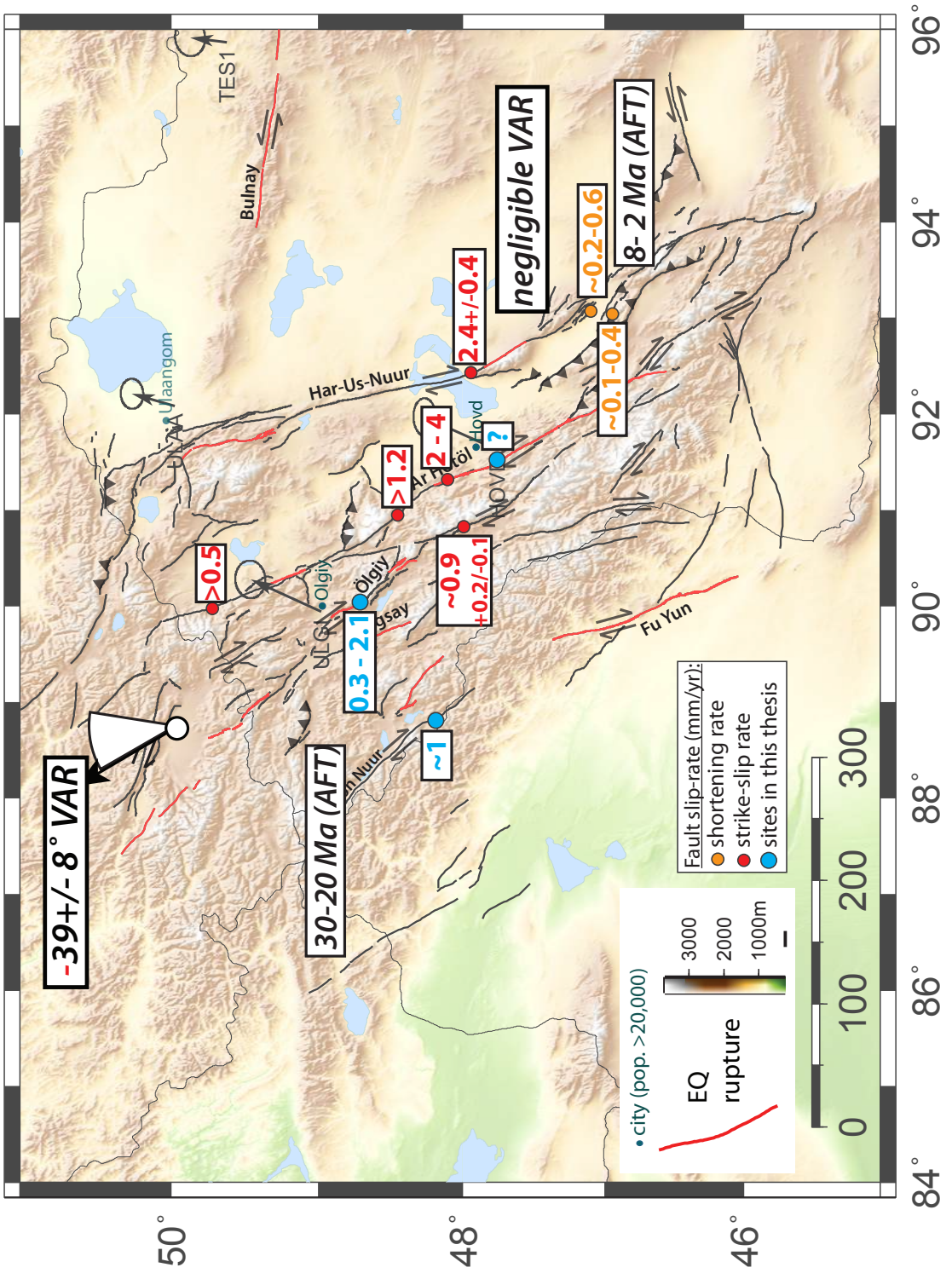
-39+/- 8° VAR
30-20 Ma (AFT)
negligible VAR
8- 2 Ma (AFT)
TES1
Bulnay
Ulaangom
Har-Us-Nuur
Ar Hotöl
Hovd
Olgiy
Ölgiy
Fu Yun
>0.5
0.3 - 2.1
~1
>1.2
2 - 4
~0.9
+0.2/-0.1
2.4+/-0.4
~0.2-0.6
~0.1-0.4
Fault slip-rate (mm/yr):
shortening rate
strike-slip rate
sites in this thesis
city (pop. >20,000)
EQ rupture
3000
2000
1000m
0
100
200
300
84°
86°
88°
90°
92°
94°
96°
50°
48°
46°

## 6.1 Summary of results and interpretations

In Chapter 2, I described evidence for Quaternary faulting activity on the major faults in the Altay (Figure 6.1). Several fault strands that were not known to be active are confirmed as having Quaternary evidence of faulting, by the preservation of deformation features at the surface related to both cumulative Quaternary displacement and single earthquake events. The average slip and length of known, and previously unknown, ancient earthquake ruptures were used to estimate the combined rate of slip of the faults over the past 1000–2000 years to be at least 6.5 mm $yr^{-1}$, or 1.3 mm $yr^{-1}$ on average on each of the five major fault zones. The total Cenozoic strike-slip fault displacement on individual faults was estimated as at least 3–8 km, from offsets of major rivers and the width of pull apart basins. I suggest that the strike-slip displacement may be underestimated by the displacement of rivers, although using the widths of the pull-apart basins should be more reliable. More quantitative results are clearly needed to compare the rates of faulting and deformation expected for the range of total displacements observed, but the work in Chapter 2 advances several key aspects of our understanding of the active faulting in the Altay. One is that several faults that were previously unrecognised or were thought to be relatively unimportant are indeed active on Quaternary timescales as well as during the last 1–2 thousand years in large magnitude earthquakes— in particular faults along the Ölgiy, Sagsay, and Hoton Nuur fault systems. Another key result is that a slip rate calculated based on the sum of earthquake moment

**Figure 6.1** ***(preceding page)*:** SRTM DEM summary map of the known rates and dates from the Altay Mountains. Shown in the figure are: active faults and earthquake ruptures from Chapter 2, known constraints on the Quaternary rate of slip from previous work and Chapter 3, the palaeomagnetic vertical axis rotations (VAR) are shown for the Chuya Basin (*Thomas et al.*, 2002), and the lack of rotation is indicated in the Dzereg Basin, and the estimates for the timing of Cenozoic cooling from AFT data are indicated from my work and *Yuan et al.* (2006) in the western Altay, and estimates from *Jolivet et al.* (2007) and *Vassallo* (2006) in the eastern Altay.

release over the last 1–2 thousand years is lower than what would be expected from the modern day strain rate estimated from GPS, because the strike-slip faulting rate is expected to be greater than the shortening strain rate, based on the geometry of the faults. This implies that some earthquake moment release is missing from the record, and probably more large palaeo-surface ruptures exist on faults that have not been thoroughly investigated in the region. Alternatively it may imply that GPS measurements overestimate shortening strain. The discovery of palaeoearthquakes and evidence for quaternary faulting activity also highlights the earthquake hazard present across the whole of the Altay Mountains.

In Chapter 3, I used cosmogenic $^{10}$Be and U-series dating to constrain the average Quaternary rates of fault slip. At the Ölgiy site on the Ölgiy fault, the data from both methods are in good agreement, and suggest a very robust estimate of 0.3–2.1 mm yr$^{-1}$ for the average slip rate (Figure 6.1). Results from the Ar Hötöl site on the Hovd fault were more difficult to interpret, and suggest that either the slip rate is very low, faulting at the surface has migrated sometime in the last few hundred thousand years, or that the results are not directly correlated to the displacements observed at the surface. The discrepancy in results confirms that multiple Quaternary dating techniques should be applied to calculate accurate slip rates, which is an important aspect of the results presented in this thesis. The application of U-series dating, complimented by $^{10}$Be cosmogenic dating, is a relatively new approach in quantifying average Quaternary slip rates. The application of U-series was augmented by sub-sampling of stratigraphic layers of the carbonate rind, and incorporating the results to produce a statistical constraint on the continuous growth of pedogenic carbonate through time. Important tectonic implications also arise from this work. The slip rate calculated on the Ölgiy fault is indistinguishable from rates calculated on the eastern-most Altay faults, and there is no requirement for either the Har-Us-Nuur or Hovd faults to be slipping significantly faster than the Ölgiy

fault, as was previously suggested (*Nissen et al.*, 2009b; *Frankel et al.*, 2010). Results from the Hoton Nuur fault, which is one of the western-most active faults, will test this hypothesis.

Both Chapters 4 and 5 are investigations into the deformation of the Altay on a geological time scale. In Chapter 4, I presented the second palaeomagnetic study from Cenozoic rocks conducted in the Altay (Figure 6.1). Samples collected from the Dzereg Basin in the eastern Altay provide reliable palaeomagnetic directions that pass a fold test and include a magnetic reversal. The declinations are not significantly rotated with respect to the expected directions, which is in contrast to anti-clockwise rotations of $39 \pm 8^{\circ}$ estimated from the Chuya Basin in the Siberian Altay (*Thomas et al.*, 2002). It is possible that the Chuya Basin data overestimate the regional vertical axis rotation if some localised faulting associated with the formation of the basin has affected the sample orientations. However if the rotation in the Chuya Basin is significantly greater than in the Dzereg Basin, the lack of palaeomagnetic rotations on the Har-Us-Nuur fault suggest that either this fault is significantly younger than the faults surrounding the Chuya Basin, or that it is behaving in a manner that is kinematically different from the other Altay faults, and is not rotating. Based on the low-temperature thermochronology results from other workers that suggest very late stage Cenozoic cooling of the massifs surrounding the Har-Us-Nuur fault (*Vassallo*, 2006; *Jolivet et al.*, 2007), perhaps the former is true. However, based on stratigraphic studies (*Howard et al.*, 2003), there is some evidence for a much longer period of topographic uplift in the region, suggesting a rather complicated, and currently unresolved, history for the Dzereg Basin.

In Chapter 5, I present results from a low-temperature thermochronology study of rocks collected in a transect along the eastern side of the Altay drainage divide, to provide constraint on the cooling history and evolution of mountain topography. The Altay have an asymmetrical shape, with high continuous topography in the west and

basin and range topography in the east, as well as a drainage divide located on the far western side of the mountains (Figure 6.1). From previous fission track studies, the eastern and northern Altay were suggested to have initiated or experienced intensified uplift only within the last 3–10 Ma, though the fission track length models that were applied often result in late-stage cooling that is an artifact of the annealing model (*Vassallo*, 2006; *Jolivet et al.*, 2007; *Buslov et al.*, 2008; *De Grave et al.*, 2008). These estimates of very recent and rapid cooling are in contrast with results from the central Altay, which suggest that Cenozoic cooling has occurred over the last 20–30 Ma, in one sample from Chapter 5, and in results from *Yuan et al.* (2006) and possibly *Glorie et al.* (2012b,a), although the timing of cooling is poorly constrained by fission track length models because the samples have not been completely reset since the Mesozoic. An important result from Chapter 5 is that the Mesozoic tectonism in the region was active until at least the late Cretaceous, if not until the Paleocene, suggesting that some of the topography in the Altay may be inherited from a previous phase of deformation.

## 6.2 Hypotheses for the active deformation of the Altay

One important aim of this thesis is to compare quantified rates and styles of deformation across a range of time scales, for the purpose of better understanding the evolution of the kinematics of active faulting in the Altay. In order to reconcile the estimates of rotation, cumulative dextral slip, and horizontal GPS shortening rates, I provide a geometrical calculation based on the length of, and distance between, the active faults of the Altay (from *Walker and Jackson*, 2004, Figure 6.2). A simplified view of the kinematics of deformation relates the amount of rotation ($\theta$) to the distance between faults and cumulative slip on the faults, and the rotation to the

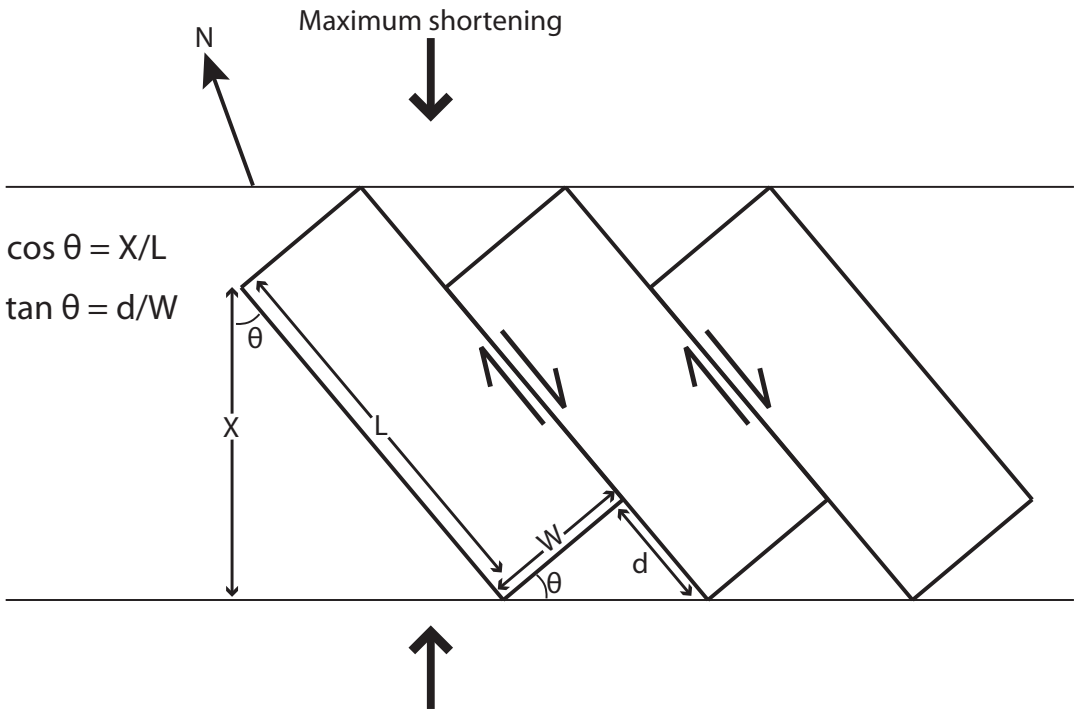


**Figure 6.2:** Simplified diagram for relating the geological displacements along dextral faults to anti-clockwise rotation, modified from *Walker and Jackson* (2004). W is the distance between faults, L is the length of faults, horizontal shortening is L-X, d is the cumulative dextral displacement along the faults, and $\theta$ is the amount of vertical axis rotation. For simplicity, I use 30 km as an estimate for the average distance (W) between faults in the Altay, and a fault length of 500 km.

length of the faults (L) and horizontal shortening (L-X):

$$\tan\theta = \frac{d}{W} \tag{6.1}$$

$$\cos\theta = \frac{X}{L} \tag{6.2}$$

The block model in Figure 6.2 certainly oversimplifies the kinematics of faulting, but still can provide a guideline for comparing rates and amounts of deformation. I first evaluate the 40° of vertical axis rotation estimated from the Chuya Basin (*Thomas et al.*, 2002). Using an average distance between faults of 30 km and

average fault length of 500 km, the cumulative displacement on faults is expected to be 25 km and the total horizontal shortening is 117 km. With the assumption that Cenozoic deformation has been active for at least 20 to 30 Ma, the average shortening rate is between 4 to 6 mm $yr^{-1}$ and the average strike-slip rate (for each of 5 fault zones) is 0.8 to 1.2 mm $yr^{-1}$ . These estimates of long-term deformation rates from the of the age of mountain building and total vertical axis rotation are remarkably similar to the horizontal shortening rate observed in GPS ($\sim$7 mm $yr^{-1}$) and the Quaternary rates of strike-slip faulting on individual fault strands (0.5 to 2.5 mm $yr^{-1}$).

However, several discrepancies arise when considering 40° of rotation of the Altay faults. The total predicted fault displacement of 25 km is significantly greater than what is observed on the Altay faults (between 3–8 km). There are a number of potential reasons for the difference between the observed and predicted total slip. First, it is likely that the river offsets, and even the pull-apart basin width, underestimate the total fault displacement (see Section 2.5.1 in Chapter 2). It is not possible to determine by how much the offsets are an underestimate. The large degree of rotation also presents a kinematic problem. The rotation of the faults will have affected both the style and presumably slip rate of active faulting. If the regional strain field has been consistently directed NE–SW over the duration of Cenozoic deformation, the faults have rotated from an orientation that is more closely aligned with the maximum principle stress, and very non-optimal for faulting, to one more optimal for strike-slip, and even further to oblique-reverse slip. There is also a 'space problem' because as the faults rotate, somewhere there must be accommodation for shortening and extension at the termination of the faults. In order to interpret the kinematics of up to 40° of rotation for the Altay, the degree of rotation must be better quantified than the two existing, and contrasting, palaeomagnetic studies of the region conducted thus far.

The kinematics of deformation in the Altay, and the comparison of GPS shortening strain to longer term strike-slip displacement and rates, are not as simple as suggested by the kinematic model. If a large portion of the shortening strain is being accommodated as crustal thickening (or uplift), then the component of shortening due to vertical axis rotation, and dextral faulting, will be much smaller than in the above calculation. The crustal thickness of the Altay region is not estimated to be particularly high, though it is certainly thicker than the region of central Mongolia and the Baikal rift (e.g. *Zorin et al.*, 1990). A larger crustal thickness, though not very well constrained, does imply some form of vertical tectonics have occurred in the Altay region, but it is not possible to separate the Cenozoic deformation from the previous, Paleozoic and older, phases of deformation in the region due to the assembly of Central Asia. If there is a significant amount of shortening by crustal thickening over the duration of Cenozoic deformation in the Altay, the suggestion of 40° of rotation from the Siberian Altay is an overestimate. If a portion of shortening is taken up by crustal thickening, as opposed to rotation facilitated by strike-slip faults, less cumulative strike-slip fault displacement would be expected. For example, if the estimates of cumulative fault displacement measured from river offsets of 3–8 km are used in Equation 6.1, a total rotation of 5.7° to 14.9° would be expected. This in turn implies total horizontal shortening of 2.5 to 16.8 km, which can be extrapolated over the duration of mountain building (20–30 Ma), resulting in shortening rates over the whole of the Altay between 0.1 to 0.8 mm $yr^{-1}$. If the river displacements are reliable recorders of fault offset, this low rate suggests a significant contribution of shortening from crustal thickening, if the long term shortening rate is close to the GPS shortening rate of 7 mm $yr^{-1}$. This constraint is not in agreement with the Quaternary and last 1–2 thousand year record of strike-slip faulting, dependent on the duration of strike-slip faulting. If the strike-slip faults have been active for 20–30 Ma, displacements of 3–8 km would result from averaged slip-rates

of 0.1–0.4 mm $yr^{-1}$ per fault, significantly lower than the measured rates summarised above (0.5–2.5 mm $yr^{-1}$).

However, if palaeomagnetic results from the Dzereg Basin are considered separately from the Chuya Basin, then the rotation and average slip rates estimated from the dextral fault displacements is not unreasonable, given the palaeomagnetic results of no resolvable rotation presented in Chapter 4. These results only represent the vertical axis rotations for the eastern-most fault in the Altay, the Har-Us-Nuur fault, which generally has a more north-south strike, is separated from the high topography of the central Altay (Figure 6.1), and the restraining bend mountains formed along the fault are suggested to be relatively young. It is possible that the Har-Us-Nuur fault is younger than the majority of active faults in the Altay, and has not had time to accommodate significant degrees of rotation. Yet if the central Altay has undergone very little rotation over the whole of the Cenozoic, it is possible that rotation has not been an important component of shortening, at least on geological time scales. The modern day strain field requires rotation, based on strike-slip earthquakes accommodated on faults that are not parallel to the maximum shortening direction (*Bayasgalan et al.*, 2005). It may be that oblique and reverse faulting have been very important for accommodating a large portion of the deformation in the Altay over longer time scales. Because the Har-Us-Nuur fault is quite distinct from the other Altay faults, and may have a different rotational history, more work is necessary to constrain rotations from the centre of the range and better evaluate the evolution of the kinematics of deformation.

The two comparisons of relative rates of fault displacement, shortening rate, and total rotation can be taken as end-member models of the kinematic deformation in the Altay. In one case, deformation is accommodated by pure strike-slip faulting and rotation, without the need for a large component of vertical tectonics. In the other case, from the observed fault displacement, the majority of shortening is ac-

commodated by reverse faulting and crustal thickening. Based on the observations and interpretations discussed, I suggest that the deformation in the Altay is currently dominated by right-lateral strike-slip faulting, but with some component of shortening and crustal thickening achieved on oblique-reverse faults. *Baljinnyam et al.* (1993) also suggest that strike-slip faulting is the primary component of active faulting in the Altay, based on the high elevations of the intermontane basins (1500–2200 m) and low relief, implying little contribution from reverse faulting. There is evidence that reverse faulting, and uplift, does occur in the Altay, but much of it seems to be related to transpressional deformation, due to local fault orientations that are optimal for reverse slip (see discussion in Chapter 2). Also, cooling histories derived from AFT data suggest that the region has experienced at least some tectonic uplift, but that the topography in the western Altay may be partly inherited. It is therefore reasonable that there is not a large contribution to shortening from dip-slip faulting, and certainly not as large as would be required in kinematic models incorporating low cumulative strike-slip displacements measured from river displacements.

## 6.3 Future Work

Whilst there are many poorly constrained quantities in the above discussion, it is still a useful exercise for helping to better understand the kinematics, and ultimately the dynamics, of deformation in the Altay. Thus far in the discussion, I have identified advances in our understanding of the deformation of the Altay, as well as further questions to be answered and quantities to be measured. The work presented here in some ways leads to more questions than it answers, particularly on how strain is distributed across the Altay faults over varying time scales. The data are still sparse in terms of quantifying deformation, even with the inclusion of results for Quaternary slip-rates, rotation rates, and uplift rates presented here and by others. One or two

spot measurements of slip-rate are not enough to evaluate the distribution of strain over time on a single fault strand, because rates may vary along strike (e.g. *Kirby et al.*, 2007). Quantification of slip-rates on multiple sites distributed along the full length of the faults would benefit our understanding of the Quaternary kinematics of faulting, by allowing the comparison of rates through space and time. My work has shown that slip-rate studies must involve more than one method of Quaternary geochronology to provide robust results. Also the question of how Quaternary slip is distributed across several surface strands of a fault is important, and has not been addressed here. If several strands of faults are active over the time period being measured, a spot measurement of slip-rate on a single alluvial surface will underestimate the average slip-rate.

Low-temperature thermochronology studies cover a large portion of the Altay region, but there are still gaps in the record in terms of understanding Cenozoic cooling, uplift, and generation of topography. AFT dating has been applied in this thesis, with some problems in interpreting the Cenozoic uplift in the region because the AFT system has not been reset since the Mesozoic. U-Th/He dating can often reveal the lower temperature history of samples where AFT results are lacking, because the U-Th/He system is reset at lower temperatures. U-Th/He has not been widely applied in the Altay, but the method has the potential to reveal more detail on the thermal history of the region and can be incorporated with AFT results.

The discrepancy in Quaternary rotation rates derived from palaeomagnetic studies is also an outstanding issue. Several scenarios could lead to the differences in the degree of rotation between the Siberian Altay and along the Har-Us-Nuur fault. Problems with local scale rotation may have led to large amounts of rotation in confined regions (e.g. the Chuya Basin). If the Har-Us-Nuur fault has only recently been reactivated, very low rotation rates would be expected from the Dzereg Basin. If the Har-Us-Nuur fault is kinematically unique from the rest of the Altay, the ac-

tive deformation might not require rotation. More palaeomagnetic studies from other parts of the Altay may resolve this issue, but only if it is possible to find appropriate Cretaceous and younger sediments.

The landscape has the potential to reveal patterns of tectonic deformation due to faulting and uplift (e.g. *Dorsey*, 2006; *Densmore et al.*, 2007b), but has not yet been exploited in the Altay. Coupled with catchment-wide erosion rates, a thorough analysis of the topography and river patterns, and how they differ across the region, may help to to understand how the tectonic deformation is reflected the landscape. This work can help connect quantification of tectonic deformation between the Quaternary and geological time scales presented in this thesis.

Finally, in order to address seismic hazard and fully document the history of earthquakes and the earthquake cycle over the last 1–2 thousand years, much more information is needed on the timing of known (and unknown) earthquake palaeosurface ruptures. This can be accomplished by seismic trenching, and will be aided by advances in quality and availability of satellite imagery over the next few years. I end this section with the suggestion that, while a first order estimate of the kinematics of deformation is possible with the known rates, duration, and cumulative amounts of deformation, many of the constraints are rough estimates based on one or two studies, and more work is necessary to fully address the dynamics of deformation. The Altay are an extensive region of active, far-field continental deformation, with a seismic moment release over the past century that is comparable to, or even greater than, areas such as southern California (*Scholz*, 2002), yet there are few estimates of the rates and amounts of deformation.

## 6.4 Broader impacts and concluding remarks

A significant motivation of this thesis was simply the lack of prior available quantification and characterisation of deformation in the Altay Mountains. As a result,

there was some bias in the previous conclusions made on the overall kinematics and rates of deformation in the region. Two major conclusions often reached are that (1) the eastern most fault zones of the Altay, particularly the Har-Us-Nuur and Hovd zones, are moving more quickly than other faults in the region, and (2) that topography in the Altay is extremely young and Cenozoic deformation only initiated in the last $5 \pm 3$ Ma. In some ways, my work challenges these broad conclusions about the timing and rates of deformation in the Altay, but this may be because other parts of the mountain range may tell a different story. This is not to state that other workers are wrong, but simply that further observation and quantification of the Altay faults and deformation suggest that faults in the northwestern parts of the Mongolian Altay are indeed active, and not moving at significantly slower rates than those in the eastern Altay, and that the evolution of deformation through geologic time may be more complex and long-lasting than originally suggested.

In this discussion, I demonstrated that average rates of deformation can be compared over three different time scales: from GPS shortening strain rates, which are not dissimilar to strike-slip rates derived from the earthquake record (Chapter 2), to average Quaternary rates of slip, and in turn to geological constraints of shortening and fault slip. The simplified kinematic model of deformation, deduced from models of similar kinematics in central Iran in *Walker and Jackson* (2004), provides insight into the accommodation of shortening strain by the rotation of strike-slip faults. I stress that the model I present is simplified, and does not take into account the diffuse deformation that is likely occurring throughout the Altay, or the more dynamical aspects of continental deformation in the region. Diffuse deformation of the 'blocks' is evident throughout the Altay as anastomosing faults, often with a surface expression as several continuous strands through a wide fault zone. The spatial pattern of active faulting in the Altay can be considered in terms of dynamics of the deformation in the region and the topic of lithospheric strength.

Two two end-member models of the deformation of continental lithosphere exist (e.g. *Thatcher*, 1995). In the microplate end-member (or plate tectonics), faults are discrete boundaries that exist in some form through the whole of the lithosphere, and the surrounding lithosphere comprises undeforming blocks whose motion can be described by rotations about Euler poles. The contrasting model essentially invokes a continuously deforming lithosphere, reflected at the surface as brittle faults that do not necessarily represent localised strain at depth. In the Altay, the anastomosing distribution of complex and interacting faults with average spacing on the order of 10–30 km suggests that the microplate model is not applicable, and the deformation is better described by continuous deformation. The strength of the lithosphere is also an important consideration in understanding the dynamics of continental deformation. *Burov and Watts* (2006) elegantly demonstrated that lithosphere in which the strength resides only in the crust, with a weak lithospheric mantle (the 'crème brûlée' model) cannot support a long-standing mountain range in a collisional system. It follows that, on the geological time scale of a mountain range, some strength must reside in the lithospheric mantle. The Altay is an example of a mountain range that has not only persisted for a very long time— on the order of a few hundred million years if the Paleozoic and Mesozoic history of the region is considered, but also an area of continental deformation located in the very far field of the collision zone. In order for the Altay region to accommodate 7 mm $yr^{-1}$ of shortening over 2500 km away from the collisional margin, the continental lithosphere must be relatively strong. Whether the strength of the lithosphere and the continuous deformation of the continent is variable on different time scales, has yet to be answered.

Finally, one aspect of my work that requires consideration is the possible implication for the assessment of earthquake hazard. While there are few people living in the Altay when compared to other regions of active faulting, there are several population centers that are within a few 10s of kilometres of active faults that are known

to have produced earthquakes in the last few hundreds of years. In some ways, it is fortunate that the major cities of the Altay— Hovd, Ölgiy, and Ulaangom, are located adjacent to historical earthquake ruptures, because if repeat times are long enough, they may not be expected to experience another earthquake in the near future (Figure 6.1). The respective Ar Hötöl, Sair Uul, and Jid earthquakes likely occurred sometime in the last 1000 years, and based on slip rates of 1–2 mm $yr^{-1}$ and the average slip in a mid-magnitude 7 earthquake of 2–4 m, it can be broadly estimated that the faults have a repeat time of 2000–4000 years for a similar sized event. However, the uncertainty on some of the constraints may be quite large, particularly the duration of time since the last earthquake. It is possible that surface ruptures may be preserved for even longer than 1000 years, as the Jid event was determined to have occurred nearly 900 years ago (*Walker et al.*, 2006). If this is the case, and if fault slip rates are at the high end of the range suggested, then a large event may be expected on a fault strand with historic ruptures. Most of the faults that have surface ruptures also have evidence of repeated events, in the form of large offsets and cumulative sag ponds and mole tracks, and it is not unreasonable to expect another large earthquake in western Mongolia. Repeated earthquakes are well constrained from the Fu Yun fault *Klinger et al.* (2011).

Approximately half of the Mongolian population lives in the countryside in felt tents, called *gers*, that are relatively resistant to damage from earthquake shaking, but migration to the cities is consistently increasing as people give up nomadic lifestyles. City buildings are built to a poor standard, and are in many cases remanent tower blocks from the pre-1990 Soviet occupation of the country. Thus the risk of earthquake damage is likely quite severe in population centers in the country, and more work on both quantifying the earthquake hazard, and increasing the resilience of the local populations, is certainly necessary given the earthquake record of western Mongolia. Currently, the hazard map of Mongolia predicts a high level of shaking for

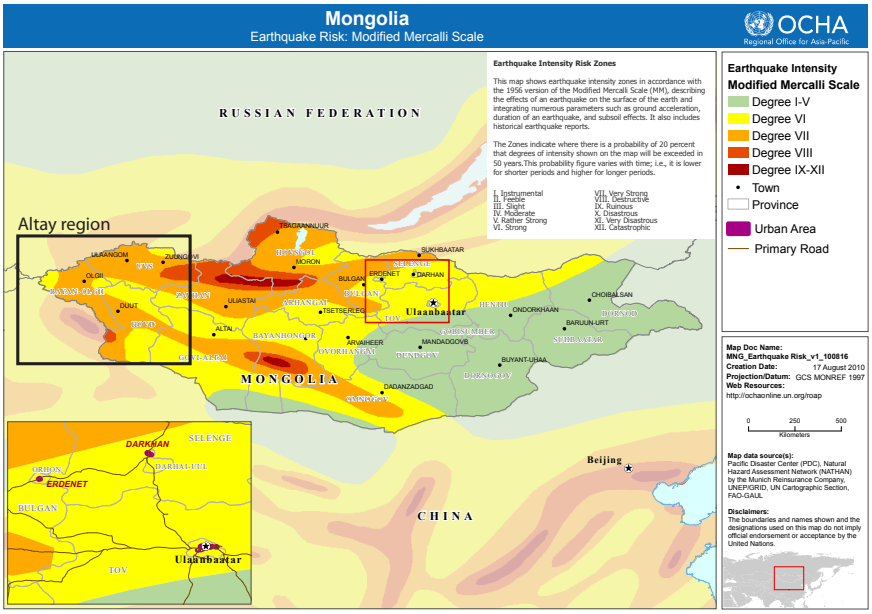


**Figure 6.3:** Repeat of Figure 1.7 in Chapter 1. Earthquake hazard map of Mongolia, from the United Nations Office for the Coordination of Humanitarian Affairs Regional Office for Asia and the Pacific (OCHA-ROAP, `http://preventionweb.net/go/15692`). The modified Mercalli scale intensities indicate a 20% probability that the degree of of shaking intensity will be exceeded in the next 50 years. The map is largely based on the locations of earthquakes in the last century, but also takes into account factors such as subsoil effects on expected ground accelerations.

the region surrounding the Bulnay, Göbi Altay, and Fu Yun faults, and relatively little risk for the Altay Mountains region within Mongolia (Figure 6.3). The hazard map for Mongolia is probabilistic, and is mostly based on earthquakes that have occurred within the last century. The work presented in this thesis implies a serious error in the probabilistic hazard map of Mongolia, and indeed any similarly constructed hazard map for regions accumulating low, intracontinental strain (*Stein et al.*, 2012). The map lacks crucial information about the pre-1900 earthquake history of the region, and does not include faults that are known to be a risk, based on their earthquake record during the last 1–2 thousand years, and even beyond through the Quaternary. These faults are certainly active, and should be included in any assessment of earthquake hazard.

# Bibliography


Allen, M. B., and S. J. Vincent (1997), Fault reactivation in the Junggar region, northwest China: the role of basement structures during Mesozoic-Cenozoic compression, *Journal of the Geological Society*, *154*, 151–155. 1.4

Badarch, G., W. D. Cunningham, and B. F. Windley (2002), A new terrane subdivision for Mongolia: implications for the Phanerozoic crustal growth of Central Asia, *Journal of Asian Earth Sciences*, *21*, 87–110. 1.4, 1.4, 5.1.1

Balco, G., J. O. Stone, N. A. Lifton, and T. J. Dunai (2008), A complete and easily accessible means of calculating surface exposure ages or erosion rates from $^{10}$Be and $^{26}$Al measurements, *Quaternary Geochronology*, *3*, 174–195, doi:10.1016/j.quageo.2007.12.001. 3.3.4, 3.3.5, 3.5, 3.4.2, 3.7

Baljinnyam, I., A. Bayasgalan, B. A. Borisov, A. Cisternas, M. G. Dem'yanovich, L. Ganbaatar, V. M. Kochetkov, R. A. Kurushin, P. Molnar, H. Philip, and Y. Y. Vashchilov (1993), Ruptures of major earthquakes and active deformation in Mongolia and its surroundings, in *Geological Society of America Memoir*, vol. 181, pp. 1–61, The Geological Society of America. 1.1, 1.2, 1.3, 1.3, 1.7, 2.1, 2.2.1, 2.3.2, 2.3.2, 2.3.3, 2.3.4, 2.3.4, 2.39, 2.3.5, 2.3.5, 2.5.2, 2.5.3, 2.5.4, 2.5.4, 2.6, 3.3.2, 3.16, 3.4, 3.4.1, 3.4.2, 4.1, 6.2

Barbarand, J., A. Carter, I. Wood, and T. Hurford (2003), Compositional and structural control of fission-track annealing in apatite, *Chemical Geology*, *198*, 107–137, doi:10.1016/S0009-2541(02)00424-2. 5.2

Bayasgalan, A., J. Jackson, J.-F. Ritz, and S. Carretier (1999), Field examples of strike-slip fault terminations in Mongolia and their tectonic significance, *Tectonics*, *18*, 394–411. 1.3, 2.5.2

Bayasgalan, A., J. Jackson, and D. McKenzie (2005), Lithosphere rheology and active tectonics in Mongolia: relations between earthquake source parameters, gravity, and GPS measurements, *Geophysical Journal International*, *163*, 1151–1179, doi:10.1111/j.1365-246X.2005.02764.x. 1.1, 1.2, 1.3, 2.2.1, 2.5.2, 2.5.5, 3.1, 3.16, 3.27, 4.1, 4.1, 4.5.2, 6.2

Behr, W. M., D. H. Rood, K. E. Fletcher, N. Guzman, R. Finkel, T. C. Hanks, K. W. Hudnut, K. J. Kendrick, J. P. Platt, W. D. Sharp, R. J. Weldon, and J. D. Yule (2010), Uncertainties in slip-rate estimates for the Mission Creek strand of the

southern San Andreas fault at Biskra Palms Oasis, southern California, *Geological Society of America Bulletin*, *122*, 1360–1377, doi:10.1130/B30020.1. 3.3.3, 3.3.5

Berberian, M., M. Qorashi, J. A. Jackson, K. Priestley, and T. Wallace (1992), The Rudbar-Tarom earthwuake of 20 June 1990 in NW Persia: preliminary field and seismological observations, and its tectonic significance, *Bullentin of the Seismological Society of America*, *82*, 1726–1755. 2.4.1

Birkland, P. W. (1984), *Soils and Geomorphology*, 430 pp., Oxford University Press, New York. 3.3.3

Blisniuk, P. M., and W. D. Sharp (2003), Rates of late Quaternary normal faulting in central Tibet from U-series dating of pedogenic carbonate in displaced fluvial gravel deposits, *Earth and Planetary Science Letters*, *215*, 169–186, doi:10.1016/S0012-821X(03)00374-1. 3.2, 3.3.3

Briggs, S. M., A. Yin, C. E. Manning, M. Grove, Z. L. Chen, and X. F. Wang (2007), Late Paleozoic tectonic history of the Ertix Fault in the Chinese Altai Mountains and its implications fr the development of the Central Asian Orogenic System, *Geological Society of America Bulletin*, *119*, 944–960, doi:10.1130/B26044.1. 1.4, 5.1.1

Briggs, S. M., A. Yin, C. E. Manning, Z.-L. Chen, and X.-F. Wang (2009), Tectonic development of the southern Chinese Altai Range as determined by structural geology, thermobarometry, $^{40}Ar/^{39}Ar$ thermochronology, and Th/Pb ion-microprobe monazite geochronology, *Geological Society of America Bulletin*, *121*, 1381–1393, doi:10.1130/B26385.1. (document), 1.4, 1.4, 5.1.1, 5.2

Broecker, W. S. (1963), A preliminary evaluation of uranium series inequilibrium as a tool for absolute age measurement on marine carbonates, *Journal of Geophysical Research*, *68*, 2817–2834. 3.3.3, 3.2

Bronk Ramsey, C. (1995), Radiocarbon calibration and analysis of stratigraphy: the OxCal program, *Radiocarbon*, *37*, 425–430. 3.3

Bronk Ramsey, C. (2009), Bayesian analysis of radiocaron dates, *Radiocarbon*, *51*, 337–360. 3.3.3

Brown, E. T., E. J. Brook, G. M. Raisbeck, F. Yiou, and M. D. Kurz (1992), Effective attenuation lengths of cosmic rays producing $^{10}$be and $^{26}$al in quartz: implications for exposure age dating, *Geophysical Research Letters*, *19*, 369–372. 3.3.4

Brown, E. T., D. L. Bourlès, B. C. Burchfiel, D. Qidong, L. Jun, P. Molnar, G. M. Raisbeck, and F. Yiou (1998), Estimation of slip rates in the southern Tien Shan using cosmic ray exposure dates of abandoned alluvial fans, *GSA Bulletin*, *110*, 377–386. 3.3.5, 3.3.5, 3.4.2

Brown, E. T., R. Bendick, D. L. Bourlès, V. Gaur, P. Molnar, G. M. Raisbeck, and F. Yiou (2002), Slip rates of the Karakorum fault, Ladakh, India, determined using cosmic ray exposure dating of debris flows and moraines, *Journal of Geophysical Research*, *107*, 2192, doi:10.1029/2000JB000100. 3.2

Brown, E. T., R. Bendick, D. L. Bourlès, V. Gaur, P. Molnar, G. M. Raisbeck, and F. Yiou (2003), Early Holocene climate recorded in geomorphological features in Western Tibet, *Palaeogeography, Palaeoclimatology, Palaeoecology*, *199*, 141–151, doi:10.1016/S0031-0182(03)00501-7. 3.3.5

Brown, R., M. Summerfield, and A. Gleadow (1994), Apatite fission track analysis: its potential for the estimation of denudation rates and implications for models of long-term landscape development, in *Process Models and Theoretical Geomorphology*, edited by M. Kirby, pp. 23–53, John Wiley and Sons Ltd. 5.3

Brune, J. N. (1968), Seismic moment, seismicity, and rate of slip along major fault zones, *Journal of Geophysical Research*, *73*, 777–784. 2.5.4

Bullen, M. E., D. W. Burbank, J. I. Garver, and K. Y. Abdrakhmatov (2001), Late Cenozoic tectonic evolution of the northwestern Tien Shan: new age estimates for the initiation of mountain building, *GSA Bulletin*, *113*, 1544–1559, doi:10.1130/0016-7606(2001)113¡1544:LCTEOT¿2.0.CO;2. 1.4

Bürgmann, R., and G. Dresen (2008), Rheology of the lower crust and upper mantle: Evidence from rock mechanics, geodesy, and field observations, *Annual Reviews of Earth and Planetary Science*, *36*, 531–567, doi:10.1146/annurev.earth.36.031207.124326. 1.1

Burov, E. B., and A. B. Watts (2006), The long-term strength of the continental lithosphere: 'jelly sandwich' or 'crème brûlée'?, *GSA Today*, *16(1)*, 4–10, doi:10.1130/1052-5173(2006)016¡4:TLT SOC¿2.0.CO;2. 1.1, 6.4

Buslov, M. M., D. A. Kokh, and J. De Grave (2008), Mesozoic-Cenozoic tectonics and geodynamics of Altai, Tien Shan, and Northern Kazakhstan, from apatite fission-track data, *Russian Geology and Geophysics*, *49*, 648–654, doi:10.1016/j.rgg.2008.01.006. 5.1.1, 5.4, 6.1

Butler, R. F. (1992), *Paleomagnetism*, 319 pp., Blackwell Scientific Publications, Boston. 4.3

Calais, E., M. Vergnolle, V. San'kov, A. Lukhnev, A. Miroshnitchenko, S. Amarjargal, and J. Déverchère (2003), GPS measurements of crustal deformation in the Baikal-Mongolia area (1994–2002): Implications for current kinematics of Asia, *Journal of Geophysical Research*, *108*, 2501–2513, doi:10.1029/2002JB002373. 1.1, 1.2, 1.2, 1.3, 2.5.4, 3.1, 3.16, 3.27, 4.1

Carlson, W. D., R. A. Donelick, and R. A. Ketcham (1999), Variability of apatite fission-track annealing kinetics: I. Experiemental results, *American Mineralogist*, *84*, 1213–1223. 5.2

Carver, G., G. Plafker, M. Metz, L. Cluff, B. Slemmons, E. Johnson, J. Roddick, and S. Sorensen (2004), Surface rupture on the Denali fault interpreted from tree damage during the 1912 Delta River $m_w$ 7.2–7.4 earthquake: implications for the 2002 Denali fault earthquake slip distribution, *Bulletin of the Seismological Society of America*, *94*, S58–S71. 2.3.5

Chen, W. P., and P. Molnar (1977), Seismic moments of major earthquakes and the average rate of slip in Central Asia, *Journal of Geophysical Research*, *82*, 2945–2969. 2.3.5

Chen, Z., J. Liu, H. Gong, F. Han, S. M. Briggs, E. Zheng, and G. Wang (2011), Late Cenozoic tectonic activity and its significance in the Northern Junggar Basin, Northwestern China, *Tectonophysics*, *497*, 45–56, doi:10.1016/j.tecto.2010.10.018. 5.1.1, 5.4

Cowie, P. A., and C. H. Scholz (1992a), Physical explanation for the displacement-length relationship of faults using a post-yield fracture mechanics model, *Journal of Structural Geology*, *14*, 1133–1148. 2.2.2

Cowie, P. A., and C. H. Scholz (1992b), Displacement-length scaling relationship for faults: data synthesis and discussion, *Journal of Structural Geology*, *14*, 1149–1156. 2.2.2

Cowie, P. A., and C. H. Scholz (1992c), Growth of faults by accumulation of seismic slip, *Journal of Geophysical Research*, *97*, 11,085–11,095, doi:10.1029/92JB00586. 2.2.2

Cunningham, D., S. Davis, and G. Badarch (2003a), Crustal architecture and active growth of the Sutai Range, western Mongolia: a major intracontinental, intraplate restraining bend, *Journal of Geodynamics*, *36*, 169–191, doi:10.1016/S0264-3707(03)00046-2. 1.5, 2.1, 2.2.1, 2.3.1

Cunningham, D., A. Dijkstra, J. Howard, A. Quarles, and G. Badarch (2003b), Active intraplate strike-slip faulting and transpressional uplift in the Mongolian Altai, in *Special Publications*, vol. 210, pp. 65–87, Geological Society, London. 1.3, 1.3, 1.4

Cunningham, W. D. (1998), Lithospheric controls on late Cenozoic construction of the Mongolian Altai, *Tectonics*, *17*, 891–902. 1.3, 1.4, 2.4.1, 5.1.1

Cunningham, W. D. (2005), Active intracontinental transpressional mountain building in the Mongolian Altai: Defining a new class of orogen, *Earth and Planetary Science Letters*, *240*, 436–444, doi:10.1016/j.epsl.2005.09.013. 1.5, 2.3.5, 2.5.1, 4.5.2, 5.1.1

Cunningham, W. D. (2007), Structural and topographic characteristics of restraining bend mountain ranges of the Altai, Gobi Altai and easternmost Tien Shan, in

*Geological Society, London, Special Publications*, vol. 290, pp. 219–237, The Geological Society of London, doi:10.1144/SP290.7. 1.3, 1.5, 2.1, 2.2.1, 2.3.2, 2.3.2, 2.3.3, 2.3.4, 2.5.5, 4.2

Cunningham, W. D. (2011), Cenozoic normal faulting and regional doming in the southern Hangay region, Central Mongolia: implications for the origin of the Baikal rift province, *Tectonophysics*, *331*, 389–411. 1.4, 1.5

Cunningham, W. D., B. F. Windley, D. Dorjnamjaa, G. Badamgarov, and M. Saandar (1996), A structural transect across the Mongolian Western Altai: Active transpressional mountain building in central Asia, *Tectonics*, *15*, 142–156. 1.3, 1.3, 4.2, 4.2

De Grave, J., and P. Van den haute (2002), Denudation and cooling of the Lake Teletskoye region in the Altai Mountains (South Siberia) as revealed by apatite fission-track thermochronology, *Tectonophysics*, *349*, 145–159. 1.4, 5.1, 5.2, 5.1.1, 5.4, 5.4, 5.13

De Grave, J., M. M. Buslove, and P. Van den haute (2007), Distant effects of India–Eurasia convergence and Mesozoic intracontinental deformation in Central Asia: Constraints from apatite fission-track thermochronology, *Journal of Asian Earth Sciences*, *29*, 188–204, doi:10.1016/j.jseaes.2006.03.001. 1.4, 5.1, 5.2, 5.1.1, 5.4

De Grave, J., P. Van den haute, M. M. Buslove, B. Dehandschutter, and S. Glorie (2008), Apatite fission-track thermochronology applied to the Chulyshman Plateau, Siberian Altai, Region, *Radiation Measurements*, *43*, 38–42, doi:10.1016/j.radmeas.2007.11.068. 1.4, 5.2, 5.13, 6.1

De Grave, J., M. M. Buslov, P. Van Den Haute, J. Metcalf, B. Dehandschutter, and M. O. McWilliams (2009), Multi-method chronometry of the Teletskoye graben and its basement, Siberian Altai Mountains: new insights on its therm-tectonic evolution, in *Geological Society, London, Special Publications*, vol. 324, pp. 237–259, Geological Society of London. 5.1, 5.4

DeLong, S. B., and L. J. Arnold (2007), Dating alluvial deposits with optically stiumlated luminescence, AMS $^{14}$C and cosmogenic techniques, western Traverse Ranges, California, USA, *Quaternary Geochronology*, *2*, 129–136, doi:10.1016/j.quageo.2006.03.012. 3.2

Delvaux, D., K. Theunissen, R. Van der Meer, and N. Berzin (1995), Dynamics and paleostress of the Cenozoic Kurai-Chuya depression of Gorny-Altai (South Siberia): tectonic and climate control, *Russian Geology and Geophysics*, *35*, 31–51. 2.3.3

Demarest, H. H. (1983), Error analysis for the determination of tectonic rotation from paleomagnetic data, *Journal of Geophysical Research*, *88*, 4321–4328. 4.4, 4.2

Densmore, A. L., M. A. Ellis, Y. Li, R. Zhou, G. S. Hancock, and N. Richardson (2007a), Active tectonics of the Beichuan and Pengguan faults at the eastern margin of the Tibetan Plateau, *Tectonics*, *26*, doi:10.1029/2006TC001987. 3.2

Densmore, A. L., S. Gupta, P. A. Allen, and N. H. Dawers (2007b), Transient landscapes at fault tips, *Journal of Geophysical Research*, *112*, doi:10.1029/2006JF000560. 6.3

Devyatkin, E. V., G. G. Martinson, V. F. Shuwalov, and P. Khosbayar (1975), Stratigraphy of Mesozoic deposits of Mongolia, *The Joint Soviet-Mongolian Scientific Research Geological Expedition, Leningrad, Nauka (in Russian)*, *13*, 25–49. 4.1, 4.2, 4.5.2

Donelick, R. A. (1993), A method of fission track analysis using bulk chemical etching of apatite, Patent 5267274, U.S.A. 5.2

Donelick, R. A., P. B. O'Sullivan, and R. A. Ketcham (2005), Apatite fission-track analysis, in *Reviews in Mineralogy and Geochemistry: Low-Temperature Thermochronology: Techniques, Interpretations, and Applications*, vol. 58, edited by P. W. Reiners and T. A. Ehlers, pp. 49–94, Mineralogical Society of America. 5.2, 5.2

Dorsey, R. J. (2006), Quaternary landscape evolution in the San Jacinto fault zone, Peninsular Ranges of Southern California: transient response to strike-slip fault initiation, *Geomorphology*, *73*, 16–32, doi:10.1016/j.geomorph.2005.06.013. 6.3

Dumitru, T. A., and M. S. Hendrix (2001), Fission-track constraints on Jurassic folding and thrusting in southern Mongolia and their relationship to the Beishan thrust belt of northern China, *Geological Society of America*, *194*, 215–229. 1.4, 5.1.1

Dunai, T. (2000), Scaling factors for production rates of in situ produced cosmogenic nuclides: a critical reevaluation, *Earth and Planetary Science Letters*, *176*, 157–169. 3.3.5

Dunai, T. J., and F. M. Stuart (2009), Reporting of cosmogenic nuclide data for exposure age and erosion rate determinations, *Quaternary Geochronology*, *4*, 437–440, doi:10.1016/j.quageo.2009.04.003. 3.3.5

Dundon, K., and E. Ganbold (2009), Glaciation of Rhyolite Valley, Höh Serh Range, Mongolian Altai, in *Proceedings of the twenty-second annual Keck Research Symposium in Geology*, edited by A. P. de Wet, 22nd ed., pp. 250–254, Keck Geology Consortium. 1.6

Engdahl, E. R., R. van der Hilst, and R. Buland (1998), Global teleseismic earthquake relocation with improved travel times and procedures for depth determination, *Bulletin of the Seismological Society of America*, *88*, 722–743. 1.2

England, P., and P. Molnar (1990), Surface uplift, uplift of rocks, and exhumation of rocks, *Geology*, *18*, 1173–1177. 5.1.1

Faure, G. (1986), *Principles of Stable Isotope Geology*, Wiley, New York. 3.2

Fisher, R. A. (1953), Dispersion on a sphere, *Proceedings of the Royal Society of London, Series A*, *217*, 295–305. 4.4

Fletcher, K. E. K., W. D. Sharp, K. J. Kendrick, W. M. Behr, K. W. Hudnut, and T. C. Hanks (), $^{230}$Th/U dating of a late Pleistocene alluvial fan along the southern San Andreas fault, *Geological Society of America Bulletin*, *122*, 1347–1359, doi:10.1130/B30018.1. 3.3.3

Fletcher, K. E. K., T. K. Rockwell, and W. D. Sharp (2011), Late Quaternary slip rate of the southern Elsinore fault, Southern California: dating offset alluvial fans via $^{230}$Th/U on pedogenic carbonate, *Journal of Geophysical Research*, *116*, doi:10.1029/2010JF001701. 3.2

Frankel, K. L., J. F. Dolan, R. C. Finkel, L. A. Owen, and J. S. Hoeft (2007), Spatial variations in slip rate along the Death Valley-Fish Lake Valley fault system determined from LiDAR topographic data and cosmogenic $^{10}$Be geochronology, *Geophysical Research Letters*, *34*, doi:10.1029/2007GL030549. 3.2

Frankel, K. L., K. W. Wegmann, A. Bayasgalan, R. J. Carson, N. E. Bader, T. Adiya, E. Bolor, C. C. Durfey, J. Otgonkhuu, J. Sprajcar, K. E. Sweeney, R. T. Walker, T. L. Marstellar, and L. C. Gregory (2010), Late Pleistocene slip rate of the Höh Serh-Tsagaan Salaa fault system, Mongolian Altai and intracontinental deformation in central Altai, *Geophysical Journal International*, *183*, 1134–1150, doi:10.1111/j.1365-246X.2010.04826.x. 1.3, 1.7, 2.3.3, 2.17, 2.3.3, 2.24, 2.25, 2.4.1, 2.5.1, 3.2, 3.3, 3.1, 3.3.2, 3.4, 3.4.2, 3.5.1, 6.1

Freeman, S. P. H. T., P. Bishop, C. Bryant, G. Cook, A. Fallick, D. Harkness, S. Metcalfe, M. Scott, R. Scott, and M. Summerfield (2004), A new environmental sciences AMS laboratory in Scotland, *Nuclear Instruments and Methods*, *B31*, 223–224, doi:10.1016/j.nimb.2004.04.010. 3.3.4

Galbraith, R. F. (1981), On statistical models for fission track counts, *Mathematical Geology*, *13*, 971–988. 5.2

Gan, W., P. Zhang, Z.-K. Shen, Z. Niu, M. Wang, Y. Wan, D. Zhou, and J. Cheng (2007), Present-day crustal motion within the Tibetan Plateau inferred from GPS measurements, *Journal of Geophysical Research*, *112*, doi:10.1029/2005JB004120. 1.1

Garland, R. (2010), Constraining quaternary fault slip-rates in Greece and Mongolia using remote sensing and uranium series dating of carbonate cements, Masters thesis, University of Oxford.

Gillespie, A. R., R. M. Burke, G. Komatsu, and A. Bayasgalan (2008), Late Pleistocene glaciers in Darhad Basin, northern Mongolia, *Quaternary Research*, *69*, 169–187, doi:10.1016/j.yqres.2008.01.001. 1.6, 1.6

Glorie, S., J. De Grave, M. M. Buslov, F. I. Zhimulev, M. A. Elburg, and P. Van den haute (2012a), Structural control on Meso-Cenozoic tectonic reactivation and denudation in the Siberian Altai: insights from multi-method thermochronometry, *Tectonophysics*, *544–545*, 75–92, doi:10.1016/j.tecto.2012.03.035. 1.4, 5.2, 5.1.1, 5.13, 6.1

Glorie, S., J. De Grave, D. Delvaux, M. M. Buslov, F. I. Zhimulev, F. Vanhaecke, and M. A. Elburg (2012b), Tectonic history of the Irtysh shear zone (NE Kazakhstan): new constraints from zircon U/Pb dating, apatite fission track dating and palaeostress analysis, *Journal of Asian Earth Sciences*, *45*, 138–149, doi:10.1016/j.jseaes.2011.09.024. 1.4, 5.2, 5.1.1, 5.13, 6.1

Gosse, J. C., and F. M. Phillips (2001), Terrestrial in situ cosmogenic nuclides: theory and application, *Quaternary Science Reviews*, *20*, 1475–1560. 3.2, 3.3.4, 3.3.5

Grunert, J., and F. Lehmkuhl (2004), Aeolian sedimentation in arid and semi-arid environments of Western Mongolia, in *Paleoecology of Quaternary Drylands*, vol. 102, edited by W. Smykatz-Kloss and P. Felix-Henningsen, pp. 195–218, Springer. 1.6

Grunert, J., F. Lehmkuhl, and M. Walther (2000), Paleoclimatic evolution of the Uvs Nuur basin and adjacent areas, *Quaternary International*, *65/66*, 171–192. 1.6, 1.6

Hallet, B., and J. Putkonen (1994), Surface dating of dynamic landforms: Young boulders on aging moraines, *Science*, *265*, 937–940. 3.3.5, 3.3.5

Hendrix, M. S., S. A. Graham, A. R. Carroll, E. R. Sobel, C. L. McKnight, B. J. Schulein, and Z. Wang (1992), Sedimentrary record and climatic implications of recurrent deformation in the Tian Shan: Evidence from Mesozoic strata of the north Tarim, south Junggar, and Turpan basins, northwest China, *GSA Bulletin*, *104*, 53–79. 1.6

Hetzel, R., I. Dunkl, V. Haider, M. Strobly, H. von Eynatten, L. Ding, and D. Frei (2011), Peneplain formation in southern Tibet predates the India-Asia collision and plateau uplift, *Geology*, *39*, 983–986, doi:10.1130/G32069.1. 1.5, 5.1.1

Howard, J. P., W. D. Cunningham, S. J. Davies, A. H. Dijkstra, and G. Badarch (2003), The stratigraphic and structural evolution of the Dzereg Basin, western Mongolia: clastic sedimentation, transpressional faulting and basing destruction in an intraplate, intercontinental setting, *Basin Research*, *15*, 45–72. 1.4, 2.3.1, 4.1, 4.2, 4.2, 4.3, 4.3.1, 4.5.2, 5.1.1, 5.4, 6.1

Howard, J. P., W. D. Cunningham, and S. J. Davies (2006), Competing processes of clastic deposition and compartmentalized inversion in an actively evolving transpressional basin, western Mongolia, *Journal of the Geological Society, London*, *163*, 657–670, doi:10.1144/0016-764904-073. 5.1.1, 5.4

Hubert-Ferrari, A., R. Armijo, G. King, B. Meyer, and A. Barka (2002), Morphology, displacement, and slip rates along the North Anatolian Fault, Turkey, *Journal of Geophysical Research*, *107*, doi:10.1029/2001JB000393. 2.2.3

Hurford, A. J. (1990), Standardization of fission track dating calibration: recommendation by the Fission Track Working Group of the I.U.G.S. Subcommission on Geochronology, *Chemical Geology*, *80*, 171–178. 5.2, 5.2, 5.2.1

Hurford, A. J., and A. Carter (1991), The role of fission track dating in discrimination of provenance, in *Developments in Sedimentary Provenance Studies, Geological Society Special Publication*, vol. 57, edited by A. C. Morton, S. P. Todd, and P. Haughton, pp. 67–78, Geological Society, London. 5.2.1

Jackson, J. (2001), Living with earthquakes: know your faults, in *Journal of Earthquake Engineering, Special Issue 1*, vol. 5, pp. 5–123, Imperial College Press. 1.1, 2.2.2

Jackson, J. (2002), Strength of the continental lithosphere: Time to abandon the jelly sandwich?, *GSA Today*, *12(9)*, 4–10, doi:10.1130/1052-5173(2002)012¡0004:SOTCLT¿2.0.CO;2. 1.1

Jackson, J. A. (1997), *Glossary of geology*, $4^{th}$ ed., 769 pp., Alexandria, Virginia, American Geological Institute. 1.5, 5.1.1

Jacoby, G. C., D. E. Bunker, and B. E. Benson (1997), Tree-ring evidence for an A.D. 1700 Cascadia earthquake in Washington and northern Oregon, *Geology*, *25*, 999–1002. 2.3.5

Jaffey, A. H., K. F. Flynn, L. E. Glendenin, W. C. Bentley, and A. M. Essling (1971), Precision measurement of half-lives and specific activities of $^{235}$u and $^{238}$u, *Physical Review*, *4*, 1889–1906. 5.2

Jibson, R. W., E. L. Harp, W. Schulz, and D. K. Keefer (2006), Large rock avalanches triggered by the M 7.5 Denali Fault, Alaska, earthquake of 3 November 2002, *Engineering Geology*, *83*, 144–160, doi:10.1016/j.enggeo.2005.06.029. 2.4.1

Jolivet, M., M. Brunel, D. Seward, Z. Xu, J. Yang, F. Roger, P. Tapponnier, J. Malavieille, N. Arnaud, and C. Wu (2001), Mesozoic and Cenozoic tectonics of the northern edge of the Tibetan plateau: fission-track constraints, *Tectonophysics*, *343*, 111–134. 1.4, 5.1.1

Jolivet, M., J. F. Ritz, R. Vassallo, C. Larroque, R. Braucher, M. Todbileg, A. Chauvet, C. Sue, N. Arnaud, R. De Vicente, A. Arzhanikova, and S. Arzhanikov (2007),

Mongolian summits: An uplifted, flat, old but still preserved erosion surface, *Geology*, *35*, 871–874, doi:10.1130/G23758A.1. 1.1, 1.4, 1.5, 2.5.1, 4.1, 5.1, 5.2, 5.1.1, 5.4, 5.4, 5.4, 5.4, 5.13, 6.1

Ketcham, R. A. (2005), Forward and inverse modeling of low-temperature thermochronometry data, in *Reviews in Mineralogy and Geochemistry: Low-Temperature Thermochronology: Techniques, Interpretations, and Applications*, vol. 58, edited by P. W. Reiners and T. A. Ehlers, pp. 275–314, Mineralogical Society of America, doi:10.2138/rmg.2005.58.11. 5.4

Ketcham, R. A., R. A. Donelick, and W. D. Carlson (1999), Variability of apatite fission-track annealing kinetics: Iii. extrapolation to geological time scales, *American Mineralogist*, *84*, 1235–1255. 5.2, 5.2

Ketcham, R. A., R. A. Donelick, and M. B. Donelick (2000), AFTSolve: A program for multi-kinetic modeling of apatite fission-track data, *Geological Materials Research*, *2*, 1–32. 5.4

Ketcham, R. A., A. Carter, R. A. Donelick, J. Barbarand, and A. J. Hurford (2007), Improved modeling of fission-track annealing in apatite, *American Mineralogist*, *92*, 799–810, doi:10.2138/am.2007.2281. 5.4, 5.9, 5.4

Khil'ko, S. D., R. A. Kurushin, V. M. Kochetkov, I. Balzhinnyam, and D. Monkoo (1985), Strong earthquakes, paleoseismogeological and macroseismic data, in *Earthquakes and the bases for seismic zoning of Mongolia, Transactions*, vol. 41, pp. 19–83, The Joint Soviet-Mongolian Scientific Geological Research Expedition: Moscow, Nauka. 2.1, 2.3.1, 2.3.2, 2.3.2, 2.3.4, 2.3.4, 2.6

Khosbayar, P. (1973), New data on Upper Jurassic and Lower Cretaceous sediments of western Mongolia, *Academy of Sciences, USSR, Doklady (Earth Sciences Section)*, *208*, 115–116. 4.1, 4.2

Kirby, E., N. Harkins, E. Wang, X. Shi, C. Fan, and D. Burbank (2007), Slip rate gradients along the eastern Kunlun fault, *Tectonics*, *26*, doi:10.1029/2006TC002033. 6.3

Klinger, Y., M. Etchebes, P. Tapponnier, and C. Narteau (2011), Characteristic slip for five great earthquakes along the Fuyun fault in China, *Nature Geoscience*, *4*, 389–392, doi:10.1038/NGEO1158. 1.2, 2.1, 2.2.1, 2.3.5, 2.3.5, 2.5.4, 2.6, 6.4

Kock, S., J. D. Kramers, F. Preusser, and A. Wetzel (2009), Dating of Late Pleistocene terrace deposits of the River Rhine using Uranium series and luminescence methods: potential and limitations, *Quaternary Geochronology*, *4*, 363–373, doi:10.1016/j.quageo.2009.04.002. 3.2, 3.3.3

Ku, T.-L., W. B. Bull, S. T. Freeman, and K. G. Knauss (1979), $Th^{230}$-$U^{234}$ dating of pedogenic carbonates in gravelly desert soils of Vidal Valley, southeastern California, *Geological Society of America Bulletin*, *11*, 1063–1073. 3.2, 3.3.3

Kurita, N., A. Numaguti, A. Sugimoto, K. Ichiyanagi, and N. Yoshida (2003), Relationship between the variation of isotopic ratios and the source of summer precipitation in eastern Siberia, *Journal of Geophysical Research*, *108*, doi:doi:10.1029/2001JD001359 (D11). 1.6

Kurushin, R. A., A. Bayasgalan, M. Ölziybat, B. Enhtuvshin, P. Molnar, C. Bayarsayhan, K. W. Hudnut, and J. Lin (1997), The surface rupture of the 1957 Gobi-Altay, Mongolia, earthquake, *Geological Society of America, Special Paper*, *320*. 1.2

Lacassin, R., A. Replumaz, and P. H. Leloup (1998), Hairpin river loops and slip-sense inversion on southest Asian strike-slip faults, *Geology*, *26*, 703–706, doi:10.1130/0091-7613(1998)026¡0703:HRLASS¿2.3.CO;2. 2.2.3

Lal, D. (1991), Cosmic ray labeling of erosion surfaces: in situ nuclide production rates and erosion models, *Earth and Planetary Science Letters*, *104*, 424–439. 3.2, 3.3.4, 3.3.5, 3.5, 3.4.2, 3.7

Laslett, G. M., W. S. Kendall, A. J. W. Gleadow, and I. R. Duddy (1982), Bias in measurement of fission-track length distributions, *Nuclear Tracks*, *6*, 79–85. 5.2

Laslett, G. M., A. J. W. Gleadow, and I. R. Duddy (1984), The relationship between fission track length and track density distributions, *Nuclear Tracks*, *9*, 29–38. 5.2

Laslett, G. M., P. F. Green, I. R. Duddy, and A. J. W. Gleadow (1987), Thermal annealing of fission tracks in apatite 2. a quantitative analysis, *Chemical Geology*, *65*, 1–13. 5.2, 5.4, 5.4

Lehmkuhl, F. (1998), Quaternary Glaciations in Central and Western Mongolia, in *Mountain Glaciations*, vol. 6, edited by L. A. Ower, pp. 153–167, Quaternary Proceedings. 3.5.3

Lehmkuhl, F., and F. Haselein (2000), Quaternary paleoenvironmental change on the Tibetan Plateau and adjacent areas (Western China and Western Mongolia), *Quaternary International*, *65/66*, 121–145. 1.6, 2.5.3

Lehmkuhl, F., and L. A. Owen (2005), Late Quaternary glaciation of Tibet and the bordering mountains: a review, *Boreas*, *34*, 87–100, doi:10.1080/03009480510012908. 2.5.3

Lehmkuhl, F., M. Klinge, and G. Stauch (2004), The extent of Late Pleistocene glaciations in the Altai and Khangai Mountains, in *Quaternary Glaciations - Extent and Chronologies. Part III: South America, Asia, Africa, Antarctica*, edited by J. Ehlers and P. I. Gibbard, pp. 243–254, Elsevier, Amsterdam. 1.6

Levashova, N. M., V. M. Kalugin, A. S. Gibsher, J. Yff, A. B. Ryabinin, J. G. Meert, and S. J. Malone (2010), The origin of the Baydaric microcontinent, Mongolia: constraints from paleomagnetism and geochronology, *Tectonophysics*, *485*, 306–320, doi:10.1016/j.tecto.2010.01.012. 1.4, 5.1.1

Lin, A., and S. Lin (1998), Tree damage and surface displacement, the 1931 M 8.0 Fuyun Earthquake, *The Journal of Geology*, *106*, 751–758. 2.3.5

Ludwig, K. R. (2003), Isoplot 3.00: A Geochronological Toolkit for Microsoft Excel, in *Geochronological Centre Special Publication*, vol. 4, Berkeley. 3.3.3

Matmon, A., D. P. Schwartz, R. Finkel, S. Clemmens, and T. Hanks (2005), Dating offset fans along the Mojave section of the San Andreas fault using cosmogenic $^{26}$Al and $^{10}$Be, *GSA Bulletin*, *117*, 795–807, doi:10.1130/B25590.1. 3.3.5

Matmon, A., K. Nichols, and R. Finkel (2006), Isotopic insights into smoothening of abandoned fan surfaces, Southern California, *Quaternary Research*, *66*, 109–118, doi:10.1016/j.yqres.2006.02.010. 3.3.5

McElhinny, M. W. (1964), Statistical significance of the fold test in palaeomagnetism, *Geophysical Journal of the Royal Astronomical Society*, *8*, 338–340. 4.5.1

McKenzie, D. (1972), Active tectonics of the Mediterranean region, *Geophysical Journal of the Royal Astronomical Society*, *30*, 109–185. 1.1

Meisling, K. E., and K. E. Sieh (1980), Disturbance of trees by the 1857 Fort Tejon earthquake, California, *Journal of Geophysical Research*, *85*, 3225–3238. 2.3.5

Merrill, R. T., M. W. McElhinny, and P. L. McFadden (1998), *The Magnetic Field of the Earth*, vol. 63, 531 pp., Academic Press. 4.3, 4.3.2, 4.4

Molnar, P., and Q. Deng (1984), Faulting associated with large earthquakes and the average rate of deformation in central and eastern Asia, *Journal of Geophysical Research*, *89*, 6203–6227. 2.3.5

Molnar, P., and P. Tapponnier (1975), Cenozoic tectonics of Asia: effects of a continental collision, *Science*, *189*, 419–426. 1.1, 2.5.5

Morinaga, Y., S.-F. Tian, and S. Masato (2003), Winter snow anomaly and atmospheric circulation in Mongolia, *International Journal of Climatology*, *23*, 1627–1636, doi:10.1002/joc.961. 1.6, 2.5.3, 2.5.5

Munkhuu, U. (2006), The 2003 Chuya sequence (North Altay range): tectonic context and seismological study, Phd thesis, University of Nice. 2.3.1, 2.3.1, 2.6

Nishiizumi, K. (2002), $^{10}$Be, $^{26}$Al, $^{36}$Cl, and $^{41}$Ca AMS standards, in *Conference on Accelerator Mass Spectrometry*, O16-1, p. 130. 3.3.4

Nishiizumi, K., E. Winterer, C. Kohl, J. Klein, R. Middleton, D. Lal, and J. Arnold (1989), Cosmic ray production rates of $^{26}$Al and $^{10}$Be in quartz from glacially polished rocks, *Journal of Geophysical Research*, *94*, 17,907–17,915. 3.3.4, 3.3.5

Nissen, E. (2008), Active mountain-building in Mongolia and Iran, Dphil thesis, University of Oxford. 3.5.1, 5.2

Nissen, E., B. Emmerson, G. Funning, A. Mistrukov, B. Parsons, D. P. Robinson, E. Rogozhin, and T. J. Wright (2007), Combining InSAR and seismology to study the 2003 Siberian Altai earthquakes—dextral strike-slip and anticlockwise rotations in the northern India–Eurasia collision zone, *Geophysical Journal International*, *169*, 216–232, doi:10.1111/j.1365-246X.2006.03286.x. 1.2, 2.1, 2.2.1, 2.3.3, 2.5.4, 2.6, 3.1, 3.16, 3.27, 4.1

Nissen, E., R. Walker, E. Molor, and M. Fattahi (2009a), Late Quaternary rates of uplift and shortening at Baatar Hyarhan (Mongolian Altai) with optically stimulated luminescence, *Geophysical Journal International*, *177*, 259–278, doi:10.1111/j.1365-246X.2008.04067.x. 1.3, 1.5, 2.3.1, 2.5.1, 3.2, 4.2

Nissen, E., R. T. Walker, A. Bayasgalan, A. Carter, M. Fattahi, E. Molor, C. Schnabel, A. J. West, and S. Xu (2009b), The late Quaternary slip-rate of the Har-Us-Nuur fault (Mongolian Altai) from cosmogenic $^{10}$Be dates and luminescence dating, *Earth and Planetary Science Letters*, *286*, 467–478, doi:10.1016/j.epsl.2009.06.048. 1.1, 1.3, 2.3.1, 2.3.1, 2.3.1, 2.3.5, 2.5.1, 2.6, 2.5.5, 2.5.5, 3.2, 3.3.5, 3.3.5, 3.4, 3.4.2, 3.5.1, 4.2, 5.1, 6.1

Owen, L. A., B. F. Windley, W. D. Cunningham, J. Badamgarav, and D. Dorjnamjaa (1997), Quaternary alluvial fans in the Gobi of southern Mongolia: evidence for neotectonics and climate change, *Journal of Quaternary Science*, *12*, 239–252. 1.6

Pallàs, R., A. Rodés, R. Braucher, D. Bourlès, M. Delmas, M. Calvet, and Y. Gunnell (2010), Small, isolated glacial catchments as priority targets for cosmogenic surface exposure dating of Pleistocene climate fluctuations, southeastern Pyrenees, *Geology*, *38*, 891–894, doi:10.1130/G31164.1. 3.3.5

Price, P. B., and R. M. Walker (1962), Chemical etching of charged-particle tracks in solids, *Journal of Applied Physics*, *33*, 3407–3412. 5.2

Price, P. B., and R. M. Walker (1963), Fossil tracks of charged particles in mica and the age of minerals, *Journal of Geophysical Research*, *68*, 4847–4862. 5.2

Putnam, A. E., J. M. Schaefer, D. J. A. Barrell, M. Vandergoes, G. H. Denton, M. R. Kaplan, R. C. Finkel, R. Schwartz, B. M. Goehring, and S. E. Kelley (2010), In situ cosmogenic $^{10}$Be production-rate calibration from the Southern Alps, New Zealand, *Quaternary Geochronology*, *5*, 392–409, doi:10.1016/j.quageo.2009.12.001. 3.2

Richards, B. W. M. (2000), Luminescence dating of Quaternary sediments in the Himalaya and High Asia: a practical guide to its use and limitations for constraining the timing of glaciation, *Quaternary International*, *65/66*, 49–61, doi:10.1016/S1040-6182(99)00036-1. 3.2

Richter, C. F. (1958), *Elementary Seismology*, 768 pp., San Francisco, W.H. Freeman. 1.2, 2.3.5, 2.3.5

Ritz, J. F., E. T. Brown, D. L. Bourlès, H. Philip, A. Schlupp, G. M. Raisbeck, F. Yiou, and B. Enkhtuvshin (1995), Slip rates along active faults estimated with cosmic-ray exposure dates: application for the Bogd fault, Gobi-Altai, Mongolia, *Geology*, *23*, 1019–1022. 3.2

Ritz, J.-F., D. Bourlès, E. T. Brown, S. Carretier, S. Chéry, B. Enhtuvshin, P. Galsan, R. C. Finkle, T. C. Hanks, K. J. Kendrick, H. Philip, G. Raisbeck, A. Schlupp, D. P. Schwartz, and F. Yiou (2003), Late Pleistocene to Holocene slip rates for the Gurvan Bulag thrust fault (Gobi-Altay, Mongolia) estimated to $^{10}$Be dates, *Journal of Geophysical Research*, *108*, doi:10.1029/2001JB000553. 1.5

Schlupp, A., and A. Cisternas (2007), Source history of the 1905 great Mongolian earthquakes (Tsetserleg, Bolnay), *Geophysical Journal International*, *169*, 1115–1131, doi:10.1111/j.1365-246X.2007.03323.x. 1.2

Scholz, C. H. (1982), Scaling laws for large earthquakes: consequences for physical models, *Bulletin of the Seismological Society of America*, *72*, 1–14. 2.2.2

Scholz, C. H. (2002), *The Mechanics and Earthquakes and Faulting*, $2^{nd}$ ed., Cambridge University Press. 2.2.1, 2.2.2, 6.3

Scholz, C. H., R. Ando, and B. E. Shaw (2010), The mechanics of first order splay faulting: The strike-slip case, *Journal of Structural Geology*, *32*, 118–126, doi:10.1016/j.jsg.2009.10.007. 2.5.5

Schwartz, D. P., P. J. Haeussler, G. G. Seitz, and T. E. Dawson (2012), Why the 2002 Denali fault rupture propagated onto the Totschunda fault: Implications for fault branching and seismic hazards, *Journal of Geophysical Research*, *117*, doi:10.1029/2011JB008918. 2.2.1, 2.5.3

Sengör, A. F. C., and B. A. Natal'In (1996), Paleotectonics of Asia: fragments of a synthesis, in *The tectonic evolution of Asia*, edited by A. Yin and T. M. Harrison, pp. 486–640, Cambridge University Press, New York. 1.4, 5.1.1

Sengör, A. M. C., B. A. Natal'In, and V. S. Burtman (1993), Evolution of the Altaid tectonic collage and Palaeozoic crustal growth in Eurasia, *Nature*, *364*, 299–307. 1.4, 5.1.1

Sharp, W. D., K. R. Ludwig, O. A. Chadwick, R. Amundson, and L. L. Glaser (2003), Dating fluvial terraces by $^{230}$Th/U on pedogenic carbonate, Wind River Basin, Wyoming, *Quaternary Research*, *59*, 139–150, doi:10.1016/S0033-5894(03)00003-6. 3.2, 3.3.3

Shi, J.-b., X.-y. Feng, S.-m. Ge, Z. Yang, M.-x. Bo, and J. Hu (1984), The Fuyun earthquake fault zone in Xinjiang, China, in *Continental seismicity and earthquake prediction*, pp. 325–346, Seismology Press, Beijing. 2.3.5

Shuvalov, V. F. (1968), More information about Upper Jurassic and Lower Cretaceous in the southeast Mongolian Altai, *Academy of Sciences, USSR, Doklady (Earth Sciences Section)*, *197*, 31–33. 4.1, 4.2

Shuvalov, V. F. (1969), Continental redbeds of the Upper Jurassic of Mongolia, *Academy of Sciences, USSR, Doklady (Earth Sciences Section)*, *189*, 112–114. 4.1, 4.2

Siame, L., O. Bellier, R. Braucher, M. Sébrier, M. Cushing, D. Bourlès, B. Hamelin, E. Baroux, B. de Voogd, G. Raisbeck, and F. Yiou (2004), Local erosion rates versus active tectonics: cosmic ray exposure modelling in Provence (south-east France), *Earth and Planetary Science Letters*, *220*, 345–364, doi:10.1016/S0012-821X(04)00061-5. 3.3.4, 3.3.4, 3.4.2

Sjostrom, D. J., M. S. Hendrix, D. Badamgarav, S. A. Graham, and B. K. Nelson (2001), Sedimentology and provenance of Mesozoic nonmarine strata in western Mongolia: a record of intracontinental deformation, in *Palaeozoic and Mesozoic tectonic evolution of Central and Eastern Asia: from continental assembly to intracontinental deformation*, vol. 194, edited by M. S. Hendrix and G. A. Davis, pp. 361–388, Geological Society of America Memoir. 1.4, 4.1, 4.2, 4.2, 4.1, 4.3.1, 4.5.2

Sloan, R. A., J. A. Jackson, D. McKenzie, and K. Priestley (2011), Earthquake depth distributions in central Asia, and their relations with lithosphere thickenss, shortening and extension, *Geophysical Journal International*, *185*, 1–29, doi:10.1111/j.1365-246X.2010.04882.x. 1.2, 2.2.1, 3.1, 3.16, 3.27, 4.1

Sobel, E. R., and T. A. Dumitru (1997), Thrusting and exhumation around the margins of the western Tarim basin during the India-Asia collision, *Journal of Geophysical Research*, *102*, 5043–5063. 5.1.1

Staiger, J., J. Gosse, R. Toracinta, B. Oglesby, J. Fastook, and J. Johnson (2007), Atmospheric scaling of cosmogenic nuclide production: climate effect, *Journal of Geophysical Research*, *112*, doi:10.1029/2005JB003811. 3.3.5

Stein, S., R. J. Geller, and M. Liu (2012), Why earthquake hazard maps often fail and what to do about it, *Tectonophysics*, *562–563*, 1–25, doi:10.1016/j.tecto.2012.06.047. 1.7, 6.4

Stone, J. O. (2000), Air pressure and cosmogenic isotope production, *Journal of Geophysical Research*, *105 (B10)*, doi:10.1029/2000JB900181. 3.2, 3.3.5, 3.5, 3.4.2, 3.7

Strobl, M., R. Hetzel, S. Niedermann, L. Ding, and L. Zhang (2012), Landscape evolution of a bedrock peneplain on the southern Tibetan Plateau revealed by in situ-produced cosmogenic $^{10}$Be and $^{21}$Ne, *Geomorphology*, *153–154*, 192–204, doi:10.1016/j.geomorph.2012.02.024. 5.1.1

Tagami, T., and P. B. O'Sullivan (2005), Fundamentals of fission-track thermochronology, in *Reviews in Mineralogy and Geochemistry: Low-Temperature Thermochronology: Techniques, Interpretations, and Applications*, vol. 58, edited by P. W. Reiners and T. A. Ehlers, pp. 19–47, Mineralogical Society of America. 5.2, 5.3, 5.2

Tapponnier, P., and P. Molnar (1979), Faulting and Cenozoic tectonics of the Tien Shan, Mongolia, and Baykal regions, *Journal of Geophysical Research*, *84*, 3425–3459. 1.4, 5.1, 5.1.1

Tarasov, P., N. Dorofeyuk, and E. Metel'tseva (2000), Holocene vegetation and climate changes in Hoton-Nur basin, northwest Mongolia, *Boreas*, *29*, 117–126. 1.6, 2.5.3

Tarasov, P. E., O. Peyron, J. Guiot, S. Brewer, V. S. Volkova, L. G. Bezusko, N. I. Dorogeyuk, E. V. Kvavadze, I. M. Osipova, and N. K. Panova (1999), Last Glacial Maximum climate of the former Soviet Union and Mongolia reconstructed from pollen and plant macrofossil data, *Climate Dynamics*, *15*, 227–240. 1.6

Tauxe, L. (2010), *Essentials of Paleomagnetism*, 489 pp., University of California Press. 4.3, 4.4.1

Tauxe, L., and D. V. Kent (2004), A simplified statistical model for the geomagnetic field and the detection of shallow bias in paleomagnetic inclinations: was the ancient magnetic field dipolar?, in *Timescales of the Paleomagnetic field*, edited by J. E. T. Channell, D. V. Kent, W. Lowrie, and J. G. Meert, pp. 101–115, American Geophysical Union, Washington, DC, doi:10.1029/145GM08. 4.4

Thatcher, W. (1995), Microplate versus continuum descriptions of active tectonics deformation, *Journal of Geophysical Research*, *100*, 3885–3894. 6.4

Thomas, J. C., R. Lanza, A. Kazansky, V. Zykin, N. Semakov, D. Mitrokhin, and D. Delvaux (2002), Paleomagnetic study of Cenozoic sediments from the Zaisan basin (SE Kazakhstan) and the Chuya depression (Siberian Altai): tectonic implications for central Asia, *Tectonophysics*, *351*, 119–137. 1.3, 2.3, 4.1, 4.1, 4.5.2, 6.1, 6.2

Torsvik, T. H., R. Van der Voo, U. Preeden, C. Mac Niocaill, B. Steinberger, P. V. Doubrovine, D. J. J. van Hinsbergen, M. Domeir, C. Gaina, E. Tohver, J. G. Meert, P. J. A. McCausland, and L. R. M. Cocks (2012), Phanerozoic polar wander, palaeogeography and dynamics, *Earth Science Reviews*, *114*, 325–368, doi:10.1016/j.earscirev.2012.06.007. 4.4, 4.2, 4.5.2

Traynor, J. J., and C. Sladen (1995), Tectonic and stratigraphic evolution of the Mongolian People's Republic and its influence on hydrocarbon geology and potential, *Marine and Petroleum Geology*, *12*, 35–52. 1.4, 5.1.1

van Calsteren, P., and L. Thomas (2006), Uranium-series dating applications in natural environmental science, *Earth-Science Reviews*, *75*, 155–175, doi:10.1016/j.earscirev.2005.09.001. 3.3.3, 3.3.3

Van der Voo, R. (1990), The reliability of paleomagnetic data, in *Reliability of Paleomagnetic Data, Tectonophysics*, vol. 184, edited by R. Van der Voo and P. W. Schmidt, pp. 1–9, Elsevier Science Publishers, Amsterdam. 4.3

van der Woerd, J., F. J. Ryerson, P. Tapponnier, Y. Gaudemer, R. Finkel, A. S. Meriaux, M. Caffee, G. Zhao, and H. Qunlu (1998), Holocene left-slip rate determined by cosmogenic surface dating on the Xidatan segment of the Kunlun fault (Qinghai, China), *Geology*, *26*, 695–698. 3.3.5

Vassallo, R. (2006), Chronologie et évolution des reliefs dans la région Mongolie-Sibérie: approach morphotectonique et géochronologique, Ph.D. thesis, L'Universite Montpellier II. 1.4, 2.3.1, 2.10, 2.3.2, 2.5.1, 3.16, 3.4, 3.4.2, 3.4.3, 3.5.1, 5.2, 5.1.1, 5.13, 6.1

Vassallo, R., J.-F. Ritz, R. Braucher, and S. Carretier (2005), Dating faulted alluvial fans with cosmogenic $^{10}$Be in the Gurvan Bogd mountain range (Gobi-Altay, Mongolia): climatic and tectonic implications, *Terra Nova*, *17*, 278–285, doi:10.1111/j.1365-3121.2005.00612.x. 2.5.1

Vassallo, R., M. Jolivet, J. F. Ritz, R. Braucher, C. Larroque, C. Sue, M. Todbileg, and D. Javkhlanbold (2007a), Uplift age and rates of the Gurvan Bogd system (Gobi Altay) by apatite fission track analysis, *Earth and Planetary Science Letters*, *259*, 333–346, doi:10.1016/j.epsl.2007.04.047. 1.4, 5.1, 5.2, 5.1.1, 5.4, 5.4, 5.13

Vassallo, R., J. F. Ritz, R. Braucher, M. Jolivet, A. Chauvet, C. Larroque, S. Carretier, D. Bourlès, C. Sue, M. Todbileg, N. Arzhannikova, and S. Arzhannikov (2007b), Transpressional tectonics and stream terraces of the Gobi-Altay, Mongolia, *Tectonics*, *26*, doi:10.1029/2006TC002081. 3.3.5

Vassallo, R., J.-F. Ritz, and S. Carretier (2011), Control of geomorphic processes on $^{10}$Be concentrations in individual clasts: complexity of the exposure history in Gobi-Altay range (Mongolia), *Geomorphology*, *135*, 35–47, doi:doi:10.1016/j.geomorph.2011.07.023. 3.3.5, 3.3.5, 3.15, 3.3.5, 3.4, 3.4.2, 3.5.1

Walker, R., and J. Jackson (2004), Active tectonics and late Cenozoic strain distribution in central and eastern Iran, *Tectonics*, *23*, doi:10.1029/2003TC001529. 4.5.2, 6.2, 6.4

Walker, R. T., A. Bayasgalan, R. Carson, R. Hazlett, L. McCarthy, J. Mishler, E. Molor, P. Sarantsetseg, L. Smith, B. Tsogtbadrakh, and G. Tsolmon (2006), Geomorphology and structure of the Jid right-lateral strike-slip fault in the Mongolian Altay mountains, *Journal of Structural Geology*, *28*, 1607–1622, doi:10.1016/j.jsg.2006.04.007. 1.1, 1.3, 2.1, 2.2.1, 2.3.1, 2.3.1, 2.7, 2.3.1, 2.3.1, 2.4.1, 2.4.2, 2.4.2, 2.5.3, 2.6, 6.4

Wang, Q., P.-Z. Zhang, J. T. Freymuller, R. Bilham, K. M. Larson, X. Lai, X. You, Z. Niu, J. Wu, Y. Li, J. Liu, Z. Yang, and Q. Chen (2001), Present-day crustal deformation in China constrained by Global Positioning System measurements, *Science*, *294*, 574–576, doi:10.1126/science.1063647. 1.1

Wells, A., M. D. Yetton, R. P. Duncan, and G. H. Stewart (1999), Prehistoric dates of the most recent Alpine fault earthquakes, New Zealand, *Geology*, *27*, 995–998, doi:10.1130/0091-7613(1999)027¡0995:PDOTMR¿2.3.CO;2. 2.3.5

Wells, D. L., and K. J. Coppersmith (1994), New empirical relationships among magnitude, rupture length, rupture width, rupture area, and surface displacement, *Bulletin of the Seismological Society of America*, *84*, 974–1002. 2.2.2, 2.3.2, 2.3.2, 2.3.4, 2.3.5, 2.4.1, 2.4.2

Wilson, P., M. J. Bentley, C. Schnabel, R. Clark, and S. Xu (2008), Stone run (block stream) formation in the Falkland Islands over several cold stages, deduced from cosmogenic isoptope ($^{10}$Be and $^{26}$Al) surface exposure dating, *Journal of Quaternary Science*, *23(5)*, 461–473, doi:10.1002/jqs.1156. 3.3.4

Windley, B. F., D. Alexeiev, W. J. Xiao, A. Kroner, and G. Badarch (2007), Tectonic models for accretion of the Central Asian Orogenic Belt, *The Geological Society of London*, *164*, 31–47, doi:10.1144/0016-76492006-022. 1.4, 5.1.1

Wintle, A. G., and D. J. Huntley (1982), Thermoluminscence dating of sediments, *Quaternary Science Reviews*, *1*, 31–53. 3.2

Yin, A., and S. Nie (1996), A Phanerozoic palinspastic reconstruction of China and its neighboring regions, in *The tectonic evolution of China*, edited by A. Yin and T. M. Harrison, pp. 442–485, Cambridge University Press, Cambridge. 1.4, 5.1.1

Yin, A., S. Nie, P. Craig, T. M. Harrison, F. J. Ryerson, Q. Xianglin, and Y. Geng (1998), Late Cenozoic tectonic evolution of the southern Chinese Tian Shan, *Tectonics*, *17*, 1–27. 5.1.1, 5.4

Yuan, W., A. Carter, J. Dong, Z. Bao, Y. An, and Z. Guo (2006), Mesozoic–Tertiary exhumation history of the Altai Mountains, northern Xinjiang, Chia: new constraints from apatite fission track data, *Tectonophysics*, *412*, 183–193, doi:10.1016/j.tecto.2005.09.007. 1.4, 5.1, 5.2, 5.1.1, 5.4, 5.4, 5.13, 6.1

Zhang, P.-Z., Z. Shen, M. Wang, W. Gan, R. Bürgmann, P. Molnar, Q. Wang, Z. Niu, J. Sun, J. Wu, S. Hanrong, and Y. Xinzhao (2004), Continuous deformation of the Tibetan Plateau from global positioning system data, *Geology*, *32*, 809–812, doi:10.1130/G20554.1. 1.1

Zijderveld, J. D. A. (1967), Ac demagnetization of rocks: analysis of results, in *Methods in Palaeomagentism*, edited by D. W. Collinson, K. M. Creer, and S. K. Runcorn, pp. 245–286, Elsevier, Amsterdam. 4.3.1

Zorin, Y. A., M. R. Novoselova, E. K. Turutanov, and V. M. Kozhevnikov (1990), Structure of the lithosphere of the Mongolian-Siberian mountainous province, *Journal of Geodynamics*, *11*, 327–342. 6.2

Zreda, M. G., and F. M. Phillips (2000), Cosmogenic nuclide buildup in surficial materials, in *Quaternary Geochronology: Methods and Applications*, edited by J. S. Noller, J. M. Sowers, and W. R. Lettis, pp. 61–76, American Geophysical Union, Washington, D.C. 3.3.5

# Appendix A

# Appendix 1

**Table A.1:** Profile height measurements

| Profile number | vertical height at (D) (m) | D: distance down slope (m) | vertical offset (x, m) |
|---|---|---|---|
| **F1 deposit** | | | |
| F1-1U | 2257.58 | 80 | |
| F1-1L | 2263.56 | 80 | 5.98 |
| F1-2U | 2256.34 | 80 | |
| F1-2L | 2262.21 | 80 | 5.87 |
| F1-3U | 2257.93 | 80 | |
| F1-3L | 2265.74 | 80 | 7.81 |
| F1-4U | 2257.94 | 80 | |
| F1-4L | 2263.82 | 80 | 5.88 |
| F1-5U | 2255.79 | 80 | |
| F1-5L | 2258.73 | 80 | 2.94 |
| *Average* | | | 5.70 |
| **F2 deposit** | | | |
| F2-1U | 2251.73 | 60 | |
| F2-1L | 2253.97 | 60 | 2.24 |
| F2-2U | 2252.01 | 60 | |
| F2-2L | 2254.87 | 60 | 2.86 |
| F2-3U | 2250.99 | 65 | |
| F2-3L | 2253.26 | 65 | 2.27 |
| F2-4U | 2251.14 | 60 | |
| F2-4L | 2253.60 | 60 | 2.46 |
| F2-5U | 2250.34 | 70 | |
| F2-5L | 2253.61 | 70 | 3.27 |
| *Average* | | | 2.62 |

**Table A.2:** $^{10}$Be blanks table

| Sample ID | $^{10}$Be/$^{9}$Be ratio of blank ($10^{-5}$) | Sample composition |
|---|---|---|
| B08-1 | 6.3 | vein quartz |
| B08-2 | 6.3 | vein quartz |
| B08-4 | 4.3 | meta-sedimentary |
| B08-5 | 4.3 | meta-sedimentary |
| B08-6 | 4.3 | meta-sedimentary |
| B08-7 | 4.3 | meta-sedimentary |
| B08-9 | 4.3 | meta-sedimentary |
| B08-10 | 4.3 | meta-sedimentary |
| B08-11 | | |
| MN09-OG01 | 4.898 | meta-sedimentary |
| MN09-OG03 | 4.898 | meta-sedimentary |
| MN09-OG04 | 4.898 | meta-sedimentary |

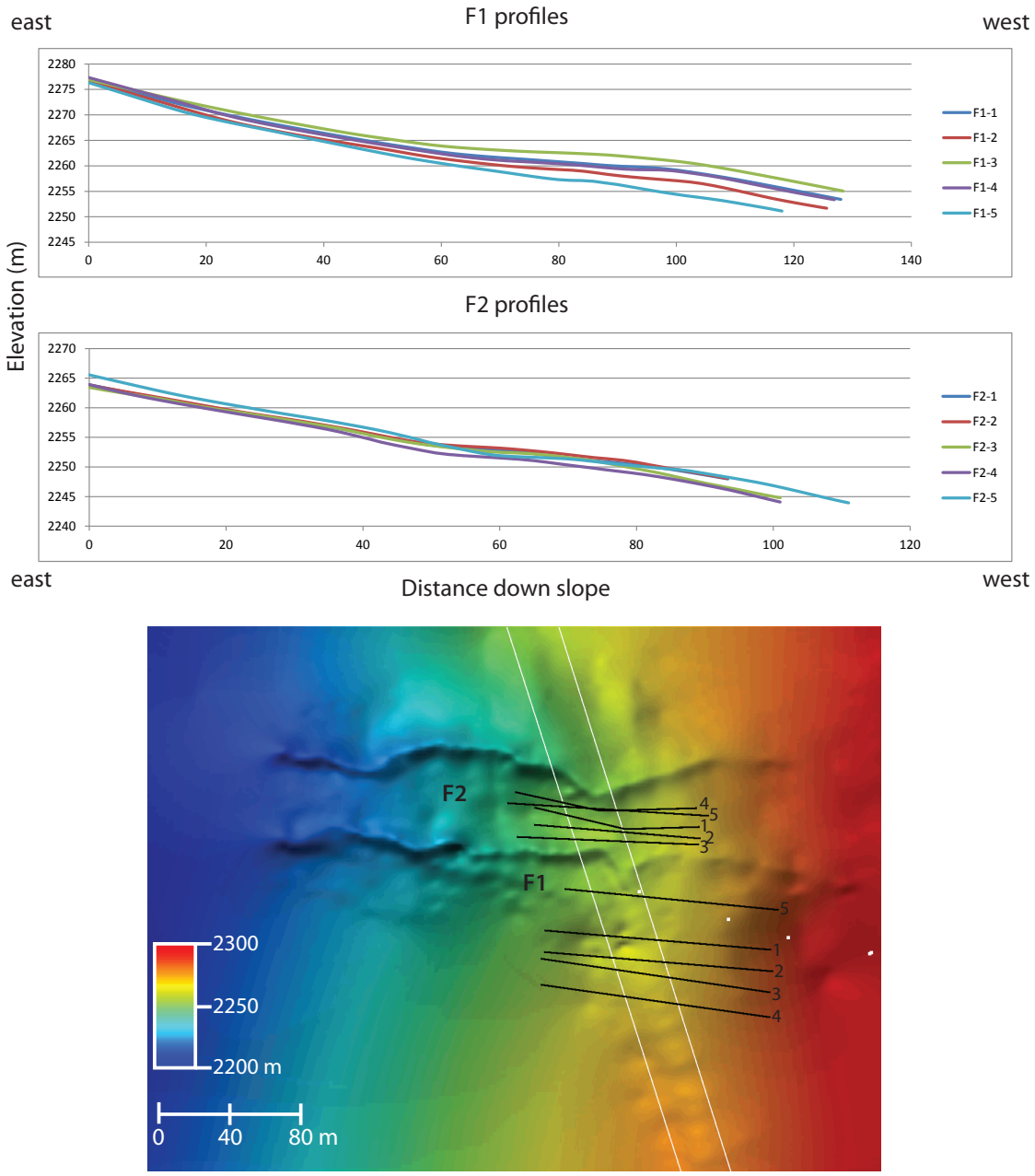


**Figure A.1:** Elevation profiles measured from east to west (down slope) on debris flows F1 and F2. The right-lateral motion of the fault displaced the gradient of the slope to place high elevated material on the west side against lower elevated material on the east side of the fault. The vertical displacement is greater on F1 because it is older than F2, and has accumulated more displacement. DEM shows the location of each profile number (in black) as well as the two N-S profiles shown in figure 3.4

.

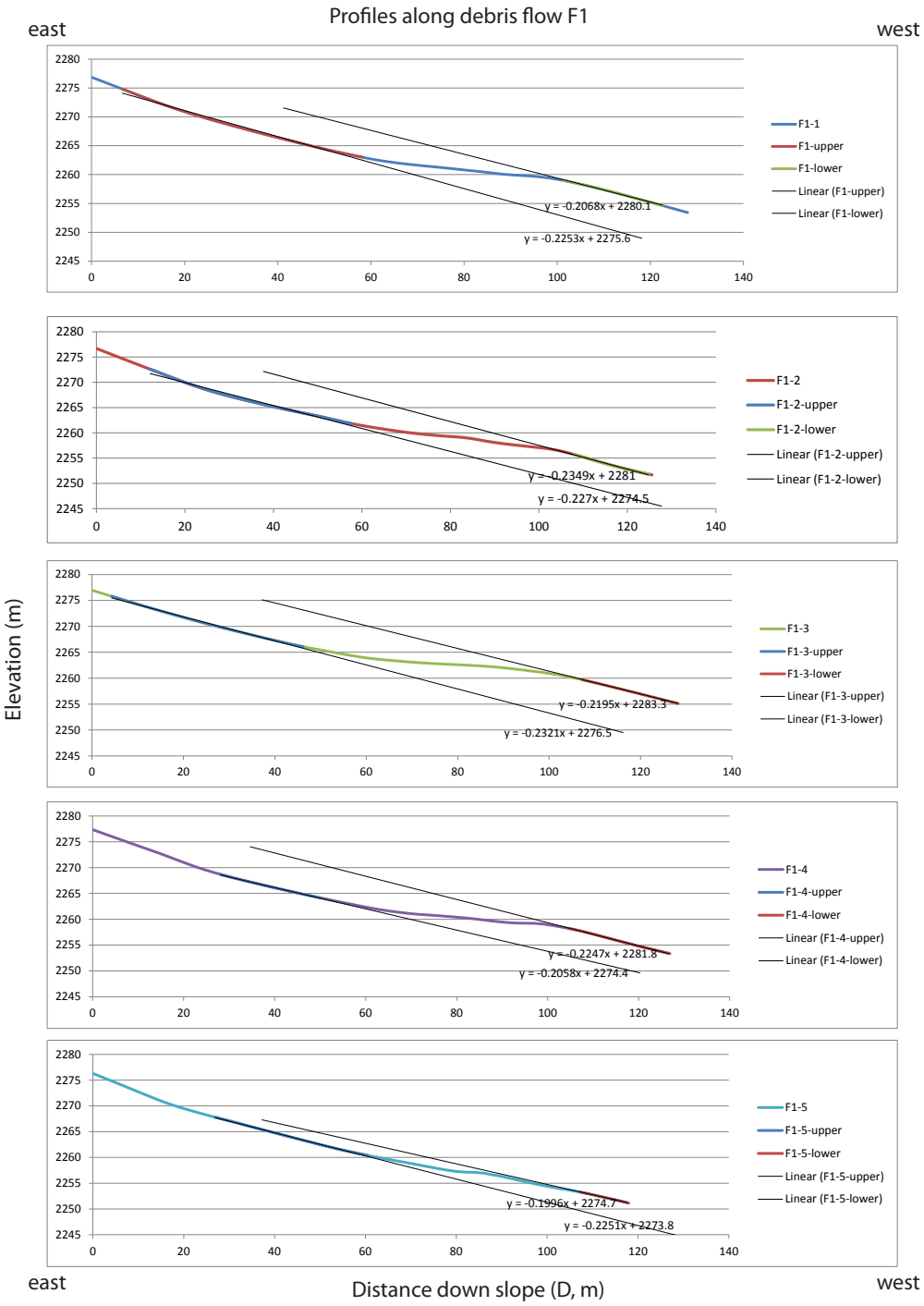


**Figure A.2:** Vertical profiles from east to west along debris flow F1. The offset of lines fitted to the slope on the upper and lower part of the flow (above and below the fault) is calculated using the equations listed on the figure. The average height offset for all profiles was used to calculate fault displacement. Profile locations are numbered in figure A.1.

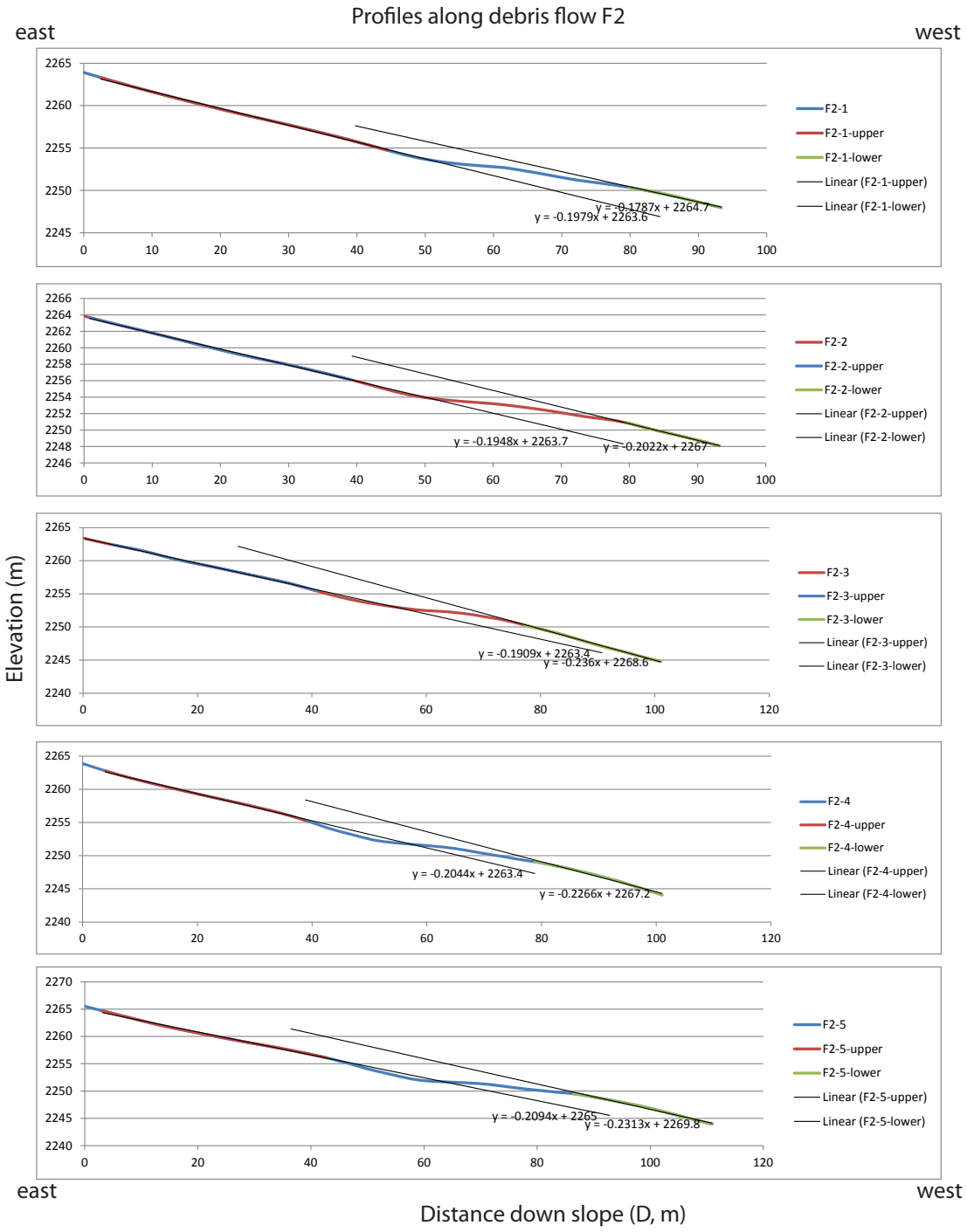


**Figure A.3:** Vertical profiles from east to west along debris flow F2. The offset of lines fitted to the slope on the upper and lower part of the flow (above and below the fault) is calculated using the equations listed on the figure. The average height offset for all profiles was used to calculate fault displacement. Profile locations are numbered in figure A.1.

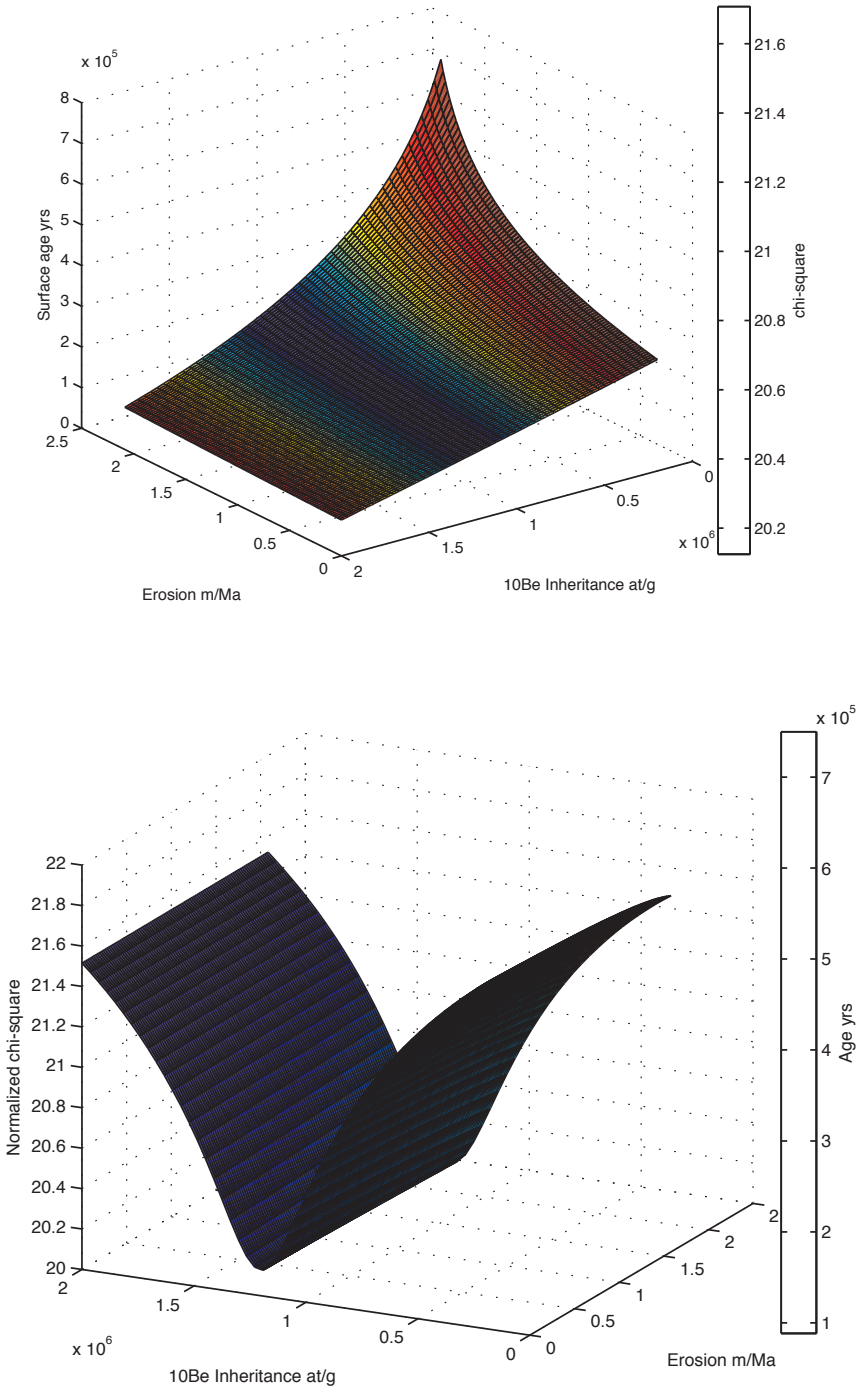


**Figure A.4:** These figures show the trade-offs between exposure age, level of inheritence, erosion rate, and $\chi^2$ values predicted by the inversion. The parameter solutions define pathways through the model space, and a higher value for $\chi^2$ implies a better fit to the data. The erosion rate is very poorly constrained in the inversion.